

Nuclear Materials & Propulsion Operation

**SEVENTH ANNUAL REPORT -
AEC FUELS AND MATERIALS DEVELOPMENT PROGRAM**

March 31, 1968

AMPTIAC

20000710 189

**NUCLEAR TECHNOLOGY DEPARTMENT
NUCLEAR ENERGY DIVISION**

GENERAL  ELECTRIC

100% QUALITY ASSURED

DISTRIBUTION STATEMENT A
Approved for Public Release
Distribution Unlimited

**Reproduced From
Best Available Copy**

LEGAL NOTICE

United States Atomic Energy Commission Contract No. AT (40-1)-2847

This report was prepared as an account of Government sponsored work. Neither the United States, nor the Commission, nor any person acting on behalf of the Commission:

A. Makes any warranty or representation, expressed or implied, with respect to the accuracy, completeness, or usefulness of the information contained in this report, or that the use of any information, apparatus, material, method, or process disclosed in this report may not infringe privately owned rights; or

B. Assumes any liabilities with respect to the use of, or for damages resulting from the use of any information, apparatus, material, method, or process disclosed in this report.

As used in the above, "person acting on behalf of the Commission" includes any employee or contractor of the Commission, or employee of such contractor, to the extent that such employee or contractor of the Commission, or employee of such contractor prepares, disseminates, or provides access to, any information pursuant to his employment or contract with the Commission or his employment with such contractor.

Printed in the United States of America

Available from

Clearinghouse for Federal Scientific and Technical Information

National Bureau of Standards, U.S. Department of Commerce

Springfield, Virginia 22151

Price: Printed Copy \$3.00; Microfiche \$0.65

DISTRIBUTION

US Atomic Energy Commission

Washington Headquarters

G. W. Cunningham	M. A. Rosen
G. K. Dicker	F. C. Schwenk
D. E. Erb	W. F. Sheely
J. S. Griffo	J. M. Simmons (2)
H. G. Hembree	R. H. Steele (NR)
J. R. Hunter	S. A. Szawlewicz
C. E. Johnson	A. Van Echo
E. E. Kintner	J. W. Vaughn (NR)
J. A. Lieberman	E. S. Wilson
J. S. Powers	Librarian, Germantown

Chicago Operations Office

M. E. Jackson, Senior Site Rep., ANL

FFTF Project Office, PNL

E. R. Astley

Idaho Operations Office

D. A. Moss
K. A. Trickett, Senior Site Rep., PNL

LMFBR Program Office, ANL

A. Amorosi
J. R. Humphreys
L. K. Kelman

Oak Ridge Operations Office

(Laboratory & Univ Div) (1)

D. F. Cope, Senior Site Rep., ORNL

C. L. Karl, CAO

J. F. Weissenberg, GE-NMPO Site Rep.

Richland Operations Office

P. G. Holsted, Senior Site Rep., PNL

J. H. Sako

San Francisco Operations Office

R. H. Ball, Senior Site Rep., GA,

San Diego, California

A. W. Larson, Senior Site Rep., GE,

Sunnyvale, California

R. L. Morgan, Senior Site Rep.,

Canoga Park, California

DTIE (20)

Air Force Materials Laboratory

H. M. Burte

G. Glenn

Technical Director

Air Force Weapons Laboratory

Lt. D. Brooks

Ames Laboratory

O. N. Carlson

W. L. Larsen

F. H. Spedding

Argonne National Laboratory

L. Baker

J. H. Kittel

M. V. Nevitt

P. Shewman

R. C. Vogel

Army Materials & Mechanics Research Center

S. V. Arnold, Asst for Technology

Atomics International

S. C. Carniglia

H. Pearlman

Babcock and Wilcox Company

C. Baroch

C. Johnson

J. Landis

L. Weissert

Battelle Memorial Institute, Columbus, Ohio

W. Berry

D. Keller

S. Paprocki

DMIC

Brookhaven National Laboratory

D. H. Gurinsky

Bureau of Mines, Albany, Oregon

H. Kato

Combustion Engineering

W. P. Chernock

S. S. Christopher

E. I. duPont de Nemours and Co., SRL

P. H. Permar

S. Rideout

General Atomic, Div of General Dynamics

S. Jaye

T. Watson

General Electric Company

APO -- Sunnyvale, California

K. P. Cohen

F. Compelli

R. Skavdahl

C. Spalaris

E. L. Zebroski

KAPL

A. E. Bibb

Library

Idaho Nuclear Corporation

W. C. Francis

Jet Propulsion Laboratory

J. Davis

Lawrence Radiation Laboratory

J. S. Kane

L. W. Roberts

A. J. Rothman

B. Rubin

Los Alamos Scientific Laboratory

R. D. Baker

D. E. Hall

J. A. Leary

R. Perkins

Mound Laboratory

L. J. Wittenberg

NASA Headquarters

J. J. Lynch

NASA Lewis Research Center

M. Ault

J. W. Creigh

T. P. Moffitt

T. A. Moss

F. E. Rom

L. Rosenblum

N. D. Sanders

N. Saunders

H. Schwartz

Naval Air Systems Command

I. Machlin

Naval Research Laboratory

R. Hawthorne

C. Serpan

Nuclear Materials and Equipment Corporation

C. Caldwell

K. Puechl

Oak Ridge National Laboratory

G. E. Boyd

J. E. Cunningham

J. H. DeVan

W. R. Grimes

W. O. Harmes

W. R. Martin

P. Patriarca

J. Scott

J. R. Weir

Ohio State University

M. Fontana

Pacific Northwest Laboratory

F. W. Albaugh

A. L. Bement

J. J. Cadwell

D. R. deHalas

R. L. Dillon

E. Evans

J. C. Tobin

R. G. Wheeler

Sandia Corporation

J. Jacobs

R. P. Stromberg

TRW Space Technology Laboratory

H. Lurie

United Nuclear Corporation

A. Strasser

University of California, Berkeley

L. Brewer

US Naval Air Systems Command (AIR-52031B)

T. Kearns

I. Machlin

Westinghouse Electric Corporation

Advanced Reactor Division

E. C. Bishop

J. C. R. Kelly, Jr.

W. E. Ray

Astronuclear Laboratory

R. T. Begley

D. C. Goldberg

Atomic Power Division

R. Allio

T. Stern

Bettis

W. J. Babyak

R. H. Fillnow

E. J. Kreigh

B. Lustman

D. H. Ahmann
N. K. Anderson (2)
W. G. Baxter
J. T. Berling
J. J. Brady, FPD
H. C. Brassfield
M. L. Bromberg
R. D. Brooks
V. P. Calkins
L. Chockie, APED
C. G. Collins (2)
E. S. Collins
J. F. Collins

P. K. Conn
J. B. Conway (2)
E. W. Filer
P. N. Flagella
R. E. Fryxell
E. S. Funston
J. O. Hibbits
E. F. Juenke
F. Kingsbury
W. C. Kuhlman
L. R. McCreight, MSD
J. A. McGurty
J. W. Morfitt

J. Moteff
G. T. Muchlenkamp
W. E. Niemuth
G. W. Pomeroy
R. B. Richards, APED
F. C. Robertshaw
C. S. Robertson
E. J. Schmidt, ATS
L. H. Sjodahl
J. P. Smith
H. R. Stephan
C. O. Tarr
F. O. Urban

J. E. VanHoomissen, NTPO
G. R. VanHouten
H. E. Wagner
J. F. White
V. C. Wilson, R&DC
R. E. Wood
Library (20)

PREFACE

This report, GEMP-1004, is the seventh annual report of the unclassified portion of the Fuels and Materials Development Programs being conducted by the General Electric Company's Nuclear Materials and Propulsion Operation under Contract AT(40-1)-2847, issued by the Fuels and Materials Branch, Division of Reactor Development and Technology, of the Atomic Energy Commission.

This report covers the period from January 31, 1967 to January 31, 1968, and thus also serves as the quarterly progress report for the final quarter of the year. During this period, two unclassified programs were terminated and the title and objectives of others were revised. The title change and status of each program is indicated below in the more detailed breakdown of this unclassified annual report, GEMP-1004, and the classified annual report, GEMP-1003, which covers the period from January 1, to December 31, 1967.

GEMP-1004, Unclassified

1. Physical and Mechanical Properties of Reactor Materials (same title), Task 1503, continuation.
2. Radiation Effects on Fast Breeder Reactor Cladding and Structural Materials (same title), Task 1304, continuation.
3. Advanced Fast Breeder Reactor Fuel Element Cladding Development (Refractory-Metal Alloy Research and Development),* Task 1115, continuation.
4. Physical Metallurgy of Fast Breeder Reactor Cladding Materials and Refractory Metals (Physical Metallurgy of Refractory-Metal Alloys), Task 1177, continuation.
5. Fast Breeder Reactor Fuel Element Cladding Research (Advanced Long-Life Reactor Fuel Cladding and Structural Materials Development), Task 1119, continuation.
6. Evaluation of Plastic Fatigue Properties of Heat Resistant Alloys (same title), Task 1516, continuation.
7. Advanced Pressure Vessel Materials (same title), Task 1521, continuation.
8. Physico-Chemical Studies of Clad UO_2 in Potential Meltdown Environments (same title), Task 1175, continuation.
9. Fast Breeder Reactor Thermocouple Development (High-Temperature Thermocouple and Electrical Materials Research), Task 1414, continuation.
10. Physico-Chemical Studies of Fe-Cr-Al-Clad Fuel Systems (same title), Task 7076, terminated FY-67.
11. High-Temperature Research on Carbides for Fuel and Structural Applications (same title), Task 7073, terminated FY-67.

*The titles presented in parenthesis are the ones used in the previous quarterly reports (GEMP-1001 and -1002).

GEMP-1003, Classified

1. High-Temperature Studies of Uranium Based Fuels (High-Temperature Studies of Substoichiometric Uranium and Uranium Solid Solutions), Task 1171, continuation.
2. Refractory-Metal Fuel Element Materials Research (same title), Task 1105, continuation.
3. Fission Product Transport Processes in Refractory Metal Fuel Elements (same title), Task 1170, continuation.
4. High-Temperature Materials Engineering Properties Evaluation (same title), Task 7017, Terminated FY-1967.
5. Fast Breeder Reactor Control, Shield, and Reflector Materials Development (Advanced Long-Life Reactor Fuel Element Moderator, Control, and Shield Materials Development), Task 1220, continuation.

CONTENTS

	Page
INTRODUCTION AND SUMMARY	11
✓ 1. PHYSICAL AND MECHANICAL PROPERTIES OF REACTOR MATERIALS (1503)	14
1.1 CREEP-RUPTURE STUDIES	14
Tungsten	14
Tungsten-Base Alloys	37
Molybdenum	41
Rhenium	58
Niobium and Niobium Alloys	63
Constant-Stress Creep Testing	65
Single Crystals	71
Stress-Rupture Parameter Analysis	71
Comparison of Test Data	79
1.2 THERMAL PROPERTY EVALUATIONS	81
Electrical Resistivity and Thermal Conductivity	81
Thermal Diffusivity	82
Enthalpy	84
1.3 SUMMARY AND CONCLUSIONS	85
1.4 PLANS AND RECOMMENDATIONS	87
✓ 2. RADIATION EFFECTS ON FAST REACTOR CLADDING AND STRUCTURAL MATERIALS (1304)	89
2.1 STATUS OF IRRADIATIONS	89
EBR-II Irradiation Program	89
ORR and ETR Irradiations	90
2.2 HEAT-RESISTANT ALLOY PROGRAM	90
Creep-Rupture Testing	90
Hot Hardness	100
Resistivity Studies	103
Transmission Electron Microscopy	107
2.3 REFRACTORY METALS AND ALLOYS PROGRAM	113
Creep-Rupture Testing	113
Hot Hardness	131
Hardness and Ultimate Strength Correlation	134
Tensile Testing	137
Resistivity Studies	147
Transmission Electron Microscopy	154
2.4 REACTOR DOSIMETRY	165
Monte Carlo Spectrum Measurements	165
EBR-II Flux Density Measurements	165
2.5 SUMMARY AND CONCLUSIONS	171
2.6 PLANS AND RECOMMENDATIONS	173
2.7 REFERENCES	174

	Page
✓ 3. ADVANCED FAST BREEDER REACTOR FUEL ELEMENT CLADDING DEVELOPMENT (1115)	178
3.1 REFRACTORY METAL ALLOY TUBING, SHEET, AND WIRE PRODUCTS	178
Seamless Tubing	180
Sheet	181
Shapes	183
Refractory Metal Alloy Wire Drawing	183
3.2 DEVELOPMENT OF MOLYBDENUM AND ITS ALLOYS FOR FAST BREEDER REACTOR APPLICATIONS	186
Molybdenum Purification	188
Molybdenum Alloys	193
W-Re-Mo Alloys	194
3.3 SUMMARY AND CONCLUSIONS	194
3.4 PLANS AND RECOMMENDATIONS	196
✓ 4. PHYSICAL METALLURGY OF FAST BREEDER REACTOR CLADDING MATERIALS AND REFRACTORY METALS (1177)	198
4.1 TUNGSTEN-RHENIUM-MOLYBDENUM ALLOYS	198
Fabrication	198
Recrystallization	199
Aging	202
Ductility	208
4.2 MOLYBDENUM	210
Fabrication	212
Recrystallization	212
Ductility	212
Aging Studies	214
4.3 FAST REACTOR FUEL CLADDING ALLOYS	214
4.4 SUMMARY AND CONCLUSIONS	214
4.5 PLANS AND RECOMMENDATIONS	215
✓ 5. FAST BREEDER REACTOR FUEL ELEMENT CLADDING RESEARCH (1119) ..	216
5.1 CHROMIUM-BASE ALLOYS	216
Material Preparation	217
Material Evaluation	219
5.2 Fe-Cr-Al-Y ALLOYS	230
Material Preparation	231
Material Evaluation	231
5.3 IRON-BASE (FERRITIC)	238
5.4 IRON-BASE (AUSTENITIC)	238
5.5 SUMMARY AND CONCLUSIONS	238
5.6 PLANS AND RECOMMENDATIONS	241
✓ 6. EVALUATIONS OF PLASTIC FATIGUE PROPERTIES OF HEAT-RESISTANT ALLOYS (1516)	242
6.1 MATERIALS SPECIFICATIONS	242
AISI 304 Stainless Steel Rod Stock	242
AISI 316 Stainless Steel Rod Stock	242
NMPO Processing – AISI 304 and 348 Stainless Steel	242
NMPO Processing – AISI 316 Stainless Steel	242
6.2 FATIGUE-TESTING EQUIPMENT	243

	Page
6.3 TEST RESULTS	247
6.4 FATIGUE DATA ANALYSIS	252
6.5 METALLOGRAPHIC AND FRACTOGRAPHIC ANALYSIS OF LOW-CYCLE FATIGUE SPECIMENS	263
6.6 SUMMARY AND CONCLUSIONS	265
6.7 PLANS AND RECOMMENDATIONS	273
✓ 7. ADVANCED PRESSURE VESSEL MATERIALS (1521)	275
7.1 EXPERIMENTAL PROGRAM	275
12Ni - 5Cr - 3Mo Maraging Steel	275
PH13-8Mo	281
Inconel Alloy 718	289
7.2 CONSIDERATION OF PRESSURE VESSEL FAILURE MODES AND RELATED PROPERTIES	300
Burst Due to Over-Pressure	301
Fatigue Cracking	303
Fast Fracture by Either Brittle Fracture or Low-Energy Tearing	309
7.3 GENERAL DISCUSSION	310
12Ni - 5Cr - 3Mo	311
PH13-8Mo	311
Inconel Alloy 718	313
7.4 SUMMARY AND CONCLUSIONS	314
7.5 PLANS AND RECOMMENDATIONS	315
✗ PHYSICO-CHEMICAL STUDIES OF CLAD UO ₂ IN POTENTIAL MELTDOWN ENVIRONMENTS (1175)	316
8.1 DYNAMIC TESTING OF ZIRCONIUM-BASE ALLOYS	316
Internal Pressure Effects	316
Effect of Oxidation on Tube Deformation	320
Testing of 50-cm-Long Zircaloy-4-Clad UO ₂ Fuel Elements	324
Dynamic Testing of Irradiated Zircaloy-2 at Constant Internal Pressure ...	326
8.2 REACTION MECHANISMS AND KINETICS	326
Oxidation of Zirconium Alloys by Steam or Air	326
Oxidation of Type 304 Stainless Steel in Steam or Air	333
Oxidation of UO ₂ by Steam	337
8.3 PHYSICAL AND MECHANICAL PROPERTIES	342
Tensile Strength of Type 304 L Stainless Steel	342
Thermal Conductivity of 304 L Stainless Steel	343
Spectral and Total Emittance Measurements of Oxidized Zircaloy-4	346
8.4 SUMMARY AND CONCLUSIONS	349
8.5 PLANS AND RECOMMENDATIONS	350
✗ FAST BREEDER REACTOR THERMOCOUPLE DEVELOPMENT (1414)	351
9.1 W VERSUS W - 25Re THERMOCOUPLE CHARACTERISTICS AT HIGH TEMPERATURE	351
Electrical Insulation Evaluation	352
Effect of Gaseous Environment	352
Sheathing Studies	353
Effect of Unmatched Thermocouple Wire Diameters	353
9.2 ELECTRICAL INSULATION FOR HIGH-TEMPERATURE THERMOCOUPLES	354
Intrinsic Variables Affecting Thermocouple Voltage	355

	Page
9.3 THERMOELECTRIC CHANGES IN W - 25Re DUE TO TRANSMUTATION...	358
Reactor Stability of W Versus W - 25Re Thermocouple	358
Reactor Testing of Thermocouple Materials	359
9.4 SUMMARY AND CONCLUSIONS	359
9.5 PLANS AND RECOMMENDATIONS	360
X PHYSICO-CHEMICAL STUDIES OF Fe-Cr-Al-CLAD FUEL SYSTEMS (7076)...	361
10.1 DIFFUSION STUDIES	361
Fe, Cr, and Al Diffusion	361
Uranium Diffusion	362
10.2 FUELED CAPSULE TESTS	365
10.3 CONCLUSIONS	367
X HIGH-TEMPERATURE RESEARCH ON CARBIDES FOR FUEL AND STRUCTURAL APPLICATIONS (7073)	369
11.1 PREPARATION AND FABRICATION OF REFRACTORY CARBIDES	369
11.2 Ta CARBIDE	371
Thermal Stability	371
Effect of Strain on Lattice Parameters	372
11.3 NON-STOICHIOMETRY IN Ta AND U MONOCARBIDES	373
Experimental Procedure	373
Discussion	376
11.4 PLANS AND RECOMMENDATIONS	378

UNCLASSIFIED

CONVERSION TABLE

To Convert From	To	Multiply By
Atmospheres	Pounds/inch ²	14.7
Calories (mean)	Btu (mean)	0.00397
Calories/gram-°C	Btu/pound-°F	1.0
Calories/sec-cm-°C	Btu/hr-ft-°F	241.8
Calories/sec-cm ²	Btu/hr-ft ²	1.32 x 10 ⁴
Calories/sec-cm ² -°C	Btu/hr-ft ² -°F	7370
Centimeters	Feet	0.03281
	Inches	0.3937
Cubic centimeters	Cubic feet	3.531 x 10 ⁻⁵
	Cubic inches	0.06103
Grams	Pounds	0.002205
Grams/cm ³	Pounds/ft ³	62.43
Grams/cm ²	psi	0.01422
Kilograms	Pounds	2.205
Kilograms/cm ²	Atmospheres	0.9678
	Pounds/ft ²	2048
	Pounds/inch ²	14.22
Kilograms/mm ²	Pounds/inch ²	1422.32
Kilowatts	Btu/sec	0.948
Liters	Cubic feet	0.0353
Meters	Inches	39.37
Millimeters of mercury	Atmospheres	0.001316
Square centimeters	Square feet	0.001076
	Square inches	0.155
Torr	mm of Hg	1.0
	Atmospheres	0.001316
Watts/cm-°C	Btu/hr-ft-°F	57.8
Watt-seconds	Btu	0.000948
Watts/cm ²	Btu/hr-ft ²	3170
Watts/cm ² -°C	Btu/hr-ft ² -°F	1760
Centimeters/sec	Feet/sec	0.03281
Meters/sec	Feet/sec	3.281

INTRODUCTION AND SUMMARY

This report, GEMP-1004, is the seventh annual report on the unclassified portion of the GE-NMPO Fuels and Materials Development Program conducted during calendar year 1967 under Contract No. AT(40-1)-2847. This report covers eleven unclassified jobs: (1) properties of reactor materials from 1000° to 3000°C; (2) radiation effects on the time-, temperature-, and stress-dependent properties of fast breeder reactor (FBR) cladding and structural materials; (3) fabrication of FBR advanced fuel element cladding; (4) physical metallurgy of FBR cladding materials and refractory metals; (5) development of advanced FBR fuel element cladding materials with improved performance capability; (6) parameters affecting low-cycle fatigue behavior of heat-resistant alloys; (7) applicability of high-strength steels to nuclear reactor pressure vessels; (8) behavior of Zircaloy-4-clad and Type 304 stainless steel-clad UO_2 in meltdown environments; (9) high-temperature thermocouple and electrical materials; (10) physico-chemical stability and reactions between Fe-Cr-Al alloys and UO_2 ; and (11) refractory carbides for fuel and structural applications.

Significant results achieved in this program were as follows:

From 1600° to 3000°C the creep-rupture data for arc-cast W was correlatable in terms of diffusion compensated creep rate versus the modulus compensated stress. Above one-half the absolute melting temperature, creep is by dislocation climb or glide of jogged screw dislocations. Arc-cast W showed no tendency to form cavities in contrast to the grain boundary separation and cavitation observed in powder-metallurgy W. Creep-rupture data (1200° to 2400°C) for arc-cast Mo showed good correlation between time to rupture and linear creep rate except at high temperatures and low stress where a change in creep mechanism was indicated. Creep-rupture data from 1600° to 2600°C are presented for W - 30Re - 30Mo, Mo - 30W, W - 25Re, and Mo - 50Re. Single crystal material of ~~W and W-30Re-30Mo~~ at 2800°C ~~and W-25Re~~ showed no detectable creep with fracture being brittle in nature. A comprehensive study of stress-rupture parameters was completed. Thermal conductivity and electrical resistivity for W - 25Re to 2400°C, thermal diffusivity for W - 25Re, 304L SS, and W from 300° to 1000°C, and enthalpies of W from 1200° to 3450°K are presented.

Irradiation of Incoloy 800 to 3×10^{20} n/cm² ($E_n \geq 1$ Mev) lowers rupture life at 540°C but increases it at 705°C with corresponding increase and decrease in minimum creep rate; ductility is decreased 1/3 to 1/2. Hastelloy X, irradiated in either ETR or EBR-II to comparable fast fluences have comparable creep-rupture properties. Hastelloy R-235 with varying B¹⁰ content at 50 ppm boron level showed increased radiation damage with increasing B¹⁰ content when tested at 870°C. Hastelloy R-235 and A-286 show shells of localized damage and gas bubbles with radii approximating the recoil distance of Li and α -particles in Fe and Ni. Embrittlement of irradiated ASTM-A302B is probably caused by carbon-defect-complex formation which recovers at 300° to 500°C as evidenced by resistivity studies.

Irradiation temperature has a pronounced effect on creep-rupture properties of Mo; for 70°C irradiations the effect at 750°C is least; for 700° and 1000°C irradiations the time to rupture at 750°C was increased by factors of 12 and 18, respectively; annealing at 1000°C of a 700°C irradiated specimen increased 750°C rupture life an additional 25 percent; delayed creep was observed at 600°, 700°, and 750°C for 70°C irradiations but not in control specimens, in 70°C irradiated specimens tested at 580°, 850°, or 900°C, or in 700°C and 1000°C irradiated specimens. Resistivity measurements indicated irradiation to saturate in Mo at about 1×10^{20} n/cm² ($E_n \geq 1$ Mev). Molybdenum, creep-rupture tested at 750°C, showed dislocation loops in matrix but not at grain boundaries in specimens irradiated at 70°C and 700°C; whereas, for the 1000°C irradiated Mo there were no matrix loops, with only occasional loops near grain boundaries. Irradiation of Nb and Nb - 1Zr at 70°C to 2.1×10^{20} n/cm² ($E_n \geq 1$ Mev) increases the room-temperature tensile yield strength about 110 and 200 percent, respectively; the 600° to 650°C yield strength is increased by 93 and 110 percent, respectively; ductility is significantly reduced; and complete recovery occurs after 1000°C anneal.

Facilities for producing refractory-metal sheet, bar, seamless tubing, and wire were put into operation and process procedures established. Purification procedures for molybdenum resulted in sheet which was ductile and free of microporosity in weld-heat-affected areas. A Mo - 5W alloy, processed using purification procedures, had stress-rupture life and deformation resistance equal to Mo - 50Re at 1600°C and superior to that alloy at 2200°C.

Lower-cost production procedures and improved room-temperature ductility properties were developed in a study of powder-metallurgy W - 30Re - 30Mo and W - 25Re - 30Mo alloys. Recrystallization, grain size, hardness, and ductility data for aging to 2000°C for up to 1000 hours are presented. Similar studies are being applied to Mo.

Fe-Cr-Al-Y alloys and Cr- and Fe-base (ferritic and austenitic) alloys are compared to austenitic stainless steel mechanical properties. All program alloys were found to possess superior tensile yield strength up to 750°C. Of these, only Cr- and austenitic Fe-base alloys have indicated 650°C creep-rupture properties comparable or superior to stainless steel.

In low-cycle fatigue, Type 348 stainless steel exhibited better strain fatigue resistance at 430°, 650°, and 816°C than Types 304 or 316 stainless steel. All three stainless steels showed cyclic strain hardening characteristics with the 316 stainless steel at 430°C ultimately showing cyclic strain softening. Results at 430°C for 348 and 316 stainless steel are in fair agreement with the Coffin-Manson and Manson-Halford relations. A hundred-fold decrease in strain rate caused, in general, a several-fold decrease in fatigue resistance of 304, 348, and 316 stainless steel at 650°C and 816°C. Fatigue curves based both on total axial and plastic strain are shifted to lower life with decrease in strain rate. Fractographic analyses indicate the crack, formed at 650°C, is approximately 1.7 mm in length at the N_5 point. The mode of crack initiation in 348 and 304 stainless steel at 650°C and 816°C and strain rates of 4×10^{-3} to 4×10^{-5} sec⁻¹ was primarily intergranular except for the highest strain rate at 650°C.

The potential of three high-strength materials for advanced pressure vessels is being evaluated. The 12Ni - 5Cr - 3Mo maraging steel possesses (1) aging characteristics which appear to be suited for aging of heavy sections, (2) promising tensile and toughness properties, (3) adequate structural stability at least to 315°C, and (4) good weldability. The precipitation-hardening stainless steel, PH13-8Mo, at aging temperatures which produce good toughness (1) may not be suited to uniform aging of heavy sections, (2) has excellent tensile and good toughness properties, (3) is stable structurally to 425°C, and (4) has good weldability and weld strength. Inconel alloy 718 has (1) excellent strength, (2) relatively low toughness which was not significantly lowered when irradiated to 1×10^{19} n/cm² ($E_n \geq 1$ Mev), (3) good structural stability to 540°C, and (4) showed good weldability but with weld strength

and toughness below parent metal level. The types of failure which need to be prevented in pressure vessel applications and the special materials properties which are related (e. g., strain hardening coefficient, dynamic yield strength, and plane strain fracture toughness) are presented.

Dynamic heating of Zircaloy-4 tubes with an internal pressure show that steam oxidation lowers deformation and deformation rates, and increases failure temperature; in the absence of oxidation, tube failure has been expressed as a function of tensile strength and heating rate. Oxidation of Zircaloy-4 in air is greater than in steam and is attributed to reaction with nitrogen in the air. The spectral emittance (at 0.65 micron) of unoxidized Zircaloy-4 varied from 0.56 at 885°C to 0.43 at 1550°C. Diffusion of oxygen in UO_{2+x} lattice is the rate controlling mechanism for oxidation of UO_2 by steam. Up to 1370°C, the oxidation of 304L stainless steel in air is 10^3 times less than in steam due to a protective Cr_2O_3 film; above 1370°C, the rates are equal as molten FeO destroys the Cr_2O_3 film.

High-temperature thermocouple characteristics of W / W - 25Re are affected by the thermoelectric emf produced along BeO, HfO_2 , or ThO_2 insulators and by the atmosphere for bare-wire (non-insulated) thermocouples. Irradiation of W versus W - 25Re thermocouples for 2 months in a 1.2×10^{14} neutron/cm²-sec thermal and 2.1×10^{13} neutron/cm²-sec fast flux resulted in similar shifts in thermal emf, causing a small (5°C) positive error.

Aluminum in Fe-Cr-Al-base claddings reduces UO_2 in cermet fuels above 1000°C. Free U formed dissolves in and diffuses through 0.38-mm cladding in 100 hours at 1000°C and in 6 hours at 1200°C. Liberated oxygen combines with Al to form Al_2O_3 at the cladding - core interface where it inhibits subsequent diffusion of Al and thus limits the quantity of U formed.

The preparation and fabrication of well-characterized carbides of Ta, Zr, Hf; the thermal stability and effect of strain on lattice parameters of Ta carbide; and the non-stoichiometry in Ta- and U-monocarbides are summarized.

1. PHYSICAL AND MECHANICAL PROPERTIES OF REACTOR MATERIALS

(1503)

J. B. Conway,* P. N. Flagella†

The purpose of this program is to measure and evaluate high-temperature (to 3000°C) physical and mechanical properties of commercially available and newly developed materials being considered for use in fueled and non-fueled high-temperature reactor applications.

1.1 CREEP-RUPTURE STUDIES

A significant amount of creep-rupture data for wrought, unalloyed, tungsten and molybdenum have been obtained over the last few years at temperatures from 1600° to 3000°C. Results have shown that wrought material, fabricated by the powder-metallurgy process, does not consistently exhibit the same strength (rupture life), creep resistance (linear creep rate), and ductility (elongation at rupture). Powder-metallurgy material was found to be characterized by considerable duplexing of the structure with a significant portion of deformation related to grain boundary separation or cavitation leading to fracture in the grain boundaries.

Wrought, arc-cast material exhibited more consistent behavior. Extremely large grains formed in high-temperature tests and deformation occurred as crystallographic slip and grain boundary sliding. No void formation was observed in the grain boundaries. Arc-cast material was considerably more ductile with fracture being transgranular.

TUNGSTEN → p 17 Stress-Rupture and Creep

Stress-rupture and creep data for wrought, unalloyed, arc-cast tungsten sheet, identifying code W(3), were obtained over a broad range of temperatures and stresses. The results are summarized in Figures 1.1 and 1.2 and indicate a change in slope for both the stress-rupture and creep rate curves at 2200°C. The slope for the creep rate curve at low stresses is consistent with the isotherms for 2400°C and 2600°C. A similar change in slope is indicated for stress-rupture data at 2400°C but not at 2600°C. The mechanism associated with slope changes has not been identified.

Creep Rate Correlation

The creep data obtained for arc-cast tungsten, W(3), from 1600° to 3000°C were evaluated based on the proposed method of Sherby¹ for pure polycrystalline metals above one-half the absolute melting temperature. The results are presented in Figure 1.3 in terms of the ratio of steady-state creep rate ($\dot{\epsilon}_s$) to the diffusion coefficient (D) plotted as a function of creep stress (σ) divided by the elastic modulus (E). Correlation of the data

*Project leader.

†Principal investigator.

¹O. D. Sherby, "Factors Affecting the High Temperature Creep of Polycrystalline Solids," Acta Met., Vol. 10, 1962, p. 135.

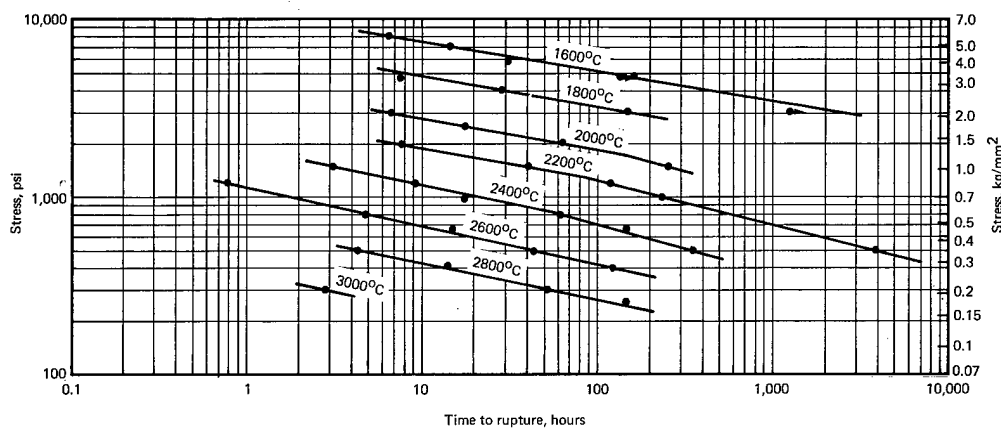


Fig. 1.1 — Stress-rupture test results for wrought, arc-cast unalloyed tungsten, W(3), sheet tested in hydrogen

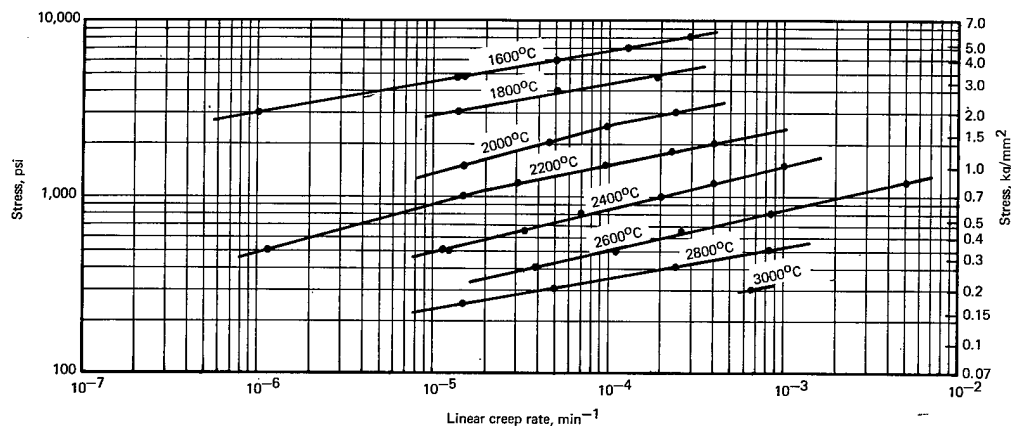


Fig. 1.2 — Creep rate test results for wrought, arc-cast unalloyed tungsten, W(3), sheet tested in hydrogen

in this manner appears to be quite good with the curve shape the same as that determined by Sherby for some other pure polycrystalline metals. The slope, n , of the linear portion of the curve is 4.2 and is consistent with Sherby's prediction that the value be approximately 5. This portion of the curve is associated with a creep process controlled by dislocation climb involving an equilibrium vacancy concentration. The non-linear portion of the curve (higher stresses) involves dislocation climb under conditions where vacancy concentration is greater than the equilibrium value.

Ductility

Evaluations of rupture elongation, for both powder-metallurgy (PM) and arc-cast (AC) tungsten, were made to obtain the results shown in Figure 1.4. (PM data are the result of testing three different vendor sources of material.) The PM sheet exhibited a decreasing trend in ductility with temperature from 1600° to 2800°C; the AC sheet showed a decrease in ductility from 1600° to 1800°C followed by a significant increase, peaking at 2200° to 2400°C, and then a decrease with further increasing temperature to 3000°C. Fracture in the PM sheet occurred only in the grain boundaries; no transgranular failures

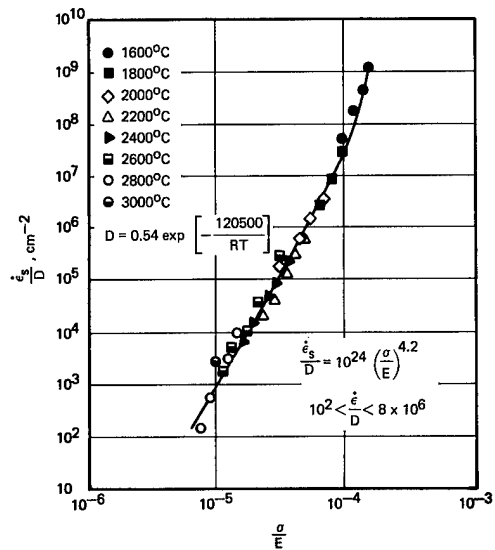


Fig. 1.3 — Ratio of steady-state creep rate ($\dot{\epsilon}_s$) to diffusion coefficient (D) versus ratio of stress (σ) to Young's modulus (E) for arc-cast W

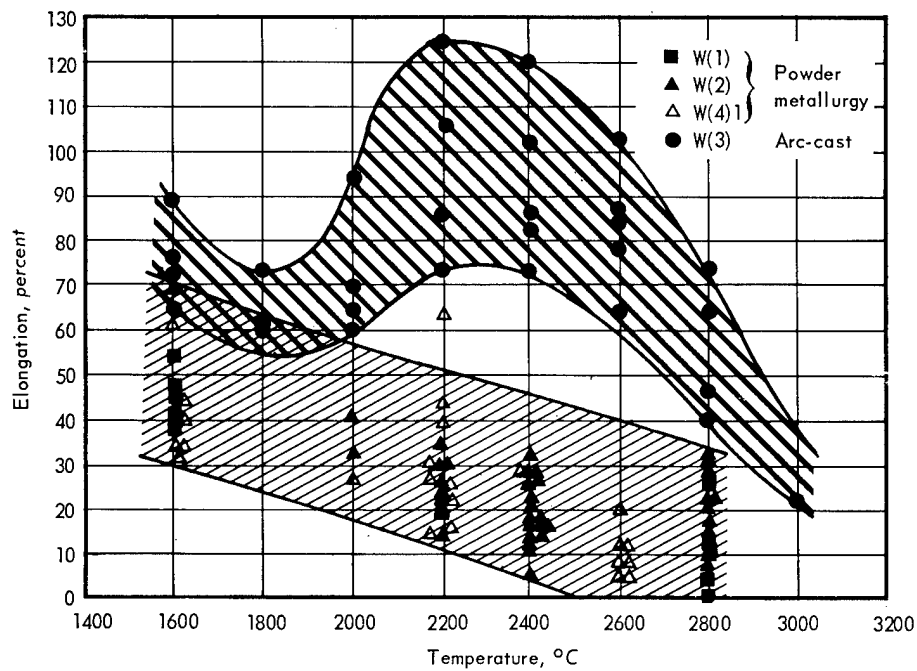


Fig. 1.4 — Elongation versus temperature for wrought powder-metallurgy and wrought arc-cast unalloyed W sheet tested in hydrogen

were observed. Failure in the AC sheet was principally transgranular with little or no grain boundary fissuring observed.

Although initial grain size appears to have an effect on the strength and ductility of these materials, the presence of many large grains after failure in the PM sheet indicates that some factor in addition to grain size must be exerting an effect. All fractures in the PM sheet occurred in grain boundaries indicating that the grain boundaries are weaker than the matrix at test conditions. The AC sheet grain boundaries remained strong and ductile leading to typical ductile transgranular deformation and ultimately resulting in "woody" tearing-type fractures with the grain boundaries appearing to play no direct part.

Reasons for reduction in ductility of the AC sheet at about 1800°C are not clear. Individual creep curves as well as instantaneous strain rate values plotted as a function of strain show a distinct discontinuity associated with the drop in ductility. Some inhibiting mechanism is apparently operative in the region of the second stage of creep (usually associated with a constant rate of dislocation flow).

Creep Analysis

Studies of creep data for arc-cast tungsten, W(3), were performed using the method proposed by Woodford² for constant-load tests. Although most analyses and interpretations of creep mechanisms are based on constant-stress tests, most experimental data for materials are obtained using the constant-load technique. For constant-load tests, actual stress on the specimen increases as strain increases since the cross-sectional area is decreasing. In both types of testing, the assumption is made that deformation occurs uniformly over the gage length until local necking is initiated.

A special computer program was written to analyze experimental strain - time data. This program was designed to yield calculated values of the instantaneous creep rate and instantaneous or true stress (the latter values are based on an assumption of constant volume deformation). For the portion of the creep curve beyond that corresponding to minimum creep rate, a plot of instantaneous creep rate versus instantaneous stress was found to be linear on logarithmic coordinates (Figure 1.5). For each temperature, then, a relationship of the form $\dot{\epsilon} = A\sigma^n$ is indicated; where $\dot{\epsilon}$ is the instantaneous creep rate beyond the minimum, σ is the instantaneous or true stress, and A and n are constants. Based on this approach, the following expression was obtained relating $\dot{\epsilon}$ to the initial stress, σ_0 , and the strain, ϵ , in a constant-load creep test:

$$\dot{\epsilon} = \frac{d\epsilon}{dt} = A\sigma^n = A[\sigma_0(1 + \epsilon)]^n. \quad (1.1)$$

Integration at constant σ_0 and solving for time, t, yields:

$$t = B(1 + \epsilon)^{1-n} + C \quad (1.2)$$

where C is the constant of integration and n is the slope of the plot shown in Figure 1.5 at any given temperature.

For a given value of σ_0 , this expression defines a linear relationship between t and $(1 + \epsilon)^{1-n}$ for the region beyond the minimum creep rate. A typical plot of this type is shown in Figure 1.6 for the tungsten data at 2400°C for which $n = 4.291$. Linearity is noted at all σ_0 values. It has been found in this analysis that the value of C [i. e., the

²D. A. Woodford, "Constant-Load Creep Data Interpreted in Terms of the Stress Dependence of Dislocation Velocity," Trans. Met. Soc. of AIME, Vol. 239, May 1967, p. 655.

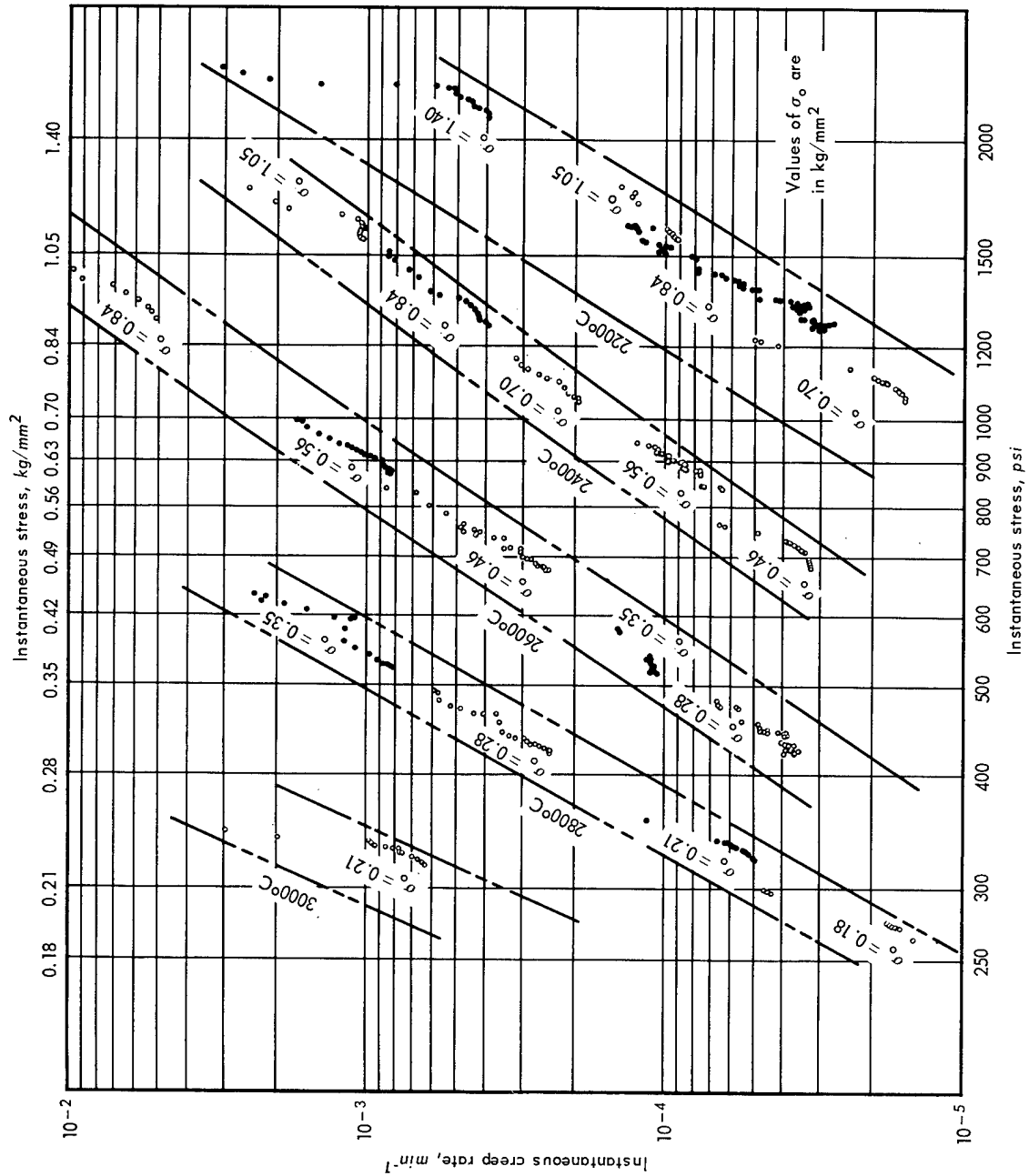


Fig. 1.5 — Creep rate versus instantaneous stress for W at various temperatures and initial stress (σ_0) values

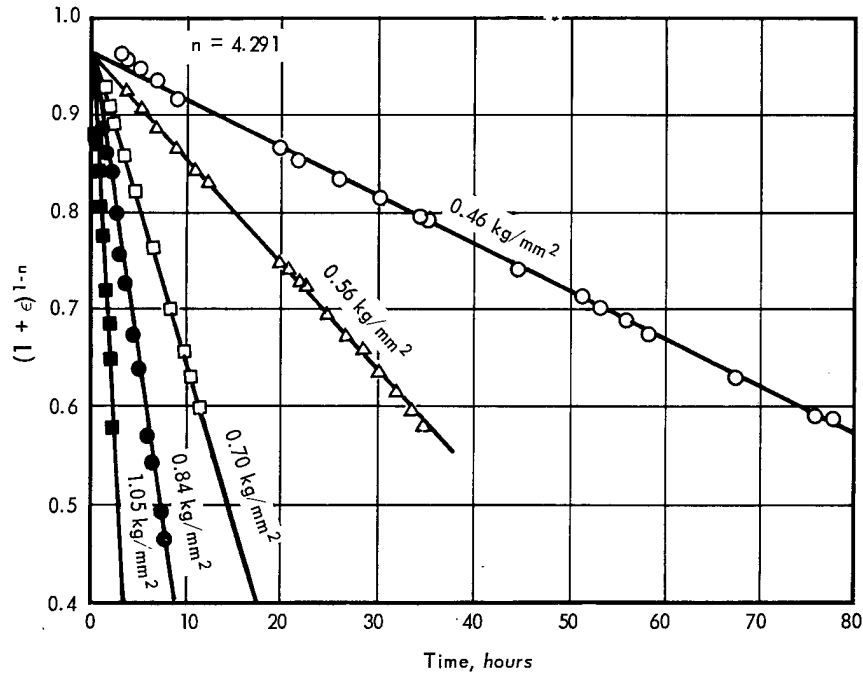


Fig. 1.6 — Tungsten W(3) data at 2400°C analyzed in terms of $(1 + \epsilon)^{1-n}$ versus time

intercept in Figure 1.6 at $(1 + \epsilon)^{1-n} = 0$ at any given temperature is related to σ_0 according to:

$$C = D\sigma_0^m \quad (1.3)$$

leading to:

$$\epsilon = \frac{1}{(E - F\sigma_0^m t)^p} - 1 \quad (1.4)$$

Expressions of this type for the tungsten data obtained in this study are:

$$T = 2400^\circ\text{C}$$

$$\epsilon = \frac{1}{(0.95 - 6.1708 \times 10^{-15} \sigma_0^{4.225} t)^{0.30386}} - 1 \quad (1.5)$$

$$T = 2600^\circ\text{C}$$

$$\epsilon = \frac{1}{(0.95 - 7.5289 \times 10^{-15} \sigma_0^{4.561} t)^{0.2922}} - 1 \quad (1.6)$$

$$T = 2800^\circ\text{C}$$

$$\epsilon = \frac{1}{(0.94 - 1.6707 \times 10^{-16} \sigma_0^{5.557} t)^{0.2247}} - 1 \quad (1.7)$$

where:

ϵ is strain

t is time, hr

σ_0 is initial stress, $\text{kg/mm}^2 \times 1422.3$

The experimental results obtained at 2400°C and those determined from the above equation are compared in Figure 1.7. The agreement is excellent when considering the problems and uncertainties associated with testing at 2400°C.

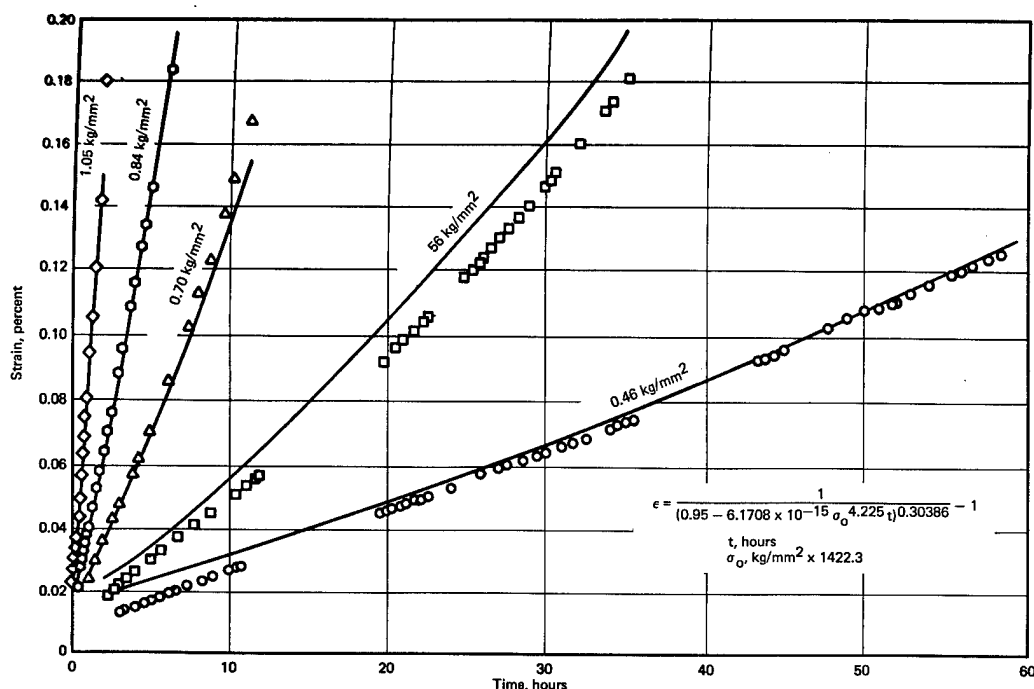


Fig. 1.7 — Strain versus time creep data for arc-cast tungsten tested at 2400°C in H₂ atmosphere

Hot Hardness

Wrought, arc-cast tungsten sheet, W(3), specimens were annealed in hydrogen at various temperatures for different times. Microhardness measurements were then made from room temperature to 1300°C. Results are given in Figure 1.8 for three specimens annealed at 1200°, 1400°, and 1600°C. As shown, a break in the curve occurs at approximately 300°C (0.16 T_m, where T_m represents the absolute melting temperature) consistent with data reported previously³ for unalloyed tungsten. Also shown is a decrease in hardness with increasing annealing temperature over the total temperature range investigated. These differences are apparently related to the grain size differences resulting from the annealing treatments. Figure 1.9 compares the grain size and typical indents obtained in determining the microhardness of specimens annealed at 1200°C and 1600°C. The specimen receiving the highest-temperature anneal (1600°C) had such large grains that the indent and resulting symmetrical deformation pattern were contained within a single grain. The specimen annealed at 1200°C shows a relatively fine-grained structure with no deformation pattern apparent. Average grain sizes associated with the data given in Figure 1.8 are 20, 28, and 88 microns for annealing temperatures of 1200°, 1400°, and 1600°C, respectively.

Microstructural Studies (R. C. Rau, S. F. Bartram, P. N. Flagella)

Microstructural studies, using optical and electron microscopy and X-ray diffraction techniques, were performed on high-purity polycrystalline tungsten after creep-rupture testing at stress levels ranging from 0.18 to 5.62 kg/mm² over the temperature range from

³"AEC Fuels and Materials Development Program Progress Report No. 67," GE-NMPO, GEMP-67, June 30, 1967, p. 55.

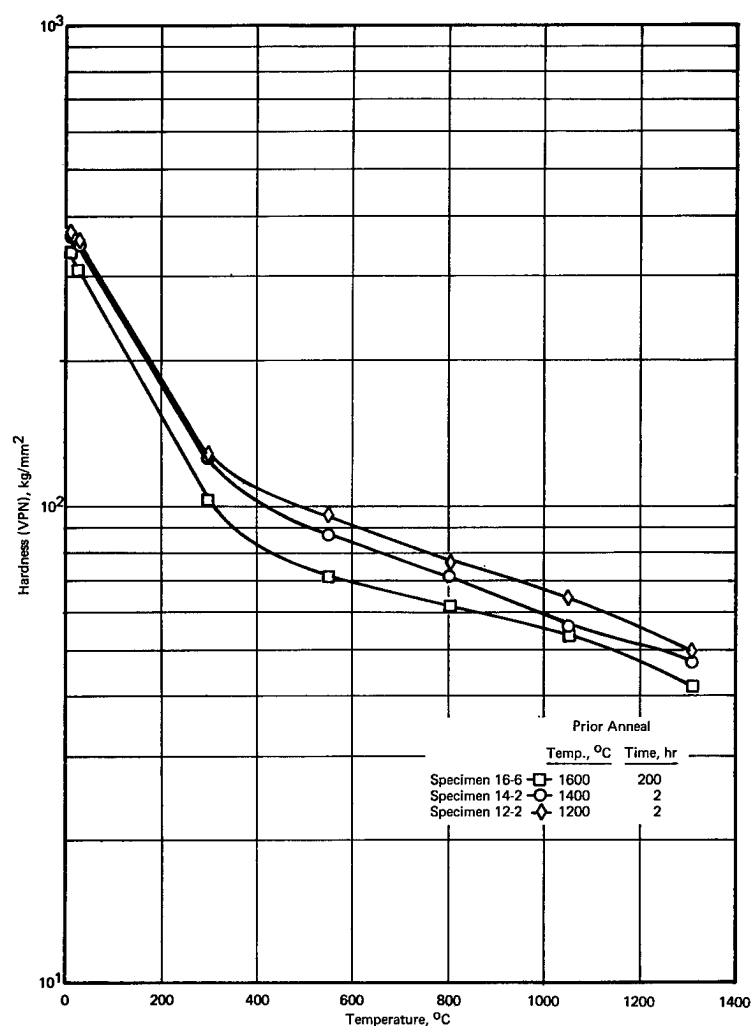
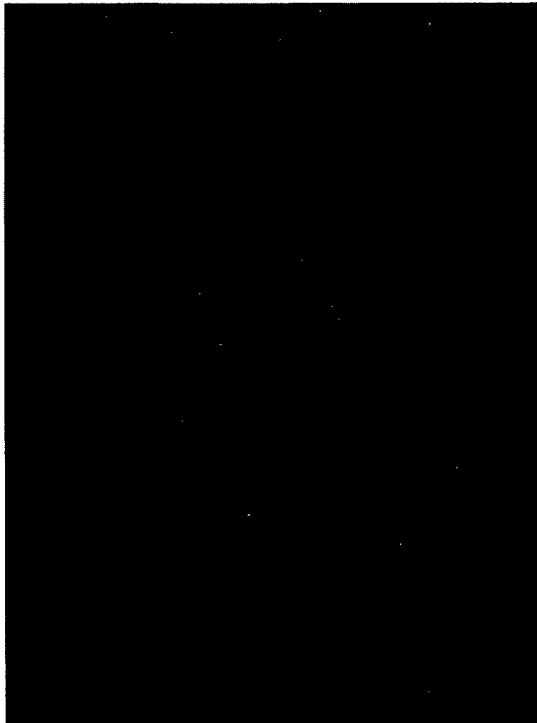


Fig. 1.8 — Hot microhardness of wrought, arc-cast tungsten sheet, W(3), after various annealing treatments

1600° to 3000°C. The objectives of these studies were (1) to characterize the dislocation microstructure in arc-cast tungsten as a function of stress and temperature, and (2) to determine the failure mechanisms in arc-cast and powder-metallurgy processed tungsten.

Dislocation Microstructures in Arc-Cast Tungsten — Development of dislocation substructures in metals during high-temperature deformation plays an important role in determining creep resistance. This substructure consists of dislocation networks or tangles, which form low-angle subgrain boundaries between slightly misoriented regions of material, and free dislocations located within the subgrains. In the present investigation, subgrain sizes, dislocation densities, and subgrain boundary tilt angles were determined in arc-cast, unalloyed tungsten and have been correlated with high-temperature creep conditions. Although the specimens used in this study had all been tested to failure, microstructural examinations were carried out on regions somewhat removed from the fracture to avoid third-stage creep effects and thus concentrate on effects related more nearly to secondary creep.

Material used for this study was 1.5-mm-thick wrought, arc-cast, polycrystalline tungsten, W(3), sheet. Creep-rupture specimens with 6.4-mm gage widths and 25.4-mm gage



1200°C anneal for 2 hours.
Indent at 1308°C.



1600°C anneal for 200 hours.
Indent at 1310°C.

Fig. 1.9 — Photomicrographs of wrought, arc-cast unalloyed tungsten sheet showing typical indents and microstructure after hot hardness testing (200X)

lengths were tested under constant load at temperatures ranging from 1600° to 3000°C and at stress levels ranging from 0.18 to 5.62 kg/mm² in a hydrogen atmosphere. All specimens were annealed at test temperature for 2 hours before stress was applied.

A number of experimental techniques were used in studying the substructure of the creep-tested specimens. Optical microscopy methods were used to determine subgrain sizes and free dislocation densities. These measurements were made using electrolytically polished and etched surfaces parallel to the stress axis. To gain increased resolution and magnification over that available by optical microscopy, replica electron microscopy techniques were used to study etch pits in some samples. Replication of the polished and etched surfaces involved a two-stage plastic/carbon technique, using chromium shadowing. Direct observations of the dislocation microstructures were made by transmission electron microscopy of thin foils prepared by a double-jet electrolytic thinning technique.⁴ These observations were used primarily for determining the dislocation separations within subgrain boundaries and for direct measurements of tilt angles between subgrains. Finally, back-reflection Laue X-ray diffraction photographs were used for indirect determinations of subgrain sizes and subgrain boundary tilt angles. This method, described previously,⁵ has the advantage over direct microscopic methods of providing bulk measurements integrated over a volume of the sample. A summary of the results for the tungsten samples examined is given in Table 1.1.

⁴R. L. Ladd and R. C. Rau, "Immersed Double-Jet Technique for Electrothinning Tungsten for Transmission Electron Microscopy," *Rev. Sci. Instrum.*, Vol. 38, 1967, p. 1162.

⁵"AEC Fuels and Materials Development Program Progress Report No. 71," GE-NMPO, GEMP-1002, December 29, 1967, pp. 18-28.

TABLE 1.1
MICROSTRUCTURAL DATA ON ARC-CAST TUNGSTEN

Sample Number	Creep Testing Conditions		Subgrain Diameter, mm		Free Dislocation Density, 10^4 per mm^2		Subgrain Boundary Tilt Angle, degrees	Dislocation Separation in Sub-Boundaries, Å		Dislocation Density in Sub-Boundaries, 10^5 per mm^2
	Temperature, °C	Stress kg/mm ² psi	Optical	X-Ray	Optical	Electron		X-Ray	Electron	
W(3)-69	1600	5.62 8000	~0.01	<0.01		4.7			525	
-71	1600	3.37 4800	~0.01	<0.01	3.5					
-50	1800	3.37 4800	0.013	0.057	7.4	12.8	0.294		780	
-87	1800	2.46 3500	0.075	0.084	1.0		0.207	897	1340	2.73
-52	1800	2.11 3000							1507	
-53	2000	2.11 3000	0.028	0.090	3.5		0.364	505	1070	4.47
-58	2000	1.76 2500			0.3					
-39	2000	1.41 2000	0.083	0.096	0.30	0.96	0.265	721		3.05
-46	2000	1.41 2000	0.075	0.077		1.5	0.365	512		5.22
-45	2000	1.05 1500	0.14	0.10	1.3		0.257	712	500	2.83
-13	2200	1.41 2000	0.067	0.10	2.6	11.1	0.321	589		3.48
-16	2200	0.70 1000	0.10	0.12	1.3		0.522	355	1250	4.79
-38	2400	1.05 1500	0.05	0.092	4.2	3.4	0.333	567		4.00
-21	2400	0.70 1000			0.71					
-85	2400	0.56 800	0.10	0.21	0.42		0.160	1152	633	8.42
-24	2400	0.56 800			1.2					
-22	2400	0.46 650			0.53					
-19	2600	0.84 1200	0.057	0.16	0.9	4.9	0.366	510		2.55
-27	2600	0.28 400	0.40	0.55	1.6		0.342	531		6.85
-28	2800	0.35 500	0.18	0.33	1.1		0.220	828		7.36
-36	2800	0.21 300	0.27	0.30	0.32		0.344	529		12.64
-49	3000	0.21 300	0.31	0.42	1.3		0.272	678		7.14

Optical microscope examination of the tested specimens showed that the structure almost invariably consisted of very large grains, often covering the entire width and thickness of the pieces. This large grain size was verified by Laue back-reflection X-ray photographs, and permitted such photographs to be obtained from single grains. A few exceptions to this large-grained microstructure were specimens tested at the lower temperatures (1600°C and 1800°C) and higher stress levels (>3 kg/mm²). In these specimens, the typical large-grained microstructure occurred at the surfaces, but a fine-grained polycrystalline texture was retained in the interior.

Substructure developed within the large grains during testing consisted of subgrain boundaries and free dislocations, both of which are revealed by etch pits, as shown in the optical micrographs of Figure 1.10. Typical back-reflection Laue photographs are shown in Figure 1.11. The pattern in Figure 1.11a shows typical clusters of small spots corresponding to the subgrain reflections from a single large tungsten grain, while that in Figure 1.11b shows spotty Debye-Scherrer rings from small randomly oriented grains in a low-temperature, high-stress specimen. Such a pattern, which must be produced by grains having a mean dimension of about 10^{-2} mm, cannot be used for subgrain measurements.

Subgrain diameters measured by direct optical examination are listed in column five of Table 1.1; those determined indirectly from the Laue photographs are listed in column six. The agreement between the results is considered quite good, although the subgrain diameters indicated by X-ray tend to be slightly larger than those measured with the microscope. This is probably due to overlap and coincidences of spots in the Laue pat-

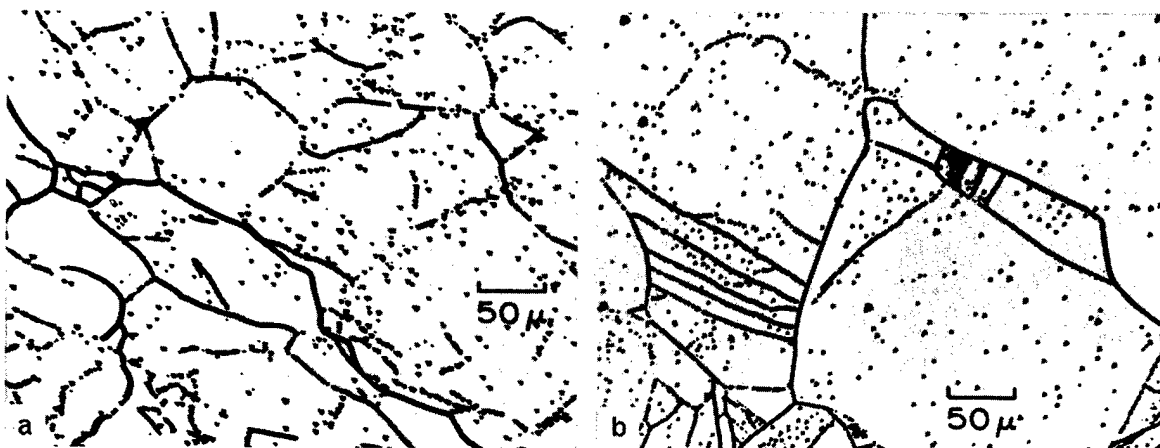


Fig. 1.10 — Optical micrographs showing etch pits delineating subgrain boundaries and free dislocations in tungsten
 (a) Specimen tested at 2000°C and 1.05 kg/mm².
 (b) Specimen tested at 3000°C and 0.21 kg/mm².

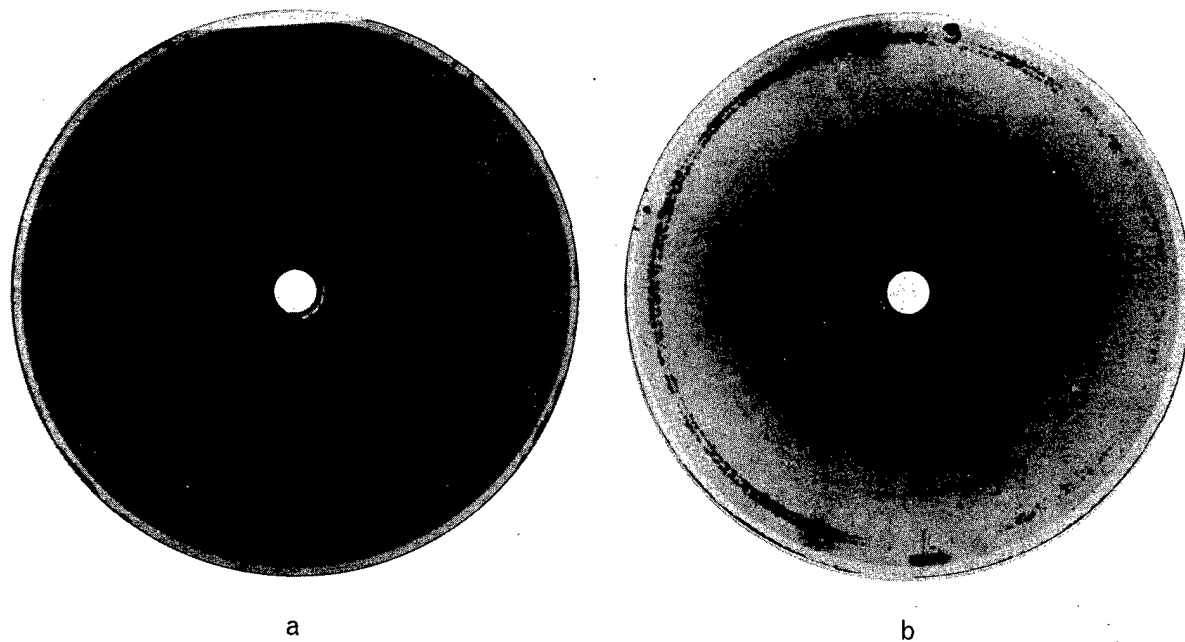


Fig. 1.11 — Typical back-reflection Laue photographs of creep tested tungsten. (a) Diffraction spot clusters due to slightly misoriented subgrains in specimen tested at 2600°C and 0.84 kg/mm².
 (b) Spotty Debye-Scherrer rings from polycrystalline region of specimen tested at 1600°C and 5.62 kg/mm².

terns, leading to low estimates of spot densities within the clusters and therefore high calculated subgrain diameters.

The subgrain sizes in tungsten are independent of test temperature and show an inverse relationship to creep stress, as indicated in Figure 1.12. This log-log plot shows a nearly linear dependence, similar to that obtained for aluminum,⁶ iron,⁷ and steels^{8,9} tested at various stress levels. In a recent review, Sherby and Burke¹⁰ correlated subgrain sizes, L , with stress, σ , for a number of metals, and showed that the data seem to obey a power relation of the type

$$\sigma = KL^\beta, \quad (1.8)$$

where β is almost equal to unity. The tungsten data of Figure 1.12 appear to follow a similar relation.

Free dislocation densities were determined by counting the etch pits within subgrains in areas such as those seen in the optical micrographs of Figure 1.10. In addition, free etch pits in some specimens were counted from composite replica electron micrographs such as that shown in Figure 1.13. Results obtained from the two counts are listed in columns seven and eight, respectively, of Table 1.1. Unlike subgrain sizes, which are a function only of creep stress, the free dislocation density depends upon both temperature and stress. The relationship is illustrated in Figure 1.14. As shown by this plot, the number of etch pits, or the density of free dislocations, increases with increasing stress at constant temperature and increases with increasing temperature at constant stress. To maintain a fixed concentration of free dislocations, the temperature must be decreased if the stress is increased.

The relationship of the free dislocation density (ρ) to stress appears similar to that observed for the linear creep rate ($\dot{\epsilon}_s$) as a function of stress (power law at constant temperature) for this same material. Good correlation of the creep rate data was obtained when $\dot{\epsilon}_s$ was divided by the diffusion coefficient (Figure 1.3) as suggested by Sherby¹¹ for polycrystalline solids. When the same technique is applied to the dislocation density data, good correlation is also obtained, as shown in Figure 1.15. The same stress dependency (4.2) is obtained for the diffusion compensated ρ as for the diffusion compensated $\dot{\epsilon}_s$ parameter. This linear portion of the curve is believed to result from creep by dislocation climb or by the motion of jogged screw dislocations involving an equilibrium concentration of vacancies. Barrett¹² indicates that slip models based on the glide of jogged screw dislocations can predict an approximate power law region with $\dot{\epsilon}_s \propto \sigma^5$ but require the ρ to be a strong function of stress (σ^3 or σ^4). The present data appear to support this model, at least for the high-temperature, low-stress region. The dislocation densities in the low-temperature, high-stress region, showing a deviation from the power law dependence, are apparently influenced by excess vacancies.

⁶I. S. Servi and N. J. Grant, "Structure Observations of Aluminum Deformed in Creep at Elevated Temperatures," Trans. of AIME, Vol. 191, 1951, p. 917.

⁷A. Goldberg, "Influence of Prior Cold Work on the Creep Resistance and Microstructure of a 0.05% Carbon Steel," J. Iron and Steel Inst., Vol. 204, 1966, p. 268.

⁸F. Garofalo, O. Richmond, W. F. Domis, and F. von Gemmingen, "Strain-Time, Rate-Stress and Rate-Temperature Relations During Large Deformations in Creep," Joint International Conference on Creep, The Institution of Mechanical Engineers, London, 1963, p. 1-31.

⁹F. Garofalo, W. F. Domis, and F. von Gemmingen, "Effect of Grain Size on the Creep Behavior of an Austenitic Iron-Base Alloy," Trans. Met. Soc. of AIME, Vol. 230, 1964, p. 1460.

¹⁰O. D. Sherby and P. M. Burke, "Mechanical Behavior of Crystalline Solids at Elevated Temperatures," Progress in Materials Science, Vol. 13, No. 7, 1967, p. 325.

¹¹O. D. Sherby, "Factors Affecting the High Temperature Creep of Polycrystalline Solids," Acta Met., Vol. 10, 1962, p. 135.

¹²C. R. Barrett, "On the Stress Dependence of High Temperature Creep," Trans. of AIME, Vol. 239, 1967, p. 1726.

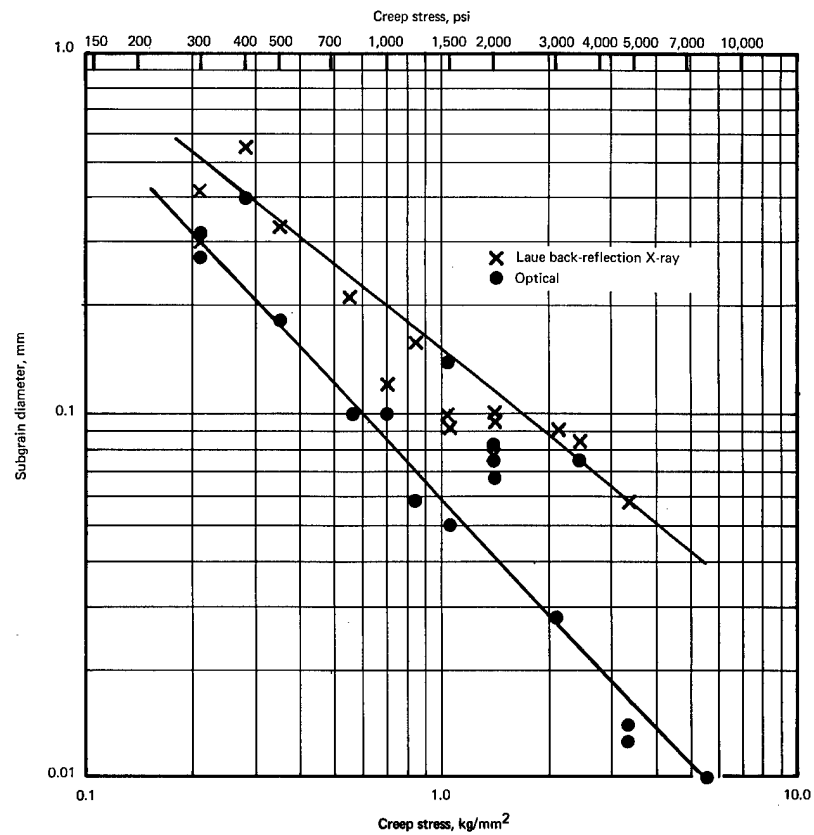


Fig. 1.12 — Effect of stress on the subgrain diameter of arc-cast tungsten as the result of creep-rupture testing from 1600° to 3000°C

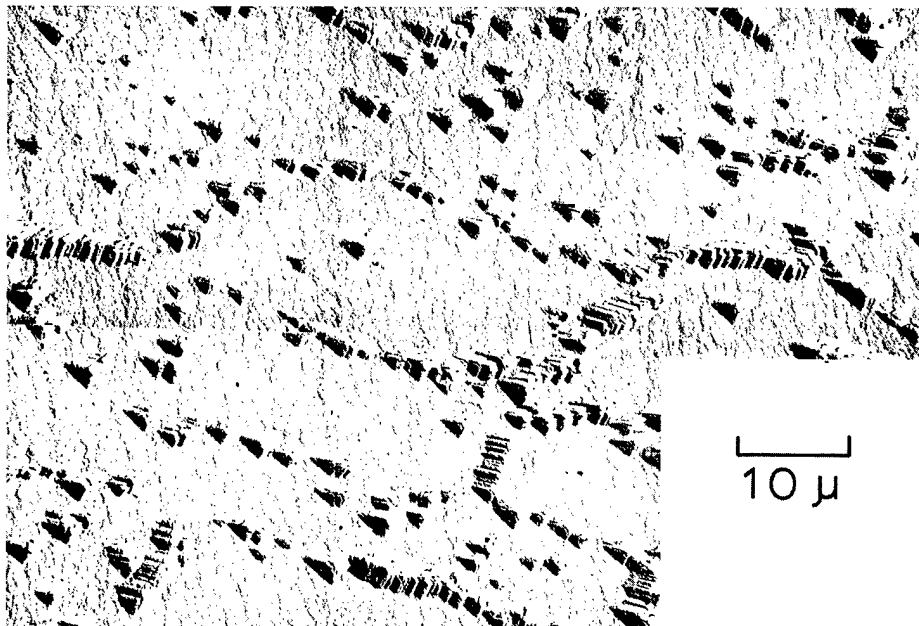


Fig. 1.13 — Composite replica electron micrograph of overlapping areas used for etch-pit counting. Tungsten tested at 1600°C and 5.62 kg/mm².

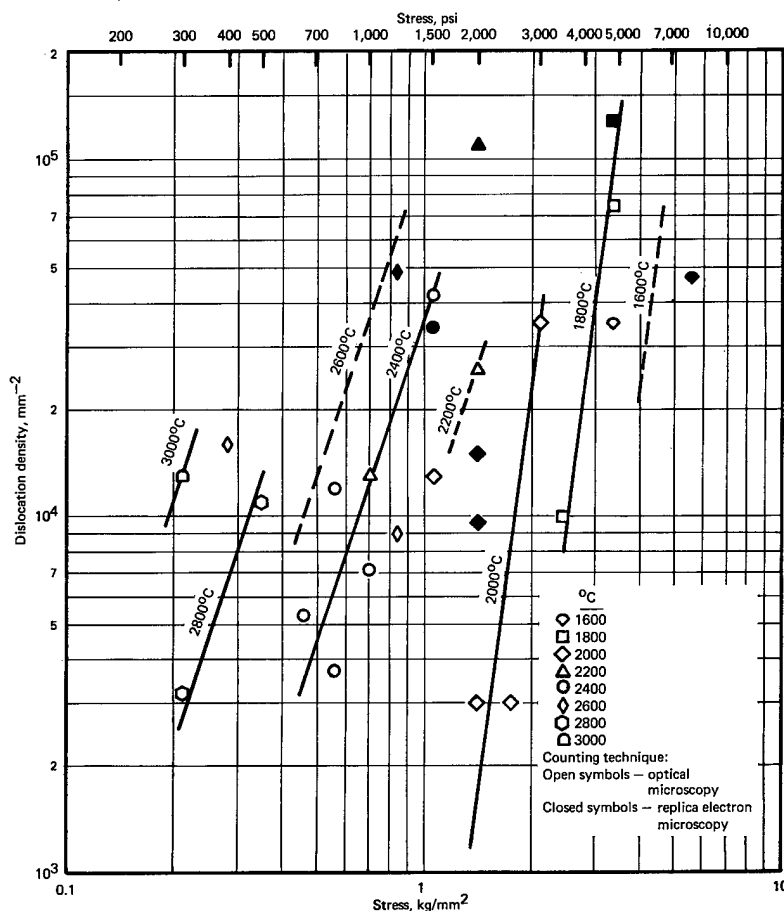


Fig. 1.14 — Number of free etch pits (dislocations) as a function of stress and temperature for wrought, arc-cast tungsten after creep tests from 1600° to 3000°C

Average misorientation angles between subgrains, determined by the back-reflection Laue technique, are listed in column nine of Table 1.1. The values obtained range from 0.16 to 0.52 degree, with the average for all samples being 0.31 degree. If the actual number of subgrains present has been underestimated, because of overlap of Laue spots, the calculated tilt angles may be somewhat too large, but the error should not exceed about 0.05 degree. These values are in good agreement with subgrain misorientations reported for other creep tested metals.^{13,14} To check the values of tilt angle directly, measurements of misorientations between subgrains in one sample were made from selected area electron diffraction patterns obtained with the electron microscope. Values obtained by this technique ranged from 0.17 to 0.47 degree, with the average being 0.29 degree, in good agreement with the X-ray results.

From the tilt angles, the average dislocation separation within the subgrain boundaries was calculated. This separation, S , is given by the expression¹⁵

¹³F. Garofalo, L. Zwell, A. S. Keh, and S. Weissmann, "Substructure Formation in Iron During Creep at 600°C," *Acta Met.*, Vol. 9, 1961, p. 721.

¹⁴R. W. Guard, "Discussion of Parker and Washburn Paper on the Role of the Boundary in Creep Phenomena," *Creep and Recovery*, American Society for Metals, 1957, p. 251.

¹⁵S. Amelinckx and W. Dekeyser, "The Structure and Properties of Grain Boundaries," *Solid State Phys.*, Vol. 8, 1959, p. 325.

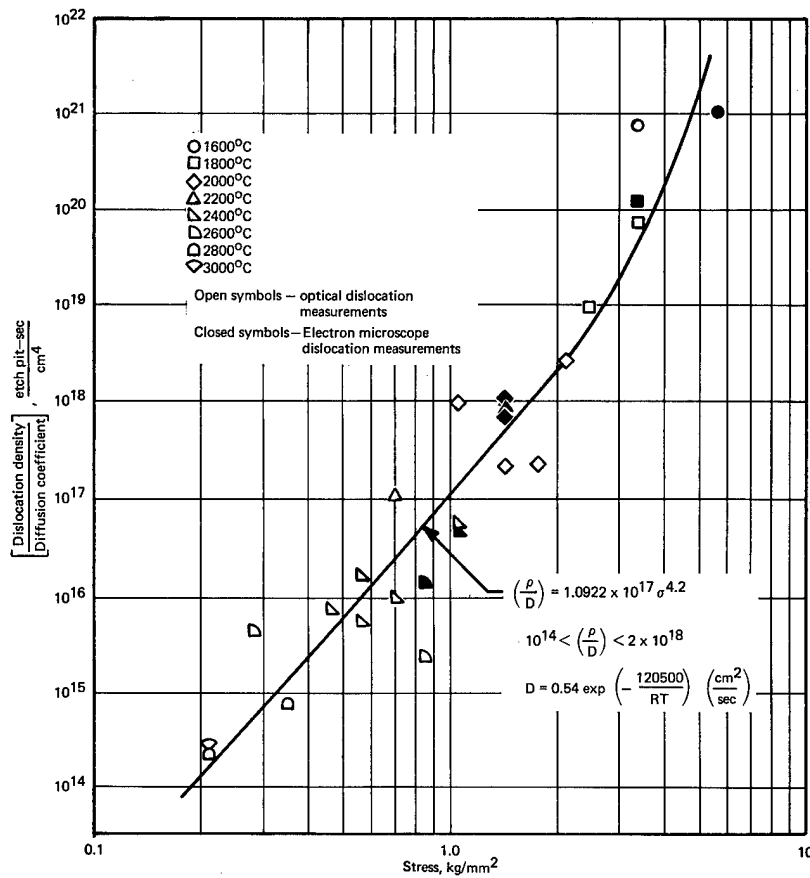


Fig. 1.15 — Correlation of diffusion-compensated dislocation density as a function of stress for wrought, arc-cast unalloyed tungsten, W(3), creep tested at temperatures from 1600° to 3000°C

$$S = \frac{b}{2 \sin \theta/2} \quad (1.9)$$

where b is the length of the Burgers vector of the dislocations and θ is the tilt angle. At small angles this expression reduces to

$$S = \frac{b}{\theta} \quad (1.10)$$

where θ is expressed in radians. Using this expression and the tilt angles tabulated in column nine of Table 1.1, the separation distances given in column ten were obtained.

Direct observations of subgrain boundary dislocation configurations and measurements of separations between the dislocations were made by transmission electron microscopy. Two subgrain boundaries analyzed crystallographically are shown in Figures 1.16 and 1.17, while typical measurements of dislocation separations are listed in column 11 of Table 1.1. Although these measured separations represent a small number of individual dislocation networks and cannot be considered good statistical values, they nevertheless verify the accuracy of the calculated values given in column ten.

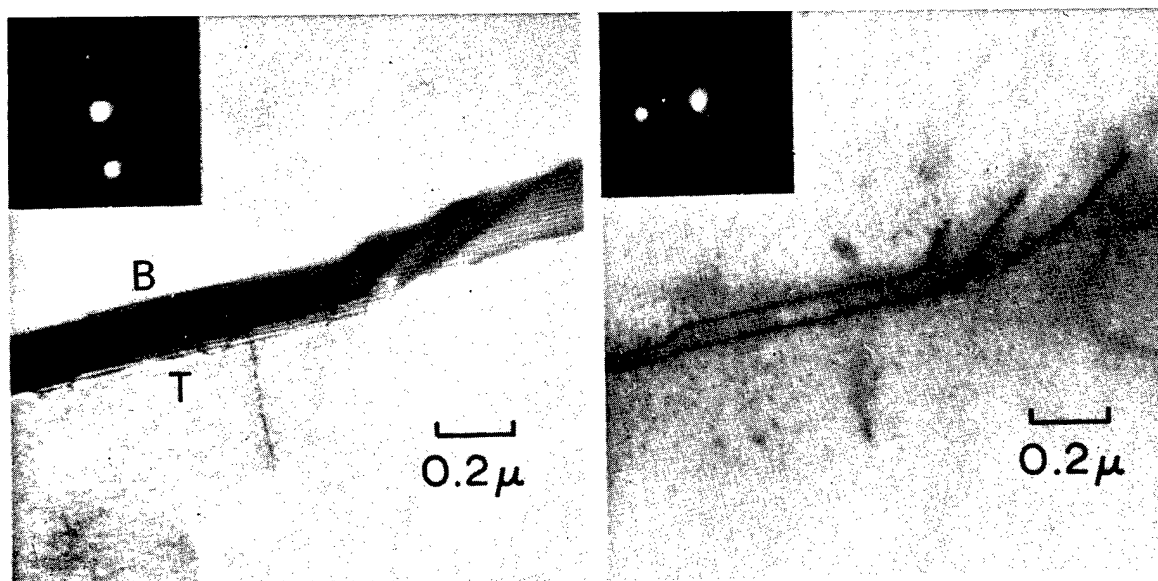


Fig. 1.16 — Transmission electron micrographs of nearly pure tilt boundary in tungsten tested at 1800°C and 2.11 kg/mm^2 . (a) Operating reflection (110) ; intersections of the boundary with the bottom and top surfaces of the foil are indicated by B and T, respectively. (b) Operating reflection $(1\bar{1}0)$.

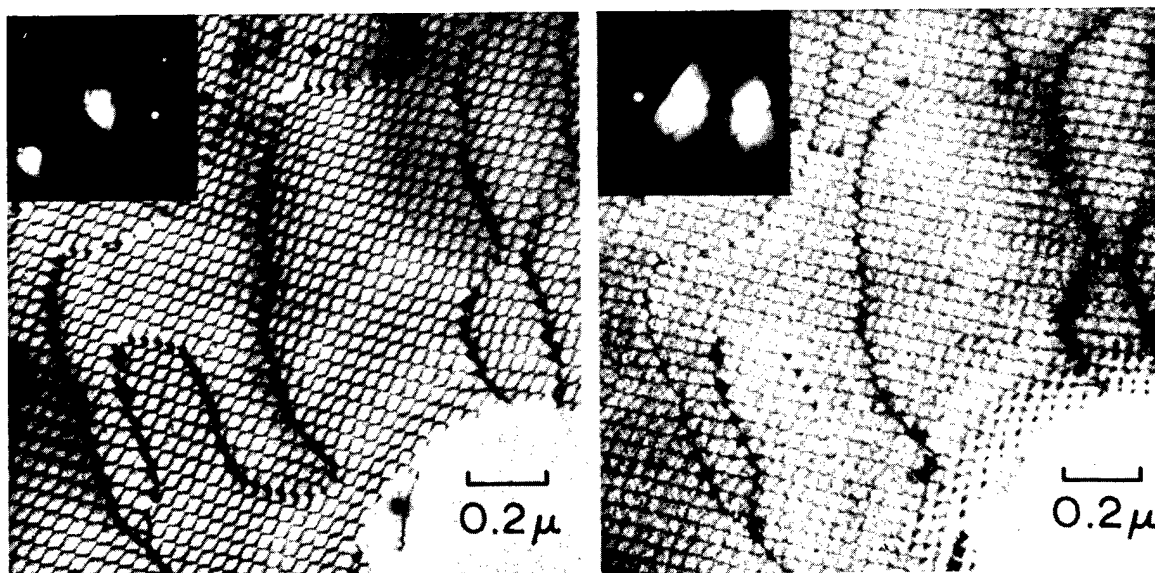


Fig. 1.17 — Transmission electron micrographs of twist boundary in tungsten at 1800°C and 3.37 kg/mm^2 . (a) Operating reflection (020) . (b) Operating reflection (110) .

Finally, from the subgrain diameter and tilt angle data, the dislocation density, ρ , in the subgrain boundaries was calculated from the expression¹⁶

$$\rho = \frac{2\theta}{Lb}, \quad (1.11)$$

where θ is the tilt angle in radians, L is the subgrain diameter, and b is the Burgers vector of the dislocations. This calculation thus gives the number of dislocations per unit area which are tied up in the subgrain boundary networks, rather than the number of free or mobile dislocations which can contribute to deformation under stress. The total number of subgrain boundary dislocations must obviously increase with increasing tilt angles and decreasing subgrain sizes.

Subgrain boundary dislocation densities were calculated from the subgrain diameters and tilt angles derived from the Laue photographs, columns six and nine, respectively, of Table 1.1, and are given in column 12 of that table. The data reveal that the number of dislocations in the subgrain boundaries tends to increase with decreasing stress at constant temperature and gradually increases as the temperature is raised. These observations indicate that during creep, free mobile dislocations within the subgrains move to and accumulate in the subgrain boundaries. Since dislocation movement during high-temperature creep is primarily diffusion controlled, longer times (i.e., lower stresses) and higher temperatures would be expected to increase the number of dislocations occupying subgrain boundaries.

The two subgrain boundaries shown in Figures 1.16 and 1.17 represent the two basic types of subgrain misorientations which can occur in body-centered cubic (bcc) metals. Figure 1.16 shows a nearly pure tilt boundary formed when subgrain misorientation occurs by a rotation about an axis in the boundary plane, while Figure 1.17 shows a twist boundary formed when such misorientation occurs about an axis perpendicular to the boundary plane. Most observed boundaries are formed by a combination of these two basic rotations.

Tilting experiments in the electron microscope reveal that the tilt boundary shown in Figure 1.16 lies on a $(11\bar{1})$ plane, inclined approximately 45 degrees from the (001) foil plane. Intersections of this boundary with the bottom and top surfaces of the foil are denoted B and T, respectively, in Figure 1.16a. It can be seen that the parallel set of closely spaced straight dislocations comprising this boundary is imaged in strong contrast in Figure 1.16a, where the (110) reflection is operating (i.e., $\bar{g} = [110]$), but is at extinction in Figure 1.16b where the $(1\bar{1}0)$ reflection is operating (i.e., $\bar{g} = [1\bar{1}0]$, $\bar{g} \cdot \bar{b} = 0$). This diffraction contrast behavior is consistent with dislocations having a Burgers vector $b = a/2[11\bar{1}]$, indicating that they are edge dislocations and that the boundary is composed primarily of extra half-planes inserted on the $(11\bar{1})$ boundary plane. The fact that a second set of widely spaced dislocations, visible in both micrographs, is superimposed on this network of parallel edge dislocations indicates that the boundary is not a pure tilt boundary, but has a small amount of twist character.

Several direct measurements across the tilt boundary of Figure 1.16 indicate that the misorientation between the subgrains is about 0.83 degree of arc, i.e., a higher than average subgrain misorientation. The measured separation of the edge dislocations in Figure 1.16a is approximately 105 Å. Making a geometrical correction for the measured slope of the boundary plane, the true spacing of the dislocations is then 183 Å. This is in very good agreement with the value of 188 Å calculated from equation (1.10) for a pure tilt boundary composed of $a/2 \langle 111 \rangle$ dislocations and having a tilt angle of 0.83 degree.

¹⁶D. McLean, "Creep Processes in Coarse-Grained Aluminum," J. Inst. Metals, Vol. 80, 1951-52, p. 507.

The twist boundary of Figure 1.17 is a very extensive planar boundary, lying on the (001) plane parallel to the plane of the foil. The extinction conditions illustrated by the photomicrographs of Figure 1.17 indicate that the network is composed of three sets of straight dislocations, two having Burgers vectors of the type $a/2 \langle 111 \rangle$ and one having $\bar{b} = a \langle 100 \rangle$, as diagramed in Figure 1.18, plus a superimposed set of randomly oriented stranger dislocations which were not identified. One of the following two interactions has occurred to form the short $a \langle 100 \rangle$ dislocation segments:

$$a/2 [111] + a/2 [\bar{1}\bar{1}\bar{1}] = a [100]$$

$$a/2 [11\bar{1}] + a/2 [\bar{1}\bar{1}1] = a [100];$$

however, the diffraction conditions observed were not sufficient to differentiate between these two equivalent possibilities.

Similar networks have been identified in the bcc metals iron^{17,18} and tantalum.¹⁹ The observed mesh shape in Figure 1.17 agrees rather well with that calculated by Carrington, Hale, and McLean¹⁷ for a network on {100}, from strictly theoretical considerations. It should be pointed out, however, that since this boundary does not lie on a {110} plane, it is not pure twist, but actually is a mixed boundary, i. e., it is not composed of pure screw dislocations. The $\langle 100 \rangle$ segments are in screw orientation, but the $a/2 \langle 111 \rangle$ segments have mixed edge and screw character.¹⁵

Using equation (1.10), the angle of misorientation between the two subgrains on either side of this boundary was calculated from the mesh size of the network. This gave a value of about 0.47 degree, in good agreement with a number of measurements on other boundaries and within the range of tilt angles determined by the back-reflection Laue method.

Failure Mechanisms in Arc-Cast and Powder Metallurgy Tungsten – Using replica electron microscopy, Stiegler et al.²⁰ studied the formation of voids or cavities at the grain boundaries of powder-metallurgy processed tungsten subjected to creep deformation at 1650°C and 2200°C. They found that at both test temperatures specimens generally failed in a brittle manner, and they attributed this failure to the growth and linking up of grain boundary cavities.

Recently, however, it has been shown that while powder-metallurgy tungsten creep-rupture tested at temperatures ranging from 1600° to 3000°C failed in a brittle, intergranular manner, specimens prepared from arc-cast material and tested under similar conditions failed in a ductile manner. High-temperature stress-rupture tests of molybdenum also showed similar differences in the failure behavior of powder-metallurgy and arc-cast material.²¹ These results indicate that different mechanisms of failure are operating in the two types of materials. To determine this basic difference, optical microscopy and electron fractography studies of creep-rupture-tested powder metallurgy and arc-cast tungsten were undertaken.

The studies were performed using selected powder-metallurgy (W-4) and arc-cast (W-3) tungsten specimens. These specimens were formed from sheet material with initial thicknesses of 0.5 mm for powder-metallurgy specimens and 1.5 mm for arc-cast specimens.

¹⁷W. Carrington, K. F. Hale, and D. McLean, "Arrangements of Dislocations in Iron," Proc. Roy. Soc., A Vol. 259, 1960, p. 203.

¹⁸S. M. Ohr and D. N. Beshers, "Crystallography of Dislocation Networks in Annealed Iron," Phil. Mag., Vol. 8, 1963, p. 1343.

¹⁹D. Hull, I. D. McIvor, and W. S. Owen, "The Distribution of Dislocations in Annealed Tantalum," J. Less-Common Metals, Vol. 4, 1962, p. 409.

²⁰J. O. Stiegler, K. Farrell, B. T. M. Loh, and H. E. McCoy, "Nature of Creep Cavities in Tungsten," Trans. ASM, Vol. 60, 1967, p. 494.

²¹P. N. Flagella, "High-Temperature Stress-Rupture Characteristics of Mo and Mo Alloys," AIAA Journal, Vol. 5, 1967, p. 281.

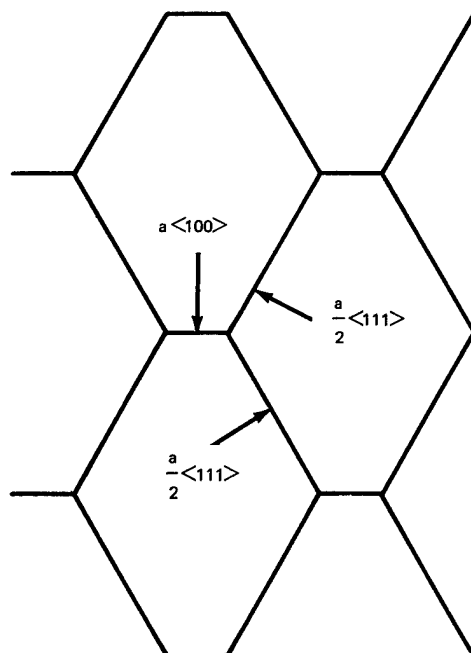


Fig. 1.18 — Schematic drawing of the three sets of dislocations comprising the twist boundary network of Figure 1.17

Specimens examined had been creep tested at 1600°, 2000°, 2200°, and 2600°C, with the results listed in Table 1.2.

For the fractographic study, fresh fracture surfaces in the highly stressed region near the original break were created by clamping the specimen in a vise with about 3 mm of the broken end protruding and sharply rapping the protruding end. These newly exposed surfaces were then replicated by the standard two-stage plastic/carbon technique, using chromium shadowing, and examined in the electron microscope.

After replication, these same pieces were mounted and mechanically polished for metallographic examination. The pieces were mounted edge-on, with the view perpendicular to

TABLE 1.2

TUNGSTEN SPECIMENS USED FOR STUDY OF FAILURE MECHANISM

Sample No.	Test Temperature, °C	Stress		Time to Rupture, hr	Elongation, %	Maximum Void Content, %	Measured Void Content, %	Ratio of Measured/Max. Void Content, %	Average Grain Size, microns
		kg/mm ²	psi						
Powder Metallurgy									
W(4)-1-73	1600	4.22	6000	51.27	32	24.2	5.58	23.1	32.5
-79	2000	2.11	3000	23.17	27	21.3	2.46	11.5	38.0
-18	2200	1.41	2000	15.29	15	13.0	2.02	15.5	48.5
-10	2200	1.12	1600	60.65	17	14.5	2.11	14.6	48.5
-8	2600	0.84	1200	8.84	8	7.4	1.11	15.0	215.5
-7	2600	0.70	1000	25.08	5	4.8	0.90	18.8	264.0
Arc-Cast									
W(3)-48	1600	4.22	6000	30.90	76				
-53	2000	2.11	3000	6.70	70				
-14	2200	1.05	1500	40.70	106				
-25	2600	0.56	800	4.77	64				

the stress axis, and were examined and photographed in the as-polished condition. In this way, any stress-induced porosity was observed in its original state, unaltered by chemical attack. Following examination for porosity, some of the specimens were etched for grain size evaluation.

Optical microscopy of the as-polished surfaces showed an abundance of grain boundary cavities in the powder-metallurgy tungsten, and an almost total lack of such cavities in the arc-cast material. Representative micrographs are presented in Figure 1.19, where a and b are powder-metallurgy material, and c and d are arc-cast material.

As illustrated by these micrographs, the powder-metallurgy material consisted of fairly equiaxed grains, which increased in average size with increasing test temperature. Grain boundary separation and cavitation were very pronounced, especially along boundaries which were transverse to the stress direction. On the other hand, arc-cast material was composed of very large grains extending across the total thickness of the specimens and showed practically no tendency to form cavities. A rare instance of a grain boundary cavity in the arc-cast specimen tested at 1600°C is indicated by the arrow in Figure 1.19c.

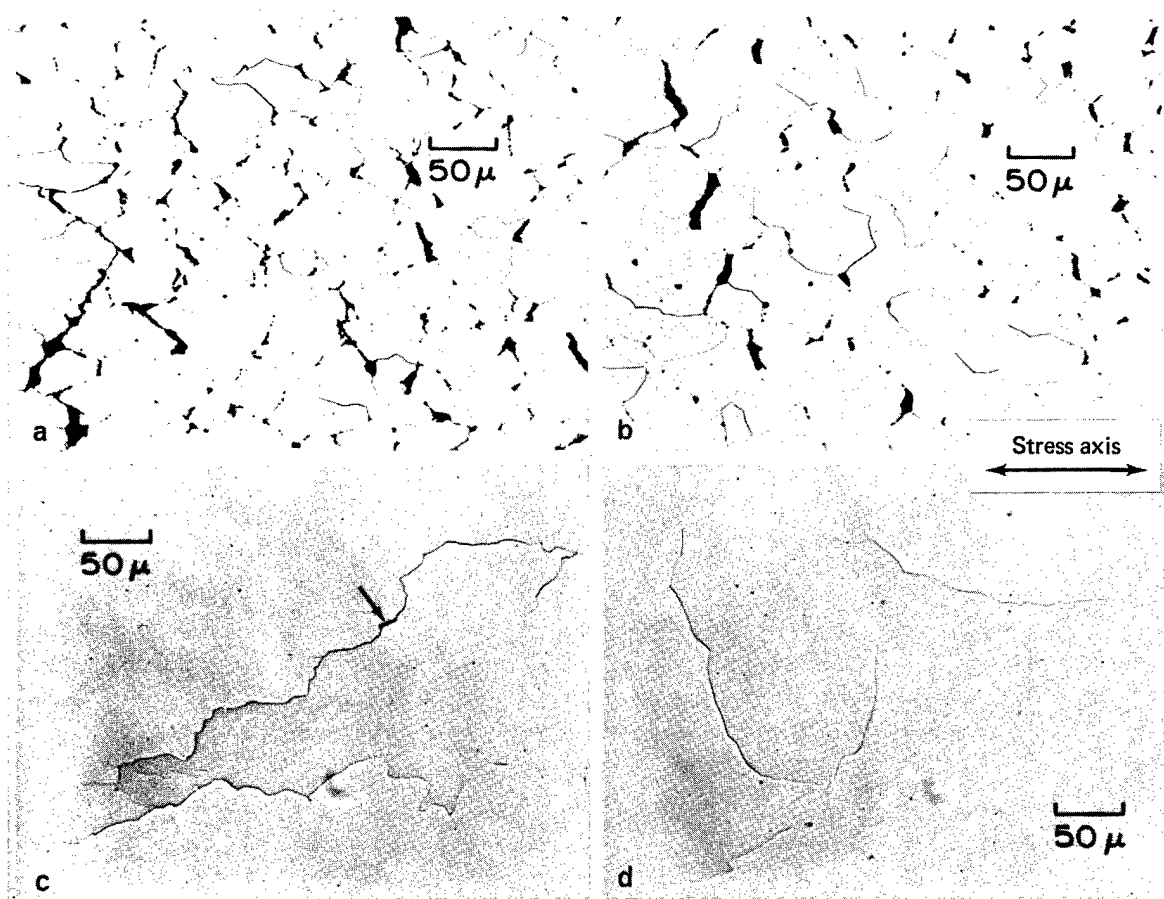


Fig. 1.19 — Optical micrographs of creep-rupture-tested tungsten in as-polished condition. (a) Powder-metallurgy specimen tested at 1600°C and 4.22 kg/mm². (b) Powder-metallurgy specimen tested at 2000°C and 2.11 kg/mm². (c) Arc-cast specimen tested at 1600°C and 4.22 kg/mm². (d) Arc-cast specimen tested at 2000°C and 2.11 kg/mm².

Replica electron microscopy of the powder-metallurgy samples showed that the fracture mode was almost totally intergranular, especially for the low-temperature, high-stress conditions, and that the exposed grain boundary surfaces contained a profusion of cavities. Typical examples are illustrated in Figure 1.20. At low temperatures the voids were usually irregular in shape, tending to be relatively flattened along the boundary surface and often containing elongated "fingers" suggestive of void coalescence, Figure 1.20a. Such cavities are termed wedged-shaped, or w-type,²² and are believed to originate primarily by grain boundary sliding.^{23,24} At higher temperatures, the shape of the cavities became more polyhedral, especially at low-stress levels, Figure 1.20b. These more rounded, or r-type²² voids, are bounded by flat crystallographic facets which correspond to low-index planes of the cubic lattice.²⁵ Such polyhedral voids form under conditions where surface diffusion permits the cavities to reduce their surface tensions and assume equilibrium shapes. Although a few examples were seen of creep cavities aligned along grain boundary triple junctions, Figure 1.20c, there was nothing to indicate that such junctions were preferred sites for voids. In general, both w-type and r-type cavities tended to be distributed uniformly over the grain boundary surfaces, in agreement with the observations of Stiegler et al.²⁰

In contrast to the powder-metallurgy material, replica electron micrographs of the arc-cast tungsten showed that the fracture at all temperatures was predominantly transgranular, as illustrated in Figure 1.21a. When grain boundary surfaces were seen, they were always relatively clean and contained only a few small irregularities suggestive of cavities, Figure 1.21b. In none of these samples was any evidence seen of cavity coalescence or polyhedral shaped voids.

An attempt was made to quantitatively correlate the observed microstructural features with the mechanical properties of the creep-tested specimens. This involved measurements of the open porosity and grain size in the powder-metallurgy specimens, Table 1.2. However, similar measurements could not be made on the arc-cast material because of the lack of porosity and the extremely large grain size.

For the powder-metallurgy tungsten, which failed with relatively little elongation in comparison with the arc-cast material, it was of interest to determine whether all of the elongation was caused by cavitation or whether other mechanisms also contributed. Accordingly, lineal measurements of open porosity were made from the as-polished surfaces at 250X magnification. These measurements were made parallel to the stress (elongation) direction at approximately 3 to 4 mm from the original fracture of each specimen in regions similar to those shown in Figures 1.19a and b. The averages of ten measurements made on each sample were converted to percentages of the length sampled, and are listed in column eight of Table 1.2.

Maximum possible void content in the stress direction, assuming that the total elongation was due to cavitation, was calculated from the measured elongations listed in column six of Table 1.2 using the relation:

$$\text{Max void content (\%)} = \frac{\text{elongation (\%)} \times 100}{100 + \text{elongation (\%)}}$$

Comparison of the values listed in column seven of the table with the measured values of column eight shows that only a portion of the total elongation can be accounted for by the cavities. This relative proportion, however, remains essentially constant as the test

²²F. Garofalo, *Fundamentals of Creep and Creep-Rupture in Metals*, Macmillan Series in Materials Science, New York, 1965, p. 213.

²³C. Zener, *Elasticity and Anelasticity of Metals*, University of Chicago Press, Chicago, 1948, p. 158.

²⁴H. C. Chang and N. J. Grant, "Mechanism of Intercrystalline Fracture," *Trans. of AIME*, Vol. 206, 1956, p. 544.

²⁵K. Farrell, B. T. M. Loh, and J. O. Stiegler, "Morphologies of Bubbles and Voids in Tungsten," *Trans. ASM*, Vol. 60, 1967, p. 485.

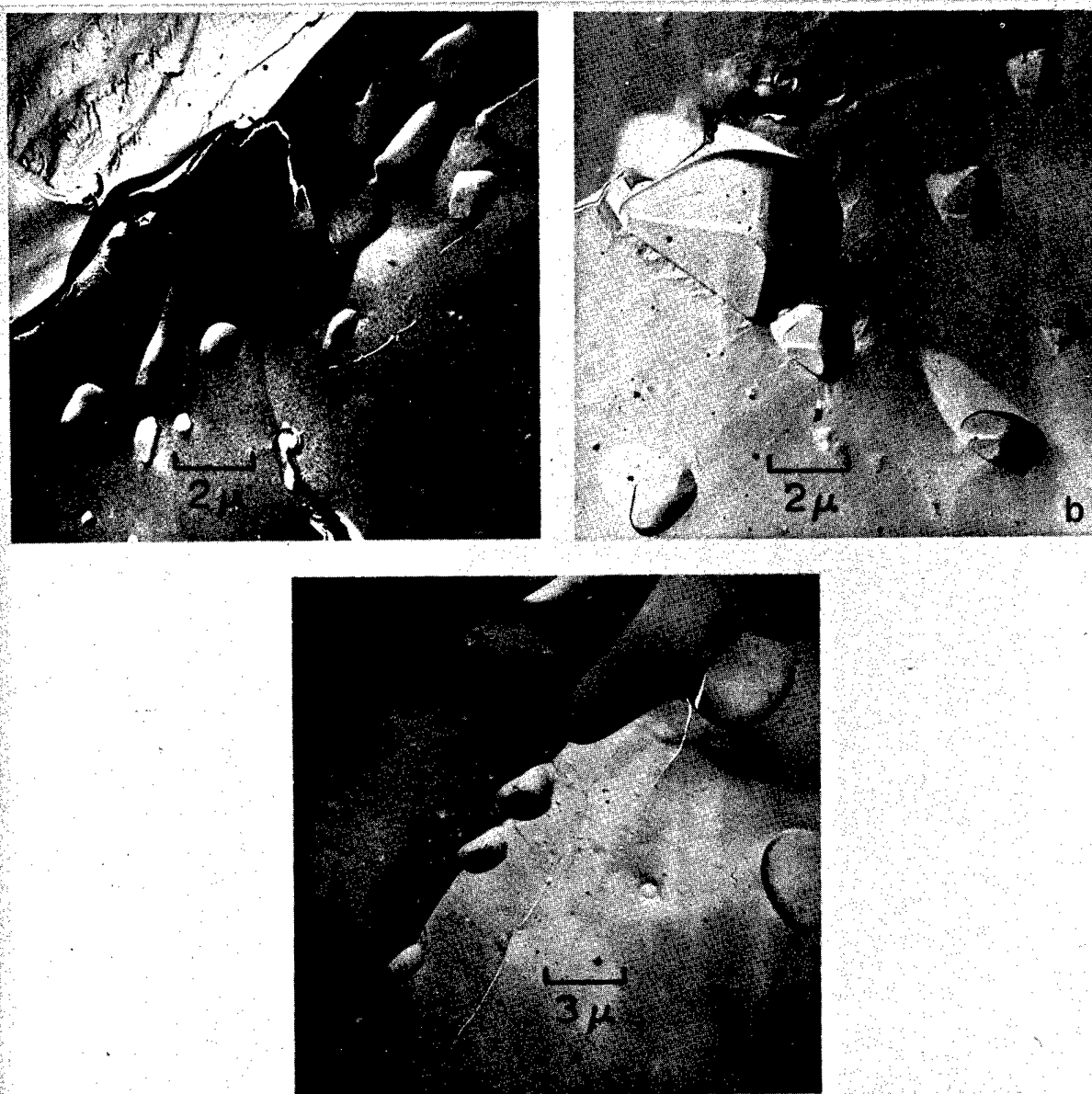


Fig. 1.20 — Electron fractographs of powder-metallurgy tungsten. (a) Irregular creep cavities in specimen tested at 1600°C and 4.22 kg/mm². (b) Polyhedral shaped voids in specimen tested at 2600°C and 0.70 kg/mm². (c) Cavities along a grain boundary triple junction in specimen tested at 2600°C and 0.84 kg/mm².

temperature increases and overall ductility decreases. As shown in column nine of the table, the portion of the elongation due to cavities is about 16 percent of that expected if cavitation were the only source of deformation.

To determine if grain deformation had occurred during creep, lineal grain size measurements were made in the longitudinal (stress) and transverse directions both in the high-stress regions where porosity measurements had been made and in the unstressed holder ends of the specimens. These measurements showed the grains to be elongated approximately 40 percent in the stress direction in all specimens, but this elongation was the



Fig. 1.21 — Electron fractographs of arc-cast tungsten. (a) Transgranular fracture in specimen tested at 2000°C and 2.11 kg/mm². (b) Grain boundary surface in specimen tested at 1600°C and 4.22 kg/mm².

same in unstressed regions as in highly stressed regions. This elongation is undoubtedly the result of prior fabrication history, since the specimens were formed with their lengths parallel to the rolling direction of the starting sheet material. The lack of measurable grain deformation during creep indicates that part of the bulk deformation must, therefore, be due to grain boundary sliding.

Although these observations illustrate the pronounced difference in failure mechanisms of powder-metallurgy and arc-cast tungsten, they do not indicate the underlying cause of this difference. Grain boundary failure, such as that observed in the powder-metallurgy material, can occur if the matrix is strengthened without a corresponding strengthening of the boundaries, or if the boundaries themselves are weakened.²⁶ Matrix hardening can be produced by a dispersion of impurities or precipitates while grain boundary weakening can occur with preferential precipitation in the boundaries, especially if a continuous film of precipitate forms. By the same reasoning, transgranular fracture, such as that observed in the arc-cast tungsten, will be favored if the grain boundaries are strengthened with respect to the matrix. Such strengthening can arise through a decrease in the amount of segregated impurities at grain boundaries, thus leading to increased grain boundary mobility and ductility. Alternatively, certain types of discontinuous precipitation at grain boundaries can strengthen those boundaries by blocking dislocation movement and preventing sliding.

In the present work, no direct evidence was observed of precipitation either within the matrix or along grain boundaries. The techniques employed, however, would not be expected to resolve very small precipitates. To detect such precipitates, transmission electron microscopy or replica electron microscopy of polished and etched surfaces would be required.

²⁶Zener, loc. cit.

TUNGSTEN-BASE ALLOYS

W - 25Re

Recent creep-rupture studies of arc-cast W - 25Re (wt %) sheet material have extended the range of data reported previously²⁷ for this material. A complete summary of all the creep-rupture data generated for arc-cast W - 25Re in this program is presented in Figures 1.22 and 1.23. As reported,²⁷ arc-cast W - 25Re is stronger than arc-cast tungsten up to 2000°C and somewhat weaker than arc-cast tungsten at temperatures above 2000°C. It is important to note that the isotherms in Figures 1.22 and 1.23 are linear even though non-linear isotherms were observed in tests of powder-metallurgy W - 25Re. Apparently, different deformation mechanisms are involved in these two types of material. Two isotherms are shown for 2400°C, in Figure 1.22; two are shown to indicate that at this temperature, the stress-rupture properties of W - 25Re depend upon elongation at rupture.

W - 30Re - 30Mo → p. 51

Stress-rupture and creep data were obtained for a number of different lots of wrought, powder-metallurgy (PM) W - 30Re - 30Mo (at. %) sheet material and one lot of wrought arc-cast (AC) material in sheet form. The PM material was produced at GE-NMPO under Task 1115, "Advanced Fast Breeder Reactor Fuel Element Cladding Development," and the AC material purchased commercially. A comparison of the stress-rupture and linear creep rate test results are shown in Figure 1.24 and 1.25. The AC material exhibits a greater rupture life than the PM material at both 1600°C and 2200°C for the stress levels investigated. This is probably related to the fact that the AC material is considerably more ductile, based on the elongation at rupture.

Photomicrographs of the PM sheet (lot 2) and the commercial AC sheet (lot 3) after creep-rupture testing are shown in Figure 1.26. Both materials tested at 1600°C and 3.37 kg/mm² show uniformly dispersed Re-rich sigma phase. The grain size for both is essentially the same, but intergranular separation is more predominant in the PM material. This is apparently the reason for the lower ductility. After testing at 2200°C and 0.56 kg/mm², the two materials are single phase, but the grain size in the AC material is approximately four times that of the PM material. Deformation appears to be primarily intergranular for the AC material, whereas cavitation or grain-boundary separation appears to contribute significantly to the deformation of the PM material. These factors may also account for the large difference in ductility for the two materials.

The linear creep rate data are essentially the same at 1600°C for the two types of material. At 2200°C, creep resistance of the AC material appears to be significantly greater at the lower stresses. This difference is apparently related to the difference in grain size at 2200°C which leads to different creep mechanisms. The PM material (lot 2) is fine grained (Figure 1.26) and has a stress versus creep rate slope of approximately 1; this indicates that diffusional creep²⁸ is the primary mechanism. The AC material (lot 3) has large grains at 2200°C (Figure 1.26) and gives a stress versus creep rate slope of approximately 5; this indicates that dislocation climb is the primary creep mechanism.²⁹

Special fabrication procedures were employed to produce high-purity W - 30Re - 30Mo sheet material. Creep-rupture tests were performed to compare this material with the previously produced (i. e., nonpurified) sheet material.³⁰ The in-process fabrication pro-

²⁷"Sixth Annual Report - High-Temperature Materials Program, Part A," GE-NMPO, GEMP-475A, March 31, 1967, p. 13.

²⁸Sherby, loc. cit.

²⁹C. Herring, "Diffusional Viscosity of a Polycrystalline Solid," J. Appl. Phys., Vol. 21, 1950, p. 437.

³⁰GEMP-67, p. 25.

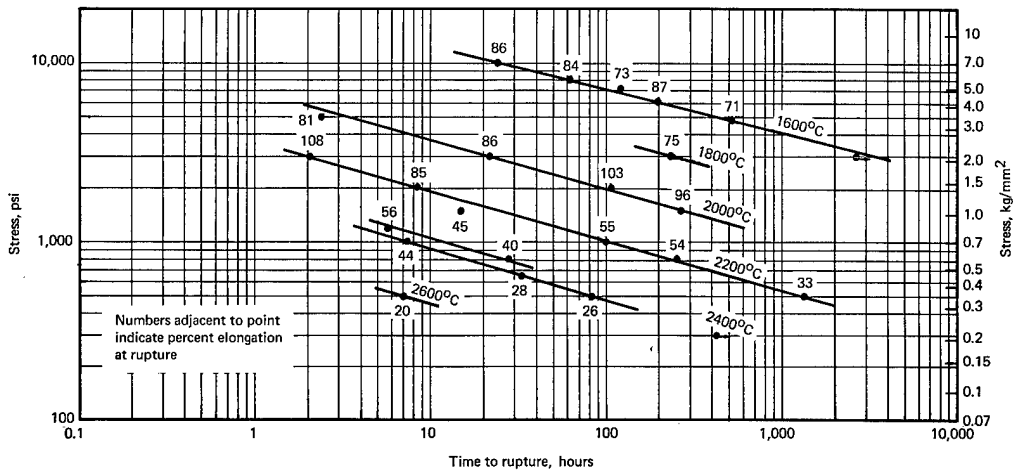


Fig. 1.22 – Stress-rupture data for arc-cast W – 25Re (wt %) alloy sheet tested in hydrogen

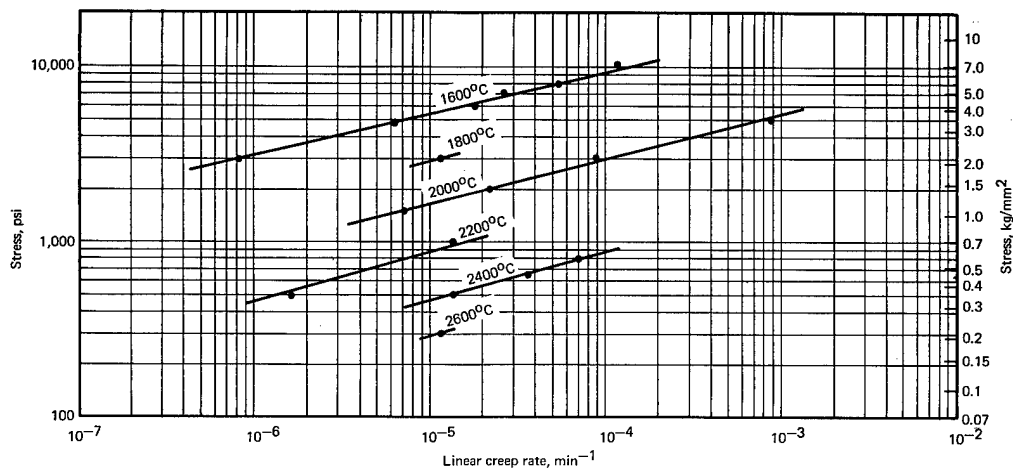


Fig. 1.23 – Linear creep rate data for arc-cast W – 25Re (wt %) alloy sheet tested in hydrogen

cedure was modified to produce four sheets (0.05-cm thick x 7 cm x 10 cm) of material, as shown in Table 1.3. Since the processing procedure differed slightly for each sheet, any effect on the mechanical properties could be determined. Specimens from each sheet were creep-rupture tested in hydrogen at 1600°C and 3.37 kg/mm² and at 2200°C and 0.56 kg/mm².

Typical creep curves, Figure 1.27, show no great difference in the rupture life, creep resistance, or ductility for the four sheets tested at the same conditions. Indication is that the variables associated with each sheet of high-purity material have a minor effect on the creep resistance and ductility, at least for the test conditions evaluated. Figure 1.27 also contains the results for AC and nonpurified PM material of the same nominal composition. The PM material, obtained as regular laboratory-produced sheet, was the least creep resistant of the group at both temperatures. Data for the commercial, recrystallized AC material show it to be somewhat more creep resistant than the regular nonpurified laboratory-produced sheet but considerably less creep resistant than the high-purity PM material.

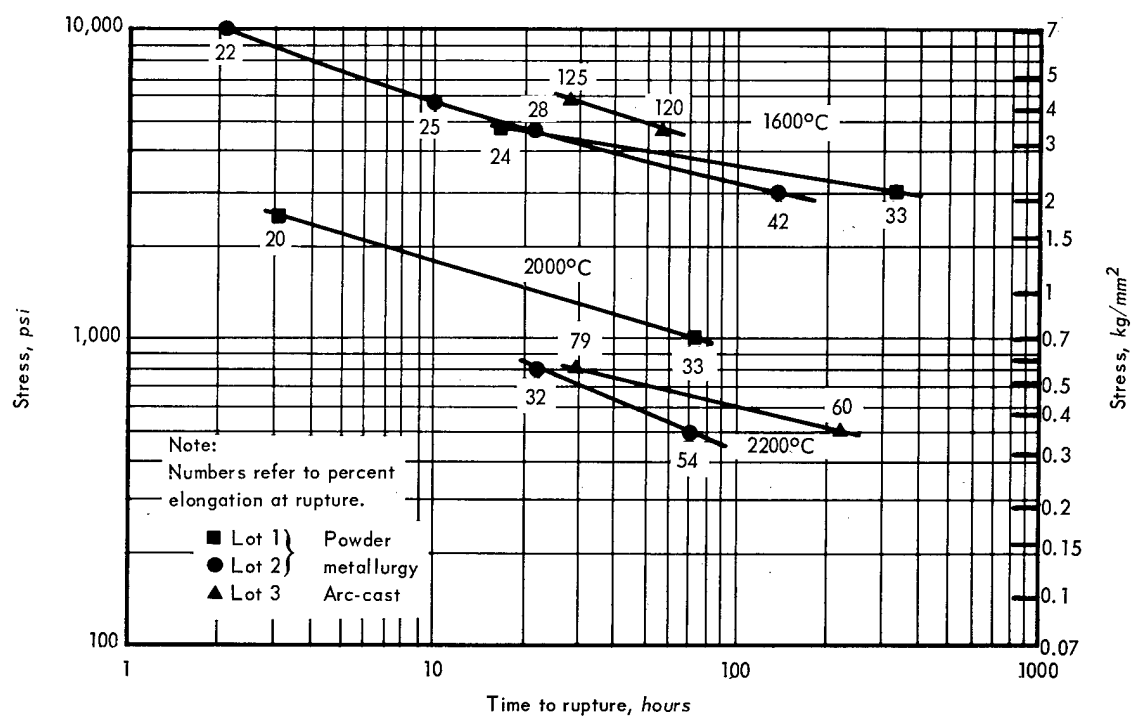


Fig. 1.24 — Stress-rupture results for W — 30Re — 30Mo (at. %) sheet tested in hydrogen

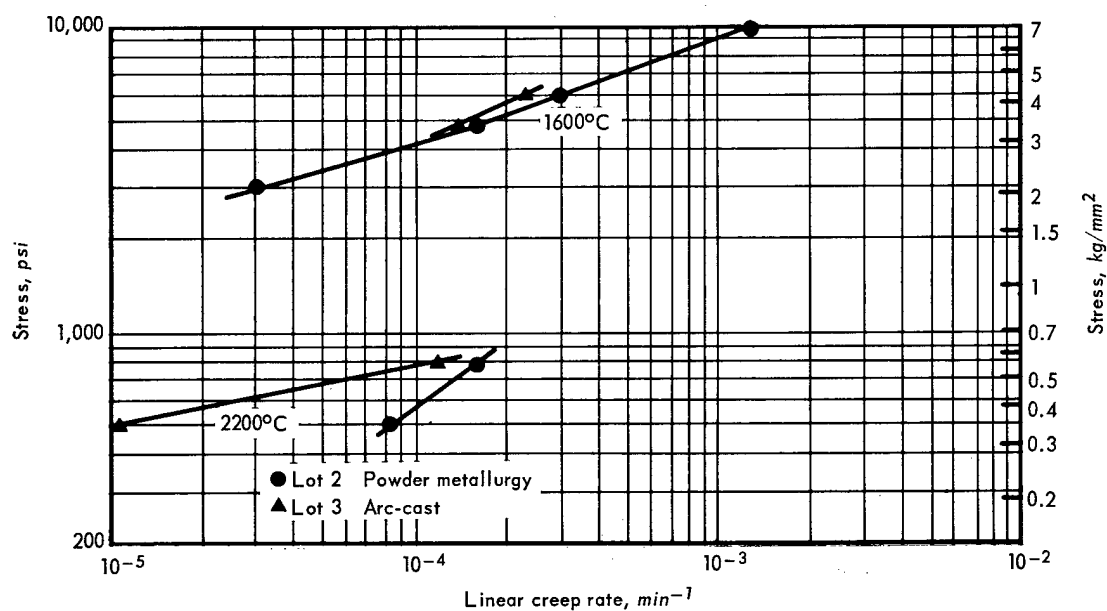


Fig. 1.25 — Creep rate results for W — 30Re — 30Mo (at. %) sheet tested in hydrogen

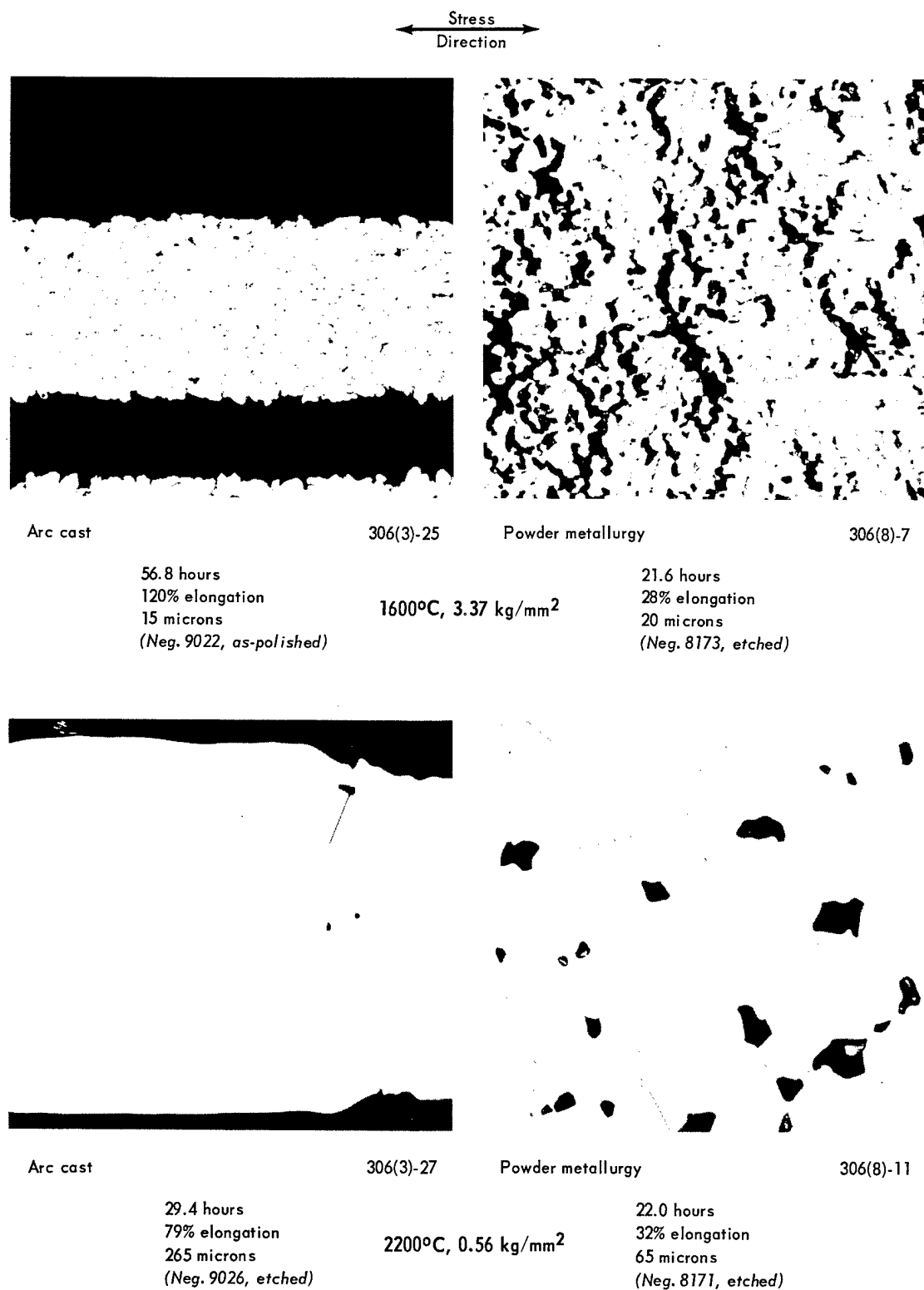


Fig. 1.26 — Photomicrographs of wrought W — 30Re — 30Mo (at. %) sheet after creep-rupture testing in hydrogen; numbers below each photomicrograph refer to time to rupture, elongation at fracture, and average grain size (250X)

TABLE 1.3
FABRICATION PROCEDURE USED TO PRODUCE
HIGH-PURITY W – 30Re – 30Mo SHEET^a

Sheet No.	Process
306(4)	Loose metal powders leached with 0.001 N HCl prior to blending. Not vapor treated.
306(5)	Same as 306(4) but powders leached with 0.001 N HNO ₃ .
306(6)	Same as 306(4) but compacted powders treated 150 hours at 1000°C in hydrogen–water vapor atmosphere prior to sintering.
306(7)	Same as 306(5) but treated as a compact similar to 306(6).

^aAll sheets were made from the identical metal powders and processed simultaneously.

Photomicrographs of the high-purity samples after testing at 1600°C and 2200°C are shown in Figures 1.28 and 1.29. No significant differences are noted between the samples tested at 2200°C. At 1600°C there appears to be some small variation in the second phase (sigma). Chemical analysis of the as-fabricated, high-purity sheet materials yielded the results given in Table 1.4. The major difference appears to be in the AC material where both the carbon and oxygen content are greater than any of the PM sheets. The special purification procedures apparently decrease the carbon content as the process is changed. These data along with the metallographic studies do not indicate the reason for the increased creep resistance of the high-purity material.

MOLYBDENUM

Stress-rupture data were previously reported²⁷ for wrought, arc-cast and wrought, powder-metallurgy, unalloyed molybdenum from 1200° to 2400°C in both hydrogen and argon atmospheres. Differences in the strength and structure for the two types of material were shown. It was also reported that essentially identical results were obtained for AC material purchased from a number of different vendor sources.

Additional data were obtained for AC material to evaluate the creep properties of unalloyed molybdenum.

Constant-load tests of wrought, AC molybdenum sheet (0.05 cm thick) were performed in hydrogen at temperatures from 1200° to 2400°C. Chemical analyses of the as-received material are given in Table 1.5. As shown, sheet material from two different vendor sources was evaluated. Test results are given in Tables 1.6 and 1.7; Table 1.8 gives the stress-rupture data previously reported for wrought, AC molybdenum rod material (0.40-cm gage diameter) along with the creep data obtained in these same tests. Figure 1.30 shows the stress-rupture curves obtained using the three sources of material; good agreement is apparent at 1600°C and 2200°C where duplicate tests were performed. Linear creep rate data for the three materials are presented in Figure 1.31. These data also show good agreement for the three materials at 1600°C and 2200°C. At 2400°C the creep rate curve decreases in slope. In fact, the data points at 2200°C and 0.141 kg/mm² (for M(9)4 material) deviate from the general trend, indicating a slope consistent with the data at 2400°C. The reason for this is not apparent but seems to be related to a unique behavior observed in an evaluation of the individual strain – time curves.

These creep curves, at constant temperature, are presented in Figure 1.32 as a function of the time required to give 10 percent strain. Plotting the curves in this way provides a comparison of the high- and low-stress tests at the same temperature. Additionally, tests at the same stress performed at different temperatures may also be compared conveniently. In this figure, creep curves obtained at 1200°C and 1600°C show a significant primary (first-

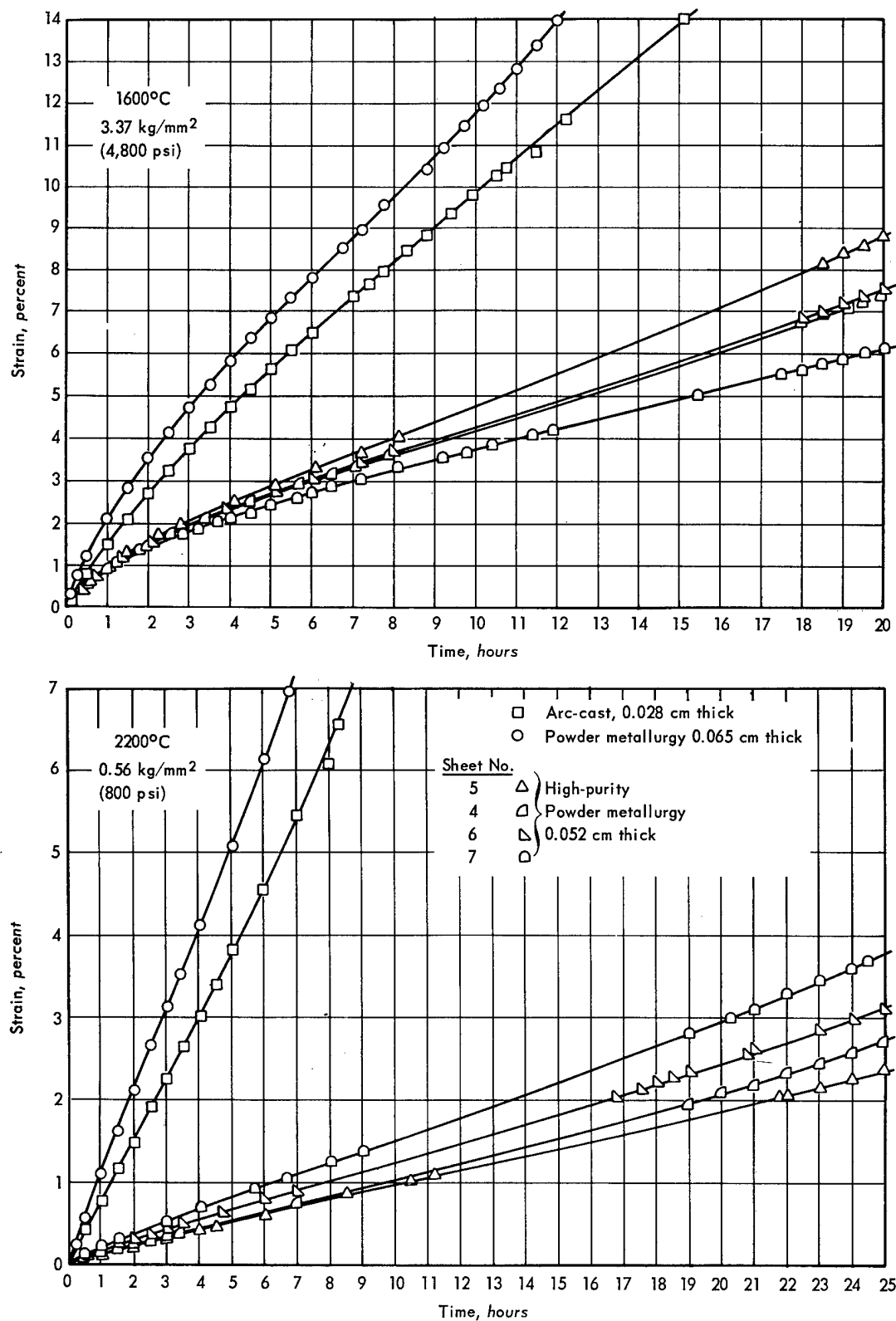
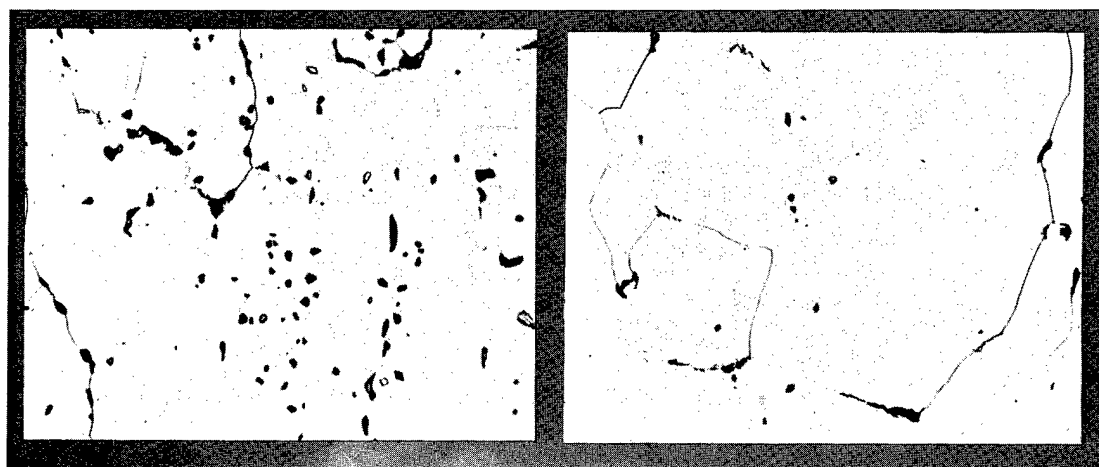


Fig. 1.27 — Creep curves for various lots of wrought W — 30Re — 30Mo (at. %) sheet tested in hydrogen

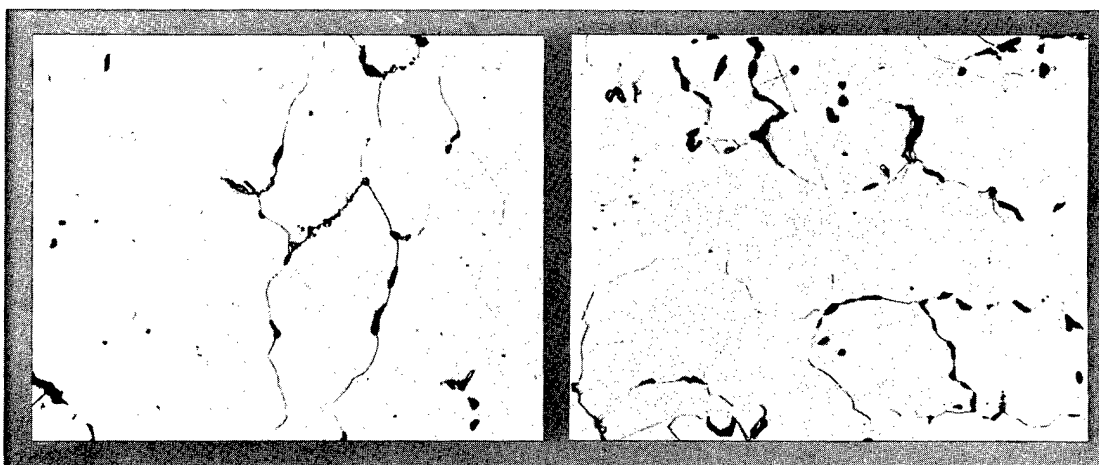


43.7 hr
21.5% elongation
165 microns
(Neg. 9893)

306(4)-12

29.6 hr
15% elongation
135 microns
(Neg. 9894)

306(5)-17



37.8 hr
14.6% elongation
165 microns
(Neg. 9895)

306(6)-18

49.3 hr
21% elongation
145 microns
(Neg. 9896)

306(7)-23

Fig. 1.28 — Photomicrographs of various lots of wrought, powder-metallurgy W — 30Re — 30Mo (at. %) sheet after creep-rupture testing at 1600°C and 3.37 kg/mm² in hydrogen; numbers below each photomicrograph refer to time-to-rupture, elongation at fracture, and average grain diameter. The figure in parentheses following the 306, under each photograph, is the lot number. (Etched, 250X)

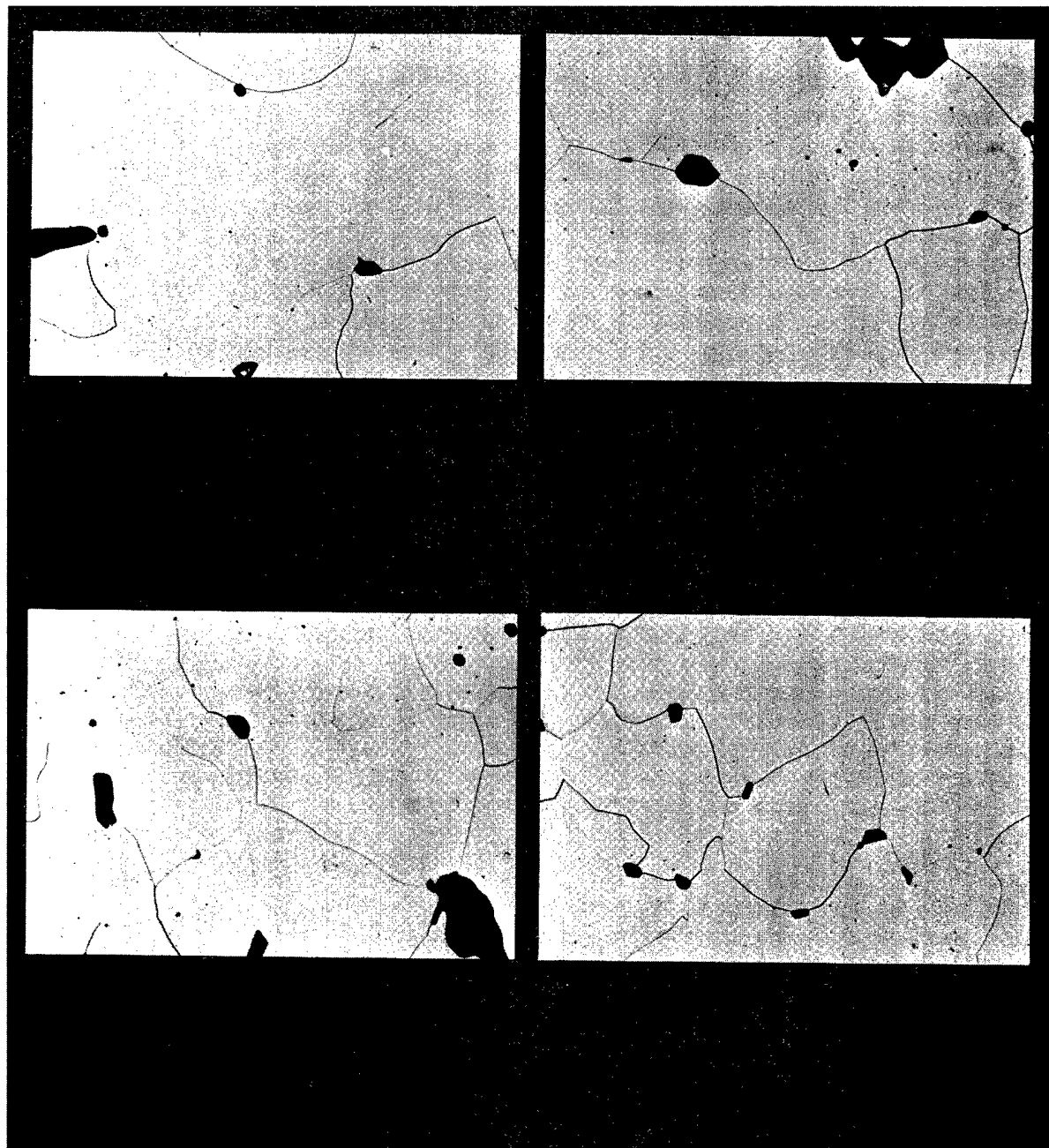


Fig. 1.29 — Photomicrographs of various lots of wrought, powder-metallurgy W — 30Re — 30Mo (at. %) sheet after creep-rupture testing at 2200°C and 0.56 kg/mm² in hydrogen; numbers below each photomicrograph refer to time-to-rupture, elongation at fracture, and average grain diameter. The figure in parentheses following the 306, under each photograph, is the lot number. (Etched, 250X)

TABLE 1.4

CHEMICAL ANALYSIS OF AS-FABRICATED W - 30Re - 30Mo
SHEET SAMPLES FROM VARIOUS LOTS

Lot No.	Impurities, ppm				Fabrication
	C	O	H	N	
2	19	4.9	0.5	0.3	PM regular laboratory process
3	<40	80	1.7	11	Per vendor } Commercial Per NMPO } AC
	41	33	4	4	
4	19	12	0.9	25	PM special purification procedures
5	16	9.8	1	0.2	
6	13	8.1	0.9	0.9	
7	7	11	0.9	4	

TABLE 1.5

CHEMICAL ANALYSIS OF
AS-RECEIVED WROUGHT,
ARC-CAST MOLYBDENUM

Material Source	Impurity Content, ppm			
	C	H	O	N
M(6)4	140	1	17	19
M(9)4	250	1	22	5

TABLE 1.6

CREEP-RUPTURE RESULTS^a FOR WROUGHT, ARC-CAST, UNALLOYED MOLYBDENUM SHEET,^b
M(6)4, TESTED IN HYDROGEN

MnO ₂ , TESTED IN WATERGLASS												
Specimen No.	Test Conditions		Time to Indicated Strain, hr							Rupture		Linear Creep Rate, min ⁻¹
	Temperature, °C	Stress, kg/mm ²	0.2%	0.5%	1%	2%	3%	5%	10%	Time, hr	Elongation, %	
4	1600	2.11	—	—	0.03	0.13	0.28	0.60	1.4	2.5	30	9.8 × 10 ⁻⁴
5	1600	1.76	—	0.05	0.18	0.53	0.98	1.9	4.2	6.9	30	3.6 × 10 ⁻⁴
6	1600	1.41	0.06	0.20	0.58	1.5	2.5	4.7	9.8	25.1	55	1.6 × 10 ⁻⁴
7	1600	1.05	0.26	0.99	2.6	6.5	10.4	18.8	38.7	99.6	64	2.9 × 10 ⁻⁵
16	1600	0.84	9.7	3.1	7.4	17.8	29.6	51.2	100.	247.	47	1.4 × 10 ⁻⁵
3	1600	0.70	3.8	12.0	24.2	48.5	73.0	122.	234.	554.	45	6.8 × 10 ⁻⁶
12	1600	0.56	8.5	26.5	57.5	124.	198.	345.	—	452. ^c	6.4 ^c	2.3 × 10 ⁻⁶
15	1600	0.35	90.5	255.	—	—	—	—	—	348. ^c	0.68 ^c	2.9 × 10 ⁻⁷
8	2200	0.56	—	—	—	—	—	0.02	0.09	0.22	40	—
9	2200	0.35	—	—	0.03	0.12	0.24	0.53	1.2	2.88	53	1.1 × 10 ⁻³
10	2200	0.21	0.10	0.40	0.97	2.0	3.0	5.1	10.1	23.8	49	1.6 × 10 ⁻⁴
11	2200	0.14	1.8	5.5	11.5	21.9	29.8	43.3	67.0	123.	52	1.3 × 10 ⁻⁵
17T ^d	2200	0.10	10.0	28.0	55.0	95.0	126.	169.	232.	244. ^c	11.0 ^c	2.7 × 10 ⁻⁶

^aAnnealed at test temperature for 2 hours in hydrogen before testing.

^b0.05-cm-thick sheet with 0.64-cm by 2.54-cm gage section.

^cTest terminated prior to rupture at time and strain indicated.

^dT denotes specimen transverse to rolling direction.

stage) creep as do the curves obtained at higher stresses at 2200°C. Curves for 0.141 kg/mm² and lower at both 2200°C and 2400°C show no apparent primary or secondary stages of creep. The creep rates reported in Table 1.5 are essentially instantaneous creep rates in the region near time zero. This change in curve shape from the more conventional creep curves obtained at the higher stresses may be related to a change in creep mechanism at low stresses.

Sherby³¹ showed that when the secondary creep rate, divided by the diffusion coefficient, is presented as a function of the stress divided by the modulus a single curve is obtained related to the mechanism of creep. The result of correlating the AC molybdenum data in this manner is presented in Figure 1.33. The 1600°C and 2200°C data show good correlation with a slope of 4.85; Sherby reported that a slope of 4 to 5 is normally obtained. The 1200°C data show a displacement that is not understood. The deviation of the data for 2400°C is apparently related to the effect of the creep-curve shape on the creep rate discussed above.

³¹Sherby, loc. cit.

TABLE 1.7
 CREEP-RUPTURE RESULTS^a FOR WROUGHT, ARC-CAST, UNALLOYED MOLYBDENUM SHEET,^b
 M(9)4, TESTED IN HYDROGEN

Specimen No.	Test Conditions		Time to Indicated Strain, hr								Rupture		Linear Creep Rate, min ⁻¹
	Temperature, °C	Stress, kg/mm ²	0.2%	0.5%	1%	2%	3%	5%	10%	Time, hr	Elongation, %		
40	1200	7.03	—	—	—	0.01	0.04	0.12	0.35	1.06	70	3.6 × 10 ⁻³	
41	1200	5.62	—	—	0.04	0.20	0.42	0.96	2.63	9.70	78	4.8 × 10 ⁻⁴	
42	1200	4.22	—	0.07	0.34	1.15	2.25	4.93	12.4	33.2	72	1.1 × 10 ⁻⁴	
44	1200	3.37	0.12	0.42	1.13	3.05	6.00	13.6	34.2	98.2	84	4.0 × 10 ⁻⁵	
36	1200	2.81	0.76	1.93	4.62	13.2	24.8	50.4	112.	214.	44	1.3 × 10 ⁻⁵	
43	1200	2.11	5.20	14.6	37.5	94.0	159.	278.	611.	1742.	52	2.4 × 10 ⁻⁶	
11	1600	1.41	0.01	0.08	0.33	1.03	1.88	3.71	8.33	17.5	34	1.8 × 10 ⁻⁴	
9	1600	1.05	0.65	1.35	2.67	5.30	8.60	14.8	29.7	59.3	57	5.0 × 10 ⁻⁵	
29	1600	1.05	0.26	0.82	2.09	5.50	9.00	16.0	33.0	81.7	51	4.8 × 10 ⁻⁵	
30	1600	0.844	1.20	2.80	6.00	14.0	23.4	42.2	87.2	241.	52	1.8 × 10 ⁻⁵	
10	1600	0.703	2.80	7.15	15.8	37.2	61.0	110.	228.	488.	35	6.8 × 10 ⁻⁶	
12	2200	0.352	—	0.01	0.04	0.15	0.27	0.55	1.25	3.40	78	1.2 × 10 ⁻³	
13	2200	0.281	—	0.03	0.15	0.48	0.87	1.71	3.72	9.92	52	4.0 × 10 ⁻⁴	
26	2200	0.211	0.11	0.58	1.35	2.90	4.45	7.45	13.6	32.1	73	1.1 × 10 ⁻⁴	
27	2200	0.176	0.54	1.76	3.82	7.93	11.9	19.5	35.0	89.0	82	4.1 × 10 ⁻⁵	
28	2200	0.141	5.45	14.5	27.0	49.0	68.5	99.4	145.	247.	50	7.2 × 10 ⁻⁶	
14	2200	0.141	5.00	11.1	20.3	37.2	53.3	77.3	108.	200. ^d	38	8.5 × 10 ⁻⁶	
49T	2400	0.211	—	0.02	0.04	0.12	0.20	0.36	0.76	1.88	48	2.0 × 10 ⁻³	
60	2400	0.190	0.02	0.06	0.14	0.30	0.56	0.78	1.52	3.89	52	1.0 × 10 ⁻³	
48T	2400	0.176	—	0.02	0.07	0.19	0.32	0.59	1.13	2.80	54	1.2 × 10 ⁻³	
23	2400	0.141	0.12	0.48	1.10	2.36	3.44	5.18	8.37	17.0	63	1.4 × 10 ⁻⁴	
53T	2400	0.120	0.63	1.90	3.81	6.86	9.25	13.0	19.2	28.3	46	4.4 × 10 ⁻⁵	
47T	2400	0.105	2.05	4.90	8.52	14.3	19.0	25.9	35.3	48.5	38	—	
54T	2400	0.084	15.1	31.0	47.2	58.9	66.1	76.9	88.7	101.	32	2.6 × 10 ⁻⁶	

^aAnnealed at test temperature for 2 hours in hydrogen before testing.

^b0.05-cm-thick sheet, 0.64-cm by 2.54-cm gage section.

^cT denotes specimen transverse to rolling direction, all others parallel to rolling direction.

^dPower failure at 88 hours caused increased strain rate.

TABLE 1.8
 CREEP-RUPTURE RESULTS^a FOR WROUGHT, ARC-CAST, UNALLOYED MOLYBDENUM ROD,^b
 M(8)1, TESTED IN HYDROGEN

Specimen No.	Test Conditions		Time to Indicated Strain, hr							Rupture		Linear Creep Rate, min ⁻¹
	Temperature, °C	Stress, kg/mm ²	0.2%	0.5%	1%	2%	3%	5%	10%	Time, hr	Elongation, %	
9	1600	1.76	—	0.02	0.12	0.44	0.82	1.60	3.30	5.18	64	4.5 × 10 ⁻⁴
10	1600	1.41	0.01	0.14	0.49	1.40	2.37	4.35	7.47	11.7	72	1.7 × 10 ⁻⁴
11	1600	1.05	0.11	0.74	2.30	5.60	8.92	13.4	23.3	58.2	53	5.0 × 10 ⁻⁵
13	1600	0.844	1.88	3.48	7.40	16.7	26.7	48.7	105.	222.	82	1.4 × 10 ⁻⁵
12	1600	0.703	5.20	17.0	26.5	45.0	68.5	120.	244.	357. ^c	15	7.0 × 10 ⁻⁶
3	2200	0.316	—	0.02	0.07	0.24	0.44	0.82	1.60	2.66	86	8.9 × 10 ⁻⁴
5	2200	0.246	0.02	0.09	0.17	0.76	1.33	2.52	5.20	9.60	78	2.8 × 10 ⁻⁴
2	2200	0.197	0.26	0.79	1.67	3.43	5.19	8.70	11.6	17.0	44	9.3 × 10 ⁻⁵
4	2200	0.162	1.05	3.32	6.11	11.56	17.0	26.2	31.5	50.0	38	3.1 × 10 ⁻⁵
1	2200	0.141	2.66	6.00	10.6	19.2	27.8	48.5	77.5	145.	64	1.9 × 10 ⁻⁵

^aAnnealed at test temperature for 2 hours in hydrogen before testing.

^b0.41-cm-dia. by 2.54-cm-long gage section.

^cTest terminated, no rupture.

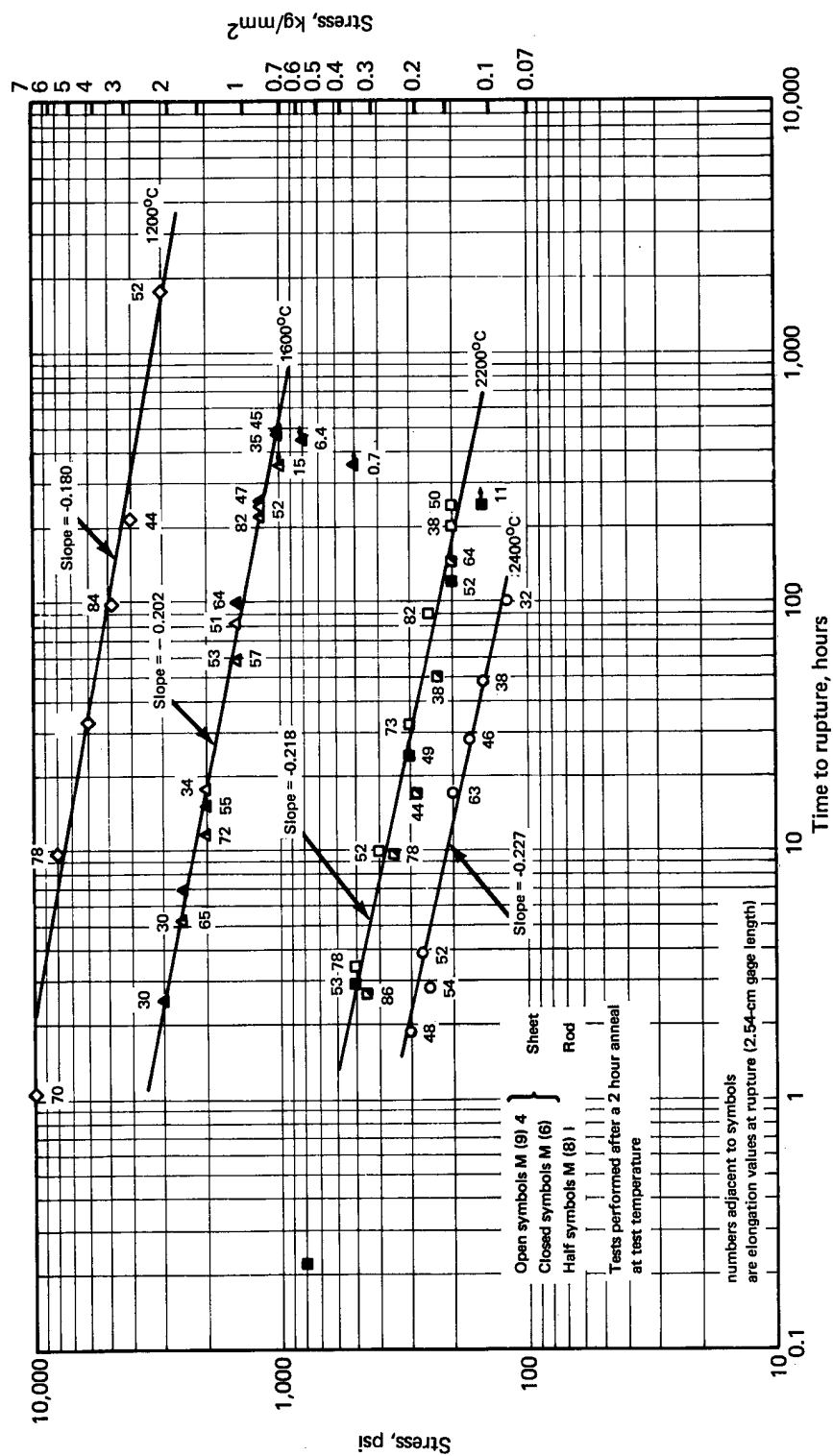


Fig. 1.30 — Stress-rupture results for wrought, arc-cast unalloyed molybdenum tested in hydrogen

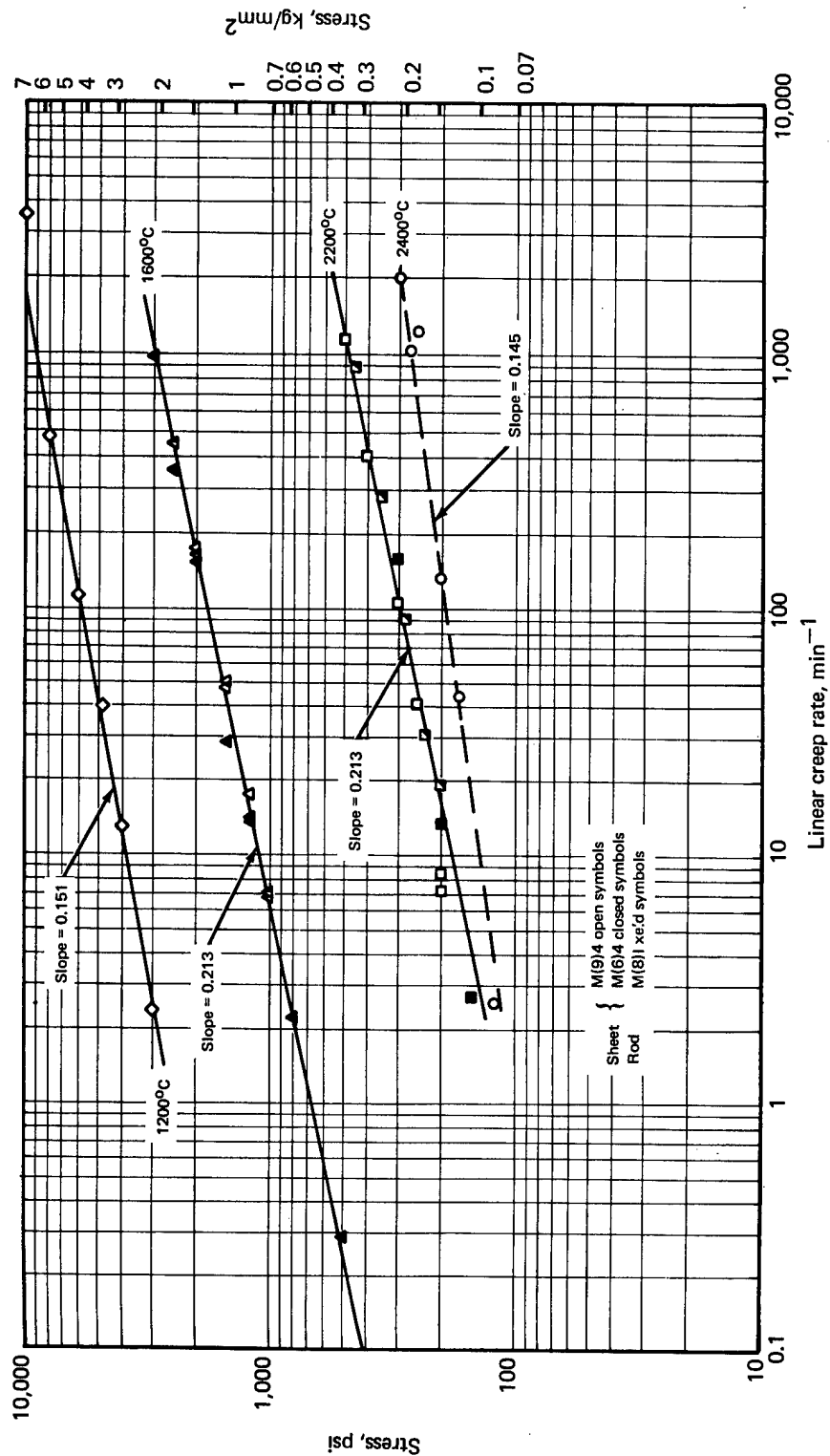


Fig. 1.31 — Creep rate results for wrought, arc-cast unalloyed molybdenum tested in hydrogen

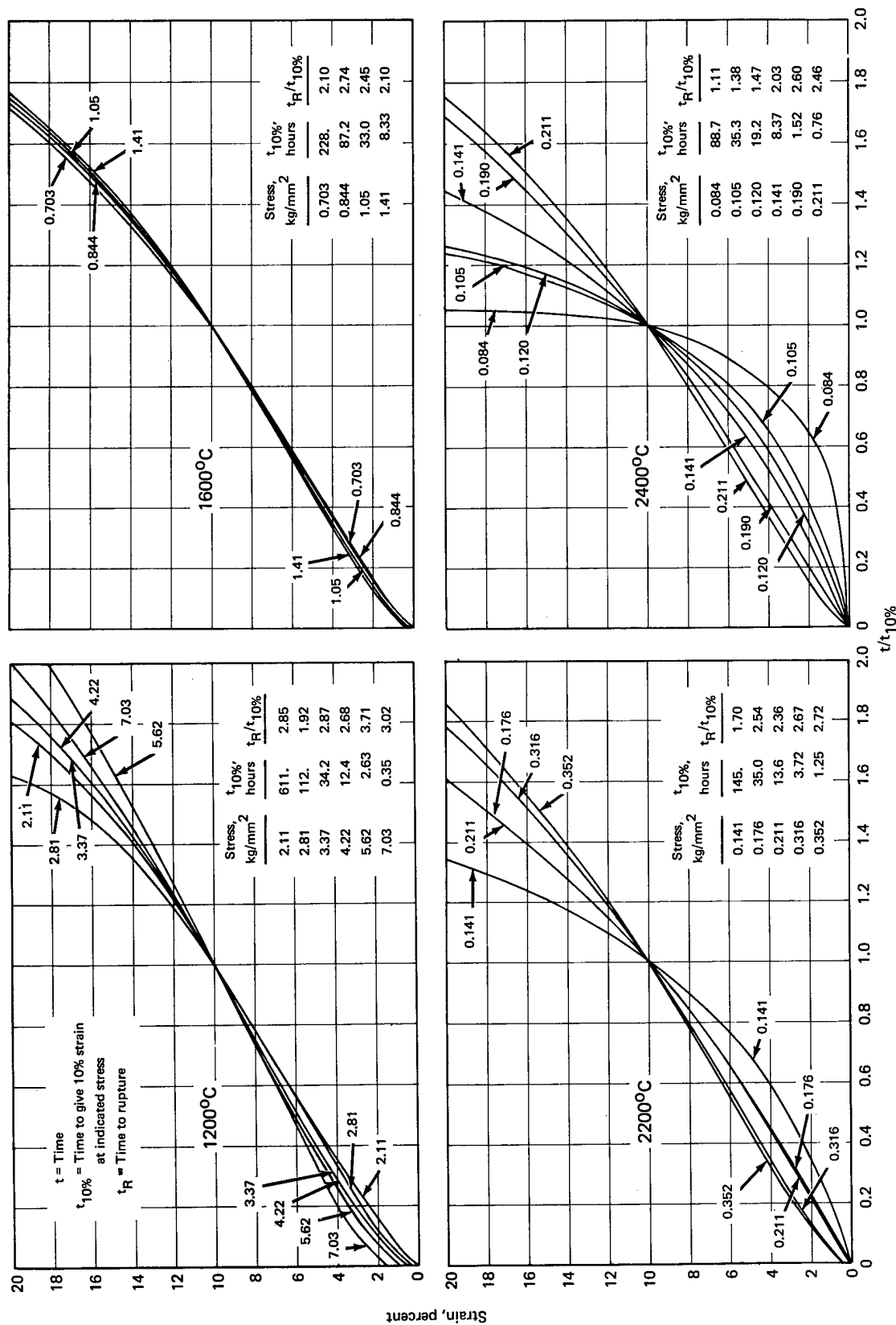


Fig. 1.32 — Constant load creep curves for wrought, arc-cast molybdenum sheet at 1200°, 1600°, 2200°, and 2400°C

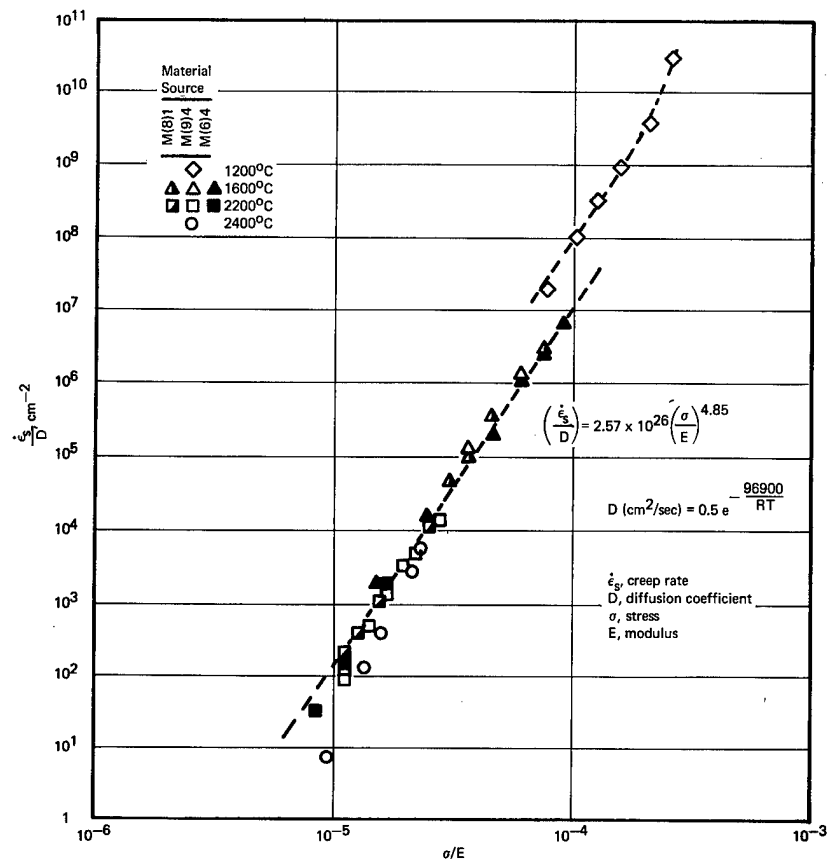


Fig. 1.33 — Correlation of linear creep rate data for arc-cast molybdenum tested in hydrogen

Monkman and Grant³² reported that when the log of the time-to-rupture is plotted against the log of the linear creep rate, a straight-line relationship is obtained with a slope of minus m , in accordance with:

$$\log t_R = \log C - m \log \dot{\epsilon}_s \quad (1.12)$$

where

t_R = rupture time

$\dot{\epsilon}_s$ = linear creep rate

m, C = constants

When m is equal to one, as it has been found to be for a number of materials, the equation becomes:

$$t_R = \frac{C}{\dot{\epsilon}_s} \quad (1.13)$$

The data for molybdenum discussed above are shown in this form in Figure 1.34. The curves for both rod and sheet material are shown to possess a slope of minus 1 but are not coincident. This displacement is due to the consistent difference in rupture life (Figure 1.30) since

³²F. C. Monkman and N. J. Grant, "An Empirical Relationship Between Rupture Life and Minimum Creep Rate in Creep Rupture Tests," Proc. ASTM, Vol. 56, 1956, p. 593.

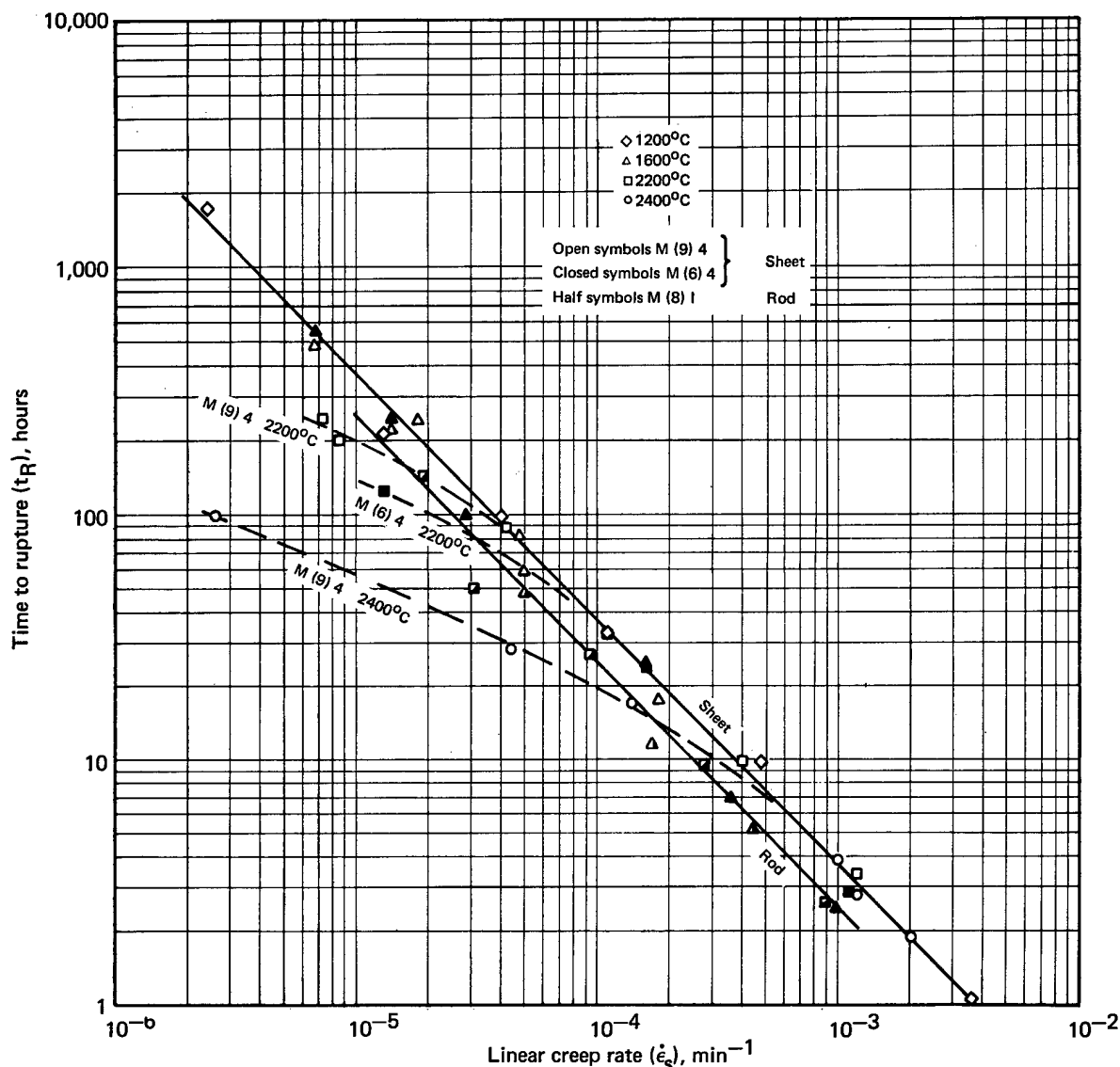


Fig. 1.34 – Rupture life versus creep rate for arc-cast molybdenum showing correlation of data to $t_R \dot{\epsilon}_s = C$

good agreement for the linear creep rate is shown in Figure 1.31. The data points in Figure 1.34 that deviate significantly from the straight lines are those showing deviations from the linear creep rate plot of Figure 1.31. The effect of the change in the creep curve shape is shown in this Monkman-Grant type of plot. Only those data at the lower stresses and higher temperatures, where no primary creep was observed, deviate from the lines in Figure 1.31.

Molybdenum-Base Alloys

Mo-5Re and Mo-5W — Creep-rupture data were reported³³ for PM Mo-5Re and Mo-5W (both at. %) alloy sheet fabricated at GE-NMPO. Sheet thicknesses were 0.05 cm and 0.08 cm for Mo-5W and Mo-5Re, respectively, with testing performed at 1600°C and 2200°C in hydrogen. Data obtained in these tests are presented in Figures 1.35 and 1.36; the data for AC molybdenum are shown for comparison. Each alloy is seen to be stronger than unalloyed, AC

³³GEMP-1002, p. 16.

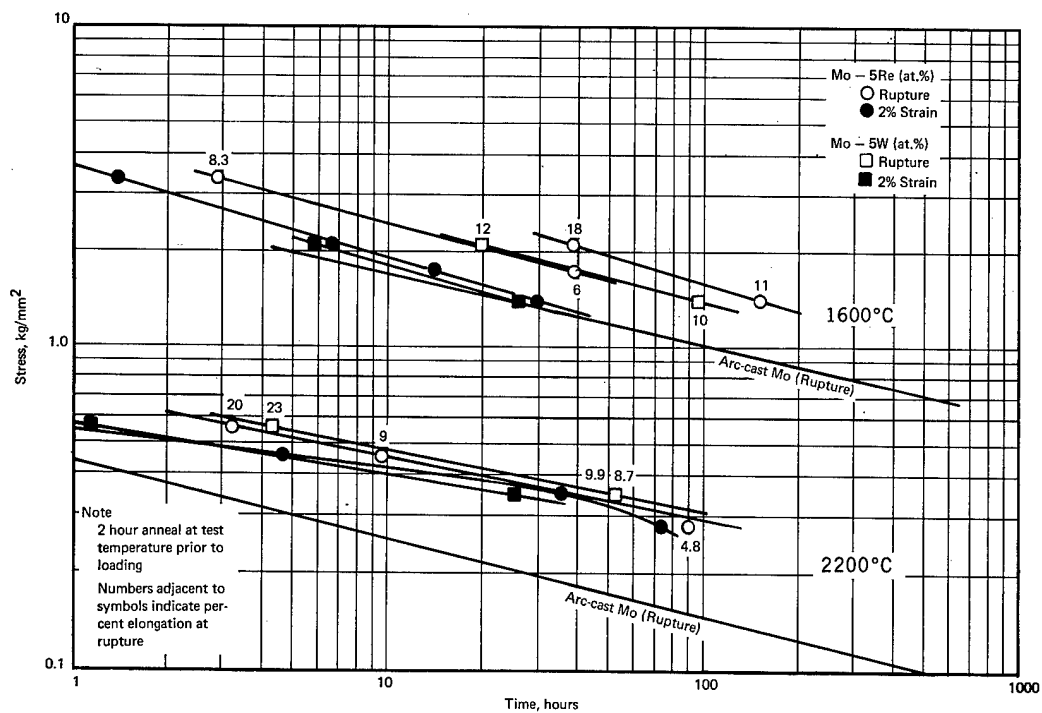


Fig. 1.35 – Stress-rupture data for powder-metallurgy Mo – 5Re and Mo – 5W alloy sheet tested in hydrogen

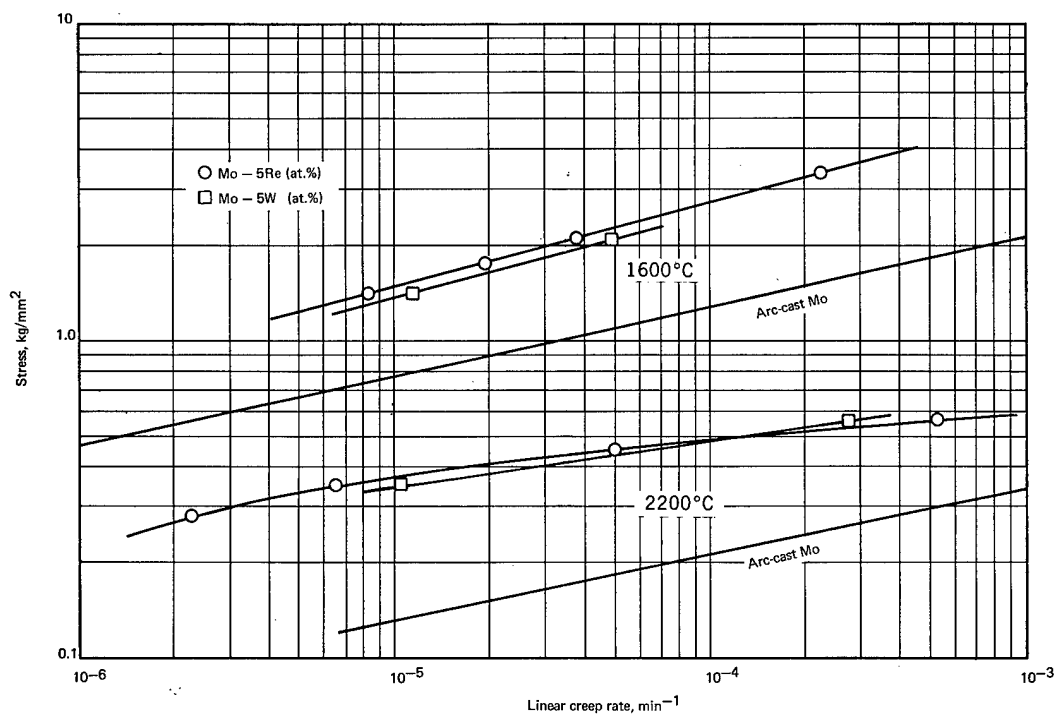


Fig. 1.36 – Linear creep rate data for powder-metallurgy Mo – 5Re and Mo – 5W alloy sheet tested in hydrogen

molybdenum. Two isotherms are presented for Mo - 5Re at 1600°C to reflect the different behavior observed in specimens from two different sheets of this material. Actually these two molybdenum alloys exhibit about the same creep-rupture behavior.

Mo - 50Re ^{Mo → p. 56} Stress-rupture and creep data (constant load) for wrought, PM Mo - 50Re (wt %) alloy sheet were previously presented³⁴ for lot 1 material at 2200°C and for lot 2 material at 1600°, 2200°, and 2400°C. The lot 2 results were obtained using specimens from sheet 1. Additional tests were performed at 1600°, 2200°, and 2400°C using specimens obtained from sheet 2 of the lot 2 material. The objective was to compare results for two different sheets of the same wrought, powder-metallurgy material obtained from the same lot. In addition, the lot 2, sheet 1 results indicated that at the higher temperatures and lower stresses, diffusional creep may be the controlling mechanism based on the increased slope of the stress versus linear creep rate plot. Further studies were therefore performed to verify this.

Table 1.9 and Figures 1.37 and 1.38 give the stress-rupture and creep data obtained for the lot 2, sheet 2 material. The sheet 2 results appear to be consistent with the sheet 1 material in terms of stress-rupture, linear creep rate, and ductility at 2200°C and 2400°C. At 1600°C, the rupture life is greater whereas the linear creep rate and ductility are lower for the sheet 1 material.

Creep curves for lot 2, sheet 2 specimens tested at the lowest stress for each of the three temperatures involved are shown in Figure 1.39. At 1600°C, the curve shows third-stage-type creep from essentially time zero, while the 2200°C curve gives the more conventional type of creep curve. At 2400°C, the creep curve displays two regions of essen-

TABLE 1.9
CREEP-RUPTURE RESULTS^a FOR WROUGHT, POWDER-METALLURGY Mo - 50Re SHEET^b
TESTED IN HYDROGEN (LOT 2, SHEET 2)

Specimen No.	Test Conditions		Time to Indicated Strain, hr								Rupture		Linear
	Temperature, °C	Stress, kg/mm ²	0.2%	0.5%	1%	2%	3%	5%	10%	Time, hr	Elongation, %	Creep Rate, min ⁻¹	
2-2	1600	3.37	0.05	0.10	0.16	0.25	0.32	0.46	0.74	2.02	102	—	
-3	1600	2.81	0.18	0.40	0.61	0.95	1.23	1.67	2.45	5.25	92	8.0 x 10 ⁻⁵	
-4	1600	2.11	0.72	1.44	2.42	3.82	4.90	6.57	9.30	16.7	85	—	
-5	1600	1.76	1.37	2.90	4.90	8.10	10.6	14.7	21.6	37.9	74	2.3 x 10 ⁻⁵	
-6	1600	1.41	2.85	6.85	12.4	20.0	25.5	33.8	47.2	81.0	60	1.3 x 10 ⁻⁵	
-1	1600	1.05	7.45	18.2	34.2	59.6	79.9	111.	162.	262.	58	4.5 x 10 ⁻⁶	
2-13	2200	0.352	0.29	0.83	1.87	3.76	5.51	8.48	12.6	14.8	21	9.5 x 10 ⁻⁵	
-15	2200	0.211	0.72	1.88	4.06	8.85	14.0	24.9	47.6	70.3	24	2.9 x 10 ⁻⁵	
-17	2200	0.141	1.03	2.77	5.52	14.4	23.2	42.0	88.2	145.	24	1.7 x 10 ⁻⁵	
-18	2200	0.105	1.28	3.50	7.60	16.5	26.2	46.7	94.1	174.	45	1.6 x 10 ⁻⁵	
2-8	2400	0.211	0.14	0.34	0.68	—	—	—	—	1.09 ^c	1.8	2.5 x 10 ⁻⁴	
-30	2400	0.211	0.15	0.37	0.72	1.33	1.83	2.51	3.20	3.48	30	2.4 x 10 ⁻⁴	
-21	2400	0.141	0.24	0.57	1.12	2.19	3.13	4.63	6.75	8.65	32	1.5 x 10 ⁻⁴	
-25	2400	0.105	0.36	0.89	1.78	3.56	5.34	8.30	13.2	20.9	46	9.4 x 10 ⁻⁵	
-29	2400	0.070	0.61	1.48	2.94	5.84	8.75	14.6	27.5	70.0	44	5.7 x 10 ⁻⁵	
-24	2400	0.035	0.97	2.66	5.50	11.3	18.4	33.6	97.7	224.	36	{ 1.2 x 10 ⁻⁵ 2.9 x 10 ⁻⁵	
1-21	2200 ^e	0.141	1.55	3.93	8.80	18.6	28.6	48.5	85.9	112.	20	1.7 x 10 ⁻⁵	

^aAnnealed at test temperature for 2 hours in hydrogen before testing.

^b0.05-cm-thick sheet, 0.64-cm by 2.54-cm gage section.

^cTest terminated; load train support failed.

^dDiffusional creep rate.

^eAnnealed at 2400°C for 2 hours in hydrogen before testing (lot 2, sheet 1).

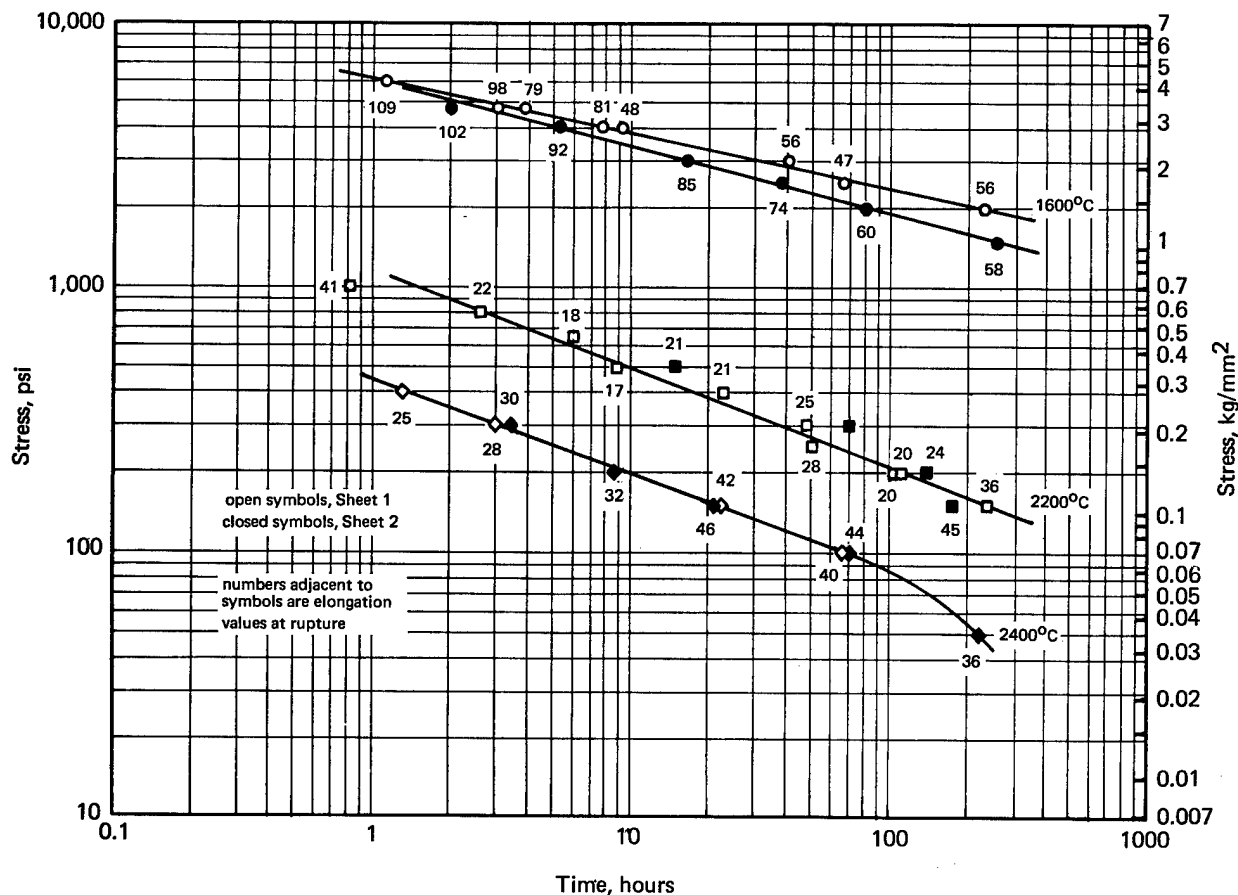


Fig. 1.37 — Stress-rupture results for wrought, powder-metallurgy Mo — 50Re (wt %) sheet (lot 2) tested in hydrogen

tially linear creep rate followed by third-stage creep. If these curves are analyzed in terms of the creep-rate curve given in Figure 1.38, it appears that the initial portion of the creep curve at 2400°C and 0.035 kg/mm² (Figure 1.39) is diffusion controlled since the creep-rate curve at 2400°C (Figure 1.38) yields a slope of essentially 1. This is consistent with the Nabarro-Herring³⁵ model for diffusional creep which indicates stress to be directly proportional to creep rate. This is further confirmed by the analysis approach proposed by Sherby³⁶ for polycrystalline metals above one-half the absolute melting temperature. Figure 1.40 shows good correlation of the results using this approach. The curve at the low-stress levels also yields a slope of 1 indicating diffusional creep. At the higher stress levels the curve slope is 2.7. According to Sherby, when a slope approximating 3 is obtained, the creep mechanism is dislocation glide based on the microcreep theory of Weertman.³⁷ He showed that when dislocation motion under stress is controlled by the velocity of solute drag along the dislocation line the creep rate is given by

$$\dot{\epsilon}_s = k D_s \frac{\sigma^3}{G^4} \quad (1.14)$$

³⁵Herring, loc. cit.

³⁶Sherby, loc. cit.

³⁷J. Weertman, "Steady-State Creep of Crystals," J. Appl. Phys., Vol. 28, 1957, p. 1185.

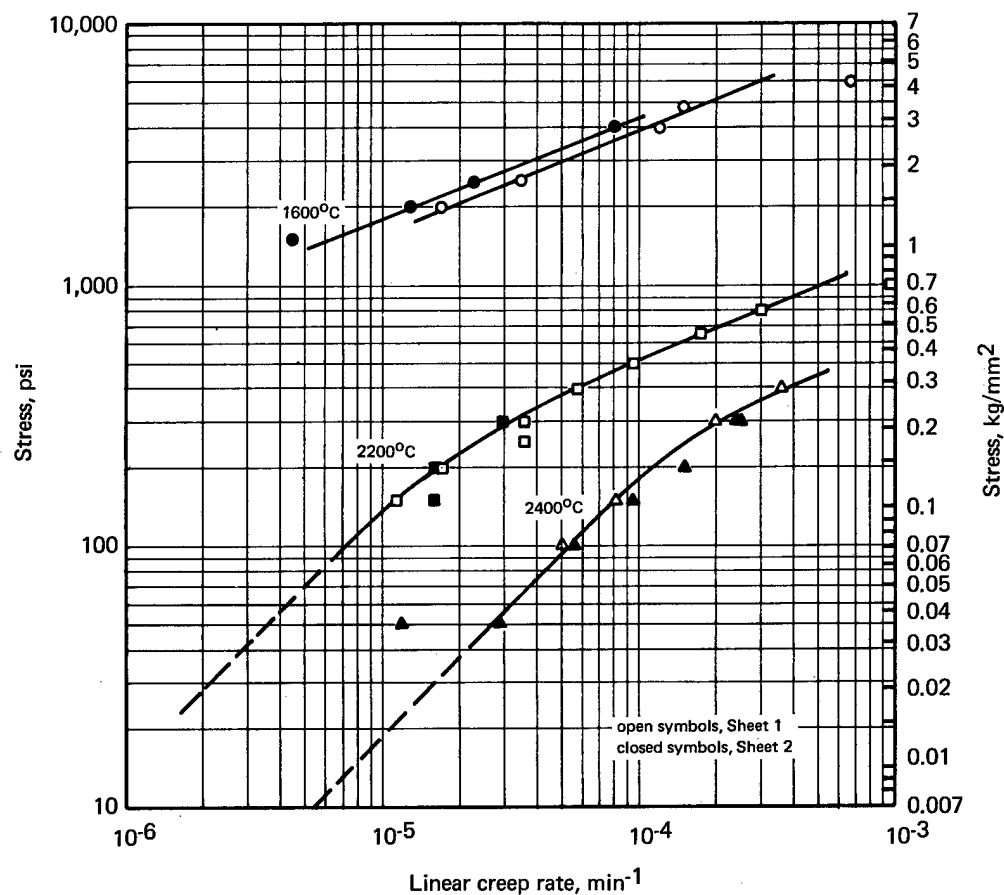


Fig. 1.38 — Creep rate results for wrought, powder-metallurgy Mo — 50Re (wt %) sheet

where k is a constant depending on the interaction force between the solute atmosphere and the dislocation, D_s is the solute diffusion coefficient, and G is the shear modulus. This equation predicts that the creep rate of solid solutions should be proportional to the third power of stress in contrast to the five power law dependence observed for pure metals.

Apparent activation energy calculations for creep were made based on the linear creep rate data obtained at the same stress level for two different temperatures. Data between 1600° and 2200°C gave a value of 84 kcal/mole and the data between 2200° and 2400°C gave a value of 121 kcal/mole.

A value of the diffusion coefficient for Mo — 50Re was calculated based on the Nabarro-Herring equation for creep rate:

$$\dot{\epsilon}_s = \frac{10 D \sigma b^3}{k T L^2} \quad (1.15)$$

where $\dot{\epsilon}_s$ is the steady-state creep rate in sec^{-1} , D is the diffusion coefficient in cm^2/sec , σ is the stress in dynes/cm^2 , k is Boltzmann's constant (1.38×10^{-16} ergs per degree), T is the absolute temperature, L is the grain diameter in centimeters, and b is the lattice spacing in centimeters. Based on the test data obtained at 2400°C and 0.070 kg/mm^2 for lot 2, sheet 1 material, the value of the diffusion coefficient was calculated to be $1.143 \times 10^{-7} \text{ cm}^2/\text{sec}$. The values of grain size and lattice spacing used were based on actual meas-

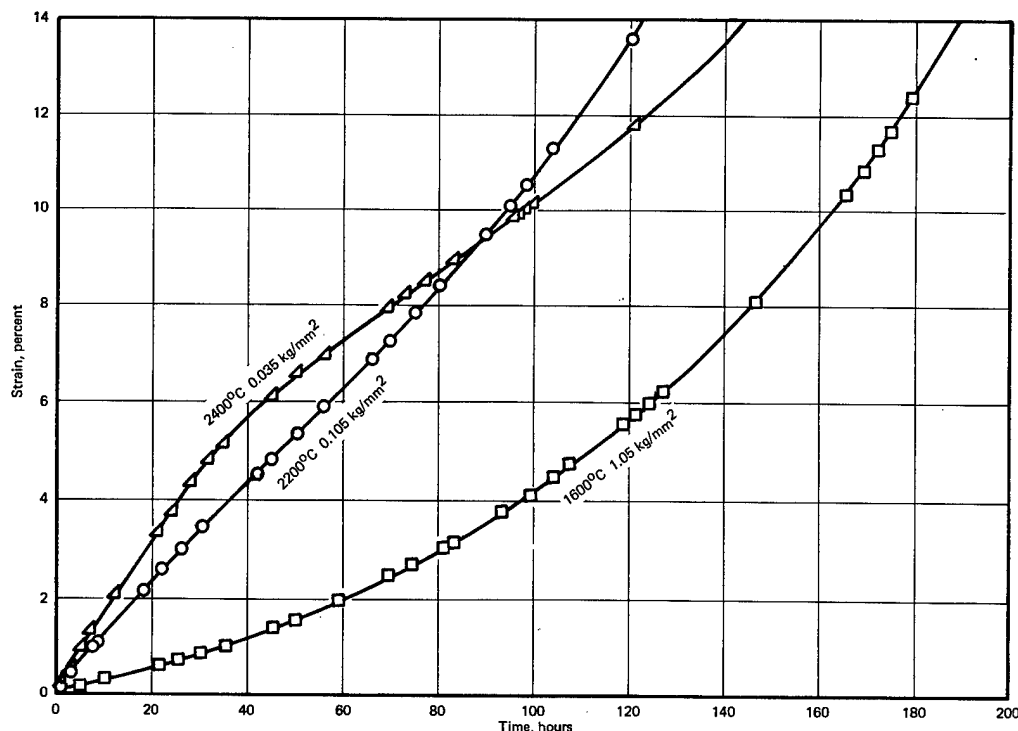


Fig. 1.39 — Creep curves for wrought, powder-metallurgy Mo — 50Re (wt %) sheet (Lot 2) tested in hydrogen

measurements of 285 microns and 3.16×10^{-8} cm, respectively. The two activation energy values discussed above were applied to the conventional diffusion expression

$$D = D_0 e^{-\frac{Q}{RT}} \quad (1.16)$$

where D is the self-diffusion rate of atoms, D_0 is a constant, Q is the activation energy for self-diffusion, R is the gas constant, and T is the absolute temperature. Diffusion rate values could then be expressed by the relations shown in Figure 1.40.

Mo - 30W ^{p. 58} The stress-rupture characteristics for both wrought, unalloyed tungsten and molybdenum sheet were shown to vary above one-half the absolute melting temperature depending on whether the material was fabricated by an AC or PM process.^{38,39} Results obtained for PM molybdenum varied depending on the material source (i. e., vendor); results for AC material were essentially identical independent of the source. Similar findings were observed for tungsten. When the stress-rupture test results for AC molybdenum and AC tungsten were analyzed in terms of homologous temperature, identical results were obtained;⁴⁰ this did not occur for the PM materials.

The phase diagram for the tungsten-molybdenum system reveals that these metals form solid solutions over the complete range of compositions. The rupture-strength relationship for alloys of the two metals may be expected to be the same as that for the elements on a homologous temperature basis except for the possible strengthening effect of the lattice dis-

³⁸P. N. Flagella, "High-Temperature Stress-Rupture Characteristics of Mo and Mo Alloys," AIAA Journal, Vol. 5, 1967, p. 281.

³⁹P. N. Flagella, "High Temperature Creep-Rupture Behavior of Unalloyed Tungsten," GE-NMPO, GEMP-543, August 1967.

⁴⁰GEMP-475A, p. 16.

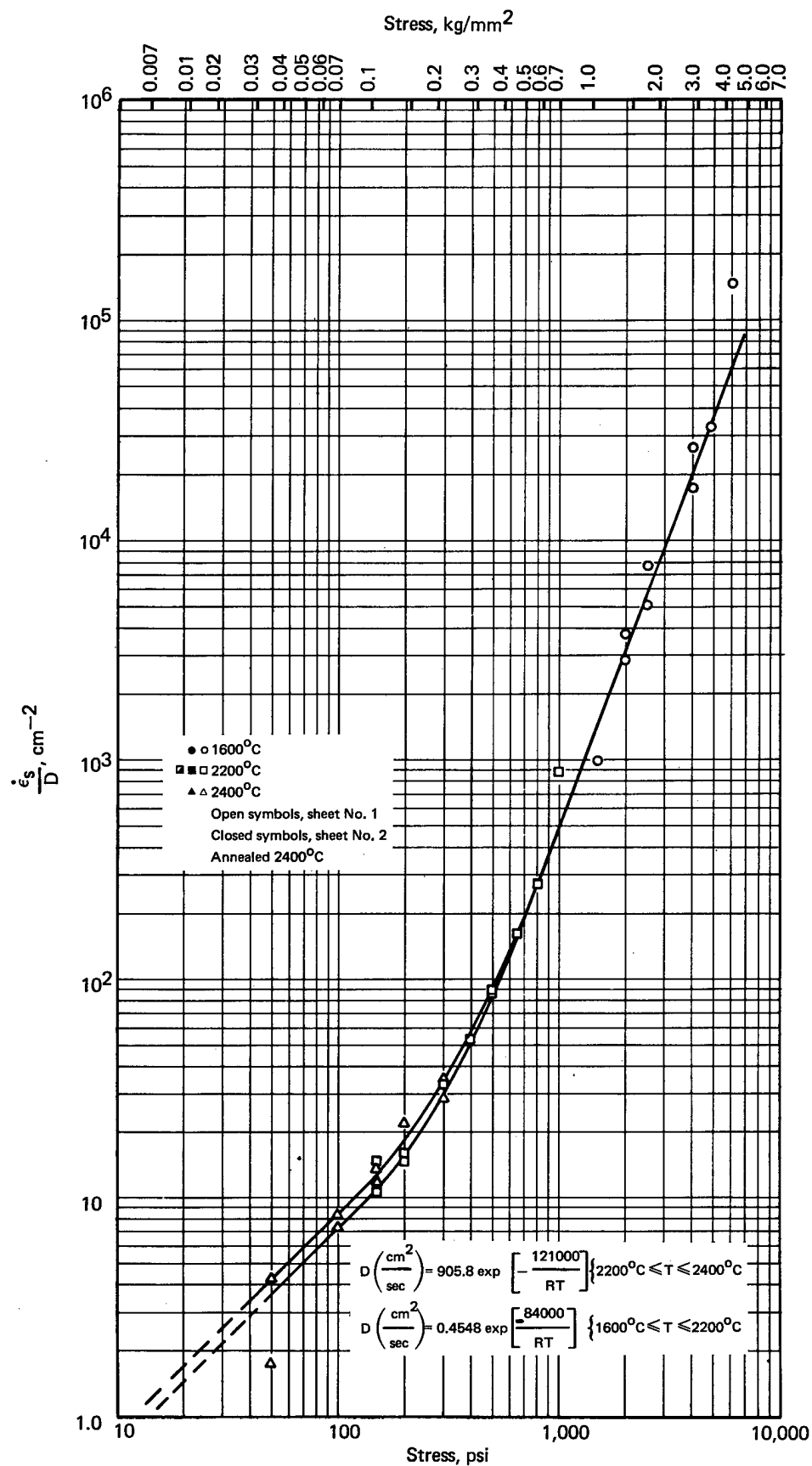


Fig. 1.40 — Correlation of creep rate data for wrought, powder-metallurgy Mo — 50Re (wt %) tested in hydrogen

tortion by the substitution of tungsten atoms for molybdenum atoms. Because of the similarity between tungsten and molybdenum, the stress-rupture characteristics of wrought, arc-cast Mo - 30W (wt %), purchased commercially (heat 30W 7694), were evaluated.⁴¹

The Mo - 30W alloy was of relatively high purity containing 69, 12, 1, and 41 ppm of C, O, H, and N, respectively. After rolling to sheet, with intermediate anneals, the material was stress-relieved for 1 hour at 1175°C in vacuum. Stress-rupture and creep tests were performed at 1600°C and 2200°C in hydrogen after annealing for 2 hours at the test temperature. Creep curves for this material are presented in Figure 1.41. For all stress levels indicated, at constant temperature, the strain is presented as a function of the time to give 10 percent strain. In this way the curve shapes over a wide range of stresses are easily shown and compared. All the creep curves for the Mo - 30W alloy display a third-stage-type creep from essentially time zero. As shown, the ratio of $t_R/t_{10\%}$ (Figure 1.41) decreases with decreasing stress at the same temperature. This is apparently not related to the fact that at 1600°C the elongation for the material at rupture decreases with decreasing stress since this is not the case at 2200°C.

Figure 1.42 gives the stress-rupture curves for the Mo-30W material at 1600°C and 2200°C along with curves for wrought, AC, unalloyed W, Mo, and W - 25Re (wt %) for comparison. As expected, the addition of tungsten to molybdenum increases the rupture life. All the materials exhibit a linear relationship between log stress and log rupture time. Isotherms for the Mo - 30W and W - 25Re alloys are nearly parallel and have slopes greater than those shown for the unalloyed tungsten and molybdenum.

The 100-hour rupture data from Figure 1.42 are shown in Figure 1.43 in terms of the homologous temperature (percent of the absolute melting temperature). Agreement is shown between the tungsten and molybdenum data but the Mo - 30W data show a 17 percent increase in the rupture stress for the same percent of the absolute melting temperature. This may be due to the lattice distortion effect mentioned above. The W - 25Re data reflect a different behavior.

Figure 1.44 shows typical specimens after testing at 1600°C and 2200°C and the resulting photomicrographs. The effect of temperature on the grain size is quite apparent being 145 microns at 1600°C and 490 microns at 2200°C. Significant intergranular separation is also noted. For the specimen tested at 1600°C this appears to occur primarily transverse to the stress direction. At 2200°C, the effect is not apparent due to the large grain size involved.

RHENIUM

→ p. 63

Studies of the creep-rupture behavior of wrought, PM (lot 2), unalloyed, rhenium sheet (0.05 cm thick) were reported^{42,43} for tests at 1600°, 2200°, and 2600°C in hydrogen. Rupture data obtained in these evaluations are presented in Figure 1.45 along with some previously reported⁴⁴ data for lot 1 rhenium which had been obtained from the same vendor at an earlier date. Some slight difference between lots 1 and 2 is quite evident from Figure 1.45 and was attributable⁴³ to different sintering procedures which led to different grain sizes in the two lots of material. Cavitation was observed in the grain boundaries of the material from both lots at fracture. Linear creep rate data for the lot 2 material are presented in Figure 1.46. In terms of rupture strength, the lot 2 material has about the same strength as AC tungsten at 1600°C and is decidedly stronger than AC tungsten at all higher temperatures.

⁴¹GEMP-1002, p. 11.

⁴²GEMP-67, p. 11.

⁴³"AEC Fuels and Materials Development Program Progress Report No. 69," GE-NMPO, GEMP-69, September 29, 1967, p. 11.

⁴⁴"Fourth Annual Report - High-Temperature Materials and Reactor Component Development Programs, Volume I - Materials," GE-NMPO, GEMP-334A, February 26, 1965, p. 23.

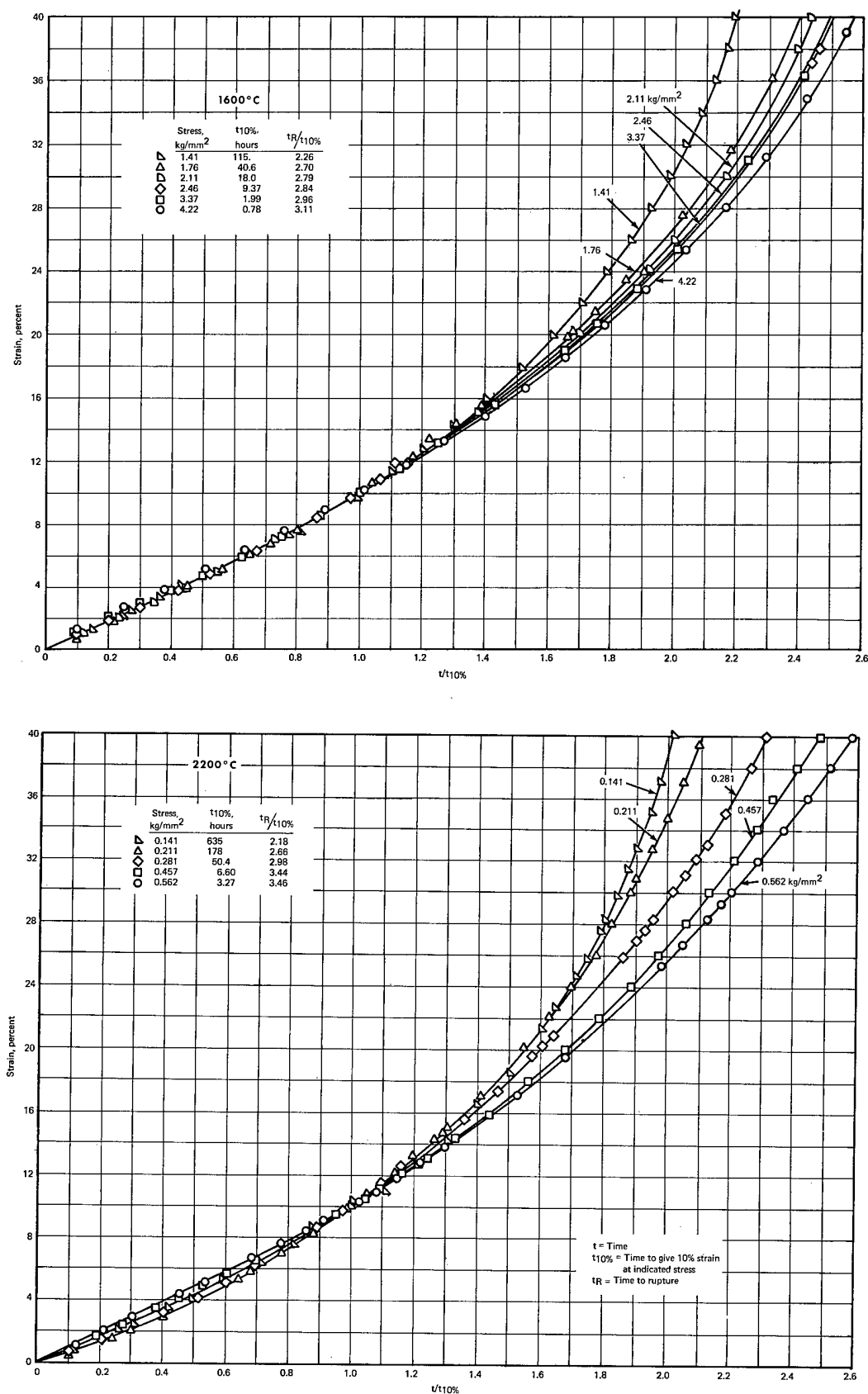


Fig. 1.41 — Creep curves for wrought arc-cast Mo — 30W (wt %) sheet tested in hydrogen

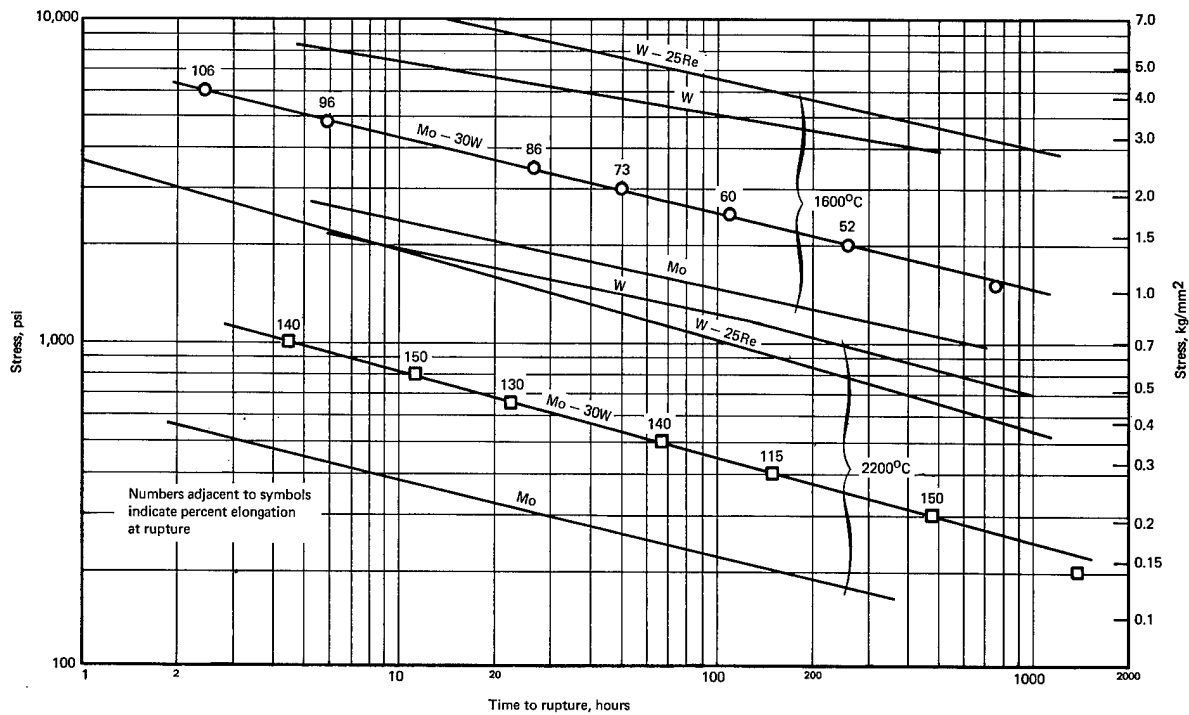


Fig. 1.42 – Stress-rupture results for wrought arc-cast Mo – 30W (wt %) sheet compared to W, Mo, and W – 25Re (wt %)

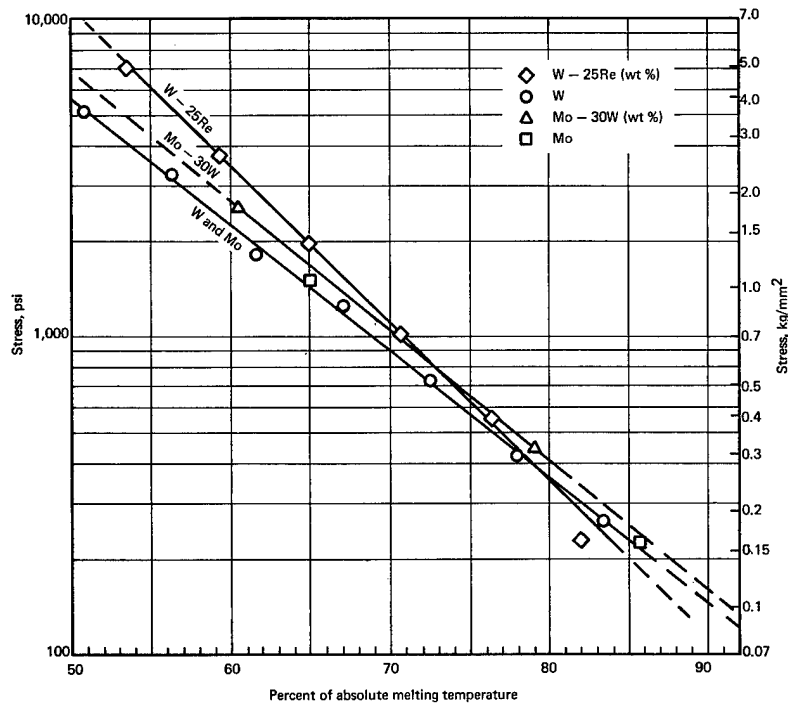
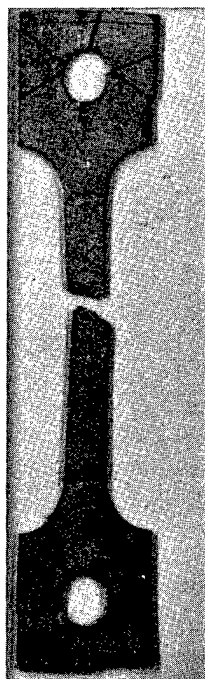
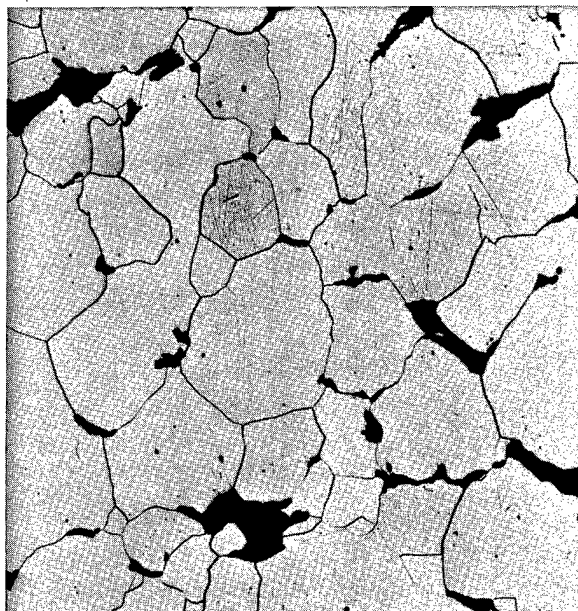


Fig. 1.43 – Stress required to cause rupture in W, Mo, Mo – 30W, and W – 25Re in 100 hours

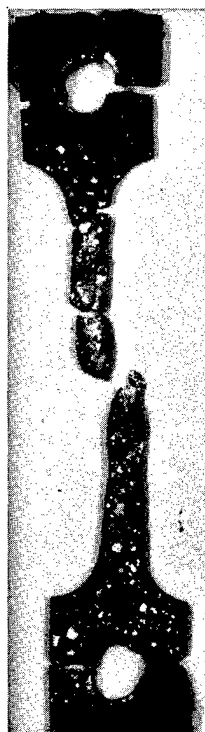


(Neg. P67-12-20D)



(Neg. 10191)
 1600°C, 1.05 kg/mm²
 764 hours, 48%
 145 microns

(100X etched)



(Neg. P67-12-20F)



(Neg. 10187)
 2200°C, 0.141 kg/mm²
 1388 hours, 72%
 490 microns

(100X etched)

Fig. 1.44 — Mo — 30W (wt %) sheet samples after creep-rupture testing in hydrogen.
 Numbers below figures are: test temperature, stress, rupture time,
 elongation at rupture, and grain size.

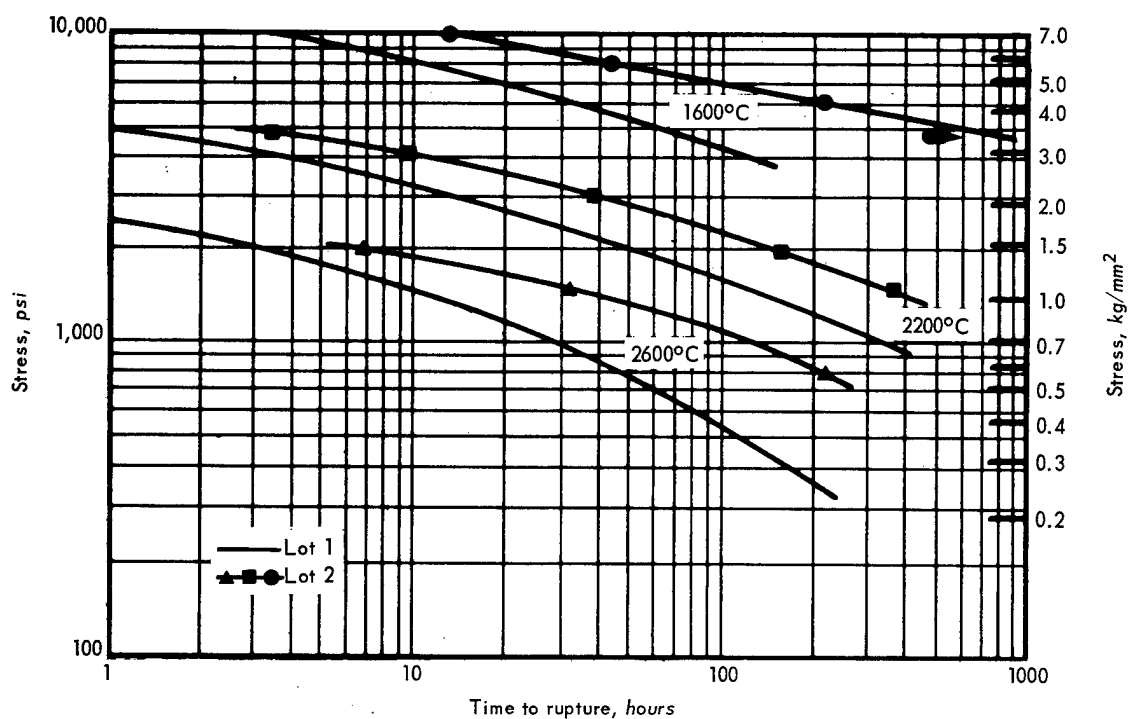


Fig. 1.45 — Stress-rupture data for lot 1 and lot 2 wrought, powder-metallurgy unalloyed rhenium sheet tested in hydrogen

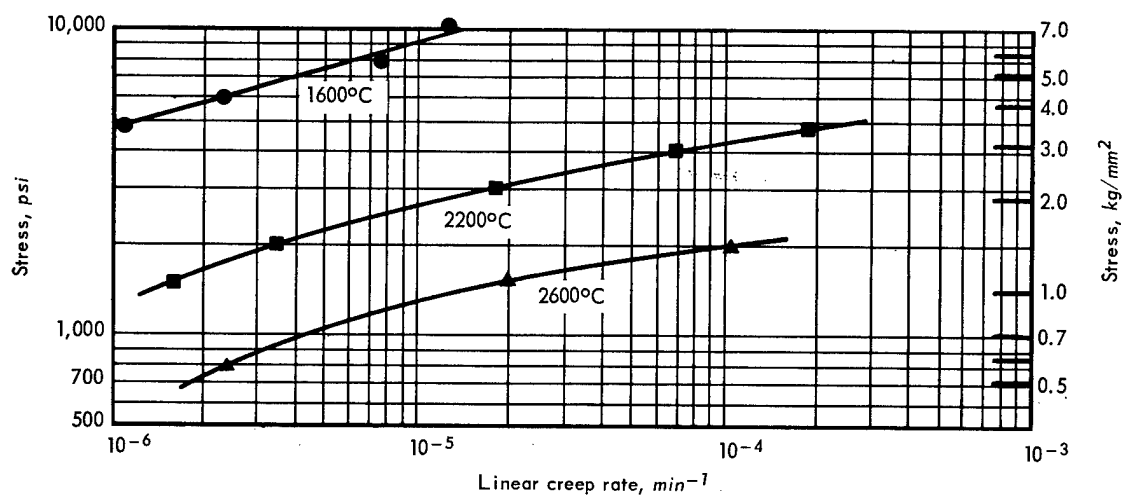


Fig. 1.46 — Linear creep rate data for lot 2 wrought, powder-metallurgy unalloyed rhenium sheet tested in hydrogen

NIOBIUM AND NIOBIUM ALLOYS

Creep-rupture testing of niobium was based on experience gained from tests⁴⁵ of tantalum at high temperatures, in either high-purity hydrogen or argon. These tests showed that the material becomes significantly contaminated with nitrogen and oxygen causing strengthening and embrittlement. The primary source of the contamination is not the test gas, since high-purity gas was used, but the result of the furnace components outgassing at high temperatures. Placing a protective tantalum foil around the specimen being tested decreased the contamination level but did not eliminate it. No such problem was encountered with the non-reactive refractory metals (W, Mo, Re) or their alloys. This is apparently due to the low level of solubility for interstitials.

Niobium, tantalum, and vanadium (Group V elements) are highly reactive and have a high solubility for the interstitial elements and hence are more difficult to evaluate in the uncontaminated condition. To overcome some of the contaminating problems associated with evaluating the creep-rupture properties of niobium, a test system was modified by incorporating an ion pump so that testing could be performed in a relatively high vacuum. In addition, modifications were incorporated to allow the system to outgas after reaching test temperature with the test specimen in a cold region of the furnace until outgassing had subsided and a good vacuum level was reached ($\sim 1 \times 10^{-6}$ Torr). By operating the system at a higher temperature than required for testing, outgassing was accelerated and possible outgassing during test was reduced. After outgassing was complete and thermal equilibrium obtained at the test temperature, the test specimen was positioned in the hot zone of the furnace, annealed for 2 hours, loaded to the desired stress level and the creep-rupture test performed.

This procedure was used to test four wrought, AC, unalloyed niobium sheet samples and one alloy, Cb-753 (Nb-5V-1.25Zr, wt %), sample at 1600°C. Impurities in ppm for the as-received materials were as follows: for Nb; C = 22, O = 282, N = 16, H = 5; for Cb-753; C = 15, O = 208, N = 44, H = 2. The test results are given in Table 1.10 and the creep curves shown in Figure 1.47. The stress-rupture data are presented in Figure 1.48 including previously published⁴⁶ data for the alloy Cb-753. The greater rupture life for the alloy over the unalloyed niobium at 1600°C and 0.703 kg/mm² is obvious. The fact that the alloy showed considerable elongation at rupture (130%) after 342 hours at 1600°C is an indication of a high-purity non-contaminating environment. Additionally, the hardness of the alloy decreased

TABLE 1.10
CREEP-RUPTURE RESULTS^a FOR WROUGHT, ARC-CAST, UNALLOYED NIOBIUM SHEET^b
AND ALLOY Cb-753 SHEET^c AT 1600°C TESTED IN VACUUM^d

Material	Specimen No.	Stress, kg/mm ²	Time to Indicated Strain, hours							Rupture		Linear Creep Rate, min ⁻¹
			0.2%	0.5%	1%	2%	.3%	5%	10%	Time, hr	Elongation, %	
Nb	1-4	0.211	0.95	2.60	5.50	12.2	20.0	35.3	70.0	182.	41	1.9×10^{-3}
	-3	0.352	—	0.03	0.18	0.86	1.88	4.28	9.60	19.3	30	5.1×10^{-3}
	-5	0.562	—	—	—	—	0.01	0.09	0.51	1.83	41	1.9×10^{-3}
	-1	0.703	—	—	—	—	—	0.04	0.18	0.54	30	1.7×10^{-5}
Cb-753	1	0.703	0.79	2.52	6.00	14.4	23.6	42.8	90.0	342.	130	1.4×10^{-4}

^aAnnealed at 1600°C for 2 hours in vacuum before testing.

^b0.053-cm-thick sheet, 0.64-cm x 2.54-cm gage section.

^c0.15-cm-thick sheet, 0.64-cm x 2.54-cm gage section.

^dFrom 1 to 2×10^{-6} Torr.

⁴⁵"High-Temperature Materials Program Progress Report No. 25," GE-NMPO, GEMP-25A, July 31, 1963, p. 12.

⁴⁶Union Carbide Corp., Stellite Division, F-30, 269-1, September 1964.

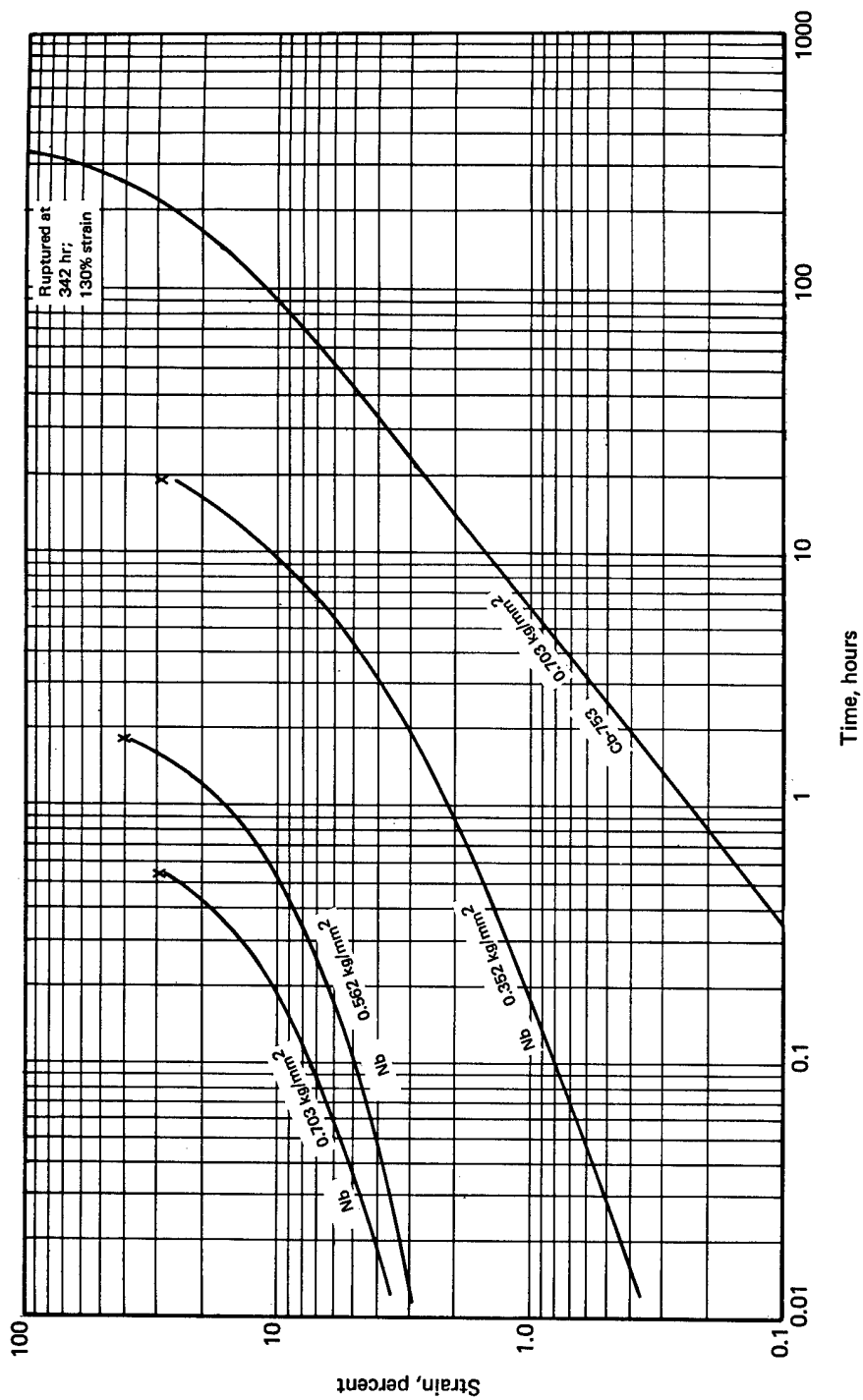


Fig. 1.47 — Creep-rupture curves for wrought, arc-cast niobium and alloy Cb-753 sheet tested at 1600°C and in a vacuum of 1×10^{-6} Torr

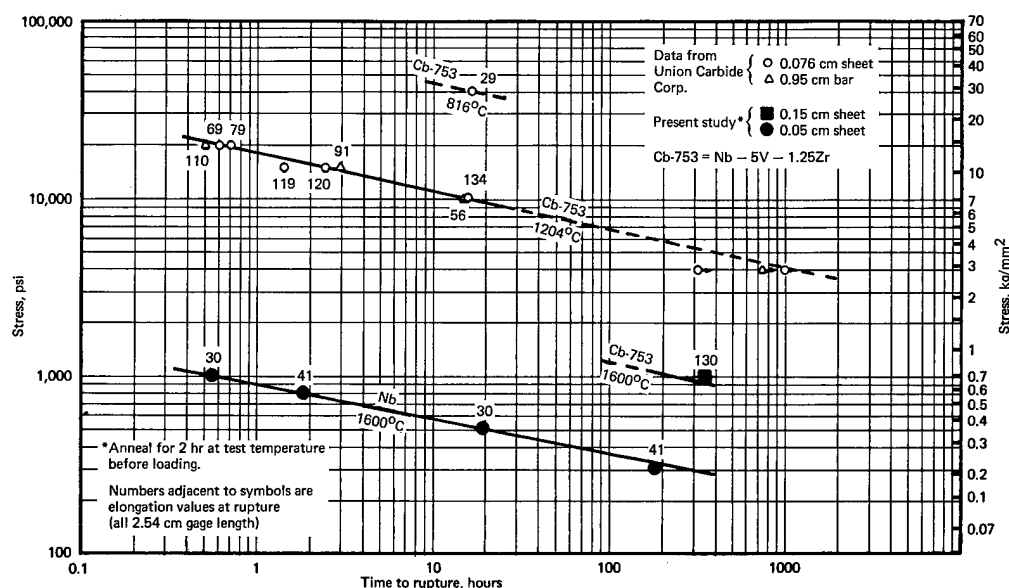


Fig. 1.48 — Stress-rupture results for unalloyed niobium and alloy Cb-753

from 183 DPH before test to 160 DPH after test. Chemical analysis and metallographic evaluations are planned for all samples to determine the extent of any otherwise undetected contamination..

CONSTANT-STRESS CREEP TESTING

All stress-rupture and creep data reported in this program to date have been obtained by constant-load testing. As the test specimen elongates, the cross-sectional area decreases and the stress increases. Most data reported in the literature are obtained in this manner, but to better understand the basic characteristics and mechanisms involved in creep, test data obtained at constant stress are desirable.

One high-temperature creep-rupture test stand was modified to perform tests at constant stress. Figure 1.49 shows a schematic diagram of the system. The electro-optical strain measuring system⁴⁷ automatically records strain versus time for the test specimen. On the basis of the strain measurement, the automatic load-control unit decreases the load on the specimen to maintain a constant stress. The assumption involved with this approach is that the strain occurs uniformly over the gage length of the specimen and that the increase in strain is proportional to the decrease in cross section (i. e., constant volume deformation). This is a valid assumption until local necking occurs which, on the basis of constant stress, does not occur until third-stage creep is observed.

Several constant-stress creep tests were performed to evaluate the system. Unalloyed molybdenum sheet specimens were tested at 1600°C and a constant stress of 2.11 kg/mm² in hydrogen and compared to the results obtained at constant load for the same material. One such comparison is shown in Figure 1.50. As expected, due to the continually decreasing load with increasing strain, the constant-stress tests show a longer time to reach the same values of strain observed in the constant-load tests.

Previous evaluations of equation forms have shown that a third-degree polynomial in $t^{1/3}$ describes the primary and secondary stages of creep for a constant-load test very well. This

⁴⁷W. L. McCullough and P. N. Flagella, "Experimental Techniques Employed in Stress-Rupture and Creep Measurements to 3000°C," GE-NMPO, GE-TM 65-5-10, April 1965.

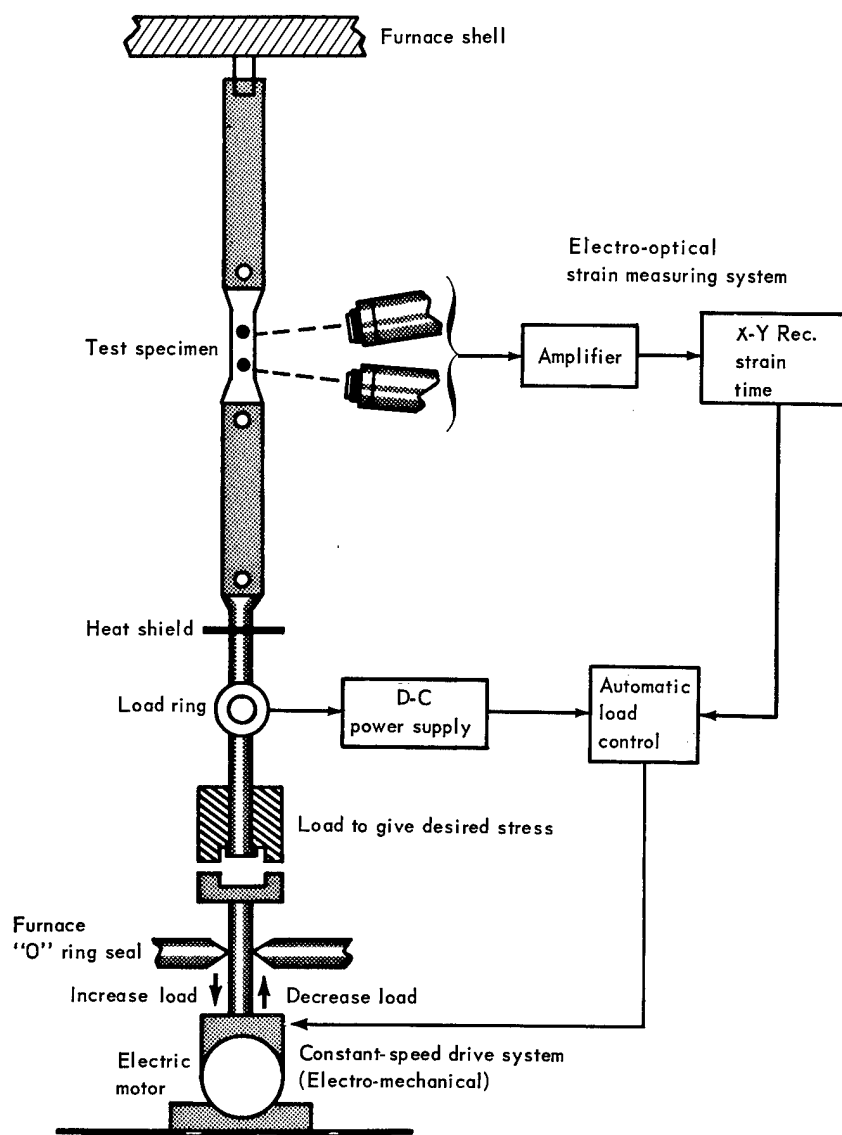


Fig. 1.49 — Schematic diagram of constant stress creep system

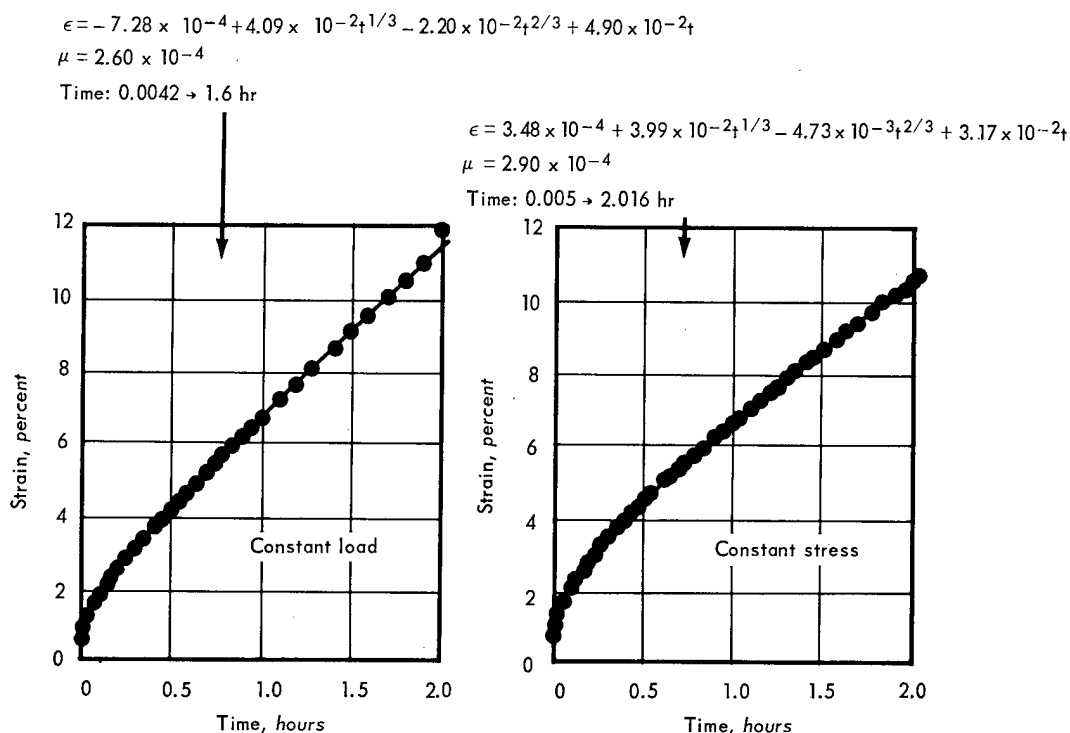


Fig. 1.50 — Comparison of constant-load and constant-stress creep tests of Mo sheet at 1600°C and 2.11 kg/mm² in hydrogen

same equation form is effective in describing the constant-stress test as shown in Figure 1.50.

Additional tests of wrought, AC molybdenum sheet were performed at both 1600°C and 2200°C in hydrogen to compare the second-stage creep rates. Figures 1.51 and 1.52 show the creep curves obtained with the time scale normalized to the time required to give 10 percent strain. This permits a more direct comparison of the creep curves to evaluate the effect of stress on the strain. Although small differences are observed between the constant-load (increasing stress) and constant-stress creep curves, the differences are not significant until approximately 15 percent strain is obtained which is beyond the region of the linear creep rate for the constant-load test. The linear creep rates for the two types of tests are essentially the same. This being the case, constant-load creep test results may be analyzed in terms of the linear (secondary) creep rate with no significant error.

The creep curves presented in Figures 1.51 and 1.52 for AC molybdenum, display the classical form at constant load and, therefore, permit analysis, correlation, and interpretation of linear creep rate behavior. Any conclusions reached in this type of analysis should be consistent with those based on an analysis of constant-stress data. Some materials, notably solid-solution alloys such as W — 25Re, Mo — 30W, and some tantalum alloys, have displayed creep curves consisting of only third-stage creep when tested at constant load. Similar curves were obtained for AC molybdenum at 2400°C (0.93 T_m) as shown in Figure 1.32. These data do not permit an analysis to be performed on the basis of linear creep rate.

To evaluate the difference due to constant-stress testing, constant-stress tests of Mo—30W (wt %) were performed at 2200°C and 0.352 kg/mm². Creep curves for two constant-stress tests and one constant-load test are shown in Figure 1.53. The results show a marked dif-

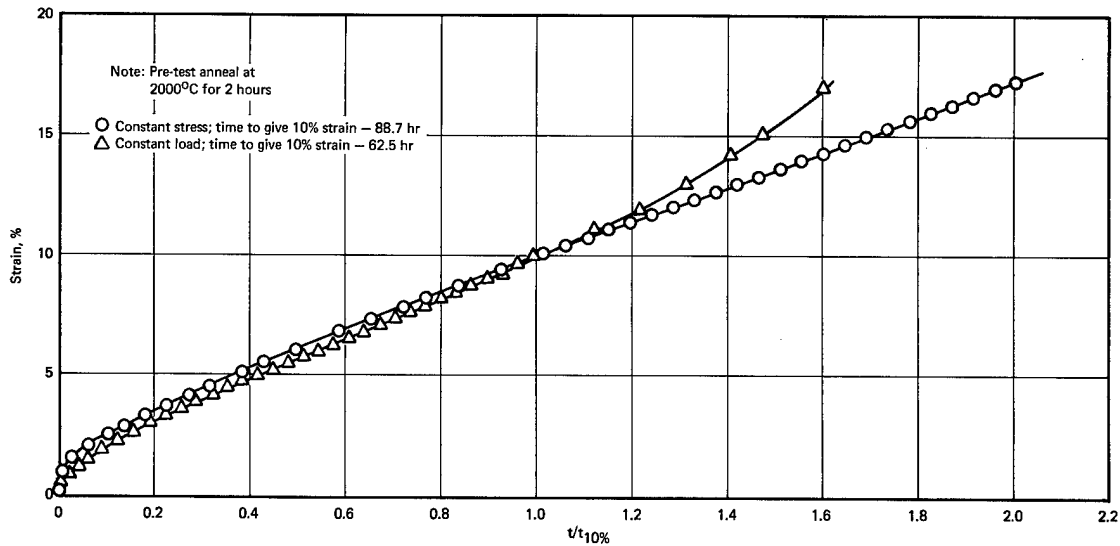


Fig. 1.51 — Comparison of constant-load and constant-stress creep curves for arc-cast Mo sheet tested at 1600°C and 0.844 kg/mm² in hydrogen

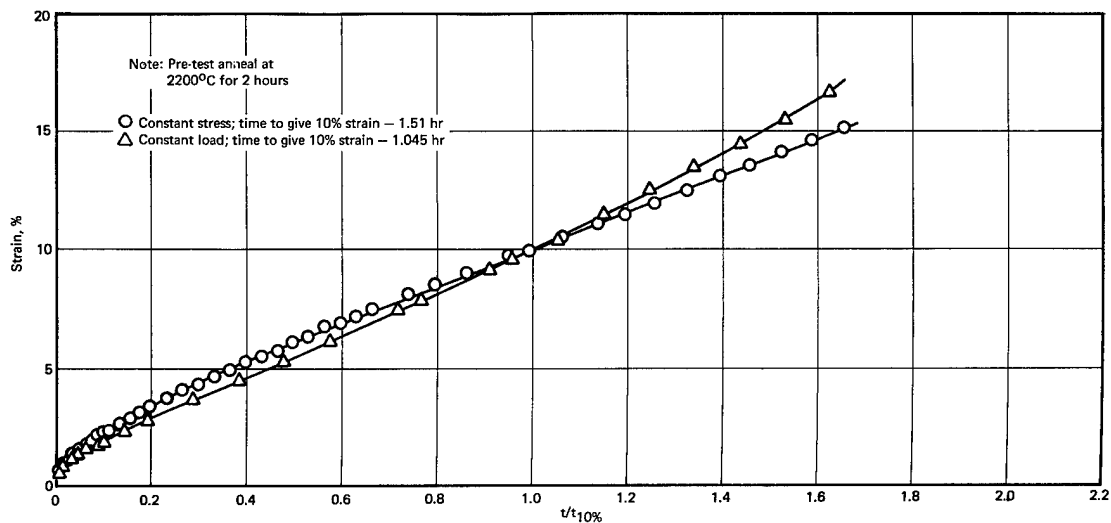


Fig. 1.52 — Comparison of constant-load and constant-stress creep curves for arc-cast Mo sheet tested at 2200°C and 0.35 kg/mm² in hydrogen

ference in the curve shapes. Whereas, the constant-load test displays a curve of increasing creep rate from time zero, one of the constant-stress tests gave essentially a linear creep curve to a strain of 65 percent. This indicates that uniform deformation over the length of the gage section occurred to at least this strain level. Strain measuring beyond this level was not possible with the test equipment and the test was terminated. The lower constant-stress creep curve in Figure 1.53 shows a decreasing rate of deformation after approximately 25 percent strain. This was caused by a greater load removal rate than actually needed to maintain constant stress. Deformation of the specimen from this test was quite uniform over the total length of the gage section (2.54 cm) after 36 percent strain as shown in Figure 1.54. The same observation was made for the sample tested to 65 percent strain.

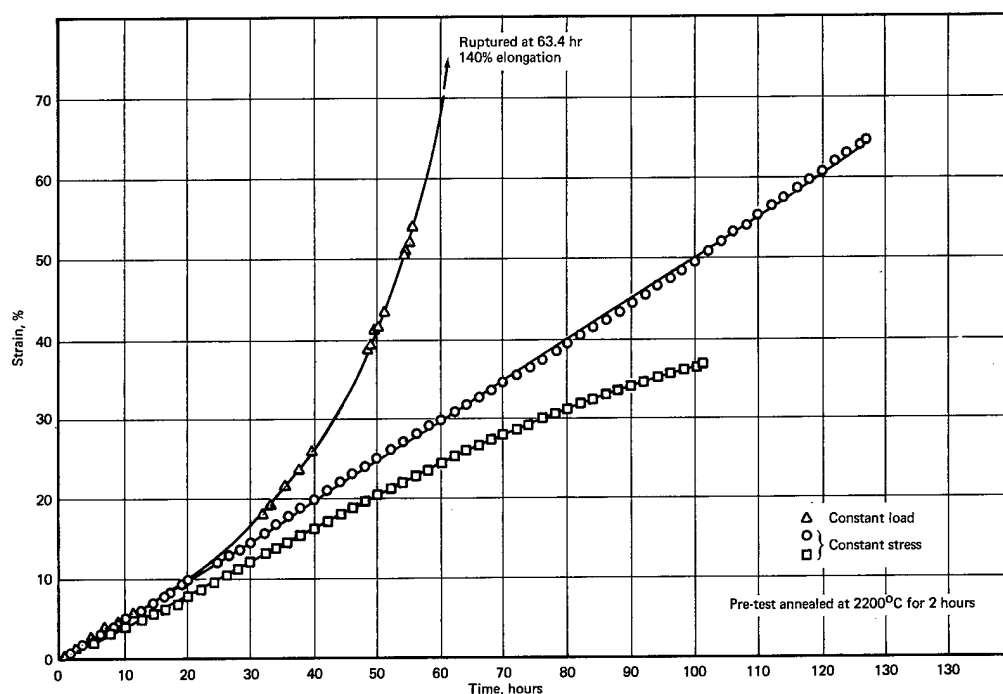


Fig. 1.53 — Comparison of constant-load and constant-stress creep curves for arc-cast Mo — 30W (wt %) tested at 2200°C and 0.352 kg/mm²

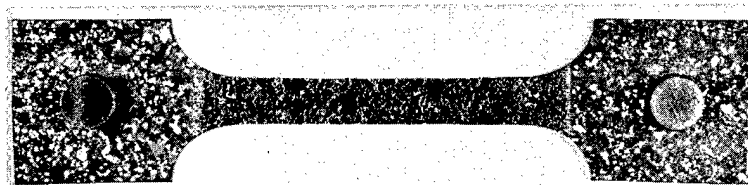


Fig. 1.54 — Mo — 30W (wt %) creep sample after testing at 2200°C and 0.352 kg/mm² showing 36% strain (2.54-cm gage length)(Neg. P68-I-12B)

Computer analysis procedures were developed to analyze constant-load creep tests in terms of instantaneous creep rate and instantaneous stress (see creep analysis section under Tungsten) to determine the dependence of strain rate on stress. This technique was employed to analyze the experimental results obtained at constant stress. Figure 1.55 shows the results for both types of testing. The constant-load test of this one sample shows the creep rate to be proportional to stress to the 4.6 power over the range from 0.35 to 0.5 kg/mm². The data points for the two constant-stress tests show reasonably good agreement with the constant-load test in terms of creep rate. The difference in the two constant-stress tests is probably due to experimental variations associated with precise temperature measurement at 2200°C, the normal precision being $\pm 10^\circ\text{C}$ at 2200°C.

Experimental creep data obtained at both constant-load and constant-stress indicate that constant-load creep data may be analyzed in terms of constant stress with no significant error due to the increasing stress as the result of strain until non-uniform deformation occurs. This appears to apply for materials exhibiting the conventional creep curve, consisting of the three stages of creep, as well as a material exhibiting only third-stage-type creep.

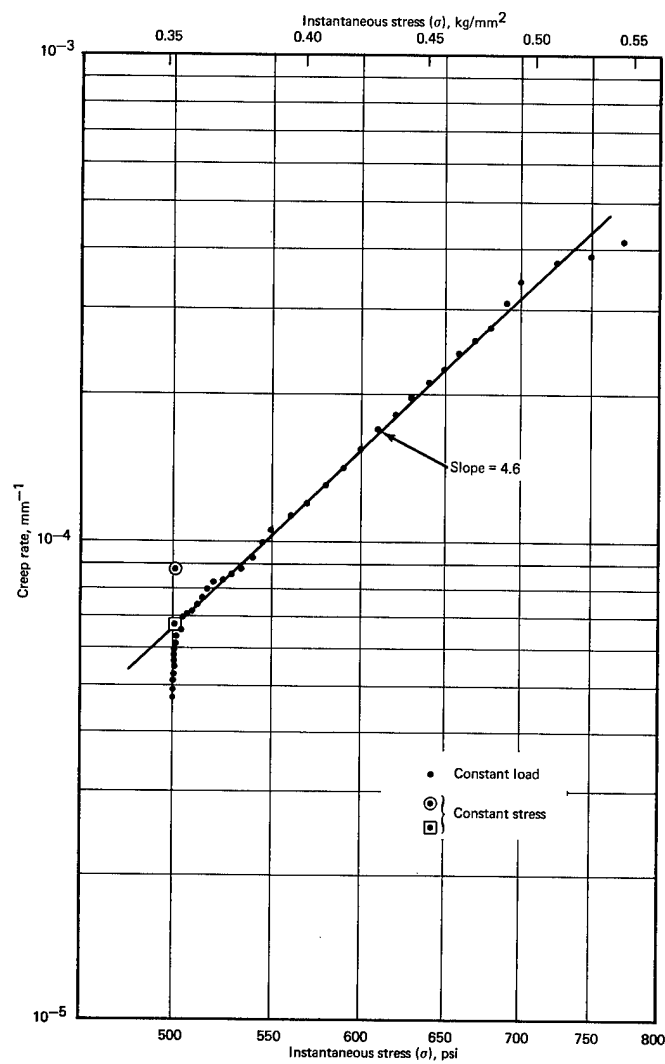


Fig. 1.55 — Comparison of constant-load and constant-stress creep tests in terms of creep rate for Mo — 30W (wt %) at 2200°C and 0.352 kg/mm²

SINGLE CRYSTALS

Unalloyed, powder-metallurgy tungsten sheet straps, 0.05 cm thick by 1.9 cm wide by 19 cm long, are used to support the sheet-type test specimens during creep testing at 1600° to 3000°C in hydrogen. During testing, large grains are sometimes developed in the straps with the sizes apparently dependent on temperature, time, and stress. One such test performed at 2200°C for 315 hours produced a single crystal of tungsten over approximately one-half the length of a strap. Using the Laue back-reflection X-ray diffraction technique, it was confirmed that the strap was a single crystal and had a nearly perfect (114) orientation with the stress axis along the (110) direction.

Creep-rupture tests of polycrystalline tungsten have been shown to exhibit correlatable characteristics consistent with other pure materials. The creep characteristics of single crystals are not understood, in general, and no data at high temperatures seem to be available for single-crystal tungsten. A creep-rupture test of the single-crystal sheet material was performed in hydrogen on a specimen having a 0.64-cm-wide by 2.54-cm-long gage section fabricated by the electrical discharge machining process (Elox). Table 1.11 lists the test conditions and results. These data show the single-crystal material to be stronger than polycrystalline, wrought, AC tungsten.

Figure 1.56 shows the single-crystal test specimen before and after testing. The significant observation is that essentially no deformation occurred prior to rupture other than that occurring locally at the 0.01-cm holes used as fiducial marks for strain measurements. The mode of fracture is not clear but near the center of the gage length there is an indication of slip along some plane of the crystal. Investigations are underway to study this region of the specimen using X-ray diffraction, metallography, and the electron microscope. These studies should provide some explanation of the mode of deformation in single-crystal, PM tungsten at extremely high temperatures.

TABLE 1.11
CREEP RESULTS OF SINGLE-CRYSTAL, UNALLOYED
TUNGSTEN SHEET TESTED IN HYDROGEN

Temperature, °C	Stress, kg/mm ²	Time, hr	Strain, ^a %
2400	0.46	22	0 (5.0)
2400	1.05	22	0 (rupture at 3.1 hr - 85%)
2600	1.05	22	0 (rupture on loading)
2800	1.05	53.6	Rupture

^aValues in parentheses refer to data for polycrystalline arc-cast tungsten.

STRESS-RUPTURE PARAMETER ANALYSIS

A comprehensive study of stress-rupture parameters was completed.⁴⁸ In addition to a detailed treatment of the three most common parameters, Larson-Miller, Dorn, and Manson-Haferd, appropriate attention was given the Graham-Walles, Murry, Chitty-Duval, and Brozzo parametric approaches. In each case, special consideration was given to the mathematical procedures employed in identifying parameter constants and in developing an analytical expression relating parameters to stress. Also, a detailed comparison was made of the relative effectiveness of these parameters in the correlation and extrapolation of experimental data. As part of this comparison, mathematical optimization procedures were employed to re-evaluate numerous sets of experimental data which have appeared in the literature.

⁴⁸J. B. Conway, "Stress-Rupture Parameters: Origin, Calculation and Use," GE-NMPO, GEMP-555, June 30, 1967.

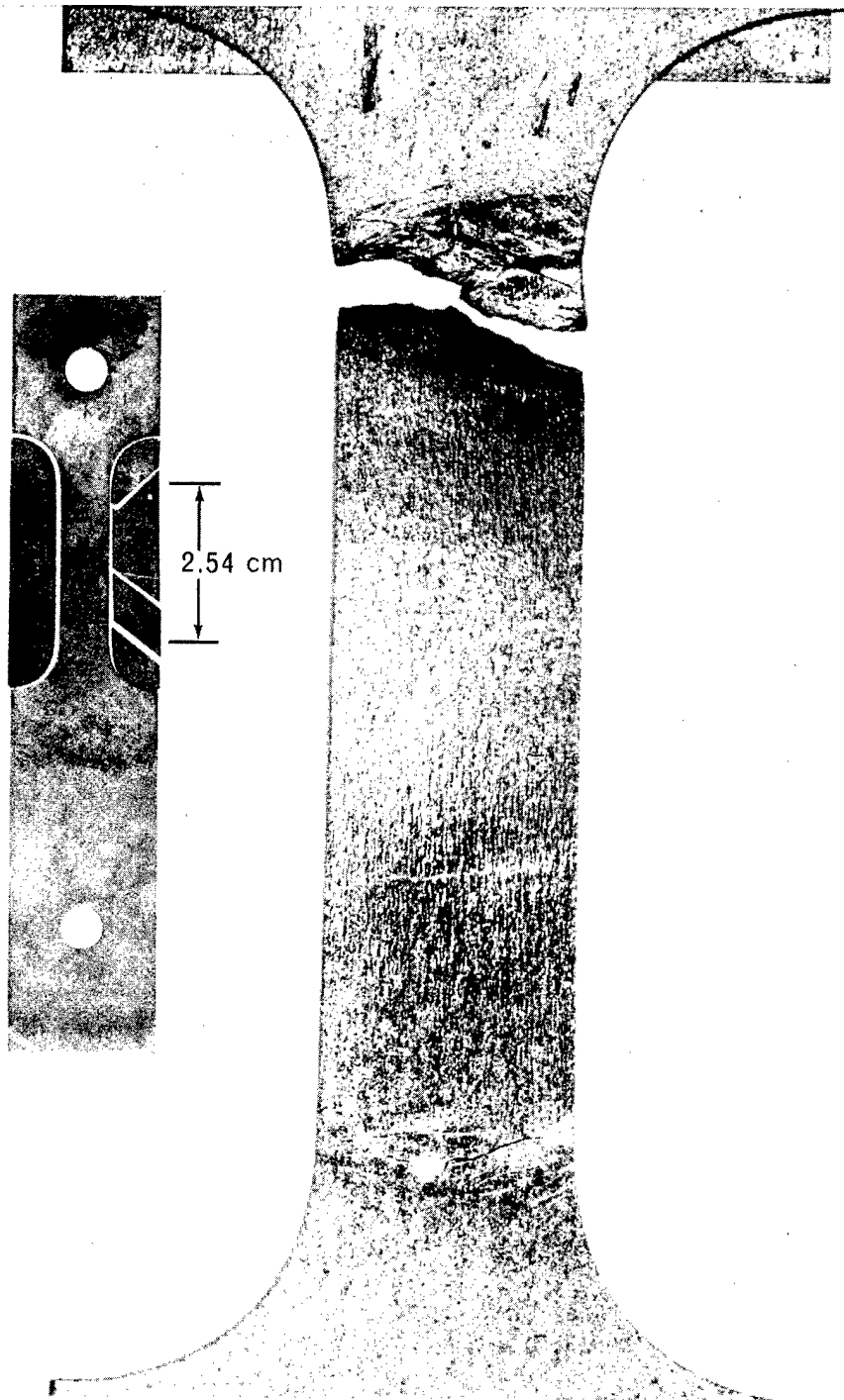


Fig. 1.56 — Single-crystal, unalloyed W sheet before and after rupture testing for 53.6 hours at 2800°C and 1.05 kg/mm² (Neg. P67-4-23A; Inset, Neg. P67-3-44A)

Several typical developments evolved during the above study are presented below.

Timken 35-15 Stainless Steel

In a recent study by Clauss,⁴⁹ the stress-rupture data for Timken 35-15 stainless steel were correlated in terms of the Larson-Miller parameter using a constant $C = 20$. A plot of this correlation is shown in Figure 1. 57a indicating a high degree of scatter about an average behavior given by the solid curve. Dashed lines are used to demonstrate that the data at each temperature seem to describe a separate line and, hence, poor correlation is indicated. Obviously, when the solid curve is used for extrapolation to lower stresses at a given temperature, rupture times are predicted which are much higher than those actually observed.

When these same data were analyzed using the optimization procedures described previously,⁵⁰ the results shown in Figure 1. 57b were obtained. In this case, the Larson-Miller constant is found to be 12.2 and results in a very excellent correlation. Extrapolation of these results to lower stresses would seem to be capable of yielding fairly acceptable results.

In Figure 1. 57c, the correlation obtained when $C = 5$ is presented. Here, too, when the C value is different from the optimum an extremely poor correlation results. It is apparent that as the C value is decreased, the isotherms assume different positions with respect to the average parameter curve until, at the optimum C value, all isotherms appear to be coincident with an average curve which can be drawn through all the points. Actually, the solid curve in Figure 1. 57b represents a polynomial developed in the least-squares optimization procedure applied to the Larson-Miller parameter.

Arc-Cast W, Mo, and W - 25Re

A linear relationship was identified⁵⁰ for the stress-rupture data of Hastelloy N when the natural logarithm of the Dorn parameter was plotted as a function of the natural logarithm of $\sinh(C\sigma)$, where C is a constant and σ is the stress. A similar approach was employed in analyzing the stress-rupture data for arc-cast W, Mo, and W - 25Re. As shown in Figure 1. 58, linear relations are obtained. Such plots can be compared to the standard master-rupture plots which usually yield a curved relationship.

When the hyperbolic sine approach is employed, it is possible to define the linear type of relationships shown. With this approach it would appear that extrapolation beyond the experimental stress range can be effected with more confidence than when the master rupture plot is curved.

In a similar analysis the Larson-Miller parameter was employed, and, as in Figure 1.58, a linear relationship was defined using the hyperbolic sine stress function. These results are presented in Figure 1. 59 where excellent linearity is seen to exist.

Timken 25-20 Stainless Steel

In an evaluation of the rupture data for Timken 25-20 stainless steel, Clauss employed the Larson-Miller approach, with $C = 20$, and found that a very unsatisfactory correlation resulted. On the parameter plot, data for each temperature described individual lines and no general correlation was noted. In the present study, these same data were analyzed using optimization procedures with the results shown in Figure 1. 60. It can be seen that all three parameters appear equally effective in the representation of these data, at least if the stand-

⁴⁹F. J. Clauss, "An Examination of High-Temperature Stress-Rupture Correlating Parameters," Proc. of ASTM, Vol. 60, 1960, p. 905.

⁵⁰"High-Temperature Materials Program Progress Report No. 63," GE-NMPO, GEMP-63, December 30, 1966, p. 13.

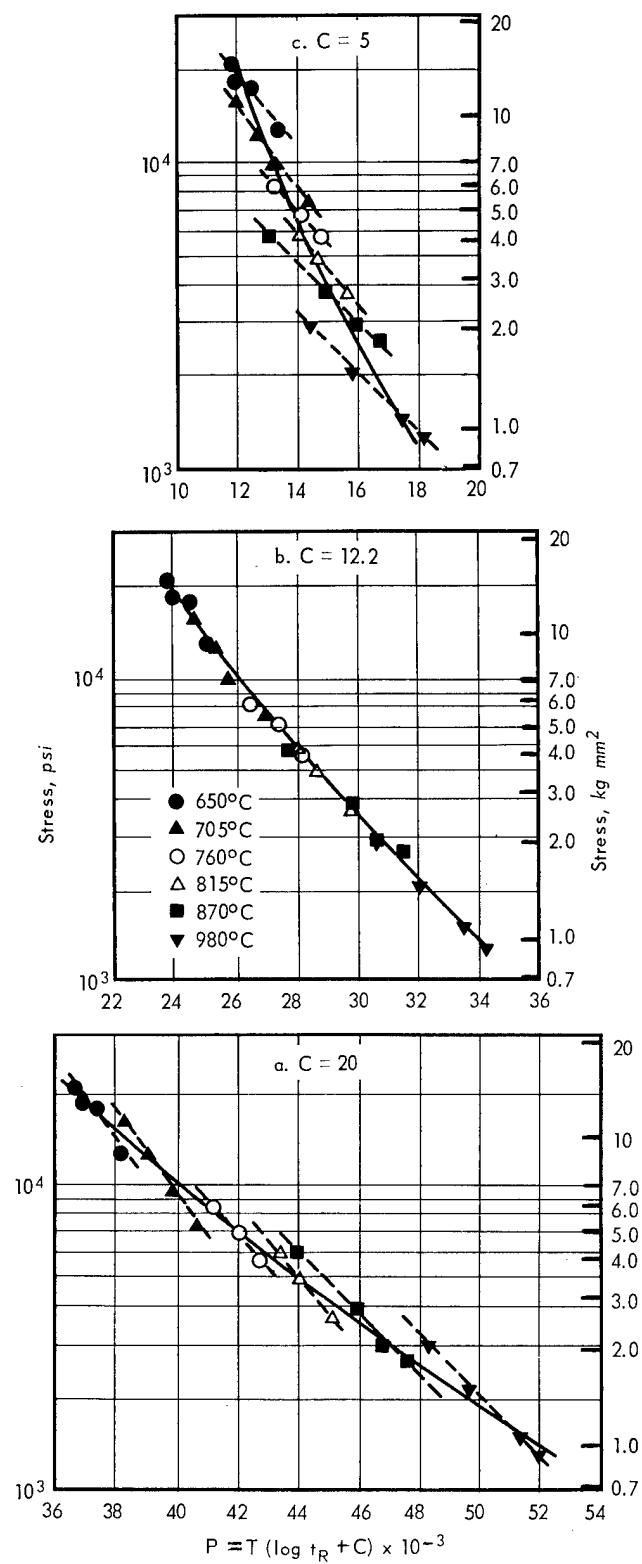


Fig. 1.57 — Larson-Miller plots of Timken 35-15 data illustrating effect of various C values

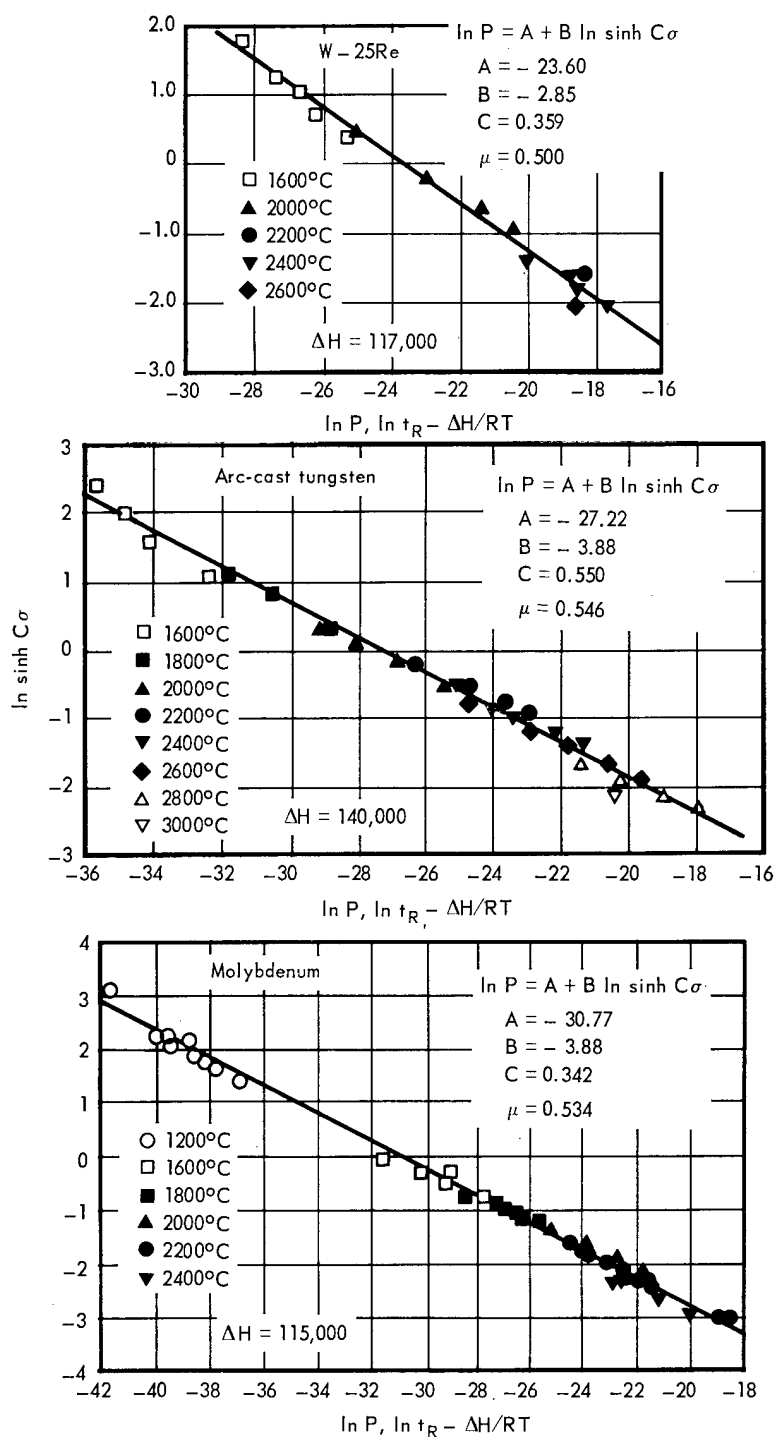


Fig. 1.58 — Dorn parameter plot for arc-cast W, Mo, and W — 25Re using hyperbolic sine stress function

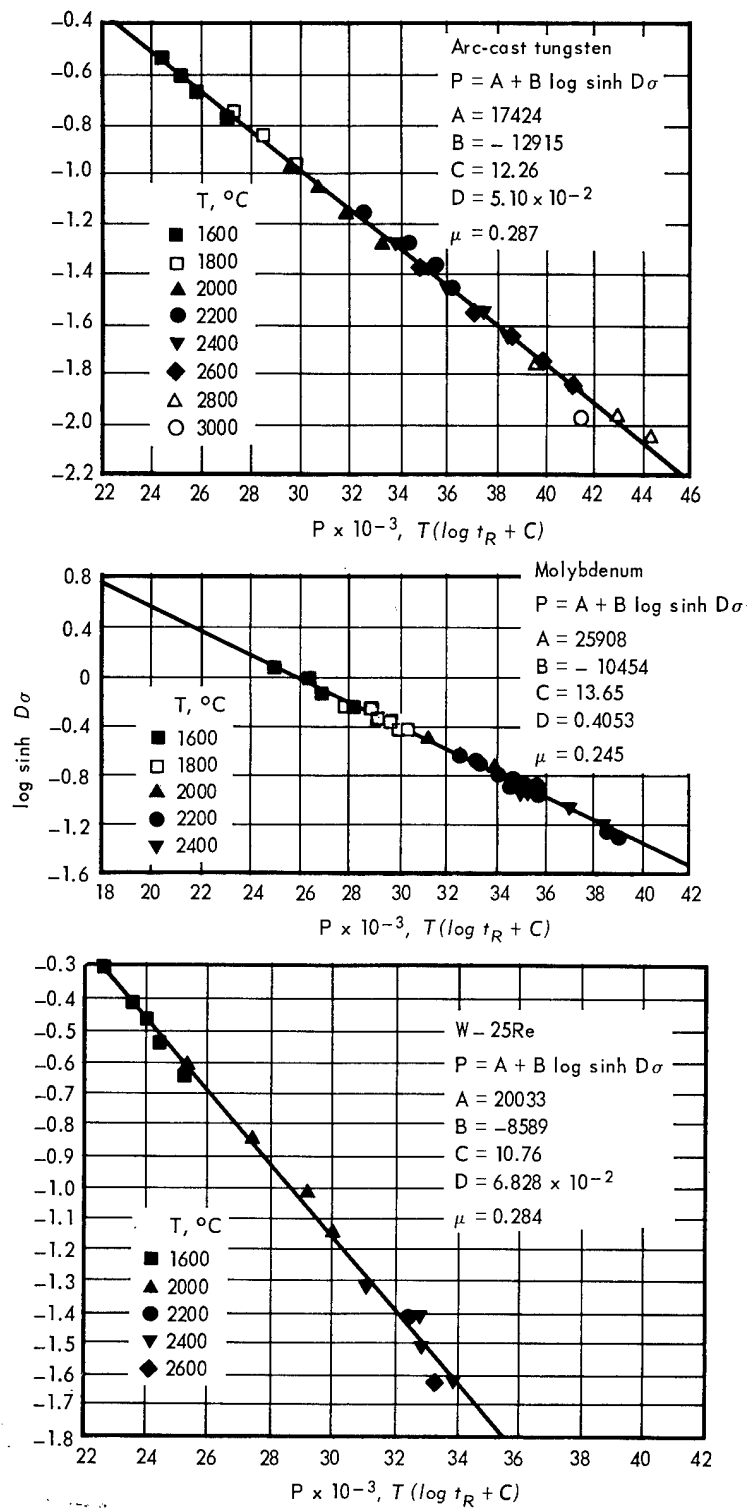


Fig. 1.59 — Larson-Miller parameter plot for arc-cast W, Mo, and W - 25Re using hyperbolic sine stress function

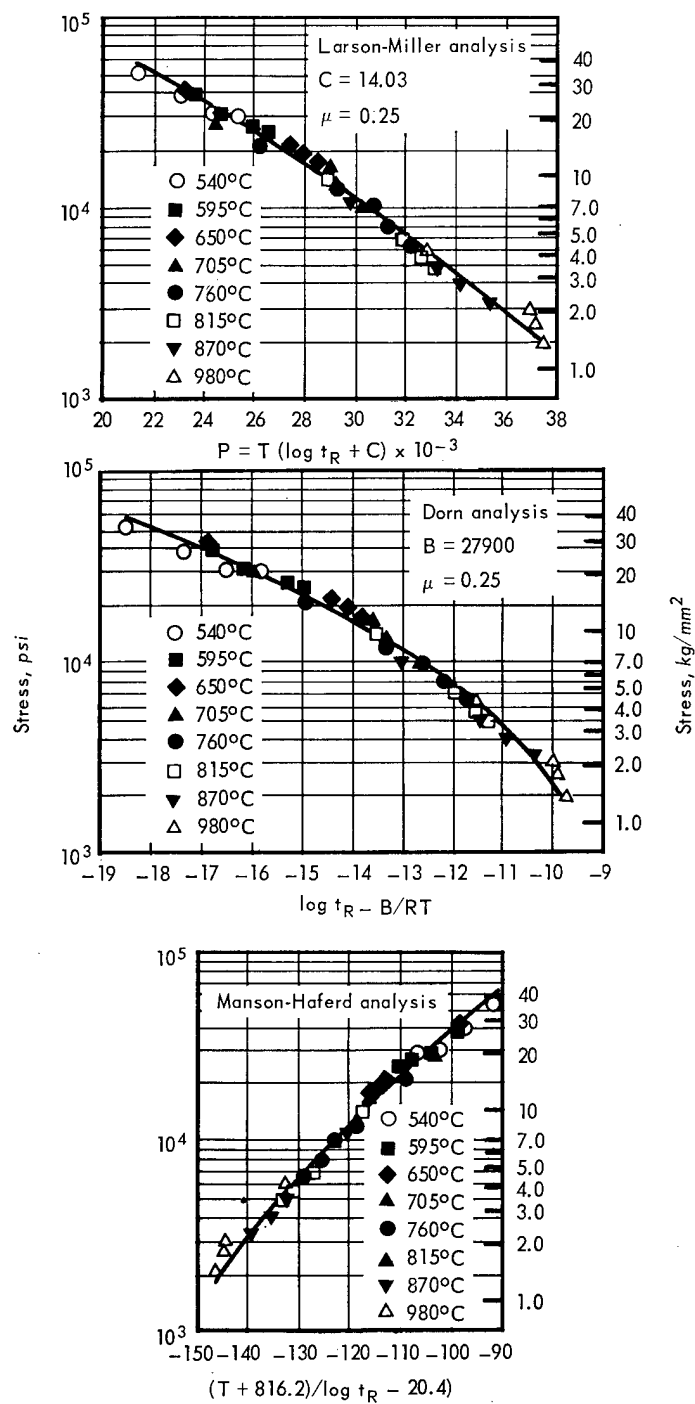


Fig. 1.60 — Rupture data for Timken 25-20 stainless steel analyzed in terms of various parameters

ard deviation, μ (based on log time) is used as a guide. For the Larson-Miller approach, the optimized C value of 14.03 yields a much better correlation than that observed in the Clauss analysis.

S-590 Alloy

Some indication of the relative extrapolative effectiveness of the Larson-Miller, Dorn, and Manson-Haferd parameters was provided in an analysis of the rupture data for S-590.⁵¹ Employing optimization procedures, and assuming a second-degree polynomial relating the parameter to log stress, master-rupture plots were prepared for the three parameters. In one case, the analysis was based on data points below 10,000 hours while in a second evaluation only data points below 2000 hours were included.

Using the master rupture plots, the predicted rupture times corresponding to conditions beyond the range of data used in making the analysis were compared to actual experimental values. This comparison is presented in Table 1.12 where the standard deviations (based on log time) for each set of results indicate the Dorn parameter to be the most effective in the case of the 10,000-hour data with the Manson-Haferd slightly less effective. Rather poor results are seen for the Larson-Miller parameter. In the 2000-hour analysis, approximately equal effectiveness is seen for the Dorn and Manson-Haferd parameters with the Larson-Miller parameter again somewhat less effective. While these results identify certain parameters as being more effective than others, it cannot be concluded that this is a general result. For other data, the Larson-Miller parameter may give the best extrapolations.

TABLE 1.12
COMPARISON OF PREDICTED AND EXPERIMENTAL RUPTURE TIMES
FOR S-590 ALLOY FOR LARSON-MILLER, DORN, AND
MANSON-HAFERD PARAMETERS

WILSON TENSILE FAILURE PARAMETERS						
Stress		Temperature, °C	Experimental Rupture Time, hr	Predicted Rupture Times, hr		
kg/mm ²	psi			L-M	Dorn	M-H
Based on S-590 data, $t_R < 10,000$ hours						
17.6	25,000	1200	43,978	62,248	42,958	41,698
21.1	30,000	1200	11,937	11,999	9,977	10,085
12.3	17,500	1350	16,964	19,508	13,493	16,378
7.0	10,000	1500	15,335	34,465	17,436	21,870
7.0	10,000	1500	11,257	34,465	17,436	21,870
				$\mu = 0.278$	0.105	0.151
Based on S-590 data, $t_R < 2,000$ hours						
35.2	50,000	1100	3,149	1,661	1,614	1,467
24.6	35,000	1200	2,243	2,582	2,206	2,304
14.1	20,000	1350	9,529	5,921	4,234	5,143
8.8	12,500	1500	5,052	6,428	4,076	5,084
17.6	25,000	1200	43,978	50,747	29,856	29,860
21.1	30,000	1200	11,937	10,069	7,518	7,715
12.3	17,500	1350	16,964	17,761	10,332	13,067
7.0	10,000	1500	15,335	35,918	13,873	19,445
7.0	10,000	1500	11,257	35,918	13,873	19,445
				$\mu = 0.244$	0.195	0.190

⁵¹R. M. Goldhoff, "Comparison of Parameter Methods for Extrapolating High Temperature Data," ASME Trans. J. of Basic Engrg., Vol. 81, 1959, p. 629.

COMPARISON OF TEST DATA

During the last few years, stress-rupture and creep data have been obtained for a number of refractory metals and alloys from 1600° to 2800°C. Stresses required to cause rupture in 1, 10, 100, and 1000 hours at 1600°C and 2200°C are given in Table 1.13 for a number of materials. Items of note are (1) at 1600°C arc-cast W-25Re has the highest 100-hour rupture stress, whereas at 2200°C powder-metallurgy rhenium has the highest value followed by tungsten; (2) available data have indicated different behavior for arc-cast and powder-metallurgy forms of the same material. Figures 1.61 and 1.62 give isochronal stress-rupture data as a function of temperature for 1 and 100 hours. The change in rupture life with respect to temperature and time is readily seen.

TABLE 1.13
STRESS TO CAUSE RUPTURE AT TIMES INDICATED FOR VARIOUS
REFRACTORY METALS AND ALLOYS

Material ^{a,b}	1600°C				2200°C			
	Stress, ^b kg/mm ² , at hours indicated				Stress, ^b kg/mm ² , at hours indicated			
	1	10	100	1000	1	10	100	1000
Tungsten								
AC	7.7*	5.2	3.6	2.5	2.0*	1.3	0.88	0.49
PM	0.84	5.5	3.5		2.3	1.6	1.1	
Molybdenum								
AC	2.5	1.5	0.98	0.62	0.46	0.28	0.17	0.098*
PM			1.3		0.70	0.59	0.38*	
Rhenium								
PM No. 1		5.6	3.1		3.5	2.2	1.2	
PM No. 2		7.4	4.8	3.2*	4.2*	2.8	1.7	
Niobium								
AC	0.63	0.39						
W-25Re (wt %)								
AC	15.*	8.8	4.9	2.8	2.5	1.3	0.70	0.38
PM	15.*	7.9	4.1		1.9	1.1	0.44*	
Mo-30W (wt %)								
AC	5.2*	3.0	1.8	1.0	1.0*	0.57	0.32	0.17
Mo-50Re (wt %)								
PM No. 1	4.3	2.7	1.7	1.1*	0.81	0.35	0.15	0.063*
PM No. 2	4.3	2.4	1.3	0.75*	0.81	0.35	0.15	0.063*
W-30Re-30Mo (at. %)								
AC		5.9*	2.8*			0.70*	0.42	0.25*
		4.2	2.2			0.74*	0.32	
Mo-5W (at. %)								
PM	4.7*	2.5	1.3		0.75*	0.48	0.31	
Mo-5Re (at. %)								
PM	4.7*	2.5	1.3		0.69*	0.46	0.31	
Re-10Os (at. %)								
PM		6.7	4.5			2.7	1.1	
Ta-10W (wt %)								
AC		7.7	4.9*		2.1*	1.2*		
Mo-TZM								
AC					0.48	0.28		
Tantalum								
AC	1.4				0.34*			
PM								
Cb-753 ^c								
AC			0.84					

^aValues with asterisk are based on extrapolations.

^bWrought sheet material, AC = arc-cast, PM = powder metallurgy.

^cNb-5V-1.25Zr (wt %).

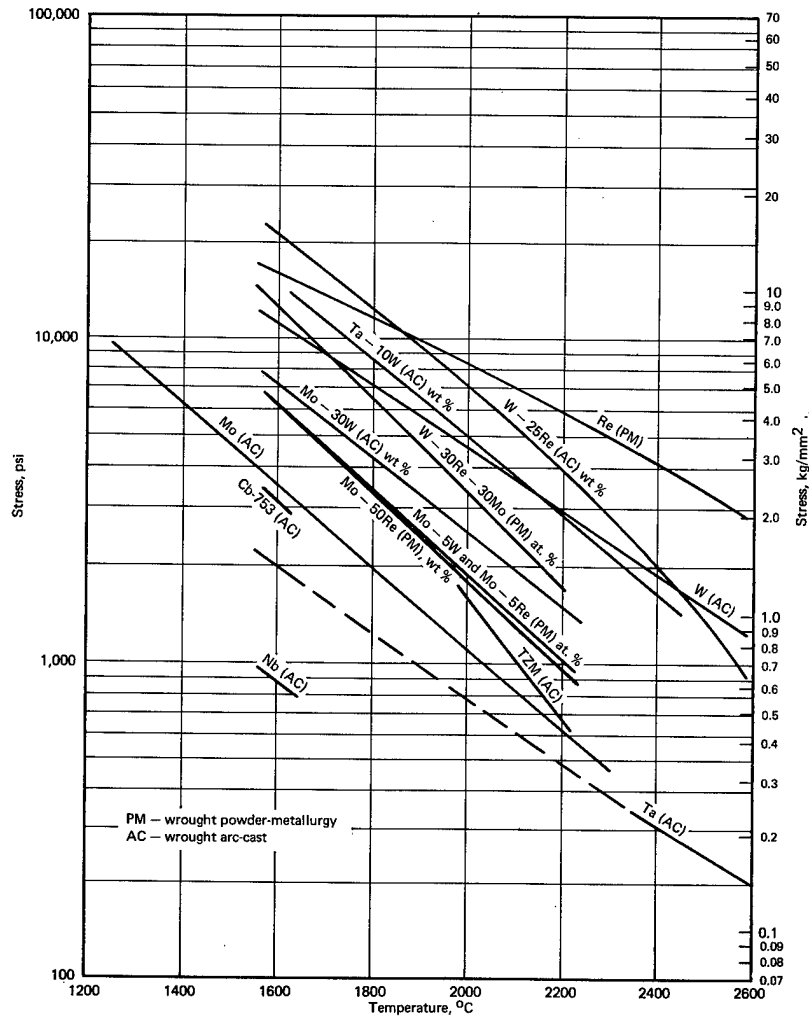


Fig. 1.61 — 1-hour isochronal stress-rupture data for various refractory metals and alloys

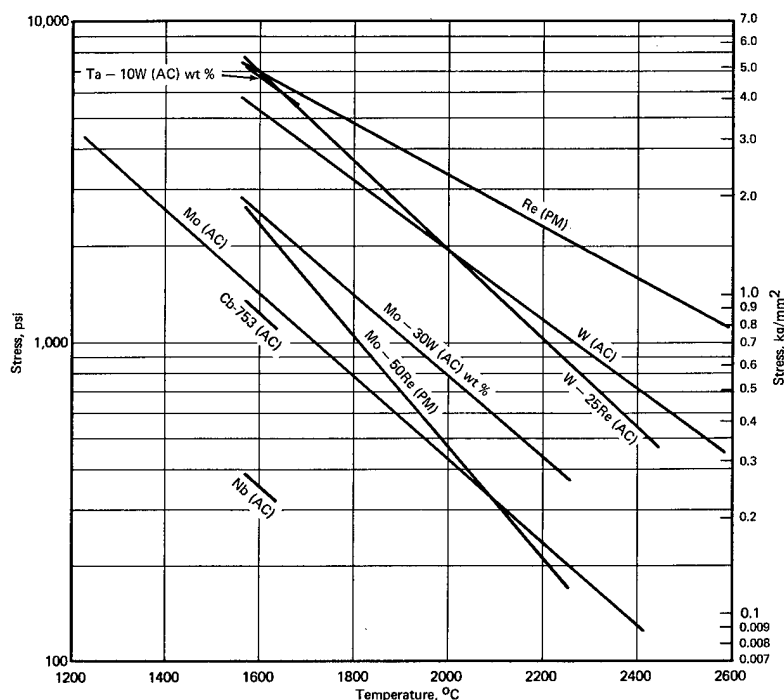


Fig. 1.62 – 100-hour isochronal stress-rupture data for various refractory metals and alloys

1.2 THERMAL PROPERTY EVALUATIONS

ELECTRICAL RESISTIVITY AND THERMAL CONDUCTIVITY

Measurements of the electrical resistivity of W – 26Re (wt %) and unalloyed tungsten were made from room temperature to 1600 °C in argon plus hydrogen. These data⁵² are presented in Figure 1.63 along with some representative literature values.^{53–57} A least squares analysis of these data yielded the following relationships:

W – 26Re

$$\rho = 1.86430 \times 10^{-5} + 3.37090 \times 10^{-8}T - 1.29457 \times 10^{-12}T^2 \quad (1.17)$$

$$\mu = 2.43036 \times 10^{-7} \text{ ohm-cm}$$

Tungsten

$$\rho = 4.33471 \times 10^{-12}T^2 + 2.19691 \times 10^{-8}T - 1.64011 \times 10^{-6} \quad (1.18)$$

$$\mu = 3.03318 \times 10^{-7} \text{ ohm-cm} \quad 300^\circ\text{K} \leq T < 1240^\circ\text{K}$$

⁵²GEMP-1002, pp. 26–31.

⁵³D. L. McElroy, "High Temperature Materials Program Quarterly Report for Period Ending April 30, 1966," ORNL-TM 1520, Part 1, pp. 53–58.

⁵⁴J. P. Moore, R. S. Graves, W. Fulkerson, and D. L. McElroy, "The Physical Properties of Tungsten," 1965 Conference on Thermal Conductivity, Denver, Colorado, October 1965, by permission.

⁵⁵R. P. Tye, "Preliminary Measurements on the Thermal and Electrical Conductivities of Mo, Nb, Ta, and W," from Niobium, Tantalum, Molybdenum, and Tungsten, A. G. Quarell, Editor, Elsevier Publishing Co., Amsterdam, 1961.

⁵⁶A. G. Worthing and E. M. Watson, "Resistance and Radiation of Tungsten as a Function of Temperature," J. Opt. Soc. A., Vol. 24, 1934, p. 114.

⁵⁷V. S. Gumenyuk and V. V. Lebedev, "Investigating Heat and Electro-Conduction of Tungsten and Graphite at High Temperatures," Fizika Metallov and Metalovedeniye (2 Jan. 1961), Nr. 1, pp. 29–33, Translation USAEC-NP-TR733.

and

$$\rho = -4.06012 \times 10^{-12} T^2 + 4.67093 \times 10^{-8} T - 1.97071 \times 10^{-5} \quad (1.19)$$

$$\mu = 1.56328 \times 10^{-6} \text{ ohm-cm} \quad 1240^\circ\text{K} < T < 2570^\circ\text{K}$$

where:

ρ = electrical resistivity, ohm-cm

T = temperature, $^\circ\text{K}$

μ = standard deviation

Previously reported data⁵² for the thermal conductivity of W - 26Re (density close to 98 percent of theoretical) are summarized in Figure 1.64. Using the resistivity data reported above, the thermal conductivity data were analyzed to yield:

$$k = 2.443 \times 10^{-8} \frac{T}{\rho} + \frac{1}{0.7493 + 7.3427 \times 10^{-3} T} \quad (1.20)$$

(standard deviation = 4.5818×10^{-2} watt/cm $^\circ\text{C}$)

where:

k = thermal conductivity, watt/cm $^\circ\text{C}$

T = temperature, $^\circ\text{K}$

ρ = electrical resistivity, ohm-cm

Also shown in Figure 1.64 are data for W - 25Re reported by Jun and Hoch⁵⁸ and other data estimated by McElroy.⁵³ Fairly good agreement is noted between these data and those obtained in the NMPO studies.

THERMAL DIFFUSIVITY

A pulse-type diffusivity technique⁵⁹ based on the use of a laser was employed to measure the thermal diffusivity of commercial, powder-metallurgy W - 25Re in the temperature range from 300 $^\circ$ to 1000 $^\circ\text{C}$. Specimens were in the form of discs 0.63 cm in diameter by 0.18 cm in thickness. A platinum-wound muffle furnace was used to provide the desired test temperatures and an oscilloscope was employed to determine the temperature - time transient of the specimen following the laser pulse. The time required for the back surface of the specimen to reach a temperature corresponding to one-half the maximum rise was then used in the usual manner to calculate diffusivity values. Data obtained for the W - 25Re alloy are presented in Figure 1.65. Also shown in this figure are diffusivity values calculated from the thermal conductivity data for the W - 26Re composition shown in Figure 1.64. As shown the agreement is quite excellent.

Diffusivity data were also obtained for arc-cast and powder-metallurgy tungsten using specimens 0.152 and 0.203 cm in thickness and 0.63 cm in diameter. All diffusivity values were in good agreement indicating no effect due to specimen thickness or material form. Average diffusivity values obtained in these tests are presented in Figure 1.66; all experimental data were within ± 2 percent of this average curve. Also shown in Figure 1.66 are diffusivity data for tungsten calculated from some recent thermal conductivity data⁶⁰ reported for this material. Except at 300 $^\circ\text{C}$ where a difference of slightly greater than 10

⁵⁸C. K. Jun and M. Hoch, "Thermal Conductivity of Tantalum, Tungsten, Rhenium, Ta - 10W, T-222, W - 25Re in the Temperature Range 1500 $^\circ$ - 2700 $^\circ\text{K}$," Third International Symposium on High-Temperature Technology, Stanford Research Institute, September 17-20, 1967. To be published.

⁵⁹R. J. Freeman, "Thermal Diffusivity Measurements on Pre- and Post-Irradiated BeO," GE-NMPO, GEMP-452, November 15, 1966.

⁶⁰Moore, Graves, Fulkerson, and McElroy, loc. cit.

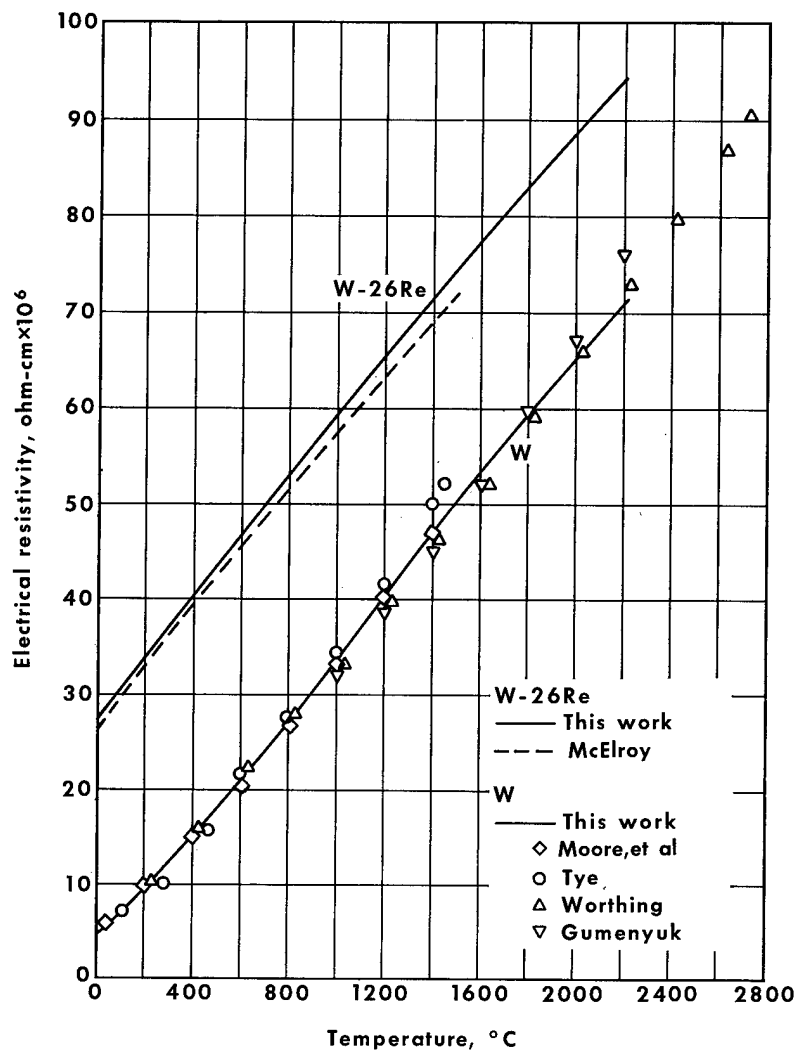


Fig. 1.63 — Electrical resistivity versus temperature for W — 26Re alloy and unalloyed W (AS-745B)

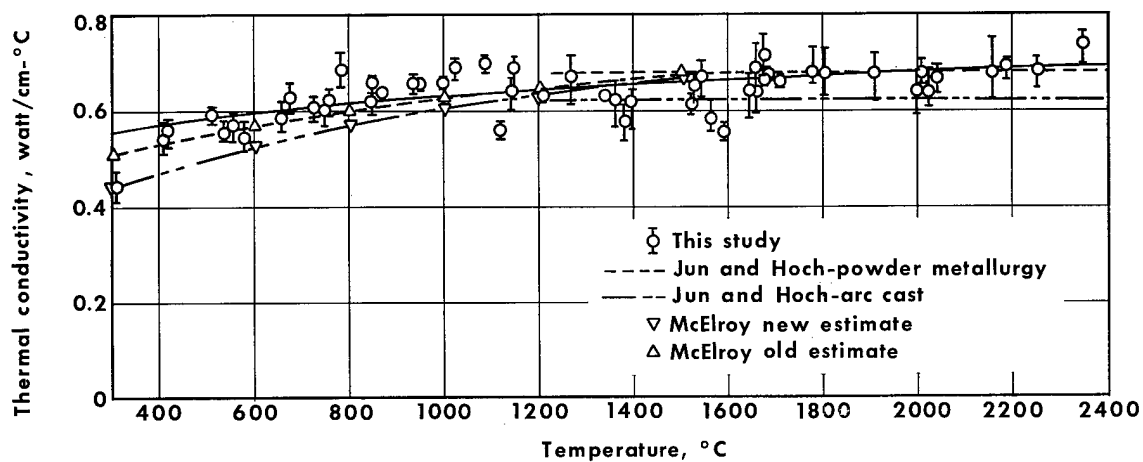


Fig. 1.64 — Thermal conductivity versus temperature for W — 26Re alloy (AS-745D)

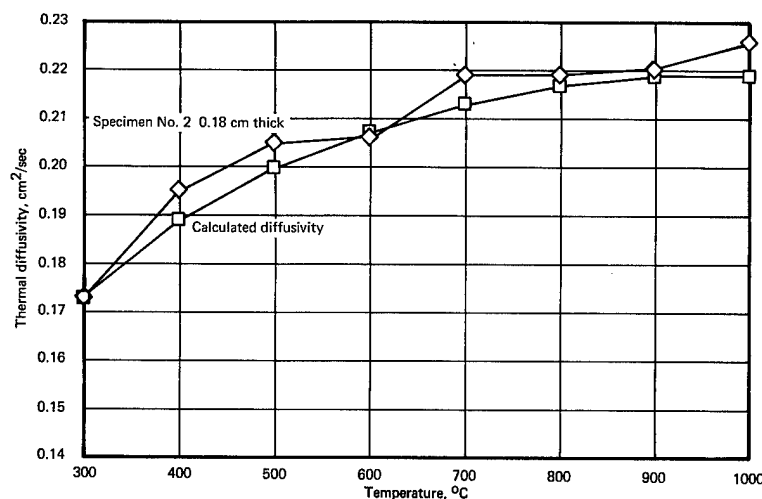


Fig. 1.65 — Thermal diffusivity versus temperature for W — 25Re (wt %) from 300° to 1000°C in argon atmosphere

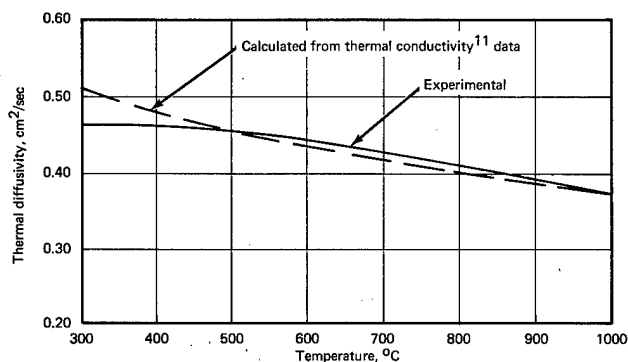


Fig. 1.66 — Average thermal diffusivity of tungsten from 300° to 1000°C in argon atmosphere (specimen thickness, 0.152 and 0.203 cm)

percent is indicated, agreement between measured and calculated diffusivity values is within 5 percent. This is excellent agreement considering the thermal conductivity data were obtained using a radial-flow steady-state technique, whereas the measured diffusivities were obtained by a transient procedure.

Diffusivity data were also obtained for 304L stainless steel in the temperature range from 300° to 1100°C. Testing was performed in argon using specimens 0.63 cm in diameter and 0.127 and 0.152 cm in thickness. The chemical composition of this material was: 18.37% Cr, 9.89% Ni, 0.024% C, 1.31% Mn, 0.70% Si, 0.014% P, 0.012% S, 0.09% Mo, and 0.05% Cu. A plot of the diffusivity data for this material is presented in Figure 1.67. It is important to note that for both specimen thicknesses the diffusivity increased slightly after the first heating to reveal an annealing effect.

ENTHALPY

Modifications were made to the drop calorimeter to permit enthalpy measurements to be made to 3000°C. Enthalpies of commercially pure (99.94%), powder-metallurgy tung-

sten were measured⁶¹ to 3250°K and are summarized in Figure 1.68. A least squares analysis of these data yielded:

$$H_T - H_{298^\circ K} = -1579.3 + 5.406T + 5.047 \times 10^{-4}T^2 + 271485X \quad (1.21)$$

where:

$$\begin{aligned} X &= \exp. (-35629.5/RT) \\ H_T &= \text{enthalpy in cal/mole} \\ R &= 1.9869 \text{ cal/mole} - ^\circ K \\ T &= ^\circ K \end{aligned}$$

applicable temperature range 1200° to 3250°K.

Differentiating the heat content equation yields the heat capacity equation:

$$C_p = 5.406 + 10.094 \times 10^{-4}T + 96728 \times 10^5 X/RT^2 \quad (1.22)$$

where:

$$C_p = \text{cal/mole} - ^\circ K$$

A comparison of the heat capacities obtained in this study with those reported in the most recent literature⁶²⁻⁶⁵ is given in Figure 1.69. Between 1200° and 2400°K agreement within 4 percent is shown for most of the data; however, this study is about 8 percent higher than that reported by Kirillin, et al.⁶³ at 3100°K. A slightly different equation was applied to Kirillin's data by West⁶⁵ to yield a slightly better representation; however, it only affected the C_p by about 2 percent (higher) at 3100°K.

1.3 SUMMARY AND CONCLUSIONS

Stress-rupture and creep data for wrought, arc-cast tungsten are presented for temperatures from 1600° to 3000°C and rupture times approaching 4000 hours. Good correlation is shown when analyzed in terms of the diffusion-compensated creep rate versus the modulus-compensated stress. The rupture ductility for arc-cast tungsten is a maximum (~20%) in the 2200° to 2400°C temperature range, whereas powder-metallurgy material shows a decrease in ductility (from 70%) with increasing temperature. Based on the counting of free dislocations for samples creep tested above one-half the absolute melting temperature, a power stress law is shown to apply indicating creep by dislocation climb or the glide of jogged screw dislocations. Optical microscopy and electron fractography studies of creep-rupture tested (1600° to 2800°C) powder-metallurgy and arc-cast tungsten indicate different mechanisms of failure operating in the two types of materials. The powder-metallurgy and arc-cast tungsten indicate different mechanisms of failure operating in the two types of materials. The powder-metallurgy material showed pronounced grain boundary separation and cavitation, whereas the arc-cast material showed no tendency to form cavities.

Stress-rupture and creep data are presented for wrought, arc-cast, unalloyed molybdenum sheet for temperatures from 1200° to 2400°C. Good correlation between the time to rupture and linear creep rate is shown except for the extremely high temperatures

⁶¹GEMP-1002, p. 34.

⁶²M. Hoch and H. L. Johnston, "A High Temperature Drop Calorimeter. The Heat Capacities of Tantalum and Tungsten Between 1000° and 3000°K," J. Phys. Chem., Vol. 65, 1961, pp. 855-860.

⁶³V. A. Kirillin, et al., "Thermodynamic Properties of Tungsten at 0° - 3500°K," Zhurnal Fizi Khimii, Vol. 37, No. 10, 1963, pp. 2249-2257.

⁶⁴G. C. Lowenthal, "The Specific Heats of Metals Between 1200°K and 2400°K," Aust. J. Phys., Vol. 16, No. 1, 1963, pp. 47-67.

⁶⁵E. D. West and S. Ishihara, National Bureau of Standards, Washington, D.C., Preliminary Data of the Enthalpy of Tungsten - private communication.

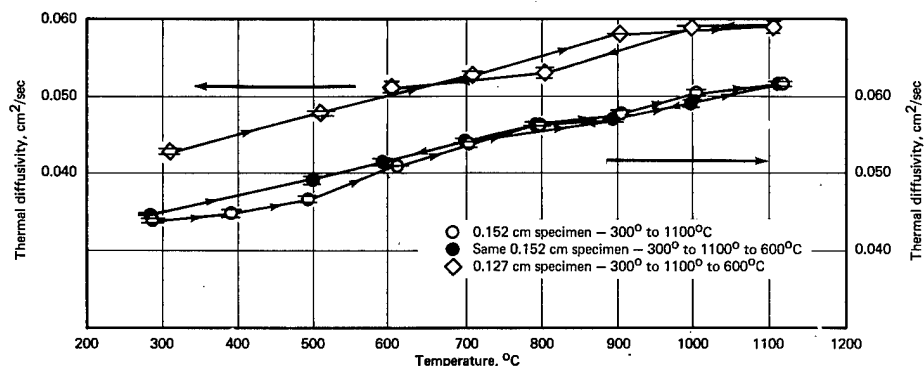


Fig. 1.67 – Thermal diffusivity of 304L stainless steel from 300° to 1100°C in argon atmosphere

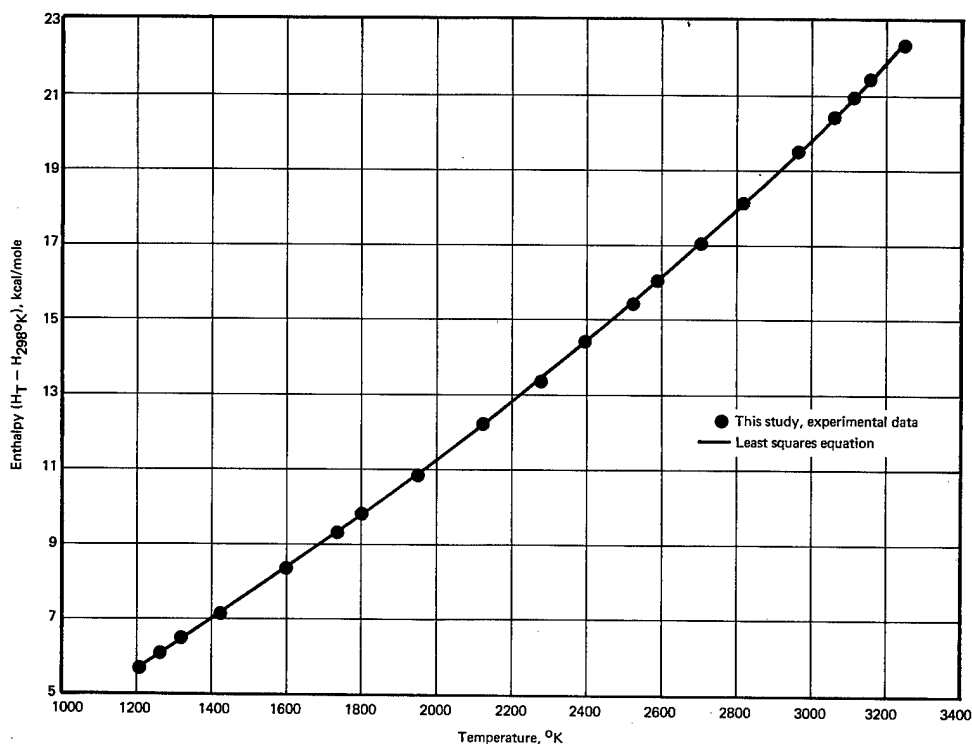


Fig. 1.68 – Enthalpy versus temperature for tungsten (99.94% purity)

and low stresses. The deviation appears to be related to a change in the creep mechanism indicated by a change in the form of the creep curve.

Creep-rupture data are presented for Re, W – 30Re – 30Mo (at. %), Mo – 30W (wt %), and W – 25Re (wt %) sheet tested in hydrogen at temperatures from 1600° to 2600°C.

Creep-rupture properties for powder-metallurgy Mo – 50Re (wt %) are presented for temperatures of 1600°, 2200°, and 2400°C. Diffusional creep is indicated at the higher temperatures and low stresses based on the creep rate versus stress relationship yielding a slope of unity. The diffusion coefficient for Mo – 50Re at 2400°C and 0.07 kg/mm² was calculated to be 1.14×10^{-7} cm²/sec.

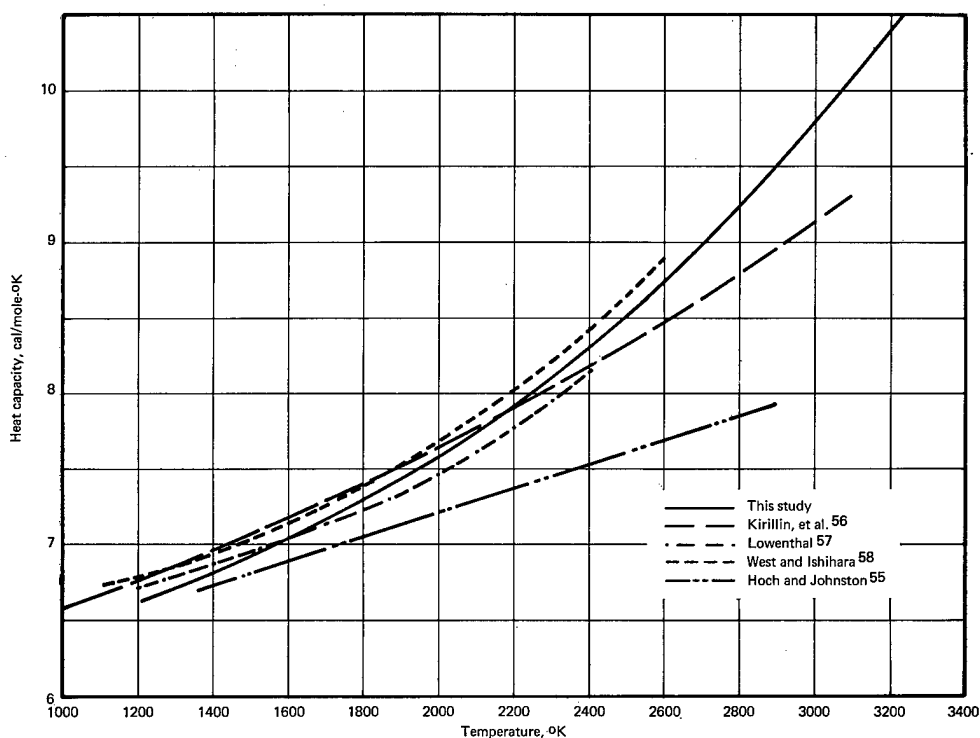


Fig. 1.69 — Heat capacity versus temperature for tungsten

Creep-rupture tests of Mo — 30W at 2200°C under constant load display a creep curve consisting only of third-stage-type creep with the elongation at rupture exceeding 100 percent. Identical tests performed at constant stress display a linear (secondary) creep rate to a strain of 65 percent.

Creep-rupture tests of powder-metallurgy tungsten at 2800°C and 1.05 kg/mm², in single-crystal form, displayed no detectable creep with fracture being brittle in nature. This result appears to be consistent with creep deformation observations for most powder-metallurgy, polycrystalline materials tested at high temperatures in that cavitation and/or grain boundary separation are the predominant mechanisms.

A comprehensive study of stress-rupture parameters was completed with special consideration given to the mathematical procedures employed in identifying parameter constants. Detailed comparisons were made of the relative effectiveness of these parameters in the correlation and extrapolation of experimental data.

Based on experimental measurements of thermal conductivity and electrical resistivity for W — 26Re (wt %), an expression describing the thermal conductivity from 400° to 2400°C is presented.

Enthalpies of unalloyed tungsten were measured from 1200° to 3450°K. Equations for heat content and heat capacity were determined from the data using a least squares analysis.

1.4 PLANS AND RECOMMENDATIONS

Stress-rupture and creep studies will be continued for commercially available and developmental refractory metal alloys as well as materials having potential application to

the LMFBR program. Evaluations will be performed in inert, reducing, and vacuum environments.

In an attempt to identify the mechanisms associated with creep resistance and deformation, optical and transmission electron microscopy studies of tested samples will be performed.

Creep tests at constant stress will be performed to afford a comparison with data obtained under constant load. The results will assist in determining the stress dependence of more complex materials.

Some physical properties will be determined for materials of interest. Properties such as enthalpy, thermal expansion, and thermal conductivity will be determined to temperatures approaching the melting point for design purposes as well as hazards evaluation. Some thermal diffusivity measurements to 1000°C are also planned.

2. RADIATION EFFECTS ON FAST REACTOR CLADDING AND STRUCTURAL MATERIALS

(1304)

J. Moteff,* F. D. Kingsbury,† J. P. Smith†

The objective of this program is to determine the effect of radiation on the time-, temperature-, and stress-dependent properties of selected heat-resistant alloys and refractory metals, to identify the causes of any changes observed in these properties, and to develop remedial measures.

The experimental program to study effects of neutron irradiation on the creep-rupture, tensile, hardness, and resistivity properties of the above classes of metals and alloys is continuing. Direct observations of defect configurations by means of the transmission electron microscope, and analysis of the neutron-induced defects and their migration behavior, are being performed and correlated with the measured changes in the mechanical properties. Detailed spectra studies are being performed to determine an accurate profile of flux and energy distribution of reactor positions used in the program.

Materials investigated in the heat-resistant alloys portion of the program include A-286, Hastelloy X, Hastelloy N (INOR-8), Hastelloy R-235, Fe-Cr-Al-Y alloys, AISI 304, 316, and 348 stainless steels, ASTM-A302B and A350-LF3 pressure vessel steels, and various Inconel and Incoloy alloys.

The refractory metals portion of the program includes investigations of V, Mo, Nb, W, Ta, and their alloys.

2.1 STATUS OF IRRADIATIONS (F. D. Kingsbury, J. P. Smith, W. S. Chenault)

EBR-II IRRADIATION PROGRAM

A planned program of fast neutron spectrum irradiations in the EBR-II reactor was initiated in conjunction with ORNL. This program is a reorientation of a previous program for a series of irradiations in the Fermi reactor. Two phases of the present program were implemented.

Phase I consisted of irradiating Fe, Ti, Ni, and Co dosimeters and 16 refractory metal tensile/creep-rupture specimens. The irradiation of 148 dosimeters resulted in complete flux mapping of the EBR-II rows 2 and 7 positions with the new 91-element reactor core configuration. Irradiation was conducted at a maximum reactor power level of 30 Mw to a total integrated exposure of 688 Mw hours. The neutron flux density profile was determined in order to interpret subsequent EBR-II material irradiations and to correlate irradiation test results from other reactors. The radiochemical analysis of the dosimeters are discussed in the dosimetry section.

*Project leader.

†Principal investigator.

Phase IIA of the program provides for the irradiation of resistivity, hot-hardness, and tensile/creep-rupture specimens at various elevated temperature and fluence values. Individual NMPO capsules, loaded into the tube bundles by ORNL personnel and awaiting insertion into the EBR-II, include 112 tensile/creep-rupture specimens, 64 hot-hardness specimens, and 264 resistivity (wire) specimens. Materials to be irradiated are the heat-resistant alloys Hastelloy X, Hastelloy R (three different B isotope dopings), Fe-Cr-Al-Y, and Mo, Cb, W, Ta, and their alloys. Additional materials including stainless steels and vanadium-base alloys are planned for Phase IIB.

ORR AND ETR IRRADIATIONS

Four refractory metal specimen capsules were irradiated in the ORR and four heat-resistant alloy capsules were irradiated, three in the ETR, one in the ORR.

2.2 HEAT-RESISTANT ALLOY PROGRAM

The objectives of this phase are to determine engineering and design data of heat-resistant alloys and to interpret these data (with supporting transmission electron microscopy) to determine the mechanisms of radiation damage. Materials tested include Incoloy 800, Hastelloy X, A-286, Hastelloy R-235, and Fe - 15Cr - 4Al - 1Y (1541 alloy).

CREEP-RUPTURE TESTING (R. A. Joseph, J. P. Smith, J. Moteff, J. A. Edwards)

All creep-rupture testing except for the 1541 alloy was performed in standard lever-loaded (5:1 ratio) dead-weight equipment. Essentially all creep data to be discussed were measured from total load train movement. To determine the order of magnitude of error inherent in this technique, several specimens were instrumented with platinum strip-type extensometers attached directly to the gage length of the specimens. Comparison of strain as determined by the load-train LVDT sensor against the optical showed that for strains above 2 percent the relative error was less than 10 percent. For strains less than 1 percent, the relative error was somewhat higher (up to 40%). These tests verified that the total load-train monitoring system utilized was satisfactory for recording strains above 1 to 2 percent, generally well below the range at which second-stage or minimum creep occurs with the possible exception of extremely brittle materials.

Incoloy 800

Specimens of Incoloy 800, irradiated at about 540°C in EBR-II to fast fluences of 0.27 and 2.7×10^{20} n/cm² ($E_n \geq 1$ Mev), were creep-rupture tested at 540°C and 705°C. Data are summarized in the graphs of Figures 2.1 and 2.2. Radiation affects the creep properties somewhat differently at the two temperatures. At 540°C the minimum creep rate ($\dot{\epsilon}$) is increased and time to rupture (t_R) is reduced compared to the unirradiated material; at 705°C, $\dot{\epsilon}$ is reduced and t_R increased (except at high stresses) compared to the control specimens. At both test temperatures radiation reduced the rupture elongation by about a factor of 3. Another significant difference is that for 540°C tests the irradiated and control lines tend to converge at low stresses but more tests are needed to verify this; on the other hand, the tendency for convergence of the unirradiated and irradiated control lines at 705°C is at high stresses. This convergence at high stress is unique among alloys investigated at NMPO; generally any convergence occurs at low-stress (longtime) tests, as appears to be the case at 540°C (Figure 2.1), indicating annealing of point defects. To determine whether the effect observed at 705°C was due to thermal aging or to combined stress and temperature, an irradiated and an unirradiated control specimen were aged at 705°C for 500 hours and then tested at 10.5 kg/mm². The irradiated specimen ruptured after 24.7 hours and had a minimum creep rate of 2.4×10^{-6} sec⁻¹, and a fracture elongation of 37 percent; these properties are essentially identical to those of the as-irradiated tests shown in Figure 2.2. This indicates that the divergence of the control

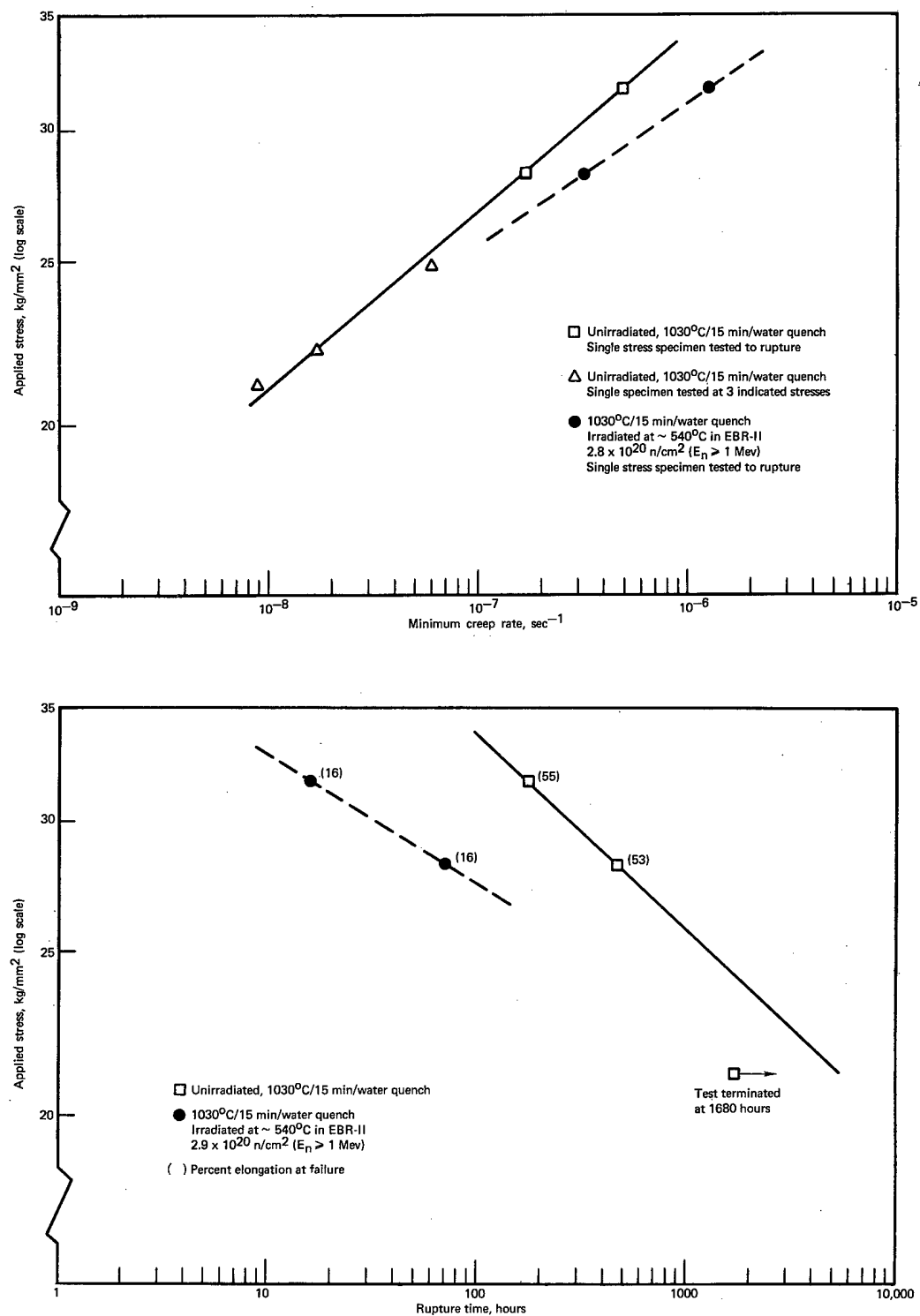


Fig. 2.1 — Minimum creep rate and stress-rupture strength for unirradiated and irradiated Incoloy 800 at 540°C

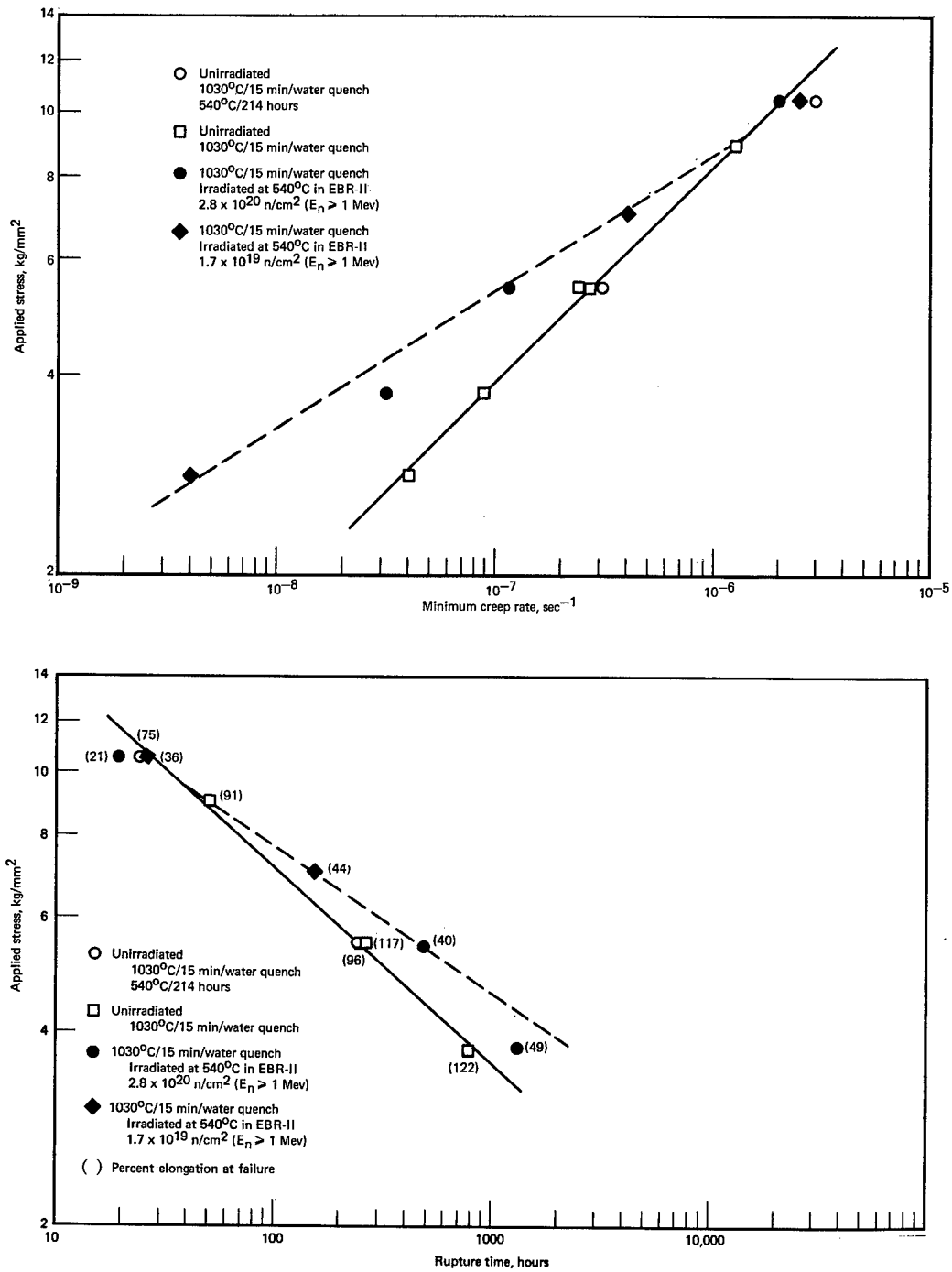


Fig. 2.2 — Minimum creep rate and stress-rupture strength for unirradiated and irradiated Incoloy 800 at 705°C

and irradiated 705°C properties (Figure 2.2) at low stress is not due solely to thermally activated migration or interaction of irradiation-induced defects; more tests are needed to determine the cause of the increased post-irradiation strength.

The creep curves for the 540°C and 705°C tests (Figure 2.3) indicate reduction in post-irradiation ductility. The major effect of radiation on ductility is the reduced third-stage creep strain.

The tests described above were of the creep-rupture variety performed at a fixed load to failure. Actual reactor operations do not result in this condition; instead, the stress varies over a rather wide range. To investigate the effects of varying stress and to determine accurately how radiation affects the low strain part of the creep curve, tests were performed in which the stress on a given specimen was varied and the strain was measured accurately with a cathetometer sighting directly on the gage length of the specimen. The low-strain range is of particular interest to designers since many cladding designs allow for 3 percent maximum strain. The procedure was to load a specimen to σ_1 and establish the linear creep rate; the load was then increased to σ_2 and again a linear creep rate was established; this was repeated for three stress levels. Finally the load was re-

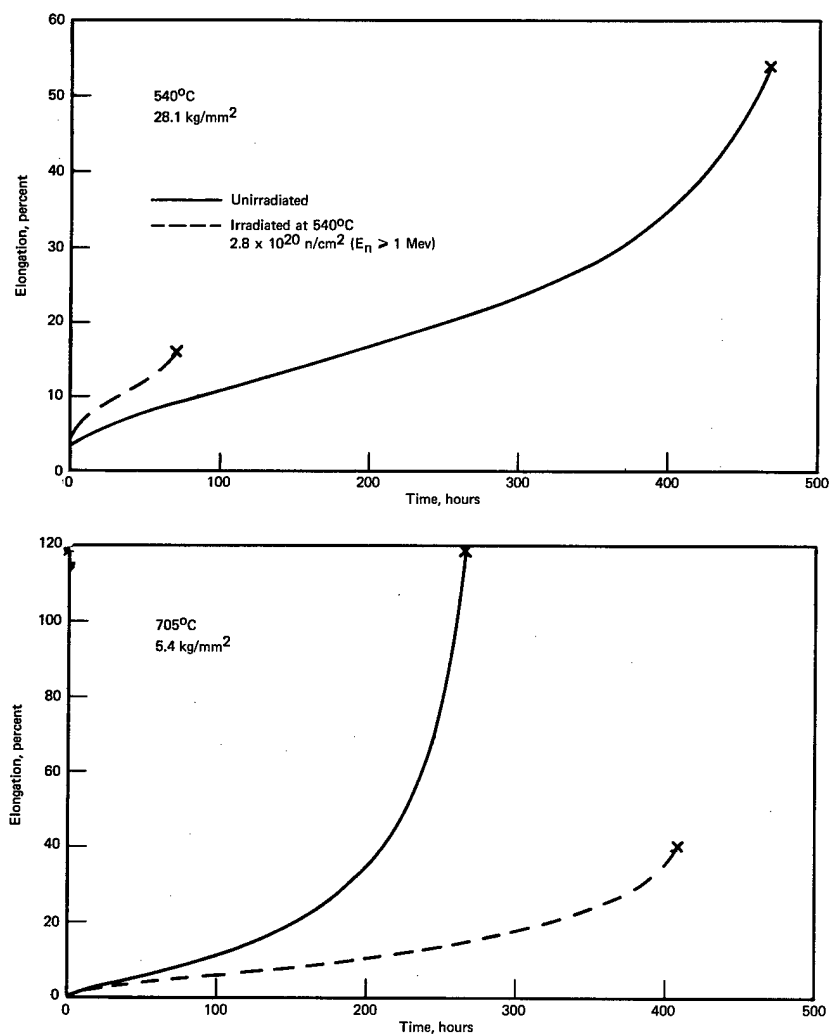


Fig. 2.3 — Creep curves for irradiated and unirradiated Incoloy 800 at 540°C and 705°C

duced to σ_1 to compare with the original creep rate at σ_1 and to determine whether the substructure had been altered. Creep data were obtained for irradiated and control specimens and are shown in Figures 2.4 and 2.5. For the unirradiated specimen (Figure 2.4) the minimum creep rate is apparently a function of prior stress or strain history, based on the fact that second-stage creep rate ($\dot{\epsilon}_s$) for σ_1 final is significantly higher than for σ_1 initial. In the case of the irradiated specimen (Figure 2.5) the $\dot{\epsilon}_s$ is essentially identical for σ_1 initial and final. In the unirradiated results, for σ_1 initial, two separate linear portions $\dot{\epsilon}_s$ appear to be present. The exact cause of this is not known; it has been observed on post-test metallography of other ruptured specimens that recrystallization is probably occurring during test since the grain size near the fracture is very fine and becomes progressively coarser in low-strain areas. This recrystallization could explain the two linear portions of the initial σ_1 and the decreased creep resistance of the final σ_1 .

The result on the irradiated specimen indicates that irradiation "freezes in the structure" and that stresses or strains in the region investigated do not alter this structure.

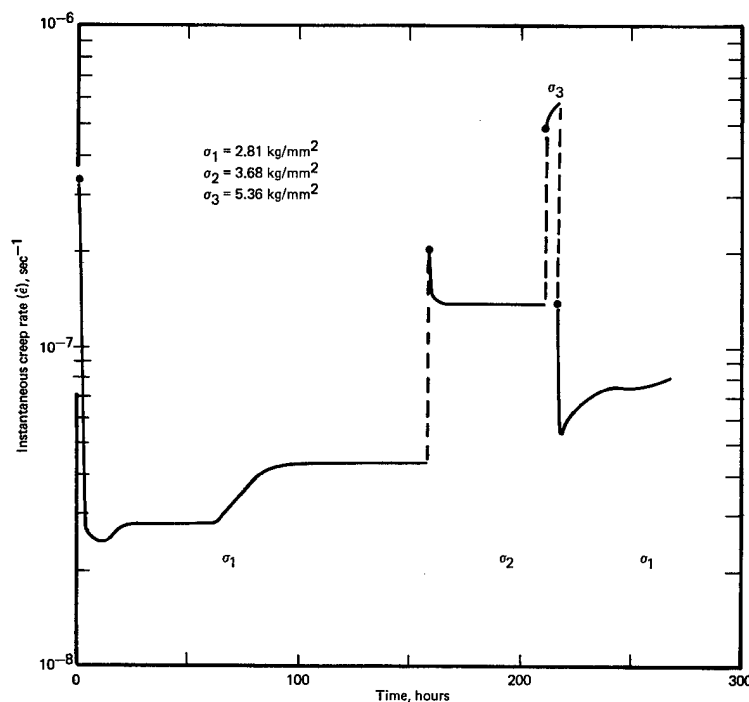


Fig. 2.4 — Instantaneous creep rate at 704°C of unirradiated Incoloy 800 as a function of creep time for various stress levels

Metallography and transmission electron microscopy will be performed to help evaluate results.

A similar series of tests was initiated at 540°C. Creep rates for the unirradiated specimens at the three lower stress levels of Figure 2.1a were all determined from one specimen; they are in good agreement with tests performed at a constant load to failure.

To more fully evaluate all available test data, correlations are being made between creep and tensile data. Tensile data discussed here were generated at GE-APO¹ on samples from the same heat and irradiation as for the specimens described above. Figure 2.6 demonstrates a reasonably good correlation of the tensile and creep data both for strength and ductility. Of particular interest were (1) the effect of fluence on the ductility but not on the strength, and (2) the minimum in the ductility curve for the irradiated specimens.

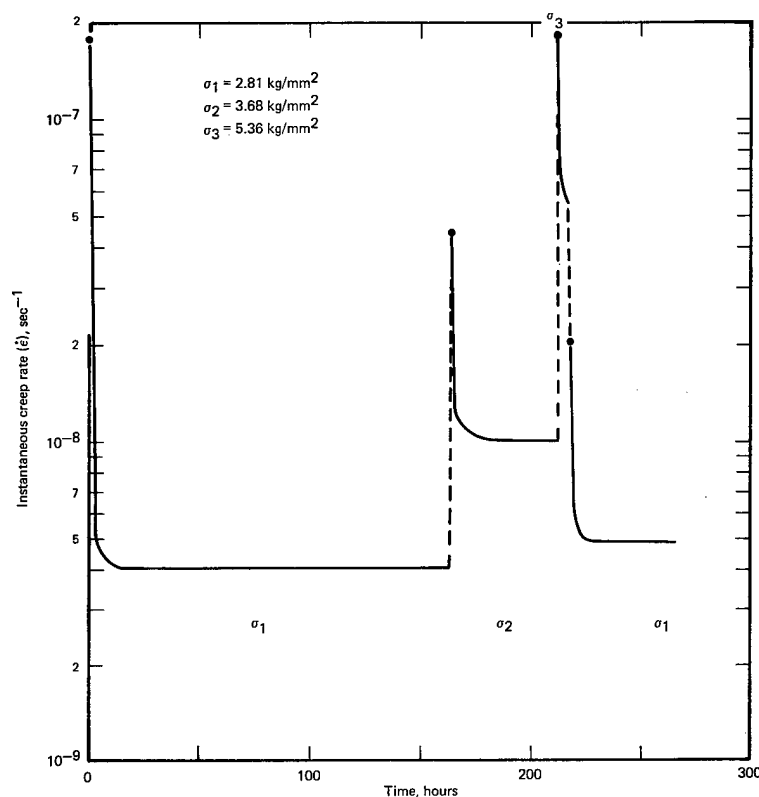


Fig. 2.5 — Instantaneous creep rate at 704°C of irradiated (2.4×10^{19} n/cm², $E_n \geq 1$ Mev) Incoloy 800 as a function of creep time for various stress levels

Stiegler and Weir² reported such a minimum for Hastelloy N. A unique approach to correlating the tensile and creep data is the application of the Monkman-Grant relationship³ ($\log \dot{\epsilon}$ vs $\log t_R$) as shown in Figure 2.7. At both temperatures, data fall on lines close to the predicted slope of -1, and available tensile data fit the curve quite well. The effective t_R for the tensile data was obtained by calculating $\epsilon/\dot{\epsilon}$ for each test where ϵ is the fracture strain. Refinements can probably be made, such as using uniform strain, although the above technique appears to work quite well to a first approximation. The slope is unity; hence $\dot{\epsilon} \cdot t_R = \text{constant}$. Although the units of this constant are strain, its physical significance is not known. It may be used as a guide to predict the minimum fracture strain since what it represents is the strain at failure obtained if no third-stage creep occurred. Since most unirradiated materials do exhibit a third-stage creep, the fracture ductility is generally somewhat higher than predicted by the Monkman-Grant relationship. On the other hand, many irradiated materials exhibit little or no third-stage creep and this relationship may predict quite closely the fracture ductility.

Hastelloy X*

Concurrent to the work described above, creep-rupture testing of Hastelloy X irradiated in EBR-II was performed in the range of 540° to 705°C. Most data were generated at 650°C since the primary intent was to compare these data with previously determined data from ETR irradiations. The 540°C and 705°C data are presented in Table 2.1 but will not be discussed because of the limited quantity. Stress-rupture life at 650°C of the

*Specimens fabricated and irradiated by GE-APO.

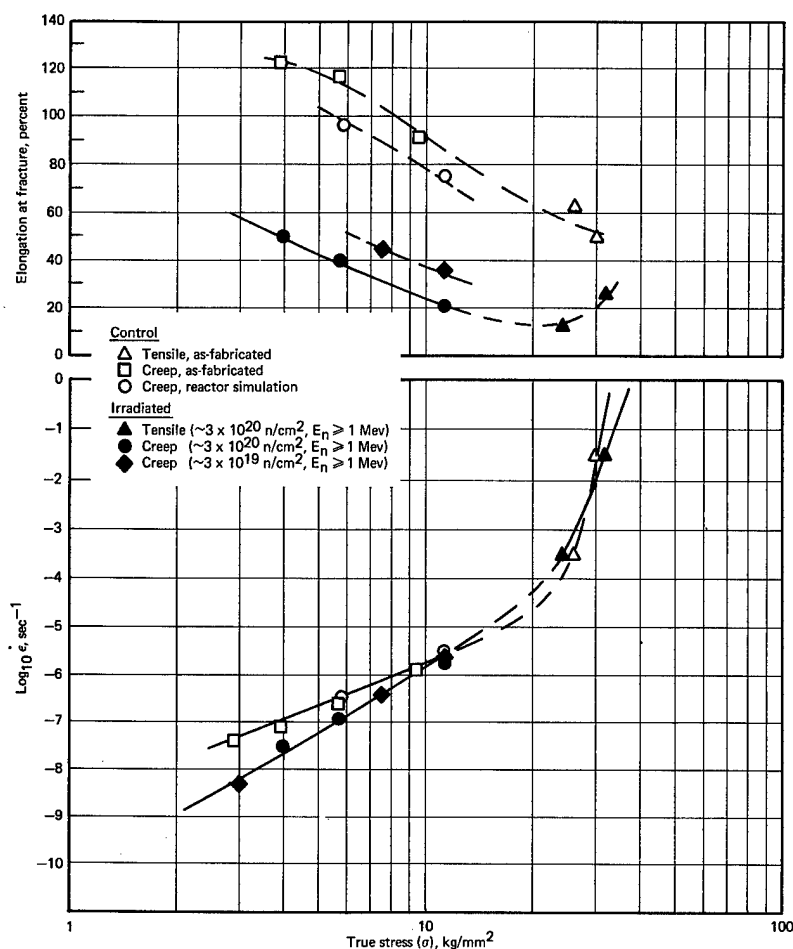


Fig. 2.6 — Strain rate and elongation as a function of true stress for Incoloy 800 tested at 705°C. To minimize structure differences due to work-hardening the true flow stress at about 6% true strain was used to correlate the tensile data with the creep data.

specimens from the EBR-II and ETR irradiations, as summarized in Figure 2.8, was essentially the same. Ductilities (not shown) from both irradiations were similar, but the EBR-II specimens showed slightly lower ductility due to the higher fluence. The point of convergence for control and irradiated lines is about 20 kg/mm². Creep data were not obtained for the ETR irradiated specimens. The strain rate-stress relationship for the EBR-II specimens (Figure 2.9) shows the creep rate to be reduced by irradiation; reduction is greater at lower stresses. The irradiated and control curves of Figure 2.9 converge at about 27 kg/mm², a stress higher than for the t_R - σ curves. Creep curves (not illustrated) for irradiated and control specimens at 650°C show that the major reason for the loss in ductility is the reduction of third-stage creep; the same was true of Incoloy 800 (Figure 2.3). The Monkman-Grant³ relationship was also applied to these data as shown in Figure 2.10. Although the lines are not so close to a slope of -1 as the Incoloy 800 data, the control and irradiated lines are parallel. Based on the criterion discussed above that $\dot{\epsilon} \cdot t_R^k = \text{constant}$, the constant $\cong 0.06$. Irradiated Hastelloy X exhibited virtually no third-stage creep and the fracture ductility was 8 to 9 percent which is not much above predicted minimum of 6 percent.

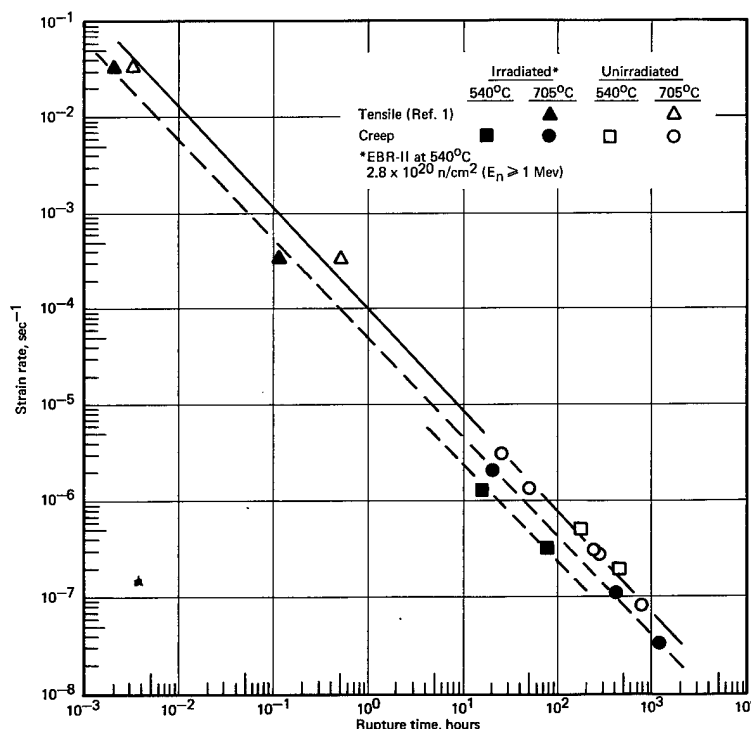


Fig. 2.7 — Monkman-Grant relationship for irradiated and unirradiated Incoloy 800 at 540°C and 705°C using tensile and creep data

TABLE 2.1

CREEP-RUPTURE DATA FOR IRRADIATED AND UNIRRADIATED HASTELLOY X						
EBR-II Irradiation Conditions		Test Conditions				
Fluence, n/cm ² (E _n ≥ 1 Mev)	Temperature, °C	Stress, kg/mm ²	Temperature, °C	Rupture Life, hr	Minimum Creep Rate, sec ⁻¹	Fracture Elongation, % in 2.54 cm
Unirradiated		39.4	540	On test	1.1 × 10 ⁻⁸	—
3.2 × 10 ²⁰	540	39.4	540	On test		
1.7 × 10 ¹⁹	540	39.4	540	636	1.7 × 10 ⁻⁸	21.7
Unirradiated		15.7	705	355	3.0 × 10 ⁻⁷	78
Unirradiated		17.1	705	229	3.6 × 10 ⁻⁷	58
3.2 × 10 ²⁰	540	15.7	705	126	7.7 × 10 ⁻⁸	5

Hastelloy R-235

Creep-rupture measurements are continuing on the special split heat of Hastelloy R-235 containing a total of 45 ppm boron with varying B¹⁰ concentration. Specimens were tested at 870°C following irradiation in the ORR at 70°C and in the ETR at 760°C. Results of the post-irradiation creep-rupture tests are shown in Figure 2.11. Only two specimens of each type were available from the ORR irradiation. Data in Figure 2.11 indicate that (1) the 760°C irradiated specimens exhibit slightly poorer properties than the 70°C specimens, and (2) the stress dependency is not significantly changed by irradiation. The amount of damage appears to be definitely a function of the B¹⁰ concentration. One specimen of each heat from the ORR irradiation was re-solutioned and aged after irradiation and before testing; results are shown in Figure 2.11. As observed in other alloys, the rupture strength is further decreased by the re-heat treatment compared to the as-irradiated

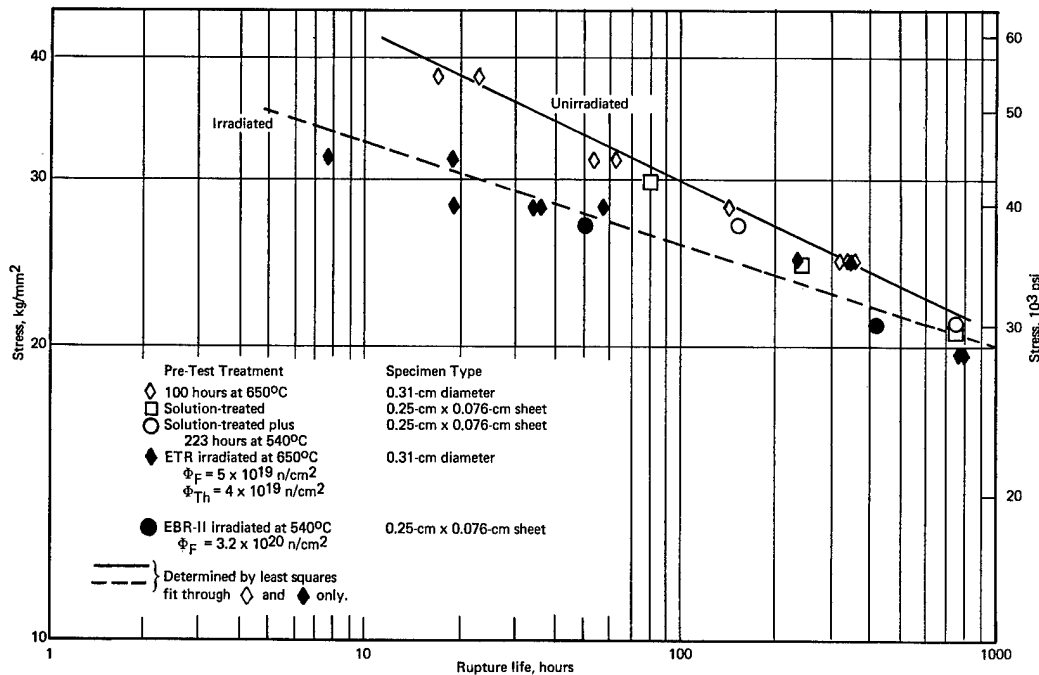


Fig. 2.8 — Stress-rupture properties of irradiated and unirradiated Hastelloy X at 650°C

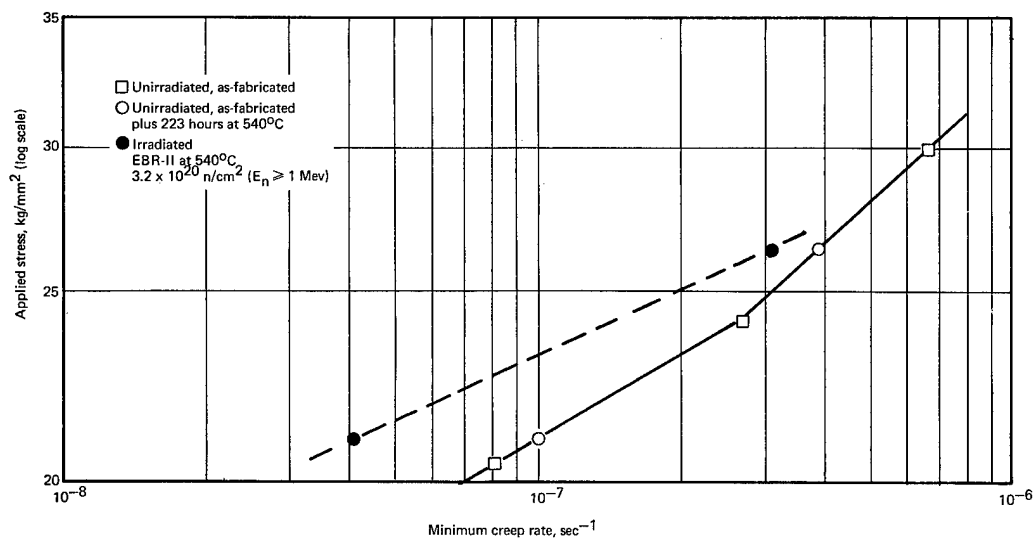


Fig. 2.9 — Minimum creep rate as a function of applied stress for unirradiated and irradiated Hastelloy X at 650°C

values. Analyses of these tests are continuing, to determine the relationship between creep rate, helium concentration, and defect density.

A-286

As discussed in a previous report,⁴ Woodford⁵ showed that the stress dependency, n , can be approximated from a single constant-load test for a fixed temperature. The expression $\dot{\epsilon} \approx A\sigma^n$ can be used in this analysis, with n , the stress dependency, equal to $(d \log \dot{\epsilon} / d \log \sigma)$ and inversely proportional to the strain rate sensitivity m ; i. e., $m = 1/n =$

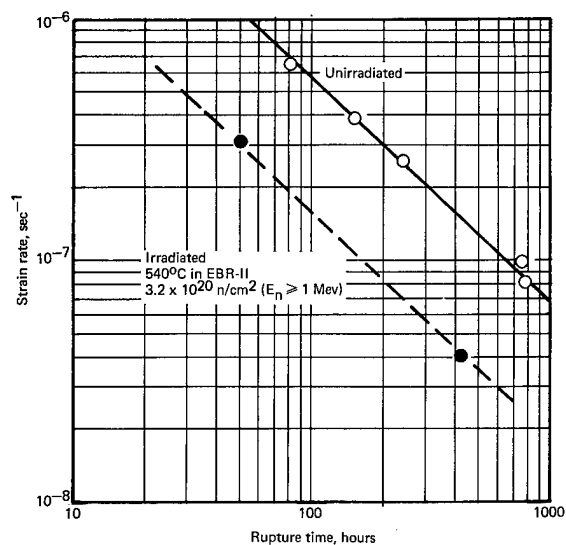


Fig. 2.10 — Monkman-Grant relationship for irradiated and unirradiated Hastelloy X at 650°C

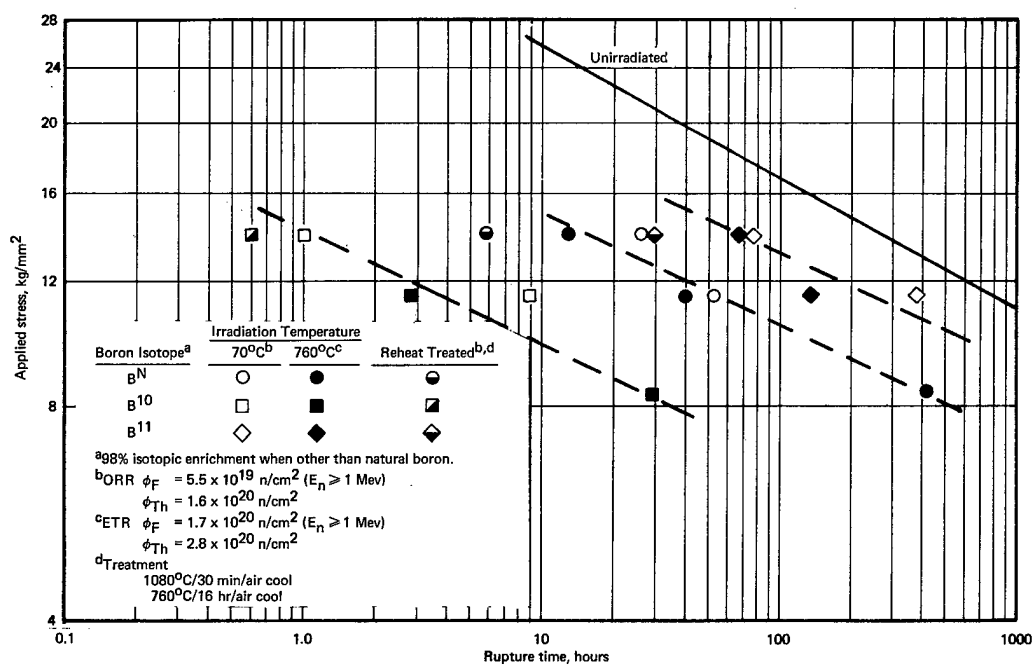


Fig. 2.11 — Creep-rupture strength and effect of post-irradiation reheat treatment on creep-rupture strength of Hastelloy R-235 at 870°C

($d \log \sigma / d \log \dot{\epsilon}$). Data presented previously⁴ showed that three different tests of Hastelloy X at 650°C and various initial stress levels yielded essentially the same value of n . This type of analysis was applied to irradiated and unirradiated test results of A-286 specimens.

The results shown in Figure 2.12 indicate about a factor of 2 increase in the stress dependency. More significantly, the minimum creep rate decreases with increasing concentration of helium atoms as generated from the $B^{10}(n, \alpha)Li^7$ reaction. In this figure the stress notation is omitted from the abscissa because the comparison is for creep tests performed at the same applied stress. Since there is essentially no primary creep, the intercept represents the minimum creep rate.

The minimum creep rate is plotted as a function of the calculated helium atom concentration in Figure 2.13; there appears to be a fairly good linear relationship. Minimum creep rate could be a function of the number of $B^{10}(n, \alpha)Li^7$ reactions which occur and is probably a function of the helium atom concentration. Strain rate sensitivity (m) is independent of helium atom concentration in the range investigated as shown in Figure 2.12. The interaction of dislocations with helium bubbles may account for the increased creep resistance; this is consistent with transmission microscopy results reported previously.⁴ The reduced ductility in irradiated A-286 could, however, be the result of decreased strain rate sensitivity (increased n or decreased m) which apparently is not a sensitive function of total helium atom concentration. The ductility change may also be a function of helium atom distribution; i. e., bubbles on those dislocations within grain boundaries may play a special role. Studies to correlate influence of changes in stress dependency and strain rate sensitivity on creep ductility and creep rates are continuing.

Fe - 15Cr - 4Al - 1Y

Data for Fe - 15Cr - 4Al - 1Y (1541 alloy) tensile and creep tests by ORNL,⁶ Harwell,⁷ and NMPO were compiled. Results of unirradiated tests are presented in Figure 2.14 as the temperature-compensated creep rate (Zener-Holloman parameter) versus stress. The ultimate strength was used for the tensile data, although the yield strength could have been used since they are virtually the same for this alloy. The applied stress was used for creep data. Considering the variation in test technique among the different laboratories and the inclusion of both tensile and creep data, a good least-squares fit to the experimental data was obtained with relatively little scatter. Figure 2.15 shows the similar parameter plots for the irradiated specimen data. This plot shows that irradiation reduces creep rate slightly but consistently for all test conditions considered, and that the stress dependency (n) for this irradiated material is not significantly changed. This is in contrast to the results discussed above for Incoloy 800, Hastelloy X, and A-286. The Woodford technique⁵ of calculating stress dependency from a single constant-load test was applied to the NMPO creep data, and the analysis predicted that the stress dependency (n) was essentially unchanged by the irradiation.

HOT HARDNESS (J. L. Kamphouse)

Incoloy 800

Hot hardness tests were performed on control and irradiated Incoloy 800 from the same material used to fabricate the control and irradiated specimens used for the creep and tensile results discussed above. A summary of the hot-hardness data is shown in Figure 2.16. There is very little difference in hardness between the irradiated and unirradiated material at any given temperature, especially from 500°C and below. At 600°C and above, the irradiated specimen appears to be slightly harder than the unirradiated specimen, possibly because the irradiation temperature was approximately 540°C; hence significant changes in strength would not be expected below this temperature. Of significance is the fact that tensile data¹ on these

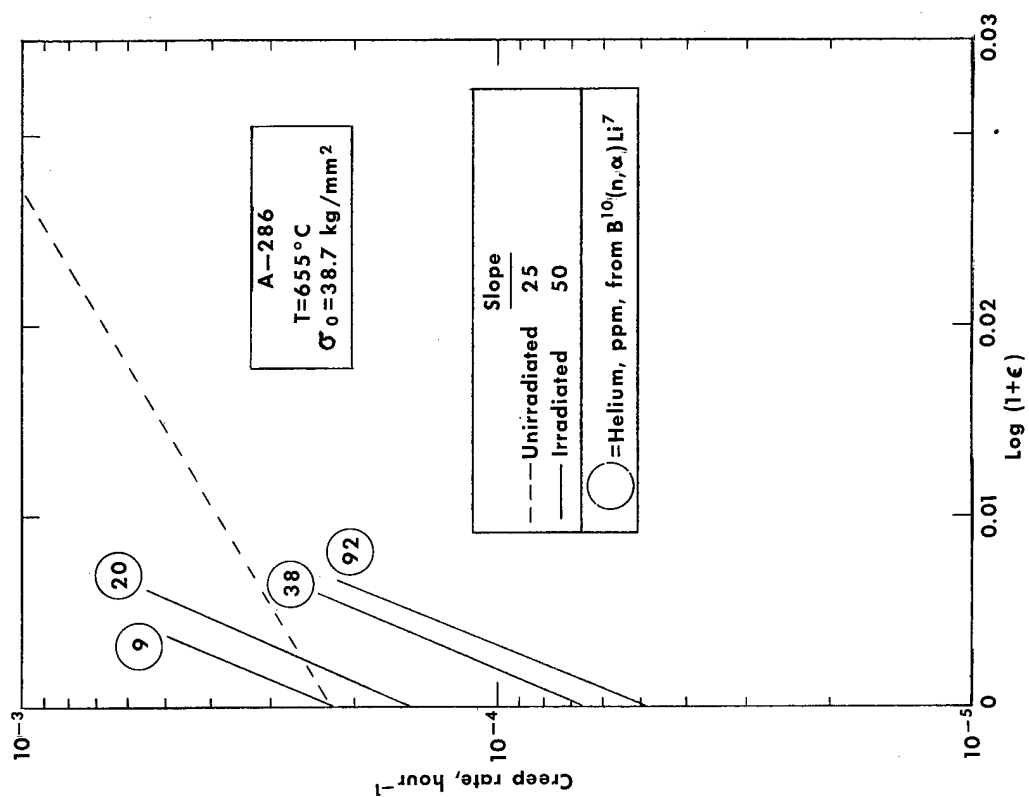


Fig. 2.12 — Creep rate as a function of $\ln(1 + \epsilon)$ for irradiated and unirradiated A-286 (AS-746F)

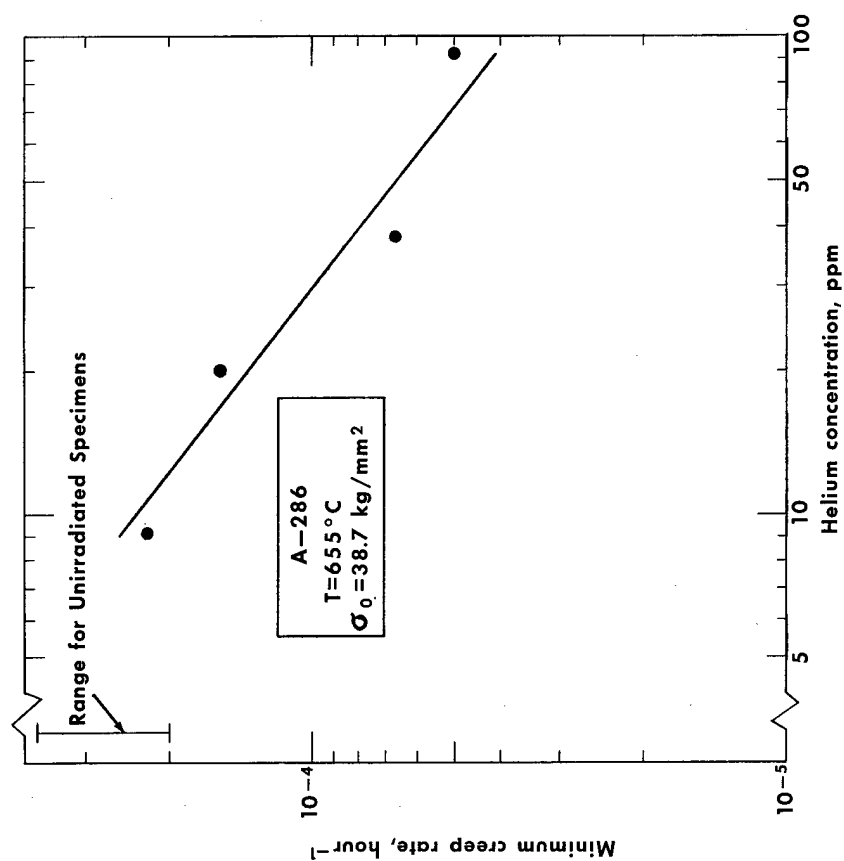


Fig. 2.13 — Minimum creep rate as a function of helium concentration for irradiated A-286 (AS-746H)

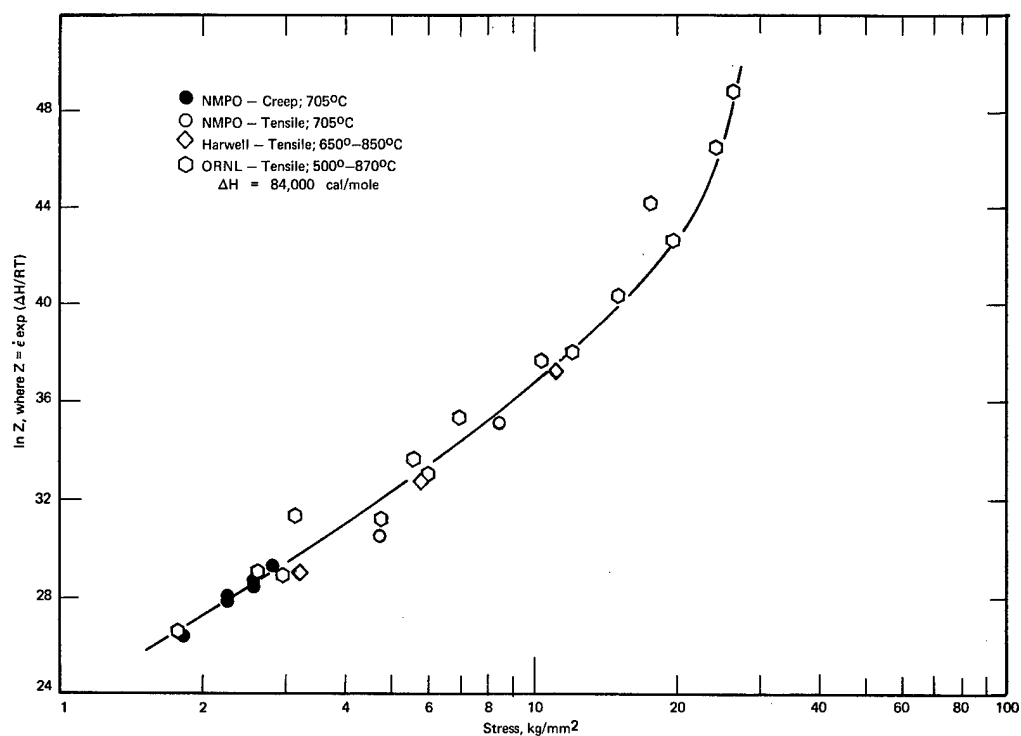


Fig. 2.14 — Variation of temperature-compensated strain rate (Z), Zenner-Holloman parameter, with stress for unirradiated Fe — 15Cr — 4Al — 1Y

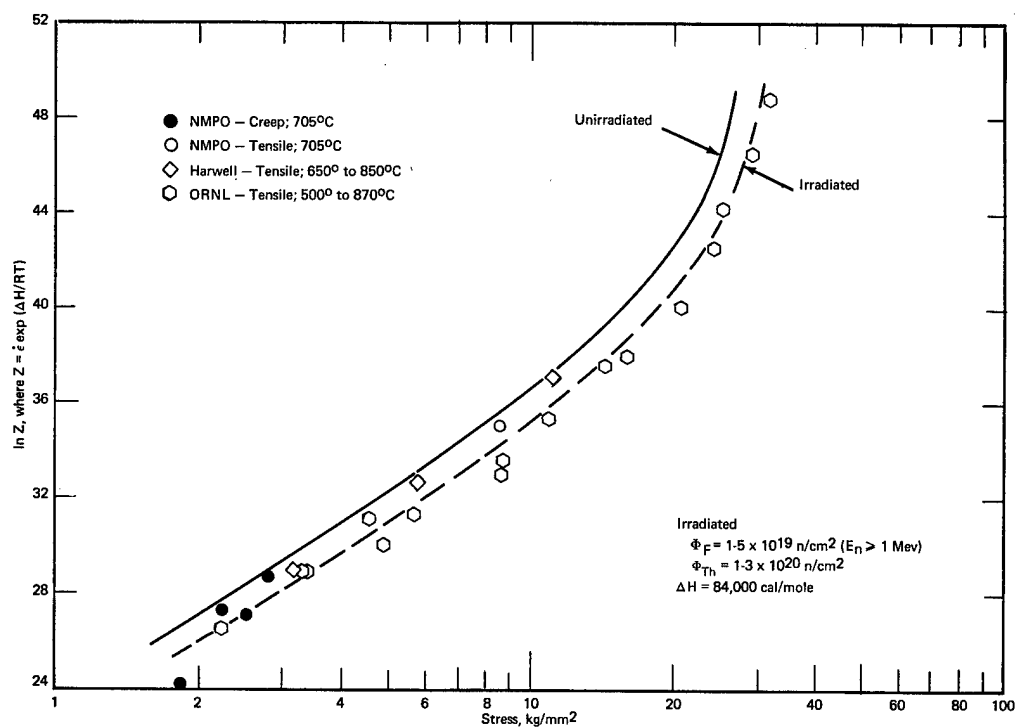


Fig. 2.15 — Variation of temperature-compensated strain rate (Z), Zenner-Holloman parameter, with stress for irradiated Fe — 15Cr — 4Al — 1Y

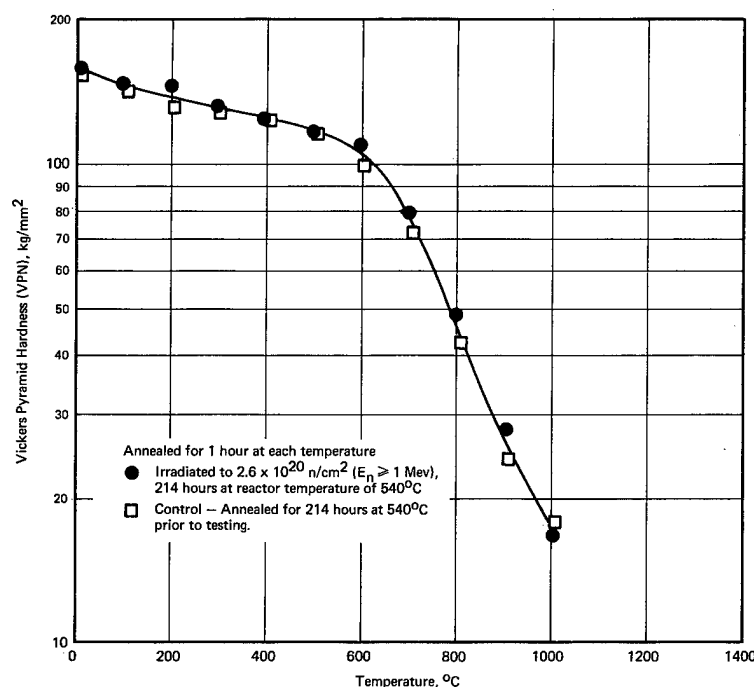


Fig. 2.16 — Hot microhardness of unirradiated and irradiated Incoloy 800

same specimens in the 600° to 700°C range show only a small strength reduction (~ 5 to 10%) due to irradiation; hence these two types of tests are in qualitative agreement.

The discontinuity at 200°C may be real because the tensile data¹ cited above show that the line through the data from the irradiated specimens crosses the line through the control data at about 200°C. That is, below 200°C the strength of the irradiated specimens is slightly higher than the control specimens, whereas above 200°C the strength of the irradiated specimens is generally lower than the control specimens.

ASTM-A302B

One unirradiated ASTM-A302B pressure vessel steel specimen and three irradiated in the IRL were hot-hardness tested from room temperature to 1000°C. During irradiation the three irradiated specimens were located at different distances from the core within a pressure vessel mock-up.⁸ The spectrum changed somewhat from one side of the mockup to the other and the fluence decreased from the side nearest the core to the side farthest away. The three specimens showed essentially the same hot hardness regardless of position in the mockup and in fact showed the same hot hardness as the unirradiated specimen.

RESISTIVITY STUDIES (L. K. Keys, J. Moteff)

ASTM-A302B

Preliminary studies presented on the A302B steels⁸ demonstrated a good correlation between mechanical properties and resistivity, although these studies were performed over a limited fluence range ($1 - 4 \times 10^{18}$ n/cm²). A second series of irradiation studies were carried out in the ORR at reactor ambient temperature in which a fluence range of approximately 1×10^{18} to about 7.1×10^{19} n/cm² was obtained, Table 2.2. In Figures 2.17 and 2.18 the fractional resistivity recovery, $\Delta\rho/\rho_0$, versus annealing temperature is given for the ORR and IRL irradiations. The general form of the recovery is the same. There are

TABLE 2.2

IRRADIATION CONDITIONS AND PRINCIPLE RECOVERY PARAMETERS FOR A302B STEELS

Sample No. Capsule		Irradiation Conditions		$\Delta(\Delta\rho/\rho_o) =$ $ (\Delta\rho/\rho_o) \text{ min} - \Delta\rho/\rho_o $		
		Fluence, nvt				
		Fast ($E_n > 1 \text{ Mev}$)	Thermal	$\Delta\rho/\rho$	$(\Delta\rho/\rho_o) \text{ min}$	
2-3	NRL-1-5 ^a	4.8×10^{18}	6.9×10^{18}	-0.0223	-0.0258	0.0035
2-5	NRL-1-3	2.7×10^{18}	3.2×10^{18}	-0.0142	-0.0229	0.0087
2-7	NRL-1-1	1.1×10^{18}	2.2×10^{18}	-0.0004	-0.0098	0.0094
2-8	ORM-49-1 ^b	1.0×10^{18}	9.0×10^{18}	-0.0093	-0.0160	0.0067
2-9	ORM-49-2	1.7×10^{18}	1.7×10^{19}	-0.0118	-0.0170	0.0052
2-10	ORM-49-3	6.0×10^{18}	3.9×10^{19}	-0.0098	-0.0280	0.0182
2-11	ORM-49-4	1.1×10^{19}	7.8×10^{19}	-0.0064	-0.0278	0.0214
2-12	ORM-49-6	7.1×10^{19}	4.6×10^{20}	-0.0427	-0.0567	0.0140
2-13	ORM-49-5	4.5×10^{19}	3.8×10^{20}	-0.0365	-0.0497	0.0132

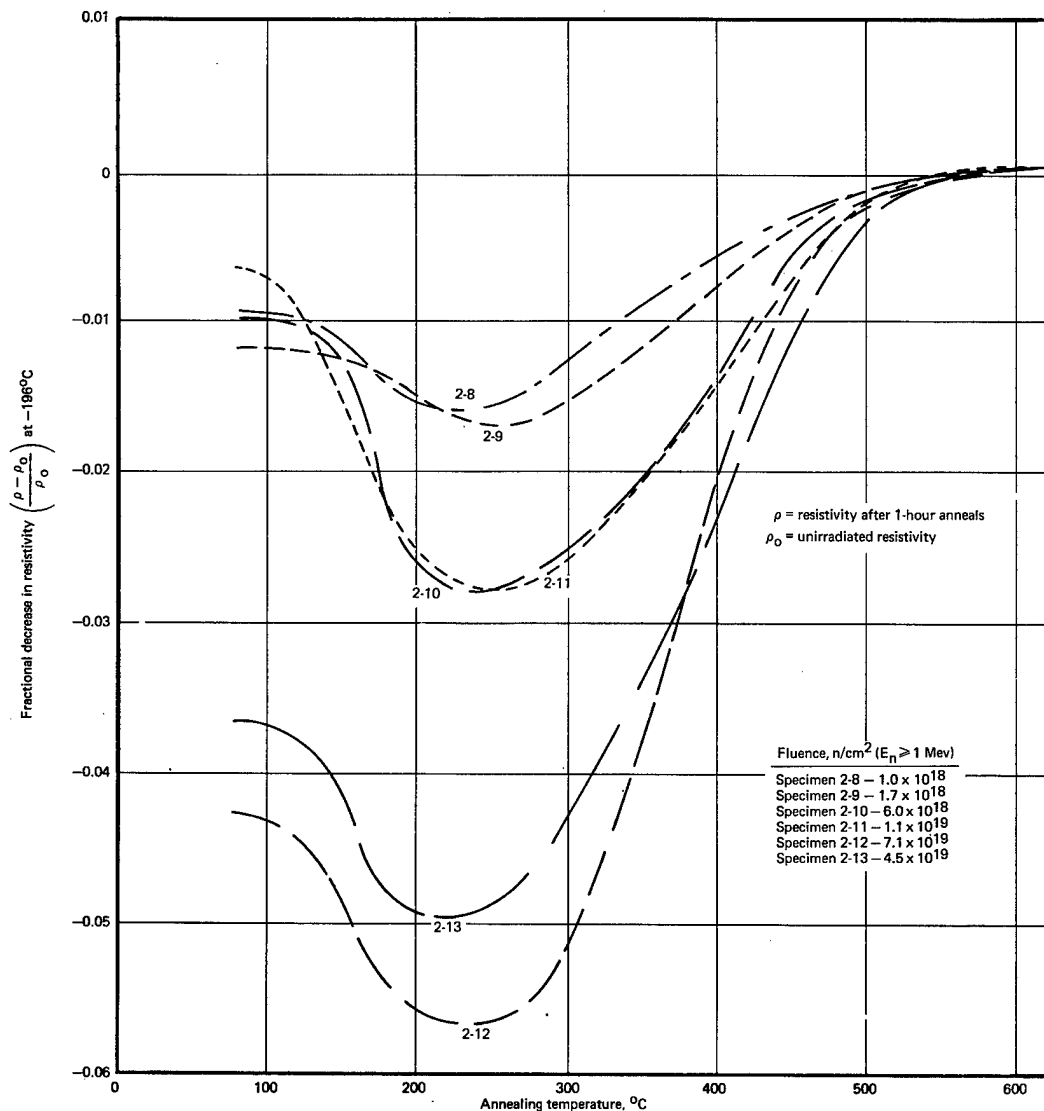
^aIndustrial Reactor Laboratory (Plainsboro, New Jersey).^bOak Ridge Reactor (ORNL).

Fig. 2.17 — Isochronal fractional resistivity recovery of irradiated A302B steel as a function of annealing temperature

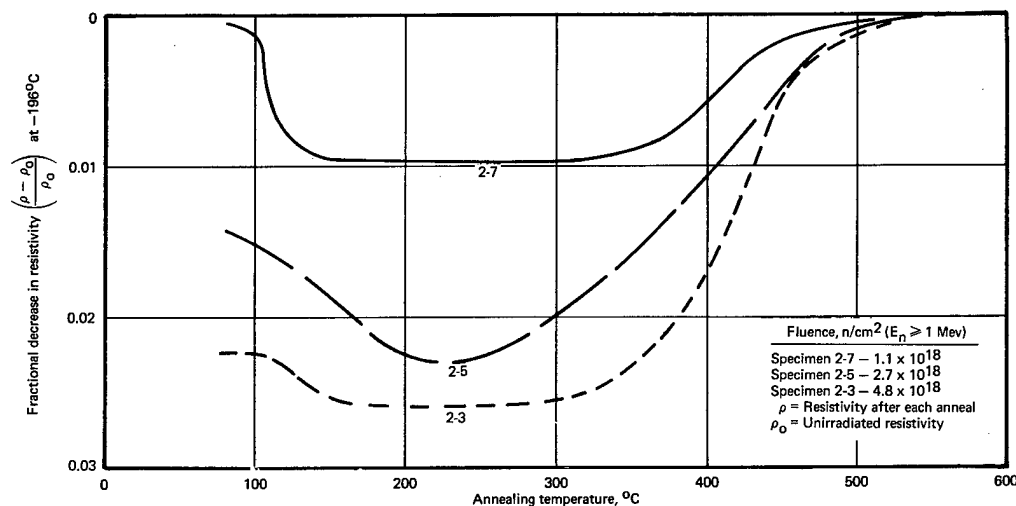


Fig. 2.18 — Isochronal fractional resistivity recovery of IRL neutron irradiated A302B steel as a function of annealing temperature

three important regions of resistivity change: (1) an initial negative resistivity change as a result of the reactor irradiation, (2) a further decrease occurring upon annealing to about 250°C, and (3) a region of increasing resistivity and recovery up to about 500°C above which recovery is complete and the resistivity behavior resembles that of the control specimens. The recovery minimum at about 250°C represents the maximum negative resistivity change due to the irradiation of these specimens. This minimum resistivity dependence ($\Delta\rho/\rho_0$) on the fast neutron fluence is shown in Figure 2.19. The value ($\Delta\rho/\rho_0$) minimum is defined as the largest negative $\Delta\rho/\rho_0$ value observed, i. e., $\Delta\rho/\rho_0$ at about 250°C. These values show a relatively smooth linear dependence on the fluence except for the lowest fluence IRL value.

Based on the work of others,^{9,10} the decrease in resistivity presumably results from the precipitation of carbon from solution by the formation of a carbon-defect complex. With increasing temperature, the carbon returns to solution and the vacancies recover and are annihilated at various sinks including carbide precipitate particles, causing the resistivity to return to its original value. Although carbon has been considered the only important interstitial impurity (because of its high concentration), other interstitials such as nitrogen may have similar effects.

In Figure 2.20 the dependence of the radiation-induced resistivity increment $\Delta\rho/\rho_0$ on the fast neutron fluence is presented for the two different irradiation experiments. Both the IRL and ORR irradiations show a negative dependence of the resistivity increment fraction on the fast neutron fluence over the total fluence region rather than the normal positive dependence expected for radiation-induced defects (vacancies and interstitials). The IRL specimens, however, show a somewhat higher fluence dependence than the ORR specimens. Several factors can contribute to the difference: (1) differences in the metallurgical conditions between the two sets of samples, (2) differences in the reactor spectrum between these irradiations, and (3) differences in the temperatures of the irradiation.

Based on the known location of the test specimens within the original block of steel and on annealing studies of unirradiated specimens, the difference in fluence dependency is believed due primarily to variations of solutioned carbon from specimen to specimen. These annealing studies indicate that the IRL specimens were probably cut from a section which had more carbon in solution; hence more was available for radiation-induced precipitation. Carbon

analysis will be obtained to verify the implications of these resistivity studies. The effects of spectra and temperature were evaluated, but are probably minor compared to effects of pre-irradiation heat treatment. Other investigators¹¹ have also shown that the heat treatment of A302B and other mild steels has a major effect on the sensitivity to fast neutron irradiation.

Figure 2.21 shows the dependence of the nil ductile transition temperature (NDT) on the fast neutron fluence for A302B steel,¹² and illustrates a good correlation with the resistivity fluence dependence.

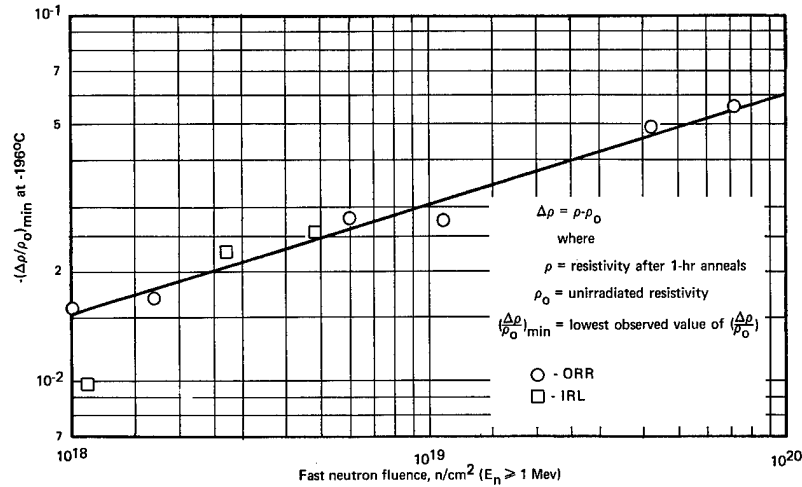


Fig. 2.19 — Dependence of the fractional resistivity minimum, $(\Delta\rho/\rho_0)_{\min}$, of irradiated A302B steels on the fast neutron fluence

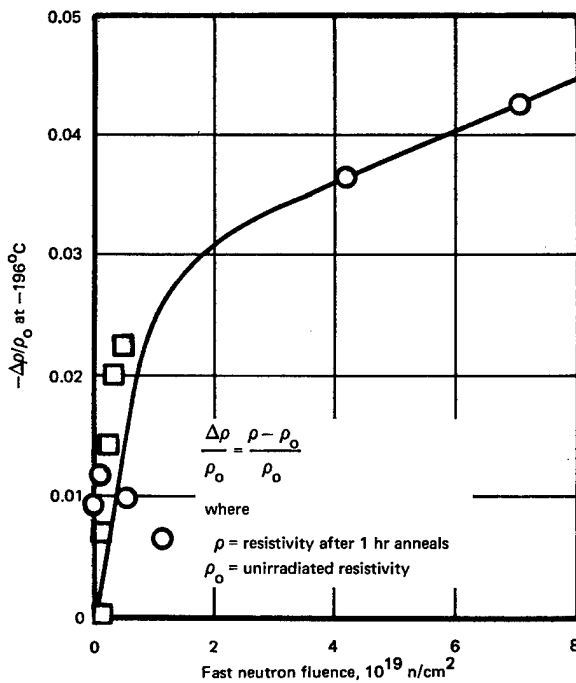


Fig. 2.20 — Fractional decrease in resistivity of IRL and ORR irradiated A302B steel as a function of fast neutron fluence

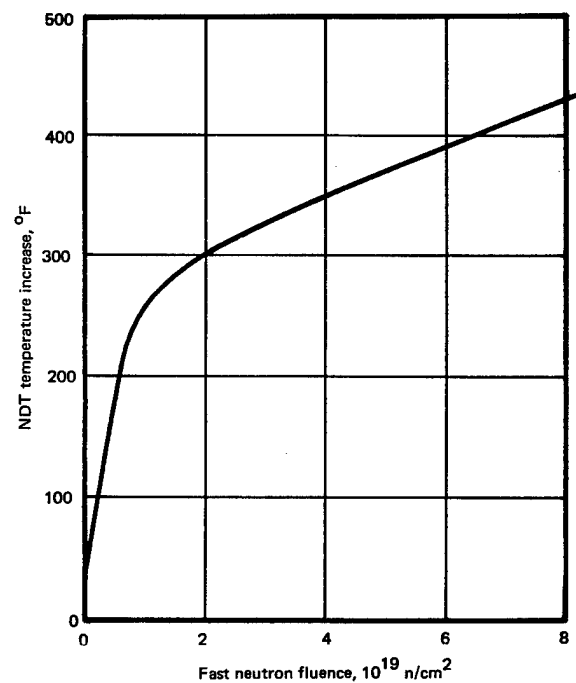


Fig. 2.21 — Increase in the nil ductility transition temperature¹⁵ of irradiated A302B steel as a function of fast neutron fluence

TRANSMISSION ELECTRON MICROSCOPY (R. C. Rau, D. A. Woodford,* J. P. Smith, J. Moteff)

Previous results¹³ on irradiated unstressed A-286 containing 0.001 and 0.010 weight percent natural boron indicated that all observable helium gas bubbles were associated with dislocations. There was no preference for bubbles to move to grain boundaries on post-irradiation thermal treatments up to 955 °C. To determine whether the combined effects of stress and temperature altered helium distributions, sections were cut from the stressed portion of the same specimens which had been creep-rupture tested at 660 °C and previously evaluated in the unstressed condition. The specimens were sectioned within 0.2 cm of the fracture and heat treated at 760°, 845°, and 955 °C. Examination of the sections from the as-tested specimens revealed very few bubbles, too few and too small in diameter to evaluate. The post-test heat-treated specimens, however, had many bubbles large enough to be evaluated. The size and size distribution appeared to be unaffected by the combined effect of stress and temperature; i.e., the results were the same as found on the specimens which were only thermally treated and not stressed. The size distribution as a function of boron content and anneal temperature is shown in Figure 2.22. There is no systematic difference between the stressed and unstressed sections taken from the specimens.

Figure 2.23 shows an area containing a grain boundary triple point and numerous matrix dislocation lines. Of significant interest are the dislocations leading into the grain boundaries; there appears to be no driving force for the helium on these dislocations to migrate to the boundary, although one would expect the dislocation to be a good diffusion pipe. Several small bubbles are present at the triple point. Figure 2.24 represents an area containing a rather high matrix bubble density compared to the few bubbles seen on the grain boundary. Significantly, all bubbles in the boundary also lie on dislocation lines within the boundary; these would probably impede dislocation movement within the boundary and thereby restrict grain boundary sliding.

The presence of shells with a high bubble density around certain precipitate particles was reported previously for A-286.¹³ Recent investigations on another alloy, Hastelloy R-235 containing 50 ppm boron enriched in B¹⁰ isotope, revealed a similar post-irradiation microstructure. Figure 2.25a illustrates the relative number of atom displacements as a function of recoil distance for both the alpha-particle and lithium. Essentially all damage is produced at the end of the recoiling particle path. The relative number of displacements caused by the lithium is somewhat higher than for the alpha-particle. Based on these factors one would expect two relatively narrow damage bands containing numerous atomic displacements as shown schematically in Figure 2.25b. Both bands (shells) were observed in A-286 and Hastelloy R-235 as shown in Figure 2.26. Figure 2.26a shows shells around three separate precipitate [Ti(N, B)] particles. For two particles an inner and outer shell are apparent. The bubbles in the outer shell are probably helium bubbles precipitated on dislocations; bubbles on the inner shell could be helium or vacancy clusters. The highly damaged matrix could limit the normal range of an alpha-particle by minimizing channeling, or the high vacancy concentration resulting from the high damage state around the lithium atom may form large voids visible on post-irradiation heat treatment. Figure 2.26b shows a similar condition in Hastelloy R-235 but probably in a different stage of development; all that is observed are concentric dislocation shells. Higher-temperature annealing will presumably reveal voids or bubbles.

*General Electric Company, Materials and Processes Laboratory, Schenectady, New York.

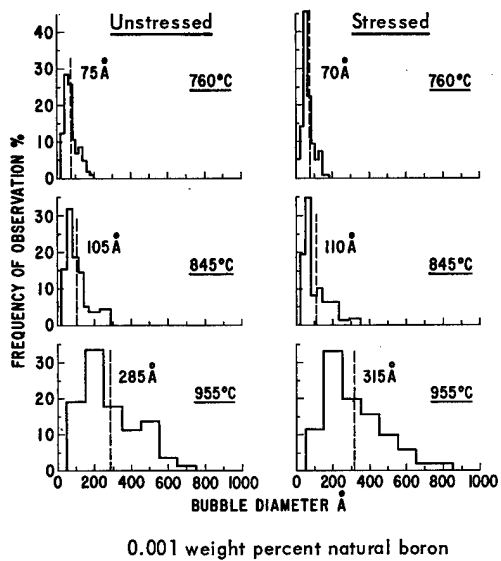
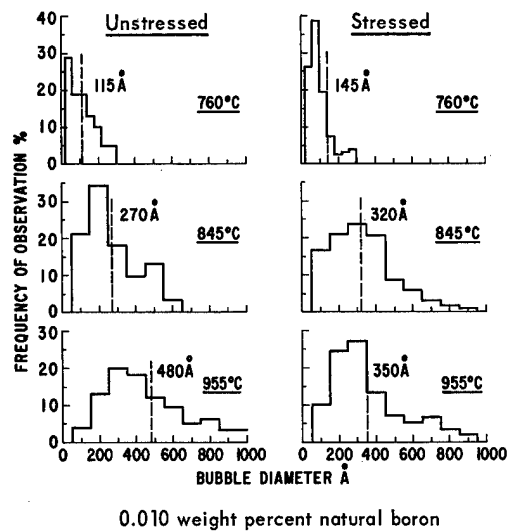


Fig. 2.22 — Size distribution of helium bubbles as a function of boron content and annealing temperature in stressed and unstressed A-286 alloy

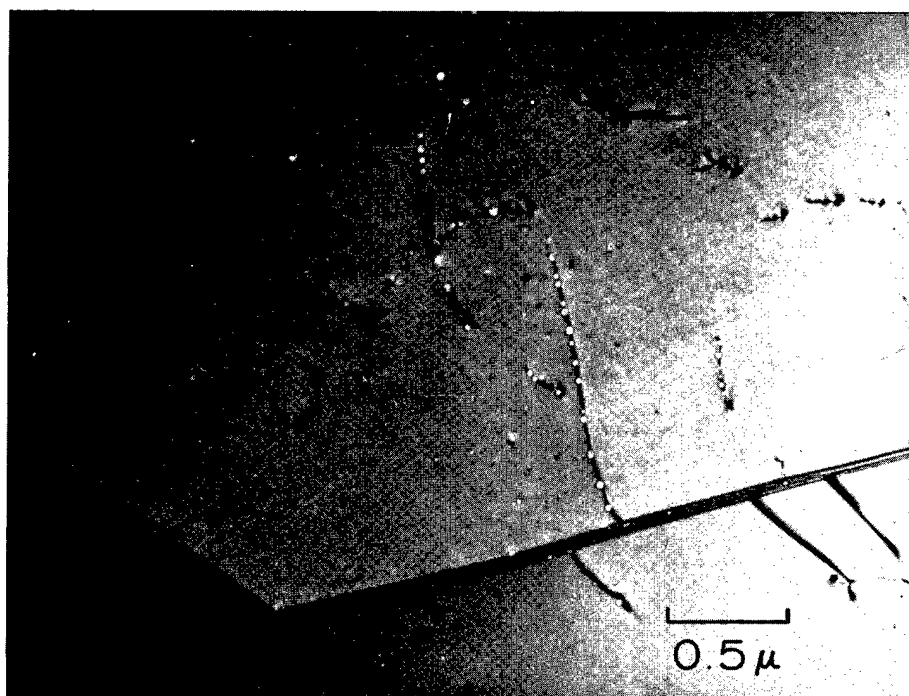


Fig. 2.23 — Transmission electron micrograph of irradiated A-286 showing helium bubbles on matrix dislocation lines and several small bubbles at the triple point

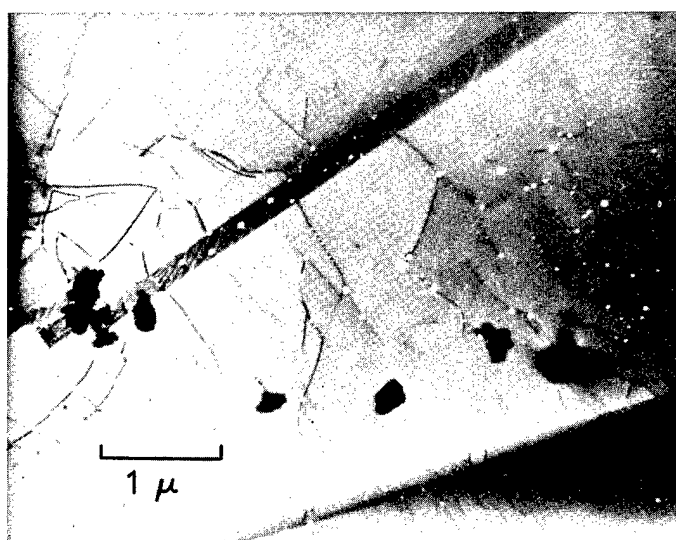


Fig. 2.24 — Transmission electron micrograph of irradiated A-286 showing bubbles attached to dislocation lines in the matrix and in the grain boundary

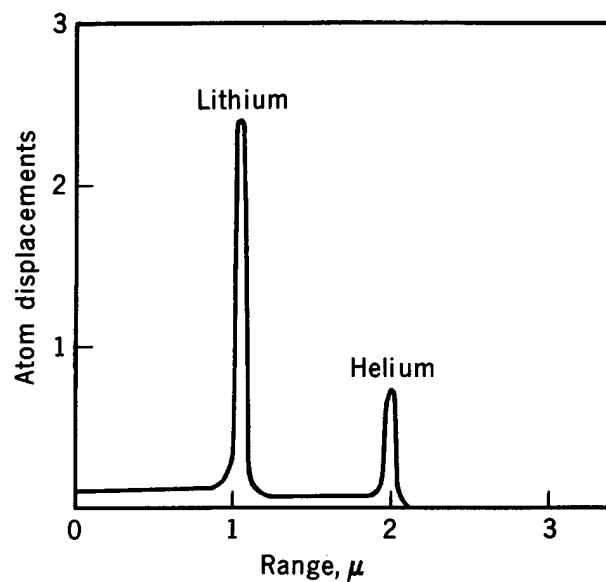
To fully explain radiation-induced changes in metals it is first necessary to describe deformation mechanisms of unirradiated alloys. An important phase of the current work is the examination of unirradiated specimens which have the same history as the irradiated specimens except for neutron exposure. Transmission electron microscope observation of unirradiated Hastelloy R-235 specimens indicates that deformation at 870°C was accompanied by the pairwise motion of dislocations through both the matrix and the coherent γ' particles.¹⁴ A good example of a slip band containing paired dislocations in a low-stress region of a tested specimen is seen in the micrographs of Figure 2.27. As discussed previously,¹⁵ this pairing is due to the creation and annihilation of an antiphase boundary by successive dislocations as they pass through the ordered γ' particles. This process retards the motion of the first dislocation and accelerates the motion of the second, causing them to draw together and move as pairs. The mobility of dislocations is largely controlled by the energy requirements for creating and annihilating an antiphase boundary; hence strengthening of coherent γ' -hardened alloys depends upon the distribution and volume fraction of γ' present.^{16,17}

The effect of strain on the interaction of dislocations with γ' particles was examined in detail, by cutting foils from three different parts of the deformed region; deformation is defined as the reduction in cross-section area. This technique involved examining foils from sections deformed at 870°C to 1, 7, and 12 percent strain.

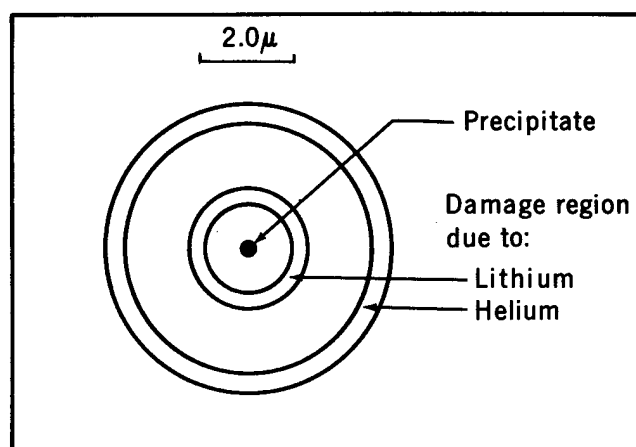
Figure 2.28a shows the microstructure in a foil taken from a region of relatively low strain (~1% reduction in area). Most γ' particles have lost coherency and are encircled by one or more dislocations. Figure 2.28b shows the microstructure in a region of intermediate strain, approximately 7 percent. At this strain level, all the γ' particles are encased in dislocation networks. The dislocation density within these networks, however, is lower than in those surrounding γ' in the high-strain (~12%) region, as shown in Figure 2.28c. Similar dislocation networks surrounding γ' particles were reported recently¹⁸ in strained Inconel X-750, but were not discussed.

This stress-induced formation of dislocation networks at the interface between γ' particles and matrix is believed to arise from the pinching off of loops from moving dislocations which bow around and are forced past the particles, leaving a loop for each passing dislocation. Increasing deformation deposits additional loops at the interface, adding to the dislocation density within the networks. As this dislocation density increases, mutual repulsive forces between the dislocations within the networks make it more difficult to add further loops, and thus lead to a hardening effect in the alloy.

In regions of high-stress concentration, dislocations would be expected to bow around coherent γ' particles rather than to shear them if the retarding force on the leading dislocation, i.e., the antiphase boundary energy of the γ' , were high enough. This is apparently true of Hastelloy R-235; no areas were observed which showed massive shearing of γ' particles by glide dislocations, as have been observed in other alloys by Copley and Kear¹⁷ and Gleiter and Hornbogen.¹⁹ The mode of dislocation immobilization in γ' precipitation hardening alloys is probably very sensitive to the alloy composition and heat treatment, since these factors influence the composition and degree of ordering of the γ' phase which in turn determine the antiphase boundary energy.



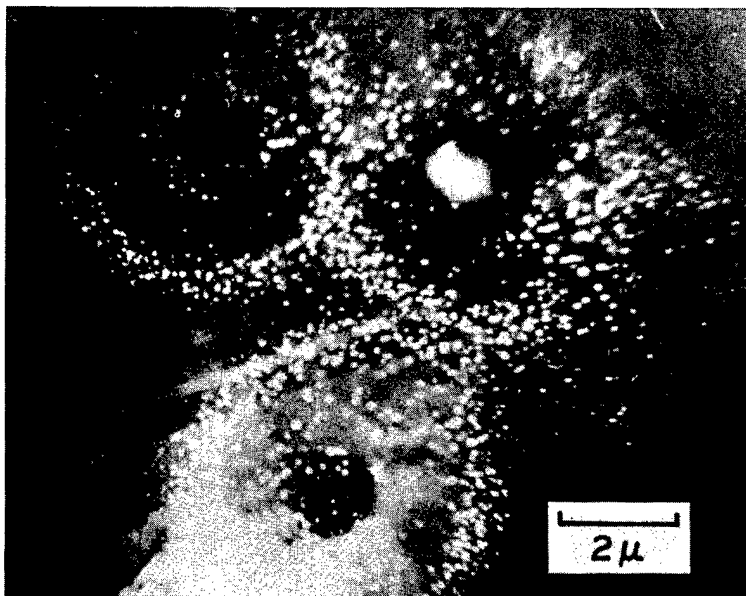
a. Relative displacement



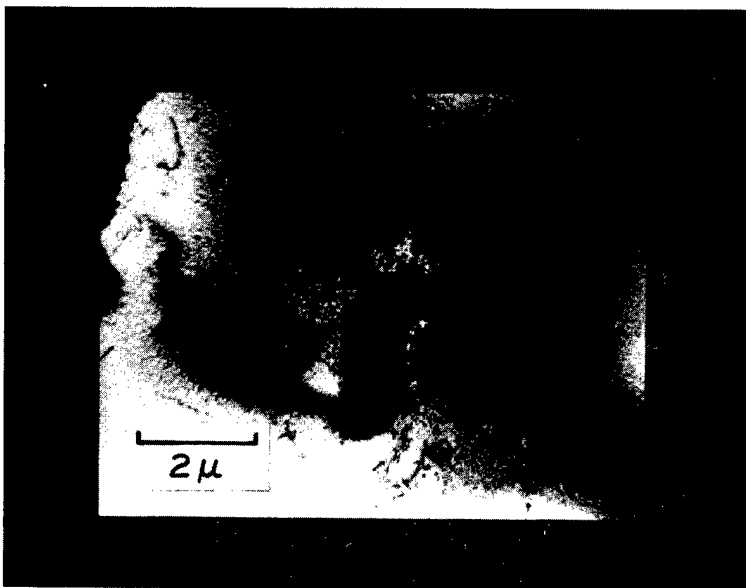
b. High-damage regions

Fig. 2.25 — Relative atom displacement and expected high-damage regions

In addition to the transmission electron microscopy discussed above, surface replication and electron microscopy is also being performed on these same Hastelloy R-235 specimens. Primary emphasis is being placed on the appearance of the structure immediately adjacent to the fracture, since past experience with similar alloys has shown that the microstructures in the unstressed condition are essentially identical before and after irradiation. Comparison of replicas from the stressed areas reveals significant differences between irradiated and unirradiated specimens, as illustrated in Figure 2.29. Of interest is the alignment of γ'



a. Helium bubbles around precipitate particles in irradiated A-286



b. Shell of dislocations around precipitate particle in irradiated Hastelloy R-235

Fig. 2.26 — Helium bubbles and shell of dislocations around precipitate particles in irradiated A-286 and Hastelloy R-235

within each grain of the unirradiated specimen (Figure 2.29a); in the irradiated specimen (Figure 2.29b) there is no tendency for alignment. This rearrangement of γ' is apparently associated with grain deformation since the unirradiated specimen exhibited approximately 18 percent elongation at rupture, but the irradiated specimen elongated only 1 percent prior to fracture. No tendency for γ' alignment was observed in the unstressed, unirradiated specimen (thermally treated but not stressed) as shown in Figure 2.30, which supports the above conclusion that the alignment is strain induced.

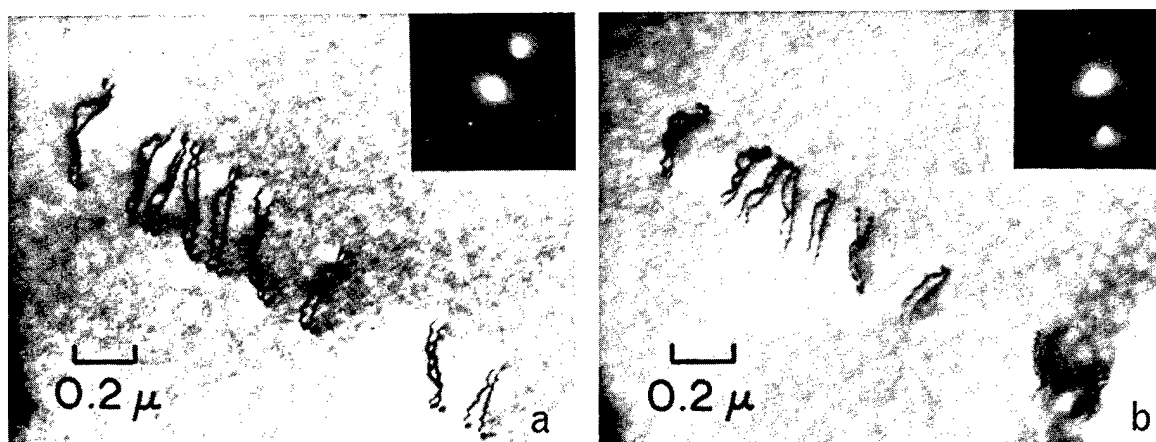


Fig. 2.27 — Slip band containing paired dislocations in low-stress region in Hastelloy R-235.
(a) (111) reflection operating. (b) (200) reflection operating.

The microstructures in Figures 2.30a and b are from the same specimen; the difference is the etchant. The structure in Figure 2.30a was obtained by using Marbles etchant; 2.30b was obtained by electro etching with 10 percent H_3PO_4 in H_2O . The H_3PO_4 etchant gives a much better definition of γ' structure, particularly in grain boundaries, where it is shown in Figure 2.30b that virtually all carbide particles (matrix as well as grain boundary) are coated with γ' . This does not occur with the Marbles etchant. Further work will emphasize the H_3PO_4 etchant because it more truly illustrates the structure. The lack of alignment of γ' in the irradiated specimen indicates that grain deformation is reduced or eliminated by irradiation. It cannot be directly concluded that this indicates matrix stiffening, since it could be the result of premature grain boundary failure.

2.3 REFRACTORY METALS AND ALLOYS PROGRAM

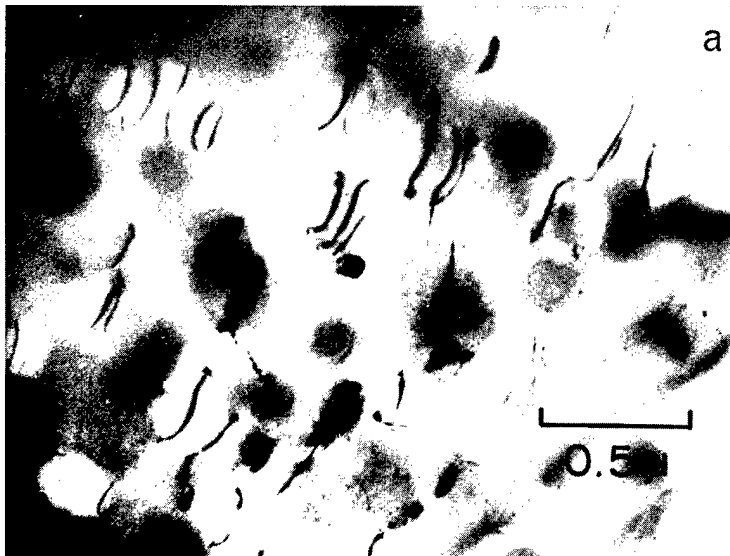
Data are presented on the creep-rupture properties of molybdenum specimens of two carbon levels. Tests were performed on specimens irradiated to neutron fluences greater than $1 \times 10^{20} \text{ n/cm}^2$ ($E_n \geq 1 \text{ Mev}$) at 70° , 700° , and 1000°C . In several cases specimens were post-irradiation annealed at various temperatures and times to determine the effect of annealing on the neutron-induced changes in the creep-rupture properties.

Elevated-temperature and room-temperature tensile test results on niobium, Nb — 1Zr, and molybdenum are discussed. Post-irradiation anneals were given to a few specimens to study thermal hardening and recovery phenomena. Hot-hardness tests on several refractory metals and alloys were completed and are compared. The recovery of radiation-induced defects in molybdenum was investigated by isochronal resistivity studies. Studies continued on the effect of changes in defect structures upon the mechanical properties. An understanding of these effects will help to define the mechanisms of neutron-induced radiation changes in refractory materials.

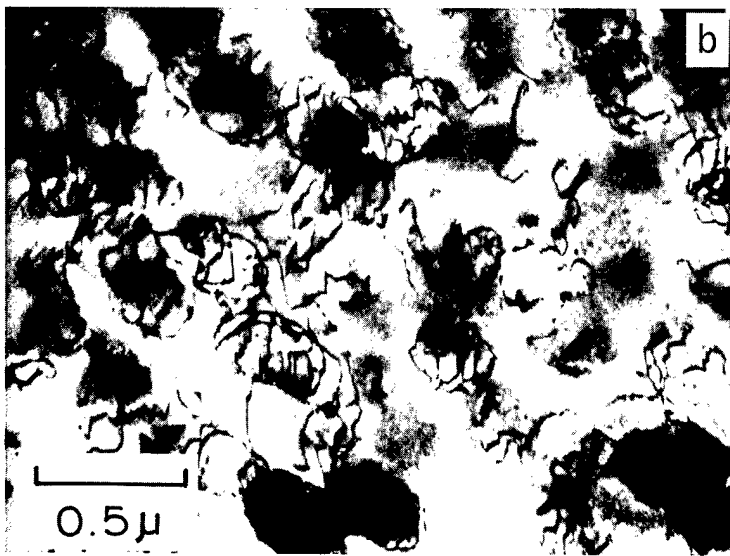
CREEP-RUPTURE TESTING (F. Kingsbury, R. Treinen, J. Motteff)

Molybdenum Rod

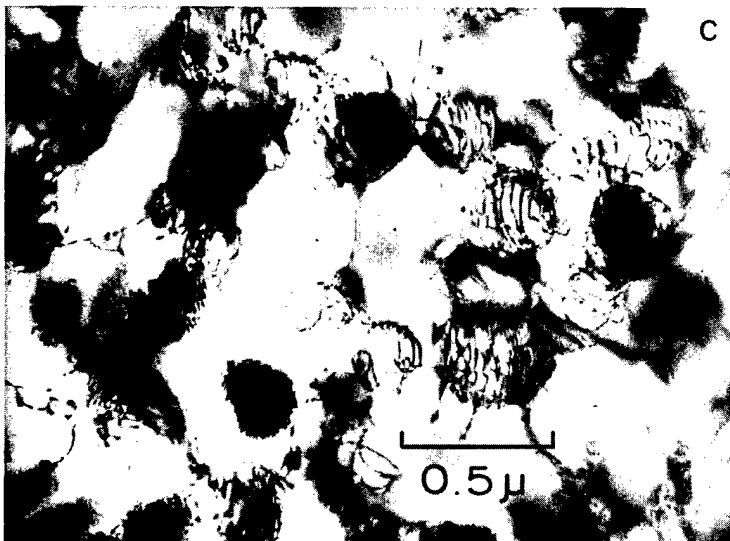
A study of the effect of irradiation temperature on the creep-rupture properties of molybdenum at 750°C was conducted. The material used in this study contained a relatively high carbon content, approximately 220 ppm. The effect of irradiation temperature was studied on recrystallized, polycrystalline specimens irradiated at 70° (reactor-ambient), 700° , and 1000°C , to fast fluences in the range 1.3×10^{20} to 1.5×10^{21}



Relatively low-strain ($\sim 1\%$) region

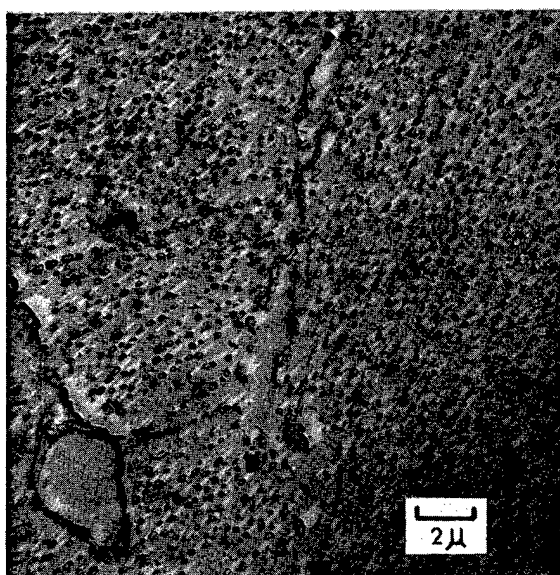


Medium-strain ($\sim 7\%$) region

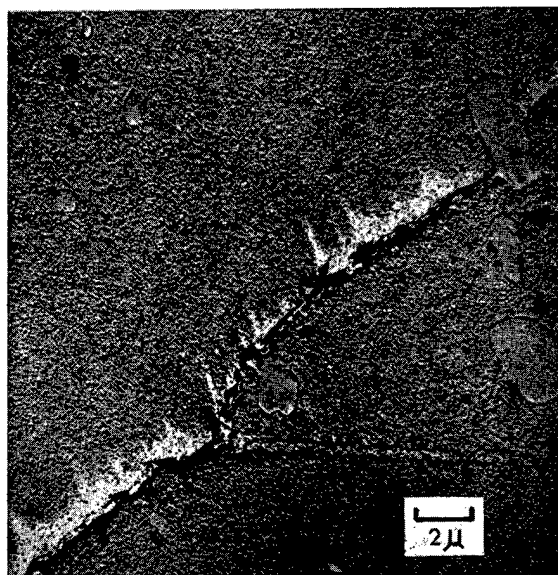


High-strain ($\sim 12\%$) region near fracture

Fig. 2.28 — Electron micrographs showing formation of dislocation networks around γ' particles as a function of strain in creep-tested Hastelloy R-235

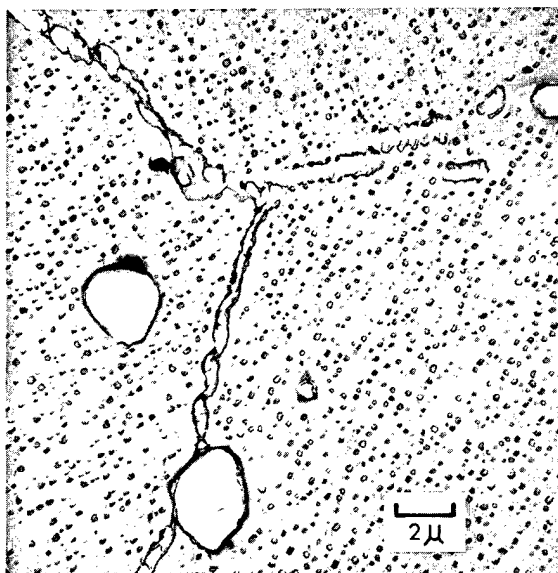


a. Unirradiated, 21% strain, t_R 200 hours

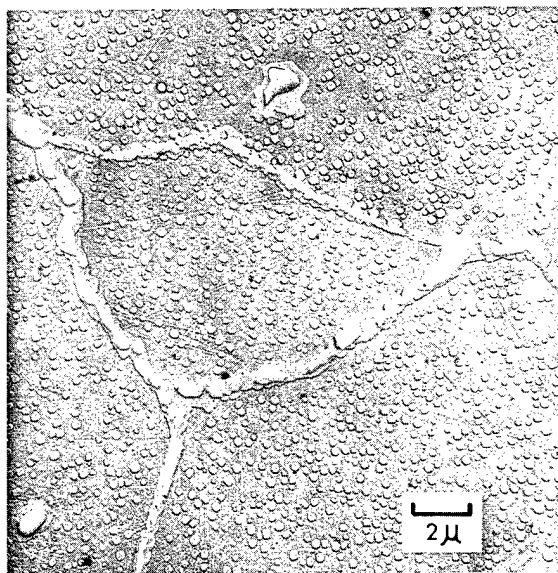


b. Irradiated, 0.6% strain, t_R 1 hour
 $\phi_F = 2.5 \times 10^{19} \text{ n/cm}^2$ ($E_n \geq 1 \text{ Mev}$)
 $\phi_{Th} = 1.6 \times 10^{20} \text{ n/cm}^2$ at 70°C in ORR

Fig. 2.29 — Longitudinal sections of creep-rupture-tested Hastelloy R-235 immediately adjacent to fracture. Creep tested at 870°C , 14.1 kg/mm^2 . (Marbles etchant)



a. Marbles etchant



b. 10% H_3PO_4 electro-etch

Fig. 2.30 — Unirradiated Hastelloy R-235 exposed 200 hours at 870°C , unstressed

n/cm^2 ($E_n \geq 1$ Mev). All irradiated specimens were tested at a common initial stress level of 18.00 kg/mm^2 (Table 2.3). Two irradiated specimens were given 1-hour post-irradiation anneals at 1000°C . A test temperature of 750°C , based on the transmission electron microscope studies of Mastel and Brimhall,²⁰ was selected for this study. Their work showed that the observable spot and loop defect density in recrystallized molybdenum, irradiated at reactor-ambient temperature to a fast neutron fluence of about $1 \times 10^{19} \text{ n/cm}^2$ ($E_n \geq 1$ Mev), decreased rapidly following post-irradiation anneals in the temperature region above 750°C . Thus it was thought that the irradiation of molybdenum above and below this temperature ($\sim 0.35 T_m$) would result in significant differences in post-irradiation creep-rupture properties. Creep-rupture properties of molybdenum at 750°C for specimens irradiated at three different temperatures are compared with a control specimen in Figure 2.31. Irradiation at the lower temperature ($\sim 70^\circ\text{C}$) resulted in the least effect on the time to rupture. There was, however, an initial period of "delayed" creep in which the creep rate remained very low for about 5 hours. The specimens irradiated at 700°C and 1000°C show a factor of 12 and 18 increase, respectively, in rupture life, with a slight decrease in ductility at the higher temperature. There is a relatively long second-stage creep behavior which increases with increasing irradiation temperature.

Two irradiated specimens were post-irradiation annealed at 1000°C in vacuum for 1 hour and creep-rupture tested. The effects of these anneals are shown in Figures 2.32 and 2.33. Annealing an ambient-temperature irradiated specimen altered the creep-rupture properties; the period of delayed creep was shortened, creep rate was reduced, and time to rupture was increased compared to the as-irradiated specimen. Changes produced by a 1000°C anneal in the creep properties of a 700°C irradiated specimen were not so pronounced. The minimum creep rate did not show a significant change, rupture life was increased by 25 percent.

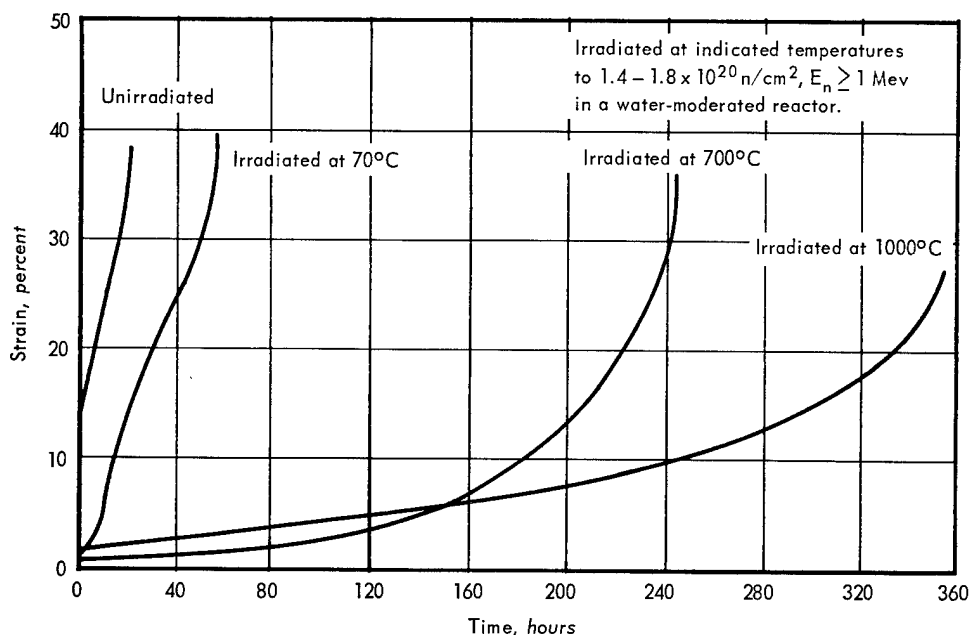


Fig. 2.31 — Creep-rupture properties of polycrystalline Mo at a test temperature of 750°C and an initial stress level of 18.00 kg/mm^2 following neutron irradiations at temperatures of 70° , 700° , and 1000°C

TABLE 2.3
MOLYBDENUM ROD^a CREEP-RUPTURE TESTS AT 750°C

Specimen No.	Fluence, n/cm ²		Irradiation Temperature, °C	Post-Irradiation Annealing	Stress, kg/mm ²	Stage I (Delayed) Creep Rate, sec ⁻¹	Duration of Stage I Creep, hr	Stage II Creep Rate, sec ⁻¹	Rupture Life, hr	Elongation, % ^b	Reduction in Area, %
	Thermal	Fast (E _n > 1 Mev)									
High-Carbon (220 ppm) Rod ^c											
1606	None	None	—	None	14.00	—	—	5.7 x 10 ⁻⁸	997.0	51.0	93.9
1615	None	None	—	None	17.00	—	—	5.4 x 10 ⁻⁷	(120.2) ^d	—	—
1610	None	None	—	None	18.00	—	—	2.13 x 10 ⁻⁶	20.4	39.5	95.7
1617	None	None	—	None	19.00	—	—	1.5 x 10 ⁻⁶	35.6	40.3	94.3
1599	None	None	—	None	20.00	—	—	4.5 x 10 ⁻⁶	8.68	38.4	92.4
1594	4.5 x 10 ²⁰	1.35 x 10 ^{20e}	~70	None	18.00	~1.4 x 10 ⁻⁷	0.5-5	1.2 x 10 ⁻⁶	56.1	40.4	92.8
1597	4.5 x 10 ²⁰	1.35 x 10 ^{20e}	~70	1000°C-1 hr-vac	18.00	~2.8 x 10 ⁻⁷	0.5-1.5	8.3 x 10 ⁻⁷	(87.5) ^d	44.6	—
1591	2.7 x 10 ²¹	1.5 x 10 ^{21f}	~70	None	18.00	~3.5 x 10 ⁻⁸	~4-20	2.8 x 10 ⁻⁷	253.4	37.6	94.3
1622	4.5 x 10 ²⁰	1.4 x 10 ^{20g}	~700	None	18.00	—	—	2.3 x 10 ⁻⁸	244.1	34.0	93.6
1623	4.5 x 10 ²⁰	1.4 x 10 ^{20g}	~700	1000°C-1 hr-vac	18.00	—	—	2.1 x 10 ⁻⁸	306.7	31.1	95.2
1612	4.3 x 10 ²⁰	1.3 x 10 ^{20h}	~1000	None	18.00	—	—	7.2 x 10 ⁻⁸	355.1	—	—

^aSpecimens from 0.508-cm-diameter arc-cast Mo rod post-grind annealed at 1200°C for 1 hour in vacuum.

^bPercent in 4.45-cm gage length.

^cHeat KDM-1002B, rod D.

^dSpecimen did not fracture; lever arm arrested against stop in latter portion of third-stage creep.

^eIrradiation test 2-236 in ETR facility E-5NE.

^fIrradiation test 2-234 in J-14NW facility.

^gIrradiation test 2-154 in ETR facility E5SW during cycle 84.

^hIrradiation test 2-136 in ETR facility E5NE during cycle 84.

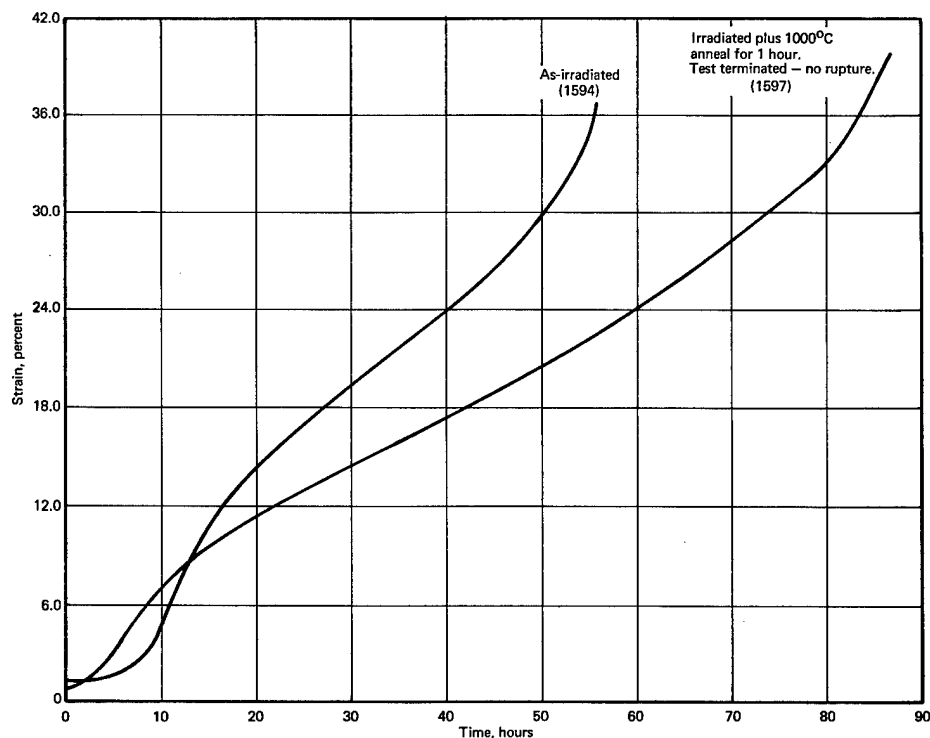


Fig. 2.32 — Effect of 1-hour 1000°C post-irradiation anneal on the creep-rupture properties of high-carbon Mo rod specimens irradiated at approximately 70°C to a fluence level of 1.35×10^{20} n/cm² ($E_n \geq 1$ Mev). Tests conducted at 750°C and 18.00 kg/mm².

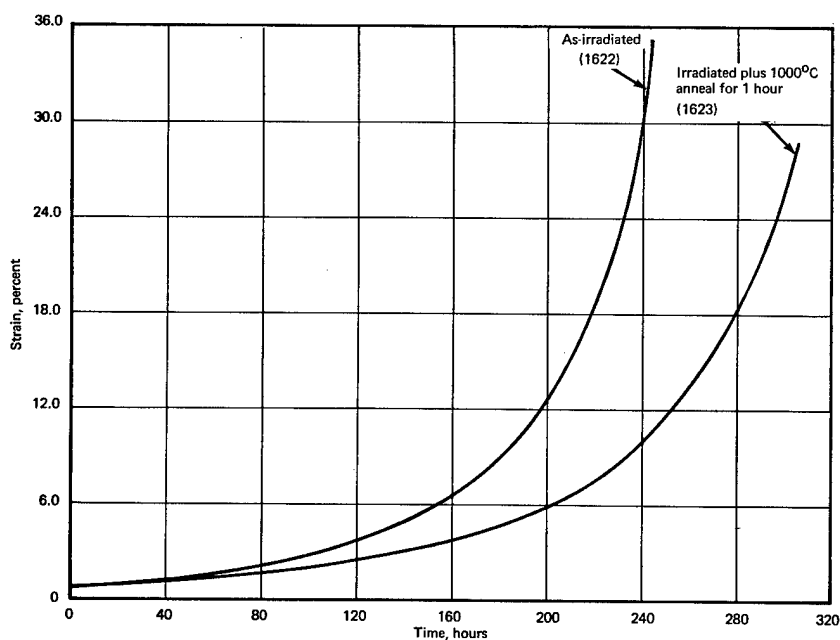


Fig. 2.33 — Effect of 1-hour 1000°C post-irradiation anneal on the creep-rupture properties of high-carbon Mo rod specimens irradiated at 700°C to a fluence level of 1.4×10^{20} n/cm² ($E_n \geq 1$ Mev). Tests conducted at 750°C and 18.00 kg/mm².

Specimen No. 1591 which was irradiated to a neutron fluence of $1.5 \times 10^{21} \text{ n/cm}^2$ ($E_n \geq 1 \text{ Mev}$) at ambient temperature permits a comparison of the effect of neutron fluence. Compared to specimen No. 1594 ($1.35 \times 10^{20} \text{ n/cm}^2$), Figure 2.34, which was irradiated to a fluence an order of magnitude lower, specimen No. 1591 exhibited a factor of 4.6 increase in time to rupture and almost an order of magnitude decrease in creep rate. A portion of the greater rupture life was due to the increased length of the delayed creep period in the higher fluence specimen.

The differences in the creep characteristics between the various specimens can also be noted in the instantaneous creep rate versus plastic strain plots of Figures 2.35 through 2.37. Specimens irradiated at ambient temperature (Figure 2.35) all show a rapidly decreasing creep rate in the initial 0.2 percent strain. This is followed by a rapidly increasing creep rate which reaches a maximum value in the 2 to 6 percent strain region. After reaching this maximum value the creep rate decreases to the usually minimum second-stage creep rate. An expanded plot of the initial 1 percent strain (Figure 2.36) shows the ordering of the inflection points in the creep rates. The initial rate of decrease is approximately constant and the minimum value at the inflection point shifts to higher strain values at decreasing creep rates.

The creep-rate strain behavior of specimens irradiated at elevated temperatures (Figure 2.37) showed two differences in the characteristics compared to the ambient-temperature irradiated specimens. No maximum is observed in the creep rate following the initial inflection point. The three specimens exhibited an increase in creep rate with increasing strain following the initial decrease in creep rate. Irradiation at 1000°C did not produce the marked inflection at the minimum creep rate observed in the 700°C irradiated specimen or the 700°C irradiated specimen with the 1000°C post-irradiation anneal. The 700°C irradiated specimens have higher creep rates over a greater range of strain (and hence time) than the 1000°C irradiated specimen. The 1000°C post-irradiated annealed specimens also showed creep rates lower than the 700°C as-irradiated specimen. These

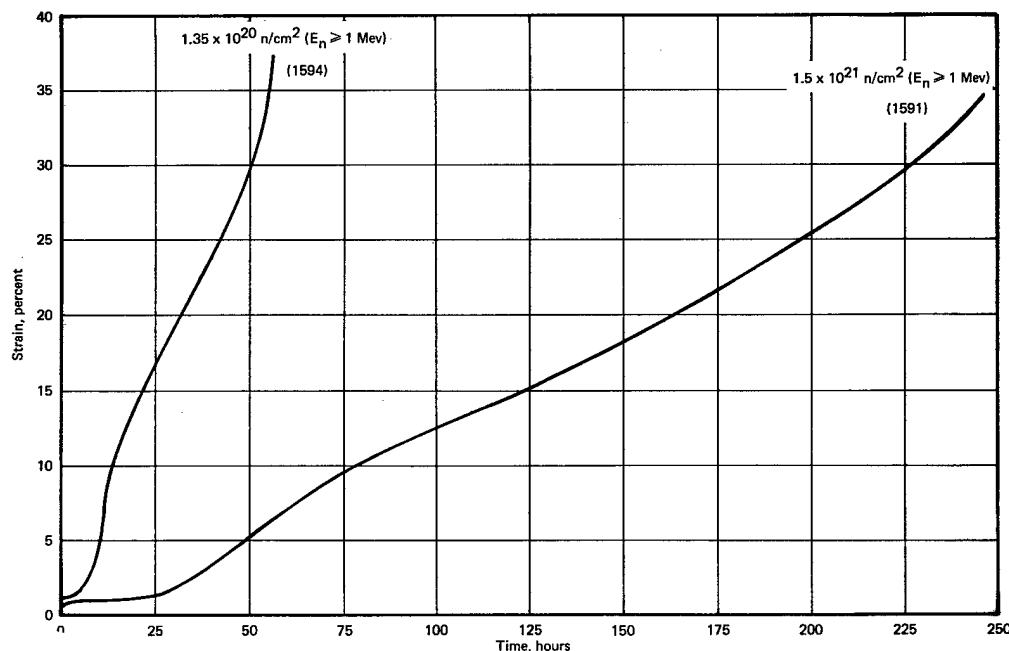


Fig. 2.34 — Creep characteristics of irradiated high-carbon Mo rod at two neutron fluence levels. Specimens irradiated at approximately 70°C and tested at 750°C and 18.00 kg/mm^2 .

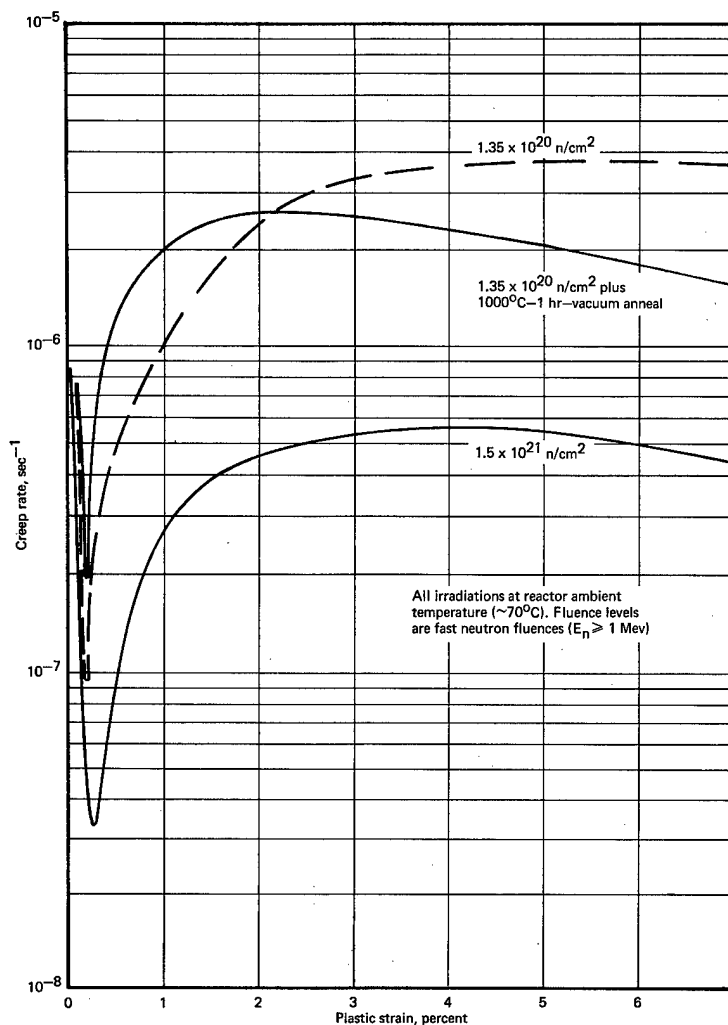


Fig. 2.35 — Creep rate versus plastic strain for ambient temperature irradiated high-carbon (200 ppm) Mo specimens tested at 750°C and 18.00 kg/mm²

results suggest that some of the more stable defects are possibly formed between 700°C and 1000°C.

It is believed that the substructure, i.e., isolated dislocations, tangles, and subgrain boundaries formed during the initial straining establish the mode of deformation in creep. Structural studies are being conducted on these high-carbon molybdenum rod specimens, both optically and by transmission electron-microscope techniques. Initial electron microscope observations will be reported in a subsequent section.

Molybdenum Sheet

Creep-rupture testing of arc-cast molybdenum sheet was conducted to gain an understanding of the effect of changes in the defect structure produced by post-irradiation annealing on the mechanical properties. Preliminary tests²¹ exhibited accelerated creep at 580°C and delayed creep at 700°C. Additional tests were conducted on material at two carbon levels, 205 ppm and 26 ppm, to confirm these results. Most tests were conducted at fixed stress levels and test temperatures; the irradiated specimens received various annealing treatments in the temperature range of 700° to 1600°C (0.34 to 0.65 T_m).

A composite strain – time plot for control, as-irradiated, and 750°C post-irradiated low-carbon molybdenum specimens tested at 580°C is shown in Figure 2.38. The accelerated creep of the as-irradiated specimen is evident. The 750°C ($0.36 T_m$) anneal produced a lower creep rate and longer rupture life than the as-irradiated specimen, but did not fully restore the creep characteristics to the control values; hence the defects causing the accelerated creep were only partly removed at 750°C.

Tests at 700°C on low-carbon molybdenum included specimens which had two neutron fluence levels (Table 2.4). All irradiated specimens were tested at 17.50 kg/mm^2 except for specimens which had been post-irradiation annealed above 1400°C. These specimens were tested at lower stresses due to grain growth which had occurred in the annealing process. Originally all low-carbon specimens were annealed at 1200°C in vacuum for 1 hour following fabrication.

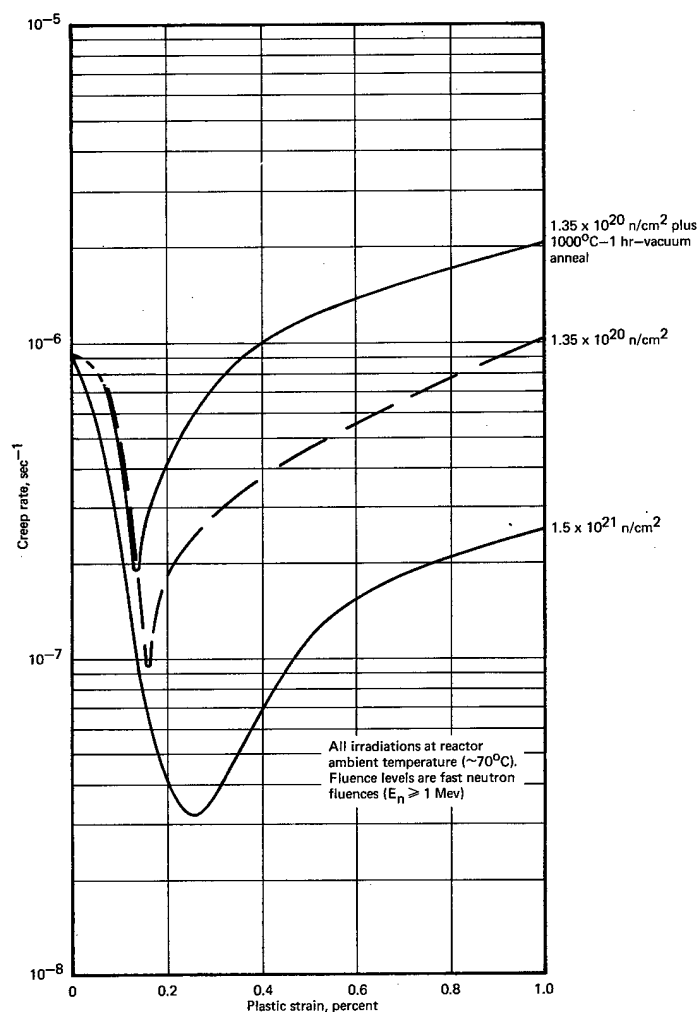


Fig. 2.36 – Creep rate versus plastic strain for irradiated high-carbon (200 ppm) Mo specimens tested at 750°C and 18.00 kg/mm^2

TABLE 2.4
LOW-CARBON MOLYBDENUM SHEET^a TESTS AT 700°C

Specimen No.	Fluence, n/cm ²		Post-Irradiation Annealing, °C	Stress, kg/mm ²	Stage I (Delayed) Creep Rate, sec ⁻¹	Duration of Stage I Creep, hr	Stage II Creep Rate, sec ⁻¹	Rupture Life, hr	Elongation, % ^b
	Thermal	Fast (E _n ≥ 1 Mev)							
2701		None	None	15.00	—	None	2.15 x 10 ⁻⁷	237.1	43.5
2712		None	None	16.50	—	None	6.74 x 10 ⁻⁷	96.8	47.9
2713		None	None	17.50	—	None	1.84 x 10 ⁻⁶	37.5	58.3
2714		None	1200°C-1 hr-H ₂	17.50	—	None	1.87 x 10 ⁻⁶	33.3	51.2
2728		None	1200°C-1 hr-H ₂	17.50	—	None	1.91 x 10 ⁻⁶	31.0	50.3
2731		None	1450°C-1 hr-vac	14.50	—	None	8.03 x 10 ⁻⁷	75.7	58.0
2716		None	1600°C-1 hr-H ₂	13.00	—	None	1.15 x 10 ⁻⁶	47.6	44.1
2700	9.3 x 10 ²⁰	3.1 x 10 ^{20c}	None	17.50	1.1 x 10 ⁻⁷	2-16	5.78 x 10 ⁻⁶	39.7	41.6
2702	9.3 x 10 ²⁰	3.1 x 10 ^{20c}	700°C-18 hr-H ₂	17.50	1.52 x 10 ⁻⁷	1-10	5.05 x 10 ⁻⁶	37.6	40.4
2704	9.3 x 10 ²⁰	3.1 x 10 ^{20c}	800°C-1 hr-H ₂	17.50	1.01 x 10 ⁻⁷	0.5-8	4.53 x 10 ⁻⁶	46.3	43.4
2705	9.3 x 10 ²⁰	3.1 x 10 ^{20c}	900°C-1 hr-H ₂	17.50	1.11 x 10 ⁻⁷	0.5-13	2.53 x 10 ⁻⁶	69.8	45.0
2706	9.3 x 10 ²⁰	3.1 x 10 ^{20c}	1200°C-1 hr-H ₂	17.50	—	None	3.75 x 10 ⁻⁷	199.7	43.8
2718	3.9 x 10 ²⁰	1.2 x 10 ^{20d}	None	17.50	7.4 x 10 ⁻⁸	0.5-18	6.47 x 10 ⁻⁶	35.4	40.1
2723	3.9 x 10 ²⁰	1.2 x 10 ^{20d}	850°C-1 hr-H ₂	17.50	6.4 x 10 ⁻⁸	0.5-4	6.36 x 10 ⁻⁶	30.6	—
2722	3.9 x 10 ²⁰	1.2 x 10 ^{20d}	900°C-1 hr-H ₂	17.50	3.2 x 10 ⁻⁷	0.5-8	3.24 x 10 ⁻⁶	50.3	44.6
2721	3.9 x 10 ²⁰	1.2 x 10 ^{20d}	950°C-1 hr-H ₂	17.50	2.0 x 10 ⁻⁷	0.5-4	1.92 x 10 ⁻⁶	74.1	40.5
2720	3.9 x 10 ²⁰	1.2 x 10 ^{20d}	1200°C-1 hr-H ₂	17.50	—	None	1.02 x 10 ⁻⁶	68.3	46.5
2725	3.9 x 10 ²⁰	1.2 x 10 ^{20d}	1450°C-1 hr-vac	14.50	—	None	3.0 x 10 ⁻⁷	176.3	54.6
2726	3.9 x 10 ²⁰	1.2 x 10 ^{20d}	1600°C-1 hr-H ₂	13.00	—	None	~3.1 x 10 ⁻⁷	173.8	42.0

^aSpecimens from 0.05-cm commercial vacuum arc-cast Mo sheet (heat C-7722), post-grind annealed for 1 hour in vacuum at 1200°C (~30 micron grain size — DPH 193). Carbon content 26 ppm; O₂ — 18 ppm. All tests at constant load in H₂.

^bPercent in 2.54-cm gage length.

^cIrradiation test capsule ORM-46 in ORR facility F-2 at reactor-ambient temperature (~70°C).

^dIrradiation test capsule GEFP2-235 in ETR facility E-5NE at reactor-ambient temperature (~70°C).

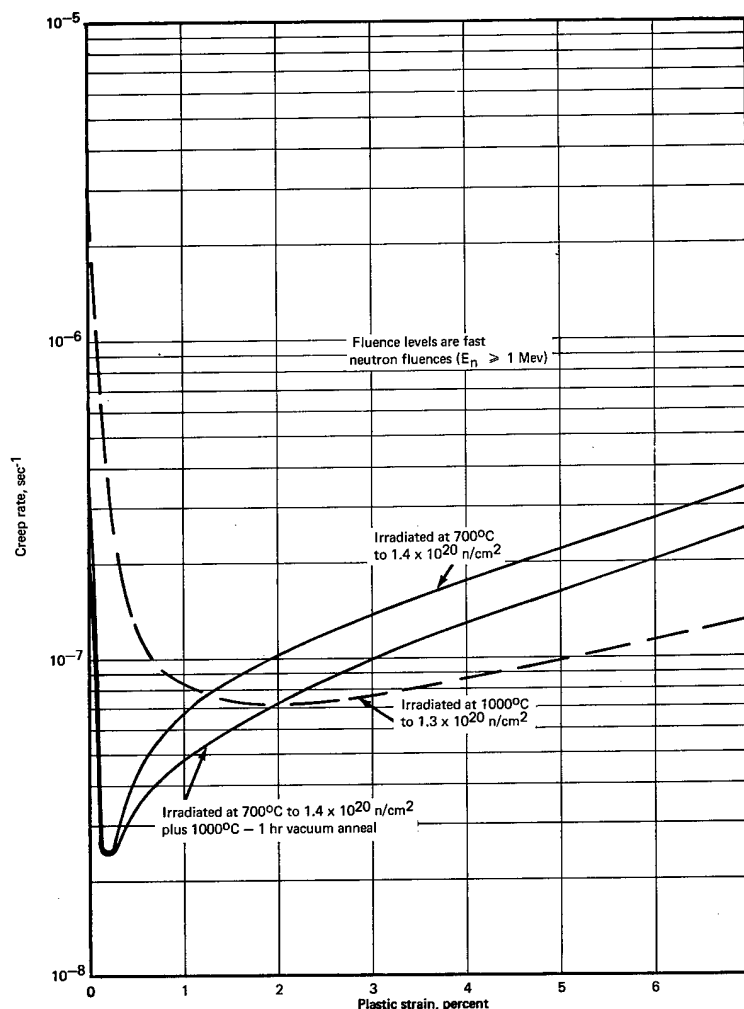


Fig. 2.37 – Creep rate versus plastic strain for elevated-temperature irradiated high-carbon (200 ppm) Mo specimens tested at 750°C and 18.00 kg/mm².

Specimens in the as-irradiated condition or post-irradiation annealed below 1000°C exhibited delayed creep (Table 2.4). The apparent length of this incubation period in which the creep rate is abnormally low tends to decrease upon annealing in the 700° to 950°C temperature range. The 700° to 800°C anneals produced only small changes in the creep rates or rupture times as shown (Figure 2.39) for the specimens irradiated to a fluence level of $3.1 \times 10^{20} \text{ n/cm}^2$ ($E_n \geq 1 \text{ Mev}$). Annealing at 900°C or 950°C produces little further changes in the incubation period but does decrease the steady-state creep rates and increase the times to rupture. A complete change in creep characteristics occurs upon annealing at 1200°C. The period of incubation (i. e., delayed creep) is not exhibited and the strain – time plots show the normal three stages of creep behavior. This is shown in Figure 2.40 for specimens irradiated to $1.2 \times 10^{20} \text{ n/cm}^2$ ($E_n \geq 1 \text{ Mev}$).

Tests at 700°C on specimens post-annealed above 1200°C are not directly comparable to the preceding results. Nevertheless, they may be compared to control specimens annealed at the same time and tested at the same stress level. Tests conducted on specimens annealed at 1450°C and 1600°C (0.60 and 0.65 T_m , respectively) did not show delayed

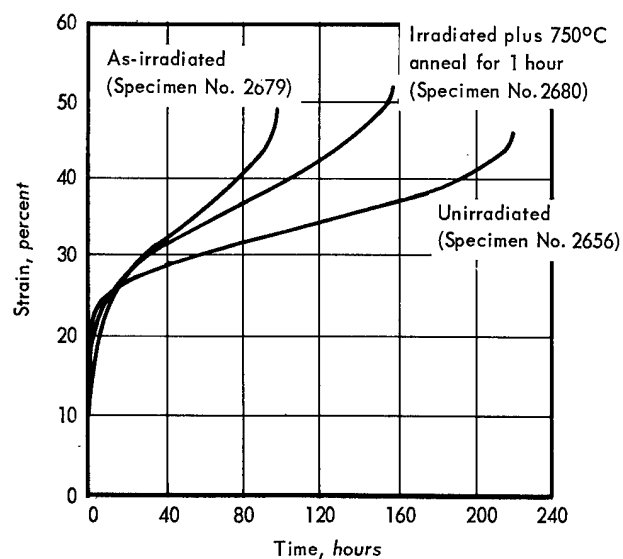


Fig. 2.38 — Effect of 750°C post-irradiation anneal on the accelerated creep of irradiated low-carbon molybdenum. Tests conducted at 580°C and 19.40 kg/mm² on sheet specimens irradiated at reactor ambient temperature to a fluence level of 4.8×10^{18} n/cm² ($E_n \geq 1$ Mev).

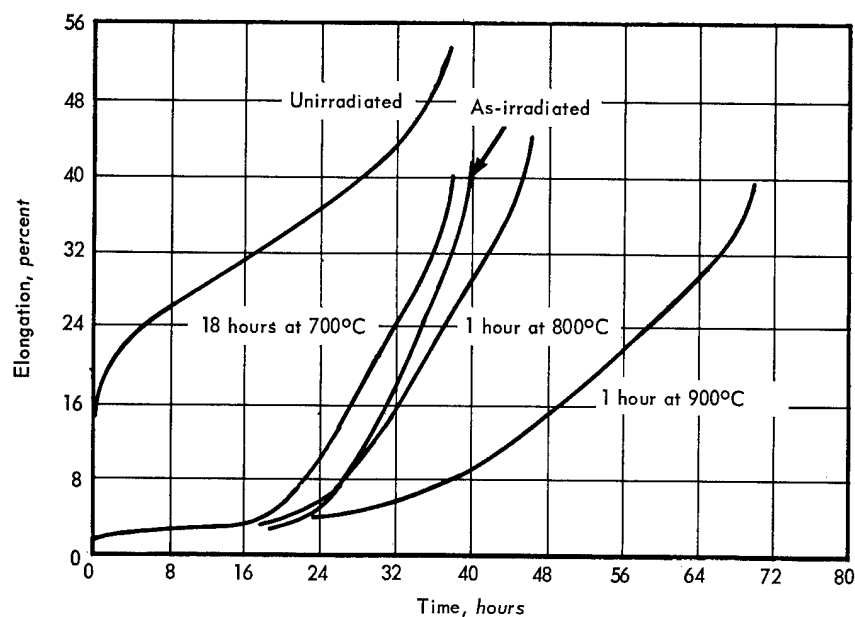


Fig. 2.39 — Effect of post-irradiation anneals at 700°C, 800°C, and 900°C on the creep properties of low-carbon molybdenum. Tests conducted at 700°C and 17.50 kg/mm² on sheet specimens irradiated at reactor ambient temperature to a fluence level of 3.1×10^{20} n/cm² ($E_n \geq 1$ Mev).

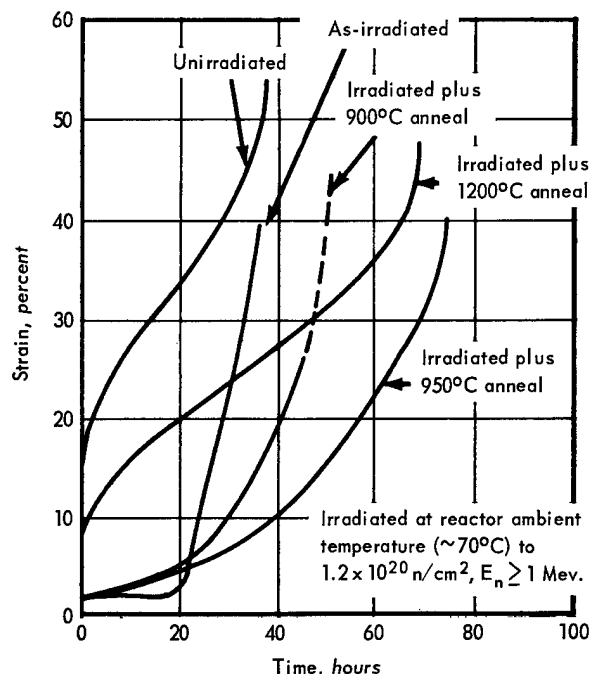


Fig. 2.40 — Effect of post-irradiation anneals at 900°, 950°, and 1200°C on creep properties of low-carbon Mo. Tests conducted at 700°C and 17.50 kg/mm² in a hydrogen atmosphere. Anneals performed at indicated temperatures for 1 hour in a hydrogen atmosphere.

creep. Pronounced neutron-induced strengthening still remains under these test conditions, as can be seen in the 1600°C annealed specimens, Figure 2.41.

A limited number of creep tests were also conducted at 700°C on high-carbon (~200 ppm) molybdenum specimens to observe the possible effect of particle – defect interaction on creep behavior. The differences in the two grades of material can be seen in the microstructures. The high-carbon molybdenum exhibited a dense, equiaxed, recrystallized grain structure with randomly distributed carbide particles. The particles were generally small but a few larger carbides were observed. Several larger carbides appeared to have voids associated with the ends of the particles (Figure 2.42). In contrast to the high-carbon molybdenum sheet, the low-carbon molybdenum microstructure (Figure 2.43) consisted of single-phase grains with no carbides observable at a magnification of 600X. The grain size of the low-carbon material was slightly larger (30-micron versus 22-micron grain sizes in the high-carbon Mo). The grains in the low-carbon material tended to be elongated in the direction of rolling.

A composite strain – time plot for the results of high-carbon molybdenum tests given in Table 2.5 is shown in Figure 2.44. The 1200°C annealed specimen exhibited no incubation period; creep rate was reduced significantly and rupture life increased 37 percent compared to the as-irradiated specimen. The 900°C anneal tended to remove the incubation period and produced a longer rupture life than the as-irradiated or 1200°C post-irradiation annealed specimen. This effect is believed related to the thermal hardening generally observed in tensile tests of irradiated body-centered cubic (bcc) materials following elevated-temperature anneals. In the present case, the thermal hardening can be related to rupture times (rupture strength) rather than to tensile strength.

The differences in the creep characteristics of the high-carbon molybdenum specimens can be readily observed in the instantaneous creep rate versus time plots of Figure 2.45.

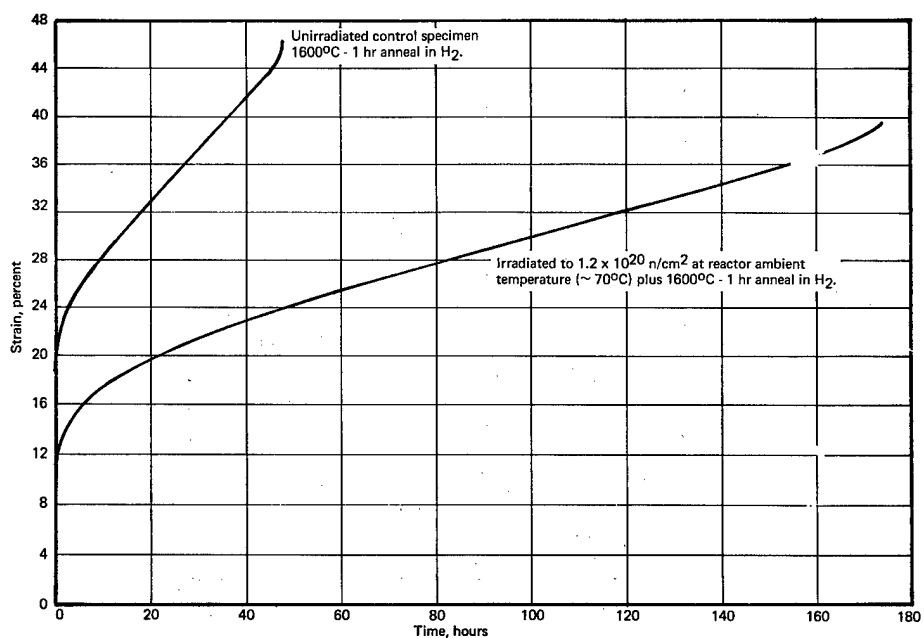


Fig. 2.41 — Strain versus time curves for low-carbon (26 ppm) Mo sheet specimens tested at 700°C and 17.50 kg/mm² in hydrogen.

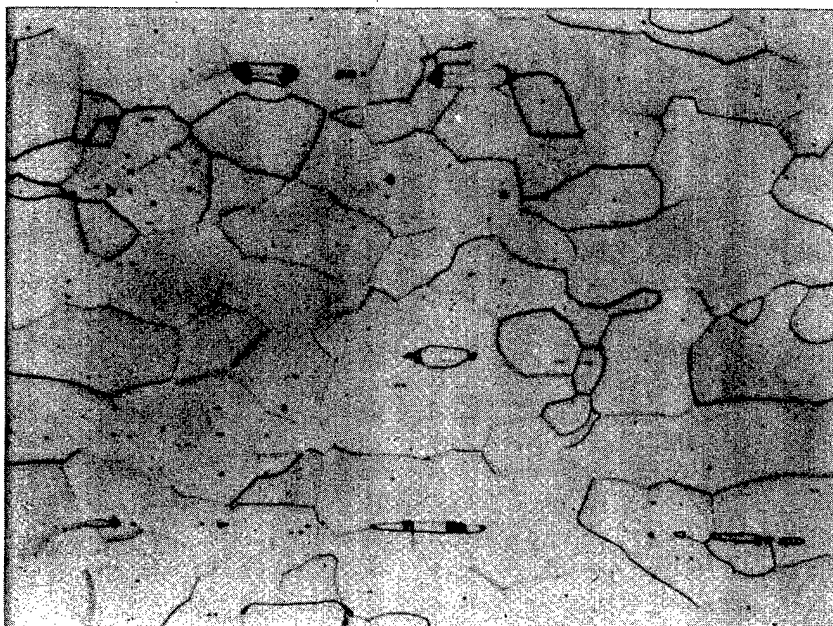


Fig. 2.42 — Photomicrograph of high-carbon (205 ppm) Mo sheet, heat C-6605, annealed at 1200°C for 1 hour in vacuum (Neg. 10280, 500X)

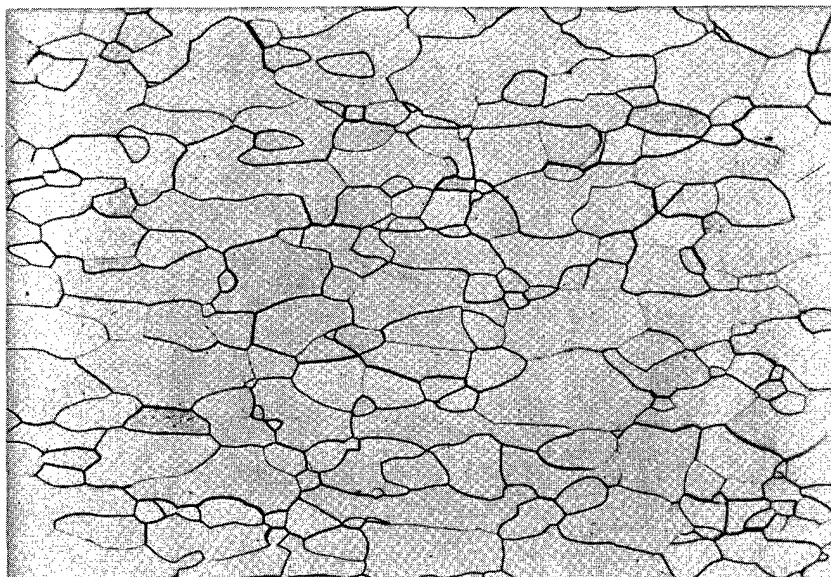


Fig. 2.43 — Photomicrograph of low-carbon (26 ppm) Mo sheet, heat 7722, annealed at 1200°C for 1 hour in vacuum (Neg. 10316, 250X)

TABLE 2.5
MOLYBDENUM SHEET CREEP RUPTURE TESTS AT 700°C AND 20.00 kg/mm²

Specimen No. ^a	Condition	Post-Irradiation Anneal	Stage-I (Delayed) Creep Rate, sec ⁻¹	Stage-I Creep Period, hr	Stage-II Creep Rate, sec ⁻¹	Rupture Life, hr	Elongation, ^b %
2103	None	None	—	—	6.09×10^{-7}	118.9	49.2
2122	Irradiated ^c	None	$\sim 2.8 \times 10^{-8}$	1 to 10	4.11×10^{-7}	180.5	46.8
2126	Irradiated ^c	1200°C for 1 hr in H ₂	—	—	2.6×10^{-7}	229.8	41.3
2127	Irradiated ^c	900°C for 1 hr in H ₂	$\sim 2.8 \times 10^{-8}$	1 to 5	2.25×10^{-7}	271.4	43.1

^aSpecimens from 0.05-cm-thick commercial vacuum arc-cast Mo sheet (heat C 6605) post-grind annealed at 1200°C for 1 hour in vacuum (~ 22 micron grain size — DPH 191). Carbon content 205 ppm; O₂ content 3 ppm. All tests at constant load in hydrogen.

^bPercent in 2.54-cm gage length.

^cIrradiation test ORM-38 in ORR facility A-2 at reactor ambient temperature ($\sim 70^\circ\text{C}$) to a fluence of 1.1×10^{20} n/cm² ($E_n \geq 1$ Mev); thermal fluence of 5.2×10^{20} n/cm².

Normal creep-rate curves are exhibited by the unirradiated and 1200°C annealed specimens; the 1200°C curve is displaced into the lower creep-rate regions. The 1-hour anneal at 1200°C probably did not remove all the radiation-induced defects (possible stable vacancy clusters). This view is supported by the results of the 1600°C anneal in the low-carbon molybdenum test data. The lower creep rate following the 1200°C anneal reflects dislocation interaction with the remaining defects.

The curves for as-irradiated and 900°C annealed specimens show the nature of the changes in creep rate during the incubation and early stages of creep. The as-irradiated specimen shows a maximum in the creep-rate curve (at ~ 40 hours) following the initial rapid decrease in creep rate (delayed creep). This maximum is not observed in the 900°C post-irradiation annealed specimen, and the specimen tends to show a continuous increase in creep rate following the delayed creep stage.

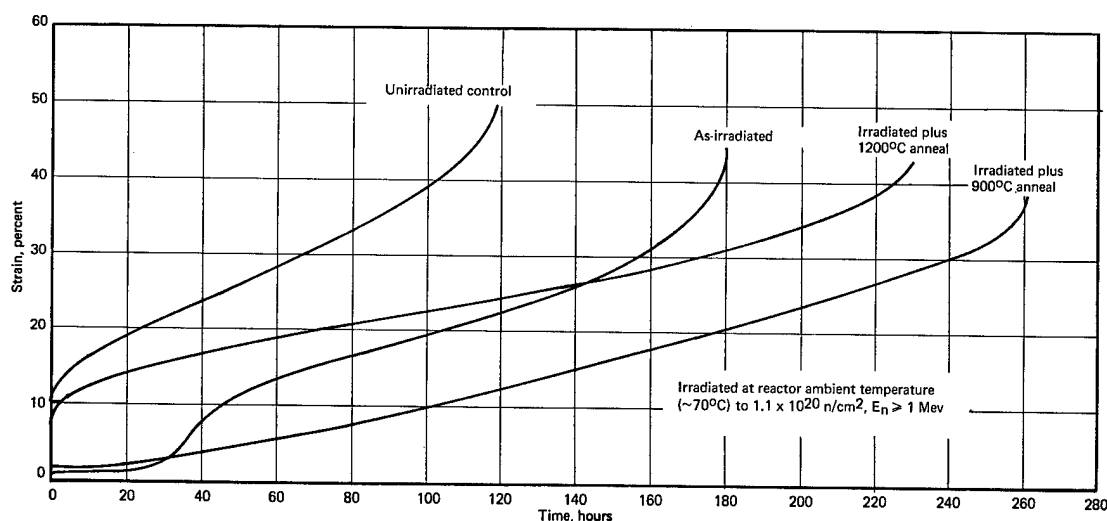


Fig. 2.44 — Effect of post-irradiation anneals at 900°C and 1200°C on creep properties of high-carbon Mo. Tests conducted at 700°C and 20.00 kg/mm² in a hydrogen atmosphere. Anneals performed at indicated temperature for 1 hour in hydrogen.

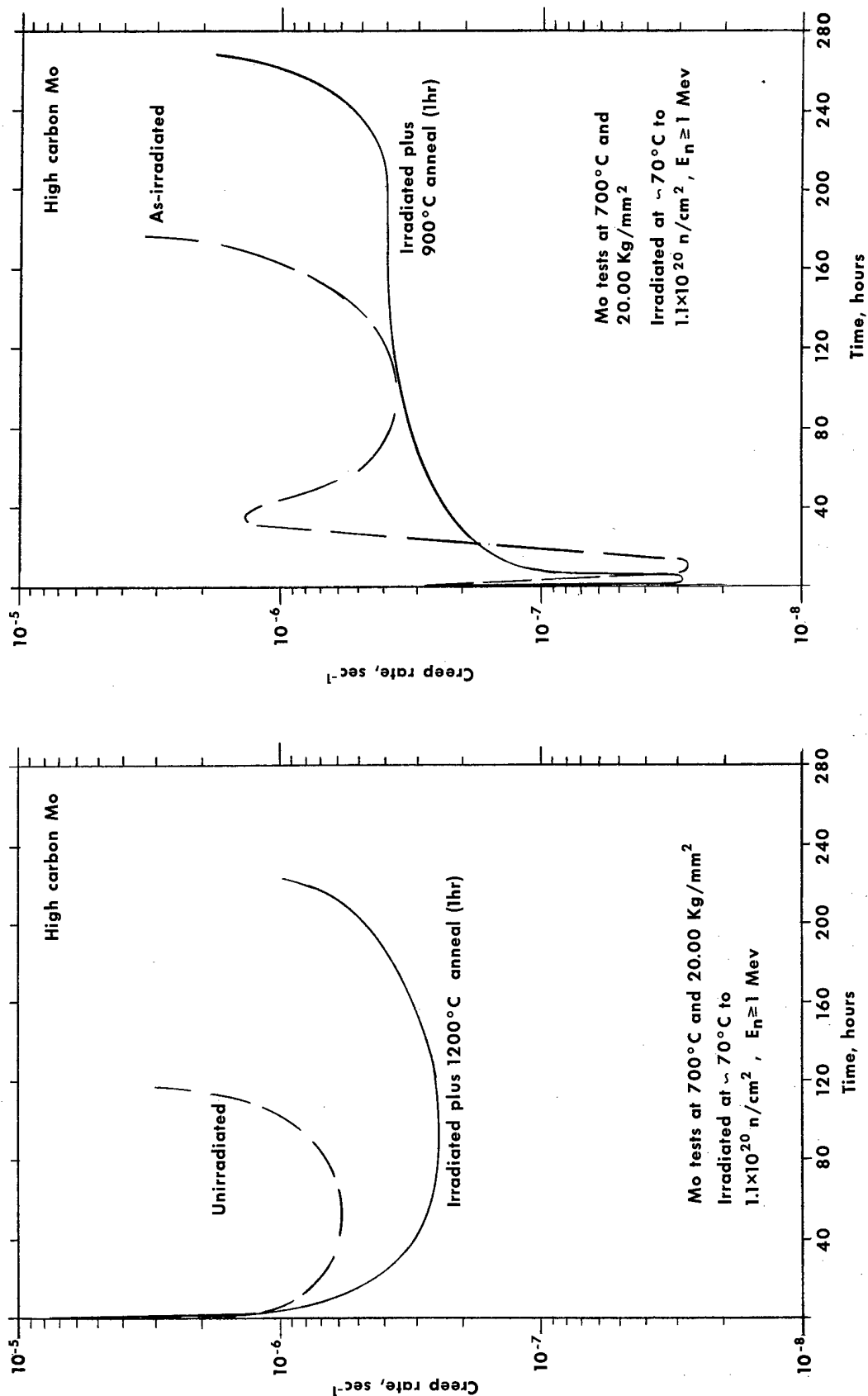
In general, the results between the low-carbon and high-carbon molybdenum sheet series of tests show agreement when compared at a similar fast-neutron fluence. The major difference between the two series exists in the effects of 900°C and 1200°C post-irradiation anneals. The 1200°C anneal in the low-carbon molybdenum test produced a longer rupture life than the 900°C anneal; the opposite was true in the high-carbon molybdenum. The temperature of maximum thermal hardening (i. e., longer time to rupture) is probably related to the carbon content since the fluence, grain size, hardness, and basic compositions of the two grades of molybdenum were very similar.

Fracture Examinations

Fracture areas of selected 700°C creep-rupture tested specimens were examined metallographically to determine possible differences between the microstructure of the unirradiated, irradiated, and post-irradiation annealed specimens. In addition to the basic parameter of post-irradiation annealing temperature, the examination included a consideration of the two carbon content levels, 26 ppm and 205 ppm.

In general, the examinations did not reveal basic differences in fracture behavior between the various conditions. The basic difference between the two carbon levels at the immediate fracture tip was the presence of elongated voids associated with the carbide particles in high-carbon molybdenum. These voids were previously observed in the original material (Figure 2.42) but they were extremely small and localized. Nevertheless, the presence of the elongated voids did not impair the fracture ductility nor change the mode of fracture. The excellent ductility of the matrix, even in the as-irradiated specimens, is apparently controlling flow and fracture behavior. Fractures were all transgranular (Figure 2.46) and were accompanied by a relatively large amount of local plastic deformation (necking down to almost a knife edge).

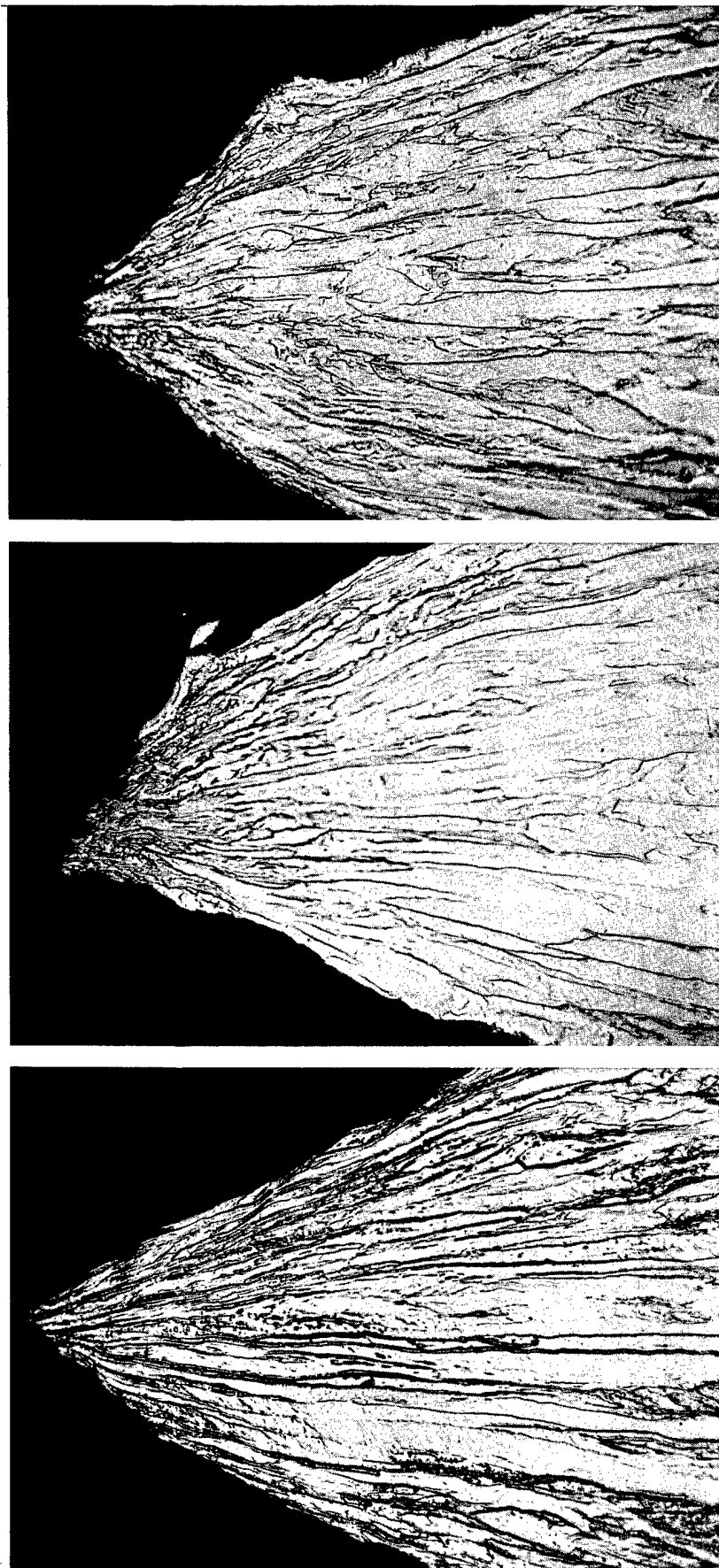
Microstructures of regions away from the immediate fracture area varied considerably between the low-carbon and high-carbon molybdenum materials. Three differences were



a. Unirradiated and 1200°C post-irradiation annealed specimens (AS-746K)

b. As-irradiated and 900°C post-irradiation annealed specimens (AS-746L)

Fig. 2.45 — Creep rate versus time curves for high-carbon Mo specimens tested at 700°C and 20.00 kg/mm² in hydrogen



Unirradiated (Neg. R-2260)

As-irradiated — $1.2 \times 10^{20} \text{ n/cm}^2$, $E_n \geq 1 \text{ Mev}$ (Neg. R-2250)

Irradiated ($1.2 \times 10^{20} \text{ n/cm}^2$) plus post-irradiation anneal at 1200°C for 1 hour (Neg. R-2254)

Fig. 2.46 — Photomicrographs of fracture area of low-carbon Mo sheet specimens creep-rupture tested at 700°C and 17.50 kg/mm^2 (500X)

noted: (1) A much finer plastically deformed grain size (Figure 2.47) in the high-carbon molybdenum due to differences in the grain sizes of the two original recrystallized molybdenum materials, (2) a considerably heavier density of low-angle grain boundary substructure in the high-carbon molybdenum, and (3) a concentration of relatively massive angular carbides in the high-carbon molybdenum (Figure 2.48a). Only a trace of carbides was noted in the low-carbon material (Figure 2.48b) and none of this carbide compared in size or shape to the chunky highly friable type present in the high-carbon molybdenum.

The grain growth which occurred in the 1600°C annealing of the low-carbon molybdenum is quite evident in the irradiated and unirradiated microstructures (Figure 2.49). When viewed at a higher magnification (Figure 2.50) the microstructure shows a relatively carbide-free matrix with agglomerated larger carbides distributed both intergranularly and intragranularly. The isolated particles of intragranular carbides are probably the result of grain boundary migration away from the particles in the grain growth process.

HOT HARDNESS (J. L. Kamphouse, J. Moteff)

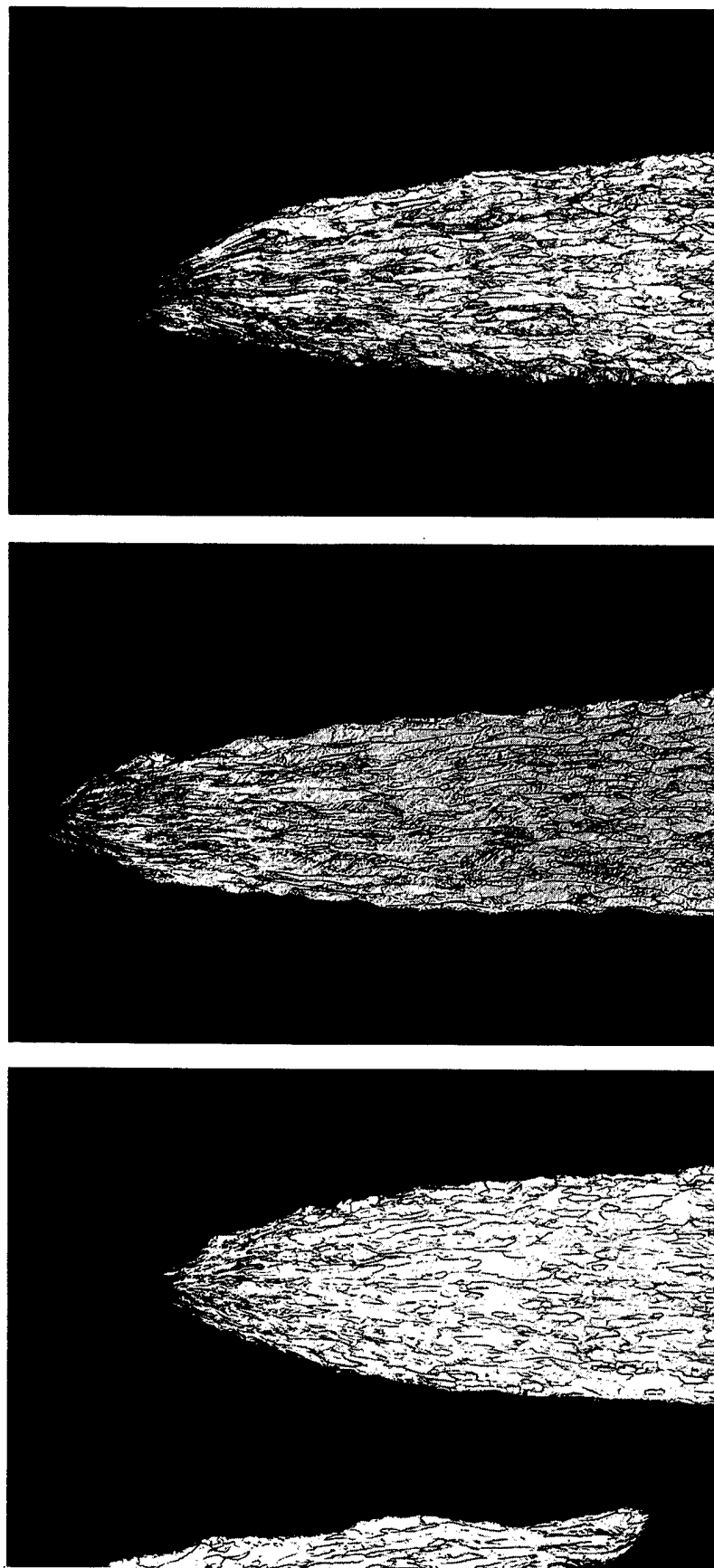
Warm-Worked Tungsten

The objective of the hot-hardness study of warm-worked and irradiated tungsten was to determine the effect of substructure on the generation of radiation-induced defects as measured by changes in the hot hardness. Four specimens were prepared, each from sections of 73 percent and 98 percent warm-worked 0.51-mm-thick tungsten sheet. Two specimens of each worked condition were recrystallized at 1760°C for 1 hour in hydrogen. One specimen of each of the four conditions (73% worked, 73% worked plus recrystallization, 98% worked, and 98% worked plus recrystallization) was irradiated at reactor-ambient temperature in the ORR Rabbit 14 facility to a fluence level of $4.1 \times 10^{19} \text{ n/cm}^2$ ($E_n \geq 1 \text{ Mev}$). One specimen of each of the original unirradiated four conditions was used for comparison.

As shown by the microhardness increment fraction curves of Figure 2.51, 73 percent worked and recrystallized material and the 98 percent worked and recrystallized material showed about the same radiation-induced hardening, primarily in the athermal component. The 73 percent warm-worked material showed much less radiation-induced hardening and the 98 percent worked material showed virtually no additional hardening.

Studies²² on the influence of dislocations on the damage structure in neutron-irradiated ($\sim 7 \times 10^{18} \text{ n/cm}^2$, $E_n \geq 1 \text{ Mev}$) molybdenum show that the spot density is about a factor of two greater in the annealed material than in the material deformed 50 percent prior to irradiation. Assuming that this type of spot defect contributes to the hardness of the irradiated tungsten, it is believed that the increase in spot density in the recrystallized tungsten and the relative ineffectiveness of the spot defects to further harden the worked tungsten may account for the greater radiation-induced hardening in the recrystallized material compared to that observed in the worked tungsten.

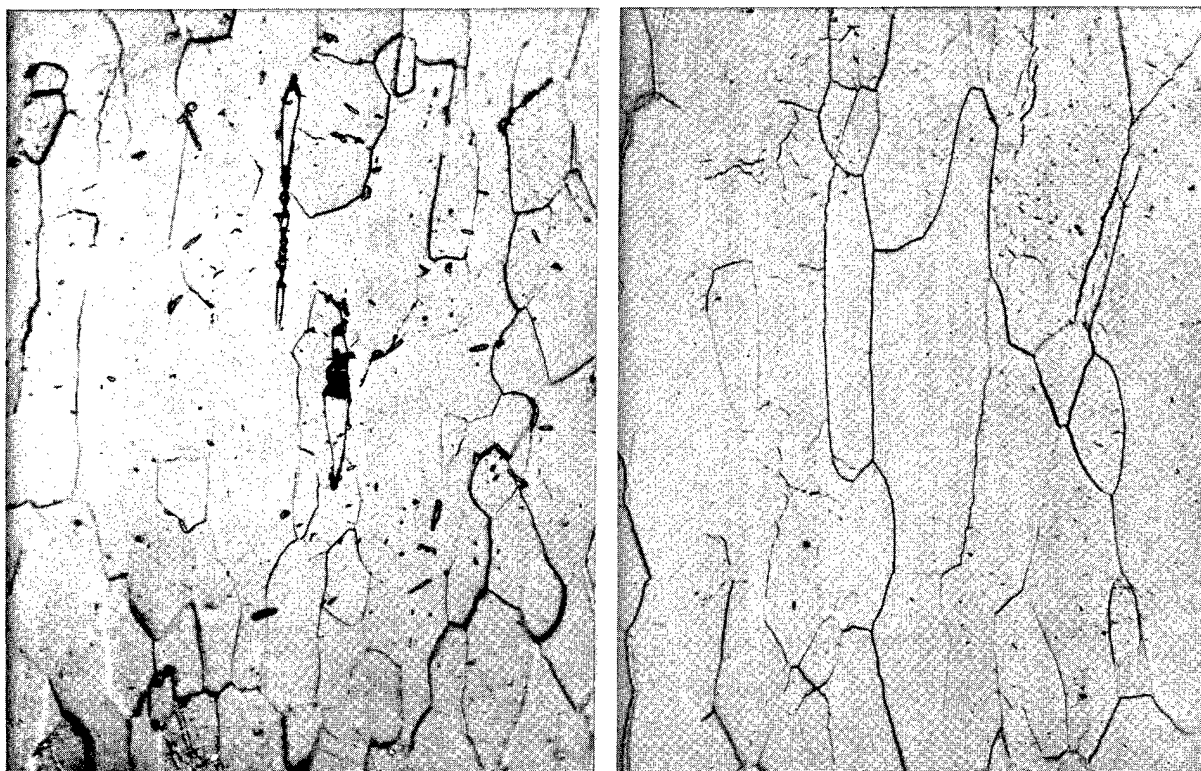
A series of isothermal anneals was performed on 98 percent warm-worked tungsten. Results presented in Figure 2.52 show some scatter in the data because some data were obtained from single indents rather than from an average of three indents as is customary when obtaining isochronal data. Because of this unavoidable data scatter at annealing times less than 10^3 seconds, a very accurate activation energy for recrystallization could not be obtained. An attempt was made to calculate the activation energy using the crosscut method,²³ and a value of 4.8 eV was obtained using data from specimens annealed at 1300°C and 1373°C as shown in Figure 2.52.



Unirradiated (Neg. R-2237)

As-irradiated — $1.1 \times 10^{20} \text{ n/cm}^2$; $E_n \geq 1 \text{ Mev}$ (Neg. R-2239)Irradiated ($1.1 \times 10^{20} \text{ n/cm}^2$) plus post-irradiation anneal at 1200°C for 1 hour (Neg. R-2241)

Fig. 2.47 — Photomicrographs of fracture area of high-carbon Mo sheet specimens creep-rupture tested at 700°C and 20.00 kg/mm^2 (100X)



a. High-carbon Mo-heat C-6605 (Neg. R-2267)

b. Low-carbon Mo-heat C-7722 (Neg. R-2268)

Fig. 2.48 — Photomicrographs showing differences in carbide size and distribution in irradiated Mo sheet specimens post-irradiation annealed at 1200°C for 1 hour and creep-rupture tested at 700°C (500X)

Niobium and Nb — 1Zr

Hot-microhardness data were obtained on irradiated and unirradiated niobium and Nb — 1Zr. The Nb — 1Zr is harder over the entire temperature range due to solid-solution hardening and/or ZrC precipitation hardening. Some thermal hardening apparently started at a temperature of about 500°C and persisted at temperatures to 1000°C for the unirradiated material. These data are given in Figures 2.53 and 2.54, respectively, and the microhardness increment fraction curves obtained are shown in Figure 2.55. These curves show recovery at the same temperatures observed in ultimate tensile strength tests.

There are apparently peaks in the increment fraction curves for tungsten, molybdenum, and niobium at $0.16 T_m$ and approximately $0.35 T_m$; the $0.16 T_m$ peak is the more prominent. Figure 2.56 gives a comparison on a homologous temperature basis of the increment fraction curves for W, Mo, and Nb²⁴, where it appears that the radiation-induced hardening of these unalloyed metals is recovered at temperatures above $0.35 T_m$.²⁵

Molybdenum Single Crystals

Hot-hardness data have been obtained on two single crystals of molybdenum of known orientations, {110} and {001}. There is a distinct difference in the data dependent on the crystallographic orientation (Figure 2.57). The specimen of orientation {110} showed little difference from polycrystalline molybdenum previously tested, although the specimen of orientation {001} was considerably softer at all temperatures. Photomicrographs (Figure 2.58) of the indents taken at 1200°C show markedly different flow patterns for the two orientations.



Unirradiated — 1600°C anneal for
1 hour in H₂ (R-2263)



Irradiated (1.2×10^{20} n/cm²) plus
1600°C anneal for 1 hour (R-2255)

Fig. 2.49 — Photomicrographs of creep-rupture tested low-carbon Mo sheet specimens tested at 700°C and 13.0 kg/mm² (100X)

Other Refractory Alloys

Hot-microhardness data were determined²⁶ on five materials in the unirradiated recrystallized condition: Ta, Ta — 10W, W — 30Re — 30Mo (at.%; 306 alloy), W — 25Re — 30Mo (at.%; 256 alloy), and Mo — 0.5Ti. These investigations were conducted to study the effects of alloying and to provide comparison data for similar specimens being irradiated in the EBR-II.

A previous discussion²⁷ of the tantalum and Ta — 10W data noted an anomalous peak at approximately 300°C. Subsequent analyses show that the tantalum material contained 33 ppm oxygen prior to testing and 65 ppm after testing. Hence the peak may be due to interstitial impurities such as oxygen.²⁸

HARDNESS AND ULTIMATE STRENGTH CORRELATION (J. L. Kamphouse, J. Moteff)

A relationship appears to exist²⁹⁻³² between hot hardness and other properties such as ultimate tensile strength and yield stress. Figures 2.59 through 2.61 show approximately linear relationships for several materials between the ultimate tensile strength, σ_u , in kg/mm² and the VPH number, H_v , in kg/mm². These linear relationships are not perfectly accurate, but they do give an estimate of the ultimate tensile strength of the material if the relatively convenient hot-hardness tests are performed first.

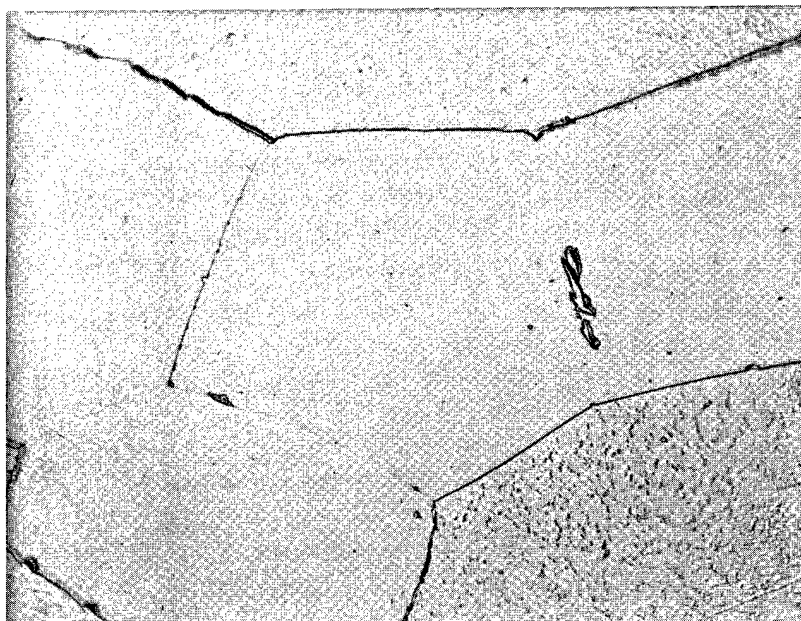


Fig. 2.50 — Photomicrograph of unirradiated low-carbon Mo sheet specimen (1600°C — 1 hour anneal) showing agglomerated carbides. Specimen creep-rupture tested at 700°C and 13.00 kg/mm². (Neg. R-2269, 500X)

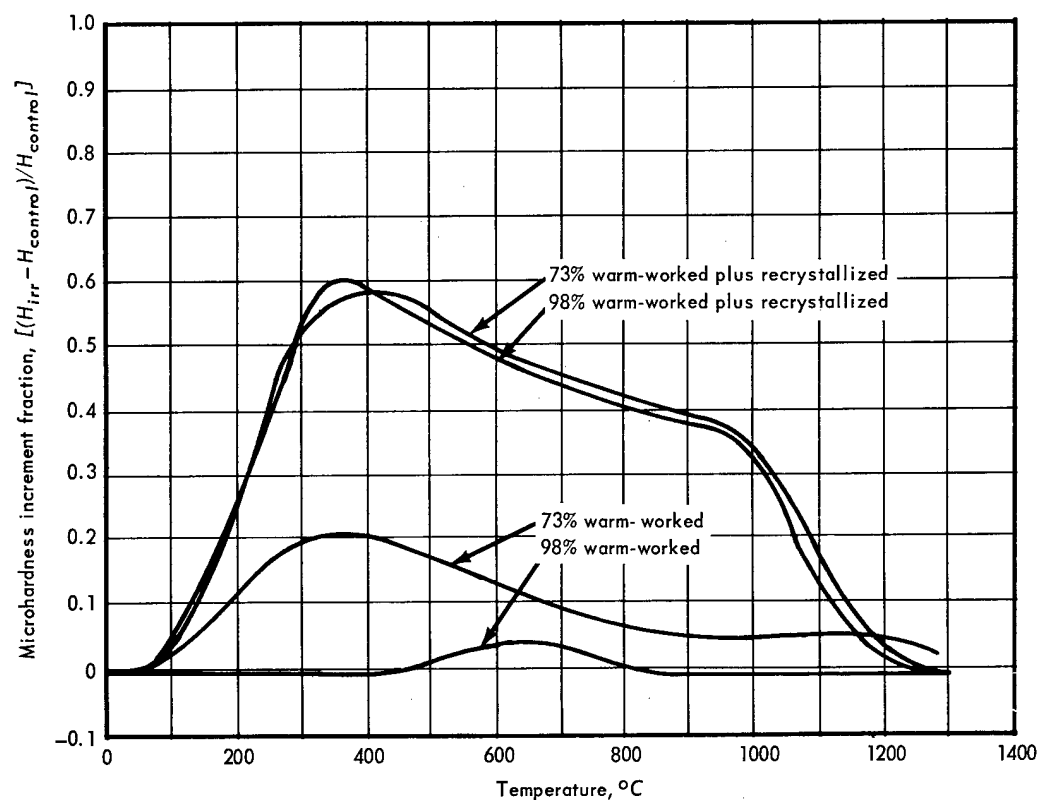


Fig. 2.51 — Hot-microhardness increment fraction for irradiated W in various conditions as a function of temperature. Specimens irradiated at ambient temperature (~70°C) in a water-moderated reactor to a fluence of 4.1×10^{19} n/cm² ($E_n \geq 1$ Mev). Recrystallized material annealed at 1760°C for 1 hour in H₂ prior to irradiation.

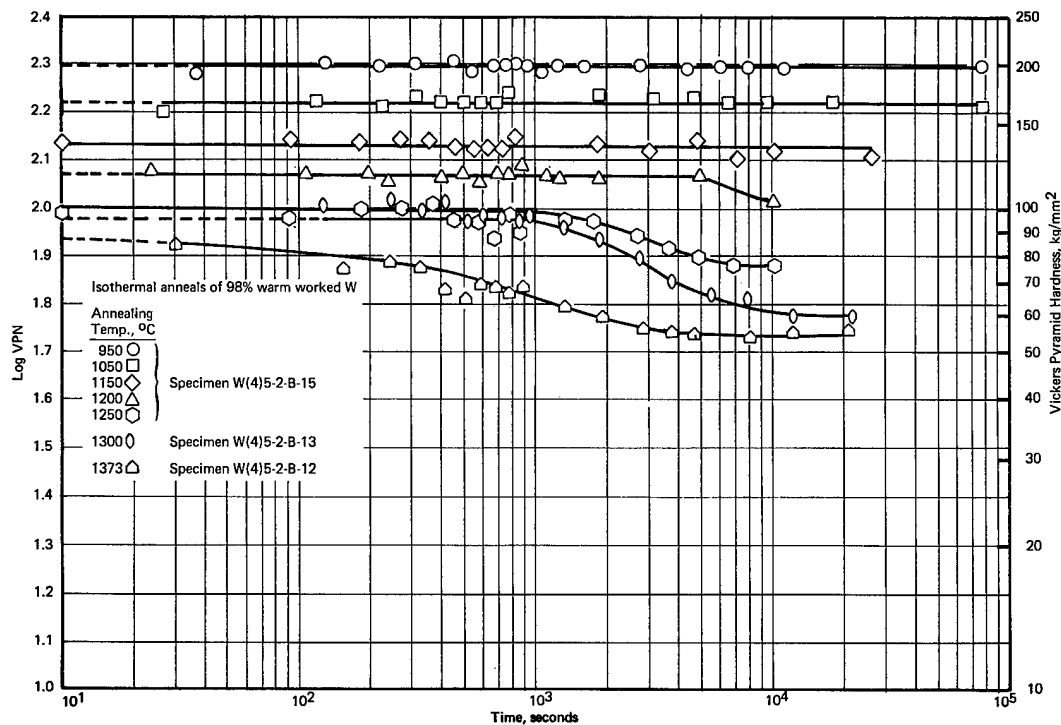


Fig. 2.52 — Isothermal hot-microhardness recovery of unirradiated 98% warm worked W as a function of annealing time.

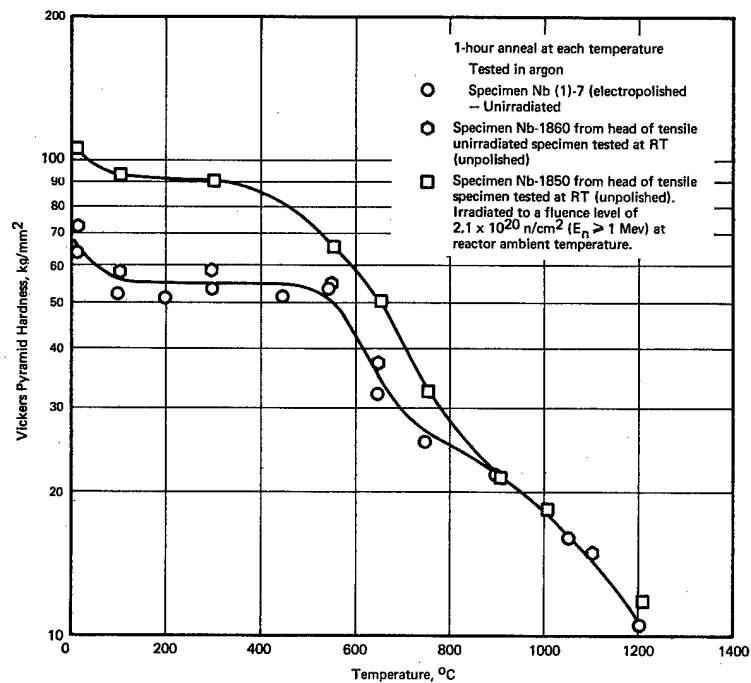


Fig. 2.53 — Hot microhardness of unirradiated and irradiated Nb as a function of temperature

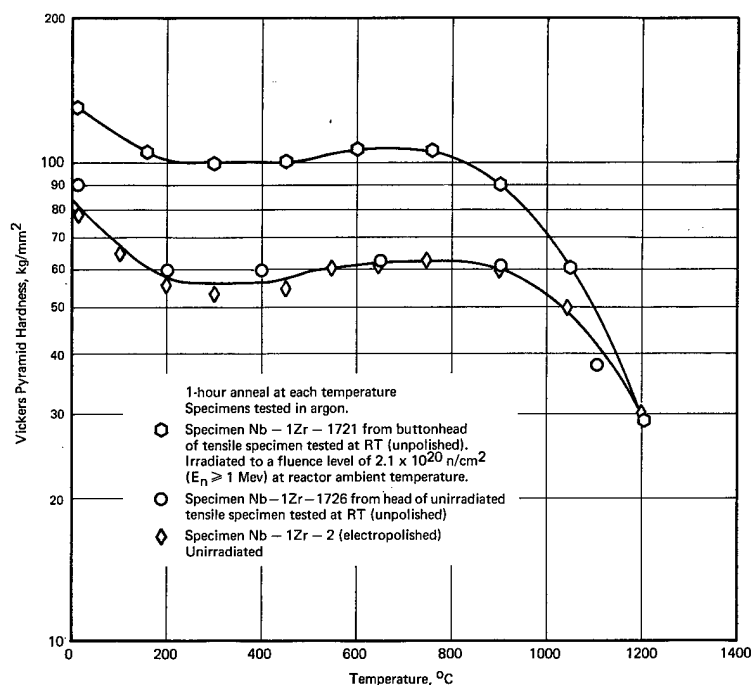


Fig. 2.54 — Hot microhardness of unirradiated and irradiated Nb - 1Zr as a function of temperature

TENSILE TESTING (W. J. Stapp, A. R. Begany)

Niobium and Nb - 1Zr

A study of the effect of annealing on the room-temperature and elevated-temperature tensile properties of irradiated (2.1×10^{20} n/cm², $E_n \geq 1$ Mev at $\sim 70^\circ\text{C}$) recrystallized niobium and Nb-1Zr was conducted. Irradiated and control sheet specimens were post-irradiation annealed at temperatures determined by hot-hardness studies. The temperatures were selected to show most advantageously the room-temperature and elevated-temperature radiation-damage recovery behavior.

The effect of post-irradiation anneals on the room-temperature engineering tensile properties of niobium appears in Figure 2.62 and Table 2.6. Recovery was complete following the 1000°C anneal. In the hot-hardness studies recovery was complete (Figure 2.53) following the 900°C anneal. Comparison of the data shows that neutron irradiation increased ultimate strength less than yield strength. Irradiation drastically reduced the uniform elongation. The tensile behavior observed in the post-irradiation anneals is similar to that observed in irradiated molybdenum,^{33,34} tungsten,³⁵ and niobium³⁶ in other studies, except that no evidence of lower yield points was observed.

The elevated-temperature (300°C and 650°C) tests were conducted after holding at test temperature for 1 hour, giving specimens, in effect, a 1-hour anneal at test temperature. The results (Figure 2.63 and Table 2.6) do not show any indication of thermal hardening, as might be suggested by an increase in the ratio of irradiated to unirradiated yield strength values at the elevated test temperatures. The dotted lines on the ultimate strength plots represent values determined from linear cross plots of hot hardness (DPH) versus ultimate tensile strength. Pronounced thermal hardening had been observed by Makin and Minter³⁶ in room-temperature tensile tests following 200° to 300°C anneals for 1 hour.

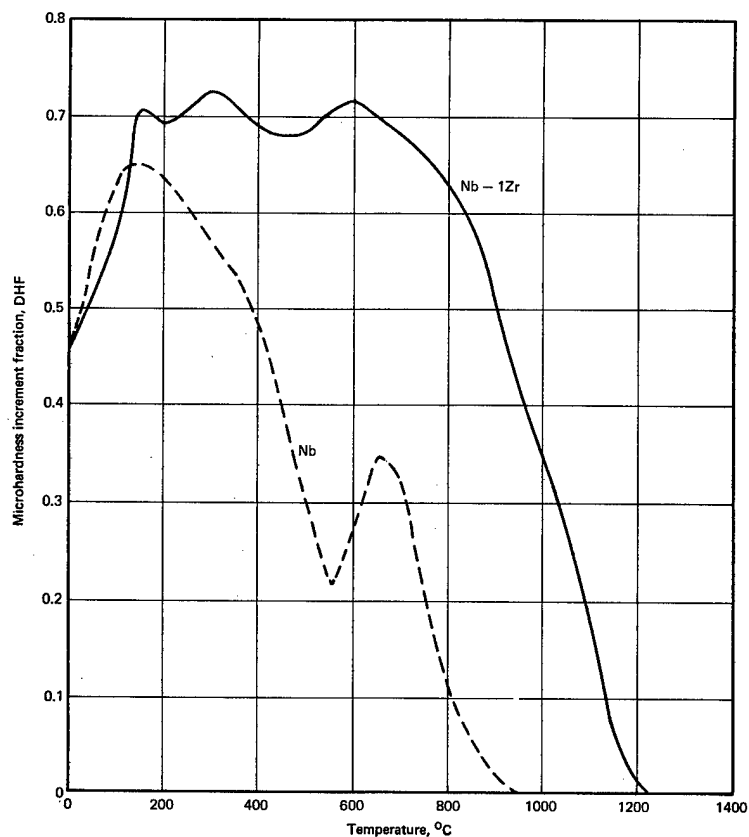


Fig. 2.55 — Hot-microhardness increment fraction for irradiated (2.1×10^{20} n/cm²; $E_n \geq 1$ Mev) Nb as a function of temperature

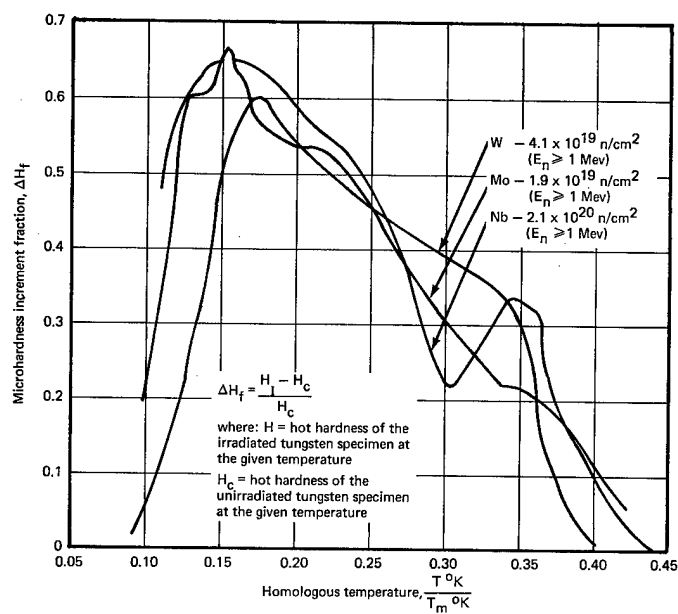


Fig. 2.56 — Microhardness increment fraction, ΔH_f , for W, Mo, and Nb compared on a homologous temperature basis

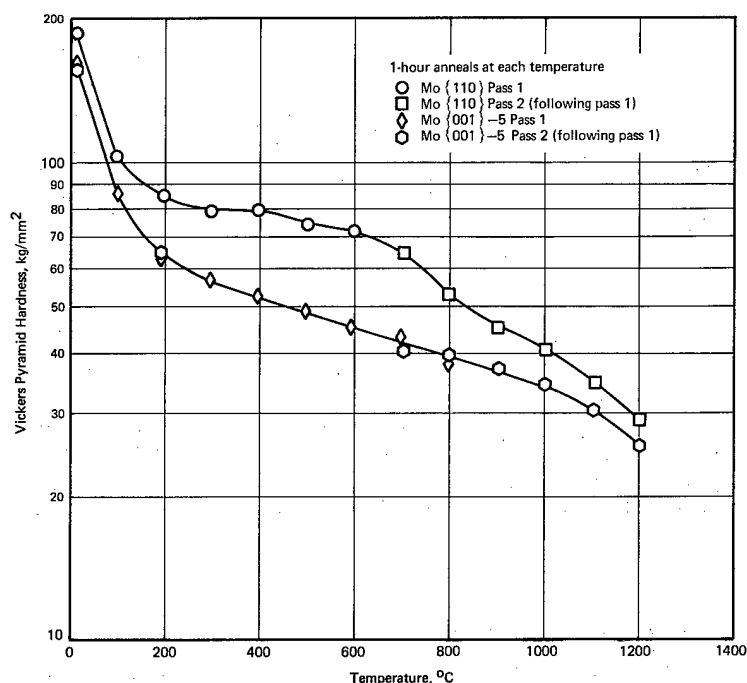


Fig. 2.57 — Hot microhardness of unirradiated single-crystal molybdenum of orientations {110} and {001}

The present results do not agree with the 600 °C temperature shown to produce complete recovery in the earlier work.³⁶ The NMPO material contained 130 ppm oxygen compared to 1600 ppm oxygen in the earlier tests. This difference and a higher neutron fluence level probably account for the higher recovery temperature. The higher strength and lower ductility levels in the specimens containing the higher oxygen level may have masked out the influence of radiation-induced defects on the mechanical properties.

The effect of post-irradiation anneals on the conventional room-temperature tensile properties of Nb — 1Zr shown in Figure 2.64 and Table 2.7 exhibit a type of thermal hardening in the 300° to 600 °C range which agrees with hot-hardness results. Complete recovery of the radiation-induced defect structure occurs after the 1000 °C anneal. Complete recovery did not occur until 1200 °C in the hot-hardness studies.

Nb — 1Zr exhibited greater strength in the irradiated condition up to a test temperature of 600 °C (Figure 2.65). Reduced ductilities were observed in both irradiated and unirradiated specimens at the 300 °C and 600 °C test temperatures.

Molybdenum

A study of the effect of post-irradiation annealing on the room-temperature tensile properties of irradiated, recrystallized molybdenum was conducted and reported.³⁷ Data were examined³⁸ in terms of the true stress versus true strain relationship to evaluate strain-hardening characteristics. The analysis employed the empirical power law expression:

$$\sigma = k (\bar{\epsilon})^n \quad (2.1)$$

where:

σ = true stress

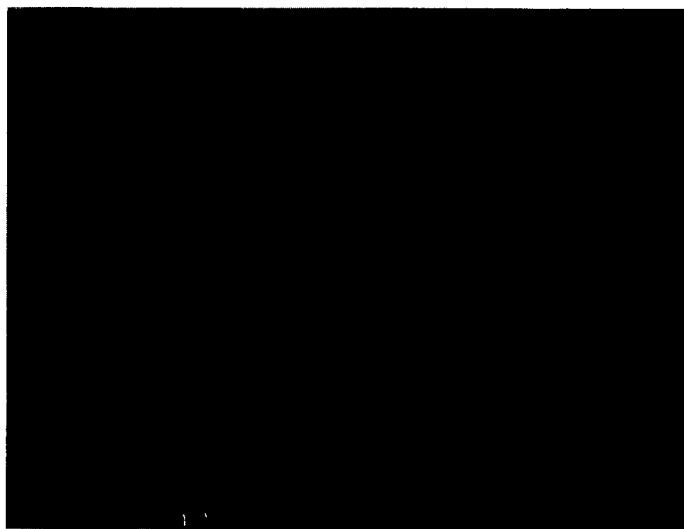
$\bar{\epsilon}$ = true strain (or natural strain)

k = constant (strength coefficient at $\bar{\epsilon} = 1$)

n = constant (strain-hardening exponent)



{100} orientation



{110} orientation

Fig. 2.58 — Photomicrographs of hot-microhardness (1200°C) indents on Mo single-crystals of two orientations (200X)

It was concluded that the increase in strength of the irradiated molybdenum was due to both source and lattice defect mechanisms.

The data were re-examined in terms of the exponential function⁴² relating true stress (σ) and true strain ($\bar{\epsilon}$):

$$\sigma = \sigma_{\infty} - (\sigma_{\infty} - \sigma_0) \exp(-\bar{\epsilon}/\epsilon_c)$$

where:

- σ_0 = stress at which plastic deformation begins
- σ_{∞} = asymptotic stress attained after deformation
- ϵ_c = characteristic strain

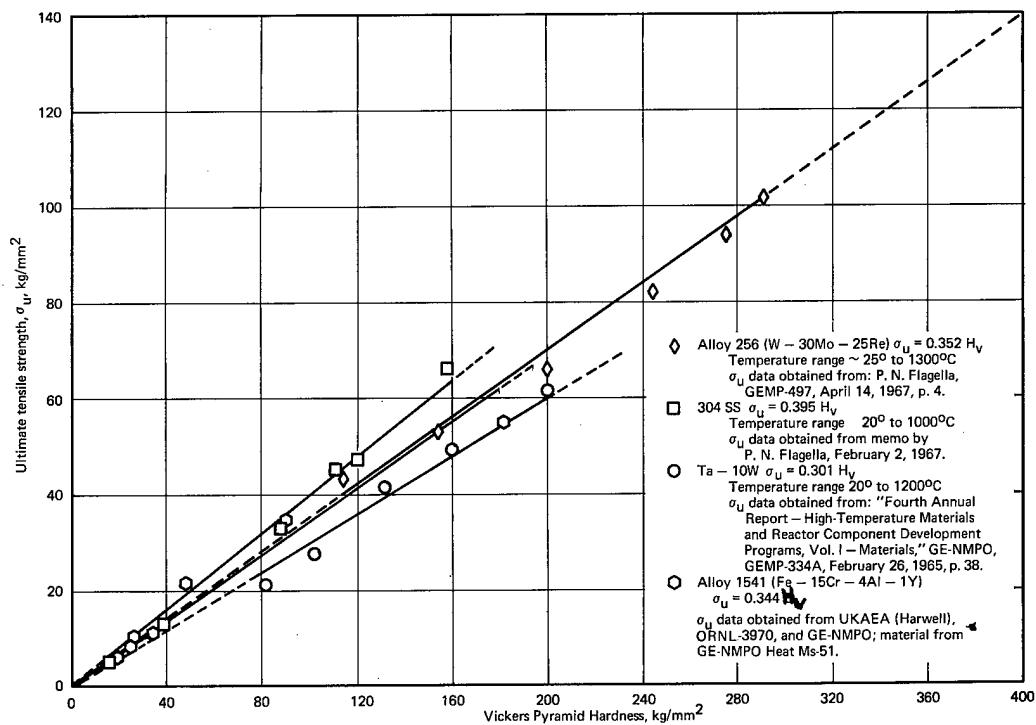


Fig. 2.59 — Ultimate tensile strength, σ_U , as a function of Vickers Pyramid Hardness, H_V , for various alloys

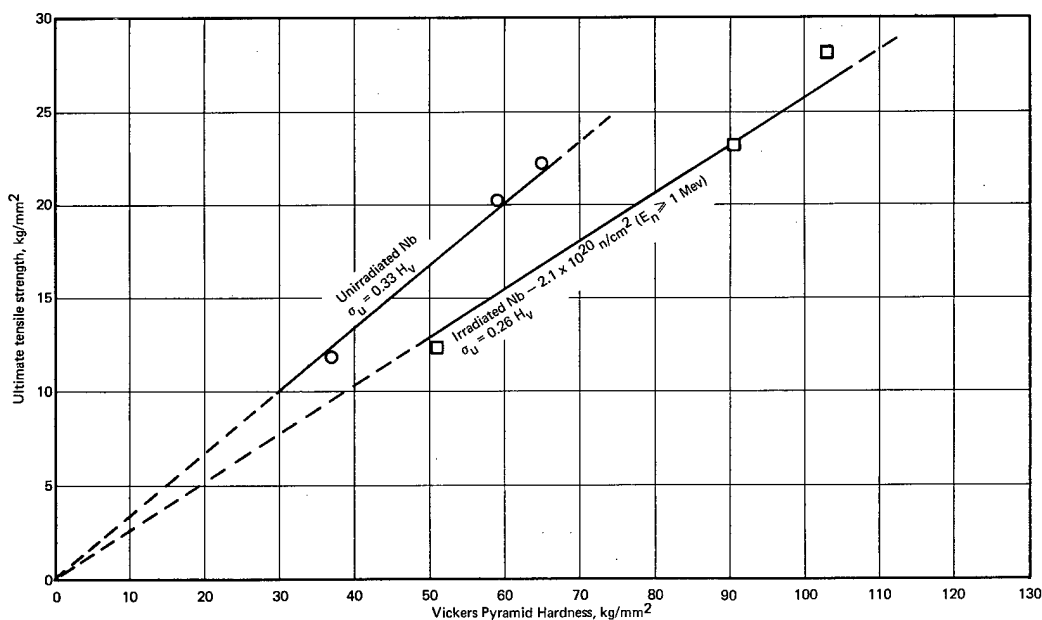


Fig. 2.60 — Ultimate tensile strength, σ_U , as a function of Vickers Pyramid Hardness, H_V , for Nb

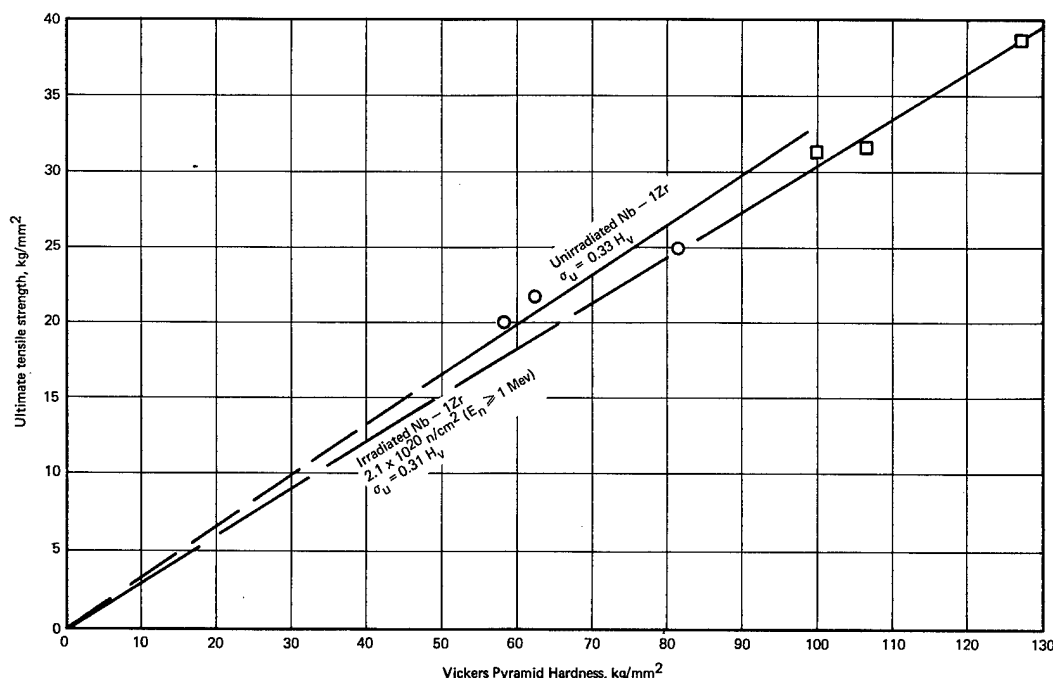


Fig. 2.61 — Ultimate tensile strength, σ_u , as a function of Vickers Pyramid Hardness, H_v , for Nb — 1Zr

Results (Table 2.8 and Figure 2.66) of the exponential function show that:

1. σ_0 is increased by radiation-induced defects to a point of elastic fracture and decreased by post-irradiation annealing to the σ_0 value of the nonirradiated material. σ_0 may be considered the lattice friction stress at zero strain or slip propagation stress.
2. Molybdenum will elongate and work-harden by the generation of dislocations. Size and/or number of radiation-induced defects are varied by annealing heat treatments, thereby affecting the characteristic strain, ϵ_c .
3. The asymptotic stress is not significantly sensitive to the number or size of the radiation-induced defects.

Hence it is again concluded that the radiation-induced increase in strength of recrystallized molybdenum is due to both the source-hardening and lattice-hardening defect mechanisms.

Fracture areas of selected room-temperature, tensile-tested molybdenum specimens were examined to determine possible differences in microstructural flow and fracture characteristics between the unirradiated, irradiated, and post-irradiation annealed conditions. Since mixed modes of fracture were expected in some cases, it was believed that optical fractography would complement the metallographic examinations and provide detailed insight into the differences in modes of fracture between the various conditions. Specifically, examination of the actual fracture faces for evidence of dimple rupture features characteristic of the ductile mode of fracture was deemed expedient. The fractographic studies were conducted at 500 diameters using dark-field illumination. Specimens in this study possessed irregular surfaces with varying amounts of localized necking on gage sections whose original dimensions were 0.5 by 6.3 mm. In general, irradiated specimens receiving a post-irradiation anneal lower than about 950°C displayed considerable embrittlement with little or no localized necking (Figure 2.67).

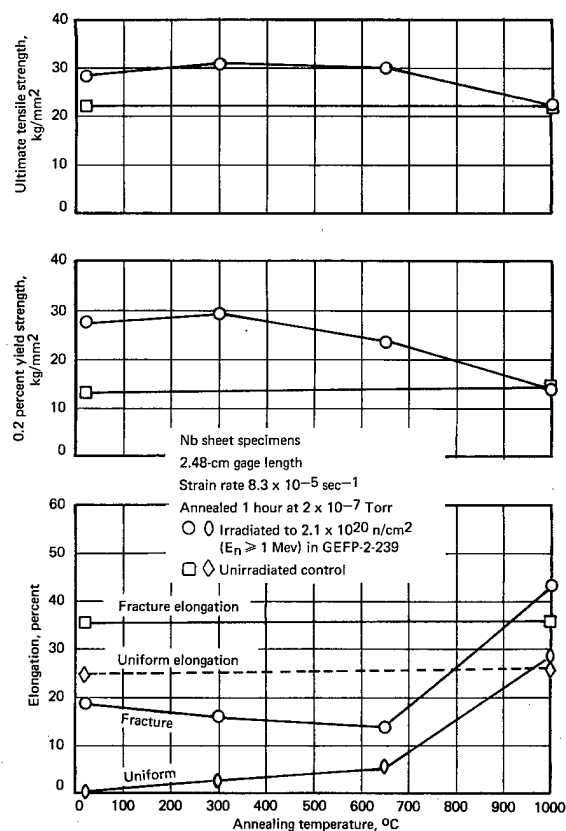


Fig. 2.62 — Room-temperature tensile properties of Nb sheet specimens versus post-irradiation annealing temperature

TABLE 2.6
NIOBIUM TENSILE TEST RESULTS

Specimen ^a No.	Condition	Post Irradiation Anneal Temperature, °C	Test Temperature, °C	Yield Strength 0.2% Offset, kg/mm ²	Tensile Strength, kg/mm ²	Uniform Elongation in 2.48 cm, %	Fracture Elongation in 2.48 cm, %
1860	Unirradiated	None	25	13.2	22.2	24.4	35.5
1862	Unirradiated	300—1 hr—vac ^b	300	13.2	20.2	9.2	13.4
1861	Unirradiated	650—1 hr—vac ^b	650	6.9	11.8	9.0	14.7
1850	Irradiated ^c	None	25	27.6	28.2	0.5	18.6
1848	Irradiated	300—1 hr—vac ^b	300	23.2	23.2	0.4	5.9
1849	Irradiated	650—1 hr—vac ^b	650	12.3	12.3	1.0	12.6
1859	Irradiated	300—1 hr—vac ^e	25	29.5	31.1	2.5	15.9
1852	Irradiated	650—1 hr—vac ^e	25	23.3	29.0	5.4	13.5
1854	Irradiated	1000—1 hr—vac ^e	25	13.8	23.4	28.3	43.0
1855	Unirradiated	1000—1 hr—vac	25	14.1	21.6	25.3	35.3

^aSpecimens from 0.5-mm-thick sheet No. 80B792, vacuum annealed at 1150°C for 1 hour after fabrication. All tests conducted in vacuum $\sim 8 \times 10^{-5}$ Torr.

^bHeating rate to test temperature 20°C/min, annealed for 1 hour prior to load application. Power turned off upon specimen fracture.

^cIrradiation test GEFP2-239 in ETR facility at reactor-ambient temperature ($\sim 70^\circ\text{C}$) to a fluence of $2.1 \times 10^{20} \text{ n/cm}^2$ ($E_n \geq 1 \text{ Mev}$) and $4.7 \times 10^{20} \text{ n/cm}^2$ (thermal).

^dElastic fracture.

^eAnnealed for 1 hour in a vacuum of 2×10^{-7} Torr.

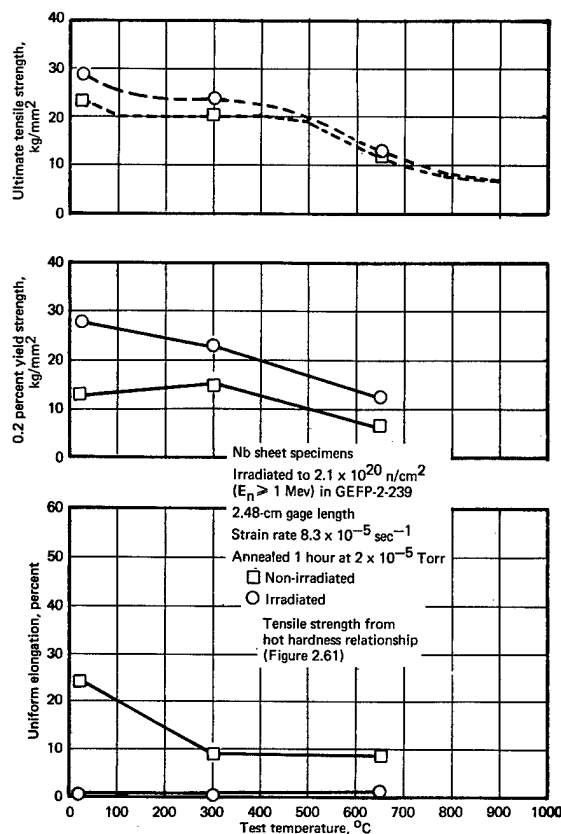


Fig. 2.63 — Elevated-temperature tensile properties of unirradiated and irradiated niobium sheet specimens

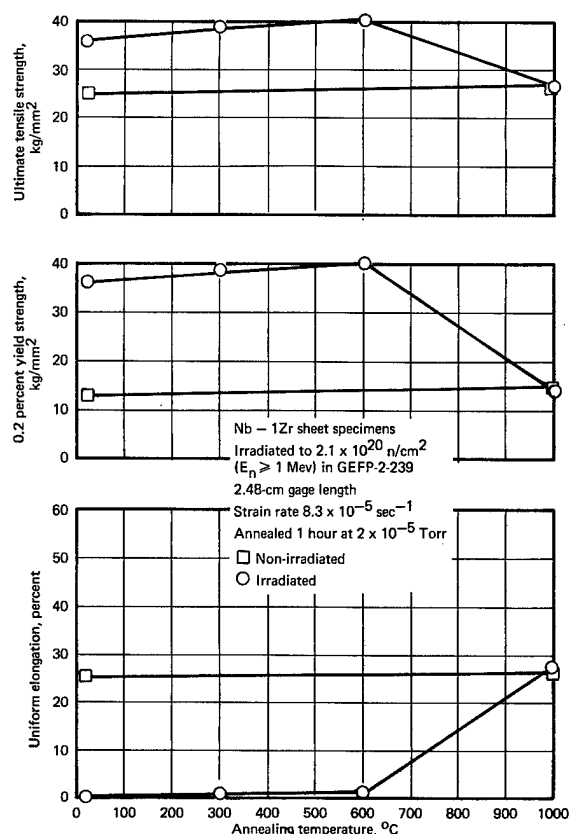


Fig. 2.64 — Room-temperature tensile properties of unirradiated and irradiated Nb - 1Zr sheet specimens

TABLE 2.7
Nb - 1Zr TENSILE TEST RESULTS

Specimen No. ^a	Condition	Post Irradiation Anneal Temperature, °C	Test Temperature, °C	Yield Strength 0.2% Offset, kg/mm ²	Tensile Strength, kg/mm ²	Uniform Elongation in 2.48 cm, %	Fracture Elongation in 2.48 cm, %
1726	Unirradiated	None	25	12.7	24.9	25.1	33.5
1729	Unirradiated	300-1 hr-vac ^b	300	8.3	20.0	10.9	15.5
1730	Unirradiated	600-1 hr-vac ^b	600	13.2	21.8	14.1	21.0
1721	Irradiated	None	25	38.7	38.7	0.2	0.4
1723	Irradiated	300-1 hr-vac ^b	300	27.4	31.3	1.6	1.6
1727	Irradiated	600-1 hr-vac ^b	600	27.8	31.5	1.5	2.6
1725	Irradiated	300-1 hr-vac ^e	25	38.7	38.6	0.7	4.9
1722	Irradiated	600-1 hr-vac ^e	25	40.0	40.5	0.9	8.0
1719	Irradiated	1000-1 hr-vac ^e	25	14.0	26.4	22.4	33.4
1724	Unirradiated	1000-1 hr-vac ^e	25	13.9	26.6	26.2	34.6

^aSpecimens from 0.5-mm-thick sheet (heat No. 27605), vacuum annealed at 1200°C for 1 hour after fabrication. All tests conducted in vacuum $\sim 8 \times 10^{-5}$ Torr.

^bHeating rate to test temperature 20°C/min, annealed for 1 hour prior to load application. Power turned off upon specimen fracture.

^cIrradiation test GEFP2-239 in ETR facility at reactor-ambient temperature ($\sim 70^\circ\text{C}$) to a fluence of 2.1×10^{20} n/cm² ($E_n \geq 1$ Mev) and 4.7×10^{20} n/cm² (thermal).

^dElastic fracture.

^eAnnealed for 1 hour in a vacuum of 2×10^{-7} Torr.

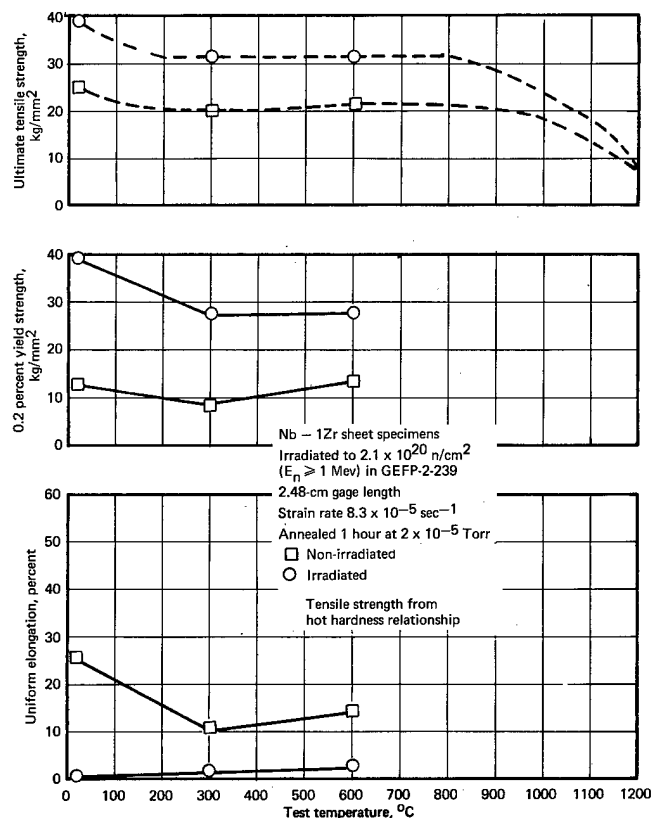


Fig. 2.65 — Elevated-temperature tensile properties of unirradiated and irradiated Nb - 1Zr sheet specimens

Metallographic examination of the unirradiated specimens showed failure to be entirely transgranular (Figure 2.68) without any trace of intergranular fracture. A moderate amount of plastic flow (necking) in the fracture area had occurred. Fractographic study of these fractures indicated a condition of quasi-cleavage; i.e., the fracture displayed characteristics of feathery cleavage (little or no plastic deformation) while possessing some plastic deformation features such as tear ridges and stretching.

The as-irradiated specimen exhibited mixed mode of fracture with intergranularity slightly in preponderance. No evidence of any appreciable wedging or ductility was observed.

The fractographic study of the post-irradiated annealed specimens showed that fracture occurred predominately by cleavage. Specimens annealed at 1025 °C and higher tended to exhibit quasi-cleavage. No post-irradiated specimens exhibited evidence of ductile dimple rupture. Specimens annealed at 950 °C and lower displayed mixed modes of fracture. In general, lowering the annealing temperature resulted in increased evidence of intergranular fracturing.

Although these observations were substantiated during metallographic examination, a possible exception to this was the following microstructural anomaly: the secondary cracking condition possessed by the 830 °C post-irradiation annealed specimen was predominantly intergranular, whereas the secondary cracking within the 700 °C annealed specimen was predominantly transgranular (see Figure 2.69).

TABLE 2.8
MOLYBDENUM TENSILE TEST RESULTS

Specimen No. ^a	Condition	Post Irradiation Anneal		Test Temperature, °C	Yield Strength, 0.2% Offset, kg/mm ²	Tensile Strength, kg/mm ²	Uniform Elongation, in 2.54 cm, %	Fracture Elongation, in 2.54 cm, %	True Stress at Zero Strain (σ ₀), kg/mm ²		Characteristic Strain (ε _c), cm/cm
		Temperature, °C	None						True Stress at Zero Strain (σ ₀), kg/mm ²	True Asymptotic Stress (σ _∞), kg/mm ²	
2100	Unirradiated	None		25	37.6	50.2	18.4	40.0	31.66	67.03	0.110
2110	Irradiated ^c	830		25	68.6	71.3	0.8	1.2	69.2	72.20	0.001
2112	Irradiated ^c	950		25	44.4	63.1	8.7	9.6	52.15	71.63	0.050
2108	Irradiated ^c	1025		25	47.6	56.6	13.6	32.7	44.51	70.65	0.092
2106	Irradiated ^c	1100		25	34.4	52.8	16.9	49.9	36.00	67.11	0.108
2121	Irradiated ^c	1200		25	31.7	48.9	16.3	41.8	31.18	62.77	0.090

^aSpecimens from 0.5-mm-thick arc-cast Mo sheet (heat C-6605), post-grind annealed at 1200°C in vacuum for 1 hour.

^bOne-hour anneals in gettered argon up to 950°C, 1-hour anneals in purified hydrogen above 950°C, at temperature indicated.

^cORM-38; irradiated to 1.2 x 10²⁰ nvt (E_n ≥ 1 Mev) at reactor-ambient temperature.

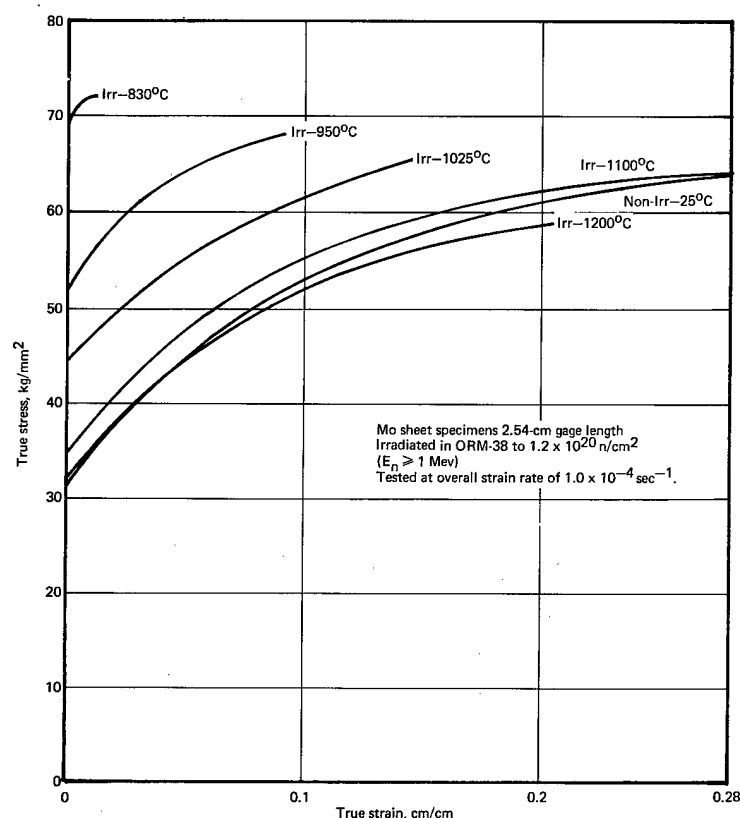


Fig. 2.66 — Room-temperature stress versus strain curves for irradiated (ORM-38) molybdenum post-irradiation annealed at indicated temperature

RESISTIVITY STUDIES (L. K. Keys, J. Moteff)

Molybdenum

The isochronal resistivity recovery of fast neutron ($E \geq 1$ Mev) radiation-induced defects in recrystallized molybdenum specimens has continued.³⁹ Six specimens were irradiated at reactor-ambient temperature ($\sim 70^\circ\text{C}$) to fast neutron fluences ranging from 1.1×10^{19} to 1.5×10^{21} n/cm^2 ($E_n \geq 1$ Mev). The various samples used and the pertinent irradiation conditions are shown in Table 2.9. The dependence of the radiation-induced resistivity increment, $\Delta\rho$, on the fast neutron fluence (for NMPO studies as well as those of Peacock and Johnson⁴⁰) is presented in Figure 2.70. The resistivity increment, $\Delta\rho$, is defined as $\Delta\rho = \rho_I - \rho_0$, where ρ_I is the as-irradiated resistivity and ρ_0 is the pre-irradiation resistivity. The resistivity increment reaches a maximum between 5×10^{19} n/cm^2 and 2×10^{20} n/cm^2 , then decreases by about a factor of 2 at 1.5×10^{21} n/cm^2 . This result is somewhat surprising in view of the asymptotic approach to saturation considered in other investigations.^{23,41} The slope of the linear portion of the curve (a slope of about 0.58) is in good agreement with that reported by Peacock and Johnson (0.54), although they observed what appeared to be saturation effects at about 3 to 4×10^{18} n/cm^2 . Results of NMPO studies and those of Kissinger, Brimhall, and Mastel⁴² yield saturation fluences much higher than those of Peacock and Johnson. Kissinger et al. observed saturation below NMPO saturation fluences. These differences result from different techniques of observation (X-ray parameter and length changes), as will be shown.

The recovery of the irradiation-induced defects in molybdenum is presented in Figure 2.71, in which the radiation-induced resistivity, $\Delta\rho$, is plotted versus annealing tempera-



Fig. 2.67 — Photomicrograph of fracture area of room-temperature tensile-tested Mo sheet specimen after irradiating to $1.1 \times 10^{20} \text{ n/cm}^2$ ($E_n \geq 1 \text{ Mev}$). Specimen given an 830°C anneal for 1 hour prior to testing. (Neg. R-2227, 100X)



Fig. 2.68 — Photomicrograph of fracture area of unirradiated room-temperature tensile-tested Mo sheet specimen (Neg. R-2236, 500X)

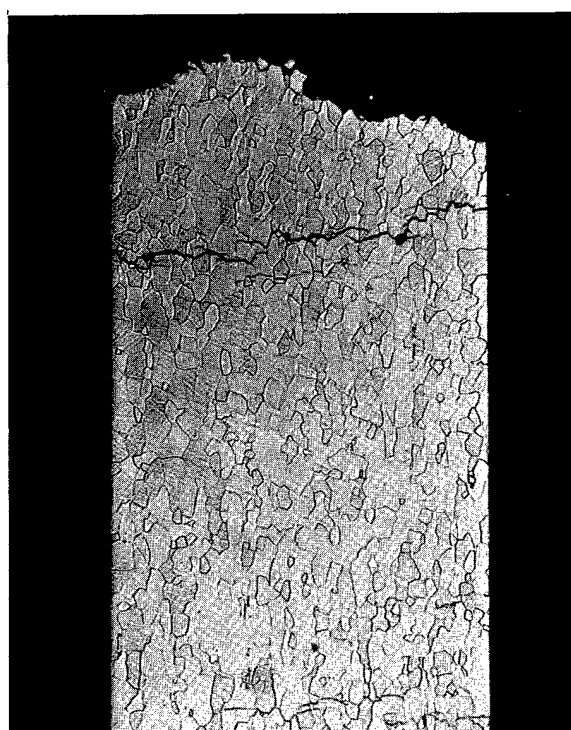


Fig. 2.69 — Photomicrograph of fracture area of room-temperature tensile-tested Mo specimen showing predominantly transgranular secondary cracking. Irradiated (1.1×10^{20} n/cm², $E_n \geq 1$ Mev) specimen given a 700°C anneal for 1 hour prior to testing. (Neg. R-2257, 100X)

TABLE 2.9
PRINCIPLE DEFECT RECOVERY STAGES IN NEUTRON-IRRADIATED MOLYBDENUM
AS DETERMINED BY ISOCHRONAL RESISTIVITY STUDIES

Sample No.	Rod	Capsule	Irradiation Condition ^a		Peak Temperature of Recovery Spectra, and Area Under Respective Recovery Peak ^b				
			Fluence, nvt		0.15 T _m , °C	(Δρ _{III}) Area, micro-ohm-cm	0.31 T _m , °C	(Δρ _{IV}) Area, micro-ohm-cm	(Δρ _{III} /Δρ _{IV}) Area, micro-ohm-cm
			Fast (E _n > 1 Mev)	Thermal					
520	C	ORM-14	1.1×10^{19}	9.3×10^{19}	153	0.396	624	0.163	2.43
527	C	ORM-18	2.3×10^{19}	1.1×10^{20}	163	0.476	620	0.227	2.10
2277	M	ORM-54	5.8×10^{19}	4.1×10^{20}	150	0.693	616	0.406	1.71
909	L	MT-138	9.8×10^{19}	3.7×10^{20}	160	0.608	619	0.536	1.13
923	L	ORM-38	1.1×10^{20}	5.2×10^{20}	157	0.701	620	0.567	1.24
914	L	MT 2-234	1.5×10^{21}	2.6×10^{21}	—	0	606	0.596	0

^aSpecimens irradiated at reactor-ambient temperatures in a water-moderated reactor (ORR or ETR).

^bPeak temperature of recovery refers to temperature of maxima in the derivative of the recovery curves. This recovery maximum is related to the melting temperature, T_m, as shown.

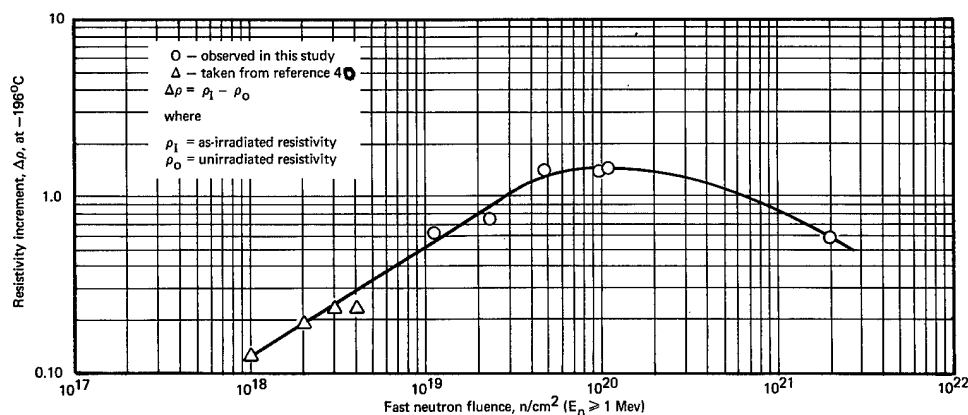


Fig. 2.70 – Total radiation-induced resistivity increment for Mo as a function of fast neutron fluence

ture. The recovery of radiation-induced defects after reactor-ambient ($\sim 70^\circ\text{C}$) irradiations resembles that for tungsten.^{43, 44} Two principal recovery regions are evident in all but the highest fluence specimen. These recovery regions are more distinct in Figure 2.72, in which the derivative $d(\Delta\rho/\Delta\rho_0)/dT$ of the normalized resistivity increment is plotted versus annealing temperature. The two principle recovery regions centered at about 160°C and 620°C , respectively, occur at almost exactly $0.15 T_m$ (stage III) and $0.31 T_m$ (stage IV) and agree quite well with the recovery observed by Ibragimov et al.⁴⁵ after a $2 \times 10^{20} \text{ n/cm}^2$ irradiation with fast neutrons. As for tungsten,⁴³ the lower temperature recovery region ($0.15 T_m$) is believed to represent the migration and recovery of self-interstitials, and the higher-temperature recovery region ($0.31 T_m$) represents the recovery of vacancies. (The term interstitial will be considered, for the remainder of this discussion, to mean self-interstitial unless specified otherwise.) Other smaller recovery regions are evident in some of the specimens, similar to tungsten.⁴⁶ The reproducibility of these smaller peaks is uncertain in NMPO studies and in the studies of others;^{40, 45, 47} their importance should not be overlooked, however, since the defects responsible for these peaks apparently contribute to the thermal hardening in this recovery region.⁴⁸ In Figure 2.73 the resistivity recovered in stage III ($\Delta\rho_{\text{III}}$) and stage IV ($\Delta\rho_{\text{IV}}$) is presented. The stage III resistivity recovery completely saturates over this range, dropping to zero at the highest fluence. The stage IV recovery, however, shows a linear fluence dependence up to about 10^{20} n/cm^2 , where a normal asymptotic approach to saturation is evident. These results are in relatively good agreement with those of Kissinger, Brimhall, and Mastel⁴² who have investigated, by lattice parameter and length change studies, the fast-neutron, radiation-induced fluence dependence in molybdenum over a range of 10^{19} to 10^{20} n/cm^2 . The results of the length change study indicate that vacancies saturate at about 10^{20} n/cm^2 or above, and that interstitials saturate at approximately 2 to $5 \times 10^{19} \text{ n/cm}^2$. The ratio of the stage III resistivity ($\Delta\rho_{\text{III}}$) recovery to the stage IV recovery ($\Delta\rho_{\text{IV}}$), presented in Figure 2.74, shows a linear dependence on the fast neutron fluence, on a semilog plot, from which intermediate values of this ratio can be predicted. Results from a resistivity recovery study of molybdenum by Ibragimov, et al.⁴⁵ after fast neutron irradiation to $2 \times 10^{20} \text{ n/cm}^2$, agree quite well with the prediction from Figure 2.74 in that a $\Delta\rho_{\text{III}}/\Delta\rho_{\text{IV}}$ ratio of almost one is obtained for approximately $2 \times 10^{20} \text{ n/cm}^2$.

These results are all consistent with the formation of increasing number of interstitial clusters (i. e., increase in the ratio of the number of interstitials in clusters to the number of free interstitials) until a fast fluence of 10^{21} n/cm^2 is reached. There are practically no free interstitials remaining above this neutron fluence level.

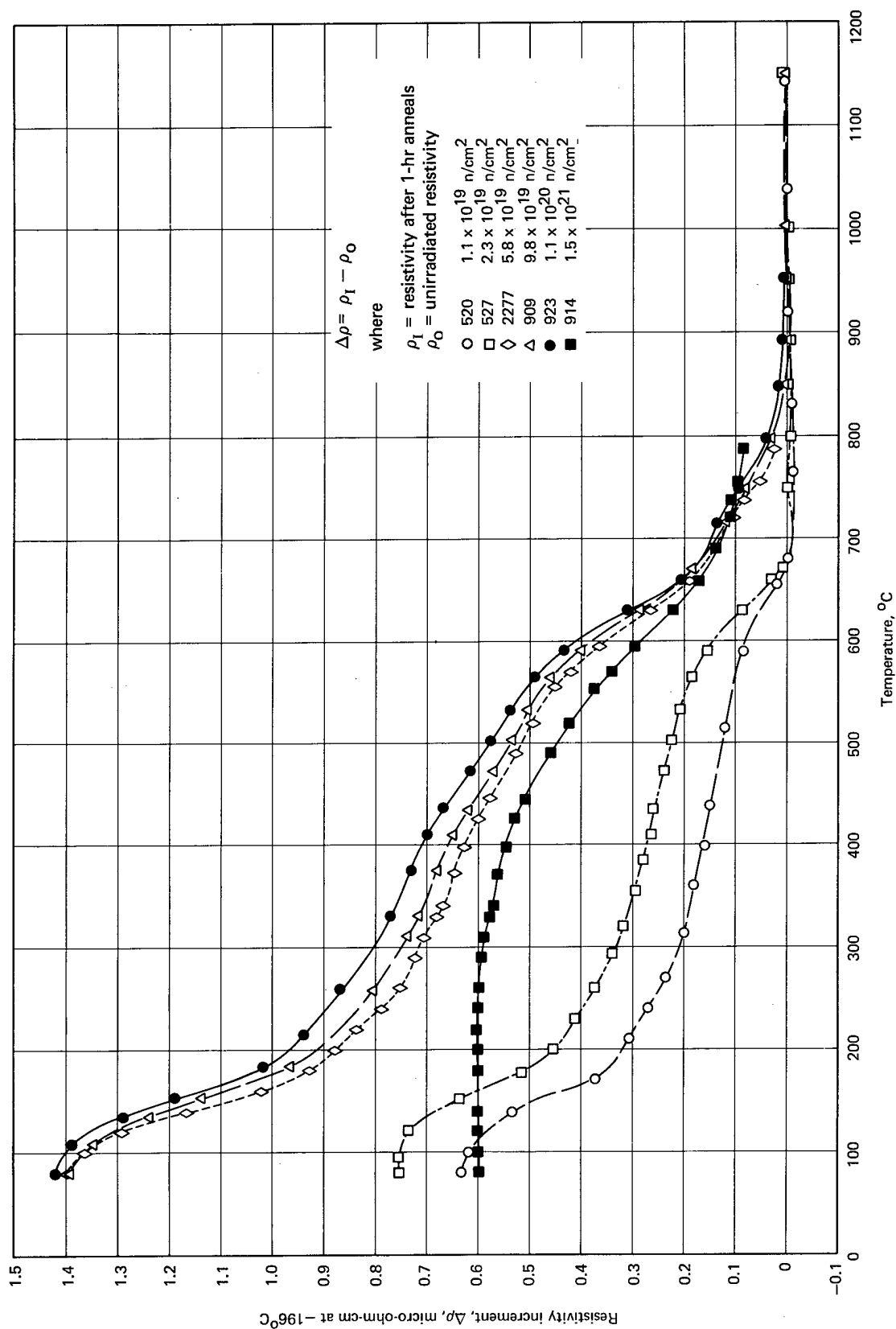


Fig. 2.71 — Isochronal resistivity recovery of neutron-irradiated, recrystallized molybdenum as a function of annealing temperature

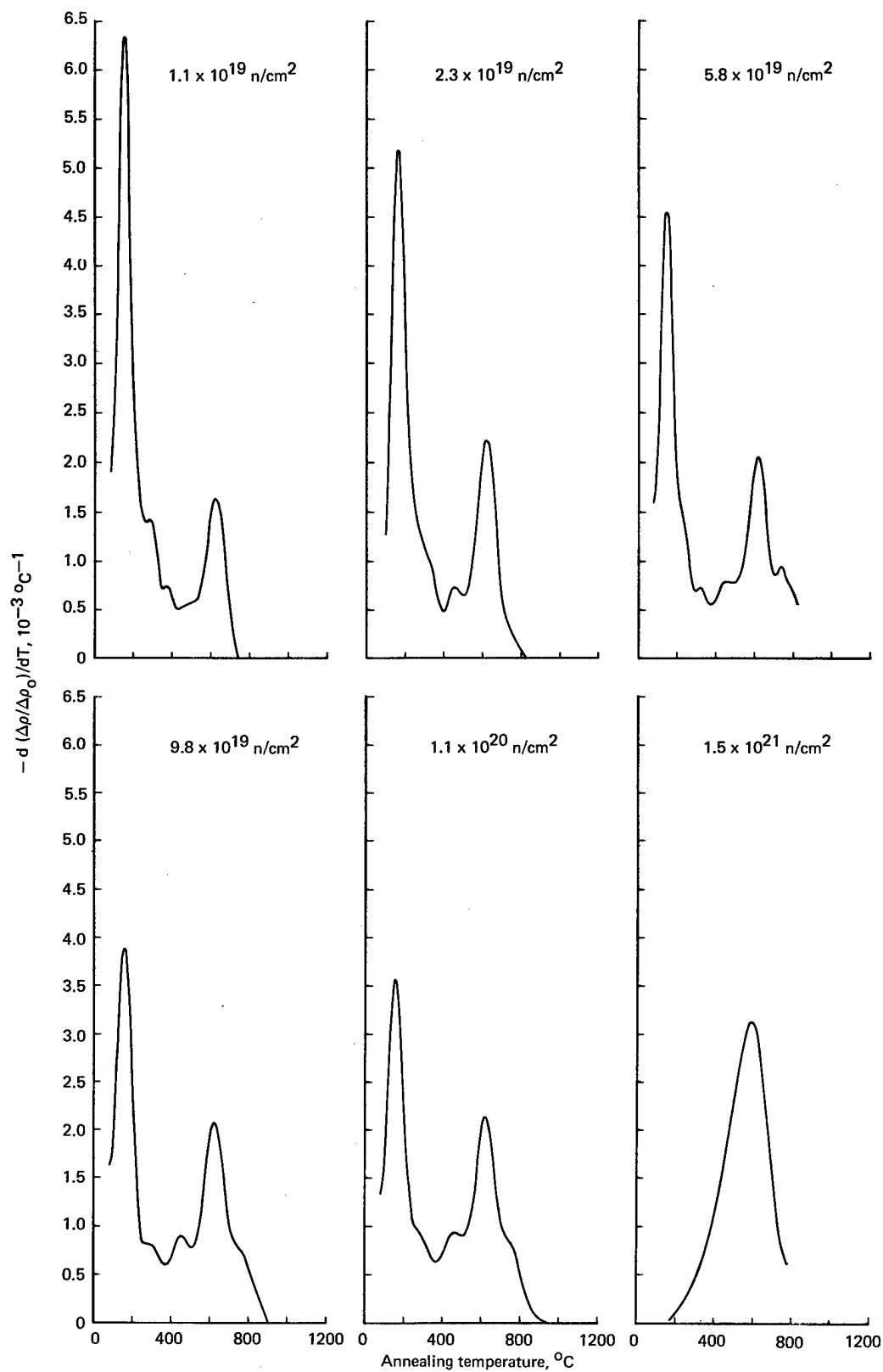


Fig. 2.72 — Derivative of the normalized isochronal resistivity recovery of neutron-irradiated, recrystallized molybdenum as a function of annealing temperature

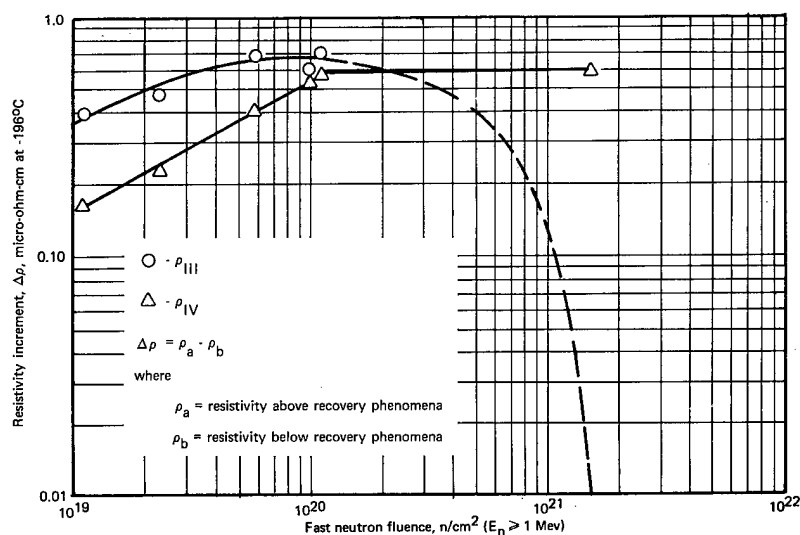


Fig. 2.73 — Resistivity recovery increments of stage III ($\Delta\rho_{III}$) to stage IV ($\Delta\rho_{IV}$) as a function of fast neutron fluence

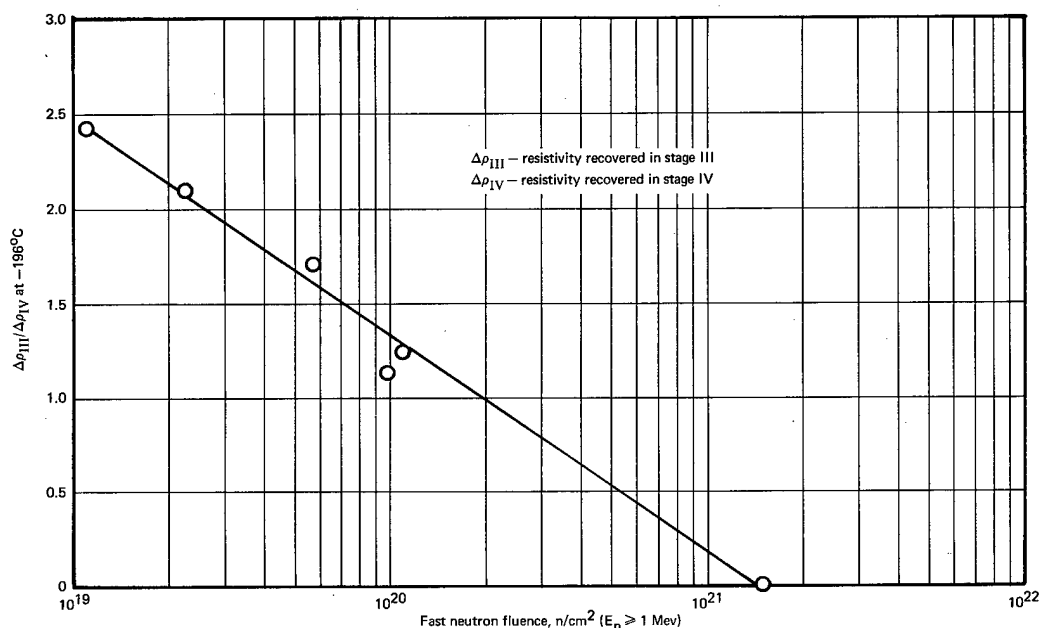


Fig. 2.74 — Ratio of resistivity recovered in stage III to stage IV as a function of fast neutron fluence

The major differences in the recovery behavior observed between tungsten and molybdenum undoubtedly arise from the differences in the homologous temperature of irradiation.⁴⁹ For tungsten, the irradiation temperature of approximately 70°C corresponds to about $0.093 T_m$, where T_m is the absolute melting temperature. For molybdenum, however, the irradiation temperature of 70°C represents about $0.12 T_m$. This represents an irradiation temperature corresponding to the onset of the stage III region in molybdenum and thus considerable recovery occurs during the irradiation. Recovery actually appears to begin at around 0°C .^{50, 51} The $0.09 T_m$ irradiation temperature for tungsten is well below the recovery region for

stage III;⁵² hence from the recovery point of view numerous point defects would be expected. Apparently irradiation within a recovery stage generates a larger ratio of cluster defects/point defects for the defects recovering in that recovery stage. This explanation is supported by the facts that the radiation-induced resistivity values observed for molybdenum are lower than for tungsten at the same radiation fluence, and that the slope observed for the neutron fluence dependence of molybdenum⁵³ is smaller than for tungsten.

The stage III recovery mechanism, considered to be the migration of point defects (interstitials), can also be compared to other metals with respect to the number of jumps such a migrating defect can make. It has been shown that a defect migrating with an activation energy Q , makes n jumps in a lifetime t before annihilation, with a vibrational frequency (ν) of approximately 10^{14} sec^{-1} , at a temperature T according to:⁵⁴

$$t = \frac{n}{\nu} e^{Q/kT} \quad (2.2)$$

Rearranging this formula, for an isochronal anneal of a time t at a temperature T , a point defect can make n jumps according to:

$$n = t \nu e^{-Q/kT} \quad (2.3)$$

Thus, for a 1-hour isochronal anneal, considering $Q \simeq 1.3 \text{ eV}$ ⁵⁵ at 160°C , about 300 jumps can be made. This parallels the number of jumps which have been found in stage III for several metals.⁵⁴

TRANSMISSION ELECTRON MICROSCOPY (R. C. Rau)

Microstructural studies using transmission electron microscopy were performed on neutron-irradiated tungsten and molybdenum. The objective of this work was to characterize radiation-induced microstructural features and, if possible, to relate those features to mechanical and physical properties. These studies concerned (1) characterization of dislocation loops in irradiated and annealed tungsten, (2) annealing of defect clusters in irradiated tungsten, and (3) effect of high irradiation temperatures on molybdenum.

Tungsten

Characterization of Dislocation Loops – Previous work^{56, 57} has shown that post-irradiation annealing at temperatures near 1100°C produces resolvable dislocation loops in tungsten irradiated to fast neutron fluences of about $4 \times 10^{19} \text{ n/cm}^2$ ($E_n \geq 1 \text{ MeV}$) or greater. It had been postulated that the loops in tungsten were probably interstitial, based mainly on results in irradiated and annealed molybdenum,⁵⁸⁻⁶⁰ but no diffraction contrast analyses had been carried out. To crystallographically characterize the loops in tungsten, tilting experiments in the electron microscope were performed on a specimen which had been irradiated to $1.5 \times 10^{21} \text{ n/cm}^2$ at reactor-ambient temperature ($\sim 70^\circ\text{C}$), and subsequently creep-rupture tested (i. e., annealed) for 315 hours at 1100°C .

Thin foil specimens were prepared electrolytically⁶¹ from an unstressed button head of the tested specimen. Preliminary scanning showed the microstructure to consist of well formed dislocation networks, making up subgrain boundaries, and a population of large dislocation loops averaging about 1000 \AA in diameter.⁵⁷ Because of the polycrystalline nature of the specimens and the apparent lack of preferred orientation, grains sampled in the thin foils had random orientations. Hence it was necessary to scan many areas to find grains in reasonably simple orientations from which meaningful tilting experiments could be performed. Figure 2.75 shows six micrographs of an extensive series obtained from an especially suitable area. The orientation of this grain was near (001), and tilting was carried out about axes near $[100]$, $[\bar{1}10]$, and $[110]$. The micrographs shown in Figure

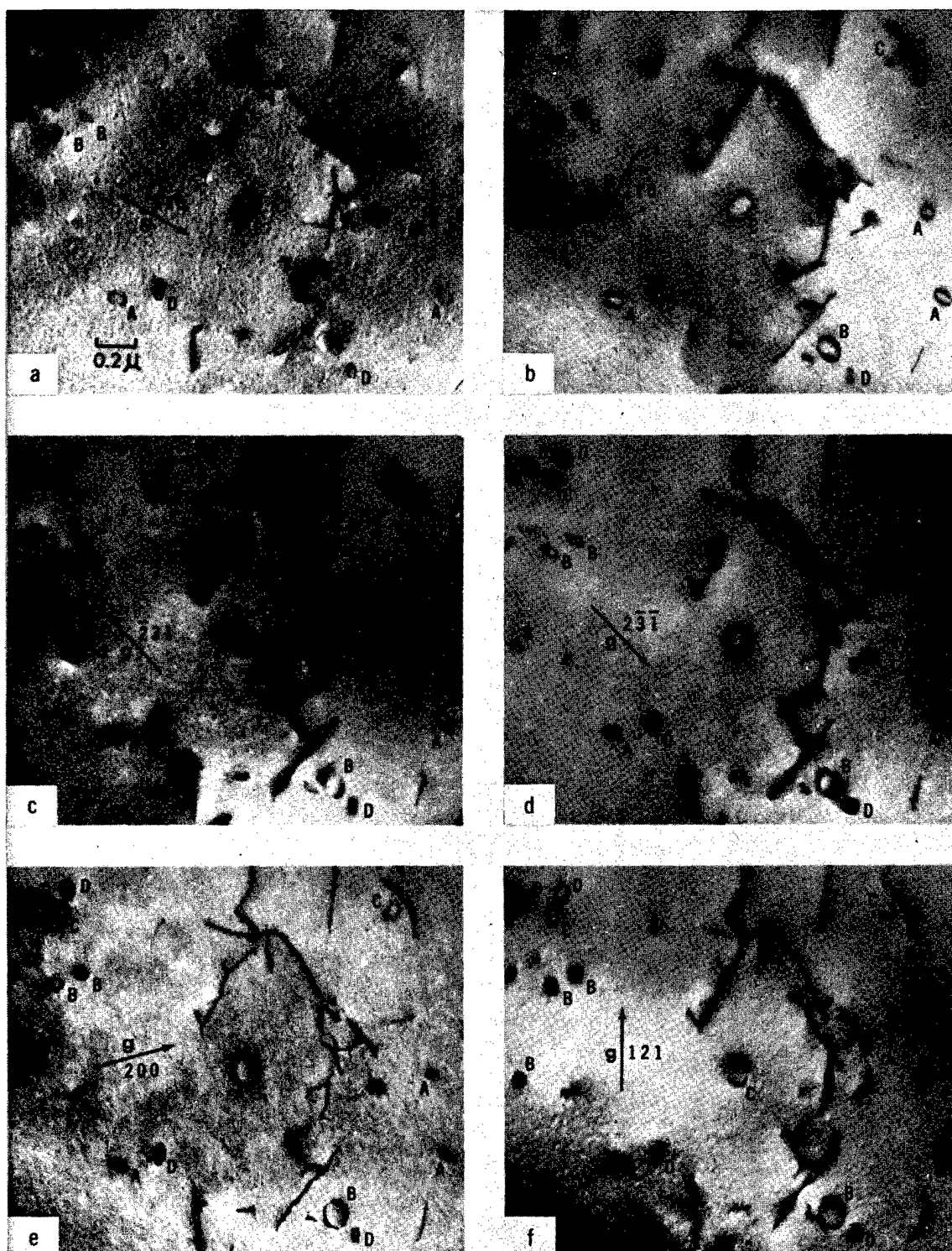


Fig. 2.75 — Dislocation loops in irradiated and annealed tungsten. All micrographs taken with $s > 0$. (a) $\bar{g} = [1\bar{1}0]$, tilt $-19^{\circ} 50'$; (b) $\bar{g} = [110]$, tilt $-10^{\circ} 30'$; (c) $\bar{g} = [231]$, tilt $+1^{\circ} 50'$; (d) $\bar{g} = [2\bar{3}1]$, tilt $+5^{\circ} 30'$; (e) $\bar{g} = [200]$, tilt $+9^{\circ} 40'$; (f) $\bar{g} = [121]$, tilt $+13^{\circ} 50'$.

2.75 illustrate the complete characterization of the loops, i.e., their Burgers vectors, habit planes, and nature.

Burgers vectors of the loops were determined by noting diffraction conditions for which the loop images were at extinction; i.e., $\bar{g} \cdot \bar{b} = 0$.⁶² For example, loops labeled A and B are out of contrast in Figure 2.75a with $\bar{g} = [1\bar{1}0]$; loops labeled C and D are out of contrast in Figure 2.75b with $\bar{g} = [110]$. In Figure 2.75c and d, with $\bar{g} = \pm [\bar{2}31]$, only B loops are out of contrast; in Figure 2.75f, with $\bar{g} = [121]$, C loops are at extinction. These conditions unambiguously identify the Burgers vector of B loops as $\pm 1/2 [11\bar{1}]$ and that of C loops as $\pm 1/2 [\bar{1}\bar{1}1]$. Similar analyses identified the Burgers vector of A loops as $\pm 1/2 [111]$ and that of D loops as $\pm 1/2 [\bar{1}11]$. The four sets of loops and their diffraction conditions in Figure 2.75 are summarized in Table 2.10.

Habit planes of the loops were determined by observing the manner in which their image shapes changed during tilting about known crystallographic directions, assuming their true shape to be circular. These observations, compared with observations of shape changes of circles drawn on a transparent tetrahedron, indicated that the loops lay on or

TABLE 2.10
MAGNITUDES OF $\bar{g} \cdot \bar{b}$ FOR OPERATING REFLECTIONS
IN FIGURE 2.75

Loop	\bar{b}	\bar{g}					
		$[1\bar{1}0]$	$[110]$	$[\bar{2}31]$	$[2\bar{3}\bar{1}]$	$[200]$	$[121]$
A	$\pm 1/2 [111]$	0	± 1	± 1	∓ 1	± 1	± 2
B	$\pm 1/2 [11\bar{1}]$	0	± 1	0	0	± 1	± 1
C	$\pm 1/2 [\bar{1}\bar{1}1]$	± 1	0	∓ 2	± 2	± 1	0
D	$\pm 1/2 [\bar{1}11]$	∓ 1	0	± 3	∓ 3	∓ 1	± 1

near $\{111\}$ planes, with each loop lying on the particular $\{111\}$ plane normal to its Burgers vector. Thus the loops are in edge orientation. The relative orientations of the four sets of $\{111\}$ loops, both with respect to each other and with respect to the micrographs of Figure 2.75, are shown in the stereoscopic drawing of Figure 2.76.

The nature of the loops was determined by the formal method of analysis of the image contrast as the sign of the quantity $(\bar{g} \cdot \bar{b})_s$ was changed.⁶³ Using standard conventions to define the geometry of dislocations and their Burgers vectors,⁶⁴ the nature of the A, C, and D loops can be deduced from Figures 2.75c and d. For example, from the identification of the habit planes, it is known that C loops slope downward to the right in the micrographs. In Figure 2.75c these loops have outside contrast, indicating that $(\bar{g} \cdot \bar{b})_s$ is positive; hence the positive edge component of the Burgers vector has the same directional sense as the \bar{g} vector. This situation obeys a right-hand rule, which indicates that the C loops are vacancy in nature.⁶³ Similar analysis of the contrast of the other loops indicates that they are all vacancy type. These results are summarized in Table 2.11.

Annealing of Defect Clusters in Irradiated Tungsten — To study the progressive effects of post-irradiation annealing on the defect structure of neutron-irradiated tungsten, a series of specimens were examined which had been irradiated to 4.2×10^{19} n/cm² ($E_n \geq 1$ Mev) at reactor-ambient temperature ($\sim 70^\circ\text{C}$). Following irradiation, the specimens received 1-hour anneals in argon at various temperatures and were tensile tested at 240°C .³⁵ The annealing temperatures and test results for both irradiated and unirradiated control samples are listed in Table 2.12.

Thin foils for transmission electron microscopy were prepared from both the unstressed button heads and the reduced areas near the fracture. Examination of foils from the button heads of unirradiated control specimens revealed that the starting microstructure contained

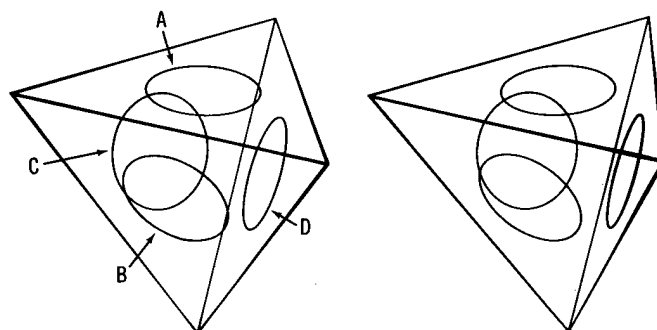


Fig. 2.76 — Stereoscopic drawing showing the appearance of loops on the four sets of $\{111\}$ planes. The tetrahedron is oriented in approximate agreement with the foil orientation of Figure 2.75.

TABLE 2.11

ANALYSIS OF THE NATURE OF LOOPS IN FIGURES 2.75c AND 2.75d

Loop	Possible \bar{b}	$\bar{g} = [\bar{2}31], s +$ $\bar{g} \cdot \bar{b}$	Image	$\bar{g} = [2\bar{3}1], s +$ $\bar{g} \cdot \bar{b}$	Image	Loop Nature
A	$\pm \frac{1}{2} [111]$	± 1	inside $\bar{g} \cdot \bar{b} < 0$	∓ 1	outside $\bar{g} \cdot \bar{b} > 0$	vacancy $\bar{b} = \frac{1}{2} [\bar{1}\bar{1}1]$
B	$\pm \frac{1}{2} [11\bar{1}]$	0	—	0	—	vacancy ^a $\bar{b} = \frac{1}{2} [\bar{1}\bar{1}1]$
C	$\pm \frac{1}{2} [1\bar{1}1]$	∓ 2	outside $\bar{g} \cdot \bar{b} > 0$	± 2	inside $\bar{g} \cdot \bar{b} < 0$	vacancy $\bar{b} = \frac{1}{2} [\bar{1}\bar{1}1]$
D	$\pm \frac{1}{2} [\bar{1}11]$	± 3	inside $\bar{g} \cdot \bar{b} < 0$	∓ 3	outside $\bar{g} \cdot \bar{b} > 0$	vacancy $\bar{b} = \frac{1}{2} [\bar{1}\bar{1}1]$

^aNature of B loops determined from other micrographs not shown in Figure 2.75

TABLE 2.12

MECHANICAL PROPERTIES AND DEFECT CLUSTER DATA FOR IRRADIATED AND ANNEALED TUNGSTEN

Specimen No.	Fast Neutron Fluence, ^a n/cm^2 ($E_n \geq 1$ Mev)	Post-Irradiation Annealing Temperature, $^{\circ}C$ T/T_M		Ultimate Strength, kg/mm^2	Elongation in 3.18 cm, %	Reduction in Area, %	Cluster Size, \AA	Cluster Density, $No./cm^3$
		$^{\circ}C$	T/T_M					
10W	Unirradiated	240 ^b	0.14 ^b	49.9	37.7	55.2	—	—
7W	4.2×10^{19}	240 ^b	0.14 ^b	66.4	0.3	8.6	35	1.0×10^{17}
16W	Unirradiated	435	0.19	49.3	34.6	64.7	—	—
11W	4.2×10^{19}	435	0.19	61.7	1.1	8.2	35	2.2×10^{16}
26W	Unirradiated	743	0.28	50.7	21.9	33.6	—	—
23W	4.2×10^{19}	743	0.28	77.6	0.5	1.8	50	8.7×10^{16}
24W	4.2×10^{19}	897	0.32	60.0	0.6	2.1	50	1.1×10^{16}
25W	4.2×10^{19}	1043	0.36	52.3	12.0	12.3	100	3.5×10^{14}

^aIrradiated at reactor-ambient temperature ($\sim 70^{\circ}C$).

^bTensile test temperature.

numerous dislocation tangles surrounding relatively dislocation-free cells, typical of worked and incompletely recrystallized metals. It was noted during subsequent examination of the irradiated specimen annealed at the highest temperature, 1043 °C, that these random tangles were partly replaced by more ordered networks of dislocations such as occur in well annealed and recrystallized metals.⁶⁵

Examination of the irradiated specimens showed the presence of radiation-induced black-dot defect clusters and the effect of post-irradiation annealing on those clusters. Figure 2.77 shows photomicrographs illustrating typical microstructures in button head foils. In the unannealed condition (Figure 2.77a) a dispersion of fine dot clusters was present throughout the matrix. Annealing at 435 °C (Figure 2.77b) produced an apparent slight decrease in cluster concentration, but annealing at 735 °C (Figure 2.77c) resulted in a noticeable densification of the clusters. Finally, annealing at 897 °C (Figure 2.77d) and 1043 °C (Figure 2.77e) caused a definite decrease in cluster concentration and led to the formation of resolvable dislocation loops.

To obtain a quantitative comparison between defect cluster densities and tensile strengths of the specimens, cluster counts were made from the electron micrographs of Figure 2.77.⁶⁶ The resulting cluster densities listed in Table 2.12 are plotted as a function of annealing temperature in Figure 2.78a. This plot bears a striking resemblance to a plot of the tensile strengths of these samples shown in Figure 2.78b. These curves and the data in Table 2.12 show that annealing produces a minimum in the strength curve at 435 °C which corresponds to a depletion of defect clusters; a maximum occurs at 743 °C which corresponds to a pronounced coarsening and densification of the clusters. Higher-temperature annealing results in a loss of strength and a reduction in the population of defect clusters, in good agreement with previous findings.^{56, 57}

This complex annealing behavior is believed to be caused by two overlapping defect recovery peaks, one occurring below 435 °C and one above. The observed cluster density curve and hence the strength curve represent the sum of the two separate recovery curves. These separate recovery curves are due to the diffusion and agglomeration of two different defect species which require different thermal energies for migration. It is significant that the 435 °C minimum occurs somewhat beyond the 0.15 T_m (stage III) recovery peak observed in electrical resistivity studies; the 743 °C maximum occurs just below the 0.31 T_m (stage IV) recovery peak.^{67, 68} Both the 897 °C and 1043 °C annealing temperatures, which produce marked recovery in the observable microstructures, are above the 0.31 T_m recovery peak.

The assignment of specific migrating defects to the stage III and stage IV recovery regions has been the subject of much controversy in the literature, primarily because of the indirect measurement techniques involved. Recent direct observations on annealing in irradiated tungsten by field ion microscopy have provided conclusive evidence that stage III corresponds to the migration of free interstitials and stage IV corresponds to the migration of vacancies.⁶⁹⁻⁷¹ On this basis the defect clusters seen in the unannealed specimen in the present study are probably interstitial clusters, and those seen in the specimens annealed at the higher temperatures are probably vacancies. The clusters in the 435 °C annealed specimen might be remnants of the early interstitial cluster population, the beginnings of the buildup in vacancy cluster population, or a combination of both.

To check these conclusions, it would be desirable to carry out electron diffraction contrast experiments on the different specimens to identify the clusters present after each annealing temperature. Such experiments cannot be performed reliably, however, when the cluster density is high or when the clusters are not resolvable as dislocation loops. Hence in the present case only, the specimen annealed at the highest temperature, 1043 °C, was suitable for analysis. Large-angle tilting experiments were carried out on a foil from this specimen following the method of Edmondson and Williamson.⁷² Figure 2.79 shows the

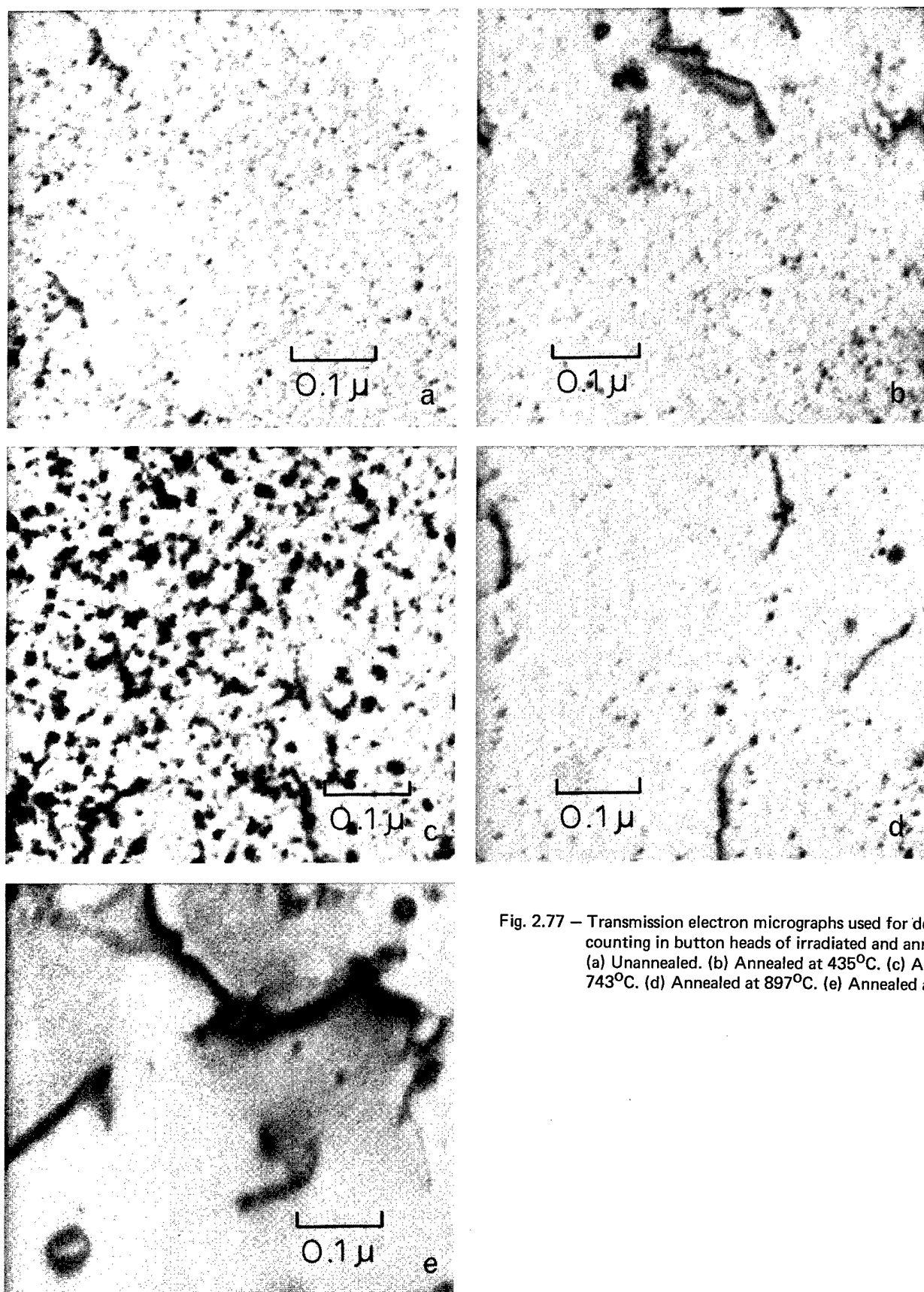


Fig. 2.77 — Transmission electron micrographs used for defect cluster counting in button heads of irradiated and annealed W. (a) Unannealed. (b) Annealed at 435°C. (c) Annealed at 743°C. (d) Annealed at 897°C. (e) Annealed at 1043°C.

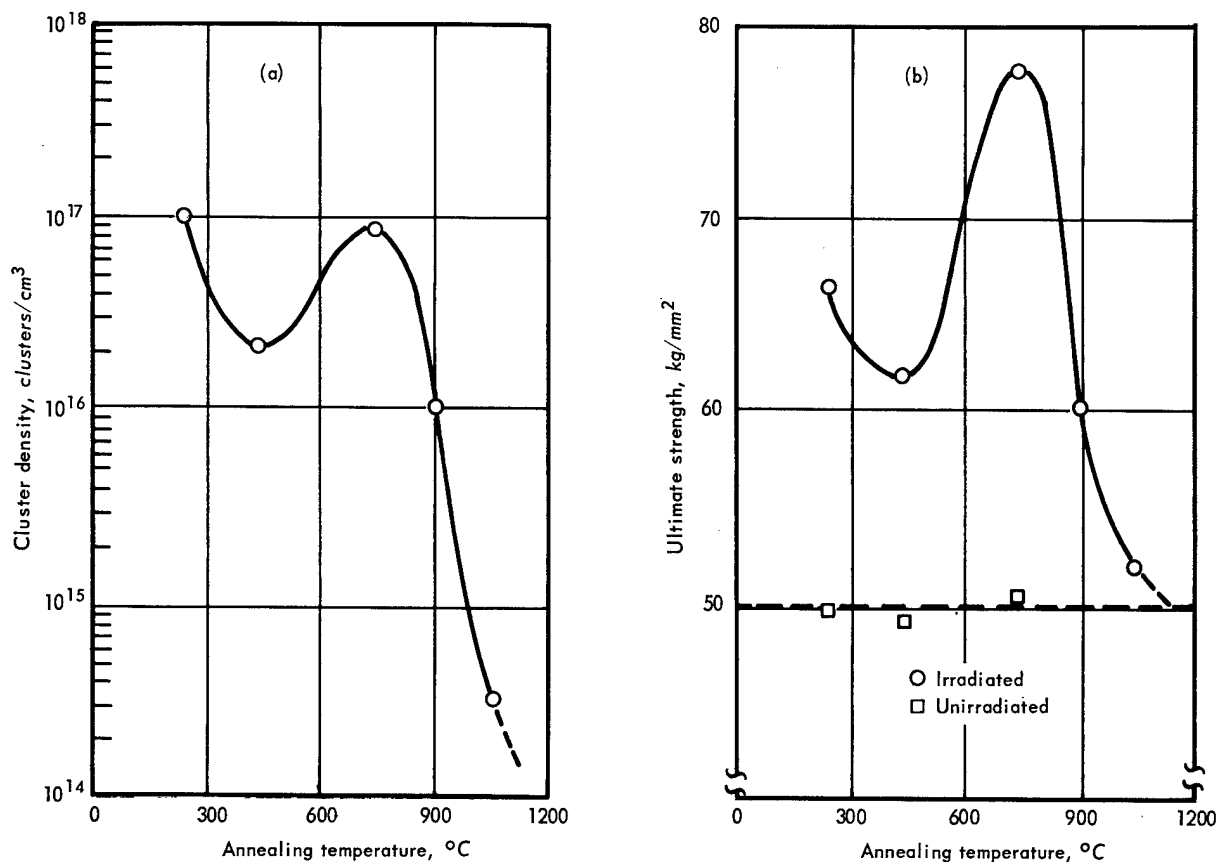


Fig. 2.78 — Effect of post-irradiation annealing temperature on defect cluster density, and ultimate tensile strength at 240°C of polycrystalline W irradiated at ~70°C to 4.2×10^{19} n/cm² ($E_n \geq 1$ Mev)

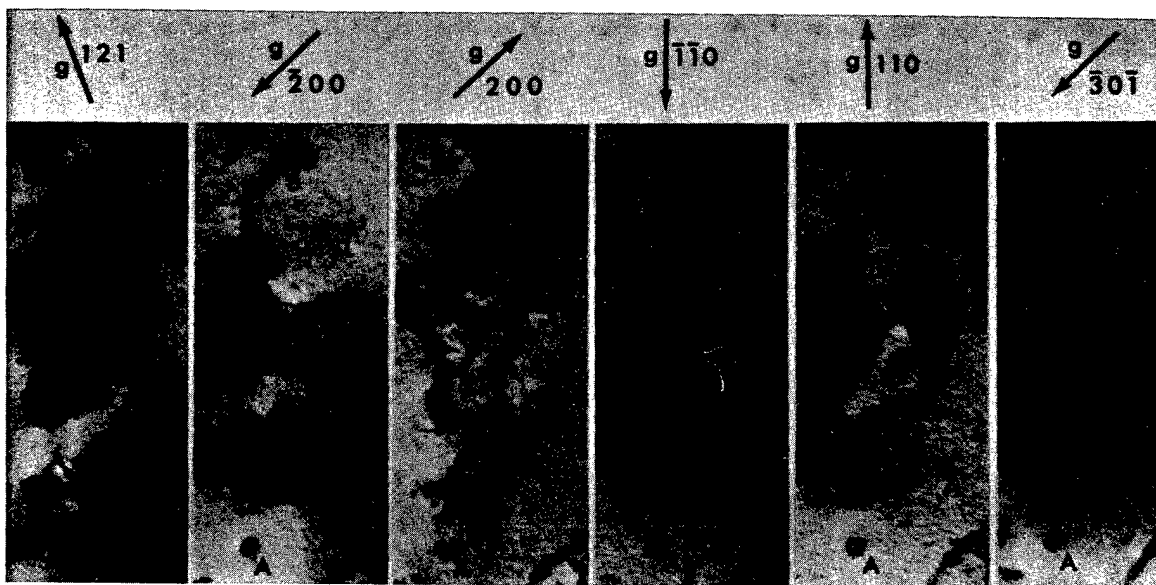


Fig. 2.79 — Series of electron micrographs used for identifying loops in tungsten irradiated to 4.2×10^{19} n/cm² at 70°C and annealed at 1043°C. All micrographs taken with $s > 0$. (a) $g = [121]$, tilt $+18^\circ 40'$; (b) $g = [200]$, tilt $+2^\circ 40'$; (c) $g = [200]$, tilt $+0^\circ 50'$; (d) $g = [\bar{1}\bar{1}0]$, tilt $-6^\circ 20'$; (e) $g = [110]$, tilt $-8^\circ 00'$; (f) $g = [30\bar{1}]$, tilt $-17^\circ 50'$.

resulting micrographs. The figure shows that loops labeled A increase in apparent size due to purely geometrical factors as the foil is continuously tilted through a relatively large angle from $+18^{\circ} 40'$ to $-17^{\circ} 50'$, but the loop labeled B decreases in apparent size. But when the diffraction conditions are changed by reversing the sign of the quantity $(\bar{g} \cdot \bar{b})_s$ (i.e., by reversing \bar{g} from $[\bar{2}00]$ to $[200]$ or from $[\bar{1}\bar{1}0]$ to $[110]$), A loop images shrink and the B loop image expands. Thus the apparent size changes due to diffraction conditions are in the opposite sense to those due to geometrical factors for both A and B loops, and both are vacancy in nature.⁷² This analysis agrees with the previous, more rigorous analysis of large loops in tungsten annealed at 1100°C (Figure 2.75), and supports the contention that vacancies migrate in stage IV.

In addition to specimens from the button heads, foils prepared from the gage sections near the fracture were also examined in the electron microscope. Detailed cluster counts were not made in the gage section foils, but it was apparent that the microstructures were generally similar to those in the button heads shown in Figure 2.77.⁶⁶ The sample annealed at 435°C was an exception; the observed cluster density in the gage section was noticeably lower than in the button head. This implies that the small clusters present after the 435°C anneal interact with and are possibly swept out by the dislocations moving along slip planes during tensile testing.⁷³

Molybdenum

Defect Structures — Transmission electron microscopy studies were begun on a series of polycrystalline molybdenum specimens irradiated at three different temperatures and creep-rupture tested at 750°C .⁷⁴ This test temperature was selected on the basis of microstructural observations by Mastel and Brimhall,⁷⁵ who found that post-irradiation annealing at temperatures above 750°C led to a rapid decrease in defect cluster densities in molybdenum which had been irradiated at reactor-ambient temperatures. The specimens used in the present investigation, and their irradiation conditions and test results, are listed in Table 2.13.

TABLE 2.13
CREEP-RUPTURE DATA^a FOR MOLYBDENUM TESTED
AT 750°C AND 18.00 kg/mm^2

Specimen No.	Fast Neutron Fluence, n/cm^2 ($E_n \geq 1\text{ Mev}$)	Irradiation Temperature, $^{\circ}\text{C}$	Rupture Life, hr	Elongation in 4.45 cm, %	Reduction in Area, %
1610	Unirradiated	—	20.38	39.5	95.7
1594	1.4×10^{20}	70	56.06	40.4	92.8
1622	1.8×10^{20}	700	244.06	37.6	94.4
1612	1.8×10^{20}	1000	355.09	31.1	95.2

^aSee Table 2.3 for complete history of specimens.

Thin foils were prepared electrolytically, using a mixture of 12.5 percent H_2SO_4 in methanol, from the unstressed button heads and the stressed regions near the fracture of the tested specimens. Examination of foils from the button head of the unirradiated control specimen showed a relatively defect-free microstructure containing only a few random dislocations. Stress at 750°C and the resulting deformation led to a microstructure of tangled networks of dislocations outlining subgrain boundaries, and free dislocations within the subgrains; these were revealed by foils from the gage section of this specimen.

Examination of button head foils from the specimen irradiated at pile-ambient temperature ($\sim 70^{\circ}\text{C}$) and tested at 750°C showed an abundance of resolvable dislocation loops, many quite large (up to 4000\AA), shown in Figure 2.80a. These loops were uniformly distributed

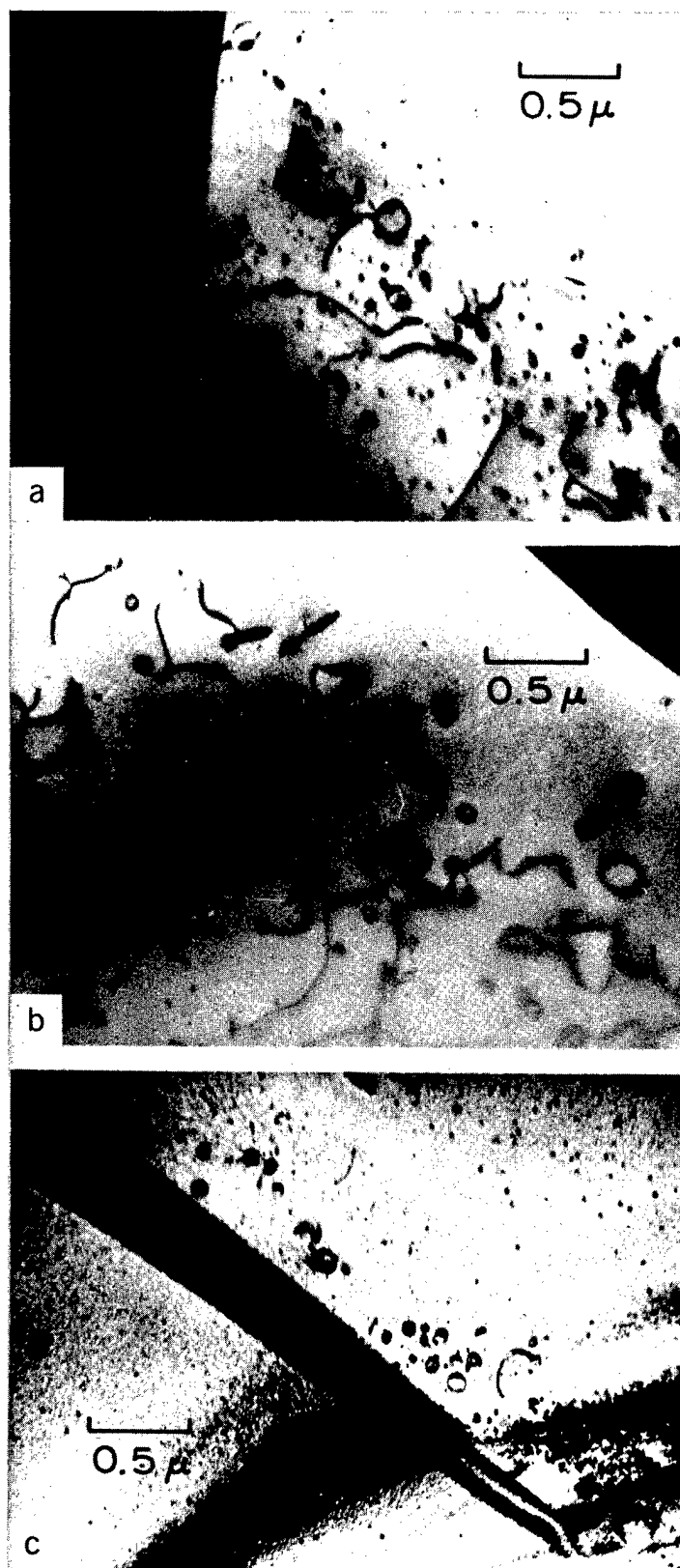


Fig. 2.80 — Microstructure in button heads of irradiated molybdenum creep-rupture tested at 750°C (a) irradiated at 70°C; (b) irradiated at 700°C; (c) irradiated at 1000°C

throughout the grains, and showed no tendency of denuding near grain boundaries. Preliminary diffraction contrast experiments indicated that the majority of the loops probably had $a/2 \langle 111 \rangle$ Burgers vectors, similar to the large loops in tungsten and in agreement with previous work on irradiated molybdenum.⁵⁸⁻⁶⁰ Large-angle tilting experiments,⁷² also preliminary, indicated that the loops were interstitial in nature. This result is consistent with other work on irradiated molybdenum.⁵⁸⁻⁶⁰

The microstructure of button head foils from the specimen irradiated at 700°C and tested at 750°C also contained a dense population of large dislocation loops within the grains (Figure 2.80b), but in this case a zone denuded of loops was present along the grain boundaries. The width of this denuded zone was about 1 micron, in agreement with recent observations by Brimhall et al.⁷⁶ on molybdenum irradiated to $3.5 \times 10^{19} \text{ n/cm}^2$ ($E_n \geq 1 \text{ Mev}$) at 600°C. Preliminary tilting experiments indicated that the loops were again interstitial in nature, and probably were in edge orientation, lying on $\{111\}$ habit planes and having $a/2 \langle 111 \rangle$ Burgers vectors.

Examination of foils from the button head of the specimen irradiated at 1000°C and tested at 750°C showed a completely different microstructure than in the other two conditions. This microstructure (Figure 2.80c) was essentially the reverse of that seen in the 700°C irradiated specimen, and consisted of an almost structureless matrix containing a scattering of small black dots together with a few scattered colonies of loops located in regions within 1 micron of the grain boundaries. These loops, which averaged about 500 to 1000 Å in diameter, were tentatively identified as vacancy in nature. This result is consistent with the recent findings of Brimhall et al.⁷⁶ who reported that 1000°C annealing of molybdenum previously irradiated at 600°C led to the nucleation and growth of vacancy clusters within the 1-micron-wide denuded zone along grain boundaries.

Examination of the foils from the stressed regions in the gage sections of the molybdenum specimens irradiated at 70°C and 700°C showed dislocation tangles and networks outlining subgrain boundaries, typical of deformed metals. Gage section foils from the 1000°C irradiated specimen showed similar dislocation structures and evidence of pinning of dislocations by the small black dots in the matrix. Several such pinned dislocations can be seen bowing out from black dots in the micrograph of Figure 2.81. The identity of these black dots is not certain; they are not believed to be clusters originating from displacement events, but rather small carbide particles which precipitated during the 1000°C irradiation. The carbon content of this series of specimens was approximately 220 ppm, well in excess of the equilibrium solid solubility limit in molybdenum. The 1000°C irradiation temperature may cause precipitation of carbides from solution. Dislocation pinning by these particles probably accounts for the enhanced strength indicated for this specimen in Table 2.13.

Large dislocation loops were scattered throughout the matrix in gage section foils from the specimen irradiated at 1000°C and tested at 750°C. A fairly complete crystallographic characterization of these loops was made from a series of micrographs, two of which are shown in Figure 2.82. This diffraction contrast analysis indicated that most of the loops were edge loops, lying on $\{111\}$ planes and having $a/2 \langle 111 \rangle$ Burgers vectors, but that they were interstitial in nature. This is in contrast to the tentative identification of vacancy loops in button head foils from this same specimen.

Finally, one rather unusual dislocation loop was found in the gage section of the 1000°C irradiated specimen. That loop is marked A in Figure 2.82a, taken with the (211) reflection operating. This loop is at extinction in Figure 2.82b, taken with the (002) reflection operating; i.e., $g \cdot b = 0$. This behavior indicates that loop A cannot have a Burgers vector of the type $a/2 \langle 111 \rangle$ commonly found in bcc metals, but suggests that it must

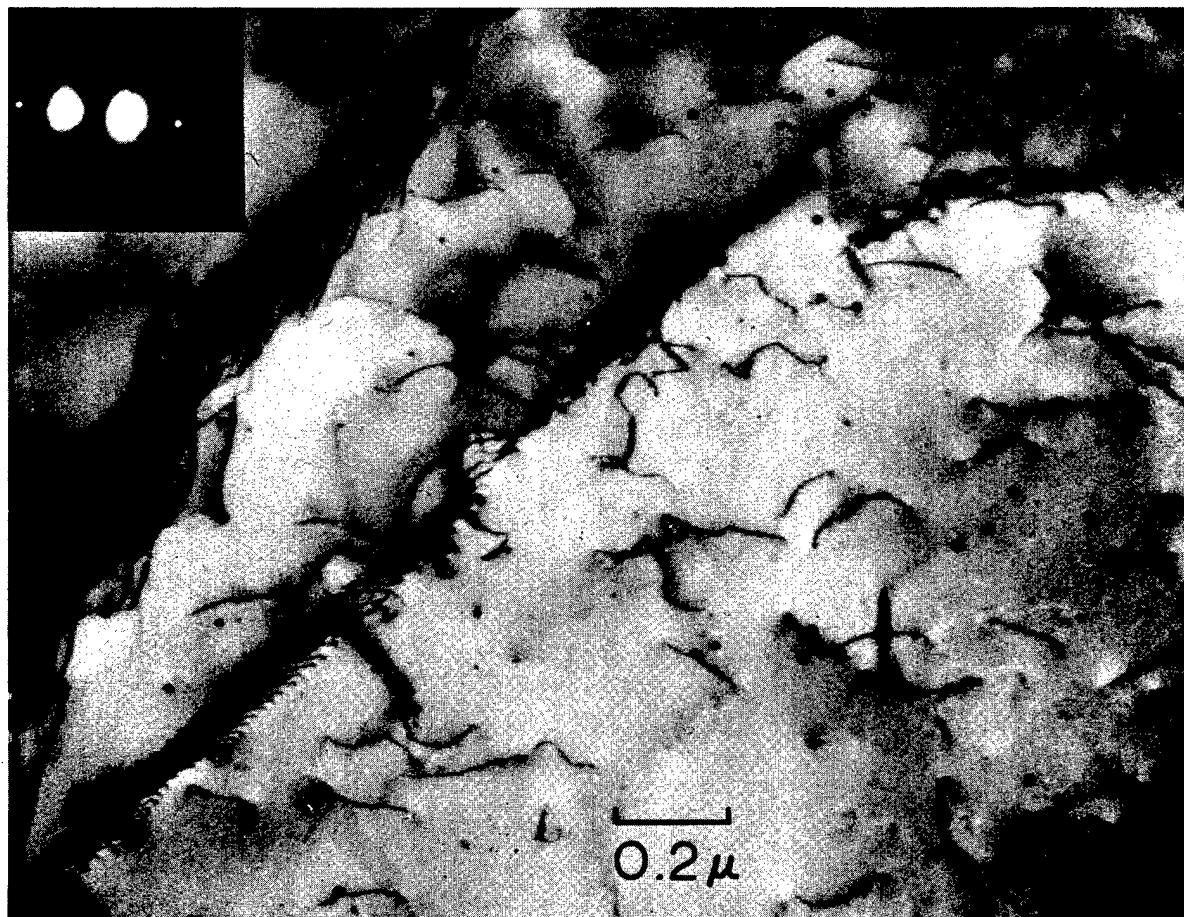


Fig. 2.81 — Pinning of dislocations by small carbide particles in stressed region of molybdenum irradiated at 1000°C and tested at 750°C

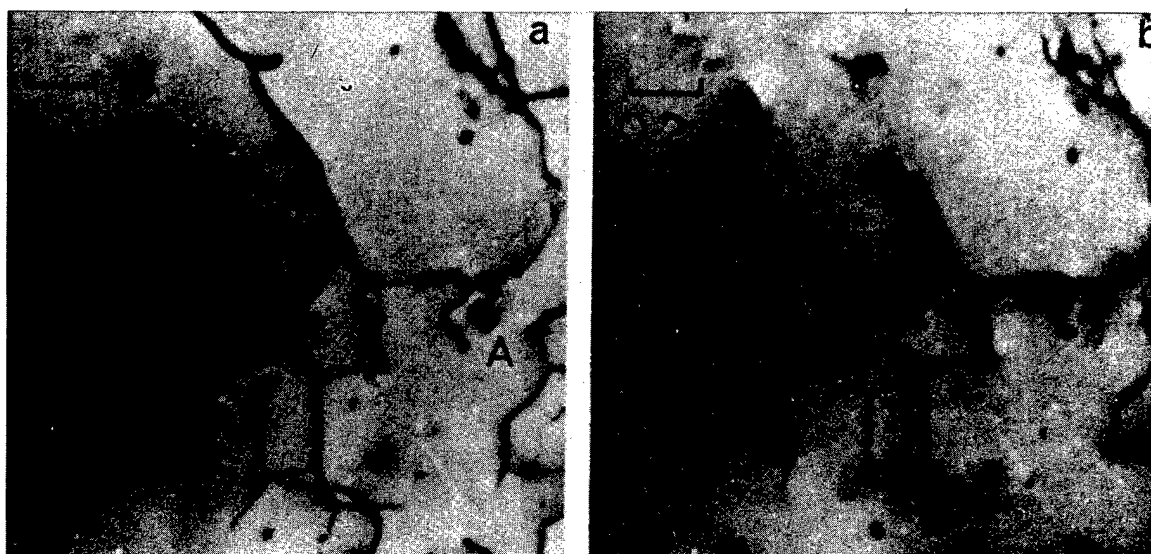


Fig. 2.82 — Dislocation loops in stressed region of molybdenum irradiated at 1000°C and tested at 750°C. Loop marked A is non- $a/2 \langle 111 \rangle$ type. (a) $\bar{g} = |211|$, tilt $+9^\circ 40'$; (b) $\bar{g} = |002|$, tilt $-5^\circ 40'$.

have a higher-energy Burgers vector such as a $\langle 100 \rangle$ or a $\langle 110 \rangle$. Although the available diffraction conditions were not sufficient to differentiate between these two possibilities, dislocation energy considerations strongly favor the a $\langle 100 \rangle$ choice.⁷⁷ Loops having Burgers vectors of this type have been found in iron bombarded with 150-keV Fe^+ ions,⁷⁸ but apparently have never been observed in neutron-irradiated bcc metals.

2.4 REACTOR DOSIMETRY

MONTE CARLO SPECTRUM CALCULATIONS (L. S. Burns, D. G. Besco, J. L. Kamphouse, J. Moteff)

The first phase of the Monte Carlo calculations of the neutron energy spectrum for various regions of the EBR-II was completed and some preliminary data are presented in this section. The neutron energy spectrum was determined for each region shown in the computer nuclear mockup in Figure 2.83. Gaps above and below the core were made equal in the mockup to utilize symmetry in the calculations. The spectrum was composed of 40 energy groups of equal lethargy between 0.01 and 14 MeV. The quadrilateral areas shown in the mockup are rotated about the reactor centerline to give a quasi three-dimensional geometry, described in the r - z plane and assumed in the ϕ rotational direction. Each region is composed of a homogeneous mixture of materials present in those regions. Neutron histories are started in the reactor and followed until they escape the configuration, are absorbed, or fall below the energy cutoff. The total number of neutrons below 0.01-MeV energy are also recorded for each region. The calculation considered elastic scattering, inelastic scattering, radiative capture, (n, α) reactions, $(n-2n)$ reactions in beryllium, and neutron absorption without secondary emission. The core was composed of 91 elements with twelve control rods and two safety rods; it was surrounded by two rows of stainless steel and the U^{238} blanket. Appropriate axial and radial power distributions with a Watts fission spectrum were used to obtain source neutrons.

For presentation the integrals of the differential neutron flux densities, $\phi'(E)$, were normalized so that the number of neutrons above 1 MeV are equal to unity. These curves are given for four regions of the core in Figure 2.84. Regions 2A and 7A represent the third of rows 2 and 7, respectively, at the core midplane and above. Regions 2B and 7B represent the third of rows 2 and 7, respectively, above the midplane nearest the top of the core. Row 7 is actually within the stainless steel reflector surrounding the core. These four regions are clearly delineated in Figure 2.83.

The integrated neutron flux densities giving the fraction of neutrons above a given energy E , $\phi(E) = \int_E^{14} \phi'(E) dE$, for each one of the four regions, along with the Watt fission spectrum for comparative purposes, are shown in Figure 2.85. The energy E has the limits $0.01 < E < 14$ MeV. In this case $\phi'(E)$ was normalized so that the area under the complete curve from 0.01 to 14 MeV is equal to unity. The fraction of neutrons, $\phi(E)$, above 0.01 MeV as obtained from these curves are simply those considered in the detailed spectrum calculation. Since there are also neutrons present at energies below 0.01 MeV, the fraction of the total neutrons greater than E in the respective regions will be smaller than that obtained from Figure 2.85 by the factor k which will also be different for each region. These factors are listed in Table 2.14.

EBR-II FLUX DENSITY MEASUREMENTS (R. L. Stuart, J. L. Kamphouse, J. Moteff)

Wire monitors which were used for the flux mapping experiment in the EBR-II rows 2 and 7 positions were counted and preliminary results for the fast neutron flux densities were determined by using the threshold reactions $\text{Fe}^{54}(n, p)\text{Mn}^{54}$, $\text{Ni}^{58}(n, p)\text{Co}^{58}$, and

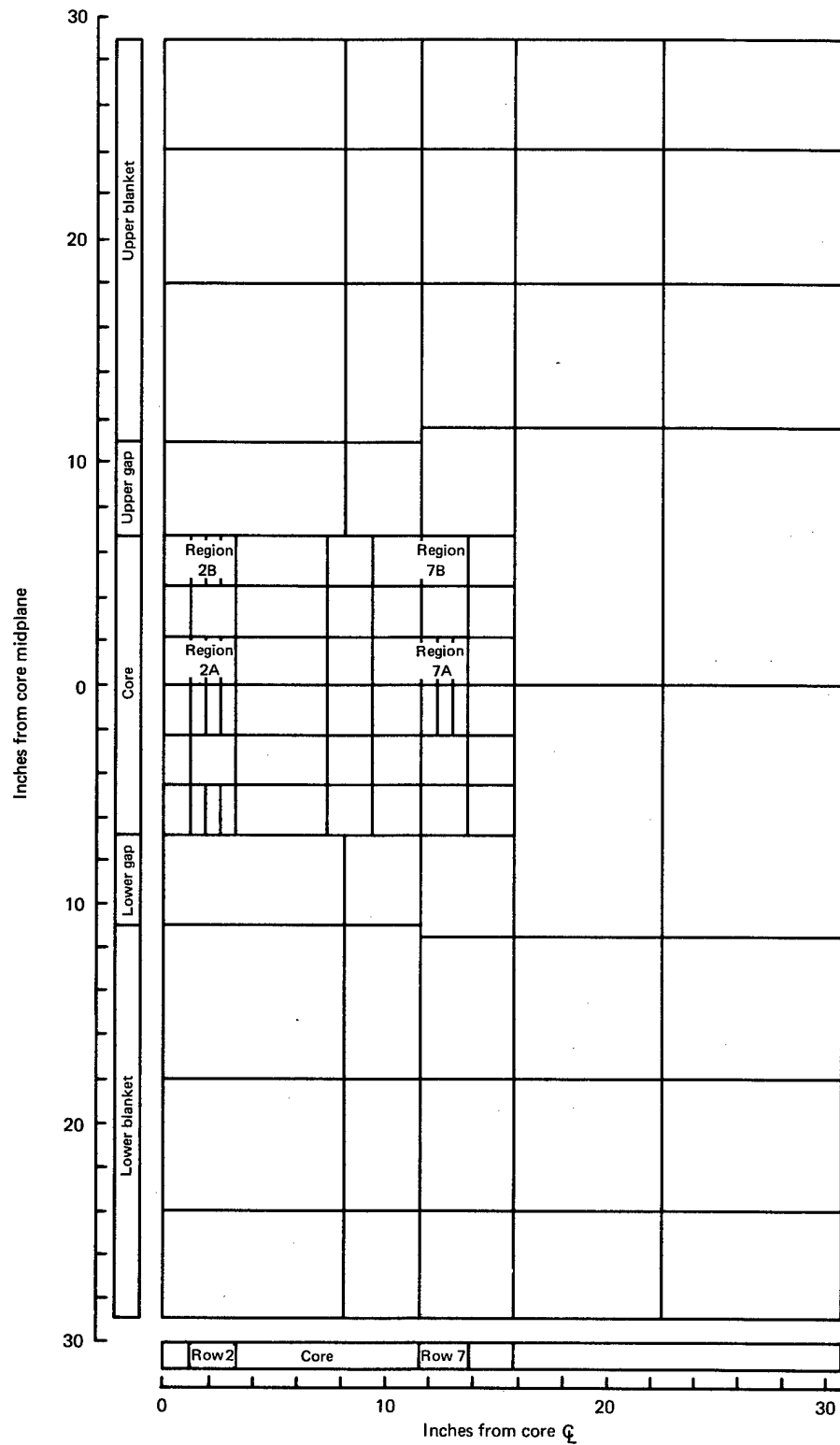


Fig. 2.83 — Computer nuclear mockup for Monte Carlo spectrum calculations in EBR-II

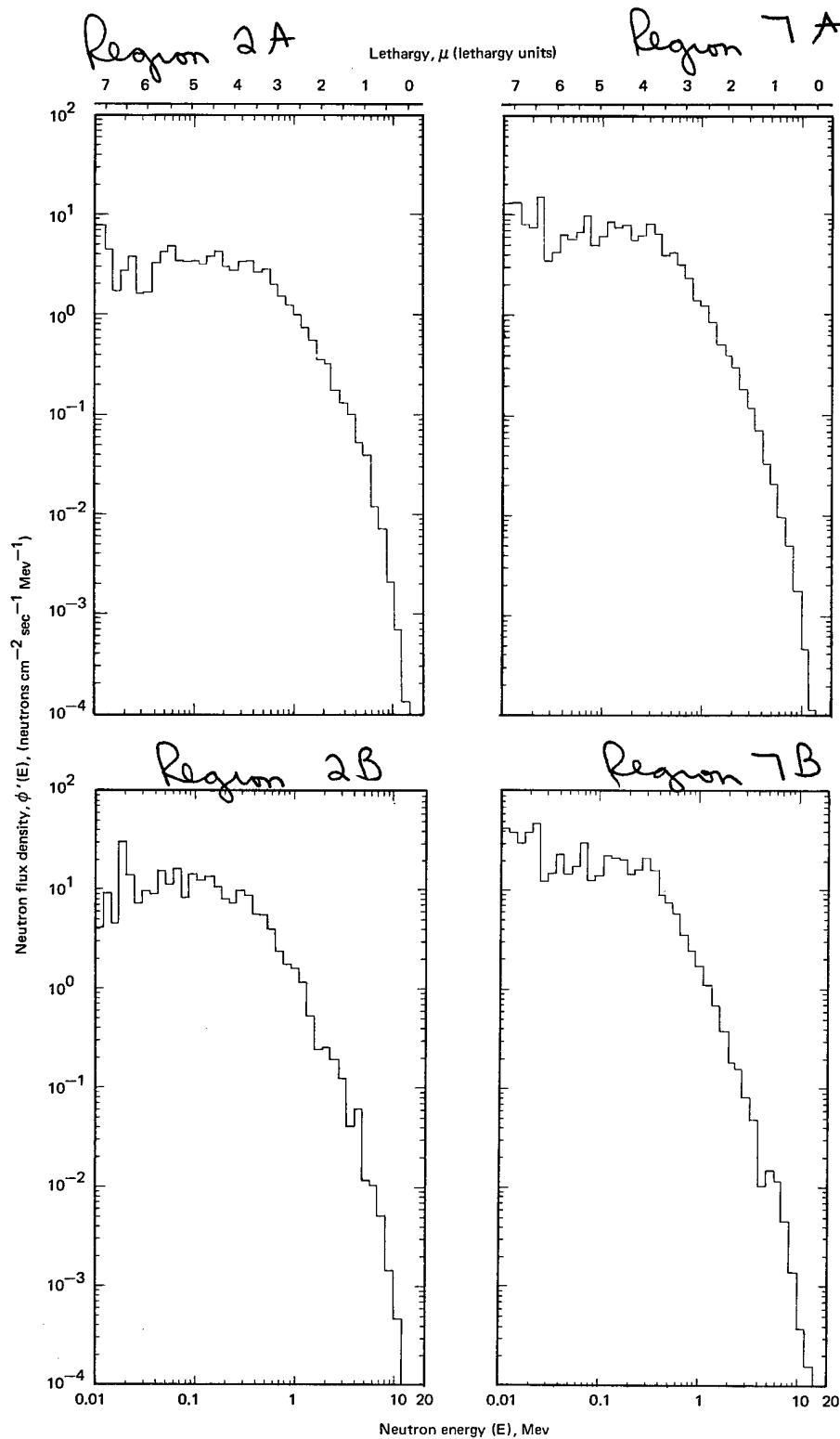


Fig. 2.84 — Monte Carlo neutron energy spectra for four core regions of the EBR-II.
Spectra normalized to unity above 1 Mev ($\mu = \ln \frac{E_0}{E}$; $E_0 = 14$ Mev)

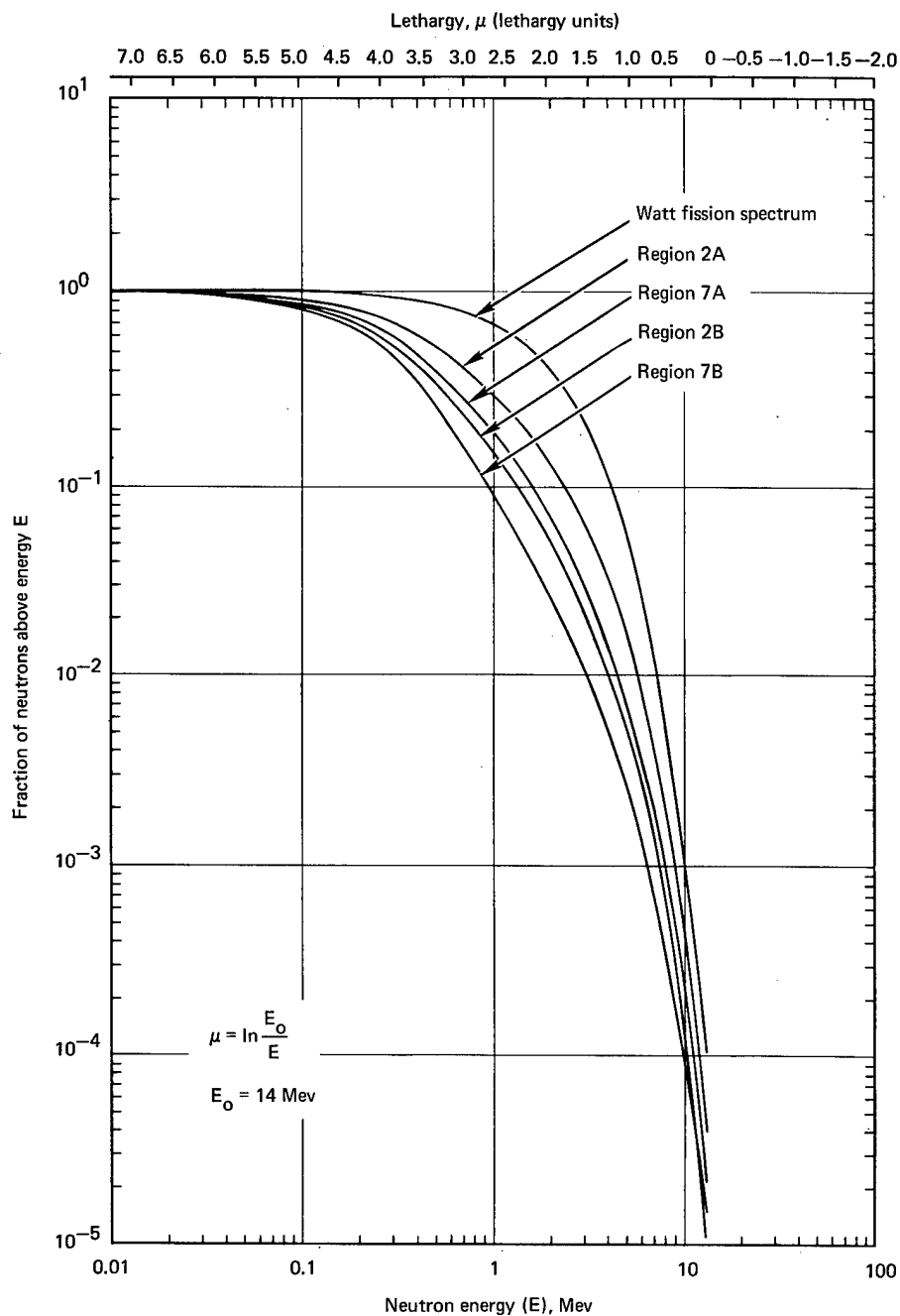


Fig. 2.85 — Monte Carlo neutron flux densities above energy E for four core regions of EBR-II. Flux densities normalized to unity above 0.01 Mev.

$\text{Ti}^{46}(\text{n,p})\text{Sc}^{46}$. The $\text{Co}^{59}(\text{n},\gamma)\text{Co}^{60}$ and $\text{Fe}^{58}(\text{n},\gamma)\text{Fe}^{59}$ reactions were used to obtain information of the neutron environment at neutron energies below those obtained with the threshold reactions. A total of 148 dosimeters were used in this experiment.

The saturated activity of the Ni^{58} fast neutron dosimeters and the Co^{59} and Fe^{58} slow neutron dosimeters was normalized to unity at the core midplane and is given as a function of position in Figure 2.86. The actual values of the saturated activity for rows 2 and 7 at the core midplane are given in Table 2.14, for regions 2A and 7A. The Ni-Co dosimeter saturated activities for regions 2B and 7B were obtained from dosimeters located 15.2 cm above the core midplane, and the iron-saturated activity for regions 2B and 7B was obtained from dosimeters located 12.7 cm above the core midplane.

Using the Monte Carlo calculated spectra shown in Figure 2.84, the $\text{Ni}^{58}(\text{n,p})\text{Co}^{58}$ and $\text{Fe}^{54}(\text{n,p})\text{Mn}^{54}$ spectrum-averaged cross sections were determined for regions 2A, 2B, 7A, and 7B. These cross sections are given in Table 2.15 along with those obtained if one were to use a Watt fission spectrum. The neutron flux density ($E_n \geq 1$ Mev) was

TABLE 2.14
SATURATED ACTIVITY VALUES FOR FOILS USED IN EBR-II DOSIMETRY EVALUATION

Region	Saturated Activity, A_∞ , dis. sec ⁻¹ mg ⁻¹			
	$\text{Ni}^{58}(\text{n,p})\text{Co}^{58}$	$\text{Fe}^{54}(\text{n,p})\text{Mn}^{54}$	$\text{Co}^{59}(\text{n},\gamma)\text{Co}^{60}$	$\text{Fe}^{58}(\text{n},\gamma)\text{Fe}^{59}$
Row 2				
A	2.61×10^8	1.66×10^7	2.17×10^8	2.41×10^5
B	1.56×10^8	1.17×10^7	4.70×10^8	2.35×10^5
Row 7				
A	9.37×10^7	5.62×10^6	3.61×10^8	2.07×10^5
B	5.77×10^7	4.23×10^6	6.92×10^8	2.07×10^5

TABLE 2.15
SPECTRUM-AVERAGED CROSS SECTIONS AND FLUX DENSITIES FOR
SEVERAL CORE REGIONS OF EBR-II

Region	Cross Section, $\bar{\sigma}_f$ ($E_n \geq 1$ Mev), millibarns ^a		Neutron Flux Density, ^b ϕ ($E_n \geq 1$ Mev), n/cm ² -sec	
	$\text{Ni}^{58}(\text{n,p})\text{Co}^{58}$	$\text{Fe}^{54}(\text{n,p})\text{Mn}^{54}$	$\text{Ni}^{58}(\text{n,p})\text{Co}^{58}$	$\text{Fe}^{54}(\text{n,p})\text{Mn}^{54}$
Row 2				
A	117	103	3.19×10^{14} (2.31×10^{14})	2.45×10^{14} (1.78×10^{14})
B	84	74	2.65×10^{14} (1.38×10^{14})	2.43×10^{14} (1.27×10^{14})
Row 7				
A	89	80	1.49×10^{14} (8.23×10^{13})	1.05×10^{14} (6.02×10^{13})
B	64	59	1.28×10^{14} (5.07×10^{13})	1.10×10^{14} (4.59×10^{13})
Watt fission spectrum	162	141		

^aCross sections calculated using AFWL TR-65-34 (WL1) values; they are based on the EBR-II Monte Carlo spectra normalized to unity above 1 Mev (see Figure 2.84).

^bValues in parentheses were obtained using the Watt fission spectrum-averaged cross sections, $\bar{\sigma}_f$ ($E_n \geq 1$ Mev), as listed in this table. The average cross sections, $\bar{\sigma}_f$, in a Watt fission spectrum are 112 and 98 mb, respectively, for the Ni^{58} and the Fe^{54} (n,p) reactions; i.e., $\bar{\sigma}_f$ ($E_n \geq 1$ Mev) = $\sigma_f/0.693$.

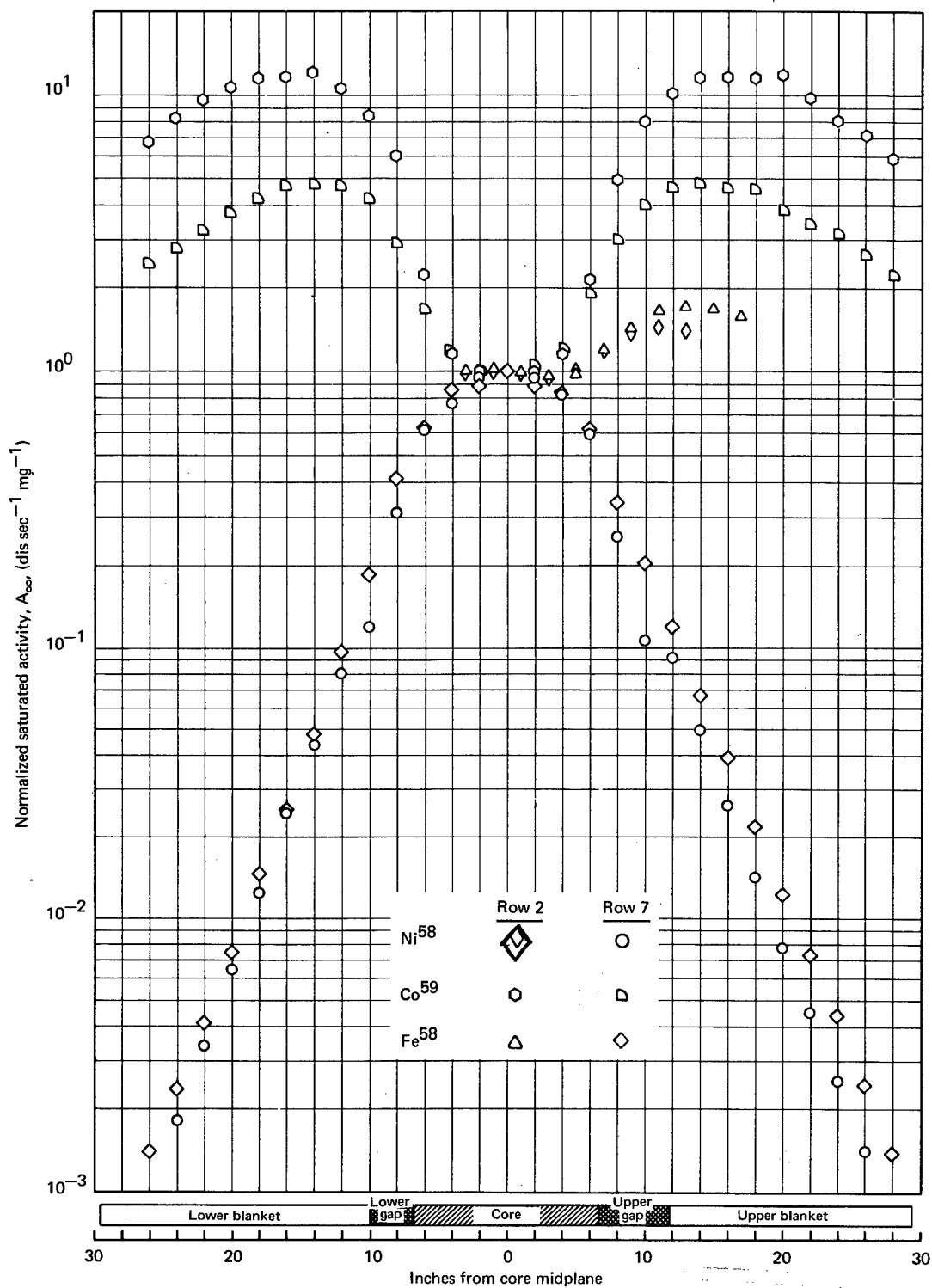


Fig. 2.86 — Saturated activity for Ni^{58} , Co^{59} , and Fe^{58} as a function of position in EBR-II, normalized to unity at the core midplane

calculated from various dosimeters located in the four regions using the spectrum-corrected cross sections. The Ni^{58} dosimeters in regions 2B and 7B were located 15.2 cm above the core midplane. The Fe^{54} dosimeters in regions 2A and 7A were located 2.54 cm above the core midplane, and the Fe^{54} dosimeters in regions 2B and 7B were located 12.7 cm above the core midplane.

The neutron flux density ($E_n \geq 1$ Mev) as measured by the Fe^{54} dosimeters listed in Table 2.15 is essentially constant in going from the midplane to 12.7 cm above the midplane for either row 2 or row 7. Although the saturated activity is reduced about 40 percent, the spectrum-averaged cross sections are increased by almost the same amount and consequently the neutron flux density ($E_n \geq 1$ Mev) remains virtually constant. The Ni^{58} dosimeters show a similar trend. Serious errors can result if a Watt fission spectrum is assumed for obtaining the cross sections to be used in determining neutron flux densities from foil activities. The uncertainties can range from a factor of 1.4 in region 2A up to a factor of 2.4 in region 7B.

2.5 SUMMARY AND CONCLUSIONS

Post-irradiation creep-rupture tests of Incoloy 800 specimens irradiated in EBR-II to fast neutron fluences ($E_n \geq 1$ Mev) up to approximately 3×10^{20} n/cm² showed that the rupture life is reduced by irradiation when tested at 540°C but increased for a test temperature of 705°C. Correspondingly the minimum creep rate is increased at 540°C but decreased at 705°C. Post-irradiation rupture elongation values and in the region of 15 to 20 percent or about one-third the unirradiated value at 540°C, and in the region of 20 to 50 percent at 705°C, which is about one-half the unirradiated values.

Post-irradiation creep-rupture properties of Hastelloy X specimens irradiated in either ETR or EBR-II comparable fast fluences are essentially the same for both types of irradiation. The ductility determined by elongation measurements is about 5 percent for specimens irradiated to a fast neutron fluence of 3.2×10^{20} n/cm² ($E_n \geq 1$ Mev) compared to about 80 percent for the control at a test temperature of 704°C.

Hastelloy R-235 containing the same total boron (50 ppm) concentration but varying B^{10} isotope content and post-irradiation creep-rupture tested at 870°C showed increasing damage with increasing B^{10} content. This clearly supports the proposed mechanisms that the B^{10} isotope, in some manner, contributes to reduced ductility of irradiated alloys.

Transmission electron microscopy studies on irradiated A-286 and Hastelloy R-235 show shells of localized high-damage regions (dislocations) and gas bubbles with radii approximating the recoil distance of lithium and alpha particles in iron or nickel. The range of the lithium particle is calculated to be approximately 1 micron and that of the alpha to be about 2 microns.

Resistivity studies of irradiated ASTM-A302B indicate that the embrittlement is probably caused by the formation of a carbon-defect complex. This complex recovers in the temperature range of 300° to 500°C with the subsequent resolution of carbon. Resistivity studies on this material correlate, over the wide range investigated, quite well with radiation-induced changes and the subsequent recovery of mechanical properties.

The effect of irradiation temperature on creep-rupture properties of molybdenum at 750°C was determined. Irradiation at 70°C resulted in the least effect on the time to rupture; irradiation at 700°C and 1000°C showed increases in the time to rupture by factors of 12 and 18, respectively. There was also a relatively long second-stage creep period which increases with an increase in the irradiation temperature. Post-irradiation annealing at 1000°C of a specimen irradiated at 700°C did not produce a significant change in the creep rate but did increase the rupture life by 25 percent over that observed in the as-irradiated (700°C) condition. →

Accelerated creep of irradiated molybdenum was observed at 580°C. Delayed creep, a period of time during the initial portion of the creep curve in which essentially no creep is observed to occur, was observed at 600°, 700°, and 750°C in specimens irradiated at reactor-ambient temperature. The accelerated creep was observed only for those specimens irradiated at the lower fluence (4.8×10^{18} n/cm², $E_n \geq 1$ Mev). Delayed creep to date has not been observed in control specimens, in tests of ambient temperature irradiated specimens at 580°, 850°, or 900°C, nor in 700°C and 1000°C irradiated specimens.

The effect of post-irradiation annealing on the 700°C creep-rupture properties of irradiated ($1-3 \times 10^{20}$ n/cm²) molybdenum at two carbon levels, 26 ppm and 205 ppm, was studied. An annealing temperature of 900°C is necessary to remove the incubation period for delayed creep. Although an anneal at 1600°C eliminated the incubation period, this heat treatment does not restore the properties to control values. The data suggest the formation of stable defects at temperatures between 900° and 1200°C which tend to strengthen the irradiated material for those test conditions.

Initial results of the effects of irradiation at reactor-ambient ($\sim 70^\circ\text{C}$) temperatures to fast neutron fluences of 2.1×10^{20} n/cm² ($E_n \geq 1$ Mev) on niobium and Nb - 1Zr tensile specimens show that the room-temperature yield strengths are increased about 110 and 200 percent respectively for the two materials. The yield strength increases at 650°C are about 93 and 110 percent, respectively, for niobium and Nb - 1Zr. The ductility of 360°C and 650°C of both metals is significantly reduced as a result of irradiation. Complete recovery occurs in the room-temperature strength and ductility of both metals following a 1000°C anneal for 1 hour.

A detailed study of the various recovery stages observed in resistivity measurements of isochronally annealed irradiated molybdenum was conducted. Molybdenum appears to saturate at about 1×10^{20} n/cm² ($E_n \geq 1$ Mev) with the saturation effect occurring as a resistivity maximum rather than the normal asymptotic approach. No significant stage III ($\sim 0.15 T_m$) temperature shift nor residual resistivity was observed at high fluences or anneal temperatures; this indicates negligible transmutation reactions. The unusual saturation behavior apparently arises from the relatively high irradiation temperature ($0.12 T_m$) leading to a removal of free self-interstitials, with only excess vacancies left behind.

Hot-hardness studies of irradiated 73 percent warm-worked tungsten and irradiated recrystallized tungsten of the same sheet showed a factor of 3 greater radiation-induced hardening in the recrystallized material. Hardening occurred primarily in the athermal portion of the curve from 280°C ($0.15 T_m$) to 1050°C ($0.36 T_m$). Tests on recrystallized tungsten following either 73 or 98 percent warm working show the same values for either original material in the unirradiated and irradiated conditions. The hardness increase was the same for both cases, indicating that the substructure was the same for both materials. The 73 percent warm-worked material showed a radiation-induced hardness increase at 316°C ($0.16 T_m$); the 98 percent warm-worked material showed no additional increase.

Hot-microhardness data were also determined for Nb, Nb - 1Zr, Mo, Mo - 0.5Ti, 306 alloy (W - 30Re - 30Mo, at. %), 256 alloy (W - 30Mo - 25Re, at. %), Ta, and Ta - 10W from 25° to 1200°C. Most tests showed that the ultimate yield strength (σ_u) increases linearly with an increase in the hot-hardness (H_v) values when compared at corresponding temperatures. The relationship $\sigma_u = A H_v$, where A is a dimensionless number with values ranging from 0.3 to 0.4.

Transmission electron microscopy was used to study the annealing behavior of small defects in irradiated tungsten and to determine the crystallography of dislocation loops formed during this annealing. These studies revealed a complex annealing process attri-

buted to the presence of two overlapping temperature regions within which different defect species become mobile. At temperatures below 435°C annealing results from migration of free interstitials; annealing above this temperature is related to vacancy migration. Dislocation loops formed during high-temperature annealing (1100°C) are vacancy in nature and pure edge in character, lying on $\{111\}$ planes and having $a/2\langle 111 \rangle$ Burgers vectors.

Microstructures of molybdenum irradiated at three different temperatures and creep-rupture tested at 750°C were studied by transmission electron microscopy. These observations revealed many interstitial dislocation loops throughout the matrix in specimens irradiated at 70°C and 700°C. In the specimen irradiated at 700°C, a zone about 1 micron wide, denuded of loops, parallels the grain boundaries. The specimen irradiated at 1000°C contained no loops within the matrix, but showed occasional loops thought to be vacancy in nature near grain boundaries. This specimen also showed evidence of small precipitates, believed to be carbides, which pin mobile dislocations.

Preliminary evaluation of the Monte Carlo spectrum calculations and the influence on fast neutron cross sections for the $\text{Ni}^{58}(n,p)$ and $\text{Fe}^{54}(n,p)$ reactions of wires irradiated in EBR-II was completed. Results show that although the experimentally determined saturated activity measured with the wire detectors is reduced about 40 percent from the core center to the core edge, the spectrum average cross sections ($E_n \geq 1$ Mev) are increased almost by the same amount. Consequently, the fast neutron fluence ($E_n \geq 1$ Mev) remains virtually constant throughout the core region. Serious errors can result if a Watt fission spectrum is assumed in the determination of the average reaction cross section of these detector wires. The resulting errors can be low by a factor of 1.4 in the center of the core up to a factor of 2.4 in the core region near the edge.

2.6 PLANS AND RECOMMENDATIONS

Investigations will continue to study the basic mechanisms of the effects of neutron irradiation on the stress-, strain-, time-, and temperature-dependent properties of selected heat-resistant alloys and refractory metals. Contributing mechanisms will be identified by considering current dislocation theories coupled with analyses of experimental data generated by creep, tensile, resistivity, and hot-hardness measurements and by direct observations of radiation-induced defects with the transmission electron microscope.

Particular emphasis will be given to the problem of radiation-induced changes in the ductility of some of these metals and alloys and to the importance of neutron spectra and fluence on both the substructure and the resulting mechanical properties.

In view of the need for information concerning the effect of neutron-induced changes in welds, a weld evaluation program will be initiated on selected candidate materials for fast breeder reactors. Selected materials will initially be limited to the heat-resistant alloys. Early work will concentrate on the general behavior of welds in unirradiated alloys.

Current investigation of the mechanisms of neutron-radiation-induced defects in various metals and alloys by isochronal and isothermal resistivity studies will be continued. Isothermal studies will be expanded to furnish migration energies and jump frequencies for various defect stages. Resistivity studies will be expanded to include iron- and nickel-base alloys, vanadium, and vanadium alloys. These resistivity studies will also be used to investigate the kinetics of bubble (or cavity) diameter changes and their influence on the cladding void volume.

Isothermal hot-hardness studies will be continued to investigate activation energies associated with various defect recovery stages in irradiated materials. Use of the hot-

hardness apparatus to study creep phenomena by varying indenter holding times will be conducted to employ hot-hardness methods for defining important temperature regions to be studied in tensile tests and to provide data for correlating and interpolating ultimate tensile strength of various irradiated alloys.

Detailed transmission electron microscopy studies to further define the kinetics of defect cluster and loop formation will be conducted. Emphasis will be placed on electron microscopy, resistivity, and density studies to define the number and size of defect loops, cavities, and/or gas bubbles for correlation with corresponding strength and hardness properties and changes in ductility.

Creep-rupture and tensile testing of irradiated specimens will be continued at temperatures above and below the prominent recovery regions to evaluate the magnitude and mechanisms of the neutron-irradiation-induced changes in properties. Particular emphasis will be given to those materials irradiated in EBR-II to fluences up to about 5×10^{22} n/cm². These studies will include detailed investigations on the radiation-induced changes in first- and second-stage creep behavior by the technique of applied stress changes on single specimens. The study of molybdenum and niobium alloys will be continued on potential LMFBR candidate materials including the vanadium-base alloys.

2.7 REFERENCES

1. Busboom, H. J. and Mathay, P. W., "Fast Neutron Damage Studies in High Nickel Alloys," GE-APED, GEAP 4985, August 1966.
2. Stiegler, J. O. and Weir, J. R., "Effects of Irradiation on Ductility," ORNL, ORNL-TM-2019, January 1968.
3. Monkman and Grant, Trans. ASTM, Vol. 56, 1956, p. 593.
4. "AEC Fuels and Materials Development Program Progress Report No. 69," GE-NMPO, GEMP-69, September 29, 1967, pp. 50-58.
5. Woodford, D. A., "Constant Load Creep Data Interpreted in Terms of the Stress Dependence of Dislocation Velocity," Trans. Met. Soc. AIME, Vol. 239, May 1967, pp. 655-659.
6. "Annual Progress Report for Period Ending June 30, 1966," ORNL, Metals and Ceramics Division, ORNL-3970, Table 20.3, p. 116.
7. Harwell, UK-AEA, private communications.
8. "Sixth Annual Report - High-Temperature Materials Program, Part A," GE-NMPO, GEMP-475A, March 31, 1967, pp. 205-208.
9. Wagenblast, H., Fujita, F. E., and Damask, A. C., "Kinetics of Carbon Precipitation in Irradiated Iron-IV Electron Microscope Observations," Acta Met., Vol. 12, 1964, pp. 347-353.
10. Fujita, F. E. and Damask, A. C., "Kinetics of Carbon Precipitation in Irradiated Iron-II Electrical Resistivity Measurements," Acta Met., Vol. 12, 1964, pp. 331-339.
11. Carpenter, G. F., Knopf, N. R., and Byron, E. S., "Anomalous Embrittling Effects Observed During Irradiation Studies on Pressure Vessel Steels," Nucl. Sci. and Engr., Vol. 19, 1964, pp. 18-38.
12. Steele, L. E. and Hawthorne, J. R., "New Information on Neutron Embrittlement Relief of Reactor Pressure Vessel Steels," ASTM, STP-380, 1965, p. 289.
13. GEMP-475A, pp. 201-204.
14. "AEC Fuels and Materials Development Program Progress Report No. 71," GE-NMPO, GEMP-1002, December 29, 1967, pp. 48-50.
15. GEMP-69, pp. 58-61.
16. Gleiter, H. and Hornbogen, E., "Theory of the Interaction of Dislocations with Coherent Ordered Zones, (1)," (In German), Phys. Status Solidi, Vol. 12, 1965, pp. 235-250.

17. Copley, S. M. and Kear, B. H., "A Dynamic Theory of Coherent Precipitation Hardening with Application to Nickel-Base Superalloys," *Trans. AIME*, Vol. 239, 1967, pp. 984-992.
18. Raymond, E. L., "Effect of Grain Boundary Denudation of Gamma Prime on Notch-Rupture Ductility of Inconel Nickel-Chromium Alloys X-750 and 718," *Trans. AIME*, Vol. 239, 1967, pp. 1415-1422.
19. Gleiter and Hornbogen, op. cit., pp. 251-264.
20. Mastel, B. and Brimhall, J. L., "The Combined Effect of Carbon and Neutron Radiation on Molybdenum," *Acta Met.*, Vol. 13, 1965, pp. 1109-1116.
21. GEMP-475A, pp. 69, 70.
22. Brimhall, J. L. and Mastel, B., "Effect of Prestrain and Subsequent Neutron Irradiation on Molybdenum," *Acta. Met.* Vol. 14, No. 4, April 1966, pp. 539-541.
23. Damask, A. C. and Dienes, C. J., "Point Defects in Metals," Gordon and Breach, New York, 1963, pp. 146-147.
24. GEMP-400A, pp. 86-90.
25. GEMP-475A, pp. 80-82.
26. GEMP-1002, pp. 61-63.
27. GEMP-1002, p. 60.
28. Tietz, T. E. and Wilson, J., "Behavior and Properties of Refractory Metals," Stanford University Press, 1965, p. 20.
29. Geary, A. L., "Fundamental and Applied Research in Metallurgy," Nuclear Metals, Inc., NMI-1258, September 17, 1963, p. 11.
30. Petty, E. R. and O' Neill, H., "Hot Hardness Values in Relation to the Physical Properties of Metals," *Metallurgia*, Vol. 63, 1961, pp. 25-30.
31. Westbrook, J. H., "Temperature Dependence of the Hardness of Pure Metals," *Trans. ASM*, Vol. 45, 1953, pp. 221-248.
32. O' Neill, H., "Hardness Measurement of Metals and Alloys," 2nd Ed., Chapman and Hall, Ltd., London, England, pp. 153-207.
33. Wronski, A. S. and Johnson, A. A., "A Hardening Effect Associated with Stage III Recovery in Neutron-Irradiated Molybdenum," *Phil.*, Vol. 8, No. 90, June 1963, pp. 1067-1070.
34. GEMP-475A, pp. 73-77.
35. GEMP-400A, pp. 76-77.
36. Makin, M. J. and Minter, F. J., "The Mechanical Properties of Irradiated Niobium," *Acta Met.*, Vol. 7, June 1959, pp. 361-366.
37. GEMP-475A, pp. 73-74.
38. "AEC Fuels and Materials Development Program Progress Report No. 67, GE-NMPO, GEMP-67, June 30, 1967, p. 55.
39. GEMP-475A, pp. 93-96.
40. Peacock, D. R. and Johnson, A. A., "Stage III Recovery in Neutron-Irradiated Molybdenum and Niobium," *Phil. Mag.* Vol. 8, 1963, pp. 275-284.
41. Holmes, D. K., "The Interaction of Radiation with Solids," North Holland Publishing Company, 1964, p. 147.
42. Kissinger, H. E., Brimhall, J. L., and Mastel, B., "Physical Characterization of Molybdenum Single Crystals for Irradiation Experiments," International Conference on Characterization of Materials, Pennsylvania State University, November 16-18, 1966.
43. GEMP-475A, p. 83.
44. GEMP-69, pp. 37-44.
45. Ibragimov, S. S., Lyashenko, V. S., and Zavyalov, A. I., "An Investigation of the Structure and Properties of Several Steels and Other Metals After Irradiation with Fast Neutrons," *J. Nucl. Energy*, Vol. 16, 1962, pp. 45-49.

46. Keys, L. K., Smith, J. P., and Moteff, J., "High Temperature Recovery of Neutron-Irradiated Tungsten," *Bulletin of the American Physical Society*, Vol. 13, 1968, p. 463.
47. Kinchin, G. H. and Thompson, M. W., "Irradiation Damage and Recovery in Molybdenum and Tungsten," *J. Nucl. Energy*, Vol. 8, 1958, pp. 275-284.
48. GEMP-69, p. 46.
49. GEMP-69, p. 42.
50. Kinchin and Thompson, *op. cit.* p. 279.
51. Nihoul, J., "The Recovery of Radiation Damage in Molybdenum," *Phys. Stat. Solidi*, Vol. 2, 1962, p. 310.
52. Kinchin and Thompson, *op. cit.*, p. 280.
53. GEMP-475A, Figure 2.23, p. 87.
54. Lomer, W. H. and Cottrell, A. H., "Analysis of Point Defects in Metals and Alloys," *Phil. Mag.*, Vol. 46, 1955, pp. 701-719.
55. DeJong, M. and Afman, H. B., "Resistometric Measurements on Molybdenum Irradiated with 2.5 Mev Electrons," *Acta Met.*, Vol. 15, 1967, pp. 1-12.
56. Lacefield, K., Moteff, J., and Smith, J. P., "Neutron Radiation Damage in Tungsten Single Crystals," *Phil. Mag.*, Vol. 13, 1966, p. 1079.
57. Rau, R. C., Moteff, J., and Ladd, R. L., "Comparison of Microstructure with Mechanical Properties of Irradiated Tungsten," *J. Nucl. Mat.*, Vol. 24, 1967, p. 164.
58. Higgins, P. R. B. and Roberts, A. C., "The Nature and Annealing Behavior of Fission Fragment Damage in Molybdenum," *J. Less-Common Met.*, Vol. 6, 1964, p. 472.
59. Downey, M. E. and Eyre, B. L., "Neutron Irradiation Damage in Molybdenum," *Phil. Mag.*, Vol. 11, 1965, p. 53.
60. Meakin, J. D. and Greenfield, I. G., "Interstitial Loops in Neutron-Irradiated Molybdenum," *Phil. Mag.*, Vol. 11, 1965, p. 277.
61. Ladd, R. L. and Rau, R. C., "Immersed Double-Jet Technique for Electrothinning Tungsten for Transmission Electron Microscopy," *Rev. Sci. Instr.*, Vol. 38, 1967, p. 1162.
62. Hirsch, P. B., Howie, A., and Whelan, M. J., "A Kinematical Theory of Diffraction Contrast of Electron Transmission Microscope Images of Dislocations and Other Defects," *Phil. Trans. Roy. Soc. A*, Vol. 252, 1960, p. 499.
63. Mazey, D. J., Barnes, R. S., and Howie, A., "On Interstitial Dislocation Loops in Aluminium Bombarded with Alpha-particles," *Phil. Mag.*, Vol. 7, 1962, p. 1861.
64. Bilby, B. A., Bullough, R., and Smith, E., "Continuous Distributions of Dislocations: A New Application of the Methods of Non-Riemannian Geometry," *Proc. Roy. Soc. A*, Vol. 231, 1955, p. 263.
65. GEMP-67, pp. 60-61.
66. GEMP-69, pp. 44-48.
67. Moteff, J. and Smith, J. P., "Recovery of Defects in Neutron-Irradiated Tungsten," *ASTM STP-380*, 1965, p. 171.
68. GEMP-475A, pp. 82-89.
69. Attardo, M. and Galligan, J. M., "A Field Ion Microscope Study of Neutron-Irradiated Tungsten," *Phys. Stat. Sol.*, Vol. 16, 1966, p. 449.
70. Attardo, J. J., Galligan, J. M., and Chow, J. G. Y., "Interstitial Removal in Stage-III Recovery of Neutron-Irradiated W," *Phys. Rev. Letters*, Vol. 19, 1967, p. 73.
71. Jeannotte, D. and Galligan, J. M., "Energy of Motion of Vacancies in Tungsten," *Phys. Rev. Letters*, Vol. 19, 1967, p. 232.
72. Edmondson, B. and Williamson, G. K., "On the Determination of the Nature of Dislocation Loops," *Phil. Mag.*, Vol. 9, 1964, p. 277.
73. Mastel, B., Kissinger, H. E., Laidler, J. J., and Bierlein, T. K., "Dislocation

- Channeling in Neutron-Irradiated Molybdenum," J. Appl. Phys., Vol. 34, 1963, p. 3637.
74. GEMP-69, pp. 29-31.
 75. Mastel and Brimhall, op. cit., p. 1109.
 76. Brimhall, J. L., Mastel, B., and Bierlein, T. K., "Thermal Stability of Radiation Produced Defects in Molybdenum," Acta Met.
 77. Dingley, D. J. and Hale, K. F., "Burgers Vectors of Dislocations in Deformed Iron and Iron Alloys," Proc. Roy. Soc. A, Vol. 295, 1966, p. 55.
 78. Masters, B. C., "Dislocation Loops in Irradiated Iron," Phil. Mag., Vol. 11, 1965, p. 881.

3/ ADVANCED FAST BREEDER REACTOR FUEL ELEMENT CLADDING DEVELOPMENT

(1115)

E. S. Funston,* C. O. Tarr†

The objective of this program is to further the technology of refractory metals and, in particular, the new refractory metals developed under this task, to permit their early utilization in the high-temperature reactor programs sponsored by the AEC. Research will continue to develop and obtain new refractory metals which will make possible marked improvements in the temperature and life capabilities of nuclear powerplants. *194*

This task was redirected during calendar year 1967 to emphasize the advanced fast breeder fuel element cladding development activities. Included in the reoriented task is the requirement to produce refractory metal thermoelement wire (W-Os) and small-diameter tungsten alloy tubing that cannot be obtained commercially.

3.1 REFRACTORY METAL ALLOY TUBING, SHEET, AND WIRE PRODUCTS

The major effort during CY-67 was directed toward developing processing procedures for the production of quality seamless W-Re-Mo tubing, sheet, and bar and W-Os wire. Special emphasis was placed on the development of fabrication procedures for seamless tubing and trial production of specific tubing sizes. In order to carry out these tasks, special processing equipment was designed and installed.¹

The key items of equipment include:

1. Facilities for the purification of metal powders, sintered compacts, and sintered mill products (acid leaching facilities and various annealing furnaces with controlled hydrogen atmosphere; -50°C to +5°C).
2. An experimental 20,000-pound capacity variable-speed draw bench for mandrel drawing of seamless tubes up to 5.0-cm OD by 366-cm finished length, Figure 3.1. A special feature of the draw bench includes an electronic control console for manual or automatic control of the drawing operation by selection of wave amplitude (force) and frequency (variable from 30 to 30,000 kc/sec). Data obtained from this equipment, including load cell read-out, yield information directly applicable to the working characteristics of each alloy.
3. Six hydraulically controlled draw benches for repetitive production runs of seamless tubing to 2.0-cm OD by 160-cm finished length, Figure 3.2.
4. Accessory equipment required to meet the quality standards for refractory alloy seamless tubing (quenching fixture to assure meeting straightness tolerances of hardened tool steel mandrels; honing fixtures to eliminate gouging or scoring of the ID surface of the tubes during the honing operation).

*Project leader.

†Principal investigator.

¹"AEC Fuels and Materials Development Program Progress Report No. 71," GE-NMPO, GEMP-1002, December 29, 1967, pp. 68-76.

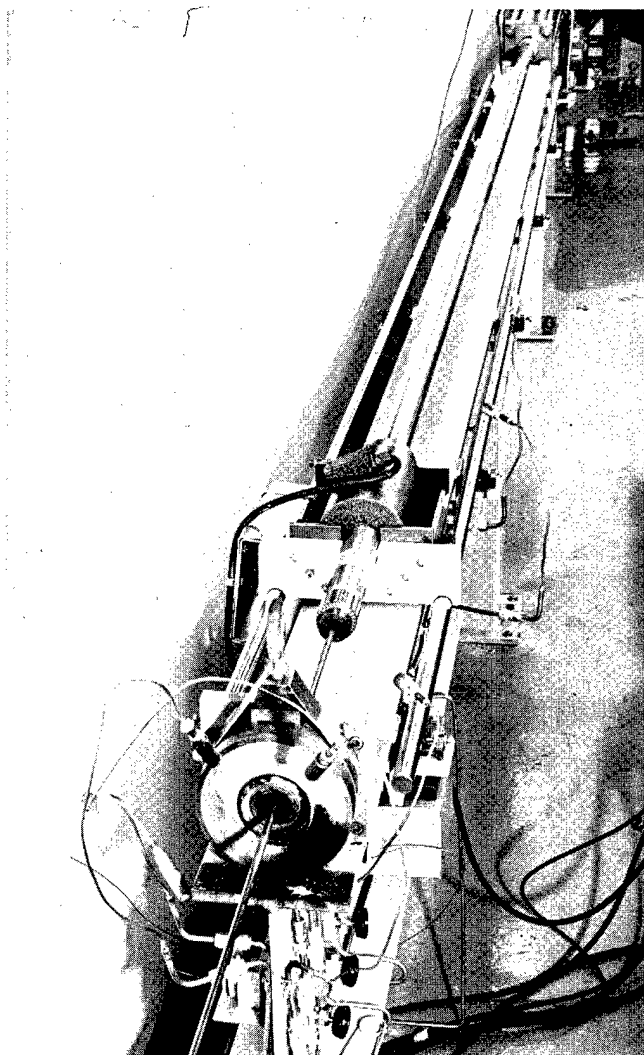


Fig. 3.1 — Draw bench for developing procedures in drawing tubing up to 5.0-cm diameter by 366-cm long, finished size. Actual draw stroke of the machine is 426 cm. Photo shows a work piece on a hardened mandrel passing through a die. The dark cylinder with an attached electric cable at the rear of the draw chuck is a tensile load cell attached to a recorder. Valves and burners for warming the workpiece and the hardened mandrel can be observed near the die holder. Commercial stroke alignment rails appear as 3.8-cm-diameter bars on each side of the draw length. (Neg. P67-10-94)

5. A beryllia-insulated, molybdenum-lined annealing furnace capable of operating continuously at 1650°C in hydrogen atmosphere, Figure 3.3. A water-cooled chamber is attached to the front of the molybdenum muffle to permit purging of the furnace with inert gas and hydrogen before the work load passes into the hot zone.
6. A wire drawing facility capable of warm drawing W-Os and W-Re alloy wire to 0.0025 cm diameter. Diamond-coated dies are employed and heating of the wire is accomplished by induction or gas burners.
7. Facilities for reclamation of rhenium from W-Re, W-Re-Mo, and Mo-Re alloys.

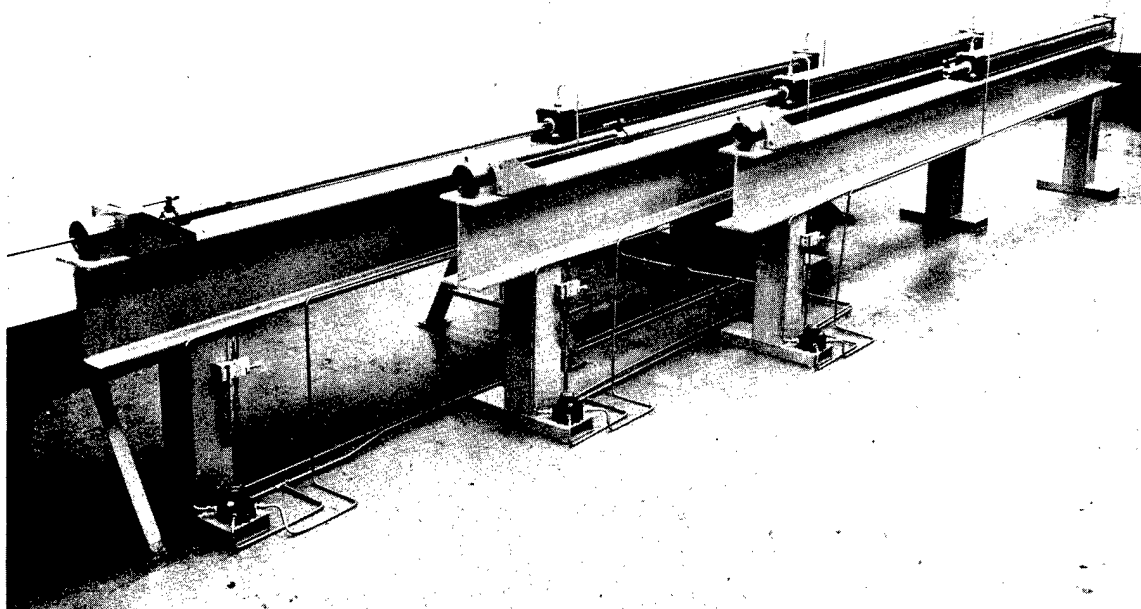


Fig. 3.2 — Repetitive work tube-drawing benches. One operator controls four benches of this type. Three benches, as shown, are controlled by hydraulic valving with motion established by a foot-operated valve mounted on the horizontal pedestal bracket below the die station of each draw bench. Speed control is provided by the micrometer flow-control valve mounted above the foot-control position. (Neg. P67-10-9B)

The processing procedures developed or selected for the fabrication of the various W-Re-Mo alloy mill products required in the program are shown schematically in Figure 3.4 and apply to both powder-metallurgy and arc-cast materials. Although the flow diagram was developed specifically for W-Re-Mo alloys, the general processing sequence can be adapted to the fabrication of tungsten and molybdenum and other solid-solution alloys of tungsten and molybdenum. The material processed from arc-cast ingots was produced from metal powders which were purified, isostatically compacted, and hydrogen sintered at NMPO. The sintered electrodes were double arc melted through the cooperation of the U. S. Department of the Interior, Bureau of Mines, Albany, Oregon.

Primary breakdown of the arc-cast or sintered billets is accomplished by extrusion at NMPO using a 1250-ton Loewy horizontal extrusion press. In FY 1968, a total of 70 billets were extruded at NMPO; a summary of the alloys which were extruded is presented in Table 3.1 and pertinent processing data are presented in Table 3.2.

SEAMLESS TUBING

For the production of seamless tubing, machined hollows (2.50 – 5.14-cm OD) of both arc-cast ingots and sintered billets were encased in molybdenum and coextruded to 1.5- or 2.0-cm-diameter product out of a 13.18-cm ID container. After extrusion, the molybdenum is removed by leaching in a concentrated nitric acid solution leaving the W-Re-Mo alloy tube hollow. The resulting tube hollow is then cut to appropriate lengths and sized and honed for warm drawing to 0.39- to 1.27-cm OD seamless tubing. Drawing is carried out at temperatures of 200°C using a WS₂ lubricant. Frequent intermediate stress relief anneals are required to eliminate laminations or in severe cases fracture of the tube.

In the case of purified molybdenum, Mo – 35Re and Mo – 5W alloys, it was necessary to wrap the hollow extrusion billet with 0.005-cm thick tungsten foil so that the nitric acid leaching treatment designed to remove the molybdenum jacket would not attack the purified

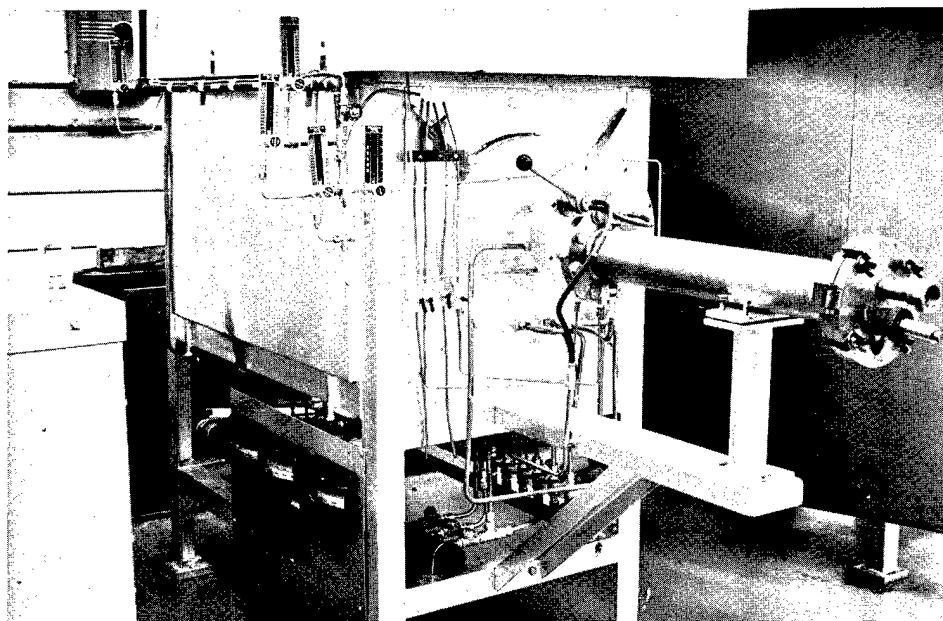


Fig. 3.3 — Beryllia-insulated, hydrogen-atmosphere furnace operated continuously at 1650°C in stress-relieving W-base alloys during processing to tubing or sheet. The fore chamber is water-cooled, and permits purging the work load with inert gas and hydrogen before entering the furnace hot zone. (Neg. P67-5-12C)

molybdenum or molybdenum alloy extrusion. The tungsten alloy foil also has been used for W-30Re-30Mo alloy extrusions to suppress surface irregularities due to selective acid attack.

Seamless tube processing of refractory alloys must be adaptable to a wide range of sizes. Extrusions of W-25Re-30Mo alloy with an ID/OD ratio of 0.471, as-extruded, represent the heaviest-walled tubular extrusions made at NMPO; the finished tube had an ID/OD ratio of 0.27. Normally, tubes are processed with a relatively thin wall having an ID/OD ratio of 0.96. The heaviest arc-cast billet of W-25Re-30Mo alloy that was extruded weighed 38 kg; and the heaviest powder-metallurgy billet processed at NMPO weighed 29 kg. Larger sizes exceed the isostatic pressing and sintering furnace capacity for metal powders at NMPO. However, through the cooperation of the Oak Ridge National Laboratory Y-12 plant, a large 14.5-cm diameter W-25Re-30Mo alloy powder compact was prepared for purification at NMPO, Figure 3.5. After sintering, the compact shrank to 11.1-cm diameter. No further processing is planned with this billet at this time.

SHEET

Hot working procedures for powder-metallurgy W-25Re alloy specifies an 80 percent gage reduction to eliminate sintering voids. A study was conducted to determine the percent hot reduction required to eliminate voids after sintering purified W-Re-Mo alloy compacts. As shown in Figure 3.6, remnants of voids remain after as much as 69 percent reduction of a sintered W-25Re-30Mo compact. After 75 percent reduction by hot rolling, however, sintering voids appear to be eliminated. Similar results were obtained for W-30Re-30Mo alloy. In this series hot rolling was carried out by heating the material to 1400°C in hydrogen; light reductions were interspaced with thorough reheating between rolling passes. These results confirm current GE-NMPO practice of specifying hot work reductions of over 80 percent to prepare W-Re-Mo alloys for subsequent cold working.

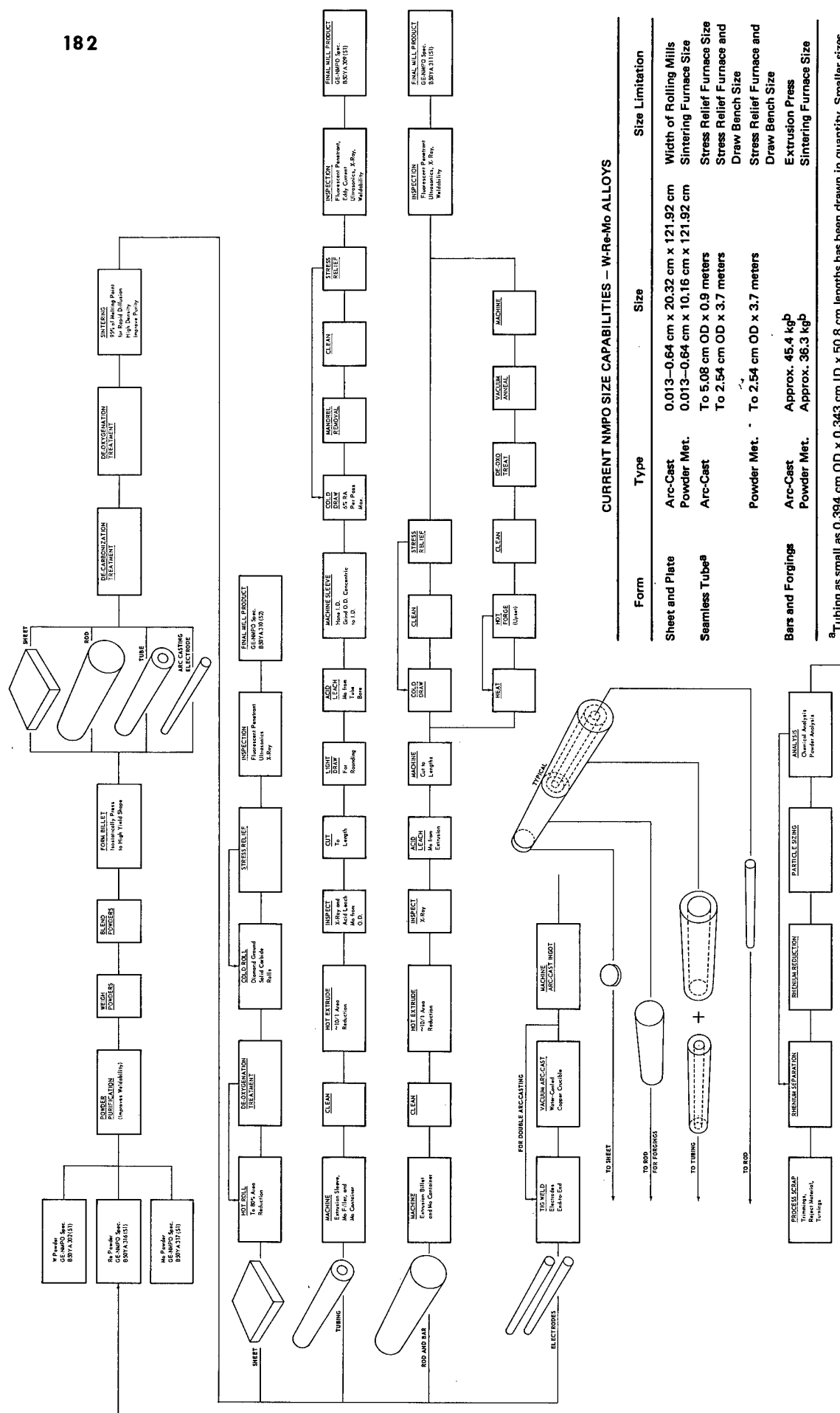


Fig. 3.4 – Flow diagram showing the various sequences involved in producing refractory metals in various forms. (AS-744)

TABLE 3.1
FY-68 EXTRUSION SUMMARY

Alloy, at. %	Bar or Rod	Tube	Remarks
W - 25Re	—	4 ^a	
W - 25Re - 30Mo	18 ^b	22 ^c	Five bars and one tube from arc-cast ingots of W - 25Re - 30Mo
W - 30Re - 30Mo	4	8	Two bars from arc-cast ingots
Mo - 35Re	2	3	Commercial Mo - 50Re (wt %) alloy
W - 0.5 Os	5 ^d	—	W - 0.5 Os for wire
Purified Mo	4	—	Two bars from arc-cast ingots
Total	33	37 ^e	

^aUltrasonic evaluation disclosed defects in one machined tube billet which was withheld from extrusion.

^bIncludes one set of isostatically pressed slabs not intended for extrusion and one large billet prepared but not extruded through July 1, 1968.

^cIncludes one W - 26Re - 30Mo alloy and one W - 30Re - 30 Mo alloy prepared for arc-melting by Bureau of Mines and mandrel extruded as tube by ORNL. Both items are now awaiting additional processing under this task.

^dExtruded from 9.65-cm-diameter billet, all others were processed from a 13.17-cm-diameter extrusion chamber.

^eIncludes eight items started for powder-metallurgy process product but diverted to arc-melted material.

SHAPES

In an auxiliary phase of this program, machining techniques on W-Re-Mo alloys were developed to permit ready-to-use test components to be supplied to advanced programs. A complex junction or welding connection of W - 25Re - 30Mo alloy produced from arc-cast ingots, to be used for a dynamic liquid metal test loop, is shown in the as-machined condition in Figure 3.7. Machining operations utilized in making this single part included surface grinding, electro-discharge machining (Elox), single-point internal thread cutting and turning, and thread grinding.

REFRACTORY METAL ALLOY WIRE DRAWING

Process development to obtain special refractory metal wire for thermocouple applications was undertaken in CY-67 and, in the last quarter, 0.0076-cm-diameter W - 0.5 Os (wt %) alloy wire was produced. The osmium addition to tungsten and W - 25Re alloy is required to compensate for the change in output emf of tungsten versus W - 25Re alloy thermocouples that occur in reactor service as a result of tungsten transmutation to rhenium and rhenium transmutation to osmium. Commercial vendors have rejected requisitions for osmium-containing alloy wires because of the toxicity of osmium. Injurious effects to NMPO personnel were avoided by use of complete coverage respiratory face masks and by the use of coatings over the material during high-temperature processing operations.

Procedures used in this work generally were conventional. Initial drawing temperatures were on the order of 650°C, light reductions were employed, and the material was given intermediate process anneals of 1400°C between each draw pass. The preferred method of cleaning the wire prior to the in-process anneals is swabbing in caustic detergent followed by a wet hydrogen treatment at 1000°C.

TABLE 3.2
PROCESSING DATA FOR REFRACTORY ALLOY EXTRUSIONS, FY 1968

Extrusion Number ^a	Alloy ^b	Product Objective	Extrusion Blank Prior to Extrusion				Completed Extrusion		Extrusion Reduction Ratio By Area	Ratio ID to OD As Extruded	Drawn Tube ID to OD Ratio
			Length, cm	OD, cm	ID, cm	Weight, g	Length, cm	OD at Center, cm			
D 76	306	Solid	5.7886	4.8158	—	1,730	48.26	1.473	8.73	—	—
D 77	50Mo—50Re	Solid	5.9055	4.8158	—	1,450	33.02	1.473	8.73	—	—
D 78	Arc-cast 306	Solid	16.0325	7.8740	—	12,780	—	—	8.20	—	—
D 79	50Mo—50Re	Tube	9.2075	4.9530	3.5941	1,171	—	—	6.77	0.725	—
D 80	Mo	Solid	Scrapped in Purification Treatment				—	—	—	—	—
D 81	256	Arc-cast Solid	12.0294	6.9215	—	7,620	—	—	7.43	—	—
D 82	50Mo—50Re	Tube	11.8364	4.6990	3.4925	1,145	—	1.930	6.45	0.743	—
D 83	306	Solid	8.9408	4.3307	—	2,133	—	1.520	10.61	—	—
D 84	50Mo—50Re	Solid	5.6890	4.8869	—	1,405	—	1.520	10.61	—	—
D 85	256	Solid	10.0022	4.3891	—	2,451	—	1.520	8.56	—	—
D 86	306	Tube	11.6586	4.7371	3.7338	1,259	—	1.930	6.51	0.788	—
D 87	50Mo—50Re	Tube	11.8948	4.6177	3.6474	995	—	—	5.49	0.789	—
D 88	256	Tube	11.2191	4.3535	3.3020	—	—	1.930	5.50	0.759	—
D 89	256	Tube	11.760	4.6355	3.3147	1,551	—	1.390	10.48	0.715	—
D 90	Mo	Arc-cast Solid	Extruded as D117 in two pieces of about equal length				—	—	—	—	—
D 91	256	Arc-cast Solid	Processed for Bureau of Mines melting and ORNL extruding				—	—	—	—	—
D 92	256	Tube	11.1125	4.4729	3.3604	1,232	—	1.390	6.11	0.751	0.87
D 93	306	Tube	11.8618	4.5948	3.6195	1,266	—	1.930	5.75	0.786	0.84
D 94	306	Tube	Scrapped in Sinter Operation				—	—	—	—	—
D 95	256	Solid	Processed for Bureau of Mines melting and ORNL extruding				—	—	—	—	—
D 96	306	Tube	11.7627	4.9047	3.5560	1,457	—	1.390	11.45	0.724	Various
D 97			Not processed to completion				—	—	—	—	—
D 98			Not processed to completion				—	—	—	—	—
D 99			Not processed to completion				—	—	—	—	—
D100	256	Tube	13.5864	5.9334	4.3180	2,852	—	1.981	8.96	0.726	0.84
D101	256	Tube	13.3350	5.9486	4.3078	2,905	—	1.981	9.28	0.724	0.84
D102	256	Tube	13.4416	5.9131	4.3688	2,786	—	1.981	8.88	0.737	0.84
D103	256	Tube	5.8420	6.0325	4.4450	1,240	—	1.981	8.29	0.736	0.84
D104	256	Tube	Used as melt stock in D118				—	—	—	—	—
D105	256	Tube	Used as melt stock in D118				—	—	—	—	—
D106	Mo	Arc-cast Solid	18.4912	7.5057	—	8,126	—	1.905	13.69	—	—
D107	256	Tube	Scrapped — Distorted in extrusion				1270	1.270	11.92	—	—
D108	256	Tube	11.8643	4.5694	3.4010	1,384	1295	1.270	11.92	0.758	0.87
D109	256	Solid	10.1244	4.3865	—	4,070	68	1.574	7.75	—	—
D110	256	Solid	11.2522	5.3035	—	4,029	45	2.540	4.33	—	—
D111	256	Melt Stock	Used for arc-cast D118				—	—	—	—	—
D112	256	Tube	11.5621	4.5034	3.3807	1,355	1271	1.270	11.92	0.751	0.87
D113	306	Tube	11.7043	4.5720	3.5255	1,334	66	1.981	5.81	0.770	—
D114	306	Tube	11.7881	4.5517	3.5255	1,295	—	1.270	11.92	0.773	0.87
D115	306	Tube	Scrapped — Distorted in extrusion				1270	1.270	11.92	—	0.87
D116	306	Tube	11.7957	4.5135	3.3223	1,445	1271	1.270	11.92	0.736	0.87
D117	Mo	Solid	20.1827	3.9700	—	2,482	132	5.227	6.30	—	—
D118	256	Arc-cast Solid	15.1739	11.8287	—	25,015	39	5.715	5.30	—	—
D119	256	Tube	10.4394	5.4838	2.5882	3,130	—	1.981	8.28	0.471	0.27
D120	256	Tube	12.7406	5.7327	2.6212	4,236	—	1.981	8.28	0.457	0.27

TABLE 3.2 (Cont.)
PROCESSING DATA FOR REFRACTORY ALLOY EXTRUSIONS, FY 1968

Extrusion Number ^a	Alloy ^b	Product Objective	Extrusion Blank Prior to Extrusion				Completed Extrusion		Extrusion Reduction Ratio By Area	Ratio ID to OD As Extruded	Drawn Tube ID to OD Ratio
			Length, cm	OD, cm	ID, cm	Weight, g	Length, cm	OD at Center, cm			
D121	256	Tube	12.7000	4.5542	2.7432	1,861	—	1.270	11.92	0.602	0.82
D122	256	Tube	12.8422	4.7625	3.5991	1,595	—	1.270	11.92	0.754	0.82
D123	256	Solid	12.0446	2.987	—	1,386	—	0.889	21.39	—	—
D124			Number not used								
D125	256	Tube	12.5730	4.8361	3.7733	1,506	—	1.905	6.38	0.781	0.96
D126	256	Tube	12.6060	4.7244	3.5204	1,557	—	1.270	11.92	0.745	0.87
D127	256	Tube	12.4561	4.7625	3.5560	1,620	—	1.270	11.92	0.745	0.87
D128	256	Tube	12.7685	4.7548	3.6830	1,492	—	1.270	12.94	0.774	0.82
D129	256	Tube			Used for D158			—	—	—	0.87
D130	256	Tube			Used for D158			1.270	—	—	0.87
D131	256	Solid			Used for D132			—	—	—	—
D132	256	Solid	11.3030	6.4338	1.6433	15,000	107	—	12.08	0.255	—
D133	256	Solid			Used for D132						—
D134	256	Tube			Used as melt stock in D158. Melt by Bureau of Mines. Made into sheet for NASA.						—
D135	256	Tube			Used as melt stock in D158. Melt by Bureau of Mines. Made into sheet for NASA.						—
D136	256	Tube			Used as melt stock in D158. Melt by Bureau of Mines. Made into sheet for NASA.						—
D137	256	Tube			Used as melt stock in D158. Melt by Bureau of Mines. Made into sheet for NASA.						—
D138	256	Tube			Used as melt stock in D158. Melt by Bureau of Mines. Made into sheet for NASA.						—
D139	250	Tube	13.0556	5.0114	3.5306	—	—	1.390	11.92	0.704	—
D140	250	Tube			Scrapped in preparation for extrusion				—	—	—
D141	250	Tube						1.270	—	—	—
D142	250	Tube	12.8905	4.7498	3.3578	2,189	—	1.905	6.44	0.706	—
D143	256	Solid	11.3030	5.1739	—	38,590	—	2.540	4.12	—	—
D144	256	Solid	10.2946	7.5082	—	7,439	—	3.556	4.29	—	—
D145	256	Solid			Not extruded in FY 1968			—	—	—	—
D146	256	Solid			Four pieces used as heavy bars, and 1 piece used as melt stock in D158						—
D147	256	Solid	11.0490	4.3738	—	2,724	—	1.346	10.35	—	—
D148	256	Tube	12.7635	6.0960	4.4450	2,951	—	1.981	9.37	0.729	—
D149	256	Tube			Used for arc-cast D118				—	—	—
D150	306	Arc-cast Solid	12.3545	7.7012	—	9,661	—	3.492	4.78	—	—
D151	W-0.5 Os	Solid	11.4782	1.5240	—	342	—	0.485	10.00	—	—
D152	256	Tube	12.0650	4.7345	3.6195	1,473	—	1.778	6.70	0.763	—
D153	W-0.5 Os	Solid			For thermocouple wire. Sizes as D151.				0.485	10.00	—
D154	W-0.5 Os	Solid			For thermocouple wire. Sizes as D151.				0.435	10.00	—
D155	W-0.5 Os	Solid			For thermocouple wire. Sizes as D151.				0.485	10.00	—
D156	W-0.5 Os	Solid			For thermocouple wire. Sizes as D151.				0.485	10.00	—
D157	256	Tube	13.3350	4.9530	3.9116	1,629	—	1.270	11.92	0.789	0.87
D158	256	Arc-cast Solid			Melted by Bureau of Mines; extruded and processed to sheet for NASA evaluation.						—

^aFour numbers not used in this series.

^b256 is GE-NSP designation for W-25Re-30Mo alloy.

306 is GE-NSP designation for W-30Re-30Mo alloy.

250 is GE-NSP designation for W-25Re alloy.

Mo-50Re is commercial designation for Mo-35% Re alloy.

Mo is GE-NSP purified unalloyed Mo.

3.2 DEVELOPMENT OF MOLYBDENUM AND ITS ALLOYS FOR FAST BREEDER REACTOR APPLICATIONS

Molybdenum is a promising candidate for containing the liquid-metal heat-transfer media in fast breeder reactors. The element resists liquid alkali metal corrosion and hydrogen embrittlement. Fuel element cladding temperatures can be increased to higher levels, i. e., greater than 650°C , because molybdenum has a significantly higher melting point than stainless steels (2610°C versus $1400^{\circ} - 1450^{\circ}\text{C}$). In addition, the resistance to radiation damage of molybdenum at service temperatures of 750°C is expected to be superior to ferritic or austenitic steels. This is particularly true with respect to the formation of helium bubbles. The low nucleation rate of helium bubbles in molybdenum and the low diffusion rates of helium to grain boundaries in molybdenum at 650°C are significant advantages over stainless steel.

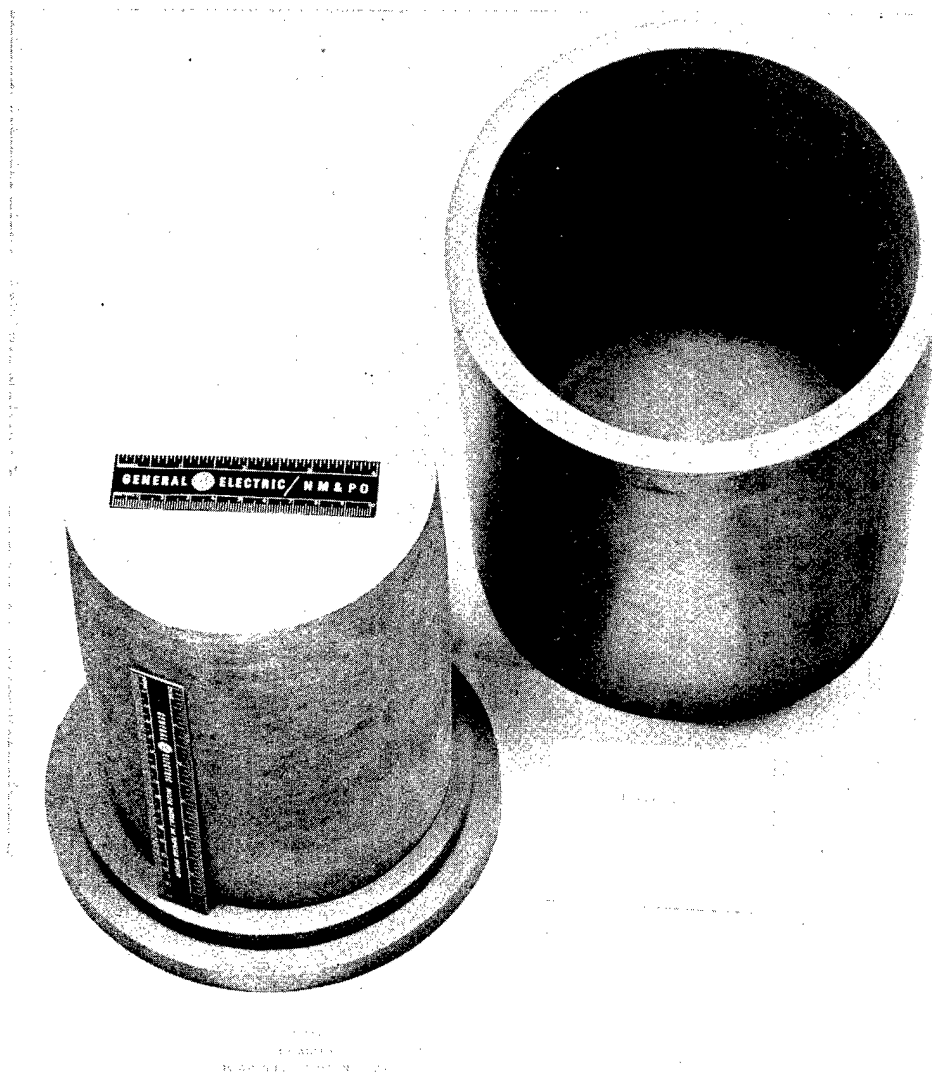


Fig. 3.5 — Compacted W — 25Re — 30Mo alloy with rubber mold used in isostatically compacting the metal powders. The specimen is laying on the mold cover. This pressing, successfully completed by Oak Ridge National Laboratory, Y-12 plant in support of this program, was conducted following purification treatment by GE-NMPO. (Neg. P67-8-3B)

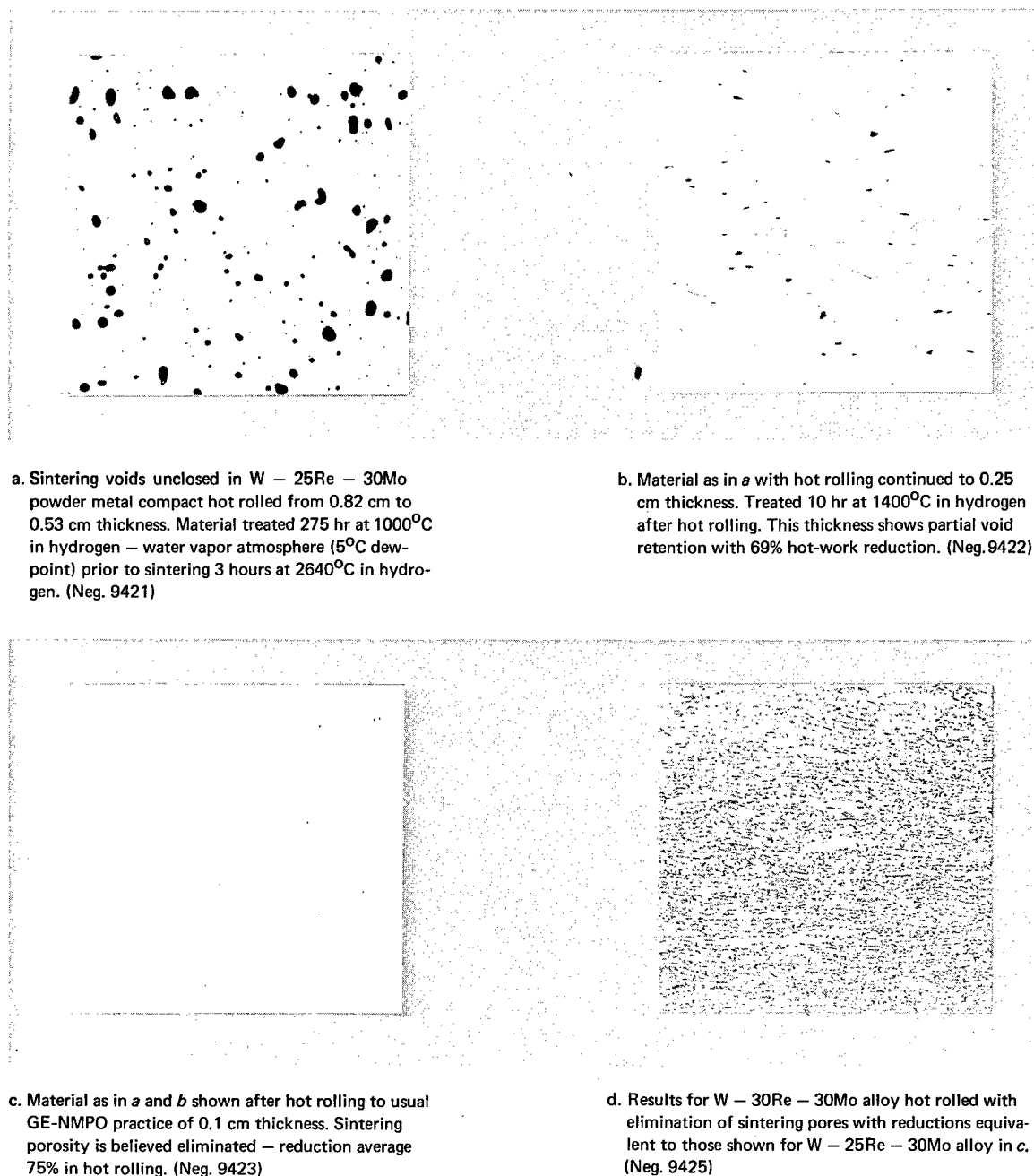


Fig. 3.6 — Photomicrograph showing the microstructures developed at major stages of the hot-rolling process on sintered W-Re-Mo alloys (Murakami etchant, 100X)

A major limitation preventing molybdenum from immediate consideration for LMFBR applications is the problem associated with ductility, particularly in weldments. Commercial molybdenum rod, tubing, and sheet stock produced by powder metallurgy techniques have been shown to develop a highly porous structure in the heat-affected area of TIG or EB weldments. Porosity in fuel element cladding stock is unacceptable. Although sound weldments can be produced in commercial arc-cast molybdenum products, the welds are brittle.

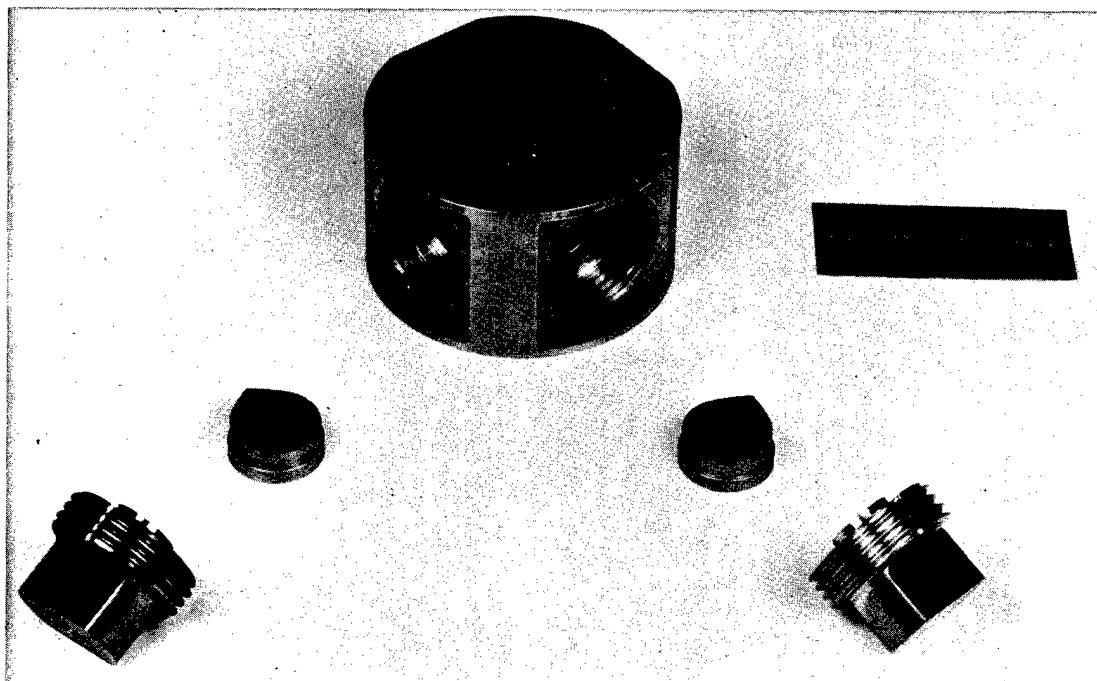


Fig. 3.7 — Welding junction and liquid-metal flow direction control, component machined from W — 25Re — 30Mo alloy. Welding of connecting tubes entering from the opposite side as shown in the photograph is accomplished through the holes shown in the foreground. The plugs shown close the welding parts. (Neg. P68-2-5C)

Research under this Task was directed toward obtaining unalloyed molybdenum products which will yield ductile non-porous EB welds. The technical approach was based upon improving the purity of the starting metal powders and maintaining the high purity during all stages of fabrication.

MOLYBDENUM PURIFICATION

The initial work directed toward improving unalloyed molybdenum for nuclear application was discussed in the preceding annual report.² At that time, treatment of metal powder compacts in hydrogen — water vapor atmospheres definitely improved the finished sheet, producing good room-temperature bend ductility in weld areas. Chemical analyses of various lots of molybdenum produced during CY-67 repeatedly showed the effectiveness of the purification treatments in lowering the carbon and oxygen levels of the molybdenum with the resultant beneficial effect on weld ductility. Reduction in the level of carbon impurities is accomplished by 1000°C, 6-week (1000 hours) treatment of the as-pressed compact in a hydrogen — water vapor atmosphere (+5°C dewpoint); carbon generally is reduced from an average of 65 ppm to 6 to 12 ppm. Oxygen impurities can be reduced from levels of 2000 to 3000 ppm in the bulk powders to approximately 40 ppm by a treatment of more than 64 hours at 1000°C in hydrogen with a low dewpoint (-40°C). Further reduction of oxygen is accomplished by similar thermal treatments after hot working operations which expose the molybdenum to air. Oxygen analyses of finished sheet were less than 20 ppm.

Although good room-temperature ductility was achieved in weldments produced in the NMPO high-purity molybdenum sheet, microporosity was not eliminated completely from the weld-affected areas. During CY-67, particular emphasis was placed on eliminating

²"Sixth Annual Report — High-Temperature Materials Program, Part A," GE-NMPO, GEMP-475A, March 31, 1967, p. 113.

all microporosity and on confirming the adequacy of the procedures developed. In the belief that microporosity in the heat-affected zone of weldments may be caused by volatilization of residual trace impurities of relatively high vapor pressure, i. e., alkali metals, etc., in the molybdenum sheet during the welding operation, attempts to eliminate or minimize the suspect trace impurities were made by leaching of the bulk powders before consolidation with various solutions including HCl, HNO₃, HNO₃ + HF + HCl, propanol, xylene, acetone, and distilled water. Credence to this hypothesis was the fact that porosity was not observed in the fused weld zone where the highly volatile metal vapors could escape when the molybdenum metal was in the liquid state (2610°C). Significantly it was found that weldments made in molybdenum sheet produced from powders which had been leached in dilute solutions of HCl (0.012M) and HNO₃ (0.014M) were free of microporosity; weldments in sheet produced from powders leached in all other solutions listed above all contained various degrees of microporosity.

To confirm the encouraging initial findings, four different batches of 0.050-cm-thick molybdenum sheet were produced using the following purification treatment:

1. Leaching bulk metal powders in dilute HCl and HNO₃ acid solutions before compacting.
2. Exposing as-compacted metal powders for prolonged periods in hydrogen – water vapor atmospheres (+5°C dewpoint) at 1000°C to lower the carbon content.

Electron beam weldments were made on sheet from each batch and all weldments were free of microporosity. The microstructure of the heat-affected zone of a weldment free of microporosity is shown in Figure 3.8. A room-temperature 2T bend across the weld of a purified unalloyed molybdenum sheet is shown in Figure 3.9. This bend represents the most stringent bend test combination considered; both the weld seam and the bend crease are parallel to the rolling direction of the sheet.

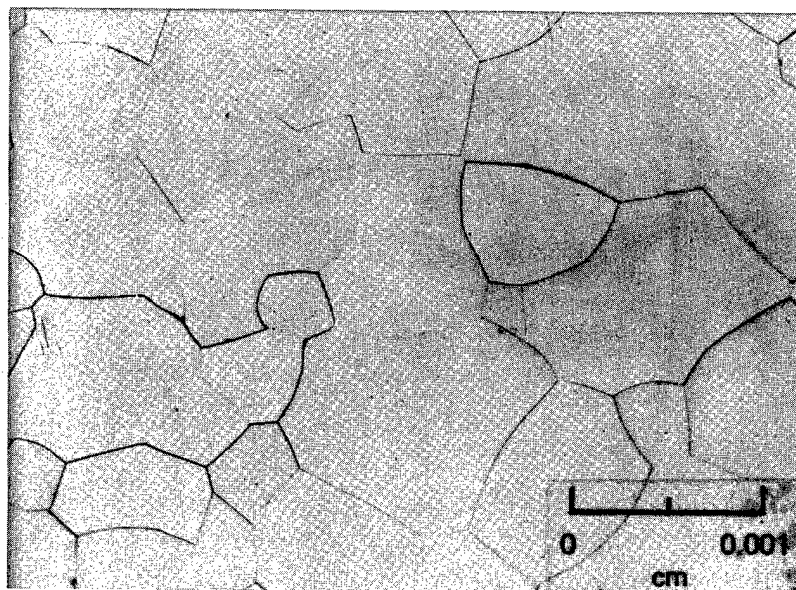


Fig. 3.8 — Microstructure of heat-affected zone in electron beam welded, purified unalloyed Mo showing absence of microporosity (Neg. MA6221, Murakami etchant, 250X)



Fig. 3.9 — Microstructure of weld zone in purified molybdenum 0.050-cm-thick sheet after 90° bend (2T) at room temperature. Weld seam and bend crease are parallel to the rolling direction.
(Neg. 10102, as-polished, 50X)

Although sheet produced from metal powders leached by dilute acid treatments have repeatedly shown a minimum of microporosity in the EB weld — heat effective zone, presumably the result of decreasing or completely removing trace element impurities, the specific trace elements involved have not been positively identified. This is because the overall level of impurities is in the low ppm range and changes in these impurities due to dilute acid leaching treatments cannot be detected and isolated by the arc-source mass spectrograph. Further studies on the purification process are in process to identify the elements contributing to microporosity in weldments.

Because of the detrimental influence of carbon and oxygen impurities on the properties of weldments, it is important to minimize contamination by these elements during the various hot and cold working operations in the processing of the sintered compact to sheet. For this reason the individual and accumulative change in carbon and gaseous impurities were determined after each major operation during processing of 24 hydrogen sintered compacts of unalloyed molybdenum to 0.038-cm-thick sheet (12 compacts were produced from powders leached in 0.012M HCl; 12 compacts were produced from powders leached in 0.014M HNO₃). Some of the pertinent results are shown in Table 3.3. Several important conclusions were reached from these studies:

1. Hot rolling purified molybdenum sheet in air from a hydrogen atmosphere results in surface contamination by oxygen, nitrogen, and carbon from the air and mill lubricants.
2. Cold rolling appears to impregnate the metal surface with rolling lubricants.
3. A hydrogen treatment (-40°C dewpoint) at 1000° to 1400°C reduces the carbon and gaseous impurities from both hot- and cold-rolled sheet.

To evaluate the influence of the dilute HCl and HNO₃ acid leaching treatments of the powder on the properties of the finished sheet, three groups of companion specimens were produced from purified molybdenum powders for bend ductility, hardness, and grain size determinations as a function of stress relief temperature (1100° — 1400°C). Processing procedures that were followed for the production of the high-purity sheet used in the evaluation were:

TABLE 3.3
CARBON AND GASEOUS IMPURITIES DETERMINED AT VARIOUS PROCESSING STAGES
IN PRODUCING UNALLOYED Mo^a

Sheet Identity	Processing Steps Completed	Reported Analytical Results, ppm			
		Carbon	Nitrogen	Oxygen	Hydrogen
N-1	Hot-roll (reduce from 0.6 cm to 0.1 cm)	19.0	6.0	77.0	1.0
C-13	Hot-roll (reduce from 0.6 cm to 0.1 cm)	15.0	5.0	41.0	2.0
C-17	Hot-roll (reduce from 0.6 cm to 0.1 cm)	27.0	—	45,9,31	—
N-8	Hot-roll (reduce from 0.6 cm to 0.1 cm)	9.0	—	21,51	—
N-1	Hot-roll + 208 hr at 1050°C in H ₂	13.0	1.0	20.0	1.0
C-13	Hot-roll + 208 hr at 1050°C in H ₂	9.0	4.0	18.0	1.0
C-17	Hot-roll + 60 hr at 1400°C in H ₂	4.0	—	13,37	—
N-8	Hot-roll + 60 hr at 1400°C in H ₂	9.0	—	9,11	—
N-3	Hot-roll + 130 hr at 1000°C in H ₂	5.0	1.0	18.0	0.8
C-16	Hot-roll + 130 hr at 1000°C in H ₂	7.0	0.6	16.0	0.6
N-3-A	Hot-roll + 130 hr at 1000°C in H ₂ , cold-rolled to 0.05 cm	27.0	2.0	22.0	1.0
N-3-A	Plus stress-relieve 20 min at 1000°C, in H ₂	7.0	1.0	16.0	1.0
C-16A	Hot-roll + 130 hr at 1000°C, in H ₂ , cold-rolled to 0.05 cm	22.0	5.0	35.0	0.9
C-16A	Plus stress-relieve 20 min at 1000°C in H ₂	8.0	0.6	10.0	0.6

^aMo received as one lot minus 325 mesh-size powder. Vendor reported 1.53 g/cm³ apparent density by ASTM B-325-58 specification, and 1.8 micron average Fisher sub-sieve diameter. Powder contained 23 ppm-C and 2920 ppm-O₂ impurities according to vendor.

1. Hydrogen-sintered compacts were hot rolled to 0.075 cm thickness in air out of a hydrogen furnace set at 1315°C. The total hot reduction was greater than 75 percent.
2. The hot-rolled sheet was treated for 175 hours in hydrogen (-40°C dewpoint) at 1000°C to remove oxygen absorbed during hot rolling.
3. The de-oxygenated sheet was cold rolled from 0.075 cm thickness to 0.050 cm thickness for a total of 33-1/3 percent reduction and stress relieved for 20 minutes at temperatures ranging from 1100° to 1400°C in hydrogen.

Table 3.4 presents the results of the tests conducted on the three companion lots of purified molybdenum sheet. Simulated EB butt welds were made on sheets from all three lots and, as demonstrated repeatedly, no evidence of microporosity could be found in the heat-affected zone of weldments made in sheet which was produced from powders leached either in dilute HCl or HNO₃ acids. Bend specimens oriented with the bend parallel and transverse to the rolling direction of both types of purified sheet and stress relieved at 1100°C and 1400°C, with one exception, withstood 90-degree bends over a 2T radius. A ram speed of 0.005 cm/min was employed. No explanation is apparent for the one specimen (oriented parallel to the rolling direction) which failed at an angle of 10 degrees other than possibly an edge effect. At a ram speed of 0.127 cm/min all specimens oriented transverse to the rolling direction and stress relieved at 1100°, 1200°, and 1300°C also withstood a 90-degree/2T bend at room temperature. However, considerably less ductility was observed in specimens oriented parallel to the rolling direction at the higher strain rate. There appears to be no difference in bend properties of the sheet as affected by the acid leaching treatment.

Grain size determinations indicate that sheet produced from the HNO₃-treated powders is slightly more resistant to recrystallization and grain growth than the sheet produced from the HCl-treated powders. This is shown in Figure 3.10 for material stress relieved at 1050°C for 20 minutes in hydrogen following cold rolling. At 1050°C, the HNO₃-treated molybdenum sheet showed incipient recrystallization and the HCl-treated molybdenum sheet

TABLE 3.4
INFLUENCE OF Mo POWDER PURIFICATION ON BEND DUCTILITY, HARDNESS, AND GRAIN SIZE OF UNALLOYED Mo

Specimen Identity	Mo ^a Used	Mo Powder Treatment	Micro-Porosity in Weld Areas	Bend vs. Rolling Direction	Bend Test Results After Stress Relief ^b				Rockwell 15-T Hardness ^d Following Stress Relief ^b at Indicated Temperatures				Grain Size After 1100°C Stress Relief ^b	Grain Size After 1400°C Stress Relief ^b	
					Angle to Fracture-Room Temperature Bend with 2T Bend Radius ^c				(15 kg Load with 1/16-inch dia Ball)						
					1100°C	1200°C	1300°C	1400°C	1100°C	1200°C	1300°C	1400°C			
Group No. 1 Vendor No. 1 (Lot 384)															
C		HCl	No	11	—	—	—	90	90.8	90.0	90.2	88.6	Fibrous grains (Elongated)	Medium (Equiaxed) Small	
C		HCl		T	90 ^c	90	90	90	—	—	—	—	Fibrous grains (Elongated)	Medium (Elongated)	
N		HNO ₃	No	11	10 ^c	50	15	90	90.2	89.2	89.6	87.9	Fibrous grains (Elongated)		
N		HNO ₃		T	90 ^c	90	90	90	—	—	—	—			
Group No. 2 (Lot 384)															
C		HCl	No	11	—	10	10	90	90.8	89.0	88.2	87.0	Coarse	Coarse	
C		HCl		T	90	90	90	90	—	—	—	—	—	—	
N		HNO ₃	No	11	5	10	30	90	90.9	90.3	89.0	87.8	Medium	Medium	
N		HNO ₃		T	90	90	90	90	—	—	—	—	—	—	
Group No. 3 (Lot 66-5-81) (Vendor No. 1)															
C		HCl	No	11	90 ^c	50	30	90	90.5	89.0	89.0	87.6	Small — 50% Equiaxed	Coarse	
C		HCl	No	T	90 ^c	90	90	90	—	—	—	—	Equiaxed	—	
N		HNO ₃	No	11	90 ^c	90	20	90	90.5	88.8	89.0	87.8	Medium	Medium	
N		HNO ₃	No	T	90 ^c	90	90	90	—	—	—	—	Equiaxed	—	

^aAnalysis (ppm) reported by Vendor No. 1 — Lot 384: — C-26, Al-14, Ca-10, Si-17, Fe-42, Mg < 10, O₂ = 1890, —325 mesh, 2.0 micron avg dia.

^bAll stress relief treatments 20 minutes at temperature in hydrogen.

^cAll bends made at 0.125 cm/minute bending punch speed except those marked "C" which were made at slower rate of 0.005 cm/minute ("C" includes all 1400°C series).

^dThe Rockwell 15-T scale in hardness converts to the more familiar Rockwell "B" scale with RT 92 = RB 97, RT 90 = RB 90, and RT 86.5 = RB 80.0.

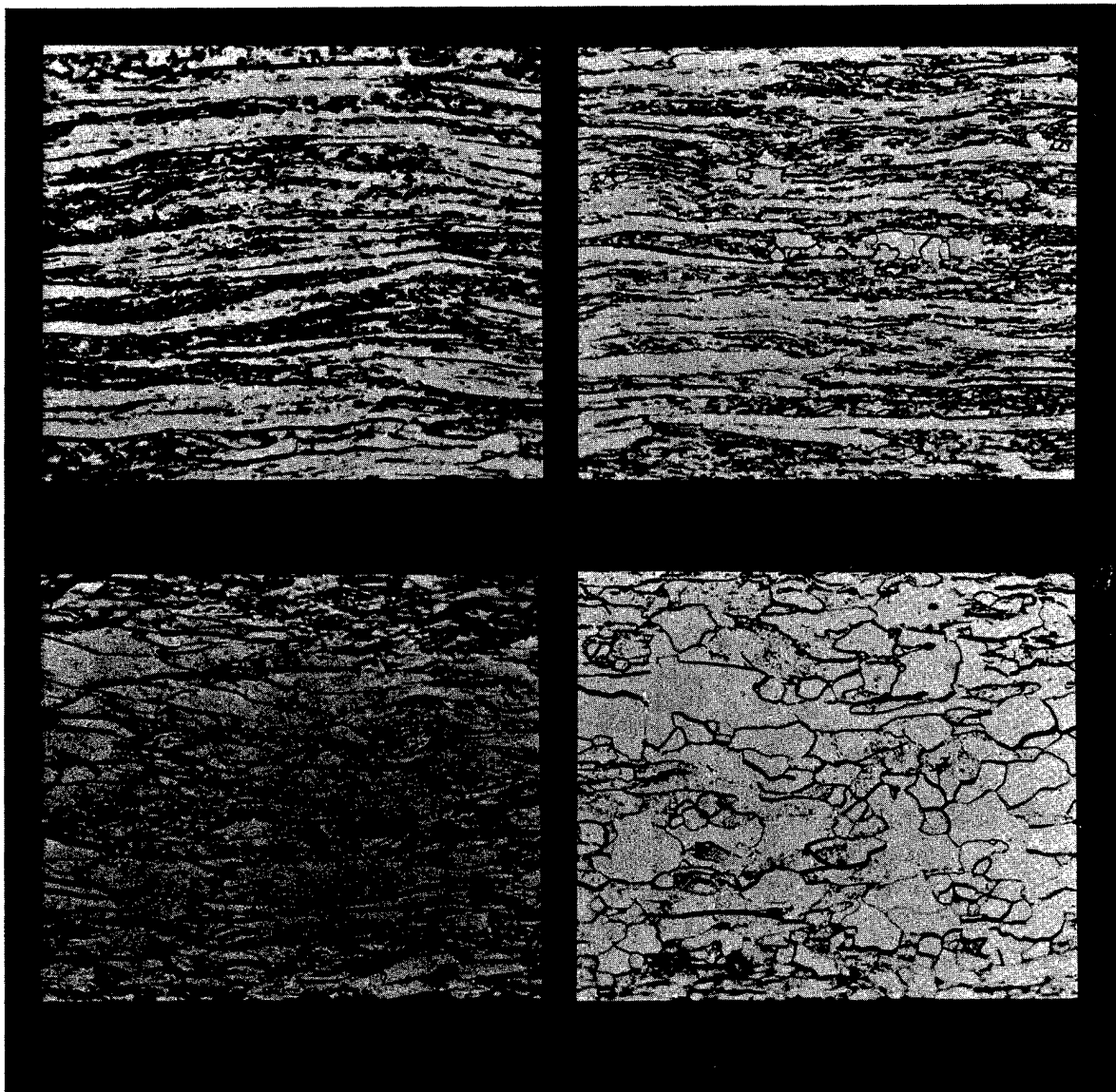


Fig. 3.10 — Photomicrograph of purified Mo before and after stress-relief at 1050°C. Metal powders used to fabricate the Mo sheet were treated with the acids indicated (Etched in methanol-sulfuric acid solution, (~200X))

showed some grain growth. As-cold-rolled, the HNO_3 -treated material was fibrous; the HCl -treated material contained a few moderate sized grains remaining from the hot-rolling operation (1350°C).

No trends were observed from the hardness data other than the normal decrease as a function of stress relief temperature.

MOLYBDENUM ALLOYS

The purification technology developed for unalloyed molybdenum for LMFBR applications also is being extended to its alloys.

Three alloys (Mo — 5W, Mo — 3Re — 5W, and Mo — 5Re, all at. %) were processed using the NMPO HCl - and wet-hydrogen purification technique which was developed for unalloyed molybdenum, as discussed above.

Sheet stock was prepared from the three alloys to verify the original test data. The HCl-treated metal powders were compacted into flat bars, treated 360 hours at 1000°C in a hydrogen – water vapor atmosphere (5°C dewpoint), and hot rolled from 0.56- to 0.1-cm-thick sheet at 1400°C. The hot-rolled sheet then was treated for 100 hours in hydrogen (-40°C dewpoint) at 1000°C to decrease the oxygen absorbed during hot rolling. The de-oxygenated sheet was cold rolled to 0.05-cm thickness. Intermediate and final anneals were carried out at 1400°C in hydrogen.

Finished sheet was evaluated for resistance to microporosity in weldments and stress rupture properties at 1600°C and 2200°C. Simulated EB butt welds were made in the longitudinal and transverse directions with respect to the rolling direction of the sheet. Radiographic inspection revealed that only the weldments in the Mo – 5W alloy and unalloyed molybdenum control sheet were free of microporosity. Further studies will be required to understand the role of small rhenium additions on microporosity.

Room-temperature bend tests were conducted on weld specimens over a 2T radius at a ram speed of 0.058 cm/min to 0.127 cm/min. Specimens from each material successfully withstood 90-degree bends when the bend crease was transverse to the weld seam and the weld seam was either transverse or parallel to the rolling direction of the sheet. When the bend crease was imposed parallel to and directly on the weld seam, bend angles of 35 to 40 degrees were recorded for the Mo – 5W alloy, 40 to 50 degrees for the W – 3Re – 5W alloy and 90 degrees for the unalloyed molybdenum control samples with the higher bend angle corresponding to the slower bend rate.

Stress-rupture data at 1600°C and 2200°C (Figure 3.11a) indicate that the NMPO-purified Mo – 5W and Mo – 5Re alloys are equal to the rupture strength of commercial Mo – 50Re. Creep data at 1600°C and 2200°C to 2 percent and 5 percent strain (Figures 3.11b and 3.11c) indicate that the Mo – 5Re and Mo – 5W alloys are more creep resistant than the Mo – 50Re alloy tested under identical stress – temperature. One-hour isochronal stress-rupture data for a number of refractory metals and alloys are given in Figure 3.12. These data show the 1-hour rupture stress of Mo – 5W and Mo – 5Re is greater at all temperatures (1200° – 2400°C) than niobium, tantalum, unalloyed molybdenum, and Mo-TZM alloy.

W-Re-Mo ALLOYS

The purification treatments developed for unalloyed molybdenum were successfully applied to W-Re-Mo alloys in a continuing effort to produce refractory alloy mill products that have usable room-temperature ductility in the weld area and that are resistant to microporosity in heat-affected zones of welds or in the base metal after longtime thermal exposure. Chemical analyses of W – 30Re – 30Mo seamless tubes that were produced indicate the carbon content to be 1.0 ppm. Similarly a Mo – 35Re tube analyzed 5.0 and 2.0 ppm carbon on samples taken 150 cm apart. These products had received a 324-hour treatment in hydrogen (5°C dewpoint) at 1000°C. Finished sheet of W – 25Re – 30Mo and W – 30Re – 30Mo similarly treated analyzed 2.0 and 6.0 ppm carbon, respectively. These data confirm the reliability of the hydrogen – water vapor treatment in reducing the carbon levels in W-Re-Mo alloys.

3.3 SUMMARY AND CONCLUSIONS

Equipment was installed for producing ^{All}sheet, ^{All}bar, seamless ^{All}tubing, and ^{All}wire of refractory metals including an electronically controlled draw bench to control the drawing speeds of seamless refractory metal tubing. Fine W – 0.5 Os wire (0.0076-cm diameter) was successfully drawn for thermocouple applications.

— top. 196

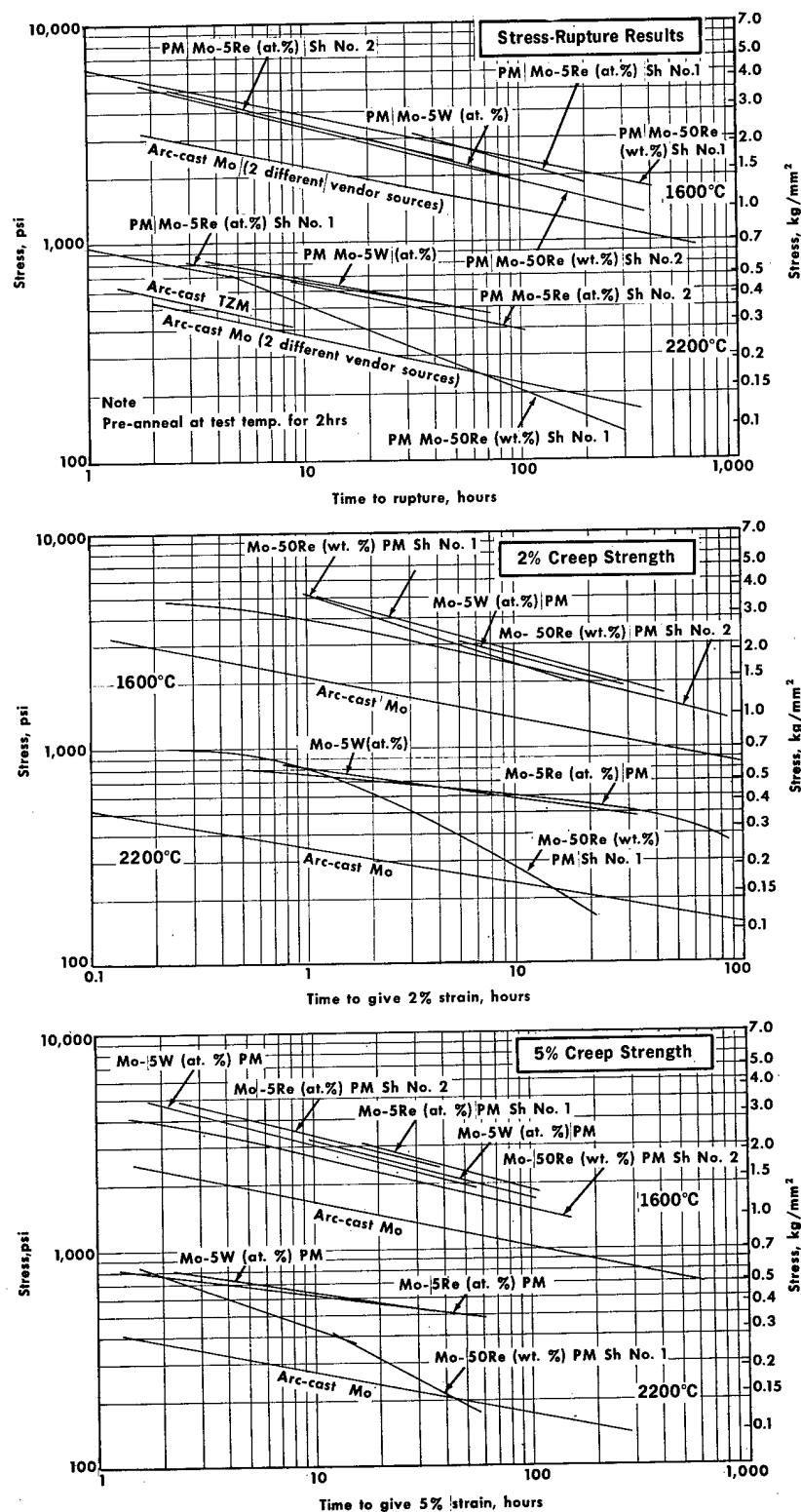


Fig. 3.11 – Stress-rupture strength, 2% creep strength, and 5% creep strength of wrought Mo and Mo alloys tested in hydrogen

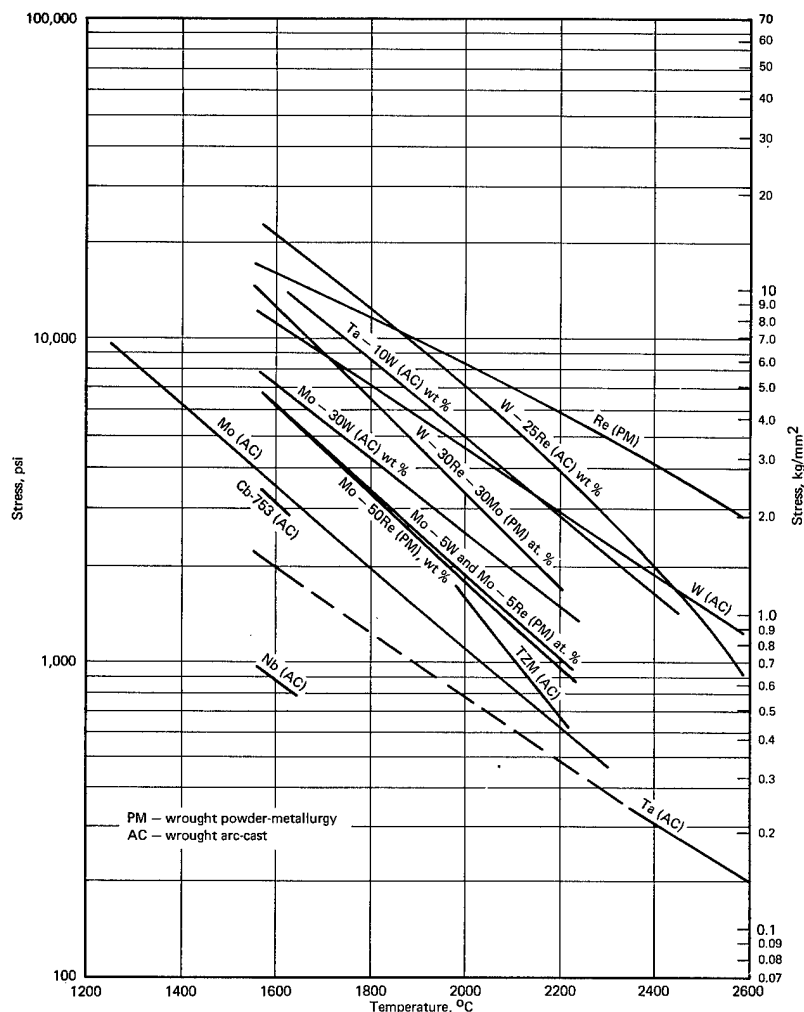


Fig. 3.12 — One-hour isochronal stress-rupture data for various refractory metals and alloys

Purification procedures developed for molybdenum have resulted in the production of unalloyed molybdenum sheet which is ductile and free of microporosity in weld-heat-affected areas. A Mo — 5W alloy processed by recently developed purification procedures has stress-rupture life and deformation resistance equal to Mo — 50Re alloy at 1600°C, and is superior to that alloy at 2200°C.

Several areas of significant accomplishment under this Task during CY-67 will be reported following resolution of patent actions.

3.4 PLANS AND RECOMMENDATIONS

Development and selection of processing procedures for obtaining purified molybdenum as nuclear-quality tubing and sheet will be emphasized. Tube-drawing procedures involving plug drawing will be evaluated for ductile molybdenum. This technique was prohibited by the high working stresses required for the stronger W-Re-Mo alloys.

Inspection and testing specifications for ductile and weldable purified molybdenum mill products will be developed.

Processing of small-diameter tubing of W-Re-Mo alloys for advanced thermocouple applications of interest to the AEC will continue. Tube-drawing procedures developed for W-Re-Mo alloys will be applied to W - 25Re and Re alloys which are of interest for LMFBR thermocouple applications. Processing of fine W - 0.5 Os thermocouple wire will continue for LMFBR applications.

4 (PHYSICAL METALLURGY OF FAST BREEDER REACTOR CLADDING MATERIALS AND REFRACTORY METALS)

(1177)

C. G. Collins,* K. M. Bohlander

The objective of this program is to define heat treatment, composition, and microstructures that result in optimum creep ductility of selected fuel cladding alloys. This objective represents a redirection of this task as of January 1968 toward emphasis on fast breeder reactor fuel cladding materials. During 1967, the task was concerned with the physical metallurgy of refractory metals, specifically W-Re-Mo alloys and molybdenum, in support of the alloy research and development efforts under task 1115. Work on refractory metals, particularly molybdenum, will continue through the remainder of the current fiscal year, with the major effort henceforth devoted to stainless steels and other selected fuel cladding alloys noted subsequently.

4.1 TUNGSTEN-RHENIUM-MOLYBDENUM ALLOYS

Studies of the W - 25Re - 30Mo and W - 30Re - 30Mo (at. %) alloys were concerned with recrystallization, ductility, hardness, and aging characteristics of original process and specially purified powder metallurgy materials. Specific objectives were to improve production procedures and properties of the sheet product.

FABRICATION

Fabrication studies centered on means of incorporating purification procedures without impairing yields or properties. As indicated in Figure 4.1, the original fabrication process for sheet material of the two alloys involved hot rolling at 1400°C to about 1-mm thickness with subsequent 5 percent reduction steps obtained in multiple passes at 200°C to final thickness. Intermediate anneals of about 15 minutes at 1400°C were made after each reduction step. Subsequently, special purification steps outlined in Figure 4.1 were incorporated in the procedure to improve weldability. Unfortunately, the temperatures initially utilized in the final purification treatment after hot rolling caused poor yields in working and limited room-temperature ductility in both alloys.

W - 25Re - 30Mo

Simpler production procedures were established for W - 25Re - 30Mo using the modified procedures indicated in Figure 4.1. Since this alloy exhibits the brittleness typical of refractory metals in the recrystallized condition, the wrought structure necessary for cold working could be retained by the following modifications: (1) carrying out the final purification treatment at temperatures below that at which recrystallization occurred, (2) omission of this final treatment, or (3) carrying out the purification treatment prior to the final hot rolling step. With a sufficiently wrought structure, it was possible to achieve reductions of 10 percent per pass at room temperature and total reductions of up to 80 percent without annealing or stress-relief treatments. With modifications No. 1

*Project leader and principal investigator.

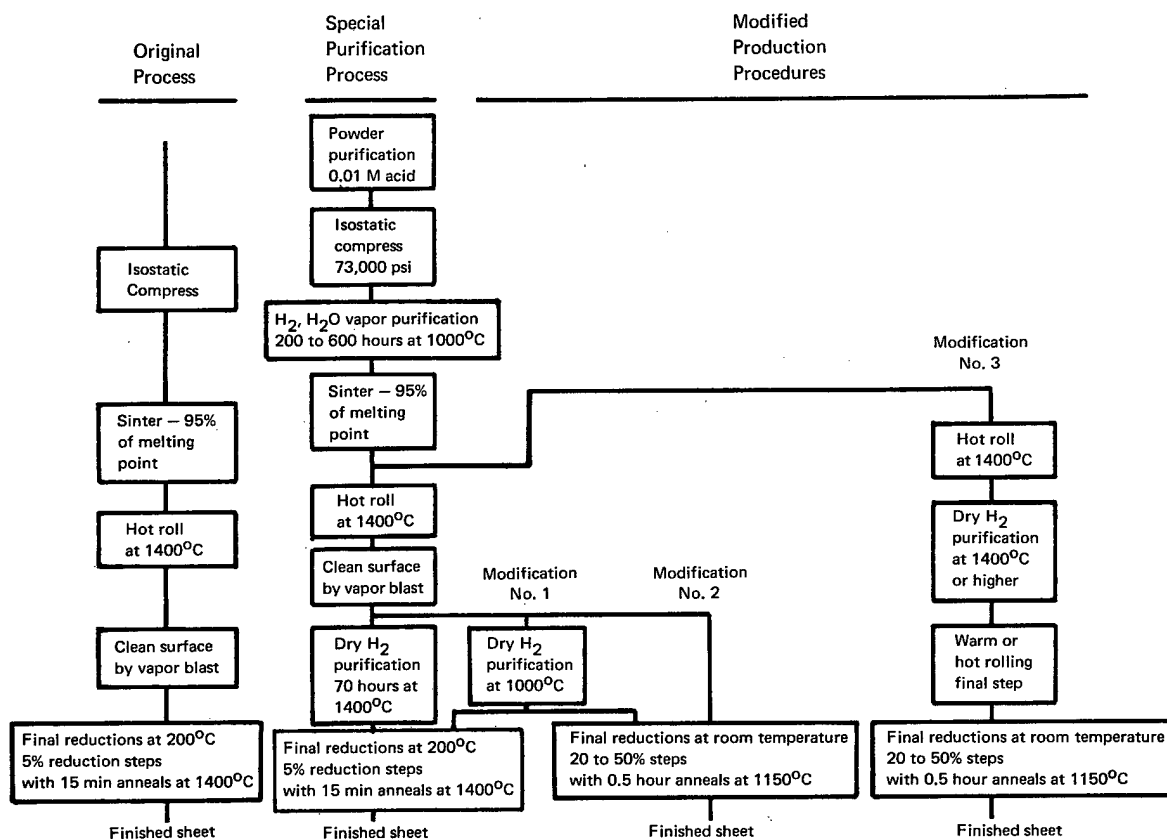


Fig. 4.1 — Production procedures for W-Re-Mo alloys

and 2 (Figure 4.1), improved yields were obtained in the processing of sheet and the final stress-relieved material possessed excellent room-temperature ductility. Present analytical data do not indicate whether the concentration of interstitial impurities, particularly oxygen, differs appreciably in sheet produced by modifications No. 1 and 2, i.e., when the final purification treatment is omitted. Weld porosity was not adversely affected by the latter procedure, however. Pending clarification of this point, studies of modification No. 3 have not been pursued.

W - 30Re - 30Mo

Similar modifications in sheet fabrication were successfully applied to the W-30Re-30Mo alloy with improvements in yield and ductility. This alloy is ductile in the recrystallized condition, although relatively poor ductility properties can arise from precipitation of a sigma phase which forms at temperatures below approximately 1700°C. Material recrystallized above the sigma solution temperatures was definitely more ductile than that recrystallized at temperatures at which sigma precipitated, even though interstitial impurities may also be involved in the ductility. Modifications in the production process therefore involved reduction and stress-relieving treatments identical to those described for the W-25Re-30Mo alloy (see Figure 4.1), and a final recrystallization anneal at 1700°C or higher to obtain a ductile-to-brittle bend transition temperature below -70°C. The final anneal also served as a further deoxidation treatment.

RECRYSTALLIZATION

Recrystallization studies to aid fabrication development were conducted on both W-Re-Mo alloys after cold reduction of sheet from the as-processed condition (produced by the original procedure outlined in Figure 4.1) and from the annealed (2000°C, 2 hr) condition. Also

included were W – 30Re – 30Mo specimens processed using special purification procedures. All materials were cold rolled at room temperature to reductions ranging from about 10 to 75 percent without intermediate anneals. A summary of the specimens prepared for this recrystallization study appears in Table 4.1.

In general, the two alloys exhibited typical recrystallization behavior; a pronounced decrease of grain size on recrystallization occurred at reductions greater than 15 to 30 percent. Data established that the final purification treatment at 1400°C for 70 hours after hot rolling amounted to a recrystallization anneal, and that the purification treatment should be 1200°C or lower if recrystallization is to be avoided.

W – 25Re – 30Mo

In the as-reduced condition, pre-annealed specimens retained the large equiaxed grain structure up to about 13.5 percent cold reduction, at which point a wrought structure became apparent. Grain sizes decreased with increasing amounts of reduction as shown in Figure 4.2, the largest decrease occurring at reductions in the range of 15 to 30 percent. Grain size in this instance refers to grain height measured in the thickness direction of the material.

TABLE 4.1
RECRYSTALLIZATION AND AGING SPECIMENS BEFORE TESTING

Specimen No.	Pre-Rolling Treatment ^a	Reduction, %	Final Sheet Thickness, cm	Hardness, DPH ^b	Grain Size, microns ^c	
					Width	Height
W – 25Re – 30Mo						
1	A	13.5	0.046	508	62.3	62
2	A	24.6	0.039	525	49.4 ^d	30
3	A	39.8	0.030	560	50.4 ^d	24.8
4	A	45.5	0.027	560	51 ^d	28.5
5	A	54.0	0.023	588	49.4 ^d	19
6	A	59.1	0.019	595	55.7 ^{d,e}	17.2
7	B	33.5	0.036	575	32.2 ^{d,e}	10.5
8	B	43.3	0.031	610	31.2 ^{d,e}	9.5
9	B	51.2	0.027	610	30.8 ^{d,e}	9.0
10	B	65.1	0.019	615	34.3 ^{d,e}	8.3
11	B	56.9	0.047	583	35.1 ^{d,e}	7.3
12	B	76.2	0.026	625	32 ^{d,e}	6.8
W – 30Re – 30Mo						
1	C	19.4	0.042	525	94.8	95
2	C	32.7	0.034	553	33.8	16.5
3	C	43.1	0.029	573	32.5 ^d	13.9
4	C	55.8	0.022	578	31.8 ^{d,e}	14.2
5	C	66.8	0.015	583	39.5 ^{d,e}	9.7
6	D	18	0.043	554	54.5	55
7	D	35.1	0.033	563	42.7 ^d	15.1
8	D	45.7	0.027	573	57.4 ^d	23.4
9	D	54.8	0.022	580	33.8 ^d	11.3
10	B	31.2	0.036	600	115.6 ^d	19.3
11	B	41.5	0.030	630	105.3 ^{d,e}	17.9
12	B	49.8	0.026	635	105.3 ^{d,e}	13.9
13	B	68.3	0.019	638	131.6 ^{d,e}	14

^aA – Annealed 2 hours at 2000°C.

B – Stress relieved at 1400°C.

C – Purified, solution annealed for 2 hours at 2000°C.

D – Solution annealed 2 hours at 2000°C.

^bAverage of 3 to 5 indentations with 2.5-kg load using microhardness tester; usual spread of values ± 10 DPH.

^cGrain sizes were determined by the linear intercept method on transverse sections.

^dIndividual grains elongated.

^eMicrostructure heavily worked, wrought.

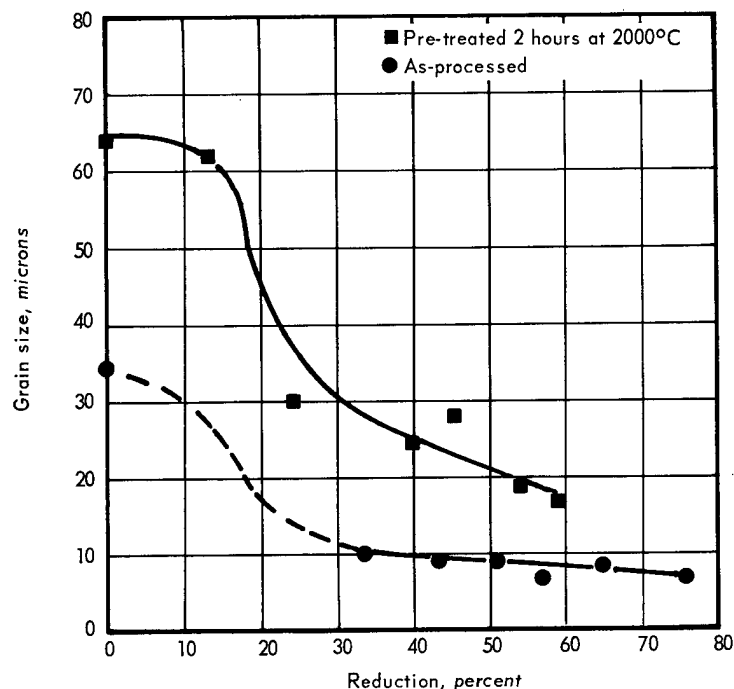


Fig. 4.2 — Influence of pre-treatment (2 hours at 2000°C) and amount of reduction in thickness by cold rolling on W — 25Re — 30Mo grain size

Isochronal anneals of 0.5 hour at 1200°, 1300°, 1400°, 1600°, 1800°, and 2000°C for both the as-processed and pre-annealed materials produced complete recrystallization at 1800°C and 2000°C regardless of the amount of reduction; at 1600°C for reductions of 40 percent or more, and at 1400°C for a reduction of 90 percent. Grain sizes after recrystallization decreased markedly at reductions of 20 to 30 percent with relatively small additional decreases for the larger amounts of reduction. Data for recrystallization at 1800°C shown in Figure 4.3 are representative of other temperatures.

Isothermal anneals for various times of material reduced 60 percent (a region of particular interest in fabrication) indicated essentially complete recrystallization at 1400°C in 8 to 9 hours, at 1300°C in approximately 100 hours, and at 1200°C in about 1000 hours. Measurements of the amount of recrystallization at various temperatures indicated that the activation energy for recrystallization was approximately 100 kcal.

W — 30Re — 30Mo

The recrystallization behavior of the W — 30Re — 30Mo alloy in the different purities and conditions examined was similar to that of the W — 25Re — 30Mo alloy. In grain sizes obtained in 0.5-hour anneals at 1800°C (Figure 4.4) the decrease in the recrystallized grain size after 10 to 30 percent reduction is similar to that of the W — 25Re — 30Mo alloy. Although the different starting conditions led to differences at low reductions, the grain size after annealing was roughly equal at reductions greater than 30 percent; hence the recrystallization behavior was not markedly influenced by purification or solution treatments or by the presence of some sigma phase. For reductions greater than 30 percent, recrystallization was complete after 0.5 hour anneals at 1600°C or above and after 2 hours at 1400°C.

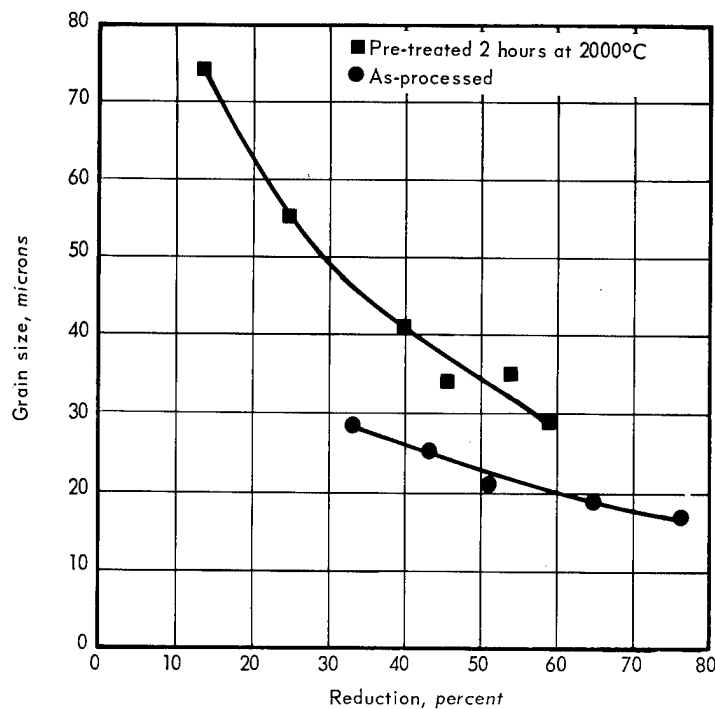


Fig. 4.3 — Grain size of W — 25Re — 30Mo as a function of reduction in thickness after 0.5 hour at 1800°C recrystallization anneal

Hardness

The hardness of the two alloys increased rapidly with increasing amounts of reduction, as indicated in Figures 4.5 and 4.6, but reductions greater than 40 percent produced little additional change. Relatively little effect of the 2-hour pre-anneal at 2000°C remained after about 20 percent cold work. In the W — 30Re — 30Mo alloy, the as-processed material attained a higher hardness with reduction than the annealed materials; this behavior is attributed to a rhenium-rich sigma phase present in this alloy in the as-processed condition. Hardness changes due to annealing and aging are noted subsequently.

AGING

Aging studies of the W — 25Re — 30Mo and W — 30Re — 30Mo alloys were conducted to assess grain growth and hardness changes of the original process materials and specially purified W — 30Re — 30Mo. Specimens were in the same pre-annealed, as-processed, and cold-worked conditions utilized in the recrystallization studies (Table 4.1). Measurements were completed on the two alloys after aging to 1000 hours at 1400°, 1600°, and 1800°C, and to 500 hours at 2000°C in helium.

Grain Growth

In general, the grain growth behavior of the two alloys was comparable. The major difference noted for the different purities and structures was that the materials pre-annealed two hours at 2000°C prior to reduction were less susceptible to secondary recrystallization.

In the W — 25Re — 30Mo alloy, the pre-annealed material exhibited good grain size stability at all aging temperatures and times, except for one specimen reduced only 5 percent which exhibited secondary recrystallization after 500 hours at 2000°C. Fairly typical results for these specimens are shown in Figure 4.7 for aging at 1800°C. The maximum grain size attained in aged specimens that had been reduced 40 percent or more was in

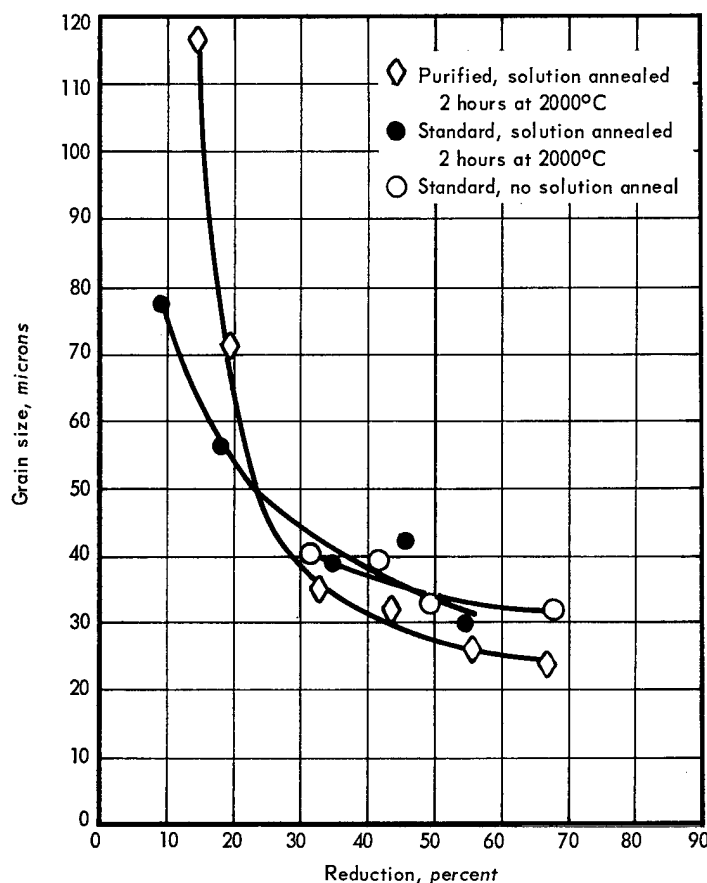


Fig. 4.4 — Grain size of W — 30Re — 30Mo as a function of reduction in thickness after 0.5-hour recrystallization anneal at 1800°C

the range of 40 to 50 microns. The lightly reduced specimens attained maximum grain sizes ranging up to 100 microns.

In contrast, the W — 25Re — 30Mo specimens in the as-processed condition, i.e., those with a wrought structure obtained by 5 percent reductions with anneals at 1400°C, exhibited secondary recrystallization in amounts roughly proportional to the amount of reduction. At 1600°C, only the specimens reduced 51 and 65 percent were affected. At 1800°C all specimens were affected, although the amount of secondary recrystallization in the two smallest reductions was not large. The 1800°C results are shown in Figure 4.8.

The overall behavior of the W — 30Re — 30Mo alloy including the specially purified material was essentially the same as that described for the W — 25Re — 30Mo alloy. As indicated in Figures 4.9 and 4.10, one specimen of the standard process material exhibited secondary recrystallization, whereas none was observed in the specially purified material. Secondary recrystallization occurred at 1800°C in the as-processed W — 30Re — 30Mo in all specimens reduced more than approximately 30 percent.

Secondary Recrystallization

Secondary recrystallization is a fairly common problem in both powder-metallurgy and arc-melted refractory metals. Its occurrence can cause loss of ductility and changes in other mechanical and physical properties. As with ordinary grain growth, the driving force for the process is the surface energy of grain boundaries. Although the causes are not well

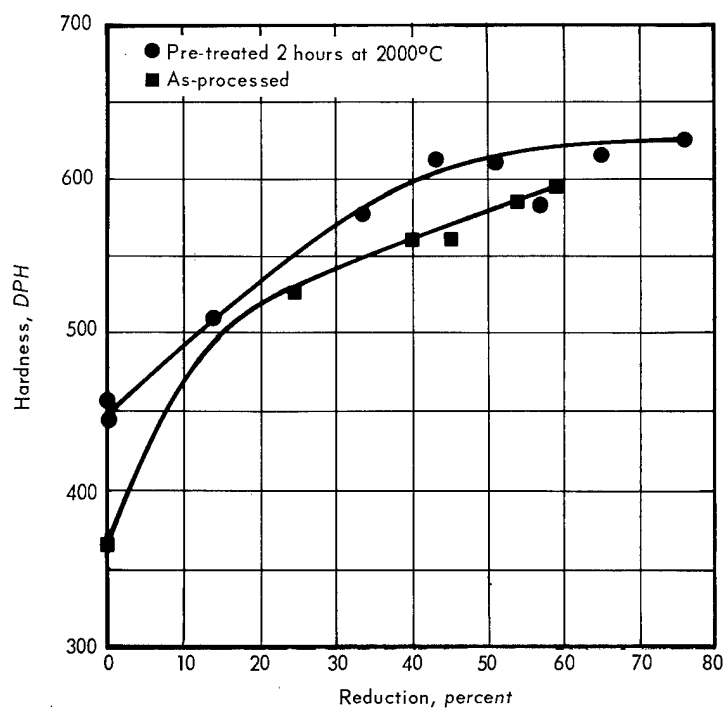


Fig. 4.5 — Hardness changes of W — 25Re — 30Mo alloy as a function of reduction in thickness by cold rolling

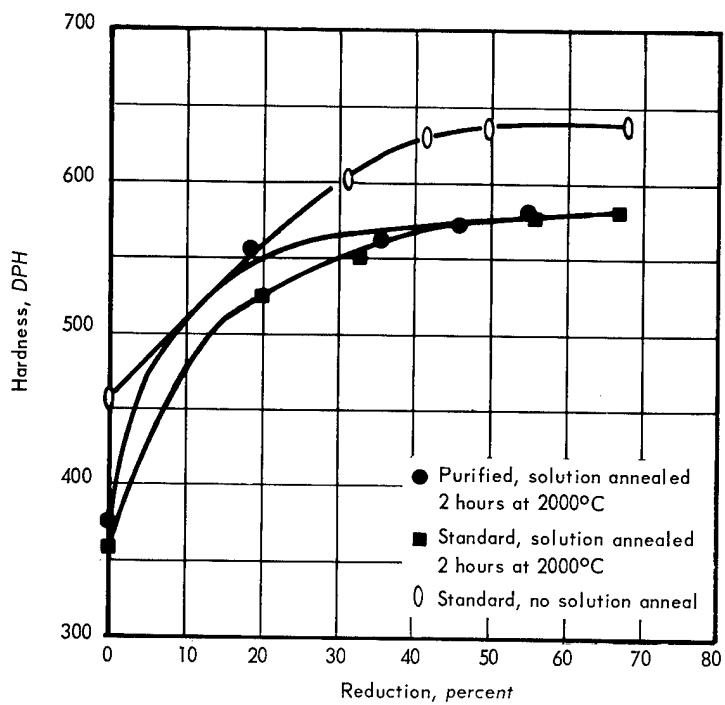


Fig. 4.6 — Hardness changes of W — 30Re — 30Mo alloy as a function of reduction in thickness by cold rolling

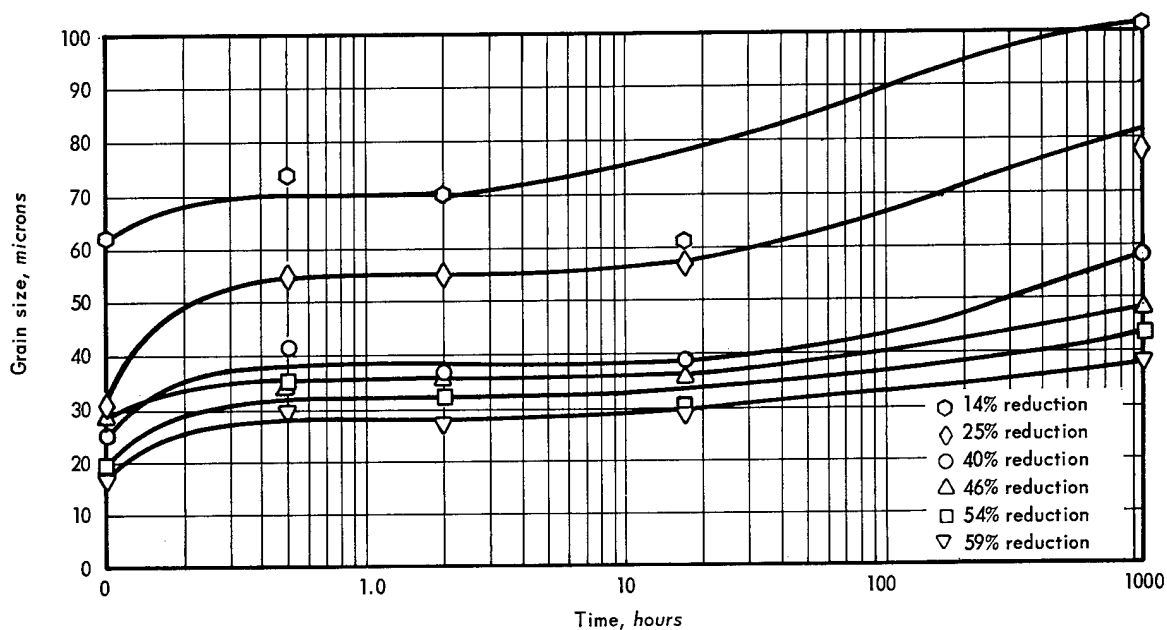


Fig. 4.7 — Grain size changes as a function of time at 1800°C for W-25Re-30Mo alloy pre-treated for 2 hours at 2000°C in H₂ before cold rolling and recrystallization anneals

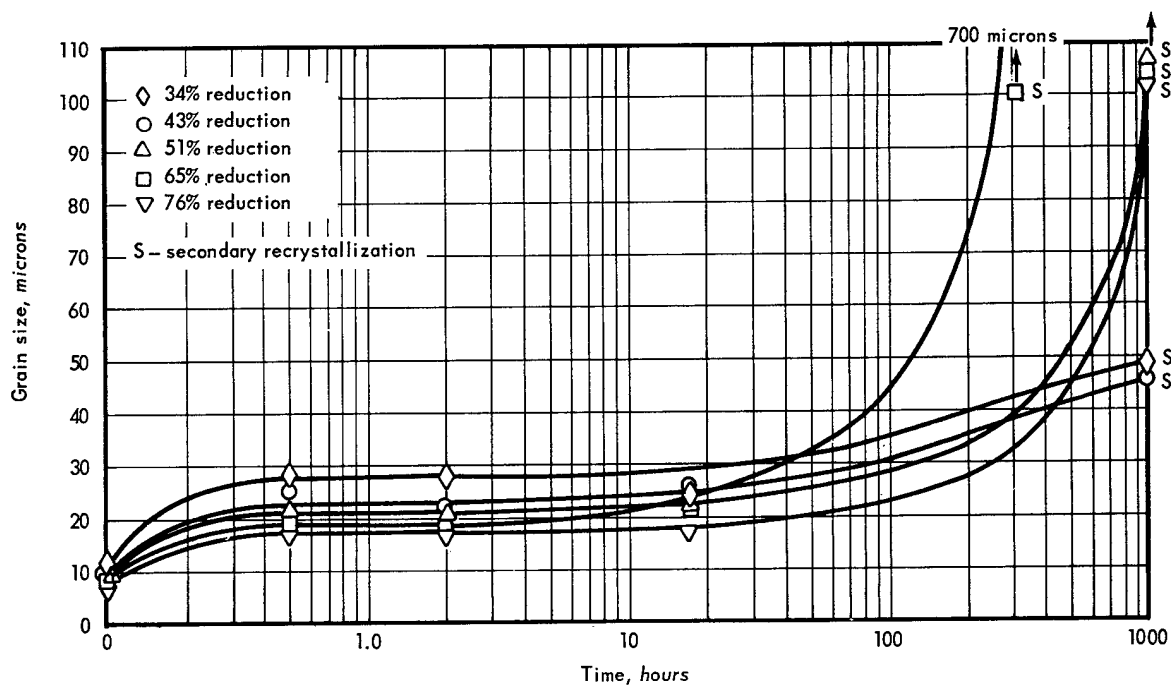


Fig. 4.8 — Grain size changes as a function of time at 1800°C for W-25Re-30Mo alloy. Samples were original process material cold-rolled from the as-fabricated condition.

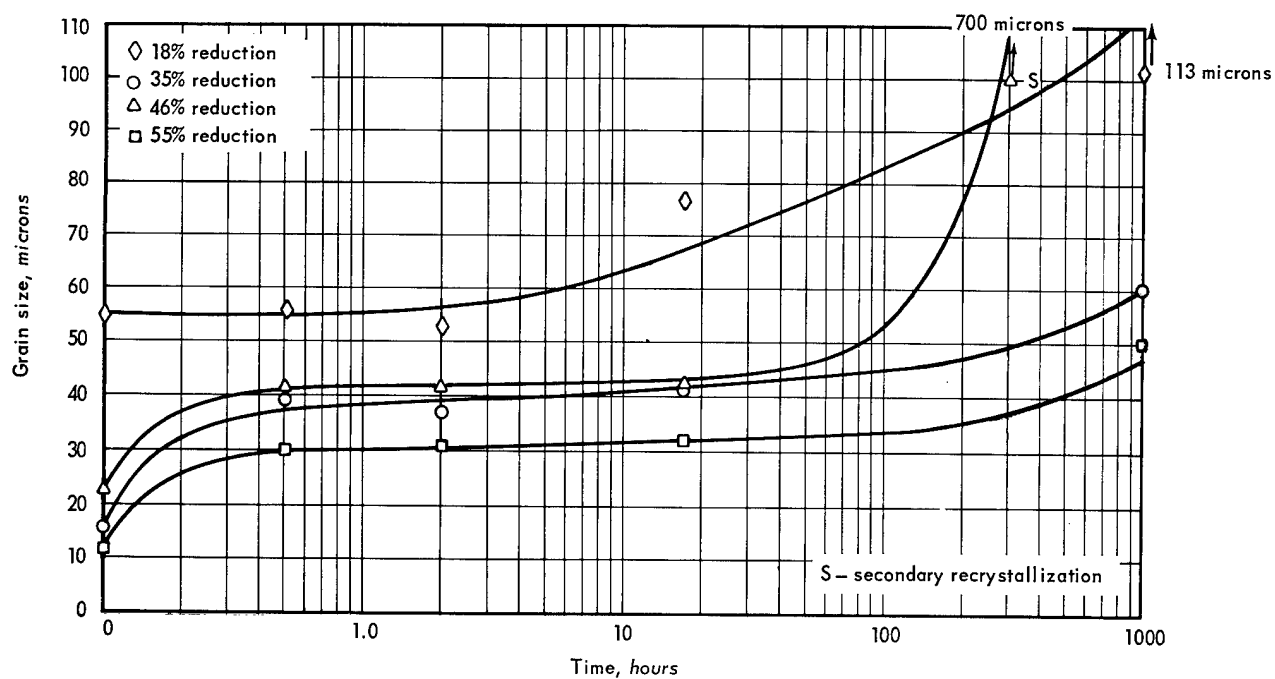


Fig. 4.9 — Grain size changes as a function of time at 1800°C for standard process W — 30Re — 30Mo solution annealed for 2 hours at 2000°C before cold rolling and recrystallization anneals

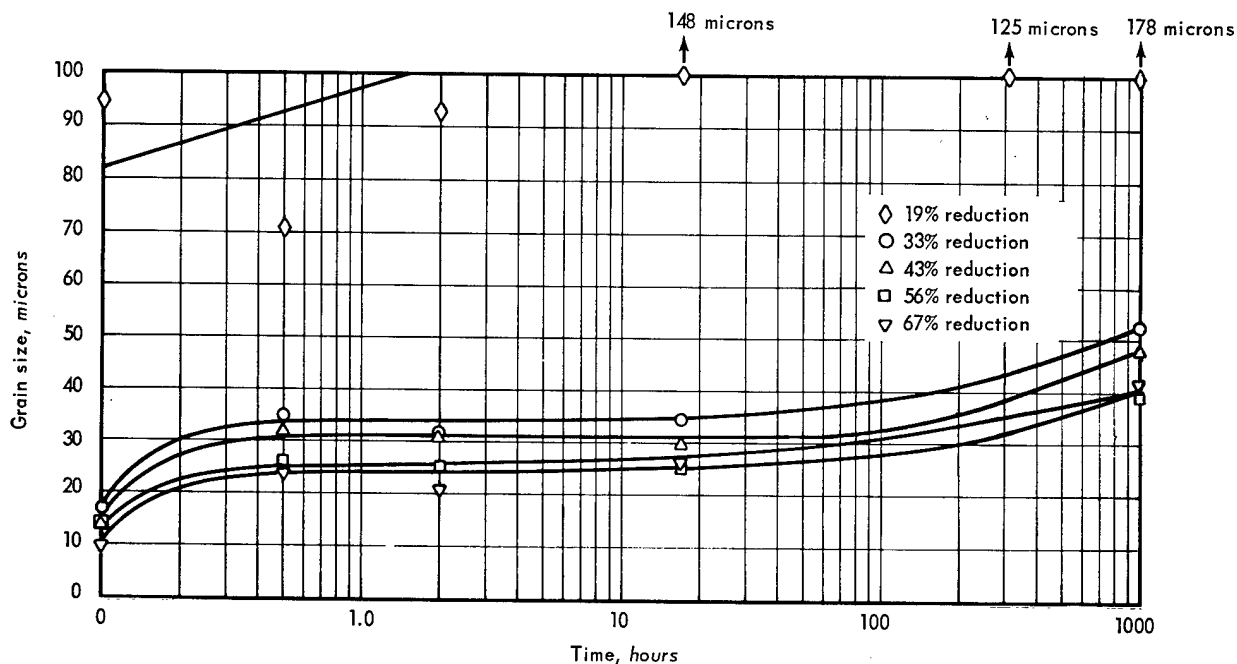


Fig. 4.10 — Grain size changes as a function of time at 1800°C for purified W — 30Re — 30Mo alloy solution annealed for 2 hours at 2000°C before cold rolling and recrystallization anneals

defined, purity, preferred orientation, and deformation are known to influence the phenomenon.

As noted in the preceding paragraphs, several specimens of both W-Re-Mo alloys exhibited areas of secondary recrystallization after aging at 1600°C or higher. Further investigation indicated that this occurred in about half the production sheets and confirmed the aging studies which indicated that it was related to amount of reduction and to purity. No definitive cause or complete solution to the problem was found.

In examinations of recent production lots of sheet materials of the two alloys, secondary recrystallization occurred in five of ten sheets produced by the original rolling procedure (small cold reductions with intermediate stress-relief anneals at 1400°C). Secondary recrystallization areas were found in four specimens after 17 hours at 2000°C in hydrogen and in a fifth specimen after an induction period of about 60 hours at 2000°C. In those materials susceptible to the phenomenon, there appeared to be a direct relationship between the amount of cold working and the occurrence of secondary recrystallization, as in the grain growth measurements described previously. This relationship was particularly apparent upon aging specimens that were cold rolled from 5 to 75 percent with no intermediate anneals, and is probably caused by strain-induced grain growth since secondary recrystallization is enhanced by both light and heavy plastic deformations.^{1,2} It is not solely a function of the amount of deformation, however. Some W-Re-Mo specimens have been cold reduced 50 to 75 percent without secondary recrystallization occurring on subsequent aging treatments, whether with or without anneals during reduction.

The possibility that the impurity concentration or inclusions – or rather the lack of these – is a factor in secondary recrystallization was investigated with some success. Indirect evidence is the fact that materials produced some time ago, with a reportedly higher impurity concentration,³ showed no secondary recrystallization in aging studies.⁴ Furthermore, although there is no statistical sampling, secondary recrystallization has only recently been observed in work under various other tasks using these materials.⁵ Direct evidence was obtained when specimens from a large sheet of W – 30Re – 30Mo, known to undergo extensive secondary recrystallization, were heated in a nitrogen atmosphere at temperatures ranging from 1000° to 1200°C and times from 3 minutes to 3 hours, annealed in argon at 2000°C for 2 hours, then cold rolled to 60 percent reduction in thickness. These specimens did not form secondary growth when aged for 100 hours at 2000°C even though some were strained by bending. In contrast, the control specimen without the nitrogen treatment formed extensive secondary growth within 17 hours at 2000°C in the same test. Chemical analyses failed to establish clearly that the nitrogen content was changed; both the nitrided and control samples indicated 10 to 20 ppm nitrogen. Considering that not all production materials exhibited secondary recrystallization, these data suggest the existence of a critical concentration of impurities which may prevent the phenomenon. For example, Fiedler⁶ found that nitrogen concentrations in excess of 0.0184 percent inhibited secondary recrystallization in silicon-iron.

¹C. D. Calhoun, "Exaggerated Grain Growth in Reactor-Grade Hafnium After Small Deformations," KAPL-3193, September 2, 1966.

²K. T. Aust, "Crystal Growth from the Solid State," General Electric Research and Development Center, Report No. 66-C-294, September 1966, p. 11.

³"AEC Fuels and Materials Development Program Progress Report No. 67," GE-NMPO, GEMP-67, June 30, 1967, p. 65.

⁴"Sixth Annual Report – High-Temperature Materials Program, Part A," GE-NMPO, GEMP-475A, March 31, 1967, pp.133–135.

⁵"710 Reactor Program Progress Report No. 24," GE-NMPO, GEMP-529 (Conf.), July 31, 1967, pp. 37–42.

⁶H. C. Fiedler, "The Behavior of Nitrogen in 3.1% Silicon-Iron," General Electric Research and Development Center, Report No. 67-C-225, June 1967.

Efforts to relate the secondary recrystallization to local inhomogeneities or to preferred orientation were not successful. Local inhomogeneities of the order of 1 percent concentration variations can be detected in the materials by X-ray fluorescence techniques. These areas probably extend only to thicknesses of a few grains in diameter since both etching and polishing resulted in variations of the composition of the same spot of 3- to 6-mm diameter. Although the measurements may not be conclusive, no correlation between these inhomogeneities and the secondary recrystallization was obtained comparing sheets known to be susceptible to it and free of it. Similar negative results were obtained in X-ray diffraction analyses of preferred orientation. At present there is no way of detecting susceptibility to the phenomenon other than actual aging tests.

Hardness Changes

The general trend of the hardness changes of the purified W-25Re-30Mo and W-30Re-30Mo alloys was almost identical to that in material not specially purified, although the purified alloys were about 20 VPH units higher (400 versus 380) than the normal material for the softest condition. Data up to 1000 hours are summarized in Figure 4.11 for specimens aged at 1200° to 2000°C. As noted previously, the increase in hardness of W-30Re-30Mo alloy at 1400°C and 1600°C at the longer aging times is attributed to the sigma phase that develops in amounts up to about 7.5 percent at these temperatures.

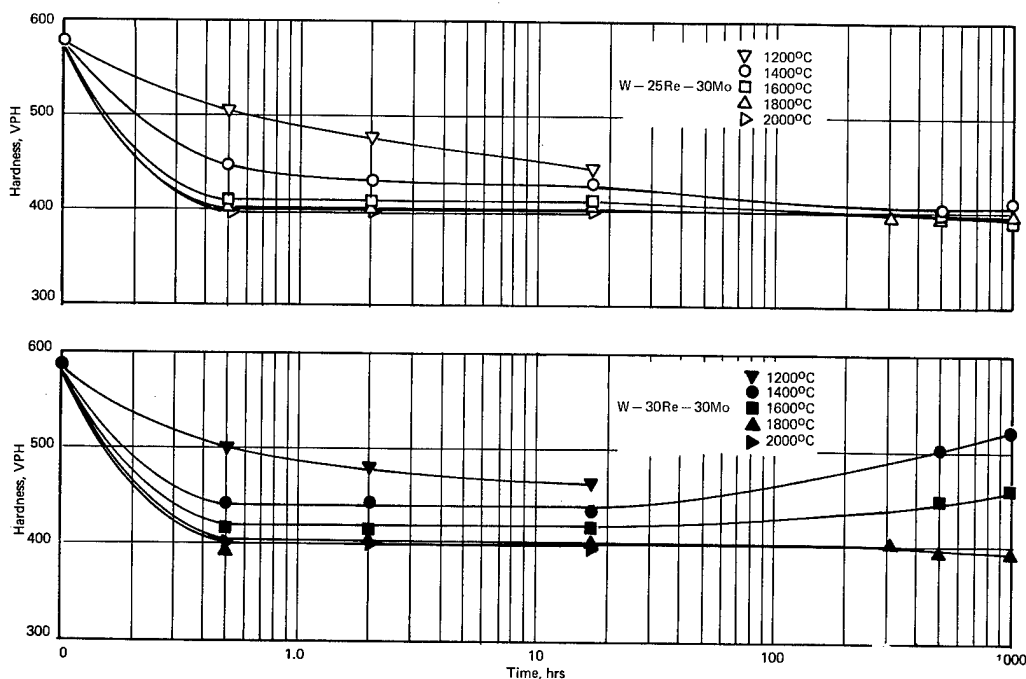


Fig. 4.11 — Change in room-temperature hardness of cold-rolled W-Re-Mo alloys after aging at elevated temperatures

DUCTILITY

Bend ductility measurements under a variety of heat treatment and microstructural conditions established that good room-temperature ductility could be achieved in W-25Re-30Mo with stress relieving at 1150°C following about 80 percent cold reduction or following a combination of hot and cold reduction of recrystallized material. This behavior was a factor in the selection of modified production procedures outlined in Figure 4.1. Similar treatment

provided only moderate ductility (40- to 50-degree bends at room temperature) in the W - 30Re - 30Mo alloy. This material is ductile in the recrystallized condition, however, provided recrystallization is carried out at temperatures above that at which the sigma phase is in solution, approximately 1700°C.

Bend ductilities were determined by means of the 4T bend test. Because of the sample quantities required, the earlier rather than the later definition of this bend test recommended by the Materials Advisory Board was followed.⁷ Bends were made both parallel and normal to the rolling direction on 0.05-cm-thick sheet specimens.

The bend ductility of the two alloys was measured as a function of amount of cold reduction. Prior to reduction, the materials were annealed 2 hours at 2000°C, a recrystallization anneal for both alloys. They were then cold rolled to reductions in thickness ranging from 10 to 60 percent. Bend tests (4T) were made on the as-reduced sheet parallel to the rolling direction. Results showed decreases in ductility of the W - 30Re - 30Mo with increasing amounts of reduction up to about 35 percent. The ductile-to-brittle transition temperatures (DBTT) were still below room temperature after 10 percent reduction, but with 35 percent reduction, room-temperature bends (parallel) of only 10 to 20 degrees were obtained. No further reduction of ductility occurred with additional cold reductions in thickness up to 60 percent. The ductile-to-brittle behavior of W - 25Re - 30Mo alloy differed from that of the W - 30Re - 30Mo in that it did not change after the 2000°C recrystallization anneal; the DBTT remained at 250° to 300°C. There was no apparent reduction in ductility in this alloy as a function of increased cold working.

Ductility changes as a function of the annealing temperature following various amounts of cold reduction of the recrystallized structure indicated that approximately 80 percent reduction was necessary to attain good room-temperature ductility (with 90-degree bends) with non-recrystallization anneals of 0.5 hour at 1150°C. Recrystallized specimens 0.5 mm thick were subjected to room-temperature bend tests parallel to the rolling direction after 50 percent reduction. Results following 0.5-hour anneals at temperatures from 800° to 2000°C in 200°C steps (Figure 4.12) show an increase in bend ductility of the W-30Re-30Mo alloy with increasing annealing temperature; 90-degree bends or greater were obtained at or above 1800°C. For the 0.5-hour time period involved, 1800°C was the lowest temperature of those examined that recrystallized the material and did not result in precipitation of sigma phase. The W - 25Re - 30Mo alloy increased in ductility to a maximum 30-degree bend after 0.5 hour at 1600°C and did not increase beyond this value at higher temperatures.

Ductility changes on aging the alloys are essentially predictable on the basis of recrystallization and sigma formation. The W - 30Re - 30Mo alloy is ductile in the recrystallized condition; hence aging at 1600°C or higher temperatures at which sigma does not precipitate does not induce brittleness, although secondary recrystallization in some cases reduced the bend angles at room temperature to 50 to 70 degrees. At 1400°C and lower, sigma formation in this alloy apparently contributed to embrittlement even when recrystallization occurred and parallel room-temperature bends of only 10 to 20 degrees were obtained after aging times greater than about 70 hours. The W - 25Re - 30Mo alloy is brittle in the recrystallized condition; hence aging for sufficient time at temperatures greater than about 1200°C resulted in parallel bends of only 10 to 20 degrees. Somewhat surprisingly, aging periods of 7 to 25 hours at 1800°C resulted in 70-degree parallel bends in this material; this relatively good ductility region was not observed at 1600°C or 2000°C.

The DBTT for different production procedures are summarized in Table 4.2. Other than material produced by the improved production procedure, which had a DBTT of less than

⁷The earlier bend definition was given in MAB-176-M, "Evaluation Test Methods for Refractory Metal Sheet Materials," November 1961. The later definition is given in MAB-192-M (same title) April 1963. Both reports by National Academy of Sciences, National Research Council, Washington, D.C.

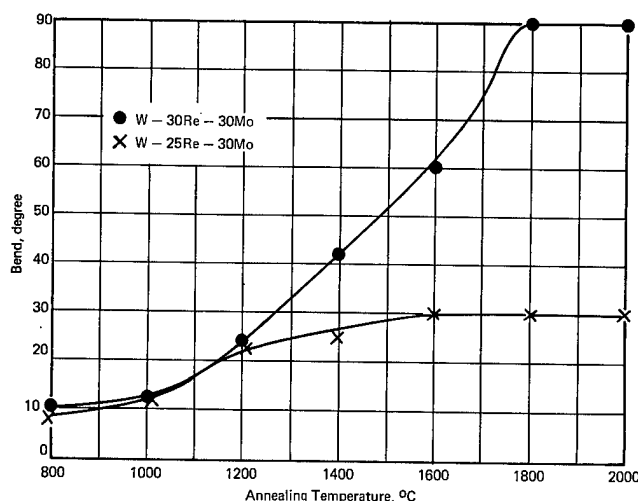


Fig. 4.12 — Influence of isochronal (0.5 hour) anneals in H_2 on the bend ductility of two W-Re-Mo alloys cold-rolled 50 per cent to 0.51-mm thickness before annealing

-70°C , the W-25Re-30Mo yielded 10- to 20-degree bends at room temperature under all conditions investigated. The normal sharp transition from ductile-to-brittle bending was evident usually from 50 to 90 degrees rather than from 0 to 90 degrees. In all cases other than the improved process material, bends parallel to the rolling direction had a higher transition temperature than those normal to the rolling direction. Parallel bends of approximately 90 degrees were obtained in the original process material at approximately 300°C for the as-processed, for the 2000°C anneal, and for the aged conditions, although some change in the shape of the curve occurred with these different treatments. Ninety-degree bends normal to the rolling direction occurred at approximately 150° to 200°C and were approximately independent of the condition of the material.

As with the W-25Re-30Mo alloy, the improved production procedure yielded W-30Re-30Mo material with a DBTT of less than -70°C . The ductile-to-brittle behavior of normally processed W-30Re-30Mo alloy, however, differed from that of the W-25Re-30Mo alloy, particularly with respect to the effects of 2000°C anneals and aging treatments at 1400°C or anneals at 2000°C . As indicated in Table 4.2, the original process material had a DBTT of 100° to 150°C (normal to the rolling direction) in the as-produced condition, somewhat lower than that of the W-25Re-30Mo alloy. In the specially purified material, the DBTT for bends normal to the rolling direction was about 400° to 500°C ; that for bends parallel to the rolling direction was greater than 500°C . This difference in behavior of the purified material is attributed, at least partly, to the sigma developed as a result of the final purification treatment. This conjecture is supported by the results for materials annealed 2 hours at 2000°C to place the sigma in solution; in this condition both the original process and purified materials had a DBTT of less than -70°C , appreciably lower than that of the original process material. Aging of the original process and purified materials at 1400°C raised the DBTT higher than 500°C in both the as-produced and solution-treated conditions; again, presumably because of the growth of the sigma phase at this temperature.

4.2 MOLYBDENUM

Studies of NMPO-processed molybdenum under this task are directed toward improving fabrication and properties of powder metallurgy material. Since molybdenum is brittle in the recrystallized condition, its fabrication in high-purity form presents the same problem

TABLE 4.2
BEND TEST DUCTILE-TO-BRITTLE TRANSITION TEMPERATURES
OF W-Re-Mo ALLOYS

Alloy	Production Process ^a	Treatment	Bend Direction ^b	DBTT, °C ^{c,d}
W - 25Re - 30Mo	Original Process	15 min final anneal at 1400°C	P	250 - 300
			N	150 - 175
W - 25Re - 30Mo	Original Process	520 hr at 1400°C	P	200 - 250
			N	100 - 125
W - 25Re - 30Mo	Original Process	2 hr at 2000°C	P	{ 30° at 150
			N	{ 90° at 300 150 - 190
W - 25Re - 30Mo	Original Process	2 hr at 2000°C, 520 hr at 1400°C	P	{ 20° at 200
			N	{ 90° at 300 20° at 100 90° at 190
W - 25Re - 30Mo	Improved Process Modification No. 2	0.5 hr at 1150°C, stress relief	P	<-70
			N	<-70
W - 30Re - 30Mo	Original Process	As-produced, 15 min final anneal at 1400°C	P	{ 50° at 25
			N	{ 90° at 150 100 - 150
W - 30Re - 30Mo	Original Process	2 hr at 2000°C	P	{ 50° at 25
			N	{ 90° at 100 -50
W - 30Re - 30Mo	Original Process	As-produced, 520 hr at 1400°C	P	~410
			N	{ 10° at 200 50° at 500
W - 30Re - 30Mo	Original Process	2 hr at 2000°C then 520 hr at 1400°C	P	{ 10° at 200
			N	{ 30° at 350-500 10° at 200 40° at 500
W - 30Re - 30Mo	Special Purified	As-produced, 15 min final anneal at 1400°C	P	{ 10° at 200
			N	{ 25° at 500 10° at 100 45° at 400 90° at 500
W - 30Re - 30Mo	Special Purified	2 hr at 2000°C	P	<-70
			N	<-70
W - 30Re - 30Mo	Special Purified Modification No. 2	1 hr at 1700°C or higher	P	<-70
			N	<-70
W - 30Re - 30Mo	Special Purified	As-produced, 520 hr at 1400°C	P	{ 10° at 200
			N	{ 30°-40° at 500 15° at 200 30°-40° at 500
W - 30Re - 30Mo	Special Purified	2 hr at 2000°C, then 520 hr at 1400°C	P	{ 10° at 200
			N	{ 40°-50° at 500 25° at 200 45° at 500

^aRefer to Figure 4.1 for outline of the different production processes.

^bP = bend made parallel with the rolling direction; N = bend made normal to rolling direction.

^cThe DBTT was based on a 90-degree bend in 4T bend tests on 0.05-cm-thick sheet. The 4T bend test was as defined in MAB-176-M.

^dEntries with degree symbol indicate bend angle at temperature cited.

described previously for W - 25Re - 30Mo; specifically, avoiding recrystallization conditions in final purification treatments. The principal options are the three modified production procedures outlined in Figure 4.1, as applied to molybdenum.⁸ Pending better definition of the important impurity concentrations, efforts have been concerned mainly with modification No. 2, i.e., omission of the final purification treatment. For this procedure the reduction, recrystallization, grain growth, and ductility measurements described in the following paragraphs indicated that stress-relieving treatments of 0.5 hour at 1000°C after 40 percent reduction at room temperature yielded sheet material with a DBTT below -70°C and good grain size stability on aging.

FABRICATION

The powder metallurgy molybdenum is readily cold rolled in the wrought condition induced by hot rolling sintered compacts from 1.1-cm to 0.1-cm thickness; reductions of up to 25 percent per pass are achieved at room temperature. As illustrated in Figure 4.13, material in the as-hot-rolled condition⁸ could be satisfactorily cold reduced up to 60 percent with and without stress relief treatments of 0.5 hour at 1000°C including cross rolling, but fracturing occurred if the material was recrystallized. Cold reductions up to 80 percent without stress relieving were achieved but the sheet contained laminations. Some lamination occurred at 60 percent reduction, but 40 percent reductions appeared sound. The sheet was successfully cross rolled provided a stress-relief treatment preceded changes in rolling direction.

RECRYSTALLIZATION

A few recrystallization anneals of cold-reduced sheet material were made to verify that the powder-metallurgy molybdenum conformed to existing data on recrystallization.⁹ Specimens of "N"- and "C"-processed molybdenum sheets were annealed at 1000° to 1200°C in the as-hot-rolled condition and after room-temperature reductions of 20, 40, 60, and 80 percent without intermediate stress-relief treatments. ("N" and "C" materials refer to nitric or hydrochloric acid leaching of powders prior to compaction.)¹⁰ In 1-hour anneals of the as-hot-rolled condition, recrystallization of the "N" material was approximately 50 percent complete at 1100°C and complete at 1200°C; the "C" material was about 50 percent recrystallized at 1050°C and complete at 1100°C. These recrystallization temperatures were lowered only about 50°C by the additional room-temperature reductions, evidently adding little to the wrought structure developed in the hot rolling.

DUCTILITY

Bend ductility measurements indicated reasonable ductility in the as-reduced condition and very good ductility after stress-relieving treatments. All bends were made parallel to the rolling direction on strip 6.4 mm wide. Tests were made at room temperature on a die with 6.4-mm span and a 2T radius punch operated at 1.27 mm per minute until the first indication of failure or until a 90-degree bend was attained. In the as-reduced condition, the hot-rolled material bent 55 degrees and the materials cold rolled 40 and 60 percent bent approximately 40 and 20 degrees, respectively. After stress relieving 0.5 hour at 1000°C, the hot-rolled material bent 80 to 90 degrees and the cold-rolled materials bent 90 degrees or more. Recrystallized material yielded bends of about 5 degrees regardless of reduction history.

⁸GEMP-475A, p. 114.

⁹"Refractory Metals and Alloys," M. Semchyshen and J. J. Harwood, editors, Interscience Publishers, New York, N.Y., 1960, pp. 290-293.

¹⁰"AEC Fuels and Materials Development Program Progress Report No. 71," GE-NMPO, GEMP-1002, December 29, 1967, pp. 65-66.

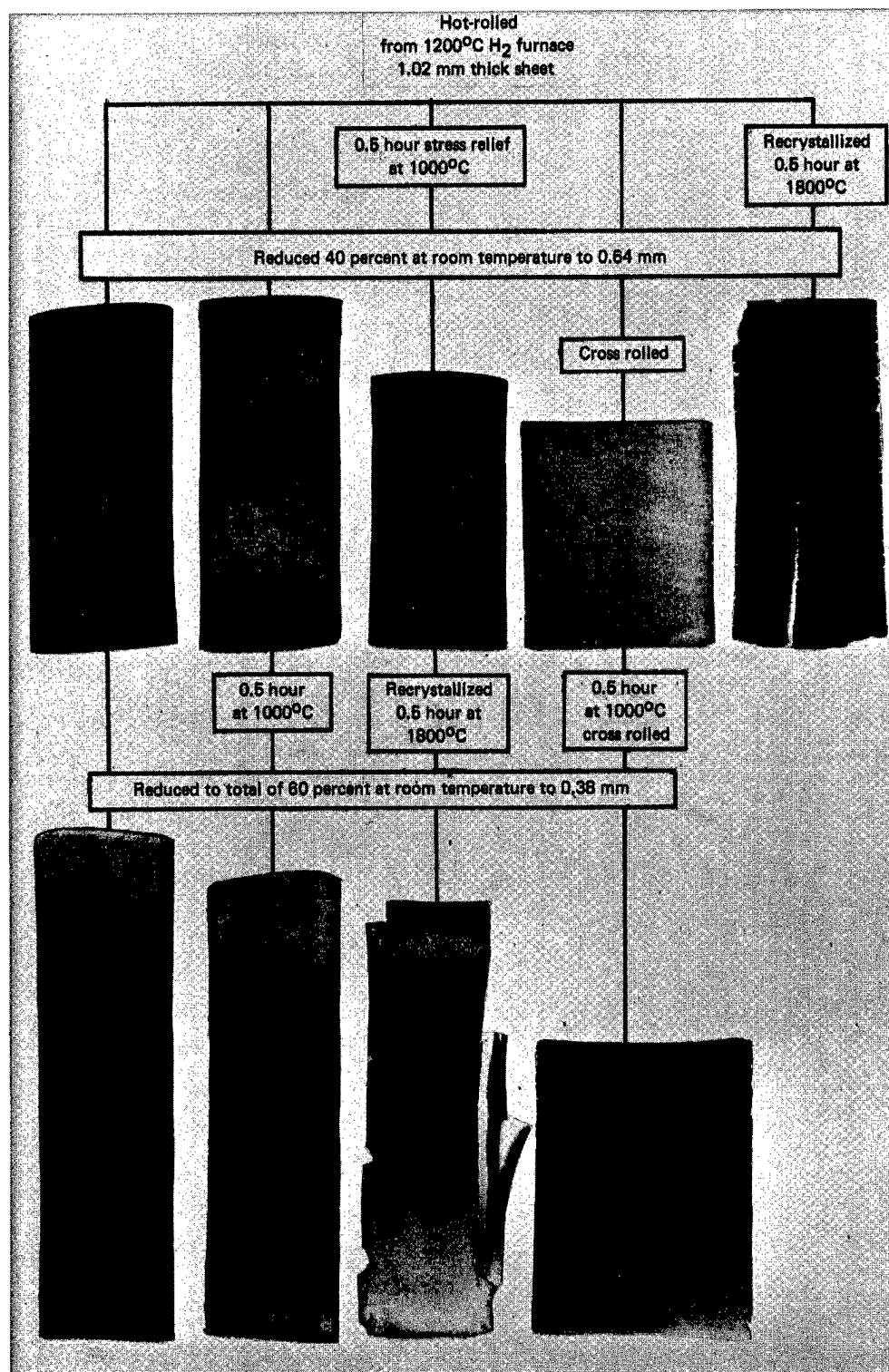


Fig. 4.13 — Unalloyed powder-metallurgy molybdenum reduced at room temperature. Preferred procedure involves 0.5 hour at 1000°C stress-relief treatment.

Additional measurements established that the DBTT of the hot-rolled material given a subsequent 40 to 60 percent reduction at room temperature and stress relieved 0.5 hour at 1000°C was below -70°C. For material with this same reduction, a stress relief of 0.5 hour at 1100°C raised the DBTT to 0°C.

AGING STUDIES

The "C" and "N" materials were aged in hydrogen for 1000 hours at temperatures of 1200° to 2000°C to assess the stability of the structures developed in processing. As in the other studies, the specimens were obtained from as-reduced hot-rolled material that was subsequently cold reduced up to 80 percent.

All materials exhibited very good microstructural stability at temperatures to 1400°C, and those reduced 20 percent prior to aging were stable at 1600°C. In this stable temperature region grain growth appeared normal; e.g., the specimen reduced 60 percent recrystallized at 1200°C to a grain size of 27 microns which, on aging 1000 hours at this temperature, increased to 39 microns. Secondary recrystallization occurred at 1600°C in materials reduced 40 percent or more and in all materials aged at higher temperatures.

4.3 FAST REACTOR FUEL CLADDING ALLOYS

The program on fast reactor fuel cladding alloys is concerned with varying heat treatment of the alloys to obtain better ductility in creep-rupture tests and, ultimately, under irradiation. Principal areas to be pursued initially are fine grain size materials, various carbon distributions obtained in work - heat-treatment combinations and in single and double aging treatments, and some work on cavitation fracture. Evaluation of the heat treatments will be based primarily on creep and rupture tests of pressurized tube specimens and of sheet specimens. All tests will be conducted in argon. Tensile tests as a function of strain rates extending to very low strain rates will be utilized as a supplementary means of evaluating heat treatments. Tests will be conducted mainly at 650°C; selected materials will also be investigated at 538°C and 760°C.

Materials included in the program are the following:

- 316 stainless steel
- 316 + Nb stainless steel
- Incoloy 800
- 12R72HV *
- 19-9DL
- Vanadium alloys¹¹
 - HSV 207
 - HSV 208
 - HSV 209
 - V - 15Cr - 5Ti
- Haynes 56

Initial efforts are concerned with 316 stainless steel and 19-9DL.

4.4 SUMMARY AND CONCLUSIONS

Studies on W - 30Re - 30Mo and W - 25Re - 30Mo (at. %) alloys led to simpler, lower-cost production procedures and greatly improved room-temperature ductility properties for powder metallurgy materials. Data were obtained on recrystallization, grain size,

*Product of Sandvik Steel, Inc., Fairlawn, N.J. Nominal composition is Fe-15Cr-15Ni-1.2Mo-0.45Ti-1.8Mn-0.5Si-0.1C.

¹¹"Vanadium Cladding Alloy Development, Quarterly Progress Report December 31, 1967," Westinghouse Electric Corp., Adv. Reactors Division, Madison, Pennsylvania, WARD-3791-13.

hardness^w and ductility^w changes on aging of these alloys at temperatures to 2000°C for periods up to 1000 hours.

Similar studies have resulted in procedures for producing molybdenum sheet; parts of this procedure are still under study. *J end*

4.5 PLANS AND RECOMMENDATIONS

Work on fast reactor fuel cladding alloys will include investigation of heat treatment and work combinations on 316 stainless steel, and 19-9DL in terms of ductility changes as a function of strain rates; creep-rupture tests will be initiated on selected materials. Other materials will be included in the studies as they become available.

Effort on the refractory metals will concentrate in two areas: (1) definition of impurity concentrations obtained in molybdenum processed by modifications No. 1 and 2 through internal friction and improved chromatographic analysis, and (2) completion of weld integrity and porosity studies currently in progress to define material purity requirements and welding conditions.

5. (FAST BREEDER REACTOR FUEL ELEMENT CLADDING RESEARCH)

(1119)

F. C. Robertshaw,* J. L. Bartos

The objective of this program is to develop improved fuel element cladding materials for fast breeder reactors and to define the properties of these materials which are of importance for fast breeder reactor applications.

More than half the material prepared for this report period under this task has been withheld pending patent clarification, at the request of the AEC Oak Ridge patent office.

The alloy systems selected for study under this program are shown in Table 5.1, together with an indication of their potential utility in various coolants. The specific alloys studied include a number which originated during the course of this program and others which were developed previously for other purposes.

TABLE 5.1

ALLOY SYSTEMS SELECTED FOR STUDY AS
FAST BREEDER REACTOR CLADDING MATERIALS

Alloy System	Applicable Coolants
Cr-base	Na, inert gases
Fe-Cr-Al-Y alloys	Na, steam, CO ₂ , inert gases, air
Fe-base (ferritic)	Na, inert gases
Fe-base (austenitic)	Na, inert gases

Start ↑ In the alloy studies conducted during the past year, primary emphasis was on developing alloys which have mechanical properties comparable or superior to austenitic stainless steel. Exploratory work was conducted to examine other properties and characteristics which are important in fast breeder cladding alloys; notably, environmental compatibility, radiation effects, and processability.]

5.1 CHROMIUM-BASE ALLOYS

→ p. 220
Although specific data were previously unavailable, interest in chromium stemmed from the prospects for high strength and sodium corrosion resistance at temperatures of interest for fast breeder reactor fuel cladding. It was thought that, unlike most other applications for which chromium-base alloys had been studied, operation in sodium or relatively inert atmospheres would minimize corrosion problems as well as the absorption of interstitial elements which cause embrittlement. Previous NMPO experience in the preparation of chromium-base alloys indicated that fabricability problems would not be prohibitive. It was concluded that chromium might play a useful role in fast breeder reactor technology; efforts were undertaken to characterize it at relevant temperatures and environments.

*Project leader and principal investigator.

Three alloys, Cr-Y, Cr-Hf-Th-Y, and Cr-TZC-Y, were selected for evaluation; previous experience had proven them relatively ductile and fairly strong. It was soon discovered that some degree of warm working was necessary to achieve strength levels better than those of stainless steel. Moreover, prepared in a practical way, these alloys had transition temperatures in bending and impact higher than room temperature. This has led to two other studies, one of which is to establish whether improved ductility can be achieved with high-purity starting materials and processing modifications. The other study is to develop new, or to evaluate existing, high-strength chromium alloys to determine how severe a ductility penalty is associated with the higher strength.

Warm-worked primary alloys and high-strength chromium-base alloys are being developed, and special procedures are being employed to improve ductility.

MATERIAL PREPARATION

Material used to evaluate the three primary chromium-base alloys was provided by 5.4-kg vacuum-induction-melted heats (M-313, M-314, M-315). Chemical analyses are listed in Table 5.2; fabrication procedures were presented previously.¹

TABLE 5.2
CHEMICAL ANALYSIS OF CHROMIUM-BASE ALLOYS

Alloy	Heat No.	Composition											
		wt %					ppm						
		Y	Th	Hf	Zr	Ti	C	O ₂	N ₂	H ₂	S	Si	Ca P
Cr-Y	M-313	0.097	—	—	0.001	—	413	18	77	5	<10	200	10 39
Cr-Hf-Th-Y	M-314	0.13	0.074	0.24	0.007	—	160	15	90	6	<10	70	10 8
Cr-TZC+Y	M-315	0.12	—	—	0.37	0.12	349	12	26	7	<10	10	10 3

Studies relating to higher-strength chromium-base alloys included preparation of binary chromium-base alloys by button arc melting to study the individual effects of alloying additions on the strength of chromium. A plot of as-cast room-temperature hardness versus alloy content (Figure 5.1) reveals the significant increase in hardness afforded by vanadium.

Based largely on these results, two 3.2-kg vacuum-induction-melted ingots were prepared and extruded. Table 5.3 indicates composition and extrusion data. After extrusion to 2.54-cm diameter, segments of alloy M-300 were encapsulated in mild steel and successfully press-forged and hot rolled at 980°C to 0.254-cm thickness. The Cr-20V-0.36Y (at. %) alloy was cold rolled 10 percent per pass with no intermediate anneals to ~~0.125 cm~~ 0.076 cm thickness. One extrusion segment of the Cr-15V-0.7Y (at. %) alloy was clad in drilled molybdenum rod, sealed by inert arc welding, soaked at 1370°C in argon for 15 minutes, and extruded to approximately 0.7-cm diameter. Subsequent zygo inspection revealed the re-extruded rod to be crack-free. Cylindrical button-head tensile specimens have been machined from segments of the re-extruded Cr-15V-0.7Y alloy.

In other efforts to exploit high-strength chromium-base alloys, three alloys were considered which had been developed under a NASA contract in which GE-NMPO participated.* Fabrication difficulties have hindered evaluation of these alloys. The compositions of these previously melted 3.2-kg vacuum induction-melted heats appear in Table 5.4. The ingots were originally extruded at approximately 1510°C from 5.4-cm diameter to 1.91-cm

*NAS3-7260 with GE-AEG.

¹"Sixth Annual Report - High-Temperature Materials Program, Part A," GE-NMPO, GEMP-475A, March 31, 1967, p. 158.

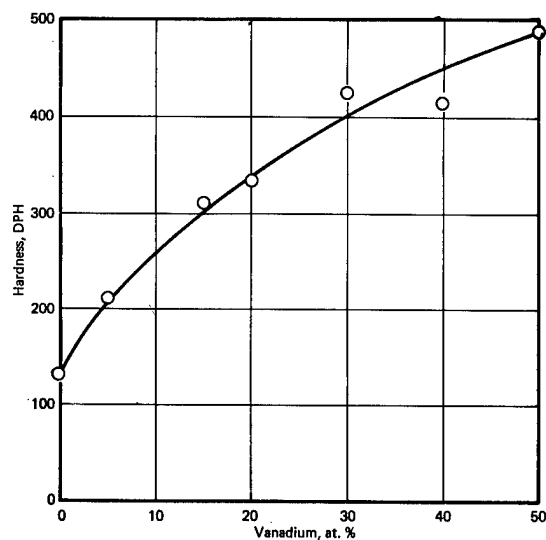


Fig. 5.1 — Room-temperature hardness versus alloy content for Cr-V alloys

TABLE 5.3

COMPOSITION AND EXTRUSION DATA FOR EXPERIMENTAL Cr-V ALLOYS

Alloy ^a	Nominal Composition, at. %			Extrusion Temperature, °C	Original Diameter, cm	Final Diameter, cm
	V	Y	Cr			
M-364	15	0.7	Bal	1205	5.4	2.54
M-300	20	0.36	Bal	1205	5.4	2.54

^aAll alloys are 3.2-kg heats.

TABLE 5.4

NOMINAL COMPOSITIONS AND IMPURITY ANALYSES FOR HIGH-STRENGTH Cr-BASE ALLOYS

Alloy Designation	NMPO Heat No.	Approximate Analysis, at. %			Gas Content, ppm		
		W	Mo	Y	O	N	H
CI-5	M-245	6.0	0.1	35	72	6	
CI-7	M-246	4.0	0.1	28	89	13	
CI-8	M-248	6.0	0.1	29	89	7	

diameter, and swaged to 0.635-cm diameter. Cylindrical button-head tensile specimens were prepared and tested in the range 1204° to 1315°C. Attempts were made to re-extrude remaining segments of the three alloys from 1.91-cm diameter to 0.7-cm diameter after encapsulating in 5.08-cm-diameter molybdenum rod, sealing by inert arc welding, and soaking at 1480° to 1510°C in argon for 15 minutes. The extruded rods appeared to be crack-free, but subsequent zygo inspection revealed severe transverse cracking which seemed to be caused by the differential thermal expansion of chromium and molybdenum. A second 3.2-kg vacuum-induction-melted ingot of the Cr – 6W – 0.1Y (at. %) alloy has been cast and will be brought to size using a modified extrusion procedure.

In efforts to assess the effect on ductility of highest-purity starting materials, experimental 80-gram button heats of several Cr-V alloys were prepared using high-purity vanadium obtained from the US Bureau of Mines, Boulder City, Nevada and iodide Cr. Nominal

analyses of the compositions melted appear in Table 5.5. Vanadium was obtained in crystal form from the US Bureau of Mines; impurity content was 20 ppm carbon, 75 ppm oxygen, 10 ppm nitrogen. Chromium was obtained in iodide crystals from Battelle Memorial Institute. It had an impurity content of 40 ppm carbon, 8 ppm oxygen, 2 ppm nitrogen.

The buttons were arc-melted under a partial pressure of argon (50.8 cm) in the presence of a titanium button to getter interstitials. Drop casting into a cylindrical copper mold was conducted in a smaller arc-melting furnace ($P_A \approx 50.8$ cm) without a titanium getter. The interstitial element content of the Cr - 20V alloy was determined to include 35 ppm oxygen and less than 1 ppm nitrogen, compared to calculated levels (based on raw material composition) of 21 ppm oxygen and approximately 4 ppm nitrogen. The alloys were encapsulated in mild steel and rolled in hydrogen at 980°C to 0.59 cm thickness where major cracking occurred. A second series of Cr-V alloys (see Table 5.5) is being prepared employing the same raw materials and melting procedures. The arc-cast buttons will be encapsulated and extruded to approximately 0.95 cm diameter from which cylindrical button-head tensile specimens will be machined to determine mechanical properties.

MATERIAL EVALUATION

Environmental Compatibility

Exploratory static sodium environment tests conducted at 650°C for 14 days on the three primary alloys and the Cr - 20V - 1Y (at. %, heat M-300) alloy were completed at ANL.² Details of these tests were reported previously.³ Weight change data are reported in Table 5.6, along with data reported by ANL for a V - 20Ti (wt %) sample. All four chromium-base alloys are clearly superior to the V - 20Ti. ANL concludes that "these exploratory tests indicate chromium-base alloys may be useful materials for service in low-oxygen sodium at 650°C."²

TABLE 5.5
NOMINAL COMPOSITIONS
OF HIGH-PURITY^a Cr-V
ARC-MELTED
BUTTON HEATS

Button No.	Composition, at. %	
	Cr	V
First Series		
1	95	5
2	90	10
3	85	15
4	80	20
5	70	30
6	60	40
7	50	50
Second Series		
1a	95	5
2a	85	15
3a	75	15
4a	65	35
5a	50	50

^aRaw materials consisted of iodide Cr and V from U.S. Bureau of Mines, Boulder City, Nevada.

TABLE 5.6
STATIC SODIUM TEST WEIGHT CHANGE DATA FOR
DEVELOPMENTAL Cr-BASE ALLOYS AT 650°C

Alloy Heat No.	Composition, wt %	Weight Loss, ^a mg/cm ²
M-313	Cr - 0.097Y	0.017
M-314	Cr - 0.24Hf - 0.07Th - 0.13Y - 0.007Zr	0.008
M-315	Cr - 0.37Zr - 0.12Ti - 0.12Y - 349 ppm C	0.005
M-300	Cr - 20V - 1Y	0.014
-	V - 20Ti	0.500

^aWeight losses are accurate to ± 0.001 mg/cm².

²Private communication, Sherman Greenberg, September 11, 1967.

³"AEC Fuels and Materials Development Program Progress Report No. 71," GE-NMPO, GEMP-1002, December 29, 1967, p. 83.

A previously described sodium capsule⁴ heated to 750°C for 1000 hours showed very small weight changes for all chromium-base alloys.

Strength and Ductility

Tensile Properties – Tensile data at 550°, 650°, and 750°C have been obtained on the three primary alloys and various experimental compositions. Table 5.7 and Figure 5.2 present these data with information concerning working conditions and pre-test hardness values. Differences in finish rolling temperature caused some variability in the hardness and short-time strength of the materials. Data indicate that warm rolling can have a profound effect on the tensile properties of these chromium-base alloys. Moreover, it is obvious that warm rolling is necessary in these alloys to achieve short-time strength levels superior to austenitic stainless steels.

Included in Table 5.7 are preliminary data on cylindrical button-head Cr – 15V – 0.7Y (at. %) alloy specimens in the as-extruded condition. Its tensile strength in the hot-extruded condition exceeds those of the warm-finished primary alloys at 750°C and 550°C. The low tensile ductility of the Cr – 15V – 0.7Y alloy at 550°C is a preliminary indication of a relatively high transition temperature.

Tensile properties of the high-strength chromium-base alloys developed under a NASA contract also appear in Table 5.7. Additional tests will be performed pending the successful fabrication of specimens.

Creep-Rupture Strength – Initial creep-rupture tests at 750°C were conducted on as-warm-rolled specimens of the three primary alloys in the type of argon-filled test capsule pictured in Figure 5.3. Data are presented in Table 5.8.

In these tests some attention focuses upon the possible influence of atmosphere contaminants on strength and ductility. The initial Cr-Hf-Th-Y specimens tested were discolored after rupture. Analyses (Table 5.8) confirmed the contamination of the specimens by nitrogen, oxygen, and carbon. Subsequently, specimens were wrapped in tantalum foil in an effort to reduce interstitial pickup. Analysis of several longtime tests wrapped in tantalum, however, revealed a significant increase in interstitial concentration and hardness (Figure 5.4). Fabrication and test procedures were checked and/or modified in further efforts to minimize contamination.⁵ The use of titanium shrouding material and a new encapsulation procedure⁶ are being evaluated. Data in Table 5.7 compare interstitial analyses of a Cr-TZC-Y specimen (CC-7) which was enveloped in a tantalum shroud and was on test for 1307 hours, with analyses of two other specimens (219 and AA-14) tested with titanium foil as a getter, using the improved encapsulation procedure. These limited data indicate that the contamination problem has been markedly reduced. Post-test analyses for interstitial element content will continue to confirm initial results.

All creep-rupture data involving the three primary alloys (warm-rolled) in which the specimens were wrapped in titanium foil and encapsulated under the improved procedure are plotted in Figure 5.5 along with data for Types 304 and 316 stainless steel. All three alloys exhibit a definite advantage over Types 304 and 316 stainless steel in creep-rupture at 750°C. Testing at 750°C and 650°C will continue in order to complete creep-rupture characterization of the primary alloys. Time extension data at 650°C and 750°C for specimens of all primary alloys compared to the stainless steels are presented in Figures 5.6

⁴GEMP-475A, p. 158.

⁵GEMP-1002, pp. 85–88.

⁶GEMP-1002, p. 86.

TABLE 5.7
TENSILE PROPERTIES OF Cr-BASE ALLOYS IN ARGON^a

Alloy	Heat No.	Condition ^b	Test Temperature, °C	Yield Strength ^c		Tensile Strength ^c		Elongation, %	Pre-Test Hardness, DPH
				ksi	kg/cm ²	ksi	kg/cm ²		
Cr-Y	M-313	Warm rolled	750	36.9	2580	38.6	2700	—	—
Cr-Y	M-313	Warm rolled	750	27.3	1910	28.8	2020	—	—
Cr-Y	M-313	Warm rolled	750	28.5	1930	37.4	2620	3.4	227
Cr-Y	M-313	+ annealed	750	31.4	2200	38.0	2660	2.0	227
		Warm rolled							
Cr-Y	M-216	Hot rolled	750	12.6	880	20.1	1410	28.4	119
Cr-Y	M-313	Hot rolled	750	10.2	710	22.5	1570	41.4	153
		+ annealed							
Cr-Y	M-313	Warm rolled	650	—	—	50.0	3500	14.7	—
Cr-Y	M-313	Warm rolled	650	42.4	2960	43.7	3060	2.1	226
Cr-Y	M-313	Warm rolled	550	49.2	3940	49.9	3490	3.2	—
Cr-Y	M-313	Warm rolled	550	58.8	4110	62.6	4390	2.2	266
Cr-Hf-Th-Y	M-314	Warm rolled	750	45.5	3180	54.7	3830	3.3	240
Cr-Hf-Th-Y	M-314	Warm rolled	750	44.9	3140	55.5	3880	5.3	—
Cr-Hf-Th-Y	M-314	Warm rolled	750	41.8	2920	53.2	3720	3.7	—
Cr-Hf-Th-Y	M-314	Warm rolled	750	52.3	3660	56.7	3970	2.9	258
		+ annealed							
Cr-Hf-Th-Y	M-314	Warm rolled	750	50.3	3520	57.0	3990	3.1	258
		+ annealed							
Cr-Hf-Th-Y	M-191	Hot rolled	750	21.2	1480	27.7	1940	6.5	170
Cr-Hf-Th-Y	M-314	Hot rolled	750	40.2	2820	41.2	2880	6.1	203
		+ annealed							
Cr-Hf-Th-Y	M-314	Warm rolled	650	51.3	3600	55.7	3900	—	—
Cr-Hf-Th-Y	M-314	Warm rolled	650	51.1	3590	59.4	4150	4.5	278
Cr-Hf-Th-Y	M-314	Warm rolled	550	48.3	3380	57.8	4050	2.9	240
Cr-Hf-Th-Y	M-314	Warm rolled	550	56.8	3980	65.0	4550	4.5	—
Cr-Hf-Th-Y	M-314	Warm rolled	550	59.6	4180	66.9	4680	3.3	278
Cr-Hf-Th-Y	M-191	Hot rolled	550	19.1	1340	31.5	2200	16.3	140
Cr-TZC-Y	M-315	Warm rolled	750	43.8	3060	61.9	4330	1.9	266
Cr-TZC-Y	M-315	Warm rolled	750	45.3	3170	48.4	3420	4.3	—
Cr-TZC-Y	M-315	Warm rolled	750	45.6	3200	57.3	4010	5.1	262
Cr-TZC-Y	M-315	Warm rolled	750	53.3	3730	62.0	4340	4.1	266
		+ annealed							
Cr-TZC-Y	M-298	Hot rolled	750	8.3	580	26.9	1880	35.4	131
Cr-TZC-Y	M-298	Hot rolled	750	13.2	925	20.1	1410	8.1	139
		+ annealed							
Cr-TZC-Y	M-315	Warm rolled	650	59.1	4140	63.6	4460	5.3	—
Cr-TZC-Y	M-315	Warm rolled	650	61.2	4280	65.4	4570	3.4	266
Cr-TZC-Y	M-315	Warm rolled	550	62.6	4390	66.4	4650	2.9	—
Cr-TZC-Y	M-315	Warm rolled	550	49.2	3440	49.9	3490	3.2	—
Cr-TZC-Y	M-315	Warm rolled	550	63.3	4430	69.7	4880	4.4	270
Cr-TZC-Y	M-298	Hot rolled	550	10.7	750	30.9	2160	15.2	134
Cr — 15V — 0.7Y	M-364 ^d	As-extruded	750	—	—	68.5	4800	29.0	—
Cr — 15V — 0.7Y	M-364 ^d	As-extruded	550	—	—	80.8	5650	0.5	—
Cl-5	—	As-hot-swaged	1310	22.8	1600	24.0	1680	14.2	—
Cl-7	—	As-hot-swaged	1040	58.9	4120	63.6	4450	20.7	—
Cl-7	—	As-hot-swaged	1310	22.7	1590	24.3	1700	19.5	—
Cl-8	—	As-hot-swaged	1040	73.2	5120	81.0	5670	19.3	—
Cl-9	—	As-hot-swaged	1310	28.5	1990	30.1	2110	48.6	—

^aSpecimens were 0.076 cm thick with a 0.63-cm-wide reduced section and a 2.54-cm gage length. Major axis of each specimen parallels rolling direction.

^bWarm rolled from 850°C; annealed in vacuum at 750°C for 2 hours.

Hot rolled from 1100°C; annealed in vacuum at 750°C for 2 hours.

^cYield strength value is approximate, based on deflectometer measurement of total load train elongation.

^dCylindrical button-head specimens.

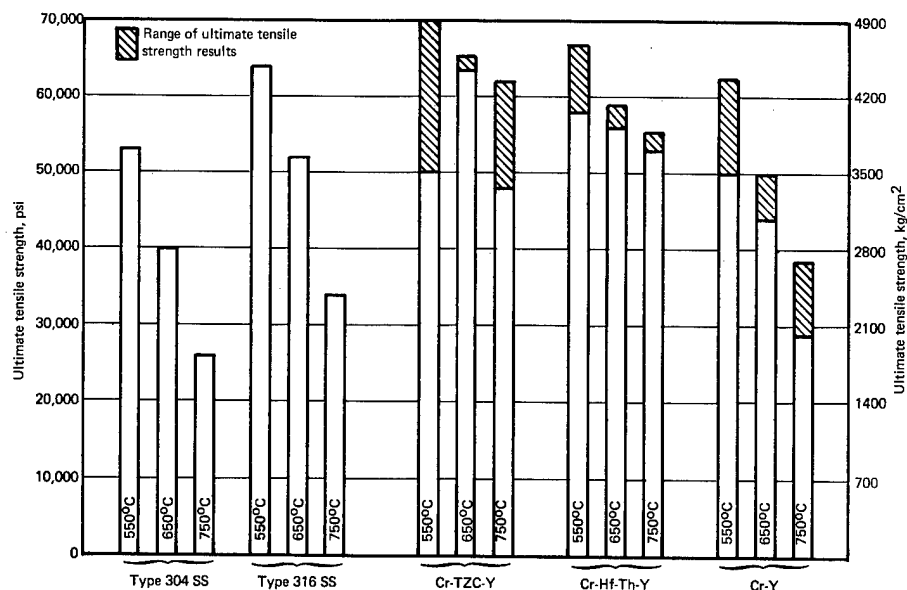


Fig. 5.2 — Ultimate tensile strengths of Type 304 and 316 stainless steel and warm rolled (850°C) Cr-base primary alloys

and 5.7. In all capsule creep tests conducted to date in this program, creep is based on total load train movement. Thus actual specimen creep is no greater, and in some cases is less than, indicated creep, which is assumed to occur within the gage section in the central 1 inch of the overall specimen length. All stainless steel data are based on a 1-inch gage length and optical readings of strain from a platinum strip extensometer. Two new systems are being procured which will permit optical strain measurements on specimens tested in argon.

DBTT in Bending — Sheet bend tests were performed on the three primary alloys and a Cr - 20V - Y (M-300) alloy after various annealing treatments. Testing was performed on a tensile machine at a crosshead speed of 0.076 cm/min over a 2T radius. Bending was continued until fracture or a 90-degree bend was achieved. Results in Table 5.9 and Figure 5.8 may be summarized as follow:

1. The DBTT for Cr-Y is about 100°C and does not vary with the annealing treatments employed.
2. The DBTT for Cr-Hf-Th-Y in the as-warm-rolled condition has not been determined, but after a 750°C anneal it is about 200°C and decreases for increasing annealing temperatures and/or times, although accompanied by a significant loss in hardness (strength).
3. The DBTT for Cr-TZC-Y has not been determined in the as-warm-rolled condition; with annealing at 750°C and 870°C after warm rolling it is apparently above 100°C. Higher annealing temperatures tend to reduce it to room temperature, again accompanied by a significant loss in hardness (strength).
4. The limited data on Cr - 20V - Y in the as-warm-rolled condition, annealed at 750°C, indicate that its DBTT exceeds 200°C.

DBTT in Impact — Subsize cylindrical notched specimens were prepared as previously described⁷ from both hot (1100°C) and warm (850°C) swaged 0.64-cm-diameter rod of the three primary alloys. Test results appear in Figure 5.9 and suggest that warm swaging and annealing at 750°C lower the DBTT of Cr-Y from 400°C for hot-swaged to approxi-

⁷GEMP-475A, p. 161.

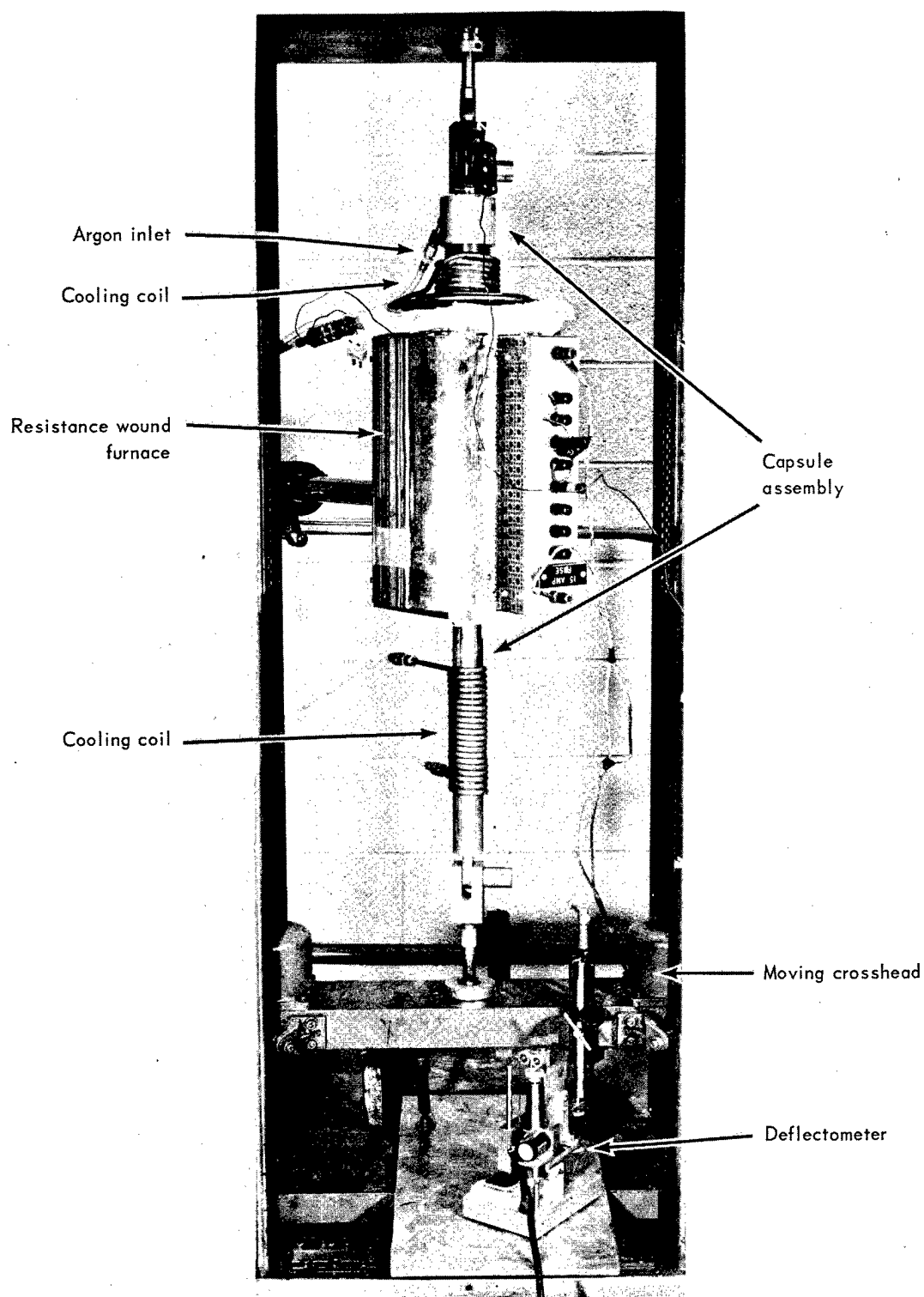


Fig. 5.3 — Arrangement used for tensile testing Cr- and Fe-base alloys in argon (Neg. P67-4-36B)

TABLE 5.8
STRESS RUPTURE RESULTS^a ON THE THREE PRIMARY Cr-BASE ALLOYS IN ARGON

Nominal Alloy Composition, at. %	Test Temperature, °C	Specimen No.	Stress		Rupture Time, hr	Total Elongation, %	Hardness, DPH		Post-Test Concentration, ppm	
			ksi	kg/mm ²			Before	After	O ₂	N ₂
Cr - 0.2Hf - 0.2Th - 0.7Y (Heat M-314)	—	As-warm-rolled	—	—	—	—	—	—	78	64
	750	BB-11	35	2464	15.7	7.1	238	231	66	98
	750	BB-1	30	2112	41.0	9.5	253	253	53	139
	750	BB-10 ^b	30	2112	25.0	7.3	232	245	74	124
	750	BB-13	25	1760	176.0	7.6	265	265	107	174
	750	BB-9	25	1760	110.7	5.1	253	270	79	202
	750	250 ^d	25	1760	122.6	12.5	224	206	—	—
	750	BB-4	20	1410	1290 ^c	1.4 ^c	233	347	146	290
	650	BB-8 ^d	45	3170	38.8	4.8	219	219	—	—
	650	251 ^d	40	2820	19.9	5.5	227	228	—	—
	650	255 ^d	35	2464	97.1	3.6	237	230	—	—
	750	219 ^d	0	0	506 ^c	—	—	—	58	58
	—	As-warm-rolled	—	—	—	—	—	—	75	34
	750	CC-4	45	3170	3.8	7.3	249	268	107	55
Cr - 0.4Zr - 0.1Ti - 0.05C - 0.7Y (Heat M-315)	750	CC-8	35	2464	1436.3 ^c	—	—	—	—	—
	750	248 ^d	35	2464	16.8	7.2	248	245	—	—
	750	257 ^d	28	1980	466.8	28.8	240	213	—	—
	750	CC-7 ^b	25	1760	1307	2.1	261	530	744	1392
	650	CC-11 ^d	45	3170	236.8	7.3	249	249	—	—
	—	As-warm-rolled	—	—	—	—	—	—	56	64
	750	247 ^d	25	1760	6.3	5.4	212	187	—	—
	750	265 ^d	20	1410	57.7	10.0	238	196	—	—
Cr - 0.7Y (Heat M-313)	650	AA-15 ^d	35	2464	141.9	16.2	209	210	—	—
	650	254 ^d	32.5	2290	102.1	7.7	266	228	—	—
	650	AA-14 ^d	30	2112	1224.4 ^c	—	227	251	59	148

^aSpecimens were 0.076 cm thick with a 0.63-cm-wide reduced section and a 2.54-cm gage length. The major axis of all specimens parallels the rolling direction.

^bTa shroud.

^cTest terminated — no rupture.

^dTi shroud.

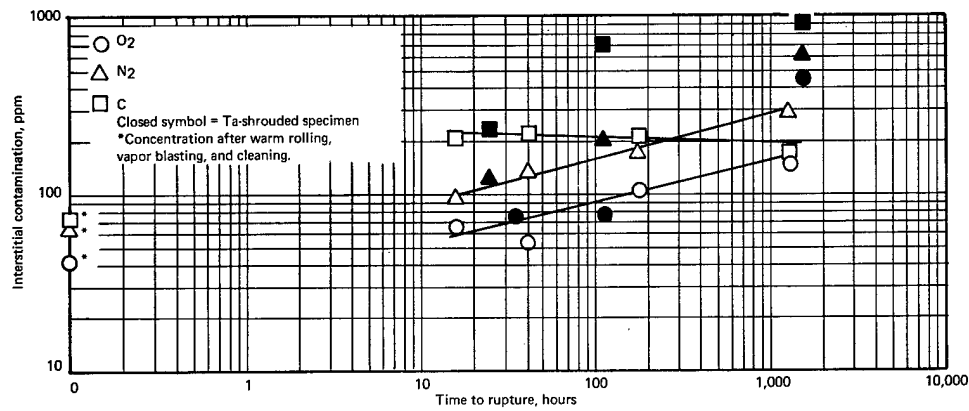


Fig. 5.4 – Effect of interstitial contamination on rupture life of Cr–Hf–Th+Y

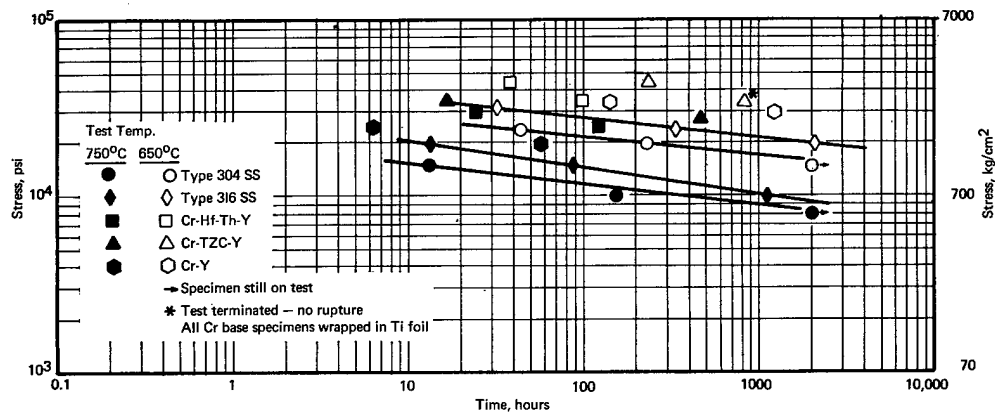


Fig. 5.5 – Stress-rupture properties of the three primary Cr-base alloys in argon.

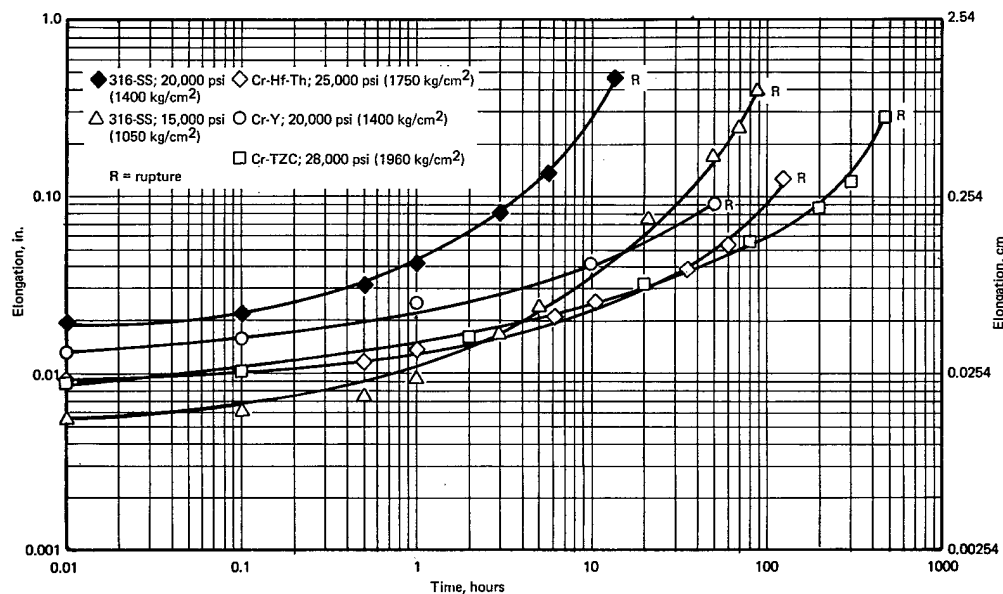


Fig. 5.6 – 750°C time extension curves for Type 316 stainless steel and the Cr-base primary alloys at various stress levels

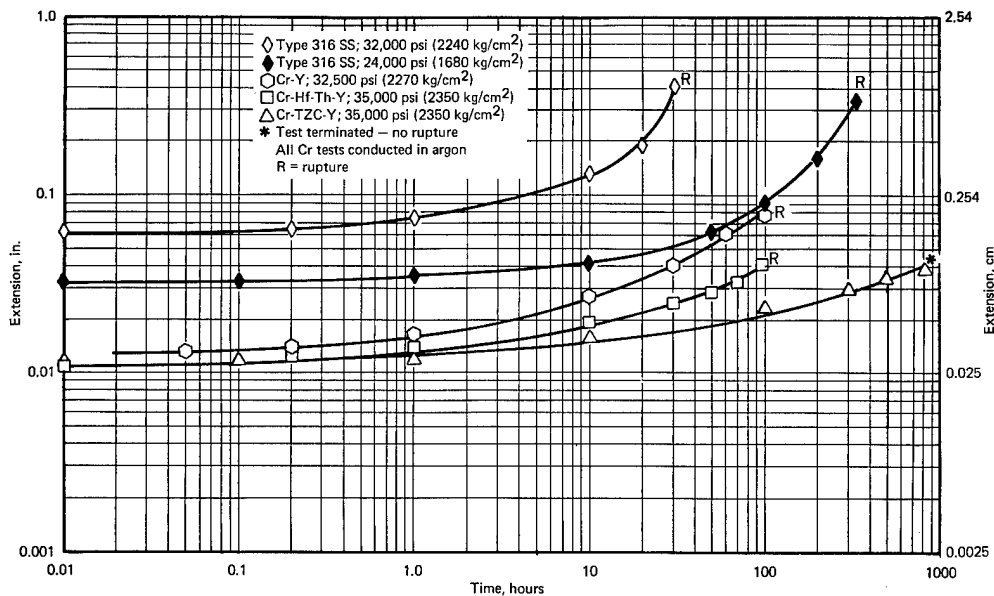


Fig. 5.7 — 650°C time — extension curves for Type 316 SS and the Cr-base primary alloys at various stress levels

mately 250°C. Annealing at 980°C after warm swaging raises the transition temperature of Cr-Y by approximately 125°C. Warm swaging and annealing, compared to hot swaging, apparently have little effect on the DBTT of Cr-Hf-Th-Y. Compared with previous results on hot-swaged material,⁸ warm swaging and annealing at 750°C of Cr-TZC-Y reduces the DBTT from approximately 500°C to 400°C.

Hot-Hardness — Hot-hardness tests were performed on the three primary alloys and several experimental compositions utilizing a previously described test apparatus.⁹ Figure 5.10 compares the hot-hardness of the three primary alloys in the warm-rolled condition with two high-strength chromium-base alloys and two experimental chromium-base alloys. The primary alloys are generally softer than the high-strength chromium-base alloys.

Thermal Stability → p. 230

Vacuum annealing stability studies were performed on the three primary alloys wrapped in tantalum foil at temperatures from 750° to 1100°C for 2 and 10 hours. Figure 5.11 incorporates previous¹⁰ 2-hour vacuum annealing data on warm-rolled sheet with 10-hour data. The change in hardness which appears when the annealing time is increased from 2 to 10 hours has initiated a more complete investigation of longtime (1000 hr) annealing and its effect on mechanical properties, taking into account the two competing processes of softening during annealing and hardening due to interstitial contamination from the test environment. Photomicrographs¹¹ of warm- and hot-rolled Cr-Y after 2-hour vacuum anneals at 750° to 1090°C show partial recrystallization in the warm-rolled specimens after the 870°C anneal. Significant grain growth occurs after the 1090°C anneal. No change in the structure of the hot-rolled material can be noted, even after the 1090°C anneal.

⁸GEMP-475A, pp. 161–162.

⁹"AEC Fuels and Materials Development Program Progress Report No. 69," GE-NMPO, GEMP-69, September 29, 1967, pp. 106–108.

¹⁰GEMP-475A, pp. 162, 164.

¹¹"AEC Fuels and Materials Development Program Progress Report No. 67," GE-NMPO, GEMP-67, June 30, 1967, p. 97.

TABLE 5.9

BEND DATA FOR Cr-BASE ALLOY AS A FUNCTION OF VACUUM ANNEALING CONDITIONS

Alloy Designation	Heat No.	Vacuum Annealing Conditions	Hardness, DPH	Temperature, ^a °C	Bend Angle, degrees	Comment
Cr-Y, W/R ^b	M-313	As-rolled	195	RT	9	Fractured
Cr-Y, W/R		750°C - 2 hr	195	RT	6	Fractured
Cr-Y, W/R		980°C - 2 hr	127	RT	9	Fractured
Cr-Y, W/R		As-rolled	195	106	90	No fracture
Cr-Y, W/R		750°C - 2 hr	195	104	90	No fracture
Cr-Y, W/R		870°C - 2 hr	178	104	90	No fracture
Cr-Y, W/R		980°C - 2 hr	127	100	90	No fracture
Cr-Y, W/R		750°C - 10 hr	200	110	90	No fracture
Cr-Y, W/R		870°C - 10 hr	136	106	90	No fracture
Cr-Y, H/R		750°C - 2 hr	140	109	5	Fractured
Cr-Hf-Th-Y, W/R	M-314	980°C - 2 hr	175	RT	90	No fracture
Cr-Hf-Th-Y, W/R		870°C - 10 hr	197	RT	90	No fracture
Cr-Hf-Th-Y, H/R		980°C - 3.5 hr	145	RT	90	No fracture
Cr-Hf-Th-Y, W/R		750°C - 2 hr	232	100	9	Fractured
Cr-Hf-Th-Y, W/R		750°C - 2 hr	232	150	10	Fractured
Cr-Hf-Th-Y, W/R		750°C - 2 hr	232	204	90	Fractured
Cr-Hf-Th-Y, W/R		750°C - 10 hr	222	110	72	Fractured
Cr-Hf-Th-Y, W/R		870°C - 2 hr	216	110	18	Fractured
Cr-Hf-Th-Y, W/R		870°C - 10 hr	197	110	90	No fracture
Cr-Hf-Th-Y, W/R		870°C - 2 hr	216	150	90	No fracture
Cr-Hf-Th-Y, W/R		870°C - 2 hr	216	209	90	No fracture
Cr-Hf-Th-Y, W/R		980°C - 2 hr	175	108	90	No fracture
Cr-Hf-Th-Y, W/R		1090°C - 2 hr	140	110	90	No fracture
Cr-Hf-Th-Y, H/R		750°C - 2 hr	196	105	7	Fractured
Cr-Hf-Th-Y, H/R		980°C - 3.5 hr	145	109	90	No fracture
Cr-TZC-Y, W/R	M-315	980°C - 2 hr	154	RT	7	Fractured
Cr-TZC-Y, W/R		1090°C - 2 hr	129	RT	90	No fracture
Cr-TZC-Y, H/R		980°C - 3.5 hr	142	RT	5	Fractured
Cr-TZC-Y, W/R		750°C - 2 hr	259	RT	12	Fractured
Cr-TZC-Y, W/R		750°C - 2 hr	259	150	7	Fractured
Cr-TZC-Y, W/R		750°C - 2 hr	259	204	9	Fractured
Cr-TZC-Y, W/R		750°C - 10 hr	252	110	15	Fractured
Cr-TZC-Y, W/R		870°C - 2 hr	227	110	5	Fractured
Cr-TZC-Y, W/R		870°C - 2 hr	227	150	18	Fractured
Cr-TZC-Y, W/R		870°C - 2 hr	227	204	9	Fractured
Cr-TZC-Y, W/R		870°C - 10 hr	211	106	9	Fractured
Cr-TZC-Y, W/R		980°C - 2 hr	154	108	90	No fracture
Cr-TZC-Y, H/R		750°C - 2 hr	181	114	7	Fractured
Cr-TZC-Y, H/R		980°C - 3.5 hr	142	108	90	No fracture
Cr-V-Y, W/R	M-300	750°C - 2 hr	366	110	9	Fractured
Cr-V-Y, W/R		750°C - 2 hr	366	152	10	Fractured
Cr-V-Y, W/R		750°C - 2 hr	366	204	9	Fractured

^aFor tests above room temperature, the specimens were heated in test position in a resistance furnace.^bW/R - warm-rolled from 850°C.

H/R - hot-rolled from 1100°C.

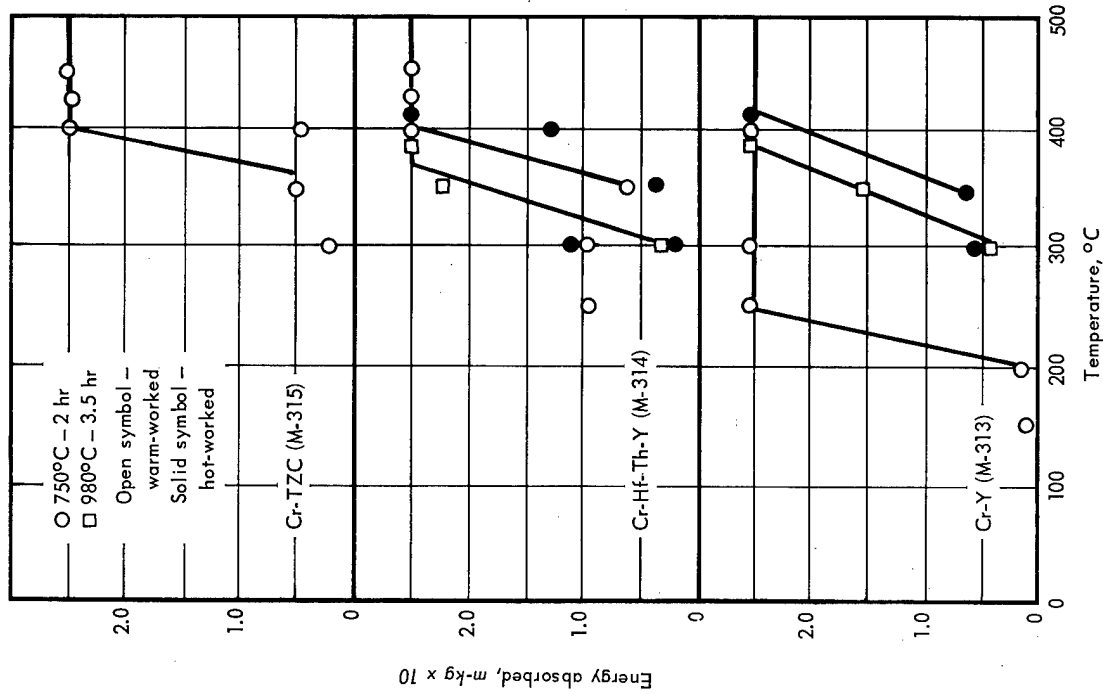


Fig. 5.9 — Impact data for Cr-base alloys as a function of vacuum annealing conditions

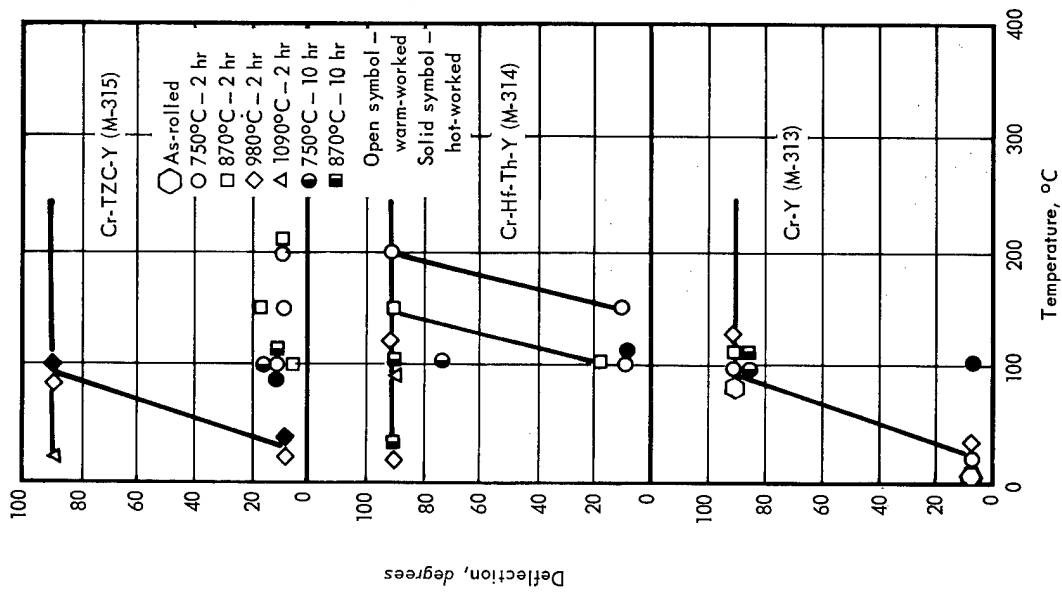


Fig. 5.8 — Bend data for Cr-base alloys as a function of vacuum annealing conditions

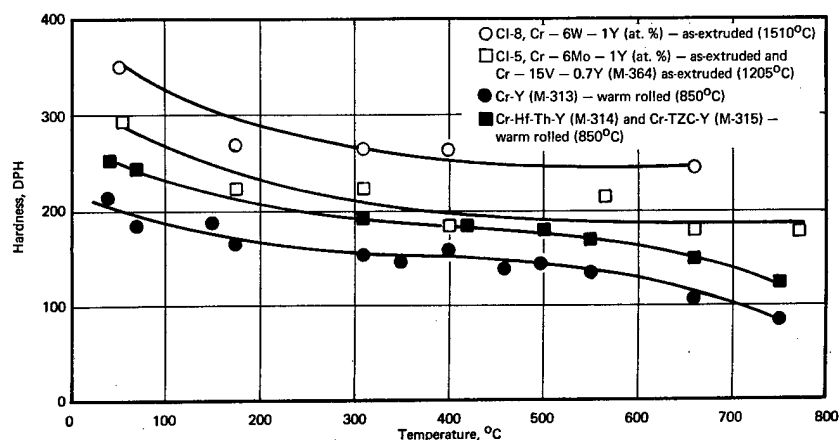


Fig. 5.10 – Hot hardness of Cr-base alloys

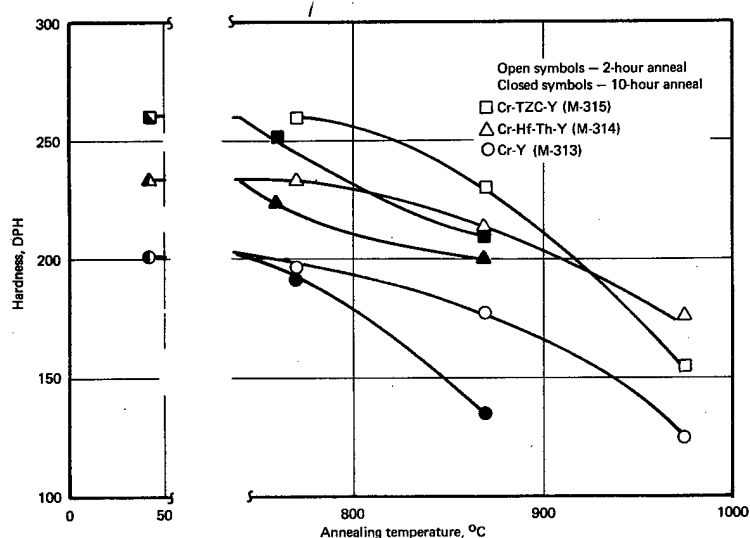


Fig. 5.11 – Room-temperature hardness versus annealing temperature for warm-rolled Cr-base alloys

Hot-hardness at 750°C as a function of time was determined for the three primary alloys and the Cr – 20V – Y (M-300) alloy in the warm-rolled condition. These tests were conducted in argon, in the previously described hot-hardness tester. The impressions were made periodically and read after the 137-hour period when the specimens cooled to room temperature. The results (Figure 5.12) show that all alloys retained essentially uniform hardness except for the Cr-Y specimen which softened after about 75 hours of exposure.

Processability

Previous exploratory efforts¹² to determine the feasibility of fabricating a chromium-base alloy in tubular form were moderately successful. Preliminary welding experiments were performed on bend specimens of warm-rolled Cr-Y sheet.¹³ A TIG weld pass parallel

¹²GEMP-475A, pp. 162–166.

¹³GEMP-67, pp. 102–103.

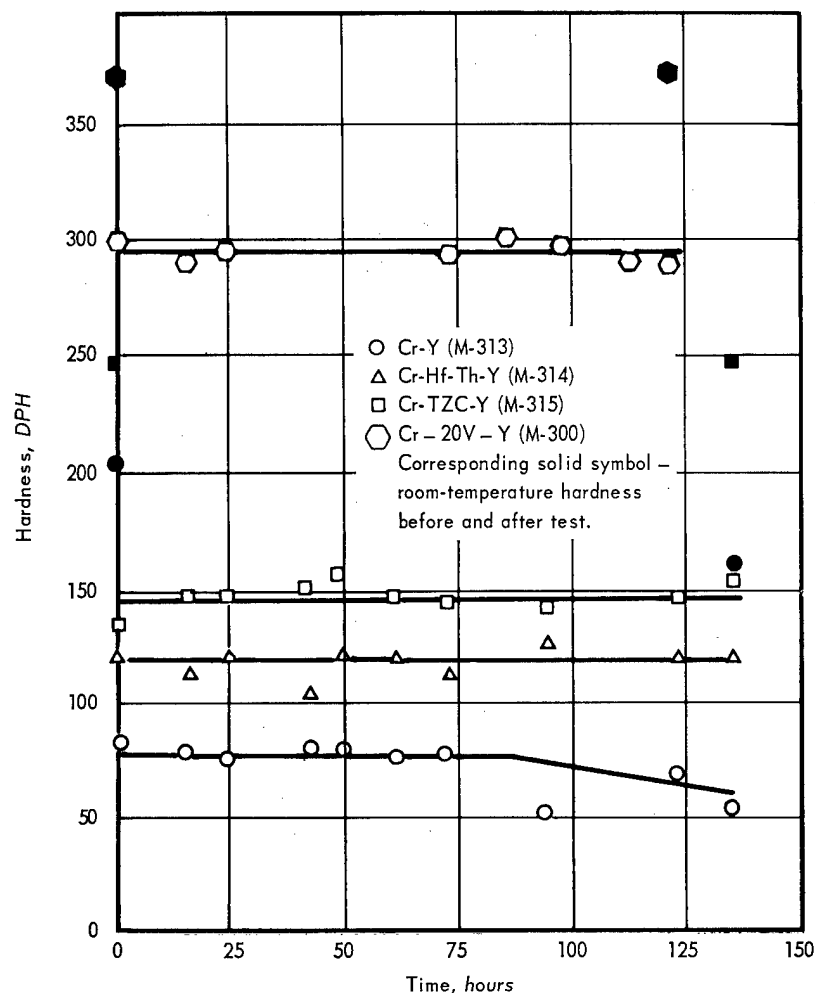


Fig. 5.12 — Hot-hardness of Cr-base alloys at 750°C

to the major axis produced a weld zone 3.2 mm wide with about 95 percent penetration in all cases. Both the weld zone and heat-affected zone were free of cracks and voids and had a common hardness of 160 DPH, compared to the 197 DPH hardness of the warm-rolled parent metal before welding. Bend tests conducted on the welded specimens indicated a DBTT similar to that obtained for the parent metal under similar annealing conditions. A typical TIG welded specimen before and after bend testing is shown in Figure 5.13. Exploratory electron-beam welds were attempted at 10^{-5} Torr, but prohibitive volatilization of chromium occurred.

Radiation Stability

Hot-rolled creep-rupture and bend specimens of the three primary alloys were included in irradiation experiment capsule ORM-53, which received an estimated dosage of 2.3×10^{20} n/cm² ($E_n \geq 1$ Mev). The capsule was irradiated in the A-2 facility of the ORR for four cycles. The specimens appeared in good condition following capsule disassembly. Testing has not yet begun.

5.2 Fe-Cr-Al-Y ALLOYS

The Fe-Cr-Al-Y alloys were investigated with the knowledge that they were low in strength compared to austenitic stainless steel, but that their oxidation resistance and tensile ductility

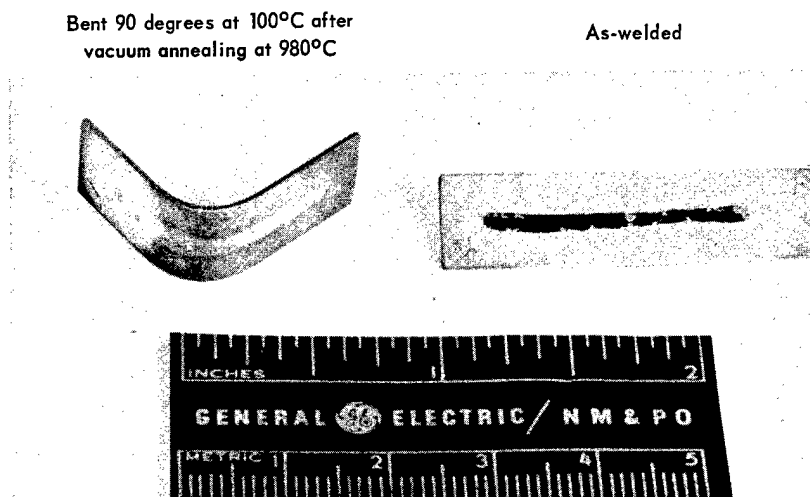


Fig. 5.13 — Welded Cr-Y alloy (M-313) bend specimens (Neg. P67-5-21)

were excellent. There were indications that their resistance to irradiation might be outstanding.¹⁴ It was also considered possible that retention of ductility in an alloy during service might be more important ultimately than an initial high-strength level compromised by loss of ductility during service. *→ p. 232*

During the past year a number of previously developed Fe-Cr-Al-Y alloys have been characterized, particularly with respect to strength in the temperature range of interest. Although a few additional studies remain to be completed, no new work is contemplated on alloys within this system.

MATERIAL PREPARATION

The sheet material used in the characterization of the Fe-Cr-Al-Y alloys was provided by six 45.5-kg heats. Melting and fabrication details were previously described.¹⁵ Analyses of the six heats appear in Table 5.10.

MATERIAL EVALUATION

Environmental Compatibility

Two Fe-Cr-Al-Y specimens were included in the capsule tested at ANL. The results in Table 5.11 indicate weight losses comparable to the reference V-20 Ti specimen and in excess of the chromium-base alloys. Previous data¹⁶ on a number of Fe-Cr-Al-Y specimens exposed to static metallic sodium (containing 22 ppm O₂) at 750°C for 1000 hours indicated that most alloys were more susceptible than chromium-base alloys similarly tested. To determine effect of longer exposure times, two additional capsules have completed over 2000 hours on test. One capsule contains vapor-blasted bend specimens (0.076 by 0.947 by 3.8 cm) of 1541* (heat MS-51), 0561 (heat MS-59), 1061 (heat MS-61), 2541 (heat MS-62), 0561+3Mo (heat MS-64), and 304 and 316 stainless steel. The other capsule contains specimens pre-oxidized in air at 1090°C for 1 hour after vapor blasting. These await inspection.

*Designation for Fe-Cr-Al-Y alloy. The first two digits denote Cr content, the third Al, and the fourth Y; i.e., 1541 is Fe-15Cr-4Al-1Y, 0561 is Fe-5Cr-6Al-1Y, etc.

¹⁴GEMP-67, pp. 25, 126.

¹⁵GEMP-475A, p. 144.

¹⁶GEMP-475A, pp. 145-147.

TABLE 5.10
COMPOSITION OF Fe-Cr-Al-Y 45.5-kg INDUCTION MELTED HEATS

Alloy Designation	Heat No.	Nominal Composition, wt %							Interstitial Concentration, ppm	
		Cr	Al	Y	C	Si	Mo	Fe	O ₂	N ₂
0561	MS-59	4.75	5.96	1.02	0.05	—	—	Bal	9	1
1041	MS-60	9.82	3.86	0.82	0.05	0.03	—	Bal	36	4
1541	MS-51	15.11	4.01	0.77	—	—	—	Bal	15.6	1.9
1061	MS-61	11.87	5.89	1.07	0.03	0.04	—	Bal	239	39
2541	MS-62	24.55	3.83	1.23	0.04	0.15	—	Bal	11	6
0561 + 3Mo	MS-64	5.34	5.87	1.46	0.04	0.09	3.42	Bal	65	12

TABLE 5.11
WEIGHT CHANGE DATA FOR Fe-Cr-Al-Y ALLOYS

Alloy Heat No.	Nominal Composition, wt %	Weight Loss, ^a mg/cm ²
MS-51	Fe - 15Cr - 4Al - 1Y	0.800
MS-60	Fe - 10Cr - 4Al - 1Y	0.130
	V - 20Ti	0.500

^aWeight losses are accurate to ± 0.001 mg/cm².

Strength and Ductility

Tensile Properties — Tensile tests were performed at room temperature, 550°, and 750°C on annealed sheet specimens of the six Fe-Cr-Al-Y alloys listed in Table 5.10. Results appear in Table 5.12 and Figure 5.14, including NMPO data for austenitic stainless steel.[†] Strength apparently increases somewhat with increasing chromium and aluminum until 750°C, when the strengths are nearly the same. The strength increase afforded by the 3 percent molybdenum addition to 0561 alloy is noteworthy. None of these alloys have tensile strengths up to 750°C as high as the austenitic stainless steels, but most of them possess equivalent or superior yield strengths at all test temperatures.

Stress-Rupture Strength — Stress-rupture tests on the Fe-Cr-Al-Y alloys were conducted in air at 550°C and 750°C using 0.076-cm-thick sheet specimens. The results shown in Table 5.13 and Figure 5.15 are conclusive in demonstrating the low stress-rupture strength of the Fe-Cr alloys compared to austenitic stainless steel. For the Fe-Cr-Al-Y compositions, however, the higher strength at 750°C of the 2541 alloy and the beneficial effect of molybdenum should be noted. At 550°C chromium level does not significantly affect stress-rupture strength, but the molybdenum addition remains advantageous. The reservoir of ductility suggested by the generally high elongation values of the Fe-Cr-Al-Y alloys is probably related to the favorable radiation behavior which has been reported¹⁷ for the 1541 alloy.

DBTT in Bending — Annealed (1000°C, 10 min) bend specimens (0.076 by 0.95 by 3.81 cm) of the six 45.5-kg heats listed in Table 5.10 were tested before and after aging at 450°C for 1000 hours. The specimens were bent over a 2T radius in a tensile machine at a crosshead speed of 0.69 cm/min until fracture or a 90-degree bend was achieved. The results (Table 5.14) indicate a rise in the DBTT of 1541 and 2541 as a result of aging. Transition temperatures of the remaining alloys were unchanged by aging. The DBTT of all annealed specimens was 0°C or lower.] →

[†]Chemical analysis, weight percent:

304 — 19.08 Cr, 9.21 Ni, 0.63 Si, 1.88 Mn, 460 ppm N₂, 417 ppm C.

316 — 17.61 Cr, 12.5 Ni, 2.62 Mo, 0.63 Si, 1.9 Mn, 580 ppm N₂, 393 ppm C.

¹⁷GEMP-67, pp. 125–126.

TABLE 5.12
TENSILE DATA^a FOR Fe-Cr-Al-Y ALLOYS
(100-lb Vacuum-Induction-Melted Heats Converted to 0.076-cm Sheet)

Alloy	Heat No.	Test Temperature, °C	0.2% Yield Strength,		Ultimate Strength,		Elongation in 2.54 cm, %
			psi	kg/cm ²	psi	kg/cm ²	
0561	MS-59	24	45,100	3170	63,400	4460	19.4
		24	45,100	3170	64,100	4510	22.9
		24	45,700	3210	65,600	4610	25.7
		550	26,500	1860	33,300	2340	46.0
		550	25,800	1810	31,600	2220	33.1
		750	8,900	630	9,600	670	24.7
		750	—	—	10,600	750	19.2
		750	8,400	590	9,400	660	22.1
1041	MS-60	24	43,300	3040	66,600	4680	28.0
		24	41,100	2890	67,000	4710	29.1
		24	40,600	2850	67,500	4750	28.4
		550	22,200	1560	30,900	2170	26.6
		550	24,600	1730	32,000	2250	20.8
		750	8,100	570	9,200	650	39.5
		750	8,000	560	9,100	640	28.4
1061	MS-61	24	54,500	3830	74,800	5260	22.7
		24	54,800	3850	74,000	5200	21.4
		24	55,700	3920	75,000	5270	22.3
		550	31,900	2240	37,600	2640	25.0
		550	30,900	2170	35,500	2500	38.7
		750	7,700	540	8,300	580	13.6
		750	—	—	9,500	670	22.4
1541	MS-51	24	49,600	3490	71,800	5050	25.7
		24	48,900	3440	71,400	5020	25.1
		24	49,800	3500	71,300	5010	24.2
		550	27,300	1920	35,000	2460	26.7
		550	27,300	1920	34,500	2430	26.2
		550	27,100	1900	33,000	2320	35.9
		750	8,000	560	9,200	650	16.9
		750	9,500	670	10,000	700	20.8
2541	MS-62	24	56,000	3940	79,300	5580	19.1
		24	54,300	3820	78,800	5540	21.2
		24	55,300	3890	79,300	5580	18.5
		550	35,300	2480	41,700	2930	35.5
		750	—	—	15,800	1110	19.7
		750	11,600	820	11,900	840	20.6
		750	12,200	860	13,300	940	—
0561 + 3Mo	MS-64	24	58,500	4110	79,300	5580	20.4
		24	58,400	4100	79,100	5560	21.8
		24	57,900	4070	78,500	5520	21.2
		550	37,400	2630	50,000	3520	29.3
		750	15,900	—	15,900	1120	18.7
		750	14,500	1120	14,500	1020	11.6
		750	16,100	1130	16,200	1140	11.6
Type 304 SS	—	24	28,300	1980	85,500	5990	74.6
		550	10,100	700	53,300	3740	35.5
		750	8,600	600	26,000	1820	19.1
Type 316 SS	—	24	35,700	2500	83,200	5830	72.5
		550	16,000	1120	64,000	4470	42.5
		750	13,000	910	34,000	2380	52.1

^aSpecimens were 0.076 cm thick with a 1.27-cm-wide reduced section and a 2.54-cm gage length. The major axis of all specimens parallels the rolling direction.

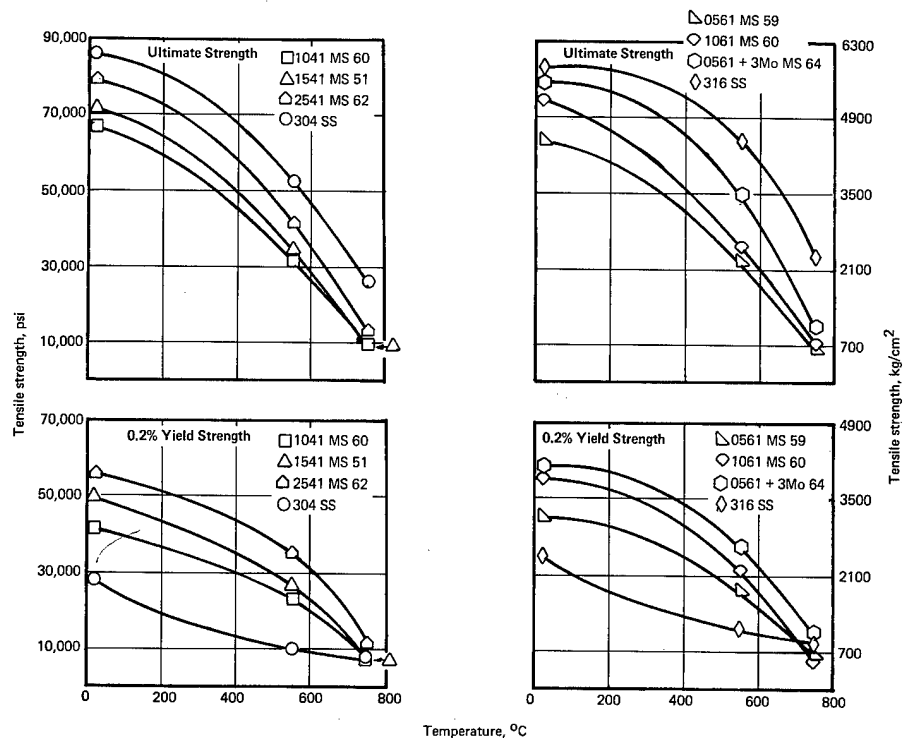


Fig. 5.14 — Tensile and yield strength of Fe-Cr-Al-Y alloys versus temperature

DBTT in Impact ^{FeB} — The DBTT of 0561 (heat MS-59) and 1041 (heat MS-60) were determined by testing Charpy V-notch specimens at various temperatures. Specimens were prepared from a 2.22-cm diameter hot-rolled (982°C) stock originating from 3.15-cm diameter extrusions. Results (Figure 5.16) suggest a DBTT between 100° and 200°C for both alloys, which is substantiated by the appearance of the fracture surfaces of 1041 (heat MS-60) shown in Figure 5.17.

A study was made to determine the correlation between DBTT as measured by subsize cylindrical notched impact specimens and Charpy V-notch specimens. Subsize specimens were machined from both halves of fractured Charpy V-notch specimens of an Fe-Cr-Al-Y alloy (MS-60—1041). The results (Figure 5.18) reveal that the subsize specimen indicates a lower DBTT than the standard Charpy V-notch. Although the subsize specimen will continue to be used for screening purposes, the ASTM standard Charpy V-notch or drop-weight test will be used in circumstances demanding comparative engineering data.

Thermal Stability

The tendency for alpha-prime precipitation in the Fe-Cr-Al-Y system has been studied.^{18,19,20} Annealed sheet specimens, 0.076 by 0.95 by 3.81 cm, of the alloys listed in Table 5.10 were heated in air at 450°C for periods up to 1000 hours. Change in hardness was used to estimate the extent of alpha-prime precipitation; results appear in Table 5.15.

¹⁸GEMP-67, pp. 104, 108, 109.

¹⁹GEMP-69, p. 100.

²⁰GEMP-1002, pp. 89, 91.

TABLE 5.13
CREEP-RUPTURE DATA^a FOR Fe-Cr-Al-Y ALLOYS IN AIR

Alloy Designation	Heat No.	Test Temperature, °C	Stress		Time to Indicated Strain, hr			Time to Rupture, hr	Linear Creep Rate, hr ⁻¹	Elongation, %
			psi	kg/cm ²	0.5%	1%	5%			
0561	MS-59	550	20,000	1400	0.2	0.5	2.5	9.5	2.0×10^{-2}	37.9
			15,000	1050	1.1	2.9	18.8	87.2	2.3×10^{-3}	60.2
			11,000	770	10.3	23.5	126.0	619	3.7×10^{-4}	71.7
		750	3,000	210	0.7	1.4	6.6	35.9	7.4×10^{-3}	44.7
			2,000	140	1.8	6.6	51	331.2	6.4×10^{-4}	61.0
			1,000	77	158.0	880.0	—	2015.3	1.1×10^{-5}	1.5
	0561 + 3Mo MS-64	550	40,000	2800	—	—	1.6	4.4	1.7×10^{-2}	27.1
			30,000	2100	2.8	6.4	25.8	70.2	1.8×10^{-3}	39.3
			20,000	1400	36.5	78.5	318.0	948.0	1.2×10^{-4}	70.2
			15,000	1050	190.0	334.0	—	867.6	4.1×10^{-5}	3.2 ^b
		750	5,000	350	0.4	0.8	3.3	14.6	—	76.9
			4,000	280	1.7	3.4	12.9	52.5	3.0×10^{-3}	89.8
			3,000	210	5.8	13.0	76.3	441.3	5.8×10^{-4}	42.3
	1041 MS-60	550	20,000	1400	—	0.4	3.9	23.9	1.1×10^{-2}	62.7
			15,000	1050	2.3	6.4	38.8	168.8	1.23×10^{-3}	48.1
			13,000	910	6.5	14.5	74.5	385.9	6.05×10^{-4}	73.4
			7,000	490	181.0	435.1	—	492.0 ^b	2.0×10^{-5}	1.10 ^b
		750	4,000	280	0.3	0.7	3.8	14.8	1.2×10^{-2}	57.6
			3,000	210	1.0	2.3	12.1	58.9	4.0×10^{-3}	51.9
			2,000	140	10.0	32.0	310.0	—	1.5×10^{-4}	—
			1,400	98	163.0	512.0	—	600.1 ^b	1.7×10^{-5}	1.1 ^b
	1061 MS-61	550	20,000	1400	0.2	0.5	2.5	11.4	2.0×10^{-2}	52.2
			15,000	1050	0.5	1.7	13.5	84.7	3.3×10^{-3}	52.4
			11,000	770	12.0	24.0	112.0	489.2	4.2×10^{-4}	105.3
		750	4,000	280	0.2	0.3	1.73	8.2	2.8×10^{-2}	65.6
			3,000	210	0.6	1.3	7.0	38.5	7.0×10^{-3}	25.9
			2,500	175	2.9	5.8	28.6	142.9	1.8×10^{-3}	—
			2,000	140	6.1	14.3	92.3	395.0	4.6×10^{-4}	34.5
	1541 MS-51	550	20,000	1400	0.7	1.7	—	49.4	2.4×10^{-3}	44.8
			15,000	1050	16.5	56.6	193.0	491.4	1.2×10^{-4}	44.3
			11,000	770	330.0	850.0	1808.0	3567.8	—	75.0
		750	3,000	210	1.0	2.2	11.5	42.9	4.3×10^{-3}	34.7
			2,000	140	12.3	26.7	145.0	624.2	3.5×10^{-4}	59.2
	2541 MS-62	550	1,100	77	510.0	—	—	2278.0 ^b	1.5×10^{-6}	0.59 ^b
		750	25,000	1750	0.2	0.3	2.7	10.8	1.5×10^{-2}	43.2
			20,000	1400	0.8	2.3	13.1	34.8	3.1×10^{-3}	47.6
			15,000	1050	2.8	6.7	46.7	213.5	9.0×10^{-4}	49.9
			5,000	350	680.0	—	—	2188.4 ^b	2.5×10^{-6}	0.59 ^b
		750	5,000	350	0.3	0.6	2.5	16.1	—	83.4
			3,500	245	1.1	2.8	16.9	73.7	2.9×10^{-3}	79.5
			3,000	210	3.4	7.2	36.3	243.2	1.3×10^{-3}	60.5
			1,100	77	272.0	1800.0	—	1946.8 ^b	2.6×10^{-6}	1.1 ^b

^aSpecimens were 0.076 cm thick with 1.27-cm-wide reduced section with 2.54-cm gage length. The major axis of all specimens parallels the rolling direction. Annealed at 1000°C for 10 minutes and water-quenched.

^bTest terminated — no rupture.

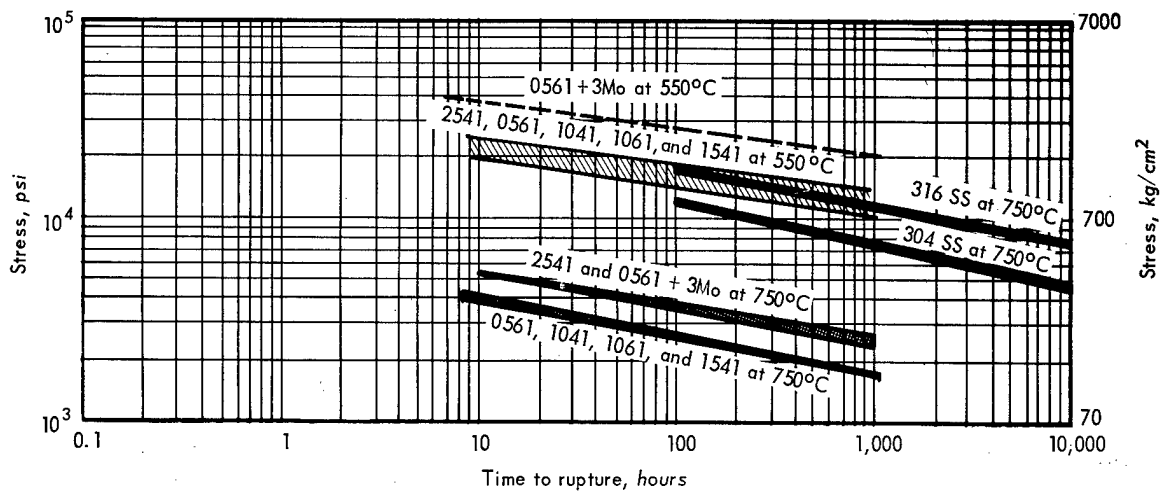


Fig. 5.15 — Creep-rupture data for Fe-Cr-Al-Y alloys

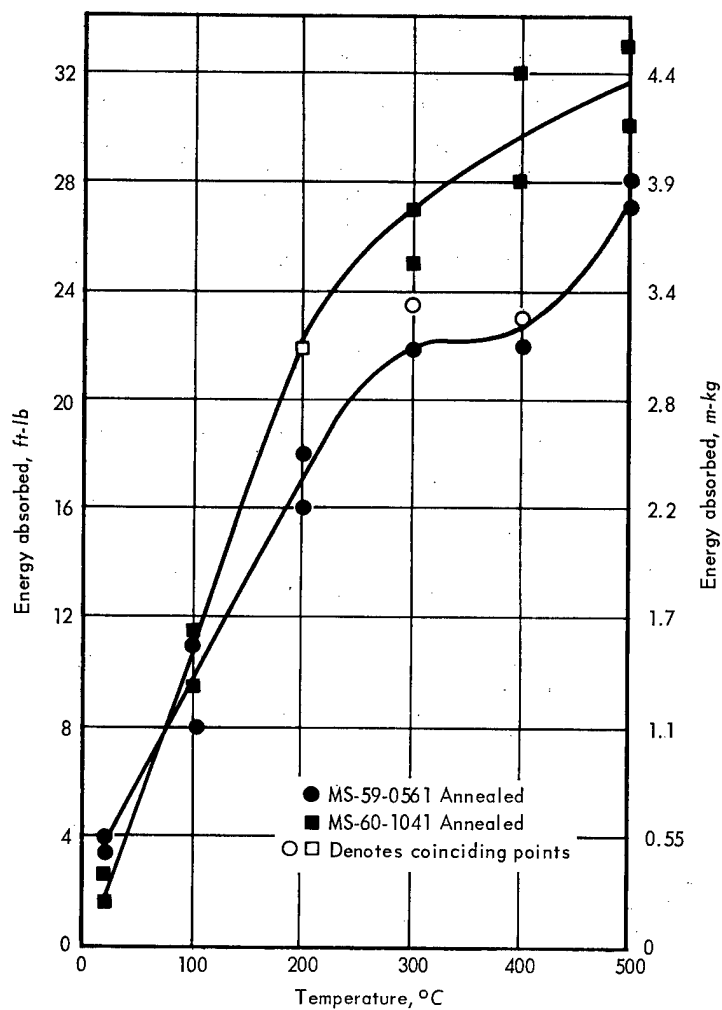


Fig. 5.16 — Charpy V-notch impact data for Fe-Cr-Al-Y alloys

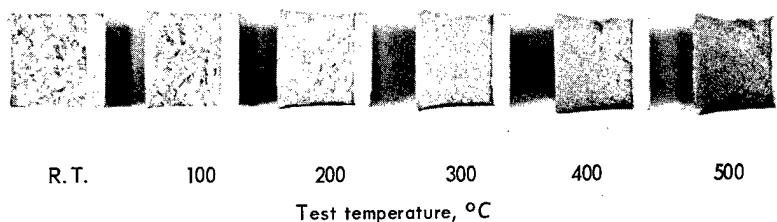


Fig. 5.17 — Fracture surfaces of 1041 alloy (Heat MS-60) (Neg. P67-8-1)

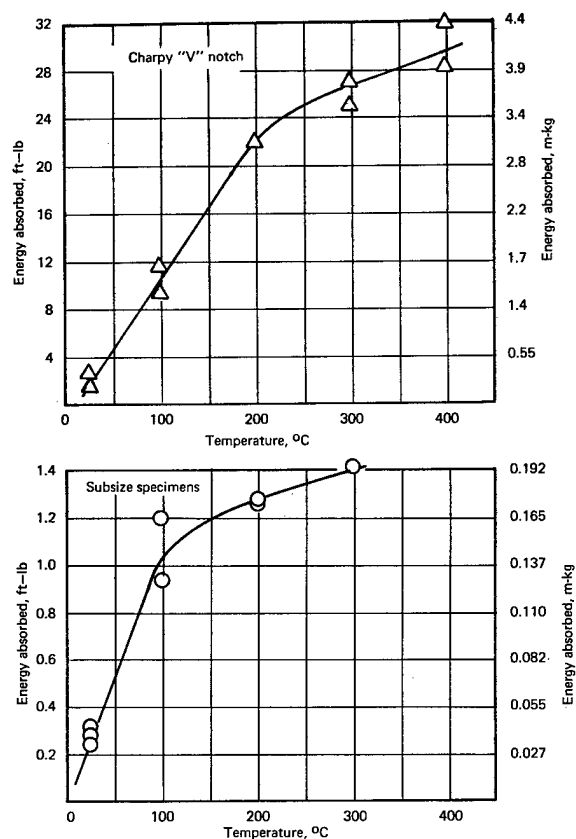


Fig. 5.18 — Impact specimen correlation study results

Alloys containing 10 weight percent chromium or less showed no significant long-term aging; the 1541 and 2541 alloys, particularly the latter, aged extensively. Aging was considerable even after 100 hours for the 2541 alloy; most of the aging in the 1541 alloy occurred beyond 500 hours. The reason for the apparent aging of the 0561 + 3 Mo alloy after 100 and 250 hours, but not at longer times, is unknown.

Results of bend tests conducted on these specimens following aging are presented under the section, DBTT in bending.

TABLE 5.14

SHEET BEND TEST OF ANNEALED AND AGED
Fe-Cr-Al-Y ALLOYS^a

Alloy	Heat No.	Specimen Condition	Bend Angle at Indicated Temperature, degrees		
			RT	0°C	-78°C
0561	MS-59	Annealed	90	90	90
0561	MS-59	Aged			90
1041	MS-60	Annealed	90	90	90
1041	MS-60	Aged			90
1061	MS-61	Annealed	90	90	45
1061	MS-61	Aged		90	30
1541	MS-51	Annealed	90	90	90
1541	MS-51	Aged	90	30	
2541	MS-62	Annealed	90	90	90 ^b
2541	MS-62	Aged	0		
0561 + 3Mo	MS-64	Annealed	90	90	35
0561 + 3Mo	MS-64	Aged	90	90	30

^aAnnealed: 1000°C for 10 minutes; water quenched.

Aged: 450°C for 1000 hours.

^bBroke as bend reached 90°; other 90° bends did not break.

TABLE 5.15

AGING OF Fe-Cr-Al-Y^a ALLOYS AT 450°C

Alloy	Heat No.	Hardness versus Time at 450°C, DPH				
		Annealed	100 hr	250 hr	500 hr	1000 hr
0561	MS-59	188	207	193	178	187
0561 + 3Mo	MS-64	216	256	255	206	224
1041	MS-60	179	183	179	165	177
1061	MS-61	209	214	217	194	220
1541	MS-51	196	200	238	220	267
2541	MS-62	228	274	341	325	391

^a45.5-kg vacuum-induction heats converted to 0.076-cm sheet.

Radiation Stability

Capsule ORM-53, which contained five bend and five creep-rupture specimens of 0561 (heat MS-59), 0561 + 3Mo (heat MS-64), 1541 (heat MS-51), 1061 (heat MS-61), and 1041 (heat MS-60), had completed irradiation under conditions described earlier in this report. Post-testing remains to be performed.

5.3 IRON-BASE (FERRITIC)

Details of this work withheld pending patent clarification.

5.4 IRON-BASE (AUSTENITIC)

Details of this work withheld pending patent clarification.

5.5 SUMMARY AND CONCLUSIONS

In the alloy studies conducted during the past year, primary emphasis has been on developing alloys which have mechanical properties comparable or superior to austenitic stainless steel. Compositions have been investigated from four alloy systems: chromium-base, Fe-Cr-Al-Y alloys, iron-base (ferritic), and iron-base (austenitic). Comparative tensile, yield, stress-rupture and creep strength, and other pertinent data are presented for the various alloys under study. Considerably more work will be required before thorough comparisons can be made, but sufficient data have been obtained for preliminary comparisons.

A comparison of the tensile and yield strengths of representative alloys within the various systems is contained in Figures 5.19 and 5.20. Data included in these and subsequent comparisons, except for the austenitic stainless steels, are based on tests of specimens from 3.6- to 5.5-kg vacuum-induction-melted laboratory heats which were extruded and rolled to approximately 0.076-cm sheet. Tests on all program alloys, other than the air-tested Fe-Cr-Al-Y system, were conducted in an argon atmosphere. The stainless steel data (based on air tests) are for commercial heats converted to 0.076-cm sheet and annealed at 1120°C for 0.5 hour and water quenched. Figure 5.19 illustrates tensile strength as a function of temperature for the various alloys. Beyond about 650°C, iron-base (austenitic) and the chromium-base alloys are clearly superior to the austenitic stainless steels. This advantage appears to increase with reducing temperatures for the iron-base

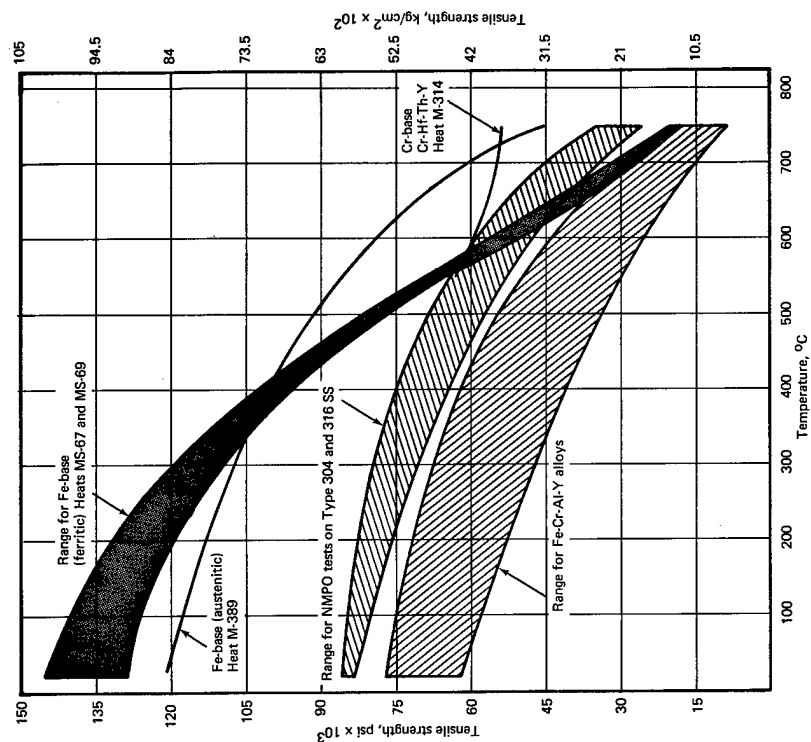


Fig. 5.19 — Tensile strength versus temperature for potential fast breeder reactor cladding material

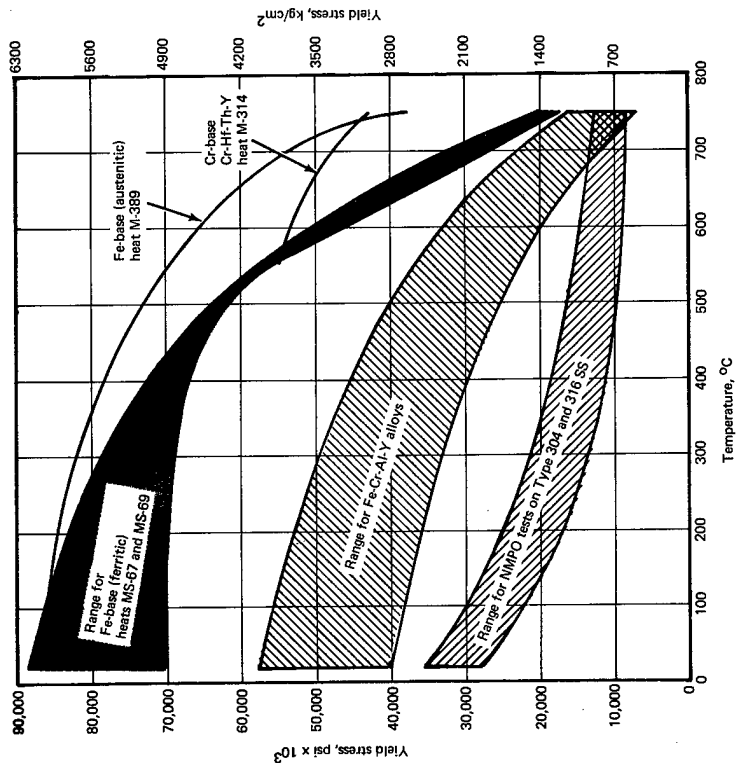


Fig. 5.20 — Yield strength versus temperature for potential fast breeder reactor cladding materials

(austenitic) but not for the chromium alloys. The outstanding comparative strength levels attained by the iron-base (ferritic) alloys up to about 550°C is noteworthy.

Figure 5.20 indicates that nearly all the alloys possess an advantage in yield strength over the stainless steels at all temperatures up to 750°C. This can be said even though, as indicated previously, the hot yield strength values for the program alloys are approximate because of the measurement technique employed.

A comparison of the 650°C stress-rupture properties of the various alloys is illustrated in Figure 5.21. Except for Fe-Cr-Al-Y alloys, only relatively limited data are available for the program alloys. Nonetheless, it seems apparent that only the chromium- and iron-base (austenitic) alloys can be expected to have stress-rupture strength comparable or superior to the stainless steels.

Creep (time – extension) curves taken from several of the stress-rupture tests are presented in Figure 5.22. These further indicate, in a preliminary way, that the chromium- and iron-base (austenitic) alloys are in a favorable strength position with respect to stainless steels. Because of the measurement technique employed in these argon tests, data for the program alloys tend to show somewhat greater creep as a function of time, short of rupture, than actually occurs.

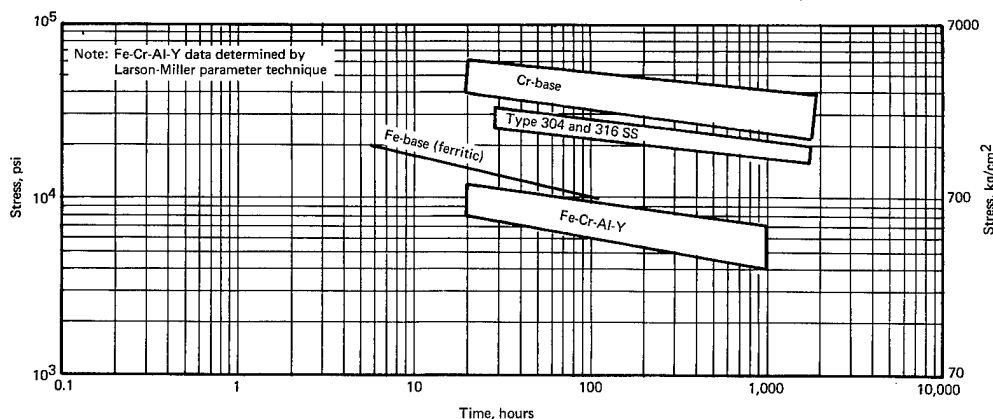


Fig. 5.21 — 650°C stress-rupture strengths of potential fast breeder reactor cladding materials

In the light of the comparative data presented, two alloy systems appear to be emerging as alternatives to stainless steel: iron-base (austenitic) and chromium-base. The iron-base (austenitic) alloys are especially attractive for their prospect of improved strength over the stainless steels. They should also possess improved and more predictable radiation and structural stability even at equivalent strength, since they are relatively pure.

Three factors other than strength can be considered with respect to the chromium-base alloys: ductility, sodium corrosion resistance, and thermal stability. None of the chromium-base alloys tested in this program have ductile-to-brittle transition temperatures in bending or impact below 100°C. Current emphasis is placed on improving this situation. The sodium corrosion resistance of chromium-base alloys appears most promising based on preliminary tests; more extensive dynamic testing is necessary to characterize the behavior of these alloys in sodium. Finally, thermal stability of chromium-base alloys, which depend upon warm-finishing for much of their strength, must be more clearly established, based upon annealing studies to date.

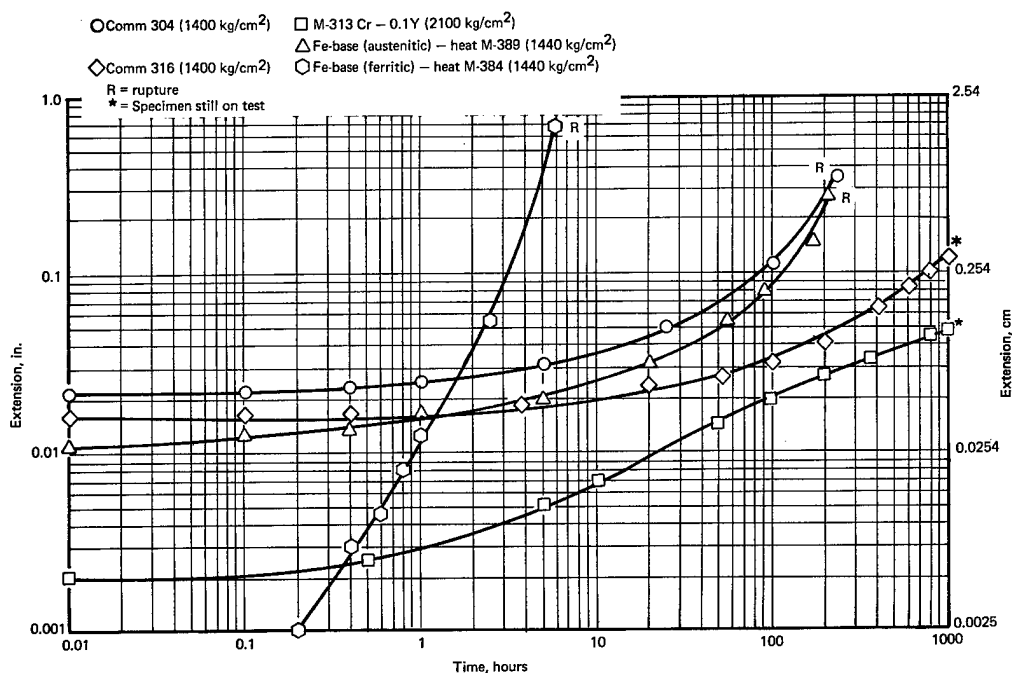


Fig. 5.22 — 650°C time-extension curves at various stresses for potential fast breeder reactor cladding materials

5.6 PLANS AND RECOMMENDATIONS

Program emphasis in the immediate future will be given to iron-base (austenitic) and chromium-base alloys. Characterization of iron-base (ferritic) and Fe-Cr-Al-Y alloys will be completed since other nuclear or non-nuclear applications may benefit, but no new alloy development within these systems will be undertaken.

Specific plans include the following:

1. Initiate strength characterization of vacuum-induction-melted developmental iron-base (austenitic) alloys.
2. Complete additional annealing and creep studies on warm-finished primary chromium-base alloys.
3. Evaluate tensile strength and ductility of high-purity and high-strength chromium-base alloys.
4. Extend strength characterization of iron-base (ferritic) alloys.
5. Continue preliminary sodium compatibility experiments on alloys from all systems.
6. Initiate post-irradiation studies on chromium-base and Fe-Cr-Al-Y alloys.

6 (EVALUATIONS OF PLASTIC FATIGUE PROPERTIES OF HEAT-RESISTANT ALLOYS)

(1516)

J. B. Conway*

The objective of this program is to determine the parameters affecting low-cycle fatigue life of metals and alloys at elevated temperatures and to generate low-cycle fatigue data for use in the design of structural components of high-performance nuclear reactor systems.

Materials currently being studied in this program are the AISI 304, 348, and 316 stainless steels. Test parameters under investigation are temperature, strain amplitude, strain rate, and length of hold times at peak strain in each cycle.

6.1 MATERIAL SPECIFICATIONS

AISI 304 STAINLESS STEEL ROD STOCK

AISI grade—heat 55697 from PNL—billets 49 cm² cross-sectional area, rolled at 1180°C to rods 16 mm in diameter—rod coiled, annealed 60 minutes at 1066°C, and water quenched—sections cut from coil, straightened, stress-relieved 30 minutes at 1010°C, and water quenched.

AISI 348 STAINLESS STEEL ROD STOCK

AISI grade—heat 55700 from PNL—rolling and heat treatment sequence same as for Type 304 stainless steel.

AISI 316 STAINLESS STEEL ROD STOCK

AISI grade—heat 65808 from PNL—ladle chemistry by weight percent:

C	Mn	Si	Cr	Ni	Mo	Co	Sn	Cu	S	P	N ₂
0.086	1.73	0.52	18.16	13.60	2.47	0.74	0.040	0.078	0.006	0.010	0.050

NMPO PROCESSING—AISI 304 AND 348 STAINLESS STEEL

Ground specimens to hourglass configuration—diametral gage section 0.635 cm—surface of gage section longitudinally polished—annealed 30 minutes at 1092°C in argon, cooling rate approximately 100°C per minute—average VHN 139 for 304 SS and 155 for 348 SS—grain size ASTM 3-5.

NMPO PROCESSING—AISI 316 STAINLESS STEEL

Sample blanks annealed 30 minutes at 1070°C in air and water quenched—ground samples to hourglass configuration—diametral gage section 0.635 cm—surface of gage section longitudinally polished—stress relieved 60 minutes at 760°C in argon, cooling rate approximately 100°C per minute—average VHN 171—grain size ASTM 3-5.

*Project leader and principal investigator.

6.2 FATIGUE-TESTING EQUIPMENT

During the past year equipment and test technique modifications were made to improve the precision and accuracy of low-cycle fatigue data being generated. A more precise method was devised for calibrating the extensometer employed to measure diametral strain; Figure 6.1 shows a photograph of the new calibration fixture. This fixture has permitted the extensometer to be calibrated in a manner that closely simulates the mode of operation during an actual test.

Another improvement consisted of fabricating Plexiglas enclosures for two uniaxial fatigue systems. One enclosure shown in Figure 6.2 permits operation in air while isolating the testing or sample zone from the immediate laboratory environment. In this way the effects of the unavoidable air currents present in the laboratory are eliminated and the test specimen temperature is more accurately controlled. This modification also permits tests to operate in inert environments if such testing becomes desirable.

Another modification which promises to improve testing accuracy involves the repositioning of the load-measuring device in the load train. This change was needed to eliminate the extraneous load resulting from frictional forces in the die-set assembly; this is presently summed along with the force on the test specimen. A sketch of this new modification is presented in Figure 6.3. The new die-set fixture is being assembled and will soon be incorporated into the current test program.

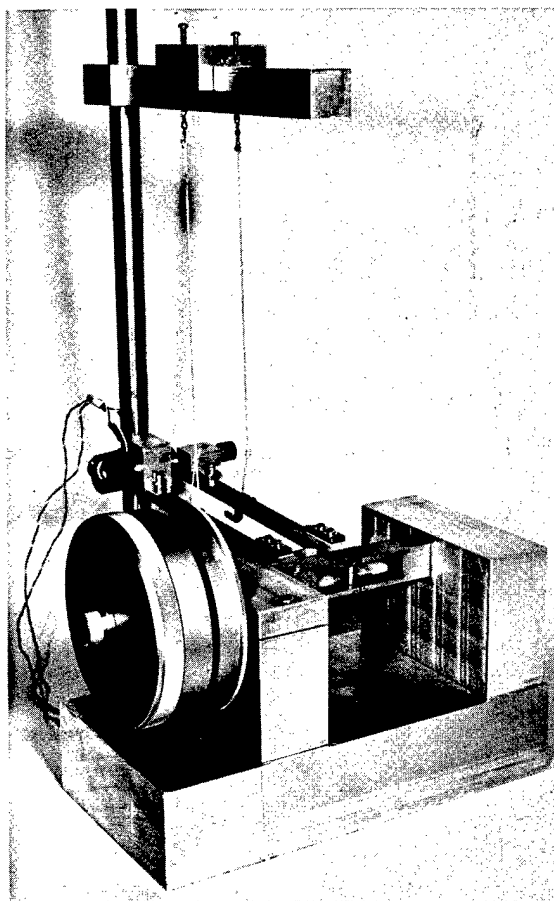


Fig. 6.1 — Calibration fixture for diametral strain extensometer (Neg. P68-2-2D)

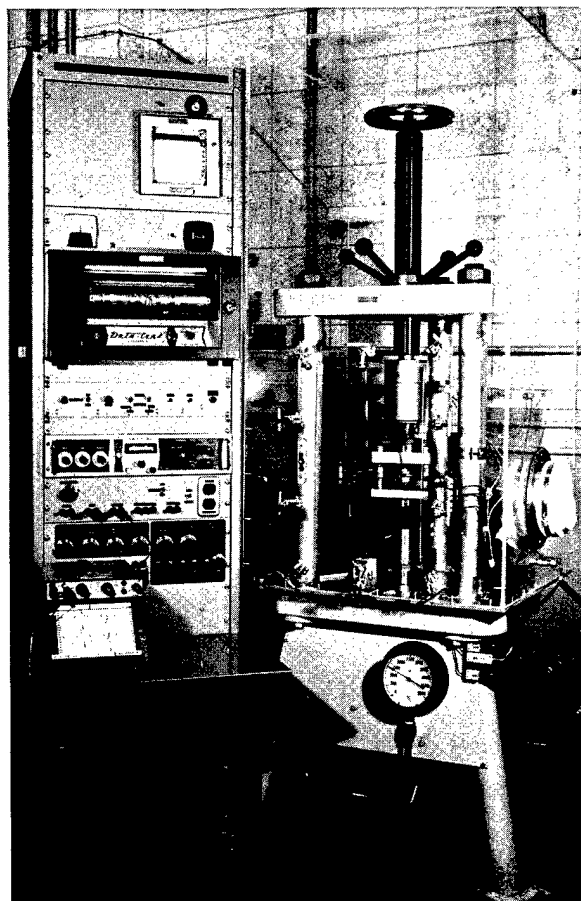


Fig. 6.2 — Typical uniaxial fatigue-testing system with Plexiglas enclosure (Neg. P68-2-2C)

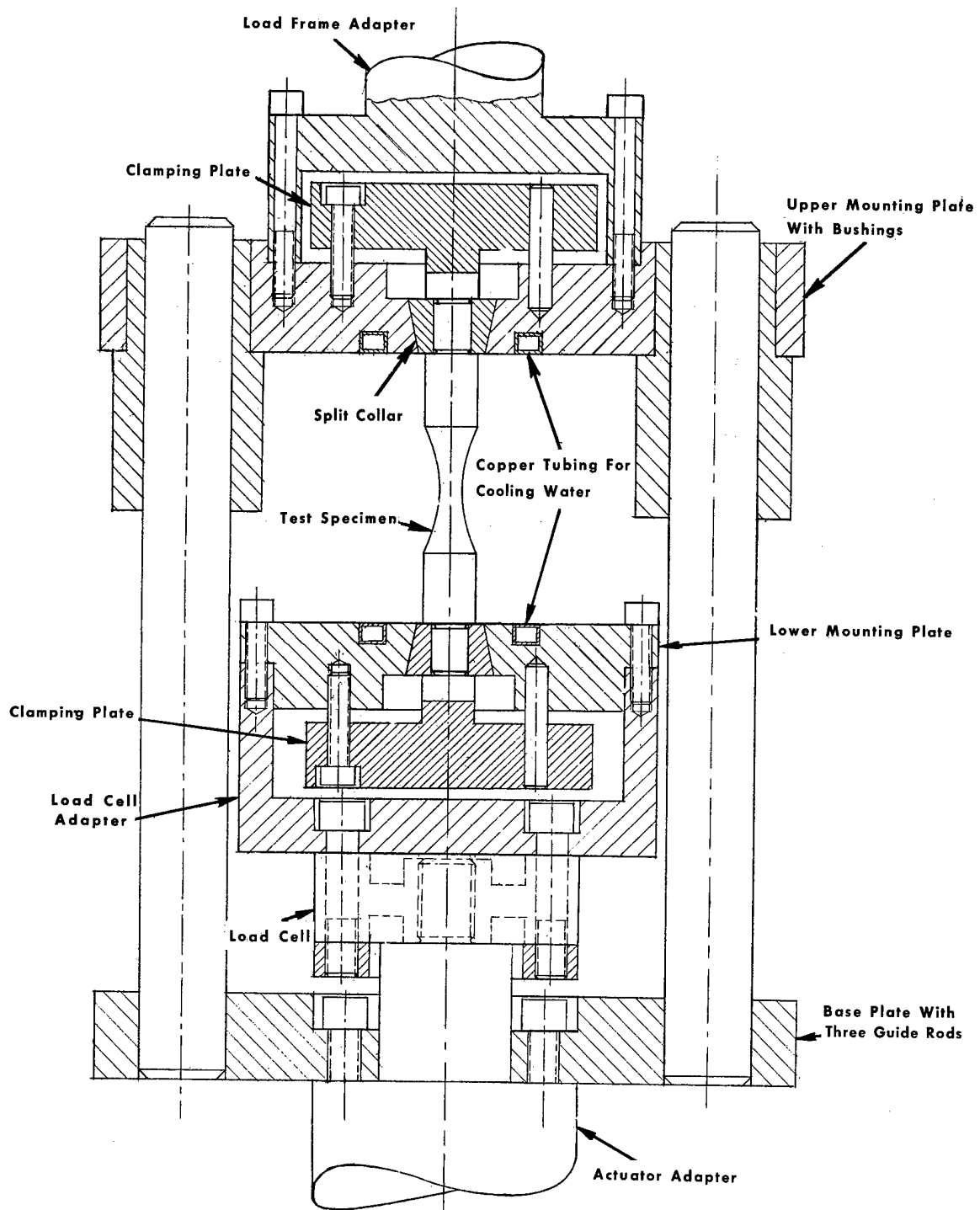


Fig. 6.3 — Sketch of test specimen and loading fixture

In another important equipment modification, a strain computer shown in Figure 6.4 was developed and installed on each fatigue-testing machine. This small analog computer continually determines relative amounts of elastic and plastic strain in the specimen and produces a signal which represents instantaneous axial strain. Once this signal has been generated it can be used for control purposes; the advantages of the diametral strain measurements in this evaluation can be combined with the ability to program and control the axial strain. Figure 6.5 compares the different strain and stress wave forms ob-

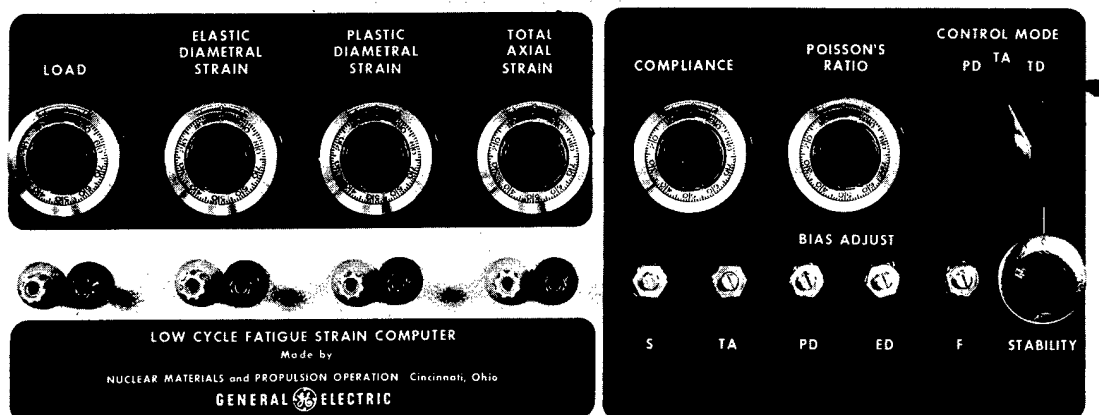


Fig. 6.4 — Front panel of low-cycle fatigue strain computer (Neg. P67-7-32)

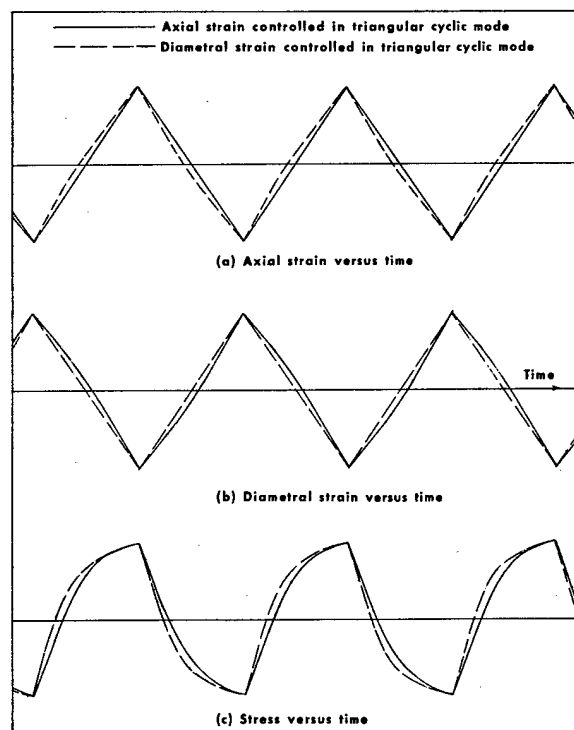


Fig. 6.5 — Comparison of stress and strain wave forms obtained with programming of axial and diametral strain (Type 348 stainless steel at 800°C)

tained¹ in diametral and axial strain control. A triangular wave form (constant strain rate) was programmed in both cases. The strain computer was used to generate the axial strain signal; the diametral strain signal was obtained directly from the diametral extensometer. Such a diagram clearly shows the intra-cycle strain rate differences, but not the more significant, long-term strain reorientation which will change the relationship between axial and diametral strain. For example, the ratio of axial strain range to diametral strain range will increase with cyclic strain hardening and decrease with strain softening. The strain range being controlled, however, will remain at a constant value.

The analog of axial strain is produced by operating upon the signals from the diametral strain extensometer and the load cell. The following relationships form the basis for the axial strain simulation:

$$\epsilon = \epsilon_e + \epsilon_p \quad (6.1)$$

$$\epsilon_e = \frac{-\epsilon_{de}}{\nu_e} \quad (6.2)$$

$$\epsilon_p = \frac{-\epsilon_{dp}}{\nu_p} \quad (6.3)$$

$$\epsilon_{de} = \frac{-F\nu_e}{AE} \quad (6.4)$$

$$\epsilon_{dp} = \epsilon_d - \epsilon_{de} \quad (6.5)$$

where:

- ϵ = total axial strain
- ϵ_e = elastic axial strain
- ϵ_p = plastic axial strain
- ϵ_d = total diametral strain
- ϵ_{de} = elastic diametral strain
- ϵ_{dp} = plastic diametral strain
- F = force on the specimen
- A = cross sectional area of the specimen at the minimum diameter
- ν_e = Poisson's ratio in the elastic region (assumed to be constant)
- ν_p = Poisson's ratio in the plastic region (assumed to be 0.5)
- E = Young's modulus

Values of A , E , ν_e , and ν_p are readily inserted into the computer as constants, but F and ϵ_d are measured. The other variables are electronically determined using d-c amplifier summing circuits. Sufficient signals are produced to provide the option of programming and controlling diametral strain, axial strain, plastic strain, or force. To calibrate the computer it is necessary only to adjust a potentiometer in the force circuit for zero plastic strain while cycling the specimen in the elastic region. This procedure establishes the ratio ν_e/AE and thus the value of ν_e if E and A are known. The value of ν_e is then set on a front-panel potentiometer dial. When plastic strain control is used it is not necessary to know ν_e or E , since the procedure of adjusting for zero plastic strain in the elastic region defines all necessary relationship.

¹T. Slot and R. H. Stentz, "Experimental Methods for Low-Cycle Fatigue Research at High Temperature," GE-NMPO, GEMP-527, June 1967.

Section 2

Figure 2.59, page 141, key to figure, fourth line from bottom

✓ Should read $\sigma_u = 0.344 H_v$

instead of $0.344 E_v$

Figure 2.70, page 150, key to figure

✓ Should read Δ - taken from reference 40

instead of . . . reference 41

Figure 2.84, page 167

Identification left off of the four different parts of the figure.

✓ Top left should be identified as Region 2A; top right, Region 7A;
bottom left, Region 2B; and bottom right, Region 7B.

Figure 2.86, page 170, key to figure

✓ Row 2 for Ni^{58} should be large diamond shape (\diamond) and row 7 for Fe^{58}
should be small diamond shape (\diamond).

Page 171, second line from top of page

✓ Should read "The Ni^{58} dosimeters in regions 2B and 7B were . . ."
instead of ". . . in regions 2A and 7A . . ."

Section 5

Page 217, second paragraph from bottom, third sentence

✓ Should read ". . . no intermediate anneals to 0.076 cm thickness."

instead of ". . . to 0.125 cm thickness."

Also remove the asterisk (*) after the work "thickness."

Section 6

The $\Delta \epsilon_t$ appearing on pages 247, 253, and 256; Tables 6.1, 6.2, 6.3, and 6.4; and Figures 6.6, 6.8, 6.10, 6.12, 6.17, 6.25, 6.28, 6.29, 6.30, and 6.31 should be $\Delta \epsilon_t$

Page 247, first paragraph, last sentence

Change to read ". . . presented for axial strain ranges . . ."

instead of ". . . strain amplitudes . . ."

Figure 6.18, page 260

Left hand ordinate should read:

Stress range, psi

GEMP-1004

Errata

Section 7

Replace Figures 7.16 (p. 305), 7.17 (p. 306), 7.18 (p. 306), and 7.19 (p. 307) with the following:

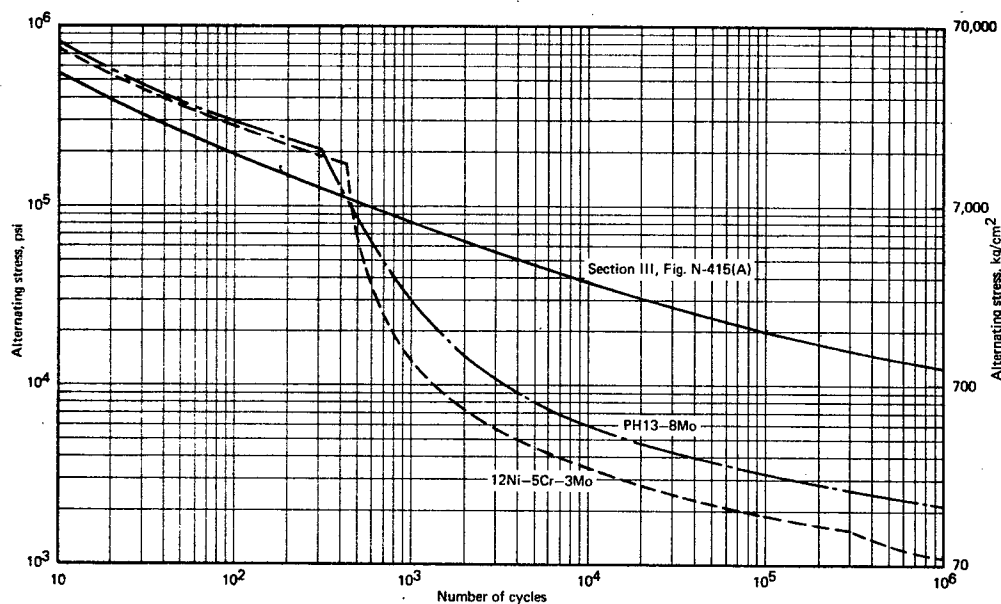


Fig. 7.16 – Comparison of calculated design fatigue curves for PH13-8Mo and 12Ni-5Cr-3Mo (using the Linear Rule to correct for the maximum effect of mean stress) with design fatigue curve for carbon and alloy steels from Section III of ASME Boiler and Pressure Vessel Code for Nuclear Vessels

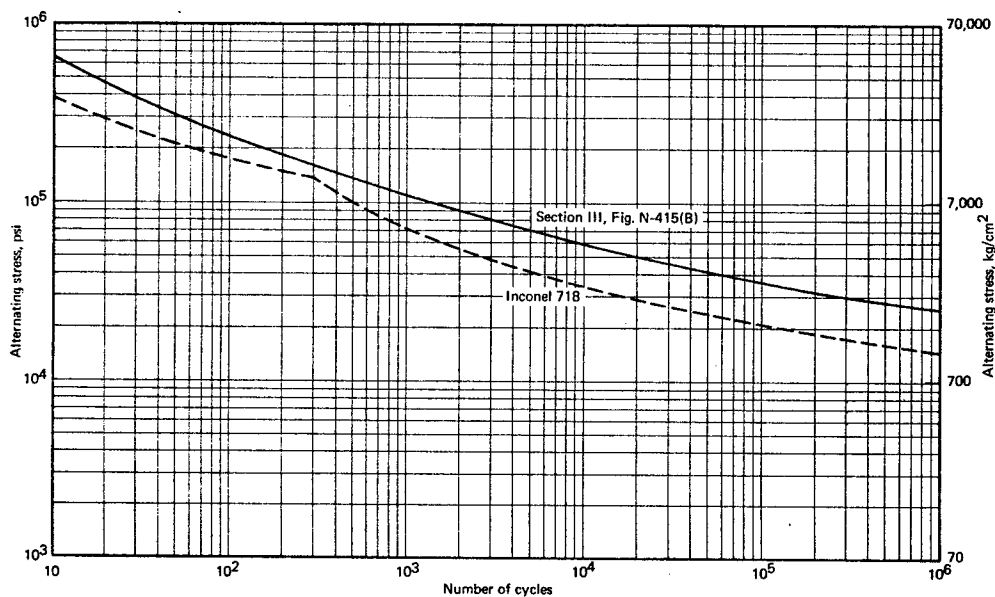


Fig. 7.17 – Comparison of calculated design fatigue curve for Inconel 718 (using the Linear Rule to correct for the maximum effect of mean stress) with design fatigue curve for 18-8 stainless steels and nickel-chrome-iron alloy from Section III of ASME Boiler and Pressure Vessel Code for Nuclear Vessels

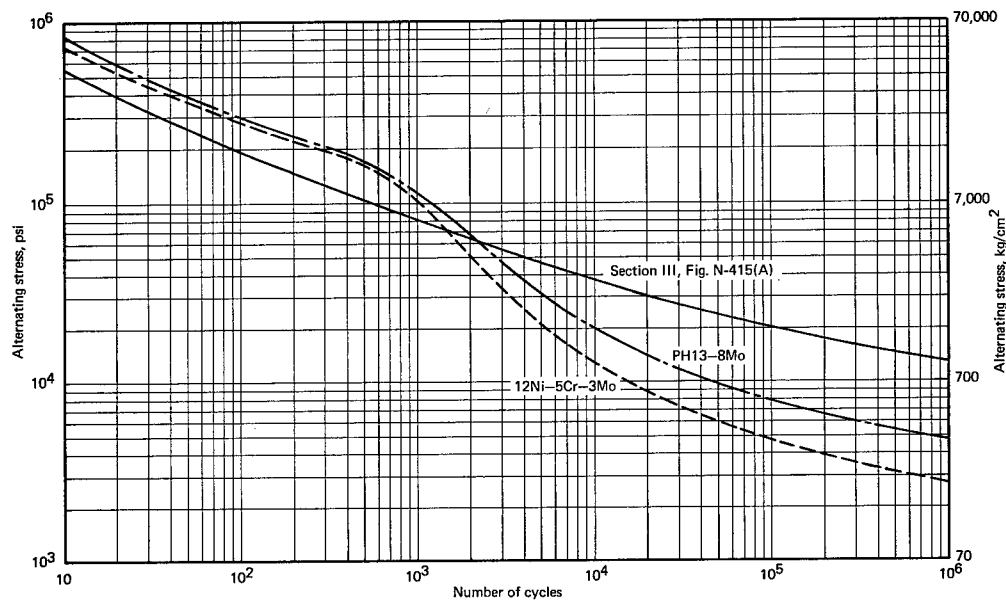


Fig. 7.18 – Comparison of calculated design fatigue curves for PH13–8Mo and 12Ni–5Cr–3Mo (using the Peterson Cubic Rule to correct for the maximum effect of mean stress) with design fatigue curve for carbon and alloy steels from Section III of ASME Boiler and Pressure Vessel Code for Nuclear Vessels

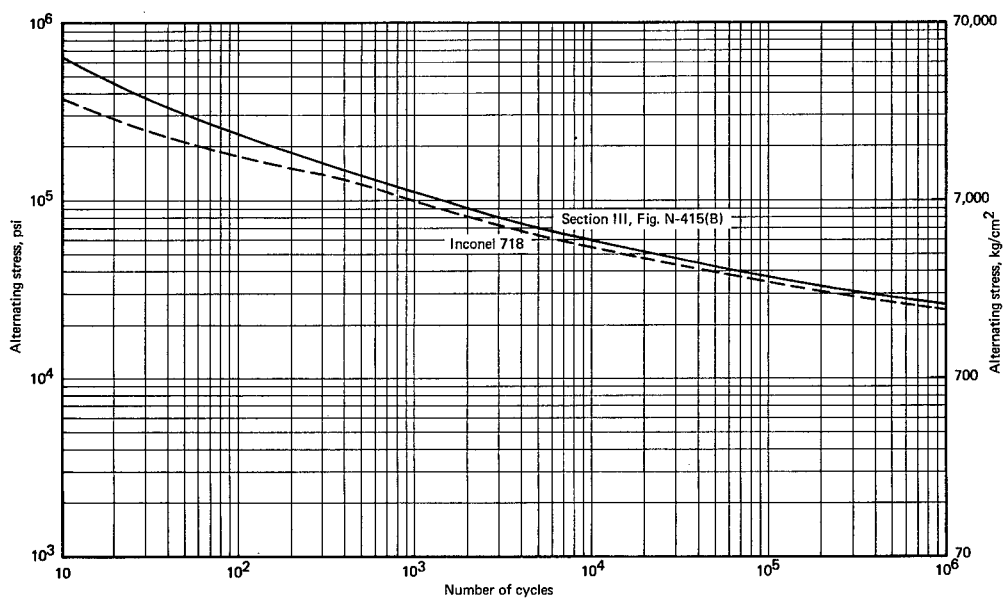


Fig. 7.19 – Comparison of calculated design fatigue curve for Inconel 718 (using the Peterson Cubic Rule to correct for the maximum effect of mean stress) with design fatigue curve for 18-8 stainless steels and nickel-chrome-iron alloy from Section III of ASME Boiler and Pressure Vessel Code for Nuclear Vessels

6.3 TEST RESULTS

During the past year fully reversed strain cycling fatigue data were obtained in an air environment for fully annealed, AISI 348, 304, and 316 stainless steel to determine effects of strain rate, strain range, and temperature. A summary of these data is presented in Tables 6.1, 6.2, and 6.3. As indicated, three strain rates, 4×10^{-3} , 4×10^{-4} , and $4 \times 10^{-5} \text{ sec}^{-1}$, were evaluated at test temperatures of 430°, 650°, and 816°C. Data are also presented for axial strain amplitudes ($\Delta \epsilon_t$) ranging from approximately 0.5 to approximately 2.5 percent.

The general effects of strain rate, strain range, and temperature on the cyclic strain fatigue characteristics of 348, 304, and 316 SS are shown graphically in Figures 6.6 through 6.11. Both total axial strain range ($\Delta \epsilon_t$) and plastic strain range ($\Delta \epsilon_p$) are presented in terms of N_5 , the cycles corresponding to a 5-percent reduction in load. Special tests were performed to identify Poisson's ratio, employed in conversion² from diametral to axial strain, for the 316 SS used in this program. Values for Poisson's ratio for the 304 and 348 SS have not been obtained yet; hence literature values were employed in the present analysis. This property is being measured for these two materials and any effect which these new data may have on the data presented here will be discussed in a subsequent report. A summary of the short-term tensile data generated to date is presented in Table 6.4.

As indicated in Figures 6.6 and 6.7, the general effect of a decrease in strain rate at 650°C and 816°C results in a severalfold decrease in the fatigue resistance of 348 SS for a given strain ($\Delta \epsilon_t$ or $\Delta \epsilon_p$) range. Figure 6.6 also shows that data obtained at 650°C and an axial strain rate of $4 \times 10^{-5} \text{ sec}^{-1}$ seem to coincide with data obtained at 816°C and $4 \times 10^{-3} \text{ sec}^{-1}$. The degree of coincidence is reduced, however, if plastic strain range data are used as the basis for the comparison, as shown in Figure 6.7.

Relationships similar to those indicated by the 348 SS data were obtained for the 304 SS as shown in Figure 6.8 and 6.9. The only apparent differences seem to be an increase in slope of the logarithmic plots of plastic strain range versus fatigue life, and slightly lower fatigue resistance for the 304 SS at the same strain levels compared to the 348 SS data. More data are needed for a meaningful interpretation of these slope differences.

Fatigue data for 316 SS are shown in Figures 6.10 and 6.11. The effect of strain rate on fatigue resistance of 316 SS is about the same as that noted for 348 and 304 SS but the temperature effect is quite different. The effect of temperature on the fatigue resistance of 316 SS is much less pronounced than that observed in tests of the other two materials; at the lowest strain rate little, if any, temperature effect on fatigue resistance is noted. This suggests that metallurgical reactions are occurring at 816°C which tend to enhance the fatigue resistance of 316 SS compared to the 650°C results. Another surprising result concerns the lower-than-expected fatigue resistance of the 316 SS at 650°C and the highest strain rate. Metallurgical evaluations are being conducted to identify the mechanisms involved.

The effects of temperature and strain range ($\Delta \epsilon_t$ and $\Delta \epsilon_p$) on the fatigue resistance of 316 SS at a constant strain rate of $4 \times 10^{-3} \text{ sec}^{-1}$ are shown in Figures 6.12 and 6.13. Based on these limited data, some consistency with the Coffin-Manson relationship, $\Delta \epsilon_p = A N_f^{-m}$, can be identified by the linear isotherms. Although N_5 was used in Figure 6.13, the same general observations follow if N_f is employed. At 430°C the value of m is essentially 0.5 but increases slightly with increasing temperature.

²"AEC Fuels and Materials Development Program Progress Report No. 67," GE-NMPO, GEMP-67, June 30, 1967, p. 135.

55
TABLE 6.1
LOW-CYCLE FATIGUE DATA^a FOR ANNEALED AISI 348 STAINLESS STEEL TESTED IN AIR AT 650°C AND 816°C

Test Temperature, °C	Specimen No.	Axial Strain			Diametral Strain			Axial Stress		Cyclic Rate		Fatigue Life		
		Total Strain Range ($\Delta\epsilon_t$), %	Plastic Strain Range ($\Delta\epsilon_p$), %	Elastic Strain Range ($\Delta\epsilon_e$), %	Total Strain Range ($\Delta\epsilon_d$), %	Plastic Strain Range ($\Delta\epsilon_{dp}$), %	Elastic Strain Range ($\Delta\epsilon_{de}$), %	Stress Range at $N_f/2$ ($\Delta\sigma$), kg/mm ²	Frequency of Loading, cycles/sec	Axial Strain Rate, ($\dot{\epsilon}_t$), sec ⁻¹	Cycles to Fracture (N_f)	Cycles to 5% Load Reduction (N_5)	Ratio N_5/N_f	
650	3-7	2.17	1.79	0.39	1.01	0.89	0.12	56.56	0.001	4.3×10^{-5}	217	193	0.889	
	3-6	2.17	1.80	0.37	1.01	0.90	0.11	55.13	0.001	4.3×10^{-5}	208	177	0.851	
	3-3	2.18	1.78	0.40	1.01	0.89	0.12	60.86	0.01	4.4×10^{-4}	370	335	0.905	
	3-8	2.18	1.78	0.40	1.01	0.89	0.12	60.14	0.01	4.4×10^{-4}	329	320	0.973	
	3-5	2.16	1.76	0.40	1.00	0.88	0.12	62.29	0.1	4.3×10^{-3}	550	471	0.856	
	3-4	2.19	1.78	0.41	1.01	0.89	0.12	62.29	0.1	4.4×10^{-3}	596	585	0.982	
	4-12	1.13	0.80	0.33	0.50	0.40	0.10	47.25	0.002	4.5×10^{-5}	871	760	0.872	
	4-10	1.13	0.81	0.32	0.50	0.40	0.10	50.83	0.002	4.5×10^{-5}	950	680	0.716	
	4-6	1.12	0.82	0.31	0.50	0.41	0.09	45.11	0.02	4.5×10^{-4}	1259	989	0.786	
	4-1	1.13	0.80	0.33	0.50	0.40	0.10	54.41	0.02	4.5×10^{-4}	1360	1133	0.833	
	4-9	1.13	0.80	0.33	0.50	0.40	0.10	52.27	0.2	4.5×10^{-3}	2635	2412	0.915	
	4-5	1.15	0.78	0.37	0.50	0.39	0.11	51.55	0.2	4.6×10^{-3}	2685	2607	0.971	
	3-12	0.61	0.33	0.28	0.25	0.17	0.09	47.61	0.004	4.9×10^{-5}	3661	3236	0.884	
	5-12	0.61	0.33	0.28	0.25	0.17	0.09	43.32	0.004	4.9×10^{-5}	7811	5464	0.700	
	3-11	0.62	0.30	0.32	0.25	0.15	0.10	45.82	0.04	5.0×10^{-4}	11596	10948	0.944	
	9-8	0.62	0.37	0.25	0.26	0.18	0.08	45.82	0.04	5.0×10^{-4}	7807	7269	0.931	
	5-3	0.62	0.34	0.27	0.25	0.17	0.08	43.67	0.4	5.0×10^{-3}	15192	15010	0.988	
	9-1	0.61	0.34	0.27	0.25	0.17	0.08	43.32	0.4	4.9×10^{-3}	17016	16676	0.980	
	9-4	0.62	0.32	0.30	0.25	0.16	0.09	44.25	0.4	5.0×10^{-3}	21432	20652	0.964	
816	5-6	2.04	1.94	0.10	1.01	0.97	0.03	22.91	0.001	4.1×10^{-5}	183	118	0.645	
	5-7	2.06	1.91	0.15	1.00	0.96	0.04	21.48	0.001	4.1×10^{-5}	233	122	0.524	
	5-5	2.11	1.88	0.23	1.01	0.94	0.07	30.06	0.01	4.2×10^{-4}	220	158	0.718	
	5-4	2.08	1.88	0.20	1.00	0.94	0.06	30.79	0.01	4.2×10^{-4}	315	176	0.559	
	5-1	2.11	1.84	0.27	1.00	0.92	0.08	38.66	0.1	4.2×10^{-3}	317	266	0.839	
	6-4	2.09	1.86	0.23	1.00	0.93	0.07	40.09	0.1	4.2×10^{-3}	326	245	0.752	
	9-2	1.08	0.91	0.17	0.50	0.45	0.05	20.76	0.002	4.3×10^{-5}	586	385	0.657	
	9-5	1.07	0.90	0.17	0.50	0.45	0.05	18.61	0.002	4.3×10^{-5}	582	439	0.754	
	9-7	1.09	0.86	0.23	0.50	0.43	0.07	28.64	0.02	4.4×10^{-4}	681	595	0.874	
	9-9	1.09	0.86	0.23	0.50	0.43	0.07	28.64	0.02	4.4×10^{-4}	729	462	0.634	
	9-6	1.11	0.84	0.27	0.50	0.42	0.08	32.93	0.2	4.4×10^{-3}	1170	746	0.638	
	9-11	1.11	0.85	0.25	0.50	0.42	0.08	34.37	0.2	4.3×10^{-3}	949	682	0.719	
	6-9	0.55	0.43	0.12	0.25	0.21	0.04	23.27	0.004	4.4×10^{-5}	1862	1554	0.835	
	6-10	0.56	0.42	0.14	0.25	0.21	0.04	19.69	0.004	4.5×10^{-5}	1892	1613	0.853	
	6-5	0.57	0.40	0.17	0.25	0.20	0.05	23.63	0.04	4.6×10^{-4}	2465	1874	0.760	
	6-8	0.58	0.40	0.18	0.25	0.20	0.05	23.63	0.04	4.6×10^{-4}	3160	2718	0.860	
	6-3	0.57	0.39	0.17	0.25	0.20	0.05	30.07	0.4	4.6×10^{-3}	4281	3379	0.789	
	6-2	0.57	0.39	0.17	0.25	0.20	0.05	32.22	0.4	4.6×10^{-3}	4896	4656	0.951	

^aControl mode: diametral strain.

Strain wave form: triangular with zero mean strain

TABLE 6.2
LOW-CYCLE FATIGUE DATA^a FOR ANNEALED AISI 304 STAINLESS STEEL TESTED IN AIR AT 650°C AND 816°C

LOW-CYCLE FATIGUE DATA FOR ANNEALED AISI 304 STAINLESS STEEL TESTED IN AIR AT 650 °C AND 816 °C														
Test Temperature, °C	Specimen No.	Axial Strain			Diametral Strain			Axial Stress		Cyclic Rate		Fatigue Life		
		Total Strain Range ($\Delta\epsilon_t$), %	Plastic Strain Range ($\Delta\epsilon_p$), %	Elastic Strain Range ($\Delta\epsilon_e$), %	Total Strain Range ($\Delta\epsilon_t$), %	Plastic Strain Range ($\Delta\epsilon_{dp}$), %	Elastic Strain Range ($\Delta\epsilon_{de}$), %	Stress Range at $N_f/2$ ($\Delta\sigma$), kg/mm ²	Frequency of Loading, cycles/sec	Axial Strain Rate, ($\dot{\epsilon}_t$), sec ⁻¹	Cycles to Fracture (N_f)	Cycles to 5% Load Reduction (N_5)	Ratio N_5/N_f	
650	10-12	2.12	1.82	0.30	1.00	0.91	0.09	43.67	0.001	4.2×10^{-5}	4.2×10^{-5}	261	197	0.755
	10-11	2.15	1.78	0.37	1.00	0.89	0.11	52.98	0.01	4.3×10^{-4}	4.3×10^{-4}	310	287	0.926
	10-9	2.11	1.78	0.33	0.99	0.89	0.10	60.43	0.1	4.2×10^{-3}	4.2×10^{-3}	566	524	0.925
	10-4	1.11	0.84	0.27	0.50	0.42	0.08	41.53	0.002	4.4×10^{-5}	4.4×10^{-5}	660	527	0.798
	10-7	1.13	0.81	0.32	0.50	0.41	0.10	46.82	0.02	4.5×10^{-4}	4.5×10^{-4}	805	748	0.929
	10-10	1.13	0.81	0.32	0.50	0.41	0.10	50.12	0.2	4.5×10^{-3}	4.5×10^{-3}	1740	1656	0.952
	120	0.58	0.36	0.22	0.25	0.18	0.07	32.84	0.004	4.6×10^{-5}	4.6×10^{-5}	2134	1533	0.718
	118	0.58	0.38	0.20	0.25	0.19	0.06	33.76	0.004	4.6×10^{-5}	4.6×10^{-5}	3124	1966	0.629
	296	0.60	0.36	0.24	0.25	0.18	0.07	37.07	0.04	4.8×10^{-4}	4.8×10^{-4}	3549	3009	0.848
	299	0.61	0.33	0.28	0.25	0.17	0.08	40.38	0.4	4.9×10^{-3}	4.9×10^{-3}	7320	7100	0.970
816	294	0.62	0.32	0.29	0.25	0.16	0.09	41.05	0.4	4.9×10^{-3}	4.9×10^{-3}	7944	7176	0.903
	10-2	2.07	1.89	0.18	1.00	0.95	0.06	24.20	0.001	4.1×10^{-5}	4.1×10^{-5}	130	80	0.615
	7-3	2.07	1.89	0.18	1.00	0.95	0.06	29.35	0.01	4.1×10^{-4}	4.1×10^{-4}	145	117	0.807
	7-1	2.08	1.88	0.20	1.00	0.94	0.06	34.01	0.1	4.2×10^{-3}	4.2×10^{-3}	260	226	0.869
	7-12	1.05	0.92	0.13	0.50	0.46	0.04	24.49	0.002	4.2×10^{-5}	4.2×10^{-5}	307	204	0.664
	7-5	1.07	0.89	0.17	0.50	0.45	0.05	26.92	0.02	4.3×10^{-4}	4.3×10^{-4}	429	379	0.883
	7-10	1.07	0.89	0.17	0.50	0.45	0.05	32.22	0.2	4.3×10^{-3}	4.3×10^{-3}	784	529	0.675
	10-3	0.53	0.45	0.09	0.25	0.22	0.03	24.34	0.004	4.2×10^{-5}	4.2×10^{-5}	788	591	0.750
	7-7	0.54	0.42	0.12	0.25	0.21	0.04	26.49	0.04	4.3×10^{-4}	4.3×10^{-4}	1338	1055	0.788
	7-9	0.56	0.41	0.15	0.25	0.21	0.05	28.50	0.4	4.5×10^{-3}	4.5×10^{-3}	2477	2346	0.947

^aControl mode: diametral strain.

Strain wave form: triangular with zero mean strain.

TABLE 6.3
LOW-CYCLE FATIGUE DATA^a FOR ANNEALED AISI 316 STAINLESS STEEL TESTED IN AIR AT 430°, 650°, AND 816°C

Test Temperature, °C	Specimen No.	Axial Strain			Diametral Strain			Axial Stress		Cyclic Rate		Fatigue Life	
		Total Strain Range ($\Delta\epsilon_t$), %	Plastic Strain Range ($\Delta\epsilon_p$), %	Elastic Strain Range ($\Delta\epsilon_e$), %	Total Strain Range ($\Delta\epsilon_d$), %	Plastic Strain Range ($\Delta\epsilon_{dp}$), %	Elastic Strain Range ($\Delta\epsilon_{de}$), %	Stress Range at $N_f/2$ ($\Delta\sigma$), kg/mm ²	Frequency of Loading, cycles/sec	Axial Strain Rate, ($\dot{\epsilon}_t$), sec ⁻¹	Cycles to Fracture (N_f)	Cycles to 5% Load Reduction (N_5)	Ratio N_5/N_f
430	14-3	1.85	1.26	0.59	0.81	0.63	0.18	76.07	0.111	4.17×10^{-3}	2202	2161	0.982
	14-4	1.77	1.30	0.47	0.80	0.65	0.15	76.92	0.111	4.03×10^{-3}	1764	1738	0.985
	14-5	1.38	0.91	0.47	0.60	0.45	0.15	63.28	0.148	4.21×10^{-3}	4118	4101	0.996
	14-7	0.91	0.63	0.28	0.40	0.31	0.09	54.91	0.222	4.11×10^{-3}	6325	6094	0.963
	14-6	0.70	0.42	0.28	0.30	0.21	0.09	50.20	0.296	4.34×10^{-3}	21898	21329	0.974
	14-8	0.49	0.24	0.25	0.20	0.12	0.08	49.92	0.444	4.66×10^{-3}	80231	71020	0.885
	21-8	2.11	1.76	0.35	0.99	0.88	0.11	60.42	0.001	4.22×10^{-5}	98	95	0.969
	16-51	2.16	1.75	0.42	1.00	0.87	0.13	70.59	0.01	4.34×10^{-4}	223	193	0.865
650	33-41	1.77	1.32	0.45	0.80	0.66	0.14	74.96	0.111	4.00×10^{-3}	522	496	0.950
	14-2	1.77	1.32	0.45	0.80	0.66	0.14	72.03	0.111	4.00×10^{-3}	553	514	0.929
	14-1	1.37	0.92	0.45	0.60	0.46	0.14	68.81	0.148	4.16×10^{-3}	1032	1006	0.975
	33-42	1.40	0.95	0.45	0.62	0.48	0.14	67.97	0.148	4.24×10^{-3}	1002	980	0.978
	27-17	1.36	0.91	0.45	0.60	0.45	0.14	66.43	0.148	4.13×10^{-3}	945	847	0.896
	16-2	1.11	0.79	0.32	0.50	0.40	0.10	50.82	0.002	4.54×10^{-5}	611	562	0.920
	21-10	1.12	0.77	0.35	0.49	0.39	0.11	58.74	0.02	4.48×10^{-4}	808	764	0.945
	27-2	0.95	0.54	0.41	0.40	0.27	0.13	62.94	0.222	4.39×10^{-3}	2089	1931	0.924
	33-32	0.96	0.55	0.41	0.41	0.27	0.13	61.09	0.222	4.45×10^{-3}	2333	2227	0.954
	27-15	0.74	0.39	0.35	0.30	0.20	0.11	52.73	0.296	4.44×10^{-3}	4304	3961	0.920
	27-18	0.76	0.38	0.38	0.30	0.19	0.12	51.75	0.296	4.56×10^{-3}	4432	4183	0.944
	21-7	0.58	0.36	0.22	0.25	0.18	0.07	42.66	0.004	4.63×10^{-5}	4400	3600	0.818
	16-11	0.60	0.32	0.28	0.25	0.16	0.09	49.34	0.04	4.82×10^{-4}	4490	4208	0.937
	33-33	0.51	0.22	0.29	0.20	0.11	0.09	46.43	0.444	4.80×10^{-3}	11761	11631	0.989
	27-4	0.52	0.23	0.29	0.20	0.11	0.09	46.99	0.444	4.68×10^{-3}	13527	13394	0.990

^aControl mode: diametral strain.

Strain wave form: triangular with zero mean strain.

TABLE 6.3 (Cont.)
LOW-CYCLE FATIGUE DATA^a FOR ANNEALED AISI 318 STAINLESS STEEL TESTED IN AIR AT 430°, 650°, AND 816°C

Test Temperature, °C	Specimen No.	Axial Strain			Diametral Strain			Axial Stress		Cyclic Rate		Fatigue Life		
		Total Strain Range ($\Delta\epsilon_t$), %	Plastic Strain Range ($\Delta\epsilon_p$), %	Elastic Strain Range ($\Delta\epsilon_e$), %	Total Strain Range ($\Delta\epsilon_d$), %	Plastic Strain Range ($\Delta\epsilon_{dp}$), %	Elastic Strain Range ($\Delta\epsilon_{de}$), %	Stress Range at $N_f/2$ ($\Delta\sigma$), kg/mm ²	Frequency of Loading, cycles/sec	Axial Strain Rate, ($\dot{\epsilon}_t$), sec ⁻¹	Cycles to Fracture (N_f)	Cycles to 5% Load Reduction (N_5)	Ratio N_5/N_f	
816	21-2	2.04	1.92	0.17	1.00	0.96	0.04	25.31	0.001	4.16×10^{-5}	169	107	0.633	
	21-4	2.08	1.87	0.21	0.99	0.94	0.05	28.68	0.001	4.15×10^{-5}	165	131	0.794	
	16-9	2.15	1.82	0.33	0.99	0.91	0.08	36.64	0.01	4.30×10^{-4}	270	215	0.796	
	21-3	2.14	1.81	0.33	0.99	0.91	0.08	33.03	0.01	4.28×10^{-4}	278	210	0.755	
	33-36	1.77	1.44	0.33	0.80	0.72	0.08	43.44	0.111	3.81×10^{-3}	358	291	0.813	
	33-37	1.77	1.44	0.33	0.80	0.72	0.08	41.48	0.111	3.81×10^{-3}	398	335	0.842	
	27-1	1.37	1.04	0.33	0.60	0.52	0.08	39.82	0.148	3.89×10^{-3}	802	658	0.820	
	27-13	1.41	1.04	0.37	0.61	0.52	0.09	37.94	0.148	3.95×10^{-3}	684	628	0.918	
	16-1	1.11	0.88	0.23	0.49	0.44	0.05	26.85	0.002	4.42×10^{-5}	497	440	0.885	
	14-9	1.12	0.87	0.25	0.49	0.44	0.06	27.97	0.002	4.47×10^{-5}	637	524	0.823	
	16-5	1.03	0.76	0.27	0.45	0.38	0.06	35.80	0.02	4.11×10^{-4}	712	547	0.768	
	33-39	0.98	0.65	0.33	0.40	0.33	0.08	37.59	0.222	4.03×10^{-3}	1485	1199	0.807	
	27-14	0.99	0.66	0.33	0.40	0.33	0.08	36.48	0.222	4.05×10^{-3}	1381	1181	0.855	
	27-16	0.72	0.47	0.25	0.30	0.23	0.06	35.08	0.296	4.03×10^{-3}	2406	1933	0.803	
	33-40	0.75	0.46	0.29	0.30	0.23	0.07	37.59	0.296	4.13×10^{-3}	1938	1742	0.899	
	16-10	0.59	0.39	0.21	0.24	0.19	0.05	25.17	0.004	4.72×10^{-5}	1832	1530	0.835	
	21-5	0.60	0.39	0.21	0.25	0.20	0.05	25.06	0.004	4.79×10^{-5}	2006	1600	0.797	
	16-8	0.61	0.39	0.22	0.25	0.20	0.05	32.45	0.04	4.85×10^{-4}	2121	1718	0.810	
	33-35	0.54	0.29	0.25	0.20	0.14	0.06	30.63	0.444	4.29×10^{-3}	6443	5984	0.929	
	27-12	0.58	0.29	0.29	0.21	0.14	0.07	32.02	0.444	4.57×10^{-3}	4961	4375	0.882	

^aControl mode: diametral strain

Strain wave form: triangular with zero mean strain

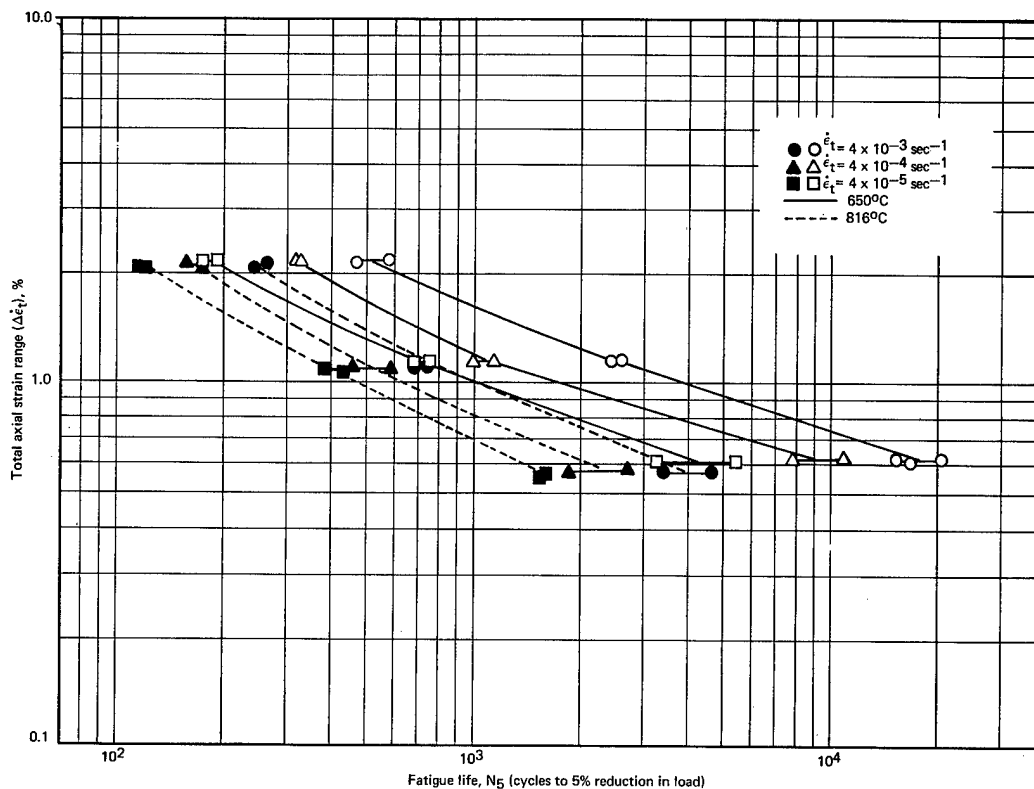


Fig. 6.6 — Total axial strain range versus fatigue life (N_5) for AISI 348 stainless steel tested in air

A comparison of plastic strain fatigue characteristics of 348, 304, and 316 SS obtained at 430°, 650°, and 816°C and a strain rate of $4 \times 10^{-3} \text{ sec}^{-1}$ is shown in Figures 6.14, 6.15, and 6.16. At 430°C³ the 316 SS is slightly less fatigue resistant than the 348 SS. No data have been obtained for 304 SS at this temperature. At 650°C the 316 SS is considerably less fatigue resistant than the 348 SS and slightly less than the 304 SS. Based on the data at 816°C, the 348 and 316 SS exhibit similar fatigue characteristics for a given strain level, whereas 304 SS is slightly less fatigue resistant than either of these two materials over the strain range evaluated.

Plots of stress range versus total axial strain range for 316 SS at 650°C and 816°C and for a constant strain rate of $4 \times 10^{-3} \text{ sec}^{-1}$ are shown in Figure 6.17. The stress values represent steady-state stress range data and were usually obtained at $N_f/2$. In general, 316 SS data for 650°C and 816°C exhibited cyclic hardening followed by the steady-state stress range indicated in Tables 6.1, 6.2, and 6.3. At 430°C, however, it exhibited cyclic hardening followed by cyclic softening; this phenomenon was observed over the entire strain range evaluated, as shown in Figure 6.18. In this evaluation, axial strain range data were calculated from diametral strain measurements obtained at the steady-state stress range which occurred after most cyclic hardening or cyclic softening had been completed.

6.4 FATIGUE DATA ANALYSIS

An analysis of fatigue data generated to date on 304, 348, and 316 SS at 650°C and 816°C for an approximate axial strain rate of $4 \times 10^{-3} \text{ sec}^{-1}$ is shown in Figures 6.19 through

³"AEC Fuels and Materials Development Program Progress Report No. 71," GE-NMPO, GEMP-1002, December 29, 1967, p. 96.

TABLE 6.4
SUMMARY OF SHORT-TERM TENSILE DATA FOR
AISI TYPES 348, 304, AND 316 STAINLESS STEEL

Fully Annealed Stainless Steel	Test Temperature, °C	Young's Modulus (E), 10 ³ kg/mm ²	Axial Strain Rate ($\dot{\epsilon}_t$), sec ⁻¹	Reduction in Area, %	Poisson's Ratio (elastic), ν_e
AISI 316	20	21.16	4×10^{-3}	a	a
	430	16.87	4×10^{-3}	60.0	0.32
	430	16.87	4×10^{-5}	57.1	0.32
	650	15.43	4×10^{-3}	60.4	0.31
	650	15.43	4×10^{-5}	33.4	0.31
	816	12.94	4×10^{-3}	56.5	0.26
	816	12.94	4×10^{-5}	49.8	0.26
AISI 304	20	20.18	4×10^{-3}	a	0.3 ^b
	20	20.18	4×10^{-5}		
	430	16.45	4×10^{-3}		0.3 ^b
	430	16.45	4×10^{-5}		
	650	15.19	4×10^{-3}		0.3 ^b
	650	15.19	4×10^{-5}		
	816	a	a		0.3 ^b
AISI 348	20	19.82	4×10^{-3}	a	0.3 ^b
	20	19.82	4×10^{-5}		
	430	16.73	4×10^{-3}		0.3 ^b
	430	16.73	4×10^{-5}		
	650	15.33	4×10^{-3}		0.3 ^b
	650	15.33	4×10^{-5}		
	816	13.39	4×10^{-3}		0.3 ^b
	816	13.39	4×10^{-5}		

^aValues are being determined.

^bAssumed values.

Poisson's Ratio (plastic) = 0.5.

6.24. In this analysis, the Manson-Halford⁴ approach was employed to predict low-cycle fatigue behavior. These calculations followed from the expression:

$$\Delta \dot{\epsilon}_t = \frac{3.5 \sigma_u}{E} N_f^{-0.12} + D^{0.6} N_f^{-0.6} \quad (6.6)$$

where:

σ_u is the ultimate tensile strength

E is the modulus of elasticity

D is $\ln \frac{1}{1-RA}$

RA is reduction in area expressed as a fraction

N_f is the number of cycles to failure

Using the short-term tensile data presented in Table 6.5, the N_f values corresponding to assumed $\Delta \dot{\epsilon}_t$ values were calculated. Based on the Manson-Halford suggestions, the lower-, average-, and upper-bound curves were positioned.

The short-term tensile property data and Poisson's Ratio needed for the conversion of diametral strain to axial strain are handbook values; hence the correlation obtained should be considered preliminary. Short-term tensile data and values for Poisson's Ratio are being generated for the alloys under investigation to secure a better correlation. As shown in Figures 6.19 through 6.24, data for the three alloys evaluated generally lie near the

⁴S. S. Manson and G. Halford, "A Method of Estimating High-Temperature Low-Cycle Fatigue Behavior of Metals," NASA TM X-52270, 1967.

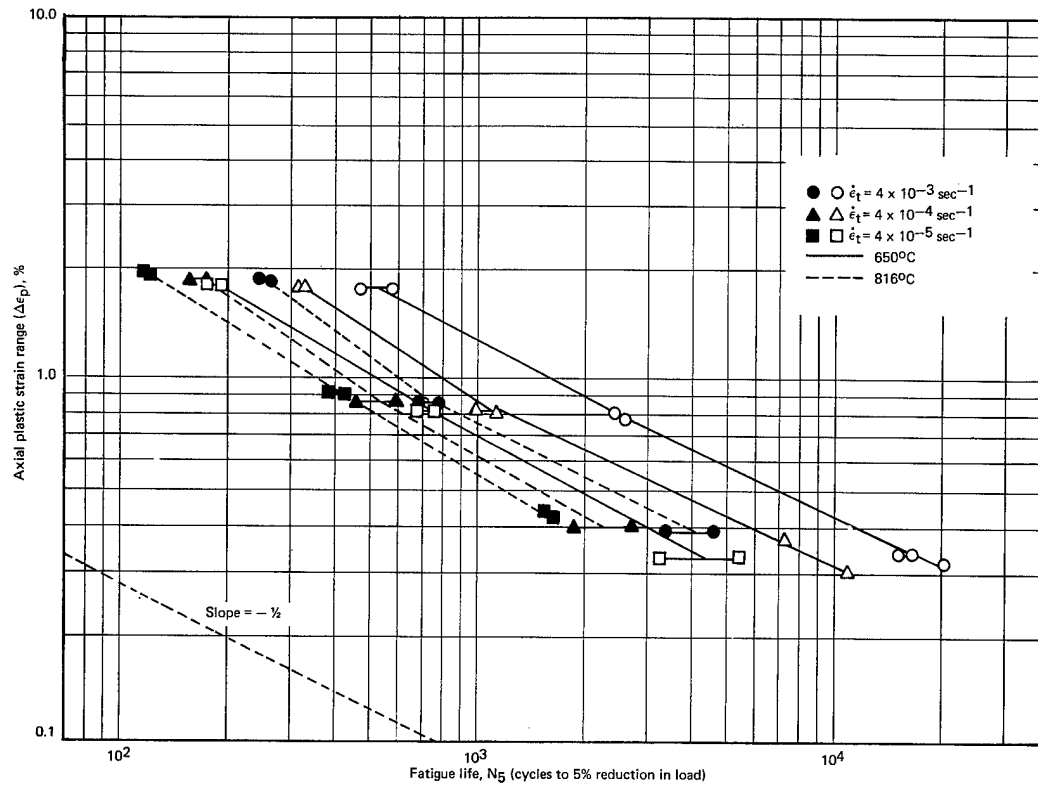


Fig. 6.7 – Axial plastic strain range versus fatigue life (N_5) for AISI 348 stainless steel tested in air

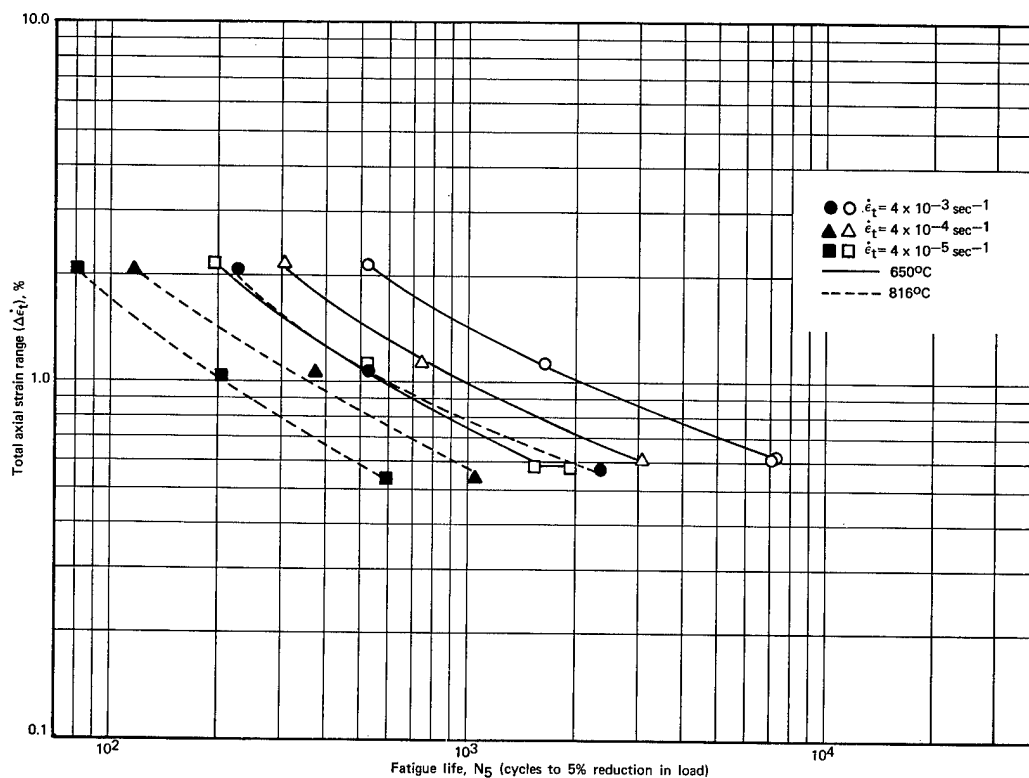


Fig. 6.8 – Total axial strain range versus fatigue life (N_5) for AISI 304 stainless steel tested in air

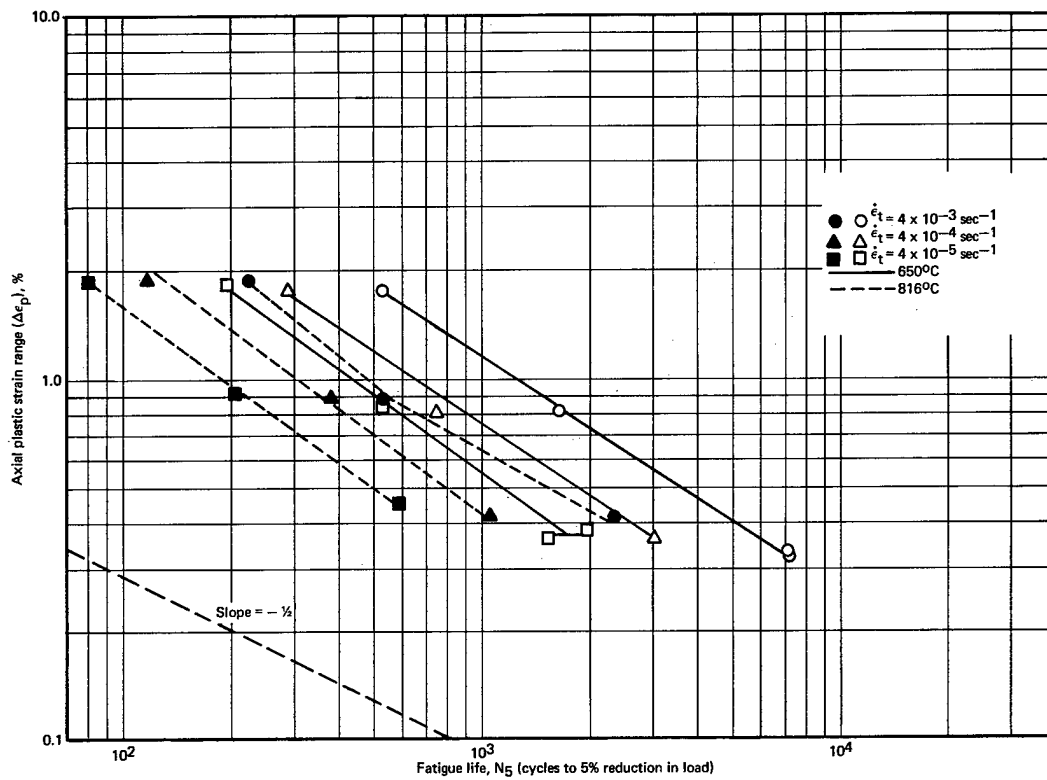


Fig. 6.9 – Axial plastic strain range versus fatigue life (N_5) for AISI 304 stainless steel tested in air

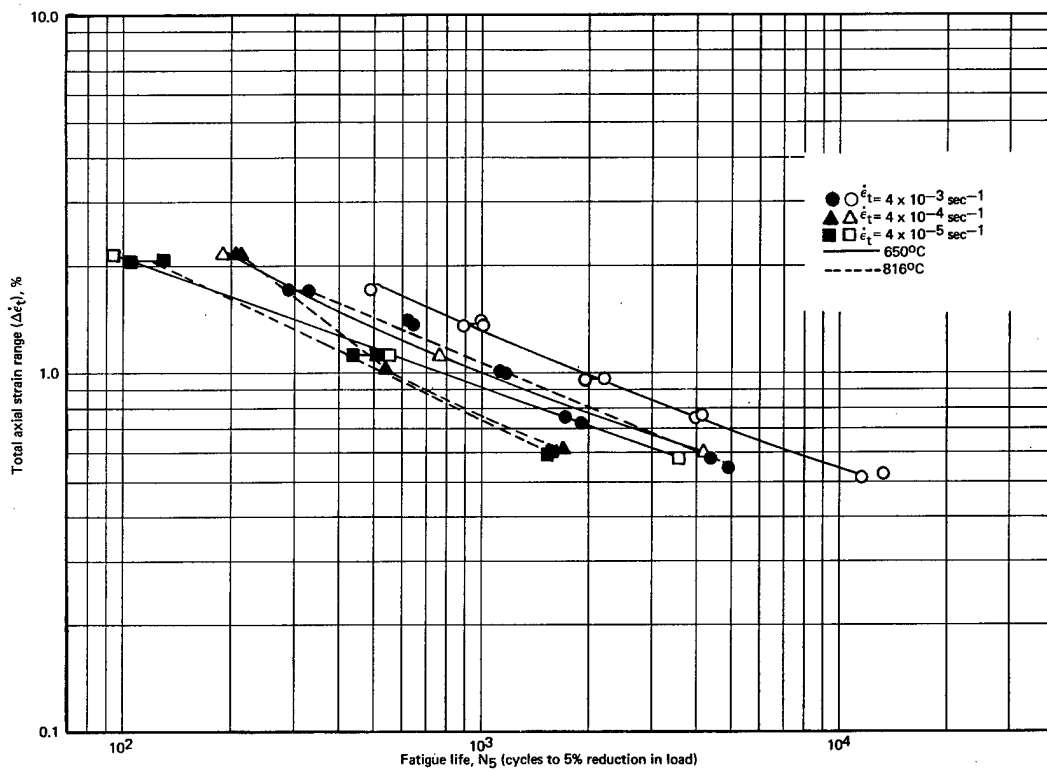


Fig. 6.10 – Total axial strain range versus fatigue life (N_5) for AISI 316 stainless steel tested in air

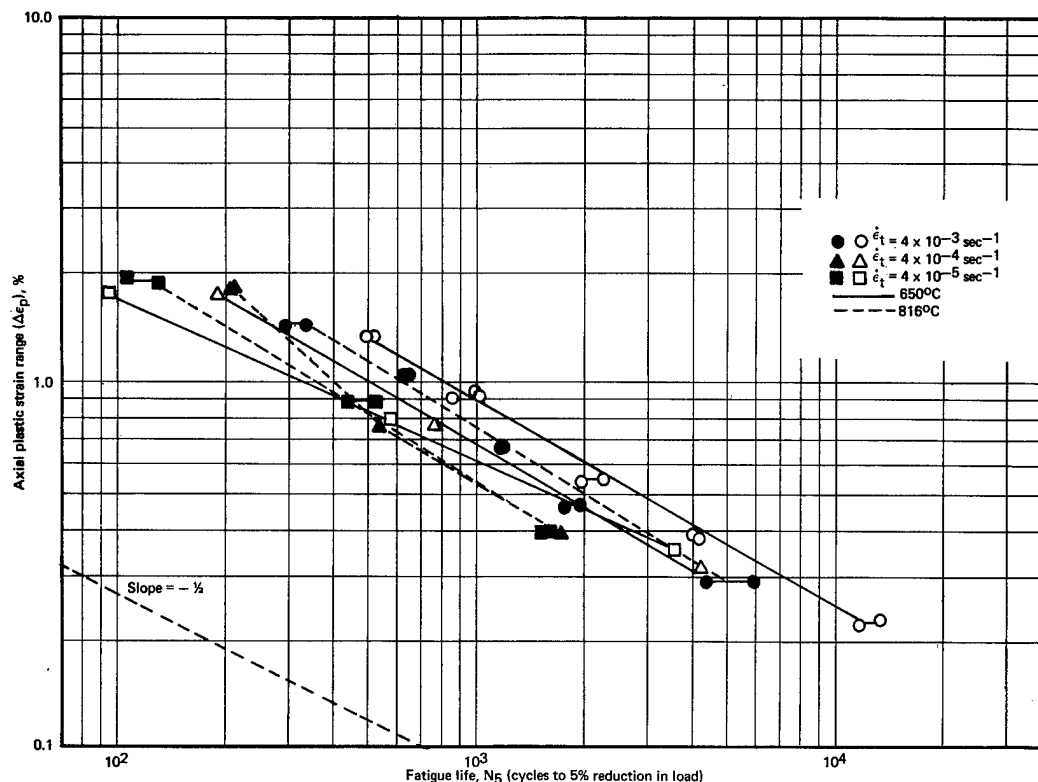


Fig. 6.11 — Axial plastic strain range versus fatigue life (N_5) for AISI 316 stainless steel tested in air

upper-bound of the predicted curve, except for the 348 SS data at 816°C. Data in the high-life region ($\Delta\dot{\epsilon}_t \sim 0.5\%$) for both 650°C and 816°C become more conservative than those predicted for the upper-bound limit using the expression mentioned. Work will continue using the short-term property data characteristic of the material being evaluated. Additional correlations that include the lower strain rate data will also be evaluated.

In all evaluations mentioned above, two definitions of fatigue life were encountered. In addition to the number of cycles to failure, N_f , the number of cycles to a 5-percent reduction in load, N_5 , was employed. A comparison of N_5 to N_f is presented in Tables 6.1, 6.2, and 6.3. Since N_5 corresponds to a fairly significant drop in the load, this point is expected to occur near the failure point. For this reason the ratio N_5/N_f should be a fraction closer to unity than to zero. If a value of 0.75 is selected, data in Tables 6.1, 6.2, and 6.3 indicate only 16 of 99 data points with N_5/N_f values below 0.75. Other interesting data obtained in this evaluation are:

1. Only 1 of 42 data points for 316 SS has a ratio of N_5/N_f below 0.75; this compares to 5 of 20 for 304 SS and 10 of 37 for 348 SS. Obviously for the 316 SS fracture is closer at hand when the N_5 point is reached.
2. Ranges of the N_5/N_f values are:
0.524 to 0.988 for 348 SS
0.615 to 0.970 for 304 SS
0.633 to 0.996 for 316 SS.
3. Twelve of the 16 N_5/N_f values below 0.75 correspond to tests at 816°C.
4. Only two of the 16 N_5/N_f values below 0.75 were obtained in tests at a strain rate of $4 \times 10^{-3} \text{ sec}^{-1}$.
5. Only three of the 16 N_5/N_f values below 0.75 correspond to strain range tests below 1 percent.

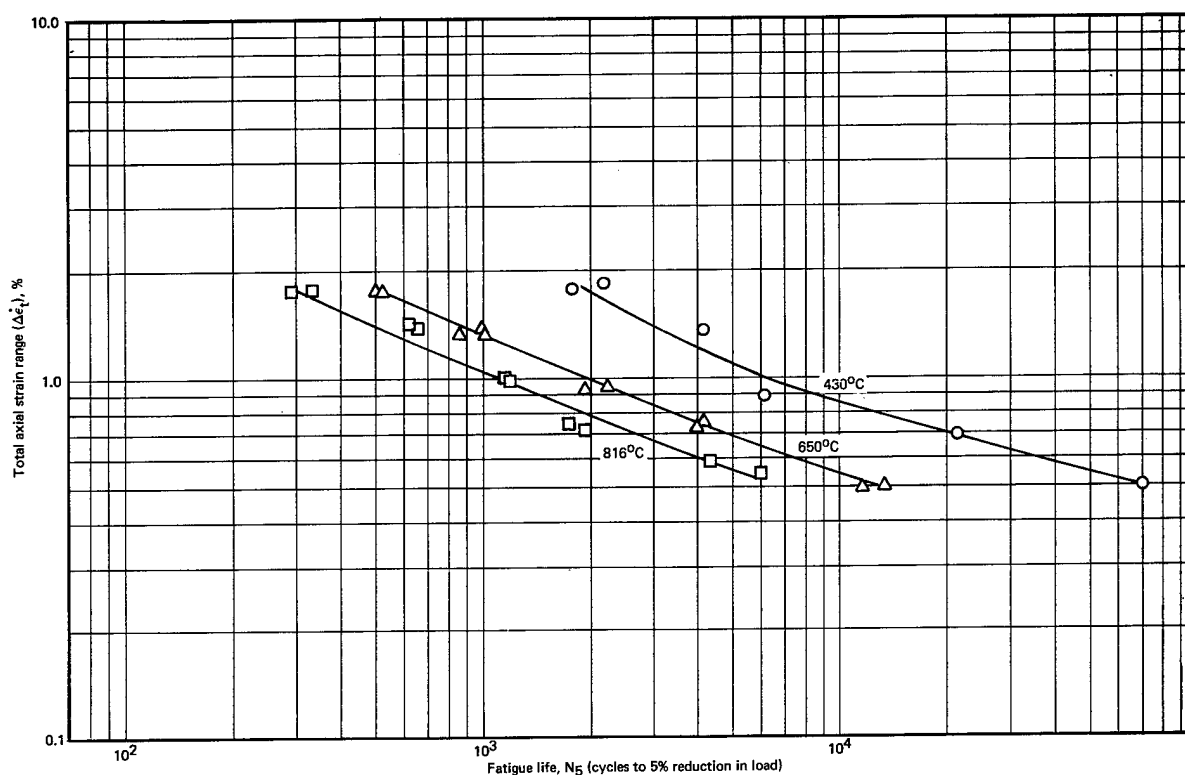


Fig. 6.12 — Total axial strain range versus fatigue life (N_5) for AISI 316 stainless steel tested in air; axial strain rate $\dot{\epsilon}_t = 4 \times 10^{-3} \text{ sec}^{-1}$

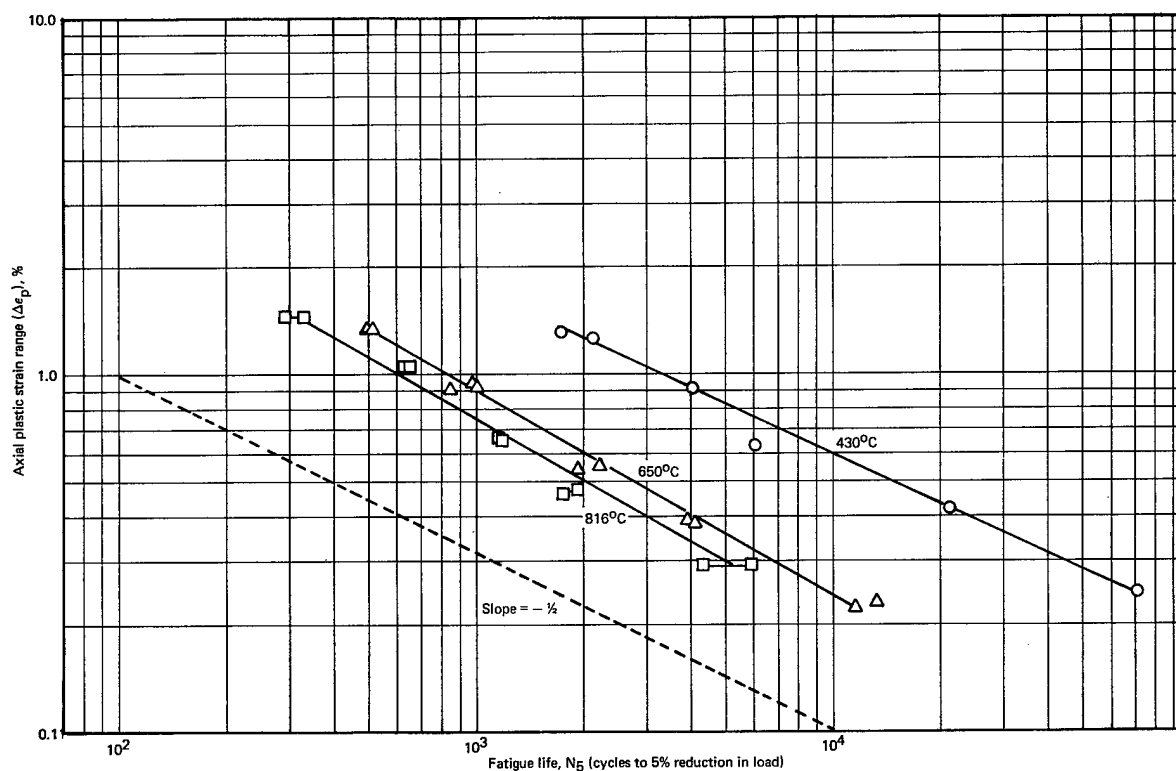


Fig. 6.13 — Axial plastic strain range versus fatigue life (N_5) for AISI 316 stainless steel tested in air; axial strain rate $\dot{\epsilon}_t = 4 \times 10^{-3} \text{ sec}^{-1}$

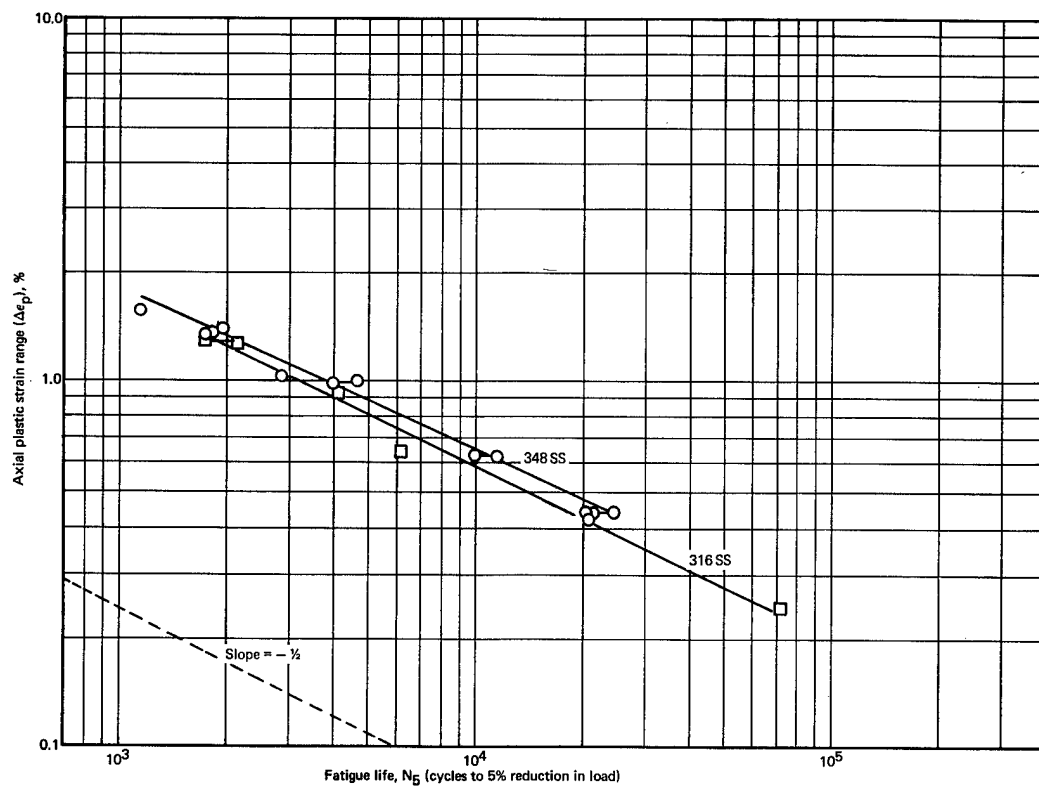


Fig. 6.14 — Axial plastic strain range versus fatigue life (N_5) for AISI 316 and 348 stainless steel at 430°C and an axial strain rate of $4 \times 10^{-3} \text{ sec}^{-1}$

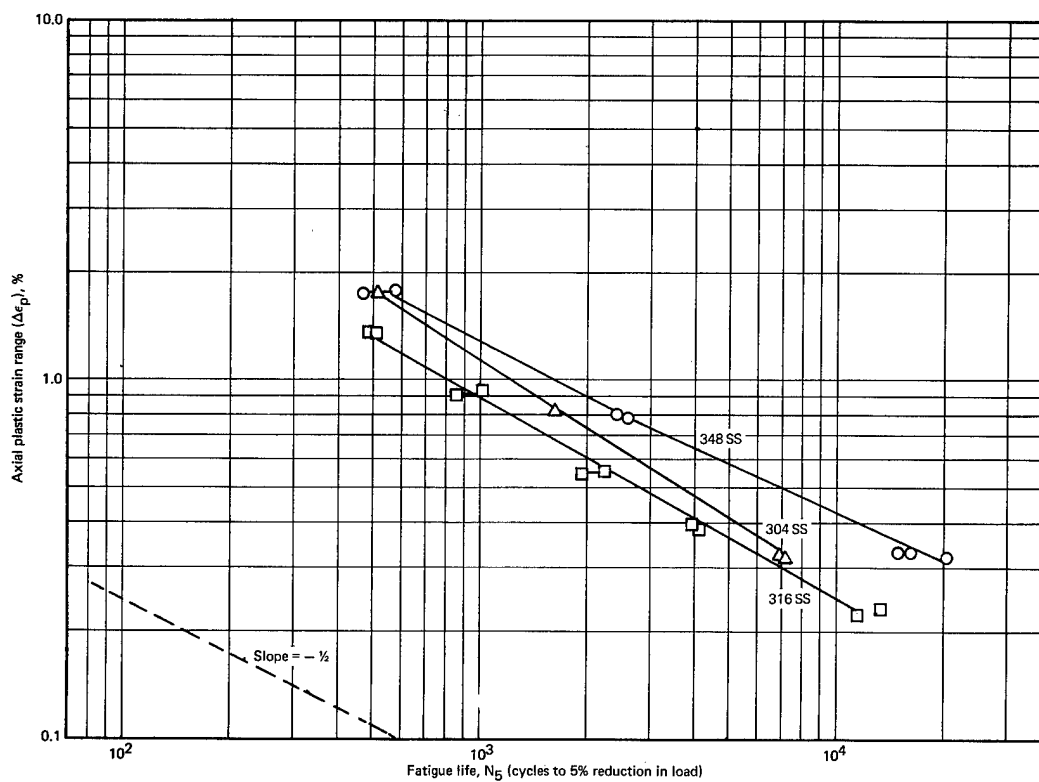


Fig. 6.15 — Axial plastic strain range versus fatigue life (N_5) for AISI 304, 316, and 348 stainless steel at 650°C and an axial strain rate of $4 \times 10^{-3} \text{ sec}^{-1}$

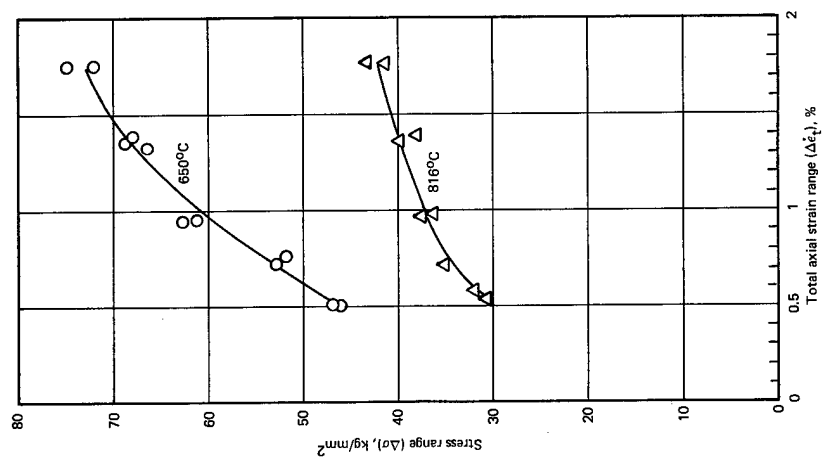


Fig. 6.17 — Stress range versus total axial strain range for AISI 316 stainless steel at a strain rate of $4 \times 10^{-3} \text{ sec}^{-1}$

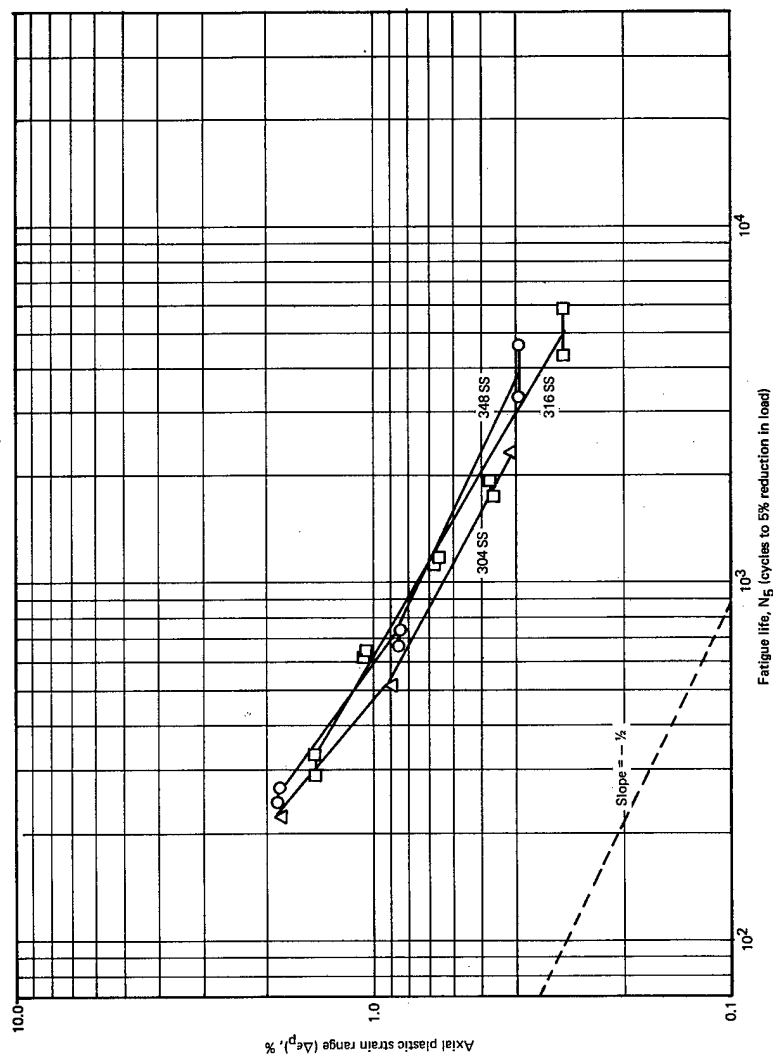


Fig. 6.16 — Axial plastic strain range versus fatigue life (N_f) for AISI 304, 316, and 348 stainless steel at 816°C and an axial strain rate of $4 \times 10^{-3} \text{ sec}^{-1}$

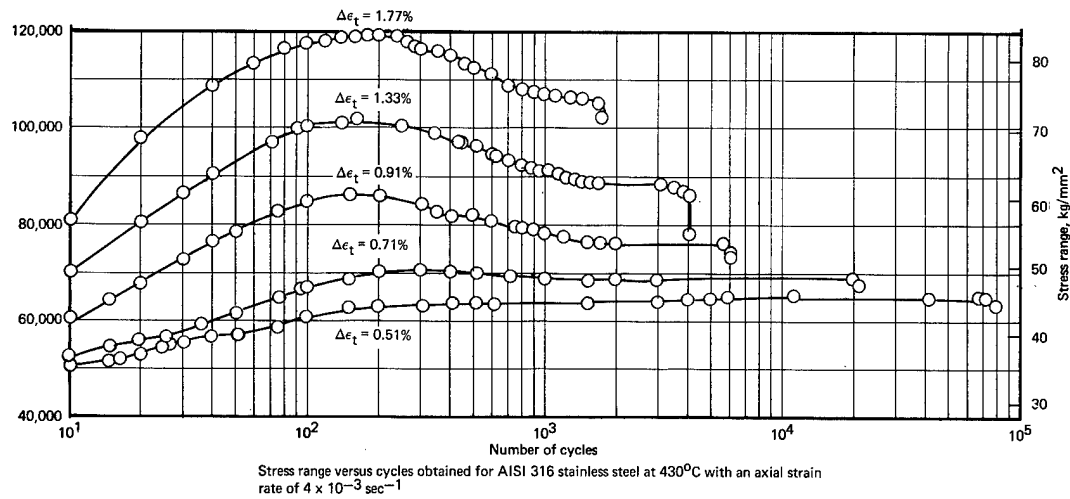


Fig. 6.18 — Stress range versus cycles for AISI 316 stainless steel at 430°C and an axial strain rate of $4 \times 10^{-3} \text{ sec}^{-1}$

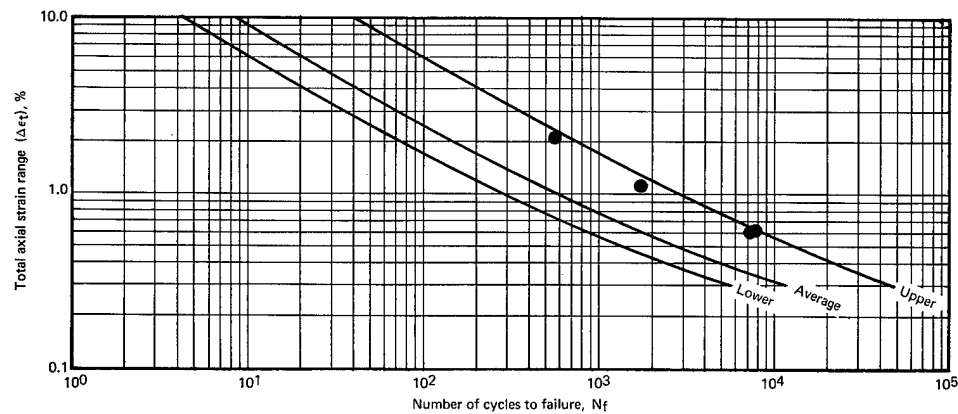


Fig. 6.19 — Correlation of high-temperature fatigue data obtained for AISI 304 stainless steel at 650°C and a constant strain rate of $\sim 4 \times 10^{-3} \text{ sec}^{-1}$

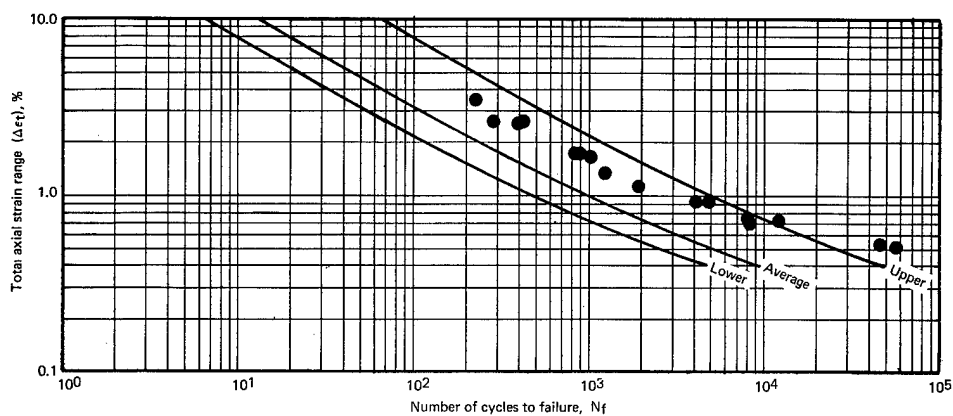


Fig. 6.20 — Correlation of high-temperature fatigue data obtained for AISI 348 stainless steel at 650°C and a constant strain rate of $\sim 4 \times 10^{-3} \text{ sec}^{-1}$

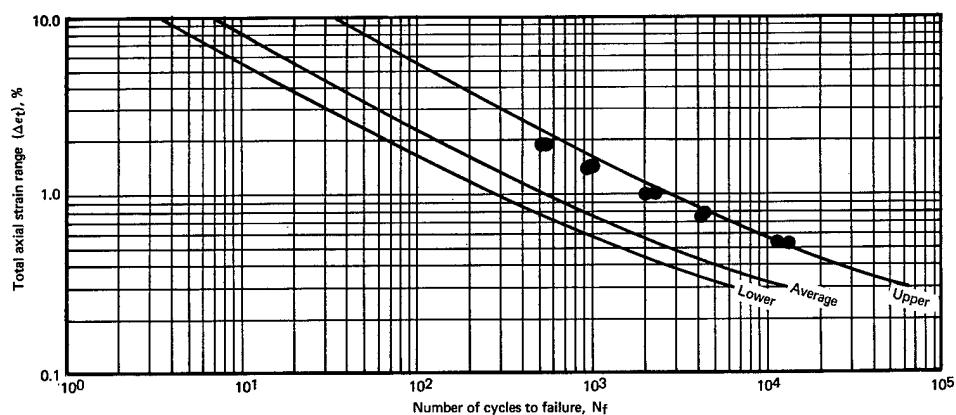


Fig. 6.21 — Correlation of high-temperature fatigue data obtained for AISI 316 stainless steel at 650°C and a constant strain rate of $\sim 4 \times 10^{-3} \text{ sec}^{-1}$

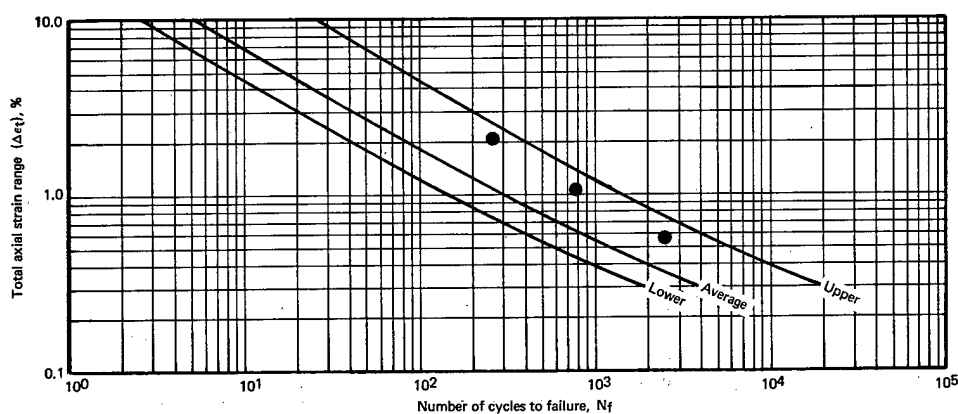


Fig. 6.22 — Correlation of high-temperature fatigue data obtained for AISI 304 stainless steel at 816°C and a constant strain rate of $\sim 4 \times 10^{-3} \text{ sec}^{-1}$

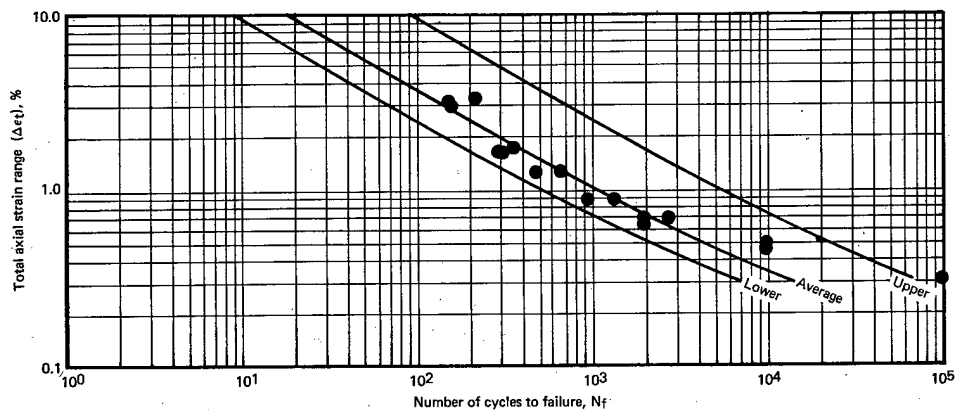


Fig. 6.23 — Correlation of high-temperature fatigue data obtained for AISI 348 stainless steel at 816°C and a constant strain rate of $\sim 4 \times 10^{-3} \text{ sec}^{-1}$

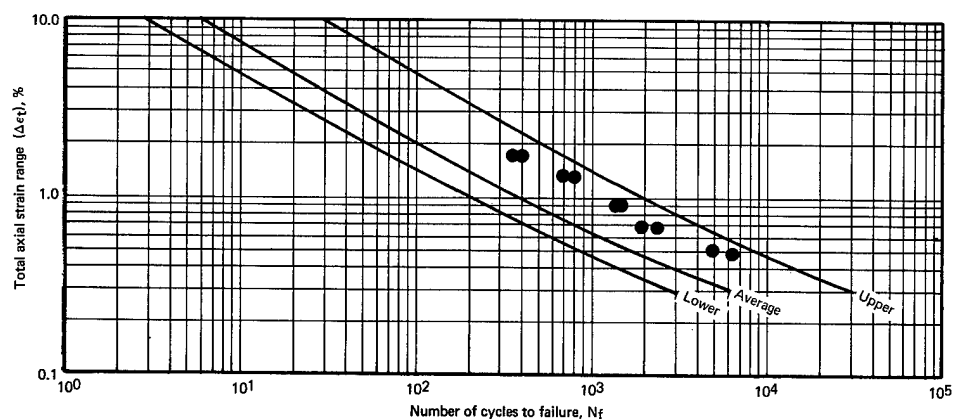


Fig. 6.24 — Correlation of high-temperature fatigue data obtained for AISI 316 stainless steel at 816°C and a constant strain rate of $\sim 4 \times 10^{-3} \text{ sec}^{-1}$

TABLE 6.5

SHORT-TERM TENSILE DATA^a FOR CORRELATION OF
HIGH-TEMPERATURE FATIGUE RESULTS OBTAINED FOR
AISI 304, 348, AND 316 STAINLESS STEEL

Material	Temperature, °C	Ultimate Tensile Strength, kg/cm ²	Young's Modulus, kg/cm ² × 10 ⁻⁶	D ^b
304	650	2882	1.546	0.867
348	650	3233	1.398	1.295
316	650	3093	1.476	0.756
304	816	1406	1.335	0.545
348	816	1575	1.272	1.87
316	816	2039	1.335	0.60

^aLiterature data.

^bD is $\ln \frac{1}{1 - RA}$

6. Only three of the 16 N_5/N_f values below 0.75 correspond to frequencies above 0.01 sec^{-1} .

Although no detailed study has been made of this relationship, attention has been focused recently on evaluating the condition of the specimen at the N_5 point. Visual observations during test have shown that the specimen is definitely cracked at this point but no quantitative data were available to define the extent of cracking. Post-test metallographic evaluations have been initiated in an attempt to acquire more specific information relating to crack initiation and propagation. A fractographic analysis based on both light and electron microscopy has been made to yield measurements of the fatigue striations. These data were used to plot crack length as a function of the number of fatigue cycles. In the two plots obtained to date (Figure 6.25), the measured N_5 point was found to correspond to a crack length of about 1.7 mm. As this study continues, some indication should be obtained of the crack initiation point or of the crack length, where the demand strain remains fairly uniform over the controlled cross section.

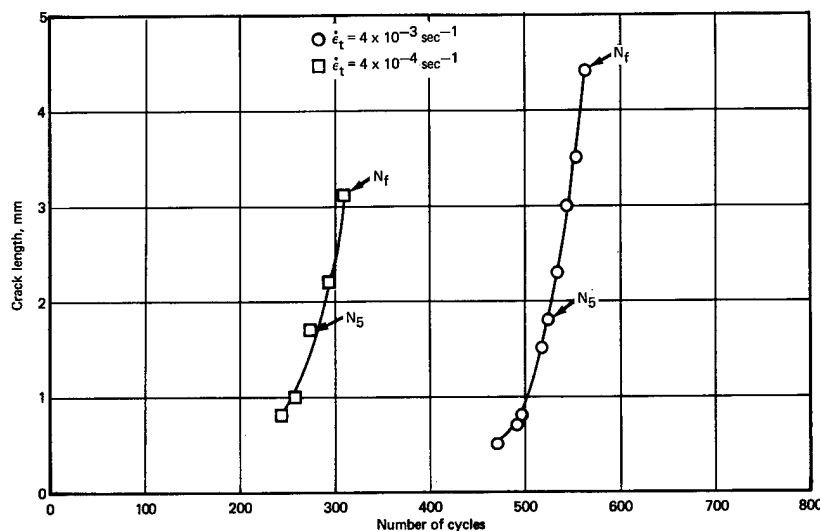


Fig. 6.25 — Relationship of fatigue cycles to crack length for AISI 304 stainless steel tested in air at 650°C; $\Delta\epsilon_t = 2.1\%$

6.5 METALLOGRAPHIC AND FRACTOGRAPHIC ANALYSIS OF LOW-CYCLE FATIGUE SPECIMENS

Post-test metallographic and fractographic analyses of low-cycle fatigue specimens were initiated. Information obtained in this study is expected to provide some understanding of behavior observed in the experimental fatigue testing program, and of basic mechanisms involved in crack initiation, crack propagation, and fracture phases of metal fatigue.

Standard metallographic techniques described previously,⁵ were used to characterize the fracture mode of AISI 304 and 348 stainless steel as a function of strain rate, strain range, and temperature. The specimens were sectioned longitudinally through the area where both the initial and final fracture occurred, and this cross section was prepared for metallographic evaluation. Photomicrographs of the structure of these two materials in the pre-test condition are shown in Figures 6.26 and 6.27. AISI 304 SS had a uniform equiaxed grain structure with twins in some grains and an ASTM grain size of 2 to 3. AISI 348 SS had a duplex grain structure with a fine-grained center surrounded by a coarse-grained outer layer. The fine-grained portion varied from one fatigue specimen to another. Because of this duplex structure, two ASTM grain sizes are reported: fine-grained material 10, and coarse-grained material 4 to 5.

Metallographic analyses were made of the cross sections of the fractures of 304 SS tested at 650°C, at two strain ranges (2 and 0.6%), and at three strain rates (4×10^{-5} , 4×10^{-4} , and $4 \times 10^{-3} \text{ sec}^{-1}$). The crack initiated and propagated transgranularly in the specimens tested at the highest strain rate at both strain ranges. In specimens tested at the lower strain rates, the cracks initiated intergranularly and propagated both trans- and intergranularly. At the final fracture in all specimens, the grains were elongated and cracks appeared on the outer surfaces. Metallographic examination revealed a grain boundary phase in all fatigue specimens. Etch pits were seen in the highly stressed areas, indicating the dislocations which formed in the stressed metal.

AISI 304 SS specimens tested at 816°C, at two different strain ranges, and at three different strain rates were also analyzed. In these specimens the crack initiated and propa-

⁵GEMP-1002, pp. 102–105.

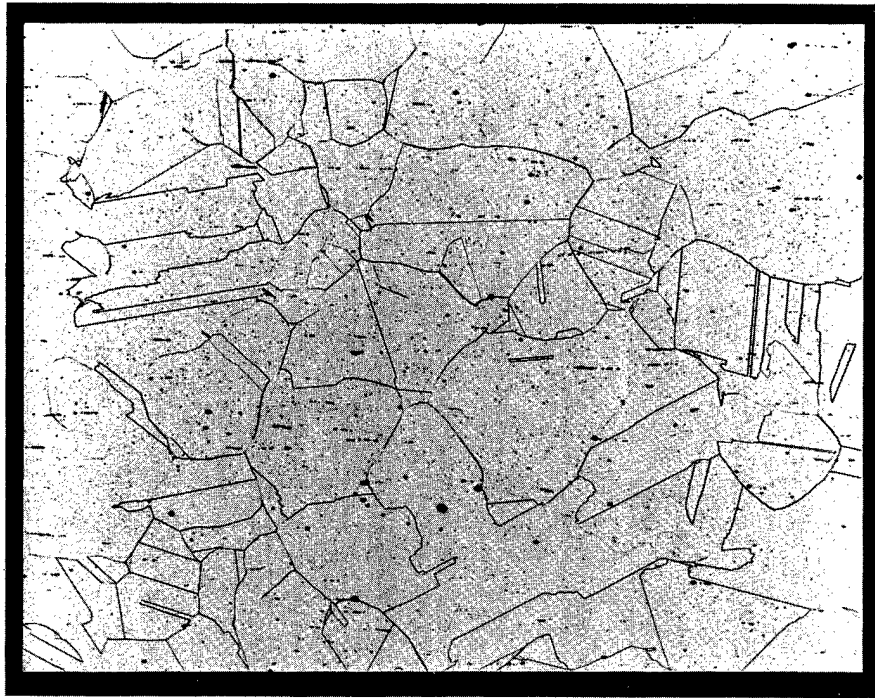


Fig. 6.26 — Photomicrograph showing pre-test structure of AISI 304 stainless steel (longitudinal cross section) used in low-cycle fatigue testing. (Neg. 10282; 22H₂SO₄, 12H₂O₂ [30%], 66H₂O, electrolytic etchant; 100X)

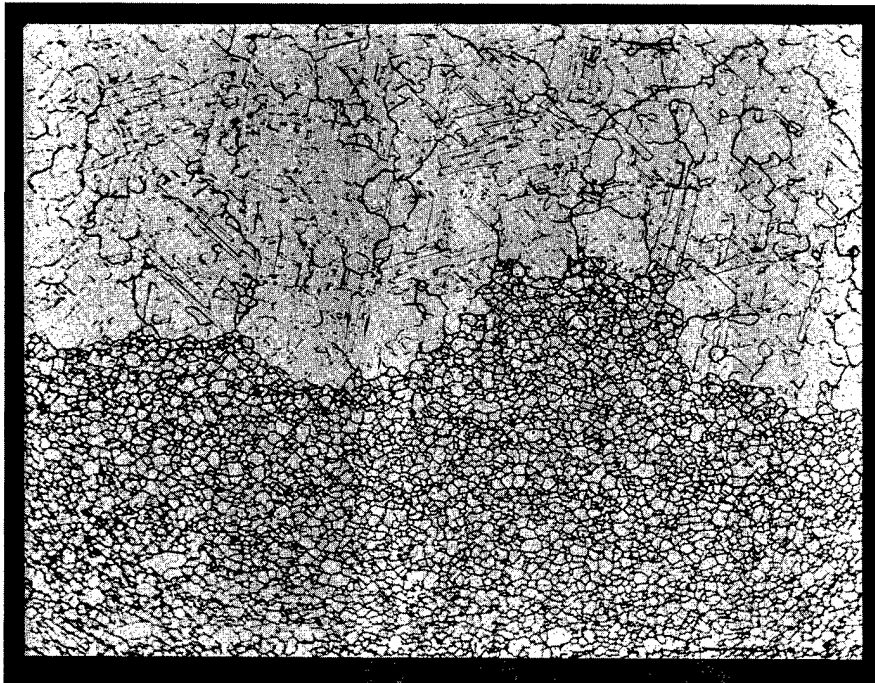


Fig. 6.27 — Photomicrograph showing pre-test structure of AISI 348 stainless steel (longitudinal cross section) used in low-cycle fatigue testing. (Neg. 10281; 50HNO₃, 50H₂O, electrolytic etchant; 100X)

gated intergranularly; at the final fracture the grains were elongated. In the highly strained regions of the 2-percent strain range specimens, subgrains were observed at the lowest strain rate, subgrains and etch pits at the intermediate strain rate, and etch pits at the highest strain rate. In the highly strained regions of the 0.6-percent strain range specimens, no etch pits or subgrains were observed at the lowest strain rate; at the intermediate strain rate etch pits were observed, and at the highest strain rate subgrains appeared. At the lowest strain rate the grain boundary phase was intermittent; at the highest strain rates it was continuous (see Figure 6.28).

Post-test metallographic analyses were performed on AISI 348 SS specimens tested at two temperatures, three strain rates, and two strain ranges. As stated previously, this material had a duplex grain structure, and the amount of fine-grained material varied from specimen to specimen. There was no change in the grain boundary phase in this material, as was seen in the 304 SS. In each specimen the crack initiated intergranularly in the large-grained areas and propagated transgranularly. Numerous secondary cracks occurred on the outer periphery of the specimens tested at the 2-percent strain range at both temperatures, but at the 0.6-percent strain range, only a few small secondary cracks appeared. The fractures varied considerably, depending upon the strain range. At the lowest strain range fractures were almost straight across except where the final separation took place (compare Figures 6.29 and 6.30). Another difference appeared in the fatigue specimens tested at 816°C at the lowest strain range; a series of cracks developed at an angle approximately 60 degrees to the fractured surface in the direction the crack was propagating (see Figure 6.31). Indications of this condition appeared in other tests but they were not nearly so pronounced.

Results of metallographic analyses of 304 and 348 SS specimens are summarized in Table 6.6.

To characterize the AISI 316 SS for the low-cycle fatigue program, longitudinal and transverse cross sections were prepared for metallographic analyses. The analysis and pre-test processing were reported previously.⁶ No differences were noted in the two cross sections, and the material had been fully recrystallized with a uniform equiaxed grain structure (Figure 6.32); ASTM grain size was 4 to 5. Twins were noted in some of the grains.

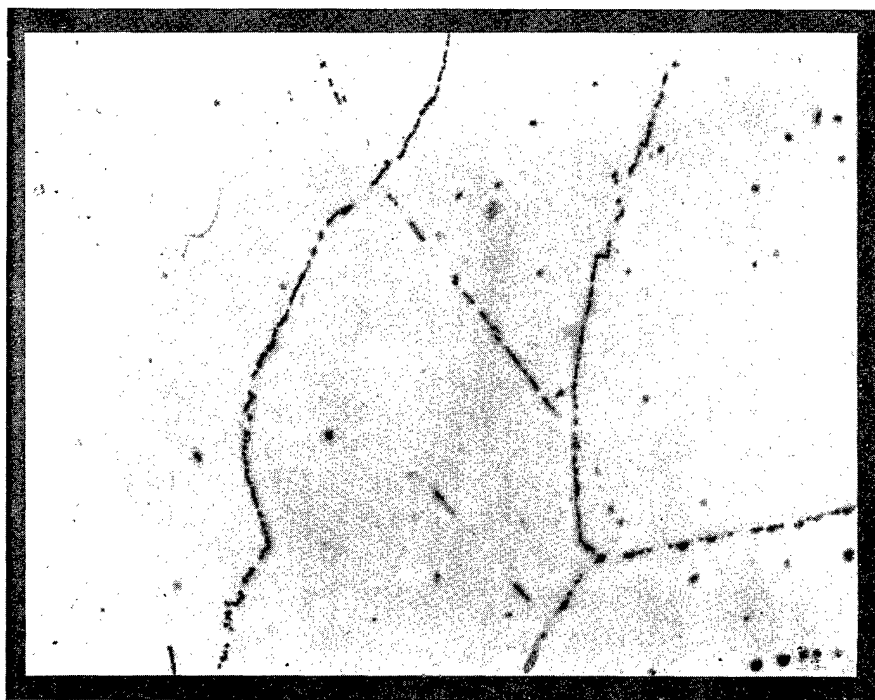
To study the fractured surfaces of low-cycle fatigue specimens at higher magnification, techniques were developed for replicating the area of interest for study in the electron microscope.⁷ These procedures are used extensively. Each striation on the fractured surface (Figure 6.33) is the result of one cycle in the fatigue test. A study is in progress to correlate this striation density with strain rate, strain range, and temperature of materials being tested. Striations could not be resolved at 1500X at the crack initiation point for the 304 SS tested at the lowest strain rate ($\sim 4 \times 10^{-5} \text{ sec}^{-1}$), and a strain range of 2 percent. This is apparently due to the low strain rate imposed during testing. In the 304 SS tested at 650°C, 2-percent strain range, and at the two highest strain rates, the cracks had propagated approximately 30 percent of the diameter ($\sim 2 \text{ mm}$) of the test specimen at the N5 point.

6.6 SUMMARY AND CONCLUSIONS

Several modifications incorporated in the four low-cycle fatigue systems this year improved strain programming versatility, load measurement sensitivity, and strain calibration accuracy.

⁶GEMP-1002, p. 94.

⁷GEMP-1002, p. 105.

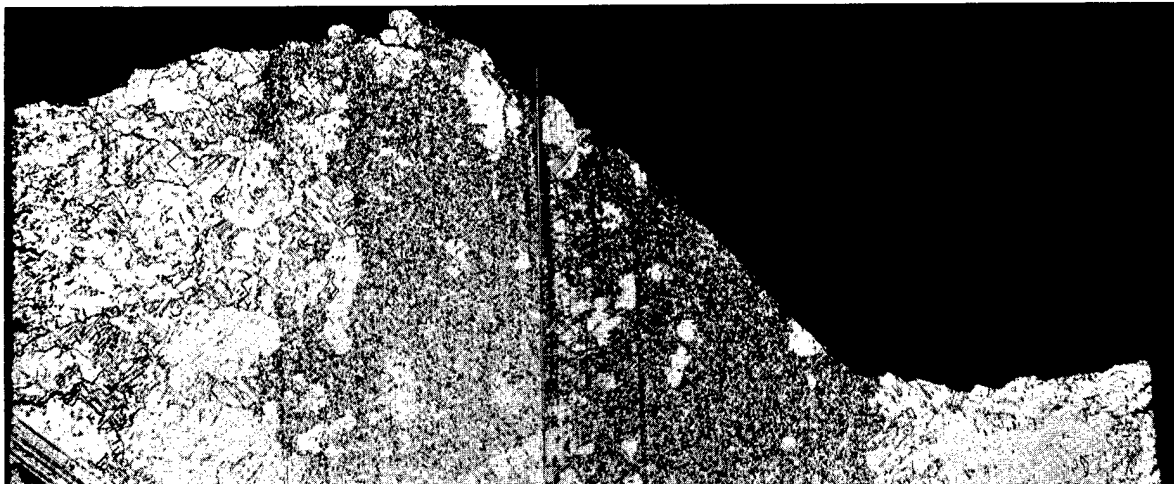


Test 10-2, $\Delta\dot{\epsilon}_t = 2.07\%$, $\dot{\epsilon}_t = 4.10 \times 10^{-5} \text{ sec}^{-1}$ (Neg. 10139)



Test 7-1, $\Delta\dot{\epsilon}_t = 2.08\%$, $\dot{\epsilon}_t = 4.2 \times 10^{-3} \text{ sec}^{-1}$ (Neg. 10138)

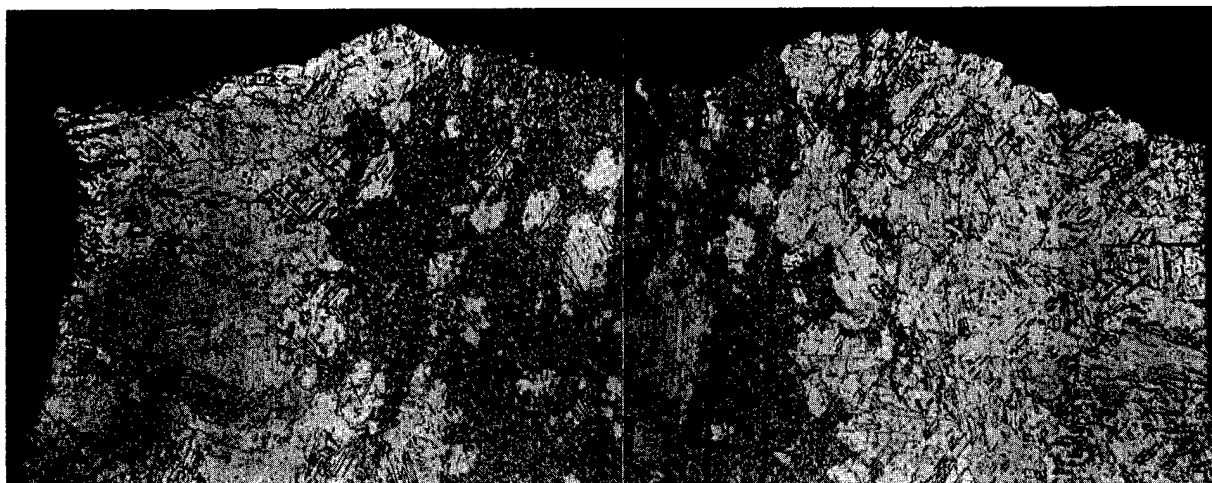
Fig. 6.28 — Photomicrographs taken near the crack initiation point showing the grain boundary phase in AISI 304 stainless steel tested at 816°C. (22H₂SO₄, 12H₂O₂ [30%], 66H₂O, electrolytic etchant; 1000X)



Neg. 10067

Test 3-7, $\Delta\dot{\epsilon}_t = 2.17\%$, $\dot{\epsilon}_t = 4.3 \times 10^{-5} \text{ sec}^{-1}$

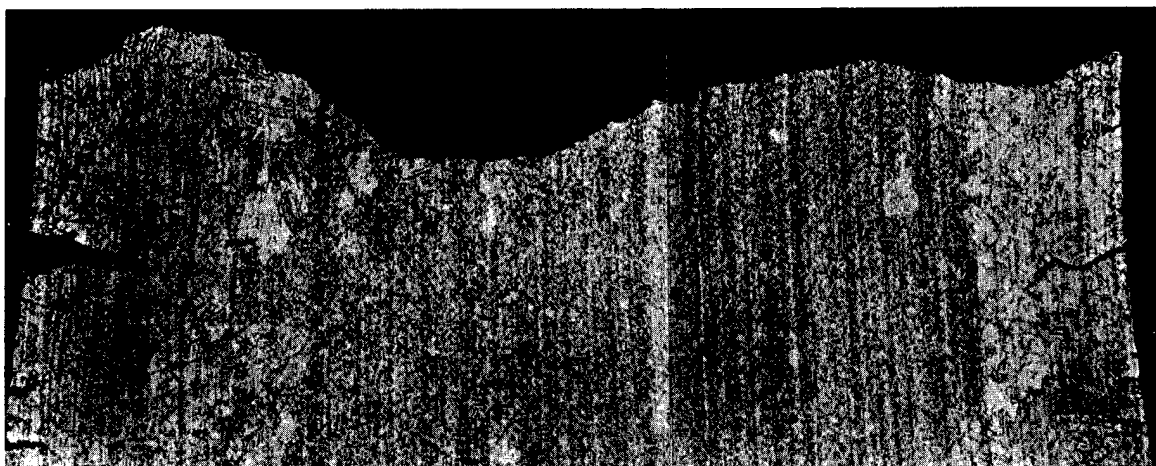
Neg. 10068



Neg. 10124

Test 3-8, $\Delta\dot{\epsilon}_t = 2.18\%$, $\dot{\epsilon}_t = 4.4 \times 10^{-4} \text{ sec}^{-1}$

Neg. 10123

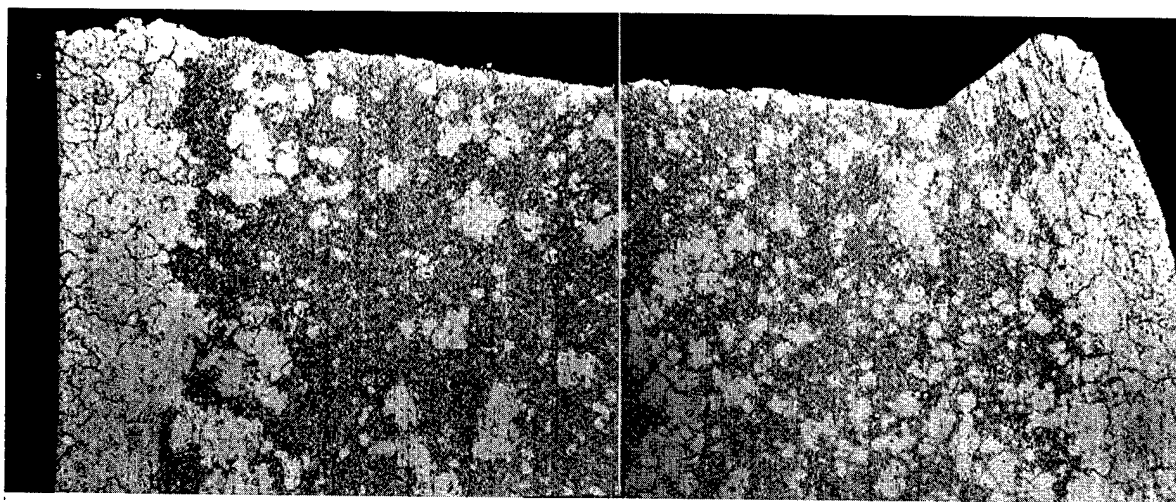


Neg. 10122

Test 3-4, $\Delta\dot{\epsilon}_t = 2.19\%$, $\dot{\epsilon}_t = 4.4 \times 10^{-3} \text{ sec}^{-1}$

Neg. 10121

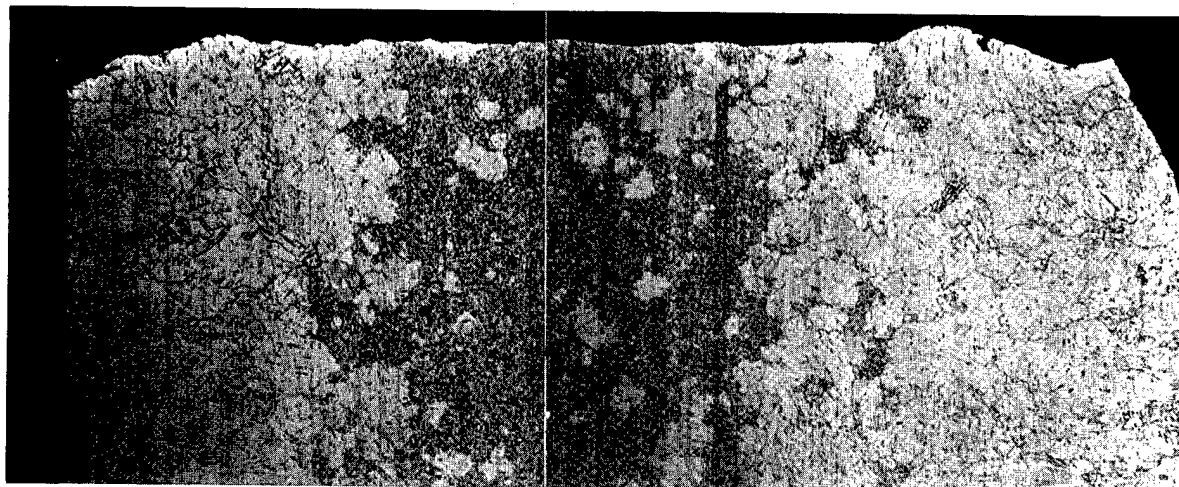
Fig. 6.29 — Composite photomicrograph of longitudinal cross section of AISI 348 stainless steel tested at 650°C. ($22\text{H}_2\text{SO}_4$, $12\text{H}_2\text{O}_2$ [30%], $66\text{H}_2\text{O}$, electrolytic etchant; $\sim 25\times$)



Neg. 10076

Test 5-12, $\Delta\dot{\epsilon}_t = 0.61\%$, $\dot{\epsilon}_t = 4.9 \times 10^{-5} \text{ sec}^{-1}$

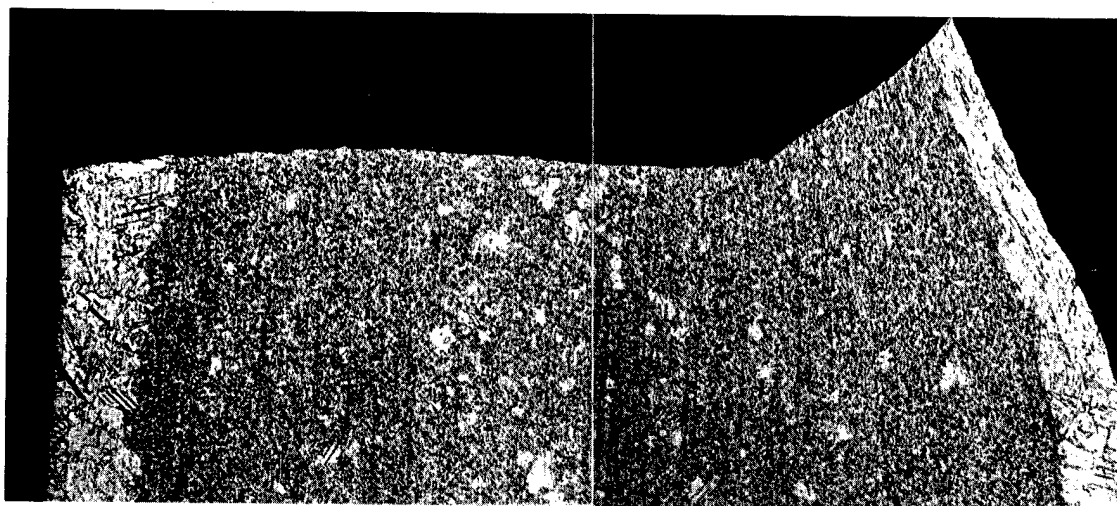
Neg. 10075



Neg. 10074

Test 3-11, $\Delta\dot{\epsilon}_t = 0.62\%$, $\dot{\epsilon}_t = 5.0 \times 10^{-4} \text{ sec}^{-1}$

Neg. 10073

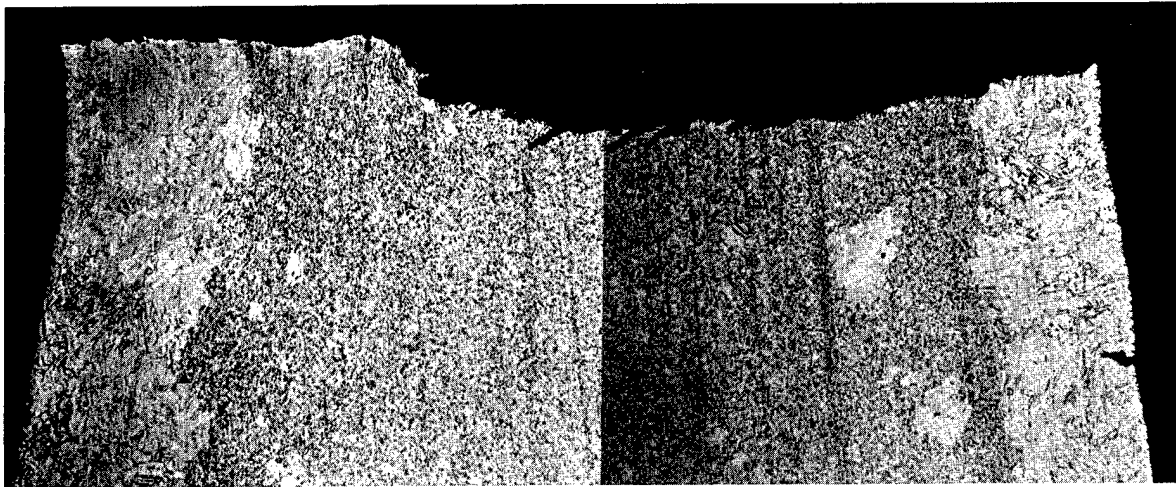


Neg. 10072

Test 5-3, $\Delta\dot{\epsilon}_t = 0.62\%$, $\dot{\epsilon}_t = 5.0 \times 10^{-3} \text{ sec}^{-1}$

Neg. 10071

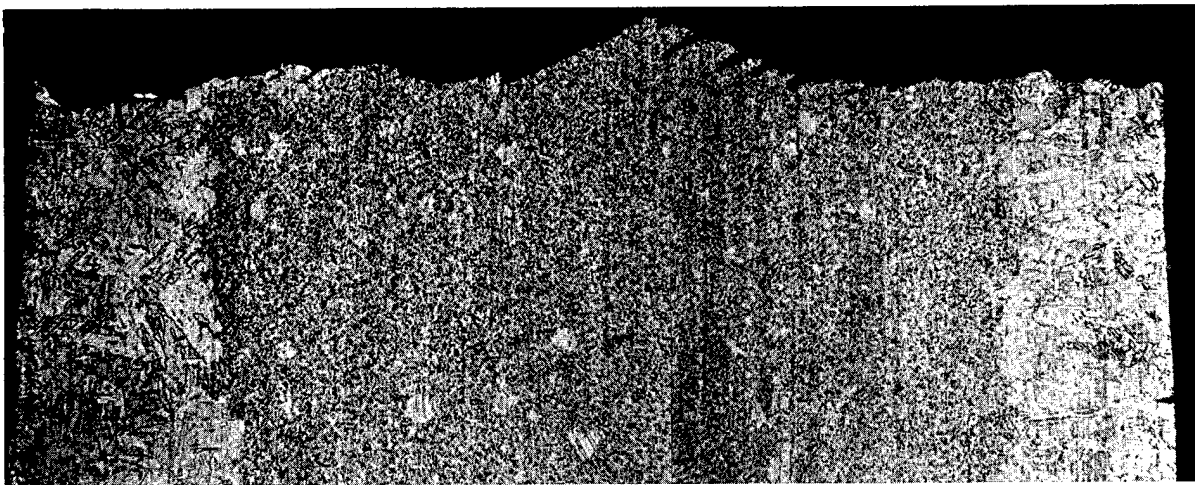
Fig. 6.30 — Composite photomicrograph of longitudinal cross section of AISI 348 stainless steel tested at 650°C. ($22\text{H}_2\text{SO}_4$, $12\text{H}_2\text{O}_2$ [30%], $66\text{H}_2\text{O}$, electrolytic etchant; $\sim 25\times$)



Neg. 10081

Test 6-10, $\Delta\dot{\epsilon}_t = 0.56\%$, $\dot{\epsilon}_t = 4.6 \times 10^{-5} \text{ sec}^{-1}$

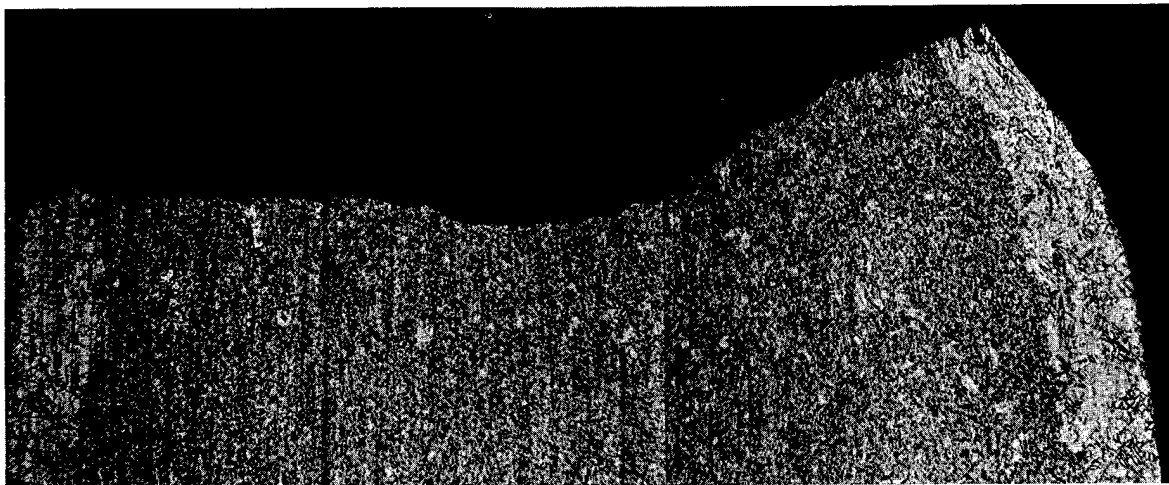
Neg. 10082



Neg. 10080

Test 6-8, $\Delta\dot{\epsilon}_t = 0.58\%$, $\dot{\epsilon}_t = 4.6 \times 10^{-4} \text{ sec}^{-1}$

Neg. 10079



Neg. 10078

Test 6-2, $\Delta\dot{\epsilon}_t = 0.57\%$, $\dot{\epsilon}_t = 4.5 \times 10^{-3} \text{ sec}^{-1}$

Neg. 10077

Fig. 6.31 — Composite photomicrograph of longitudinal cross section of AISI 348 stainless steel tested at 816°C. (22H₂SO₄, 12H₂O₂ [30%], 66H₂O, electrolytic etchant; ~25X)

TABLE 6.6
FRACTURE MODE CHARACTERIZATION OF AISI 304 AND 348 STAINLESS STEEL LOW-CYCLE FATIGUE SPECIMENS

Specimens	Test Temperature, °C	Test No.	Axial Strain Range ($\Delta\epsilon_t$), %	Axial Strain Rate ($\dot{\epsilon}_t$), sec ⁻¹	Cycles to 5 % Reduction in Load (N_5)	Mode of Crack Initiation	Intergranular Crack Length from Point of Initiation, mm	Mode of Crack Propagation to the Shear Point	Specific Observations
304 SS	650	10-12	2.12	4.2×10^{-5}	197	Intergranular	0.3	Inter- + transgranular	Continuous unidentified phase observed in grain boundaries; etch pits in highly strained regions.
	650	10-11	2.15	4.3×10^{-4}	287	Intergranular	0.1	Primarily transgranular	
	650	10-9	2.11	4.2×10^{-3}	524	Transgranular	—	Primarily transgranular	
	650	120	0.58	4.6×10^{-5}	1,533	Intergranular	0.6	Inter- + transgranular	Continuous unidentified phase observed in grain boundaries; etch pits in highly strained region.
	650	296	0.60	4.8×10^{-4}	3,009	Intergranular	0.2	Primarily transgranular	
	650	294	0.62	4.9×10^{-3}	7,176	Transgranular	—	Primarily transgranular	
	816	10-2	2.07	4.1×10^{-5}	80	Intergranular	4.0	Primarily intergranular	Intermittent unidentified phase observed in grain boundaries; subgrains in highly strained regions.
	816	7-3	2.07	4.1×10^{-4}	117	Intergranular	1.2	Primarily intergranular	Continuous unidentified phase observed in grain boundaries; a few etch pits and subgrains in highly strained regions.
	816	7-1	2.08	4.2×10^{-3}	226	Intergranular	1.0	Primarily intergranular	Continuous unidentified phase observed in grain boundaries; few etch pits in highly strained regions.

TABLE 6.6 (Cont.)
FRACTURE MODE CHARACTERIZATION OF AISI 304 AND 348 STAINLESS STEEL LOW-CYCLE FATIGUE SPECIMENS

Specimens	Test Temperature, °C	Test No.	Axial Strain Range ($\Delta\epsilon_t$), %	Axial Strain Rate ($\dot{\epsilon}_t$), sec^{-1}	Cycles to 5% Reduction in Load (N_5)	Mode of Crack Initiation	Crack Length from Point of Initiation, mm	Mode of Crack Propagation to the Shear Point	Specific Observations
348 SS	816	10-3	0.53	4.2×10^{-5}	591	Intergranular	0.7	Primarily intergranular	Intermittent unidentified phase observed in grain boundaries; no etch pits in highly strained regions.
	816	7-7	0.54	4.3×10^{-4}	1,055	Intergranular	0.8	Primarily intergranular	Continuous unidentified phase observed in grain boundaries; etch pits in highly strained regions.
	816	7-9	0.56	4.5×10^{-3}	2,346	Intergranular	0.8	Primarily intergranular	Continuous unidentified phase in grain boundaries; subgrains in highly strained regions.
	650	3-7	2.17	4.3×10^{-5}	193	Intergranular	0.2	Transgranular Transgranular Transgranular	Large amounts of secondary cracking; grain boundaries were relatively clean compared to 304 SS.
	650	3-8	2.18	4.4×10^{-4}	320	Intergranular	0.1		
	650	3-4	2.19	4.4×10^{-3}	585	Intergranular	0.1		
	650	5-12	0.61	4.9×10^{-5}	5,464	Intergranular	0.4	Transgranular Transgranular Transgranular	Limited secondary cracking; crack propagation was very regular, flat, and perpendicular to specimen axis.
	650	3-11	0.62	5.0×10^{-4}	10,948	Intergranular	0.2		
	650	5-3	0.62	5.0×10^{-3}	15,010	Intergranular	0.1		
	816	5-7	2.06	4.1×10^{-5}	122	Intergranular	<0.1	Transgranular Transgranular Transgranular	Numerous secondary cracks.
	816	5-5	2.11	4.2×10^{-4}	158	Intergranular	<0.1		
	816	5-1	2.11	4.2×10^{-3}	266	Intergranular	<0.1		
	816	6-10	0.56	4.6×10^{-5}	1,613	Intergranular	<0.1	Transgranular Transgranular	Crack propagation was very regular, flat, and almost perpendicular to specimen axis; cracks developed at ~60 degree angle to primary fracture surface in the direction of propagation.
	816	6-8	0.58	4.6×10^{-4}	2,718	Intergranular	<0.1		
	816	6-2	0.57	4.5×10^{-3}	4,656	Intergranular	<0.1	Transgranular	Crack propagation was very regular, flat, and perpendicular to specimen axis.

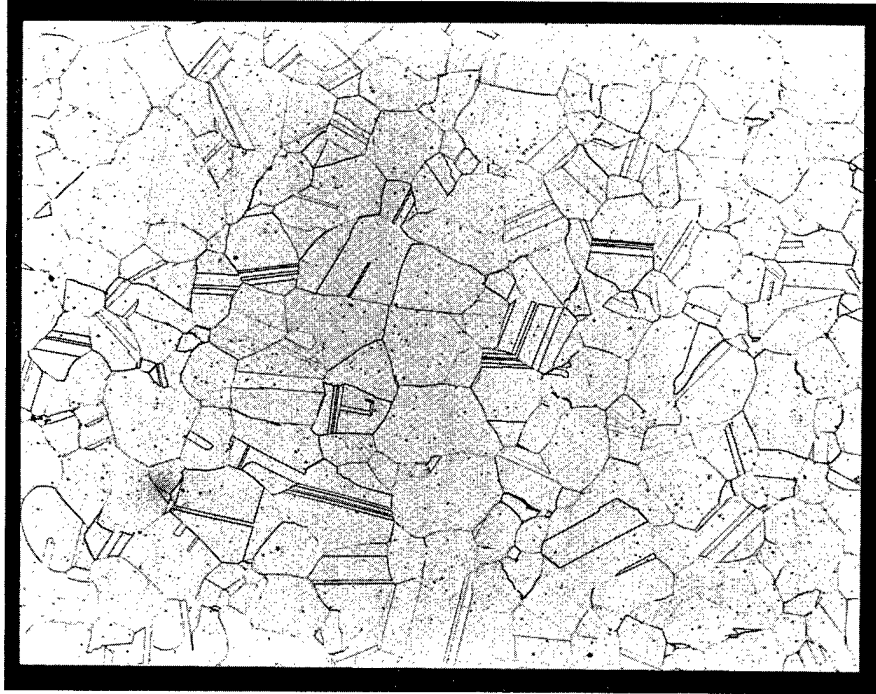


Fig. 6.32 — Photomicrograph showing pre-test structure of AISI 316 stainless steel (longitudinal cross section) used in low-cycle fatigue testing. (Neg. 10083; $22\text{H}_2\text{SO}_4$, $12\text{H}_2\text{O}_2$ [30%], $66\text{H}_2\text{O}$, electrolytic etchant; 100X)

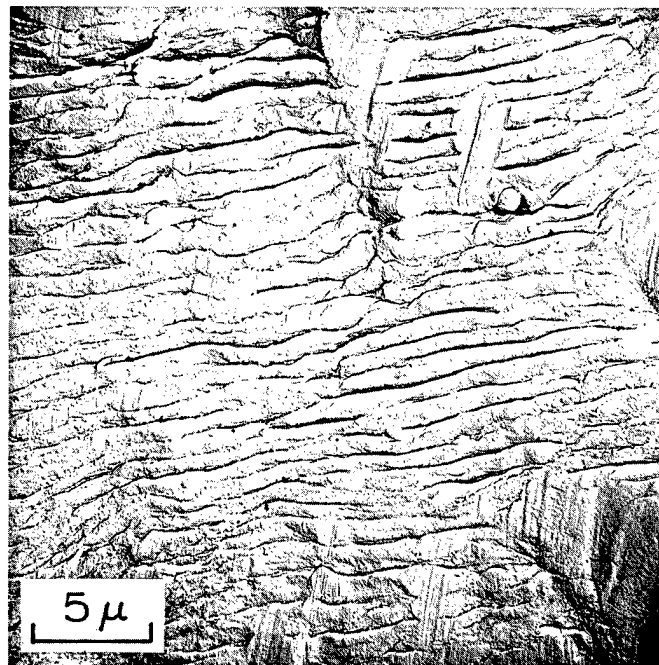


Fig. 6.33 — Electron fractograph showing striations on the fractured surface of AISI 304 stainless steel tested at 0.51% strain range, $4.5 \times 10^{-3} \text{sec}^{-1}$ strain rate, and 430°C . Note rub-marks in the top center portion of the fractograph (two-stage acetate-carbon replica). Test No. 347U (Neg. 1197B)

Low-cycle fatigue data were generated for AISI 348, 304, and 316 stainless steel to determine effects of strain range (0.3 to 2.2 percent), temperature, (430°, 650°, and 816°C), and strain rate, (4×10^{-3} , 4×10^{-4} , and 4×10^{-5} sec⁻¹).

In general, the 348 SS exhibited slightly better strain fatigue resistance for a given total axial or plastic strain level than 304 or 316 SS; this effect was observed for all three temperatures evaluated. The fatigue resistance of 316 SS for 650°C, however, is less than either the 304 or 348 SS. The 348, 304, and 316 SS exhibited cyclic strain-hardening characteristics for the various test conditions evaluated, except for the 316 SS tested at 430°C. The 316 SS exhibited cyclic strain hardening followed by cyclic strain softening over the entire strain range evaluated.

Results for 348 and 316 SS tested at 430°C are in fair agreement with the Coffin-Manson relationship that correlates low-cycle fatigue life at temperatures below the creep range. Fair agreement was obtained using the Manson-Halford approach for predicting the fatigue life of materials tested in the creep range. In general data tended to be more conservative than the average prediction had indicated.

A hundredfold decrease in strain rate caused a severalfold decrease in the fatigue resistance of 304 and 348 SS tested at 650°C and 816°C. Similar results were obtained for 316 SS tested at 650°C. At a test temperature of 816°C, however, only slight differences in the fatigue resistance of 316 SS were observed at strain ranges less than 1.0 percent for a change in strain rate from 4×10^{-4} sec⁻¹ to 4×10^{-5} sec⁻¹. This improvement in the fatigue characteristics of 316 SS at the lowest strain rate is presumably due to a metallurgical reaction.

The shape of the curves shown in plots of total axial or plastic strain versus fatigue life, N_5 , for the three materials evaluated does not seem to change as the strain rate is decreased several hundredfold but the curve is shifted to positions of lower life for given strain values.

A comparison of the ratio of N_5/N_f for the overall data showed that this ratio is generally decreased from a range of approximately 0.99 to 0.90 representing the 650°C data, to a range of approximately 0.7 to 0.85 for the 816°C data.

An attempt was made to characterize the N_5 failure criterion from the standpoint of crack length. Preliminary results of a fractographic analysis for samples tested at 650°C indicate that the crack is approximately 1.7 mm long at the N_5 point.

Results of a metallographic and fractographic analysis of 348 and 304 SS specimens tested at 650°C and 816°C and strain rates of 4×10^{-3} , 4×10^{-4} , and 4×10^{-5} sec⁻¹, showed that the mode of crack initiation was primarily intergranular for all conditions tested, except for the highest strain rate at 650°C. Under these conditions the 304 SS exhibited a transgranular type of crack initiation at both the highest and lowest strain range evaluated.

6.7 PLANS AND RECOMMENDATIONS

The effect of strain rate on fatigue characteristics of AISI 348, 304, and 316 stainless steels will be further evaluated. This continuing work will duplicate several test conditions for which only a few data points are presently available. Overall data will be statistically analyzed when these tests are completed. Several tests will also be conducted to determine the strain-rate sensitivity at 430°C of the austenitic stainless steels presently being evaluated.

Testing will be initiated to determine the effect of hold times at peak strain for AISI 348, 304, and 316 stainless steels. These data will be obtained at temperatures of 430°, 650°, and 816°C.

The various aspects of biaxial fatigue testing are being investigated. Several techniques are being reviewed for conducting biaxial fatigue tests at NMPO.

Metallographic and fractographic analyses of fatigue specimens will continue. Special emphasis is being placed on fracture analysis, although future work will include an investigation of morphology changes in the various materials being evaluated.

7. (ADVANCED PRESSURE VESSEL MATERIALS)

(1521)

F. C. Robertshaw,* H. R. Stephan,† J. E. McConnelee

The objective of this program is to determine the applicability of high-strength steels and alloys to nuclear reactor pressure vessels and similar critical applications. Materials under investigation include a 12Ni - 5Cr - 3Mo maraging steel and precipitation-hardening stainless steel, PH13-8Mo. The nickel-base alloy, Inconel alloy 718, is also being investigated together with a quenched and tempered alloy steel, HP 9Ni - 4Co - 0.2C.

All alloys studied in this program can be processed to far greater tensile and yield strength levels than the current alloys which are ASME Boiler and Pressure Vessel Code-approved and in current use. If it can be established that these alloys meet strength criteria and other significant requirements for pressure vessel applications, their eventual use may achieve one or more of the following:

1. Greater pressure vessel reliability and safety.
2. Reduced pressure vessel weight and section size.
3. Improved reactor performance resulting from higher permissible pressures and/or temperatures.

The type of materials being studied will necessitate greater unit costs for materials and processing, but it is believed that overall reactor economics may disclose an acceptable cost balance, particularly in view of such intangibles as greater safety or equal safety with less weight. to p 314

The experimental approach being followed encompasses two phases. The first phase consists of selecting and procuring candidate materials in the form of approximately 2.54-cm-thick plate, and evaluating pertinent properties, response to heat treatment, weldability, and radiation resistance. The second phase involves procurement of heavier plate (≥ 10 cm thick) to determine size effects on properties, response to heat treatment, and weldability. Ultimately one or more materials are expected to emerge as candidates for high-strength pressure vessels. For the most part all alloys currently under study are well into the first phase. The 12-5-3 maraging steel is entering the second phase.

7.1 EXPERIMENTAL PROGRAM

12Ni - 5Cr - 3Mo MARAGING STEEL

The 12-5-3 maraging steel is a heat-treatable alloy capable of high strength with excellent toughness. Heat treatment consists of solution annealing, air cooling or quenching to form martensite, and aging to effect precipitation strengthening. Because of the low carbon level (0.03C max, Table 7.1) the alloy is relatively soft (approximately R_C 30) and is work-

*Project leader.

†Principal investigator.

TABLE 7.1
DESCRIPTION OF 12Ni - 5Cr - 3Mo MATERIAL

Lot No.	Heat No.	Melting Procedure ^a	Size, cm	Condition	Vendor's Chemical Analysis														ppm		
					wt %																
					C	Mn	P	S	Si	Cr	Ni	Ti	Al	Mo	Fe	O	N	H			
Nominal analysis					0.03 Max	0.10 Max	0.010 Max	0.010 Max	0.12 Max	4.75– 5.25	11.5– 12.5	0.10– 0.35 ^b	0.20– 0.50 ^b	2.75– 3.25	Bal						
1	01378	AM + VCEM	2.7 x 61 x 61	815 ^o C for 1 hr – air cool	0.02 0.015 ^c	0.06 <0.01 ^c	0.006 0.005 ^c	0.006 0.001 ^c	0.06 0.02 ^c	5.00 –	11.90 –	0.13 0.14 ^c	0.37 0.40 ^c	3.08 3.08 ^c	Bal	–	–	–			
2	01434	AM + VCEM	0.32 dia x spool (Filler metal)	–	0.02	0.01	0.005	0.008	0.02	2.75	11.97	0.33	0.09	2.63	Bal	–	–	–			
3	IP0193	AM	2.54 x 35.6 x 57 2.54 x 15.2 x 61	815 ^o C for 1 hr – air cool	0.018	0.06	0.002	0.007	0.10	5.00	12.1	0.23	0.27	3.24	Bal	15	80	–			
4	V91230	IVM	0.155 dia x spool ~10 kg	Cold drawn	0.004	0.1	0.002	0.004	0.02	5.05	12.9	0.43	0.05	2.37	Bal	7	3.5	–			
5	60539	IVM	10.2 x 20.3 x 122 (2 pieces)	815 ^o C for 1 hr/ 2.54-cm thickness – air cool	0.006	0.01	0.005	0.004	0.02	5.08	12.15	0.25	0.24	3.00		20	80	–			
5	60540	IVM	10.2 x 20.3 x 122 (1 piece)	–	0.005	0.01	0.005	0.004	0.01	5.00	12.02	0.26	0.24	3.09		10	50	–			
6	04514	IVM	110 kg 0.155 dia wire ^e	–	0.01	0.05	0.007	0.004	0.08	4.91	12.10	0.24	0.38	3.08		–	–	–			

^aAM - Air melt; VCEM - Vacuum consumable electrode melt; IVM - Induction vacuum melt.

^b0.35 - 0.50% Al and 0.10 - 0.25% Ti are reported to offer the best combination of properties in conjunction with air-melted composition control.

^cGE-NMPO analysis.

^dForged to size.

^eMaterial in ingot form to be processed to wire as indicated for use in welding 10-cm-thick plate specimens.

able as solution annealed; after aging the alloy has a hardness of R_C 40 to 44 and is not easily worked. A standard heat treatment consists of 815°C for 1 hour, air cool, plus 480°C for 3 hours, air cool.

The aging treatment for optimum properties may vary between different heats of material. The alloy can be prepared by air melting techniques, but vacuum melting techniques are preferable. It is reportedly weldable by either TIG or MIG methods and requires no pre- or post-heating. For best properties, heat treatment by aging or solution treatment and aging are required after welding.

Table 7.1 describes the 12-5-3 material procured to date. Lots 1 and 2 were obtained first and most data subsequently reported involve these materials. Lots 3 and 4 were obtained more recently, principally to evaluate the 12-5-3 wire composition compared to the 12-3-3 composition. Lots 5 and 6 will be used to study size effects on properties, response to heat treatment, and weldability. Initial inquiries have been made to procure 20-cm-thick material.

Base Metal Studies

Aging Studies — Table 7.2 and Figure 7.1 show the effect of aging at temperatures of 425° , 450° , 480° , and 510°C for times up to 25 hours on the hardness of the four heats of the 12-5-3 alloy. Specimens were approximately 1.27-cm to 2-cm cubes. Heat No. 01378 developed the lowest hardness for the three higher aging temperatures; heat No. 1P0193 developed the highest hardness under every aging condition. This is probably due to a more favorable Ti/Al ratio and a higher molybdenum level. Heat No. 60539 and 60540, fabricated into 10.2-cm by 20.3-cm forgings, show intermediate to high hardness values except at the lowest aging temperature.

These studies indicate that the generally recommended aging treatment of 480°C for 3 hours results in about the same hardness for all four heats, but longer aging times can be used to increase the hardness from 1.5 to 4 R_C . Increased aging times may be useful when greater strength with somewhat lower toughness is desired.

TABLE 7.2
12Ni - 5Cr - 3Mo AGING STUDIES

Heat No.	Aging Temperature, °C	Aging Time, hr																	
		1	2	3	4	5	6	8	9	10	11	12	14	15	20	21	24	25	
		Rockwell C Hardness																	
01378	425	38		39.5		40				42								42	
	450	39		40			40											42	
	480	38.5		40			41				41.5							41.5	
	510	39		39			39.5				39.5							39.5	
IP0193	425	38		39.5			41.5	42			42		43			43			
	450	39		41			42	42.5			43				43.5		44		
	480	39		41			42	42.5			43				44				
	510	39.5		40			41	42.5			43		44		43.5		44		
60539	425		36		36.5			38										41.5	
	450	37		40.5			41.5		42									43.5	
	480	37.5		40		40.5		41					41.5			42.5		42.5	
	510	39		39.5		40		39.5					40			41		41	
60540	425		36			37		38.5										41.5	
	450	37.5		41			41		42.5									44.5	
	480	37		41		41		41.5					42			43.5		42.5	
	510	39		39		40		40					40			41		41	

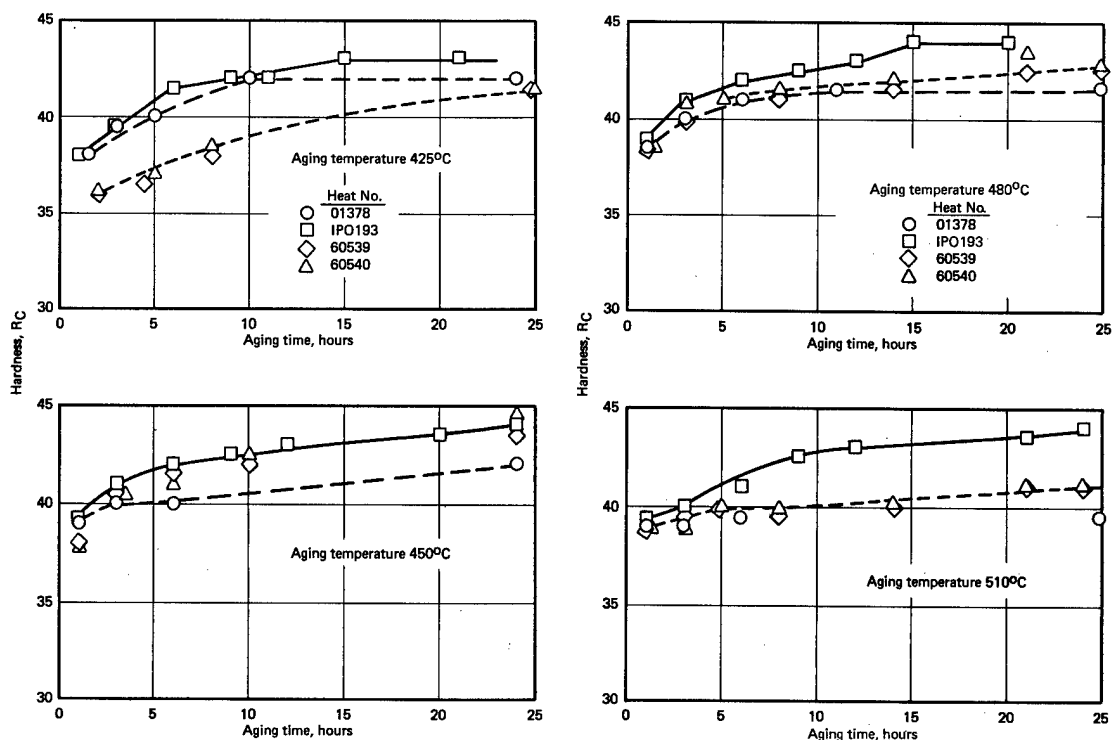


Fig. 7.1 – 12Ni – 5Cr – 3Mo aging studies

The relatively slow rate of aging to peak hardness values is an excellent feature of this alloy since it indicates no serious aging problem associated with thick sections or complicated structures.

Tensile Properties – Tensile data obtained on specimens from the 12-5-3 plate from heat No. 01378 at 25°, 315°, and 425°C in orientations transverse and parallel to the rolling direction are summarized in Table 7.3 and Figure 7.2. Although earlier tests¹ had indicated a difference in values due to orientation, additional aging has produced essentially equal and higher strength levels in both directions.

Toughness – Charpy V-notch impact tests at 25°, -40°, and -78°C on specimens oriented both transverse and parallel to the rolling direction from heat No. 01378 are shown in Table 7.4 and Figure 7.2. Additional aging has reduced the transverse values somewhat, which has reduced but not eliminated the difference between values for the two rolling directions.

As a further measure of fracture toughness, specimens are being prepared for drop-weight tear testing (DWTT) at the Naval Research Laboratory.

Fatigue Properties – Hourglass specimens are being prepared for preliminary low-cycle fatigue testing. Material from heat 1P0193 is being employed.

Radiation Effects – Tensile blanks and Charpy V-notch specimens of the 12-5-3 alloy and similar specimens of PH13-8Mo and Inconel alloy 718, were irradiated in the MTR at pile-ambient temperature to an approximate fluence of 4 to 5×10^{19} n/cm² ($E_n \geq 1$ Mev). Testing will be conducted at the Naval Research Laboratory.

¹"Fuels and Materials Development Program Progress Report No. 71," GE-NMPO, GEMP-1002, December 29, 1967, p. 109.

TABLE 7.3
TENSILE PROPERTIES OF 12Ni - 5Cr - 3Mo PLATE^a

Specimen Orientation	Specimen No.	Specimen Type ^b	Test Temperature, °C	0.2% Yield Strength		Tensile Strength		Elongation ^c in 4D, %	Reduction of Area, %
				kg/cm ²	psi	kg/cm ²	psi		
Transverse to rolling direction	K1	I	25	11,330	161,200	11,860	168,700	22	72
	K2	I	25	11,450	162,900	11,950	169,900	22	70
	K3	I	315	9,010	128,100	10,030	142,700	16	69
	K4	I	315	9,060	128,900	10,060	143,100	14	69
	K5	I	425	8,100	115,200	9,170	130,500	9	73
	K6	I	425	8,090	114,800	9,140	129,700	18	74
	2E	II	315	8,700	124,200	9,580	139,200	14	66
	3E	II	425	8,100	115,300	9,150	130,000	17	70
	L1 ^d	I	25	12,250	175,700	12,600	180,100	19	70
	L2 ^d	I	25	12,200	175,400	12,600	180,000	19	70
	L3 ^e	I	25	12,650	180,900	13,000	185,400	18	70
	L4 ^e	I	25	12,700	181,400	13,100	186,200	18	69
Parallel to rolling direction	1B	I	25	12,330	175,400	12,570	178,800	22	68
	2B	I	25	12,200	173,900	12,520	178,000	22	67
	3B	I	315	9,630	136,900	10,410	148,100	17	41
	4B	I	315	9,560	136,000	10,440	148,500	16	66
	5B	I	425	8,340	119,500	9,400	133,900	18	70
	6B	I	425	8,020	114,300	9,030	127,900	14	72
	1A	II	25	12,340	175,200	12,600	179,200	17	65
	2A	II	315	9,400	133,700	10,400	148,200	15	65
	3A	II	425	7,950	113,600	9,200	131,100	17	69
	1E ^d	I	25	12,300	176,320	12,600	180,700	18	68
	2E ^d	I	25	12,400	176,570	12,600	180,500	19	67

^aPlate heat treated at 480°C for 3 hours and air cooled before machining to specimen configuration.

^bAll specimens were standard ASTM type: I - 0.636-cm-diameter reduced section.

II - 1.27-cm-diameter reduced section.

^cElongation in four x diameter (4D).

^dSpecimen aged an additional 3 hours at 480°C and air cooled.

^eSpecimen aged an additional 6 hours at 480°C and air cooled.

Thermal Stability - Specimens of the 12-5-3 alloy aged at 480°C for 3 hours were heated for 1000 hours at 315°, 370°, 425°, and 480°C. Exposures up to 100 hours resulted in no change in hardness except at 480°C where a slight increase was noted. After 1000-hour exposures at 315°C and 370°C, hardness increases of 3 to 4 R_c were observed. The specimens heated for 1000 hours at 425°C and 480°C tended to drop in hardness. Properly aged, the alloy can apparently be made stable to at least 315°C.

Weldment Studies

Four weldments of the 12-5-3 alloy were prepared using the 2.54-cm-thick plate from heat 01378. Joint designs were similar to those shown earlier for Inconel alloy 718.² Of these, two were made using the U-joint and two with the double U-joint preparation. The former is utilized in developing weld metal properties and the latter in determining weld joint properties. The manual TIG welding method was used. The filler metal was 0.32-cm-diameter spooled bare wire of 12Ni - 3Cr - 3Mo (heat 01434). Additional details of weldment preparation were given in an earlier report.³

Weld Zone Hardness versus Heat Treatment - The effect of post-weld heat treatment on weld zone hardness was studied on several sections cut from the two U-joint weldments of 12-5-3 plate made using 12-3-3 weld wire.⁴ The first heat treatment consisted of post-

²"Sixth Annual Report - High-Temperature Materials Program, Part A," GE-NMPO, GEMP-475A, March 31, 1967, Fig. 9.1, p. 232.

³"AEC Fuels and Materials Development Program Progress Report No. 67," GE-NMPO, GEMP-67, June 30, 1967, pp. 141-145.

⁴GEMP-67, Fig. 10.1, p. 144.

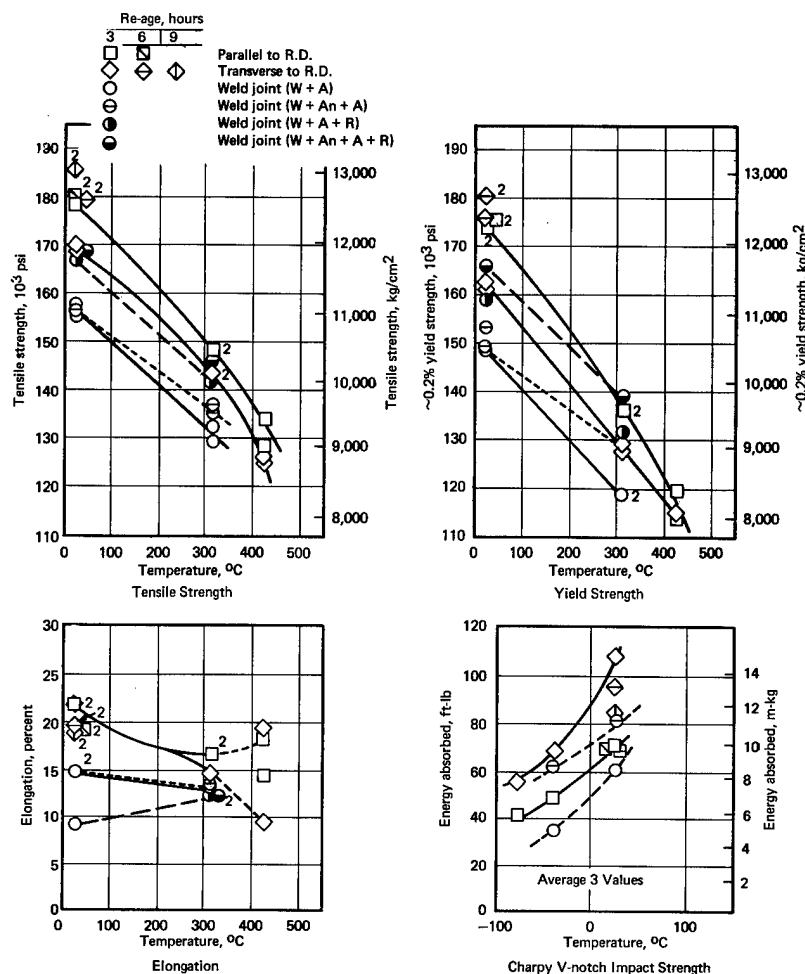


Fig. 7.2 — Tensile and Charpy V-notch impact properties of 12Ni — 5Cr — 3Mo maraging steel plate and weldments. Data points taken from Tables 7.3 through 7.6.

weld aging at 480°C for 3 hours. Figure 7.3 illustrates the results of a Rockwell C hardness transverse of weldment sections which received this treatment. Weld center hardnesses varied from R_C 30 to 35. Two sections, B and C, were then annealed for 1 hour at 815°C (air cooled) and aged at 450°C for 24 hours. Weld center hardnesses after this treatment rose to R_C 37 to 38. Figure 7.4 illustrates sections from a weldment annealed at 815°C for 1 hour (air cooled) and aged at 480°C for 3 hours. Weld center hardnesses ranged from R_C 32 to 35.

Both base metal and weld metal hardnesses are low after aging at 480°C for 3 hours (Figure 7.4). Re-aging such segments at 450°C for 24 hours or at 480°C for an additional 3 to 6 hours achieved higher centerline weld hardnesses in the range of R_C 36 to 38; base metal hardnesses increased to R_C 40 to 42. This is a further indication that aging practice must be adjusted to effect optimum properties. The disparity in weld metal and parent metal hardness is particularly important because it indicates that this 12-3-3 wire composition will not achieve optimum weld properties.

Tensile Properties — Joint tensile strength data at 25°C and 315°C of weldments heat treated in various ways are summarized in Table 7.5 and Figure 7.2. Aging of weldments at 480°C for 3 hours resulted in strengths lower than anticipated, based on base metal

TABLE 7.4
CHARPY V-NOTCH IMPACT STRENGTH OF 12Ni-5Cr-3Mo PLATE^a

Orientation of Major Specimen Axis ^b	Energy Absorbed					
	25°C		-40°C		-78°C	
	ft-lb	m-kg	ft-lb	m-kg	ft-lb	m-kg
Transverse to rolling direction	104	14.4	71	9.8	59	8.2
	103	14.3	66	9.2	54	7.5
	114	15.8	68	9.4	56	7.8
	83 ^c	11.5				
	95 ^c	14.2				
	90 ^c	12.4				
	84 ^d	11.6				
	78 ^d	11.0				
	92 ^d	12.6				
Parallel to rolling direction	70	9.7	49	6.8	42	5.8
	68	9.4	49	6.8	41	5.7
	72	10.0	50	6.9	39	5.4
	76 ^c	10.5				
	64 ^c	8.9				
	72 ^c	10.0				
	62 ^d	8.6				
	67 ^d	9.3				
	83 ^d	11.5				

^aPlate heat treated at 480°C for 3 hours and air cooled before machining to specimen configuration.

^bAll notches perpendicular to surface plate.

^cSpecimens aged an additional 3 hours at 480°C.

^dSpecimens aged an additional 6 hours at 480°C.

properties. Re-aging at 450°C for 24 hours resulted in marked improvements to levels about equivalent to base metal transverse properties reported earlier for the 3-hour age at 480°C. Post-weld annealing at 815°C for 1 hour plus aging at 480°C for 3 hours resulted in about the same properties noted above for the direct aged joint. Re-aging this weldment at 450°C for 24 hours again resulted in about the same improvement noted above for the direct aged and re-aged weldment. Both treatments with re-aging resulted in joint properties about equivalent to the transverse base metal values. Elongation values for most weld joint specimens were 12 to 15 percent except for one which was 9 percent. These values are lower than those of the base metal.

Toughness – Charpy V-notch specimens of the above weldments of the 12-5-3 plate made using the 12-3-3 weld wire showed the welded, annealed, and aged specimens to have an average absorbed energy value of 11.0 m-kg (80 ft-lb) at 25°C, compared to 8.6 m-kg (62 ft-lb) for welded and aged specimens. The values obtained at -40°C were 8.4 m-kg (61 ft-lb) and 4.7 m-kg (34 ft-lb), respectively. These values were lower than the base metal for the direct aged weld but were midway between the transverse and parallel rolling direction values for base metal when the weld was annealed and aged. Table 7.6 and Figure 7.2 summarize the Charpy V-notch data.

PH13-8Mo

The PH13-8Mo alloy is a martensitic precipitation-hardening stainless steel which has excellent toughness at high-strength levels. It is heat treated by solution annealing, air cooling or quenching, and aging. In the solution-treated condition the alloy has a hardness of approximately R_C 35 maximum; as-aged, depending on aging temperature, its hardness ranges from about R_C 36 to 48. Normally, the material is supplied from the vendor in the solution-treated condition (925°C for 0.5 hour and air cooled or quenched to below 15°C) and is only aged by the user at 510° to 590°C, depending on the properties required.

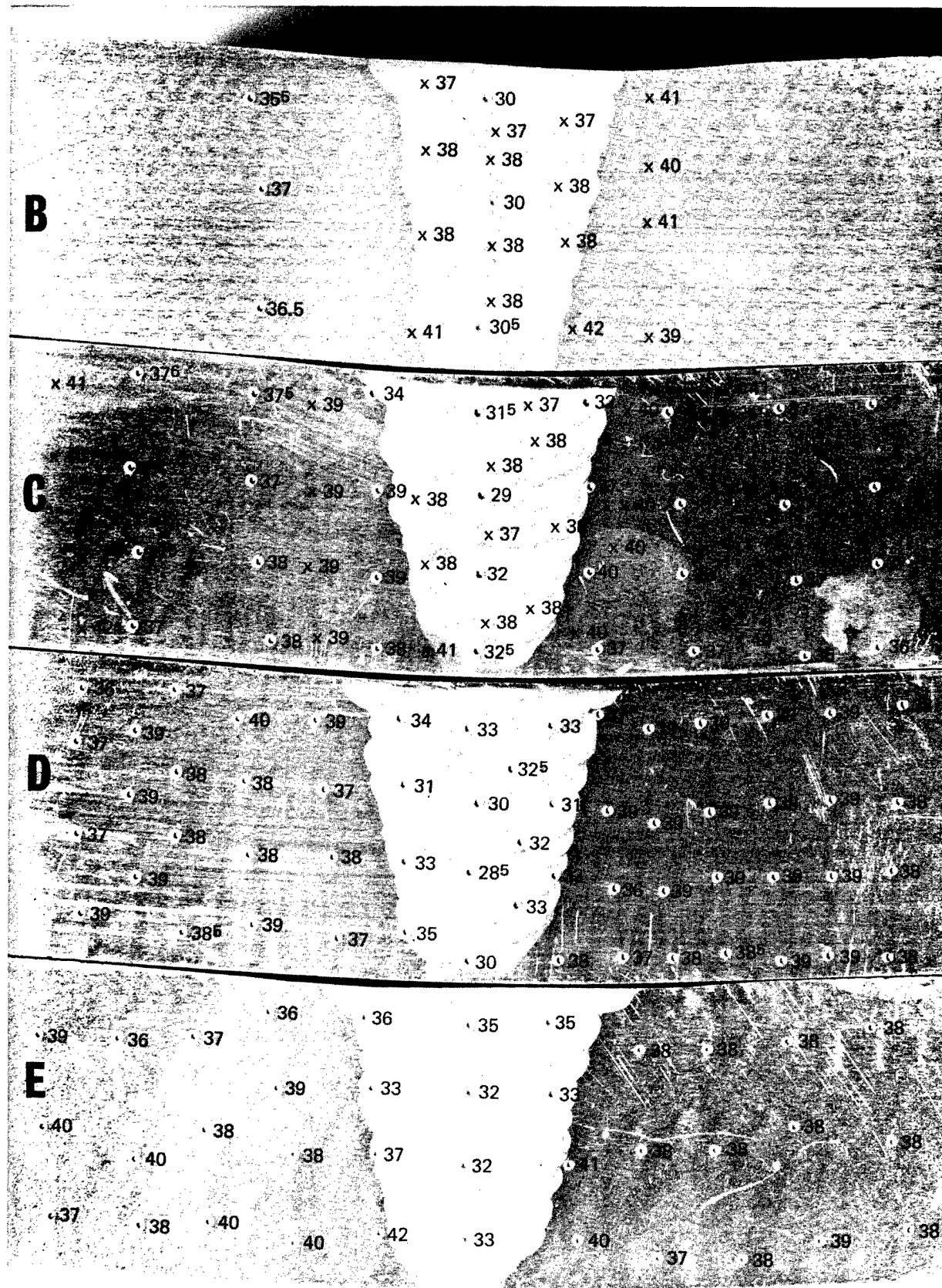


Fig. 7.3 — Sections of weldments of the 12Ni — 5Cr — 3Mo maraging steel made using 12Ni — 3Cr — 3Mo filler metal. Sections were maraged after welding at 480°C for 3 hours which resulted in the Rockwell C hardness values shown beside the indentations. After maraging, sections B and C were annealed 1 hour at 815°C, air cooled, and aged at 450°C for 24 hours. The hardnesses achieved by this treatment are shown by the numbers beside the X-marks. (Neg. P67-8-33B)

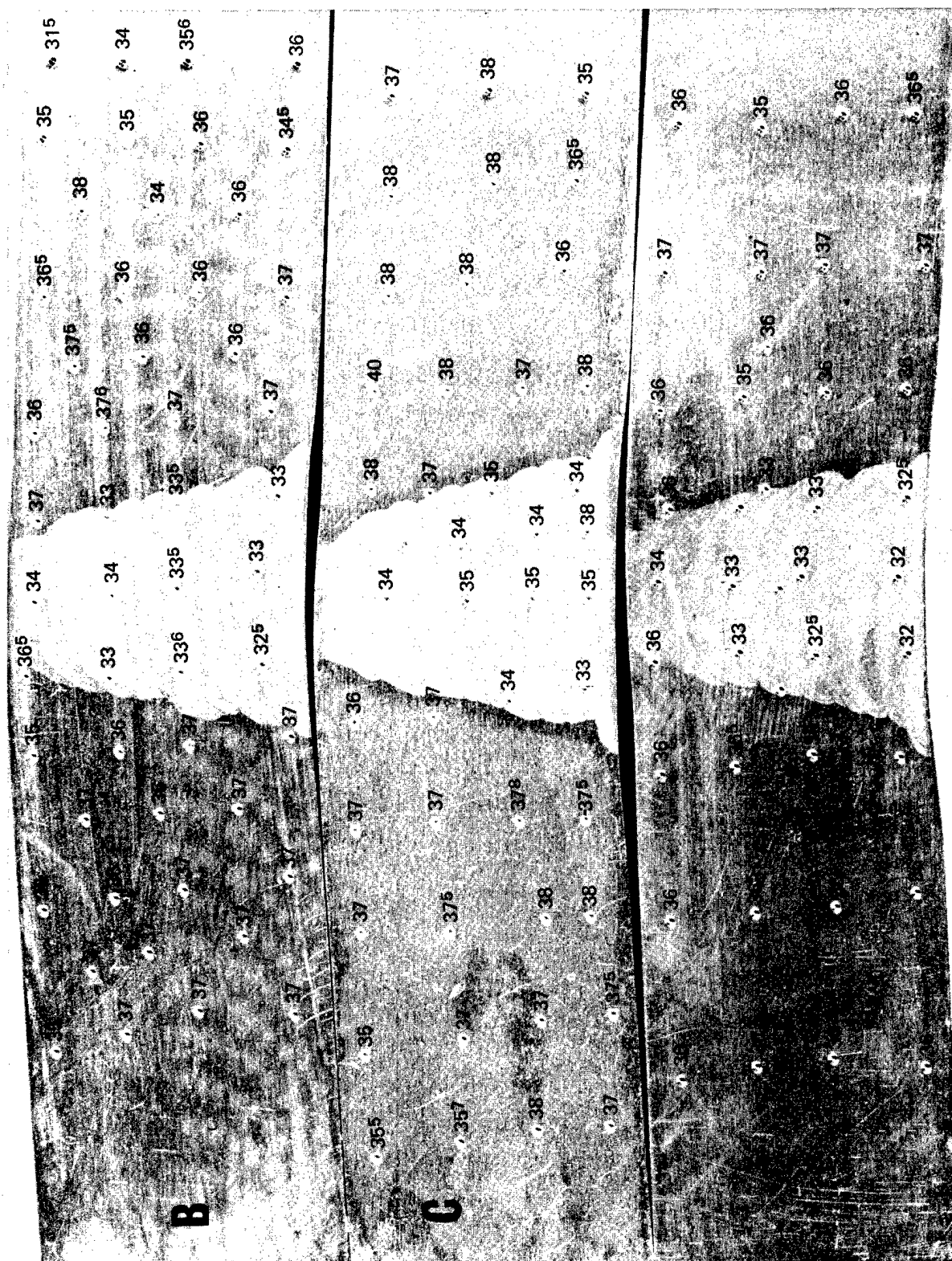


Fig. 7.4 — Sections of weldments of the 12Ni — 5Cr — 3Mo maraging steel made using 12Ni — 3Cr — 3Mo filler metal. After welding, sections were annealed at 815°C, air cooled, and aged at 480°C for 3 hours. Numbers at indentations are Rockwell C hardness values. (Neg. P67-8-33A)

TABLE 7.5
TENSILE PROPERTIES OF 12Ni – 5Cr – 3Mo WELDMENTS

Specimen Type ^a	Specimen No.	Specimen Treatment ^b	Test		0.2% Yield Strength		Tensile Strength ^c		Elongation in 4D, %	Reduction of Area, %
			Temperature, °C		kg/cm ²	psi	kg/cm ²	psi		
I	22E	W+A	25		10,430	148,800	11,100	157,100	15	64
I	22K	W+A	25		10,400	148,600	10,800	154,800	14	67
I	22F	W+A	315		8,300	118,900	9,130	132,300	13	63
I	22L	W+A	315		8,400	119,700	9,080	129,300	13	53
II	22A	W+A	25		10,900	155,300	11,600	161,300	11	61
II	22B	W+A	315		8,450	120,300	9,000	127,200	11	62
I	22G	W+A+R	25		11,280	159,800	11,845	167,900	14	59
I	22H	W+A+R	25		11,200	159,200	11,840	167,700	14	60
I	22I	W+A+R	315		9,060	130,100	10,000	142,400	12	60
I	22J	W+A+R	315		9,300	132,100	10,000	142,700	12	59
I	24A	W+An+A	25		10,500	149,500	11,100	156,500	15	65
I	24B	W+An+A	25		10,800	153,600	11,250	158,600	14	64
I	24C	W+An+A	315		9,030	127,700	9,550	135,100	13	63
I	24D	W+An+A	315		9,100	130,000	9,550	136,800	13	63
I	24E	W+An+A+R	25		11,700	166,300	11,900	169,300	9	33
I	24F	W+An+A+R	315		9,800	139,100	10,250	145,800	12	59

^aAll specimens were standard ASTM type: I – 0.636-cm-diameter reduced section.

II – 1.27-cm-diameter reduced section.

Reduced sections contained weld metal, heat-affected zone, and base metal.

^bHeat Treatments: W – Weld.

A – Aged 3 hours at 480°C and air cooled prior to machining.

R – Re-aged an additional 24 hours at 450°C.

An – Annealed 1 hour at 815°C and air cooled to room temperature.

^cAll specimens fractured in the weld.

TABLE 7.6
CHARPY V-NOTCH^a IMPACT STRENGTH
OF 12Ni – 5Cr – 3Mo WELDMENTS

Condition of Specimen ^b	Energy Absorbed			
	25°C		–40°C	
	ft-lb	m-kg	ft-lb	m-kg
W + A	68	9.4	35	4.8
	58	8.0	30	4.1
	60	8.3	37	5.1
W+An+A	80	11.0	56	7.8
	81	11.1	66	9.1
	78	10.8	61	8.4

^aNotch oriented perpendicular to surface of plate and through weld metal.

^bHeat treatment: W – Welded.

A – Aged 3 hours at 480°C.

An – Annealed 1 hour at 815°C and air cooled to room temperature.

A standard aging temperature for a good combination of strength and toughness is 565°C for 5 hours, air cool. The alloy is best prepared by a combination of vacuum induction melting plus vacuum consumable arc remelting. It is reportedly weldable by techniques used for other precipitation-hardening stainless steels with no pre- or post-heating. For best properties, heat treatment by aging or solution treating and aging are required after welding.

Table 7.7 describes the PH13-8Mo material procured to date. Lots 1 and 3 were obtained first, and the majority of the data reported are for these materials. Lot 2 was

TABLE 7.7
DESCRIPTION OF PH13 - 8Mo MATERIALS

Lot Heat No.	Melting Procedure ^a	Size, cm	As-Received Condition	Chemical Analysis, wt %																				
				C		Mn		P		S		Si		Cr		Ni		Al		Mo		N ₂		Fe
				Vendor NMPO	Vendor NMPO	Vendor NMPO	Vendor NMPO	Vendor NMPO	Vendor NMPO	Vendor NMPO	Vendor NMPO	Vendor NMPO	Vendor NMPO	Vendor NMPO	Vendor NMPO	Vendor NMPO	Vendor NMPO	Vendor NMPO	Vendor NMPO	Vendor NMPO	Vendor NMPO	Vendor NMPO	Vendor NMPO	Vendor NMPO
Nominal analysis				0.05 Max	0.10 Max	0.010 Max	0.008 Max	0.10 Max	12.25– 13.25	7.50– 8.50	0.90– 1.35	2.00– 2.50	0.010 Max											
1	VC 5281 IVM + VCEM	1.27 x 30 x 183	925°C–0.5 hr– air cool	0.042 0.024	0.02 0.02	0.003 0.006	0.004 0.002	0.02 0.02	<0.01 0.02	12.58 –	8.07 –	1.11 1.25	2.06 2.31	–	–	–	–	–	–	–	–	–	Bal	Bal
2	VC 5281 IVM + VCEM	2.54 x 46 x 46	925°C–0.5 hr– air cool	0.042 0.024	0.02 0.02	0.003 0.006	0.004 0.002	0.02 0.02	<0.01 0.02	12.58 –	8.07 –	1.11 1.25	2.06 2.31	–	–	–	–	–	–	–	–	–	Bal	Bal
3	VC 5178 IVM + VCEM	0.155 dia x spool (Filler metal)	Overaged and cold drawn	0.044	–	0.002	0.003	0.016	12.74	8.58	0.46	2.20	–	–	–	–	–	–	–	–	–	–	Bal	Bal

^aIVM - Induction vacuum melt.

VCEM - Vacuum consumable electrode melt.

obtained to provide additional material for testing and to further study aging response following welding on somewhat heavier plate. The study of plate 10-cm thick or greater has been considered. It is not certain, however, that a post-weld heat treatment can be developed which is practical for large pressure vessels, and the cost involved for experimental quantities in these thicknesses is high. Accordingly a more certain qualification will be made in the 2.54-cm thickness before proceeding to heavier plate.

Base Metal Studies

Aging Studies – Specimens from the 1.27-cm-thick plate (925°C solution-treated condition) were aged in air for various times up to 25 hours at 510°, 540°, 565°, and 590°C. Hardnesses ranging from R_C 46 to 48 were attained within 1 to 2 hours at 510°C and 540°C; after 24 hours the hardnesses dropped slightly to about R_C 45. Hardnesses of the order of R_C 42 to 43 were attained in 1 hour at 565°C and 590°C; these dropped to R_C 40 to 42 in about 4 hours, and to about R_C 36 to 39 after 24 hours. Data are given in Table 7.8 and aging curves are shown in Figure 7.5.

The alloy apparently hardens extremely rapidly to a peak hardness level and then over-ages to a lower hardness at longer times. This is particularly apparent at aging temperatures of 565°C and 590°C which, incidentally, produce the highest toughness levels. Aging temperatures above about 540°C can apparently present significant problems in large complicated structures; high- and low-strength zones might develop during aging, depending on section thickness and/or design configuration.

Tensile Properties – Tensile data obtained on 1.27-cm PH13-8Mo plate were determined at 25°, 315°, and 425°C, and are presented in Table 7.9 and Figure 7.6. The figure shows that PH13-8Mo possesses a tensile strength greater than 11,500 kg/cm² (156,000 psi) up to about 300°C, combined with a yield strength of nearly 11,000 kg/cm². These values are the lower for the two orientations tested, i. e., parallel to the rolling direction. The tensile and yield strengths of the specimens whose principal axis was transverse to the direction of rolling were higher by as much as 15 percent. Tensile elongation was approximately the same in both directions.

Toughness – Charpy V-notch impact tests were made on 1.27-cm-thick PH13-8Mo plate at 25°, -40°, and -78°C. Energy absorption values at 25°C were above 9 m-kg for both orientations; the transverse direction showed values above 10 m-kg. At lower temperatures, however, Charpy V-notch values for the transverse orientation fell off quickly to about 2.7 m-kg at -78°C, and those for the parallel orientation dropped to 4.3 m-kg. Table 7.10 and Figure 7.6 summarize impact data obtained on PH13-8Mo 1.27-cm-thick plate.

To further evaluate the fracture toughness of the PH13-8Mo alloy, specimens for drop-weight tear testing are being prepared of the 2.54-cm plate. Testing will take place at the Naval Research Laboratory.

Fatigue Properties – Hourglass specimens of material from the 2.54-cm-thick plate are being prepared for low-cycle fatigue testing.

Radiation Effects (NRL) – Tensile blanks and Charpy V-notch specimens have been irradiated in the MTR at pile-ambient temperature. The fluence level to which they were exposed is approximately 4 to 5×10^{19} n/cm² ($E_n \geq 1$ Mev). Post-irradiation testing will be conducted at the Naval Research Laboratory.

Thermal Stability – The effects on hardness and microstructure of the aged alloy after longtime heating at various temperatures are being determined. No change in hardness or microstructure was noted after exposure at 315°, 370°, 425°, 480°, and 540°C for 100 hours. Moreover, no significant hardness changes were noted after heating for 1000 hours at 315°, 370°, and 425°C. Heating for 1000 hours at 480°C and 540°C, however, resulted in softening

TABLE 7.8
PH13 – 8Mo AGING STUDIES^a

Specimen No.	Aging Temperature, °C	Aging Time, hr																			
		0	0.25	0.5	1	2	3	4	5	6	7	8	10	11	12	14	16	19	20	24	25
		Rockwell C Hardness																			
H-1	510	35				46.5		46		46				46			44.5			44.5	
H-2	540	35.5				47	47.5			47			46		46				45.5		45.5
H-4	565					43	42.5			42				40		39			37.5	37	36.5
H-6	565	35	45	45.5	46			44		44				40							39
H-5	590					42	42.5			40			39				37.5	37		36	35.5
H-3	590									40											

^aHeat No. VC5281, 1.27-cm-thick plate.

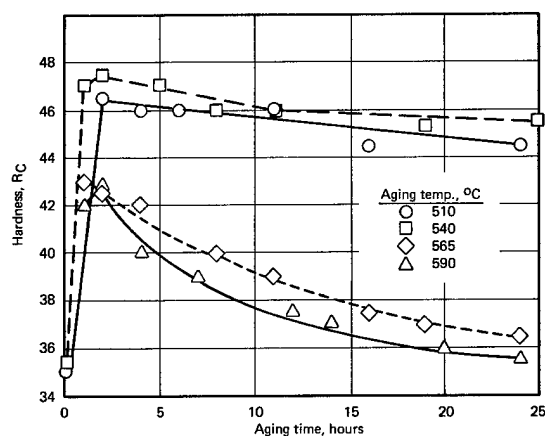


Fig. 7.5 – Aging of PH13 – 8Mo precipitation hardening stainless steel, heat No. VC 5281

TABLE 7.9
TENSILE PROPERTIES OF PH13 – 8Mo PLATE^a

Specimen Orientation	Specimen No. ^b	Test Temperature, °C	0.2% Yield Strength		Tensile Strength		Elongation in 2.54 cm, %	Reduction of Area, %
			kg/cm ²	psi	kg/cm ²	psi		
Parallel to rolling direction	N1	25	13,200	188,900	13,710	195,000	19.4	69.8
	O1	25	13,210	187,900	13,660	194,200	21.2	71.7
	P1	315	11,130	158,300	11,590	164,800	15.8	69.7
	Q1	315	11,070	157,500	11,470	163,100	14.3	69.1
	R1	315	11,065	157,400	11,870	163,800	16.7	69.1
	S1	425	9,740	138,500	10,220	145,300	22.4	74.9
Transverse to rolling direction	Ba	25	14,360	204,200	15,790	224,600	16.8	64.9
	BB	25	14,510	206,300	15,440	219,600	18.7	65.8
	BC	315	12,100	172,100	13,100	186,300	15.0	64.9
	BD	315	10,890	154,900	12,950	184,200	14.2	65.0
	BE	425	10,320	146,800	11,250	160,000	21.1	72.8
	BF	425	10,350	147,200	11,130	158,300	22.0	73.1

^aPortions of the PH13 – 8Mo plate were heat treated at 565°C for 4 hours and air cooled prior to machining to specimen configuration.

^bAll specimens were standard ASTM type with 0.636-cm-diameter reduced section.

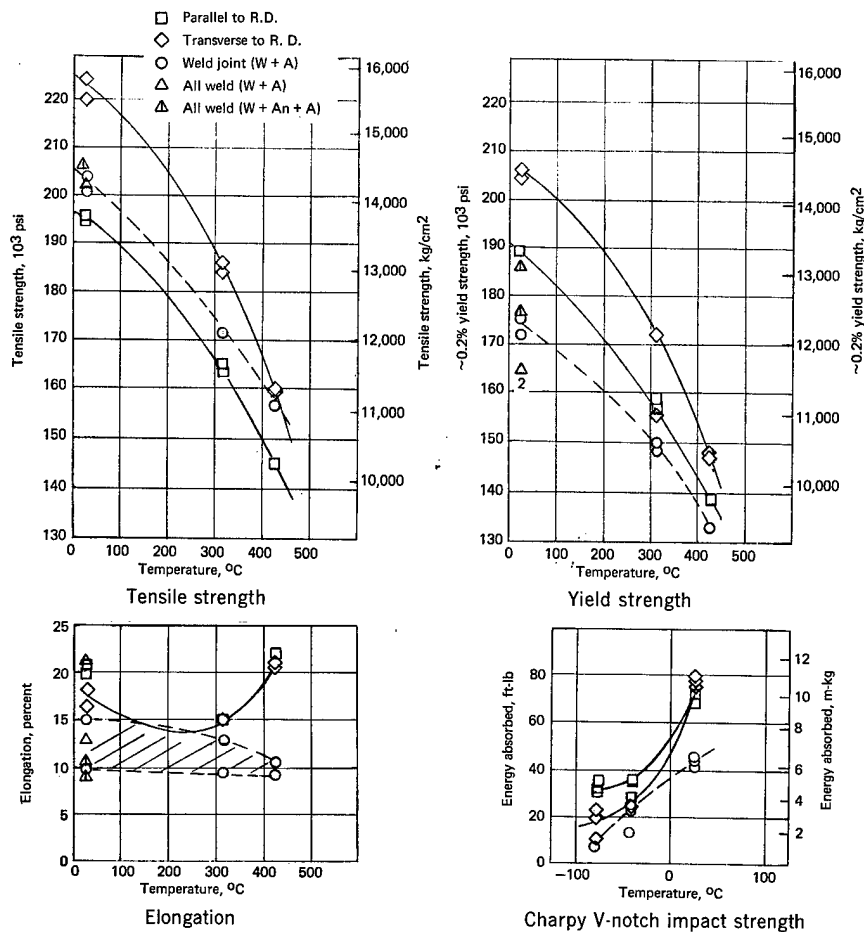


Fig. 7.6 — Tensile and Charpy V-notch impact properties of PH13-8Mo precipitation hardening stainless steel plate and weldments

TABLE 7.10

CHARPY V-NOTCH IMPACT STRENGTH OF PH13 — 8Mo PLATE^a

Major Specimen Axis ^b	Energy Absorbed					
	25°C		-40°C		-78°C	
	ft-lb	m-kJ	ft-lb	m-kJ	ft-lb	m-kJ
Transverse to rolling direction	75.5	10.4	21.5	3.0	10.0	1.4
	78.5	10.8	23.5	3.2	24.0	3.3
	80.0	11.0	24.0	3.3	19.5	2.7
Parallel to rolling direction	69.0	9.5	28.5	3.9	31.0	4.3
	69.0	9.5	36.4	5.0	31.0	4.3
	74.0	10.2	36.0	5.0	36.0	4.3

^aPortions of the PH13 — 8Mo plate were heat treated at 565°C for 4 hours and air cooled prior to machining to specimen configuration.

^bAll notches perpendicular to the surface of the plate.

from an original hardness of R_C 43 to R_C 35 to 36. For stable operation of the heat-treated alloy, the maximum use temperature is apparently less than 480°C.

Weldment Studies

Four weldments were prepared from the 1.27-cm-thick plate of PH13-8Mo, using the 0.155-cm-diameter spooled wire of normally matching composition. The manual TIG welding process was employed in conjunction with both single and double bevel weld preparations. Welding procedures were reported previously.⁵

Weld Zone Hardness Versus Heat Treatment – Figure 7.7 illustrates weld zone hardness values of two weldment sections, one after aging only (specimen W11A) and the other after annealing plus aging (specimen W11AA). The weldments shown are for the 1.27-cm-thick plate with a double V-joint weld. The improved weld hardness pattern achieved by annealing and aging after welding is apparent. More pertinent weld data are anticipated from weldments in the 2.54-cm-thick plate.

Tensile Properties – Weld-joint tensile properties of the PH13-8Mo weldments aged after welding were determined at 25°, 315°, and 425°C, and are presented in Table 7.11 and Figure 7.6. Tensile strength is intermediate between the transverse and parallel orientation

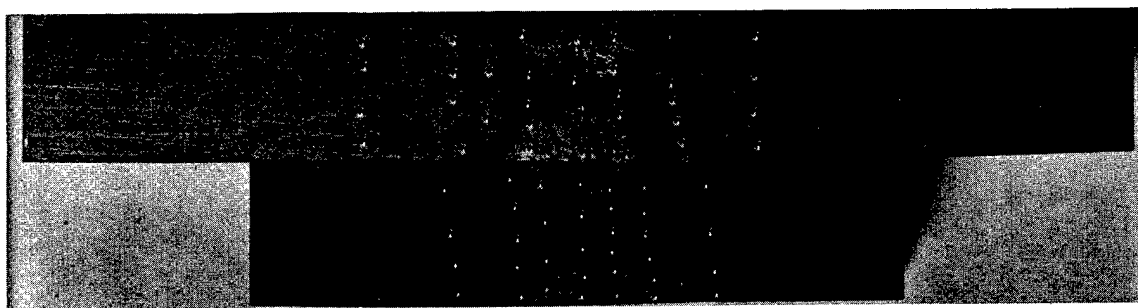


Fig. 7.7 – Macroetched cross sections from double-V PH13-8Mo weldments. W11A aged after welding and W11AA annealed and aged after welding. Numbers beside the indentations are Rockwell C hardness values (P67-8-33N)

values of the base metal; yield strength varies from about 93 percent at room temperature to 96 percent at 415°C of the base metal, parallel orientation values. Ductility of the welds is significantly lower and more variable than observed in base metal tests. Effects of other post-weld heat treatments are being studied.

All-weld specimen data in two post-weld heat-treated conditions are also presented in Table 7.11. The properties are generally quite good, although post-weld annealing and aging apparently produce higher yield strength values than aging alone.

Toughness – Charpy V-notch impact tests were completed on specimens machined from weldments aged only after welding. Table 7.12 and Figure 7.6 summarize the absorbed energy values obtained at 25°, -40°, and -78°C. The values decrease approximately linearly from 25°C to -78°C, and are about the same as those reported earlier for base metal transverse specimens at -40°C, but much lower at 25°C and -78°C. Effects of other post-weld heat treatments are being studied.

INCONEL ALLOY 718

Inconel alloy 718 is a precipitation-hardening nickel-base alloy which has a nominal composition of 53Ni, 19Cr, 19Fe, 5Nb, 3Mo, 1Ti, 0.5Al, 0.05C, and 0.004B (wt %). It is strengthened by a coherent Nb-rich gamma-prime precipitate believed to be $Ni_3(Nb, Ti$

⁵GEMP-67, p. 146.

TABLE 7.11
TENSILE PROPERTIES OF PH13-8Mo WELDMENTS

Specimen Type ^a	Specimen No.	Specimen Treatment ^b	Test Temperature, °C	0.2% Yield Strength		Tensile Strength		Elongation in 2.54 cm, %	Reduction of Area %	Location of Fracture
				kg/cm ²	psi	kg/cm ²	psi			
Joint tensile	C	W + A	25	12,160	172,800	14,120	201,300	14.0	68	Base metal
Joint tensile	E	W + A	25	12,390	176,000	14,280	203,000	8.2	22	Weld
Joint tensile	D	W + A	315	10,410	148,300	12,130	172,100	12.6	52	Weld
Joint tensile	F	W + A	315	10,540	150,000	12,110	172,000	9.2	38	Weld
Joint tensile	G	W + A	425	9,330	133,300	11,120	158,100	10.8	35	Weld
Joint tensile	H	W + A	425	9,400	133,700	11,030	157,400	9.3	34	Weld
All weld tensile	D	W + A	25	11,620	165,000	14,300	203,200	12.9	27	—
All weld tensile	C	W + A	25	11,600	164,600	14,300	203,200	20.8	58	—
All weld tensile	4	W+An+A	25	13,030	186,400	14,520	206,500	7.8	20	—
All weld tensile	3	W+An+A	25	12,500	176,800	14,400	207,400	11.0	21	—

^aAll specimens were standard ASTM type with 0.636-cm diameter reduced section.

^bHeat treatments: W — Welded.

A — Aged 4 hours at 565°C, air cooled to room temperature.

An — Annealed at 925°C for 0.5 hour, air cooled to 15°C.

TABLE 7.12
CHARPY V-NOTCH^a IMPACT STRENGTH
OF PH13-8Mo WELDMENTS

Condition of Specimen ^b	Energy Absorbed					
	25°C		-40°C		-78°C	
	ft-lb	m-kg	ft-lb	m-kg	ft-lb	m-kg
W + A	44	6.1	14	1.94	8	1.08
W + A	46	6.4	26	3.6	7	0.97
W + A	41	5.7	22	3.0	8	1.08

^aNotch oriented perpendicular to surface of plate and through weld metal.

^bHeat treatment: W — Welded.

A — Aged for 4 hours at 565°C, air cooled to room temperature.

Al). The alloy has better strength at higher temperatures than any other compositions being studied, retaining approximately 90 percent of its room-temperature strength above 480°C. This high-temperature strength was the principal reason for selection, since it offered an opportunity for temperature growth in advanced reactor systems. Several heat treatments are employed, depending on the properties required. A typical heat treatment consists of solution treating at 950°C for 1 hour, air cool followed by aging at 715°C for 8 hours, furnace cool to 620°C, hold 12 hours, and air cool. The alloy can be prepared by air melting techniques, but vacuum melting techniques are preferred. For some applications, double vacuum melting is employed. It is reportedly quite weldable by inert arc techniques, its sluggish response to age hardening favors good weldability, and it requires no pre- or post-heating. For best properties, heat treatment by aging or solution treating and aging are required after welding.

Table 7.13 describes the Inconel alloy 718 material procured for test. Preliminary inquiries were made for 10-cm-thick material, but further procurement action has been delayed pending additional qualification of the alloy, particularly with respect to fracture toughness.

Base Metal Studies

Tensile Properties — The tensile properties of the Inconel alloy 718 plate were determined at 25°, 425°, 540°, and 650°C using three different heat treatments. These data are shown in Tables 7.14, 15, and 16 and in Figure 7.8. Heat treatment I resulted in the low-

TABLE 7.13
DESCRIPTION OF INCONEL ALLOY 718 MATERIALS

Heat No.	Melting Procedure ^a	Size, cm	As-Received Condition	Chemical Analysis, wt %															
				C		P		S		Si		Cr		Ni		Ti		Al	
				Vendor	NMPO	Vendor	NMPO	Vendor	NMPO	Vendor	NMPO	Vendor	NMPO	Vendor	NMPO	Vendor	NMPO	Vendor	NMPO

Nominal analysis				0.08	0.45	0.015	0.015	0.45	0.45	17.0	50.0	0.65	0.80	2.8	4.75	1.0	0.30	0.006	Bal
				Max	Max	Max	Max	Max	Max	Min	Min	Min	Max	Min	Min	Max	Max	Max	
										21.0	55.0	1.40		3.3	5.50				
										Max	Max	Max		Max	Max				
02ACES				0.02	0.007	0.10	—	0.02	0.005	0.007	0.005	0.18	0.10	18.27	18.02	53.28	—	1.01	0.89
4878E				0.04	0.30	—	—	0.02	0.005	0.007	0.005	0.18	0.10	18.39	52.95	0.84	0.44	0.54	0.59
																	0.04	—	0.003
																	0.03	0.002	18.30
																			18.16

^aVM — Induction vacuum melt.

TABLE 7.14

TENSILE PROPERTIES OF INCONEL ALLOY 718 PLATE AFTER HEAT TREATMENT I^a

Specimen Orientation	Specimen No. ^b	Test Temperature, °C	0.2% Yield Strength		Tensile Strength		Elongation in 4D, %	Reduction of Area, %
			kg/cm ²	psi	kg/cm ²	psi		
Parallel to rolling direction	Y1 ^c	25	10,000	140,200	13,960	197,000	15.9	23
	Y2 ^c	425	9,150	129,900	12,900	183,200	19.9	33
	Y3 ^c	540	8,800	125,200	12,700	180,200	17.4	35
	D	25	9,650	137,000	13,700	193,800	17.8	22
	H	25	9,650	137,000	13,600	192,200	13.3	18
	B	425	8,300	118,000	12,570	178,700	21.6	32
	I	425	8,700	124,000	12,600	179,800	12.9	15
	C	540	8,350	119,000	12,400	176,500	16.3	33
	J	540	8,900	119,900	12,450	177,100	12.9	21
	E	650	8,150	116,000	10,400	148,000	21.0	39
	K	650	8,100	115,800	10,500	149,000	18.9	50
Transverse to rolling direction	C1	25	9,900	140,800	13,300	189,100	13.7	15.3
	C2	25	9,940	141,300	13,270	188,700	11.9	14.8
	C3	425	8,920	126,900	12,370	175,900	17.6	19.1
	C4	425	8,940	127,100	12,360	175,800	19.1	20.3
	B1	540	8,630	122,700	12,300	174,900	20.8	31.6
	B3	540	8,590	122,200	12,310	175,000	20.5	31.6
	C5	650	8,290	117,900	10,570	150,300	16.5	21.6
	C6	650	8,300	118,000	10,630	151,200	23.9	30.7

^aHeat treatment: 950°C for 1 hr, furnace cool 100 min to 715°C, hold 8 hr, furnace cool to 620°C, hold for 12 hr (including furnace cooling time), air cool to room temperature.

^bStandard ASTM type with 0.636-cm-diameter reduced section.

^c1.27-cm-diameter reduced section.

est strength levels. Heat treatment II, which is similar to I except for more rapid cooling from the solutioning temperature, results in the highest strength levels. Heat treatment III, involving a much higher solutioning temperature and a modified aging cycle, resulted in intermediate strength values. In general, heat treatment III, which was selected for improved toughness, resulted in better elongation and reduction of area values than the other two heat treatments. It is clear from heat treatments I and II that the cooling rate from

TABLE 7.15

TENSILE PROPERTIES OF INCONEL ALLOY 718 PLATE AFTER HEAT TREATMENT II^a

Specimen Orientation	Specimen No. ^b	Test Temperature, °C	0.2% Yield Strength		Tensile Strength		Elongation in 4D, %	Reduction of Area, %
			kg/cm ²	psi	kg/cm ²	psi		
Parallel to rolling direction	P1	25	11,600	165,000	14,700	209,500	21	24
	AA	25	12,150	172,400	14,800	211,100	21	33
	Q1	425	10,400	147,900	13,120	186,160	21	35
	R1	425	10,300	145,580	13,150	186,500	15	37
	S1	540	10,090	143,500	12,810	182,270	24	26
	T1	540	10,330	146,680	12,750	181,330	17	34
	U1	650	9,950	141,610	11,830	168,220	14	32
	V1	650	—	c	11,970	170,120	21	40
Transverse to rolling direction	FA	25	12,970	170,000	14,400	204,700	19	23
	FD	25	12,970	170,000	14,350	204,200	18	23
	FB	425	10,760	152,830	12,810	182,210	17	29
	FE	425	10,790	153,300	12,690	180,490	18	29
	FC	540	10,290	146,340	12,490	177,670	14	24
	FF	540	10,630	150,980	12,410	176,440	12	23
	FH	650	c	c	11,290	160,600	14	26
	FG	650	9,310	132,570	11,030	156,980	6	32

^aHeat treatment: 950°C for 1 hr, air cool to room temperature, heat to 715°C, hold 8 hr, furnace cool to 620°C, hold for 12 hr (including furnace cool time), air cool to room temperature.

^bAll specimens were standard ASTM type with 0.636-cm-diameter reduced section.

^cExtensometer slipped.

TABLE 7.16

TENSILE PROPERTIES OF INCONEL ALLOY 718 PLATE AFTER HEAT TREATMENT III^a

Specimen Orientation	Specimen No. ^b	Test Temperature, °C	0.2% Yield Strength		Tensile Strength		Elongation in 4D, %	Reduction of Area, %
			kg/cm ²	psi	kg/cm ²	psi		
Parallel to rolling direction	M	25	10,020	142,490	13,590	193,290	24	31
	N	425	8,830	125,620	12,425	176,950	24	37
	O	540	8,580	122,300	12,180	173,140	23	37
Transverse to rolling direction	A	25	11,300	160,740	13,870	197,300	18	23
	D	25	11,350	161,600	13,930	198,300	20	26
	B	425	—	c	12,510	177,930	23	33
	E	425	10,140	143,990	12,510	177,900	22	33
	C	540	9,780	139,060	12,310	175,000	20	33
	F	540	9,550	135,800	12,270	174,340	22	33

^aHeat treatment: 1070°C for 1 hr, air cool to room temperature, heat to 760°C, hold for 10 hr, furnace cool to 650°C, hold for 10 hr (including furnace cool time), air cool to room temperature.

^bAll specimens were standard ASTM type with 0.636-cm-diameter reduced section.

^cExtensometer slipped.

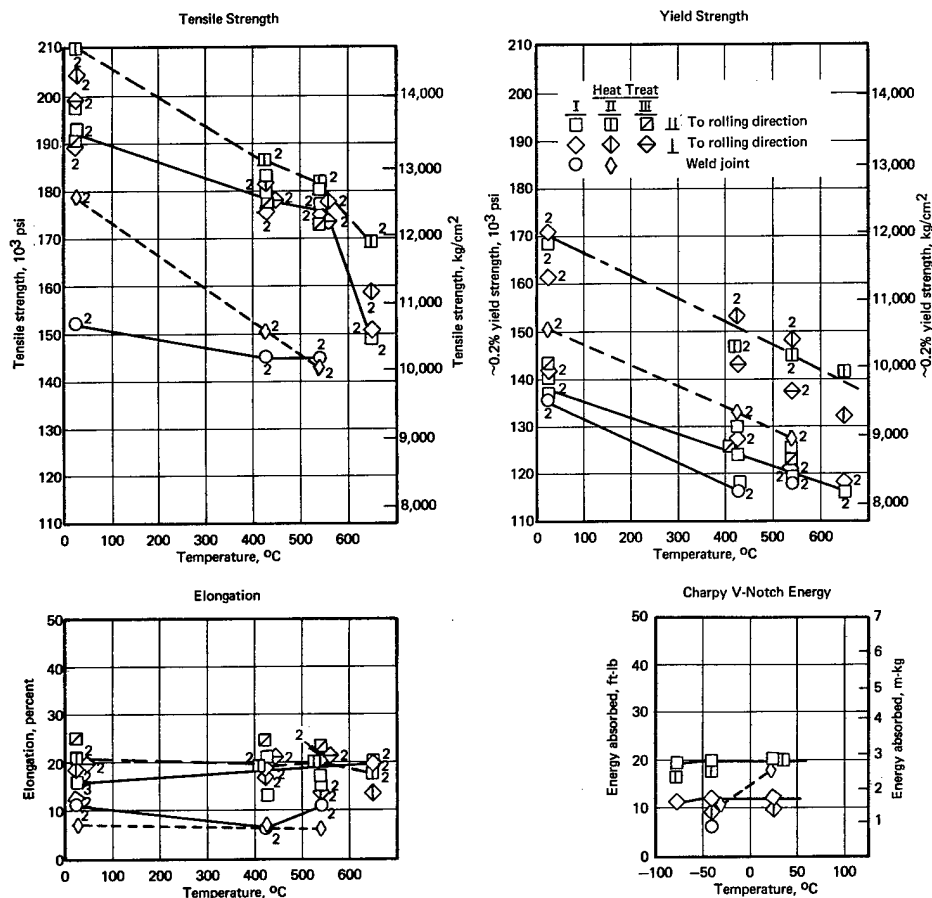


Fig. 7.8 — Tensile and Charpy V-notch impact properties of Inconel alloy 718 plate and weldments

the annealing temperature has a major effect on tensile properties. This suggests that the quenching procedures employed in the solution annealing of the type of heavier plate potentially useful in nuclear pressure vessel construction must be carefully selected to assure optimum properties.

Toughness – Charpy V-notch impact tests were completed for the parallel and transverse orientations at 25°, -40°, and -78°C for heat treatments I and II. Table 7.17 and Figure 7.8 show these data. No evidence of a transition from ductile-to-brittle fracture was noted and the cooling rate apparently had little effect on the absorbed energy levels, but a distinct toughness anisotropy exists. Charpy V-notch specimens which received heat treatment III will be evaluated. Drop-weight tear test specimens for each of the three heat treatment are being prepared and will be tested at NRL to further define the toughness of this fcc alloy.

Fatigue Properties – Specimens are being prepared for preliminary low-cycle fatigue testing. These specimens are being made from material which has received heat treatment III.

Radiation Effects – Charpy V-notch data have been obtained at NRL on Inconel alloy 718 specimens irradiated to a fluence of 1.15×10^{19} n/cm² ($E_n \geq 1$ Mev). Specimens were irradiated in the Union Carbide Research Reactor in a helium environment at less than 120°C. The specimens received heat treatment I prior to machining for irradiation. Table 7.18 and Figure 7.9 summarize data obtained. The irradiation exposure apparently did not reduce impact resistance, at least when similar test temperatures were employed. Additional control tests will be made at higher temperatures.

A second capsule containing tensile blanks and Charpy V-notch specimens of Inconel alloy 718 had been irradiated in the MTR at pile-ambient temperature to a fluence level of about 4 to 5×10^{19} n/cm² ($E_n \geq 1$ Mev). Post-testing will be conducted at NRL.

Thermal Stability – Specimens of Inconel alloy 718 representing all three heat treatments have been exposed in air at 540°C for 1000 hours. No change in hardness was noted. Another plate which had received heat treatment II was exposed for 1000 hours at 650°C and a small

TABLE 7.17
CHARPY V-NOTCH IMPACT STRENGTH OF INCONEL ALLOY 718 PLATE

Orientation of Major Specimen Axis	Heat Treatment ^a	Energy Absorbed					
		25°C		-40°C		-78°C	
		ft-lb	m-kg	ft-lb	m-kg	ft-lb	m-kg
Parallel to rolling direction	I	20	2.76	20	2.76	20	2.76
		20	2.76	20	2.76	18	2.50
		20	2.76	19	2.64	19	2.64
Parallel to rolling direction	II	20	2.76	18	2.50	17	2.35
		20	2.76	17	2.35	17	2.35
		18	2.50	18	2.50	17	2.35
Transverse to rolling direction	I	11.0	1.52	12	1.66	11.5	1.59
		12.0	1.66	12	1.66	9.0	1.24
		12.0	1.66	12	1.66	11.0	1.52
Transverse to rolling direction	II	10	1.38	9	1.24	—	—
		9	1.24	8	1.08	—	—
		—	—	11	1.52	—	—

^aHeat treatment: I – 950°C for 1 hr, furnace cool 100 min. to 715°C, hold 8 hr, furnace cool to 620°C, hold 12 hr (including furnace cooling time), then air cool to room temperature.

II – 950°C for 1 hr, air cool to room temperature, heat to 715°C, hold 8 hr, furnace cool to 620°C, hold 12 hr (including furnace cool time), then air cool to room temperature.

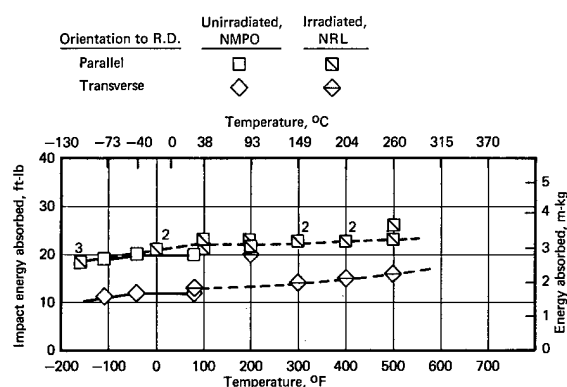


Fig. 7.9 – Effect of nuclear irradiation ($<122^{\circ}\text{C}$ $1.15 \times 10^{19} \text{ n/cm}^2$; $E_n \geq 1 \text{ Mev}$) on Inconel alloy 718

TABLE 7.18

INCONEL 718 CHARPY V-NOTCH DATA FOR IRRADIATED SPECIMENS^a

Specimen No.	Orientation ^b	Charpy V Properties ^c				Rockwell
		Temperature		Energy		Hardness,
		°F	°C	ft-lb	mg-kg	R _C
T9	T	+80	27	13	1.8	40 ^d
E3	P	+300	150	23	3.2	
T1	T	+500	260	16	2.2	
T15	T	+400	205	15	2.1	
T7	T	+200	93	20	2.8	
G3	P	+200	93	23	3.2	40 ^d
D1	P	+100	38	23	3.2	
J3	P	+300	150	22	3.0	
C3	P	±0	−18	21	2.9	
F3	P	+200	93	22	3.0	
K3	P	+100	38	21	2.9	
I3	P	−160	−107	18	2.5	
K1	P	+400	205	22	3.0	
T5	T	+80	27	12	1.7	
D3	P	±0	−18	21	2.9	
T13	T	+300	150	14	1.9	
E1	P	−160	−107	18	2.5	
H1	P	−160	−107	19	2.6	
G1	P	+500	260	23	3.2	
L1	P	+400	205	23	3.2	
H3	P	+500	260	26	3.6	

^a $1.15 \times 10^{19} \text{ n/cm}^2$, $E_n \geq 1 \text{ Mev}$ (σ 68 mb Mn^{54} fission).

^bT = Major specimens axis transverse to rolling direction.

P = Major specimen axis parallel to rolling direction.

^cMaterial given Heat Treatment I prior to radiation exposure.

^dAverage of 3 readings.

increase in hardness was noted. Tensile and Charpy V-notch impact specimens are being prepared from each plate.

Weldment Studies

Four weldments of the Inconel 718 alloy were prepared in 2.54-cm-thick plate, using joint designs described previously.⁶ Of these, two were made using the U-joint for all-weld metal specimens, and two were made with the double U-joint preparation for determining joint properties. The manual TIG welding method was employed according to procedures described earlier.⁶

Weld Zone Hardness Versus Heat Treatment – Sections of double U weldments with two different post-weld heat treatments were ground, etched, and surveyed for Rockwell C hardness. Figure 7.10 illustrates two sections from a weldment which, after welding, were aged at 715°C for 8 hours, furnace cooled to 620°C and held for 12 hours including furnace cooling time, and air cooled. Prior to welding the plate was heated at 950°C for 1 hour and air cooled. Weld center hardnesses ranged from R_C 34 to 44; base metal hardnesses ranged from R_C 38 to 46. The reason for the disparity in hardness between the two weld areas is not known but must tentatively be assigned to weld metal heterogeneity. Differences in base metal hardness are probably associated with inadvertent variations in pre-weld heat treatment.

Figure 7.11 presents the results of hardness surveys on two sections of a weldment subjected, following welding, to a solution anneal at 950°C for 1 hour followed by furnace cooling to 715°C, holding 8 hours, furnace cooling to 620°C, holding for 12 hours, and air cooling. Weld center hardnesses range from R_C 35 to 41, with base metal hardnesses of R_C 41 to 43.

Tensile Properties – Data obtained on weld-joint tensile specimens machined from double U weldments are presented in Table 7.19 and Figure 7.8. These specimens possess significantly lower strength and ductility than the base metal similarly treated. The deleterious effect on properties of slow cooling from the solution annealing temperature is again apparent. The W2 series specimens were cut from plate air cooled from 950°C prior to welding; hence they should be compared with base metal specimens given heat treatment II listed in Table 7.15. The effect of post-weld solution annealing and air cooling, and aging on weldment properties will be determined. All-weld specimens in various conditions of heat treatment are being prepared.

Toughness – Table 7.20 and Figure 7.8 contain results of Charpy V-notch tests conducted on specimens machined from weldments. The specimens aged only after welding (solution annealed at 950°C for 1 hour and air cooled prior to welding) possessed approximately the same impact strength as the base metal at 25°C but only half as much at -40°C. Even lower values at -40°C were obtained on specimens from weldments given a solution anneal (furnace cooled) and aged after welding.

HP 9Ni – 4Co – 0.20C

HP 9Ni – 4Co – 0.20C, a heat-treatable steel, has been added to the program and will be evaluated. This alloy can achieve high tensile strengths while retaining excellent toughness. It is recommended for use in the quenched and double-tempered condition. The material is reported to be quite weldable in the quenched and tempered condition, and no post-weld heat treatment is required to achieve virtually 100 percent weld efficiencies.

A plate 2.54 cm thick by 91.4 by 122 cm has been received from heat No. 3932354* and is being machined into test pieces for tensile, impact, low-cycle fatigue, DWTT, and weld

*Composition in wt % of heat 3932354: C – 0.017, Mn – 0.29, P – 0.004, S – 0.007, Si – 0.01, Ni – 9.11, Cr – 0.79, V – 0.09, Co – 4.40, Fe – balance.

⁶GEMP-475A, Fig. 9.1, p. 232.

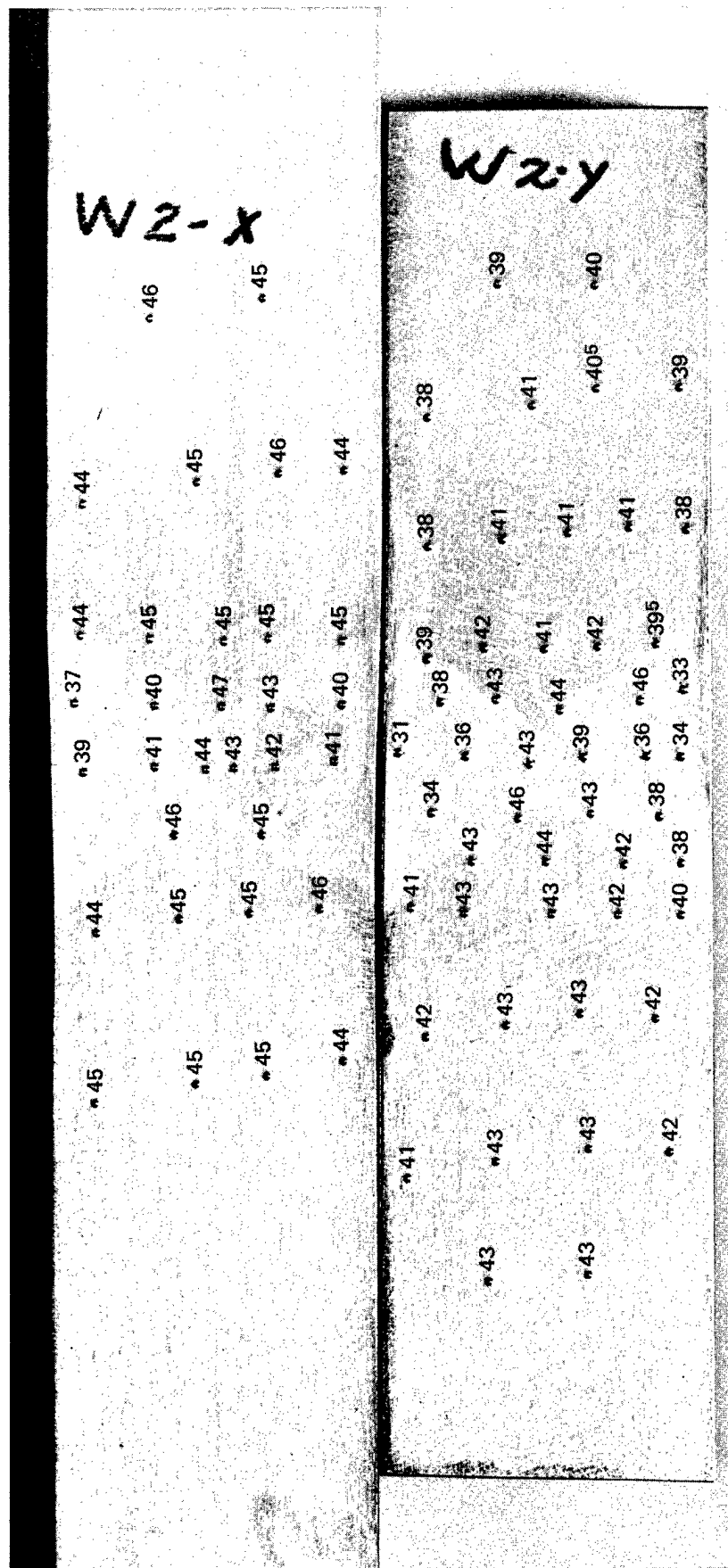


Fig. 7.10 — Macroetched cross sections from a double-U Inconel alloy 718 weldment aged at 715°C for 8 hours, furnace cooled to 620°C, held for 12 hours, and air cooled to room temperature. Numbers beside the indentations are Rockwell C values. (Neg. P67-8-33L)

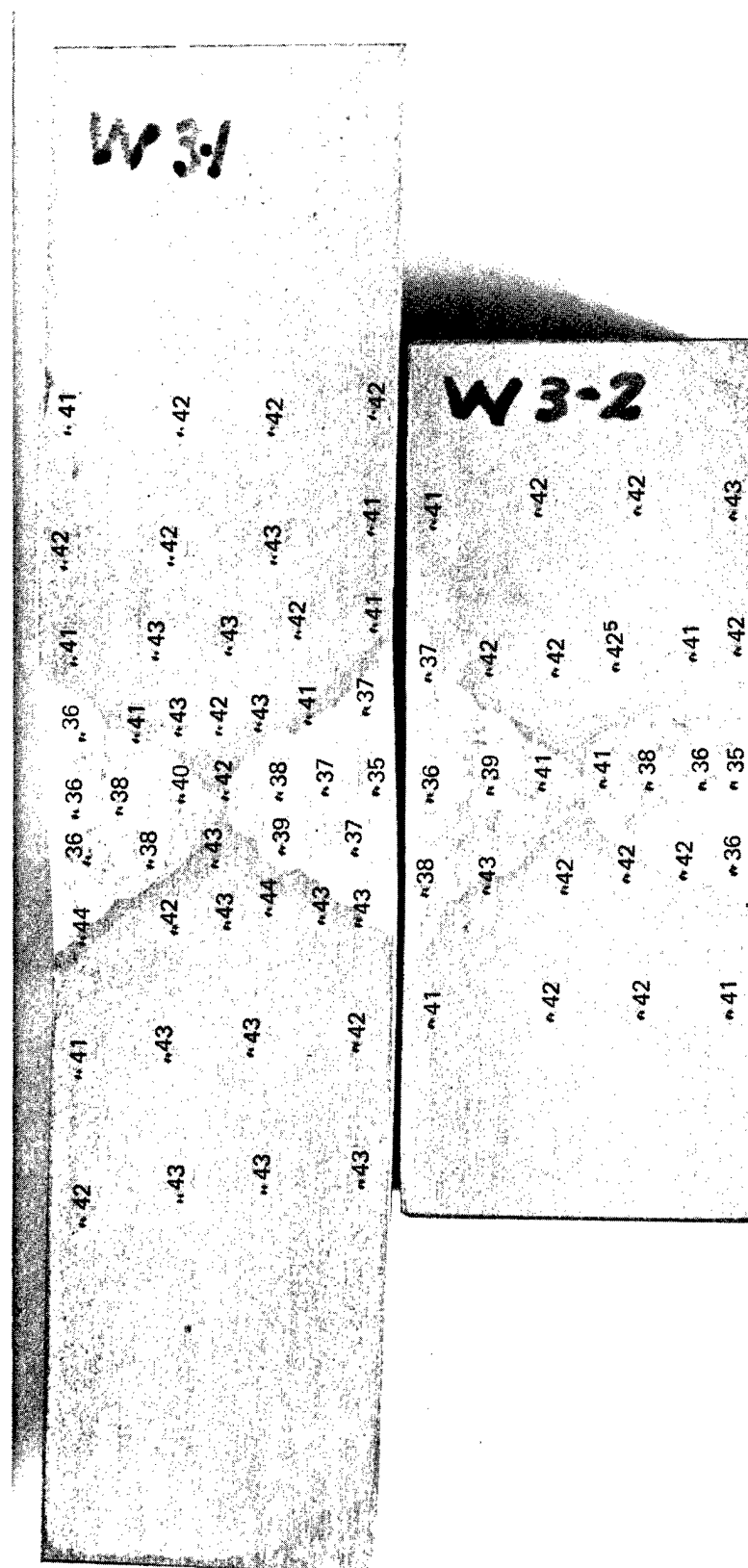


Fig. 7.11 — Macroetched cross sections from double-U Inconel alloy 718 weldment annealed (furnace cool) and aged after welding. Numbers beside the indentations are Rockwell C hardness values. (Neg. P67-8-33M)

TABLE 7.19
TENSILE PROPERTIES OF INCONEL ALLOY 718 WELDMENTS

Specimen	Specimen No.	Specimen Treatment ^a	Test Temperature, °C	0.2% Yield Strength		Tensile Strength		Elongation in 4D, %	Reduction of Area, %	Location of Fracture
				kg/cm ²	psi	kg/cm ²	psi			
Joint tensile	W3A	W+An+A	25	9,700	138,300	10,900	155,200	12.7	11	W
	W3A	W+An+A	25	9,300	132,900	10,300	147,000	12.3	13	W
	W3C	W+An+A	425	8,100	115,400	10,300	146,900	7.3	22	W
	W3D	W+An+A	425	8,900	119,800	10,000	143,200	4.9	13	HAZ ^b
	W3E	W+An+A	540	8,300	118,200	10,500	148,700	8.9	34	W
	W3F	W+An+A	540	8,100	115,290	9,200	131,100	4.1	15	HAZ ^b
	W3G	W+An+A	540	8,300	118,000	9,700	137,600	14.0	14	W
	W2E	W + A	25	10,500	149,600	12,500	178,200	6.9	30	W
	W2K	W + A	25	10,600	150,700	12,700	179,800	7.6	28	W
	W2G	W + A	425	9,500	134,700	10,900	154,800	8.5	33	HAZ ^b
	W2L	W + A	425	9,200	130,400	10,100	143,800	4.1	22	W
	W2I	W + A	540	9,200	131,140	10,400	148,300	7.3	31	W
	W2H	W + A	540	8,700	123,700	9,500	135,800	4.5	22	W

^aHeat treatment: W — Welded.

An — Annealed at 950°C for 1 hour, furnace cooled to aging temperature.

A — Aged at 715°C for 8 hours, furnace cooled to 620°C and held 12 hours, including furnace cooling time.

^bHAZ — Heat-affected zone.

TABLE 7.20
CHARPY V-NOTCH IMPACT STRENGTH
OF INCONEL ALLOY 718 WELDMENTS

Notch Location ^a	Specimen Condition ^b	Energy Absorbed			
		25°C		-40°C	
		ft-lb	m-kg	ft-lb	m-kg
HAZ ^c	W + A	21	2.90	10	1.38
Weld	W + A	16	2.11	11	1.52
Weld	W + A	20	2.76	11	1.52
BM ^d	A	20	2.76	17	2.35
BM ^d	A	10	1.38	Parallel to RD	
				9	1.24
HAC ^c	W+An+A	—	—	Transverse to RD	
				10	1.38
HAZ ^c	W+An+A	—	—	8	1.08
HAZ ^c	W+An+A	—	—	8	1.08
Weld	W+An+A	—	—	6	0.83
Weld	W+An+A	—	—	6	0.83
Weld	W+An+A	—	—	6	0.83
BM ^d	An+A	20	2.76	20	2.76
BM ^d	An+A	10	1.38	Parallel to RD	
				9	1.24
				Transverse to RD	

^aAll notches perpendicular to surface of plate.

^bHeat treatment: W — Welded.

A — Aged at 715°C for 8 hours, furnace cooled to 620°C, held 12 hours, including furnace cooling time.

An+A — Annealed at 950°C for 1 hour, furnace cooled to 715°C, held 8 hours, furnace cooled to 620°C, held 12 hours including furnace cooling time.

^cHAZ — Heat-affected zone.

^dBM — Base metal.

specimens. This material was air melted and vacuum consumable electrode remelted and arrived in the heat-treated condition. Nominal heat-treating procedures are as follow ;

Normalize: 900°-930°C - 1 hr/2.54 cm thickness, air cool

Austenitize: 845° ±10°C - 1 hr/2.54 cm thickness, water or oil quench

Temper: Double temper - each temper consists of 2 hours minimum at 540°C (for 13,360 kg/cm² minimum tensile strength).

The vendor reports the following room-temperature properties for this material:

Tensile strength, kg/cm ²	13,910 (198,000 psi)
Yield strength, kg/cm ²	13,290 (188,600 psi)
Elongation in 5.08 cm, %	17
Reduction of area, %	68.5
Charpy V-notch impact energy (avg), m-kg	9.1 (66 ft-lb)

Welding wire designed to match the base metal properties in the as-welded condition is being procured.

7.2 CONSIDERATION OF PRESSURE VESSEL FAILURE MODES AND RELATED PROPERTIES

Studies have been made to identify special material properties beyond those normally obtained which may eventually be required to properly qualify a potential pressure vessel material. This gives reasonable assurance that no major basic limitation of the concept of using high-yield-strength materials or of using a given advanced pressure vessel material is overlooked.

The first step in these studies is to consider potential failure modes and to identify special material properties or tests required to evaluate a factor of safety for each mode of failure. Six principal modes of failure have been considered:

1. Burst due to over-pressure.
2. Fatigue cracking.
3. Fast fracture including both brittle fracture and low-energy tearing.
4. Buckling collapse due to external pressure.
5. Corrosion, including stress corrosion and corrosion fatigue.
6. Progressive distortion (ratchetting).

Although the foregoing six modes of failure are potentially all significant failure modes, only the first three are considered immediately pertinent to the development of advanced pressure vessel materials. The other three failure modes are being eliminated from further studies of advanced pressure vessel materials for the following reasons.

Buckling collapse is eliminated from further consideration simply because the vast majority of pressure vessels pertinent to this program are vessels subject only to internal pressure. There is a possibility of developing an instability at the knuckle of a poorly designed dished head, but this is considered primarily a design problem unrelated to development of advanced pressure vessel materials.

Corrosion, on the other hand, is definitely a materials problem, but it is assumed that, should corrosion be a problem with these materials, a corrosion-resistant cladding could be applied in a manner similar to that currently used for the conventional low-carbon steels.

Progressive distortion or ratchetting is eliminated from further consideration because it is primarily a design problem. A well designed structure (including adequate analysis) should not be subjected to ratchetting.

The remaining three failure modes require careful consideration in the development of advanced pressure vessel materials, and are treated in some detail in the following paragraphs.

BURST DUE TO OVER-PRESSURE

Investigators have shown⁷ that burst pressure can be expressed in terms of ultimate tensile strength, strain-hardening exponent, and geometry of the vessel. For a thin-walled cylinder, Langer⁷ gives the following equation for the burst pressure:

$$P_b = \sigma_u' F_{cyl} \left(\frac{2t}{d_i} \right) \left(1 - \frac{t}{d_i} \right) \quad (7.1)$$

where

P_b = burst pressure

σ_u' = nominal stress at ultimate load, i. e., nominal engineering ultimate tensile strength

t = vessel wall thickness

d_i = vessel inside diameter

$$F_{cyl} = \left[\frac{0.25}{\epsilon_u + 0.227} \right] \left(\frac{e}{\epsilon_u} \right)^{\epsilon_u}$$

e = base of the natural logarithms

ϵ_u = true strain at ultimate load

Langer states that equation (7.1) should be used for

$$W < 1.4$$

$$\text{where } W = d_o/d_i = \frac{d_i + 2t}{d_i} = 1 + \frac{2t}{d_i}$$

and d_o = vessel outside diameter

when the strain-hardening exponent, n , is defined as the true strain at ultimate load $n = \epsilon_u$ and equation (7.1) then defines the burst pressure in terms of the nominal tensile strength, strain-hardening exponent, and vessel geometric parameters.

For a cylindrical vessel designed to Section III of the ASME Boiler and Pressure Vessel Code with the minimum permissible thickness, the design pressure, P_d , is given by the following:

$$\begin{aligned} P_d &= 2S_m \left(\frac{t}{d_i} \right) \left[\frac{1}{1+t/d_i} \right] \\ &\cong 2S_m \left(\frac{t}{d_i} \right) \left[1 - \frac{t}{d_i} \right] \end{aligned} \quad (7.2)$$

where

S_m = membrane stress allowable.

If one defines the factor of safety, FS , on burst as the ratio of the burst pressure to the design pressure, and if it is further assumed that for the high-strength materials in this program the value of S_m will always be based on the ultimate tensile strength, and using the Section III value of

$$S_m = 1/3 \sigma_u',$$

⁷B. F. Langer, "PVRC Interpretive Report of Pressure Vessel Research, Section I - Design Considerations," Welding Research Council Bulletin, No. 95, April 1964.

the factor of safety on burst due to over-pressure for a thin-walled cylinder becomes simply:

$$FS = 3 F_{cyl} \quad (7.3)$$

The definition of F_{cyl} indicates that it is a function only of the strain-hardening exponent ($n = \epsilon_u$), Langer's tabulated values of F_{cyl} as a function of n together with equation (7.3) were used in preparing Figure 7.12 which shows the relationship between the factor of safety and the strain-hardening exponent.

Gross⁸ gives plots which show the variation of yield strength and strain-hardening exponent with tensile strength for typical pressure vessel steels. Figure 7.13 combines

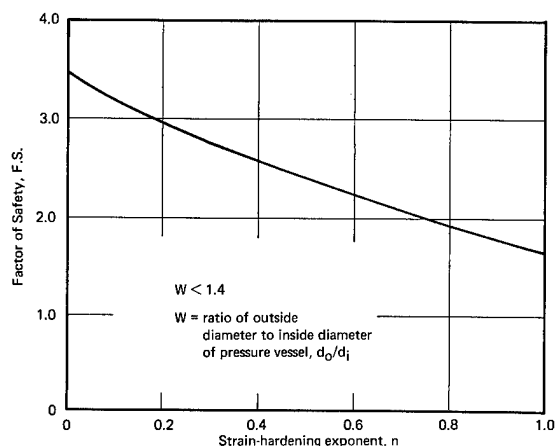


Fig. 7.12 — Factor of safety of burst of over pressure for a thin-walled cylindrical pressure vessel

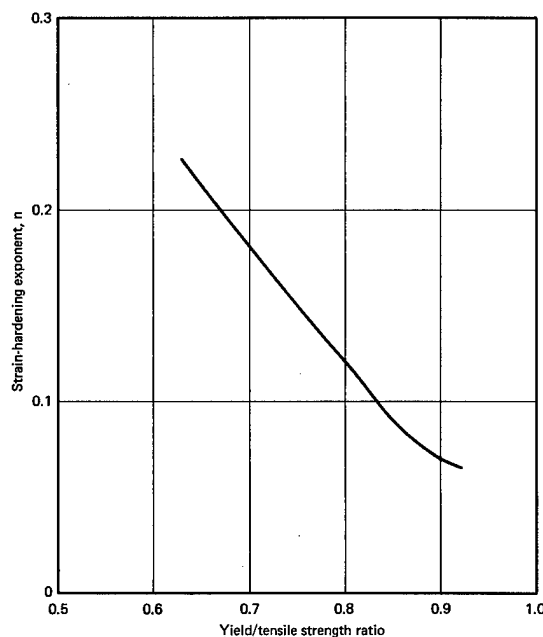


Fig. 7.13 — Variation of the strain-hardening exponent with the yield-to-tensile strength ratio for typical pressure vessel steels — based on the data of Gross

⁸J. H. Gross, "PVRC Interpretive Report of Pressure Vessel Research, Section II — Materials Considerations," Welding Research Council Bulletin, No. 101, November 1969.

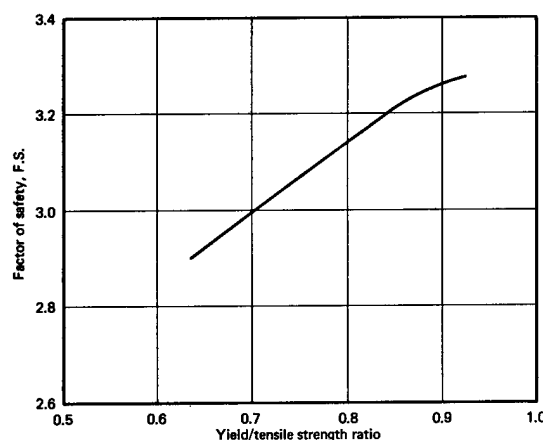


Fig. 7.14 — Variation of factor of safety with the yield-to-tensile strength ratio — obtained by cross plotting information contained in Figures 7.12 and 7.13

these plots of Gross to obtain a plot of the variation of the strain-hardening exponent with the yield-to-tensile strength ratio for the typical pressure vessel steels. The information contained in Figures 7.12 and 7.13 was combined to obtain the plot of factor of safety versus the yield-to-tensile strength ratio shown in Figure 7.14. This plot indicates that the factor of safety on burst due to over-pressure tends to increase with increasing yield-to-tensile strength ratio.

The foregoing discussion demonstrates the need for somewhat more detailed tensile data and evaluation than are normally obtained from routine tensile tests in order to evaluate the factor of safety on burst due to over-pressure. In addition to the normal data, the true strain at the ultimate (maximum) load is required. The true strain at the ultimate load is needed to define the strain-hardening exponent which, in turn, can be used to obtain a calculated factor of safety on burst. Strain-hardening exponents obtained for candidate pressure vessel materials can be compared with the data of Gross presented in Figure 7.13 to assess the behavior of these materials compared to current typical pressure vessel materials.

FATIGUE CRACKING

Coffin,⁹ Coffin and Tavernelli,¹⁰ and Manson¹¹ have shown that low-cycle (or strain) fatigue data can be related to the tensile properties of a material. Manson has presented several different techniques for doing this, but his method of Universal slopes which has been correlated with fatigue data on numerous materials was selected for these studies due to its simplicity of application. Manson gives the following equation for relating the fatigue strain range with the tensile properties:

$$\Delta \epsilon = 3.5 \frac{\sigma_u'}{E} N_f^{-0.12} + \left(\frac{D}{N_f} \right)^{0.6} \quad (7.4)$$

⁹L. F. Coffin, Jr., "A Study of the Effects of Cyclic Thermal Stresses on a Ductile Metal," Trans. ASME, Vol. 76, 1954, pp. 931-950.

¹⁰L. F. Coffin, Jr., and J. F. Tavernelli, "Experimental Support for a Generalized Equation Predicting Low-Cycle Fatigue," Trans. ASME, Vol. 84, Series D, 1962, pp. 533-591.

¹¹S. S. Manson, "Fatigue: A Complex Subject — Some Simple Approximations," Exp. Mech., Vol. 5, No. 7, 1965, pp. 2-35.

where

- $\Delta\epsilon$ = total strain range, elastic plus plastic
- E = modulus of elasticity
- σ_u' = nominal stress at the ultimate (max) load
- N_f = number of cycles to failure
- D = ductility = $[1/(1-RA)]$
- RA = reduction in area expressed as a fraction

Manson does not propose that this equation be used in lieu of actual fatigue data. Since it has correlated well with fatigue data for a wide range of materials, however, it is considered to give a good indication of the potential fatigue performance of materials. Accordingly, Manson's equation (7.4) has been used to give a preliminary indication of the potential fatigue performance of the candidate advanced pressure vessel materials.

Since these advanced pressure vessel materials are specifically intended for nuclear service, the Manson equation was used to compare potential fatigue properties of these materials with design fatigue strength curves for the currently approved materials presented in Section III of the ASME Boiler and Pressure Vessel Code for Nuclear Vessels. To make this comparison, the Code philosophy as delineated in the supplementary criteria¹² issued with the first edition of Section III was used to apply corrections for the effect of mean stress and factors of safety on stress and cycles.

Code criteria in essence assume that the materials behave in an elastic – perfectly plastic manner and that, due to residual stresses of unknown magnitude in the as-fabricated vessel, one must assume that the maximum possible mean stress exists at any point in the vessel. The Code criteria also assume a linear rule for correcting for the effect of mean stress.

Figure 7.15 helps to illustrate the manner in which the correction for mean stress has been made. After shakedown,* all possible stress states lie either within the triangular region A-O-B along line A-B, or on the alternating stress axis above point A. Line C-D from the point on the alternating stress axis represents the stress, S_N , required to produce failure in N cycles at zero mean stress to the ultimate tensile strength on the mean stress axis. This line represents the limiting combinations of mean and alternating stress required to produce failure in N cycles according to the linear rule.

However, since line A-B represents the limits of the possible stress states, point E corresponds to the highest possible mean stress point corresponding to N cycles. The corresponding alternating stress value, S_N' is the alternating stress amplitude corrected for the maximum possible effect of mean stress. Applying this procedure for a number of different values of N gives the fatigue curve corrected for the maximum effect of mean stress. The next step in obtaining the calculated fatigue design curve is to apply the Code factors of safety of 2 on stress and 20 on cycles to the fatigue curve corrected for the maximum effect of mean stress. The calculated design fatigue strength curves obtained in this manner are compared with the applicable Section III design fatigue strength curves in Figures 7.16 and 7.17.

For many materials the Peterson Cubic Rule¹³ is a better representation of the fatigue behavior under combined mean and alternating stress; hence the foregoing comparison was repeated using this rule, and results are shown in Figures 7.18 and 7.19.

*Shakedown refers to an elastic cyclic condition after a few cycles which is assumed to be assured by the Code's $3S_m$ limit on the primary plus secondary stresses.

¹²"Criteria of Section III of the ASME Boiler and Pressure Vessel Code for Nuclear Vessels," ASME, New York, N.Y., 1964.

¹³R. E. Peterson, "Brittle Fracture and Fatigue in Machinery," Fatigue and Fracture of Metals, Wiley, New York, N.Y., 1952, pp. 79-102.

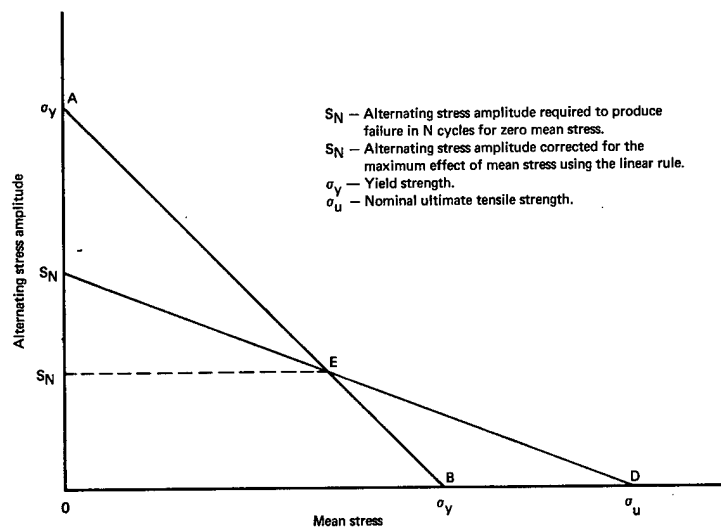


Fig. 7.15 – Modified Goodman diagram showing the application of the linear rule to obtain the correction for the maximum effect of mean stress

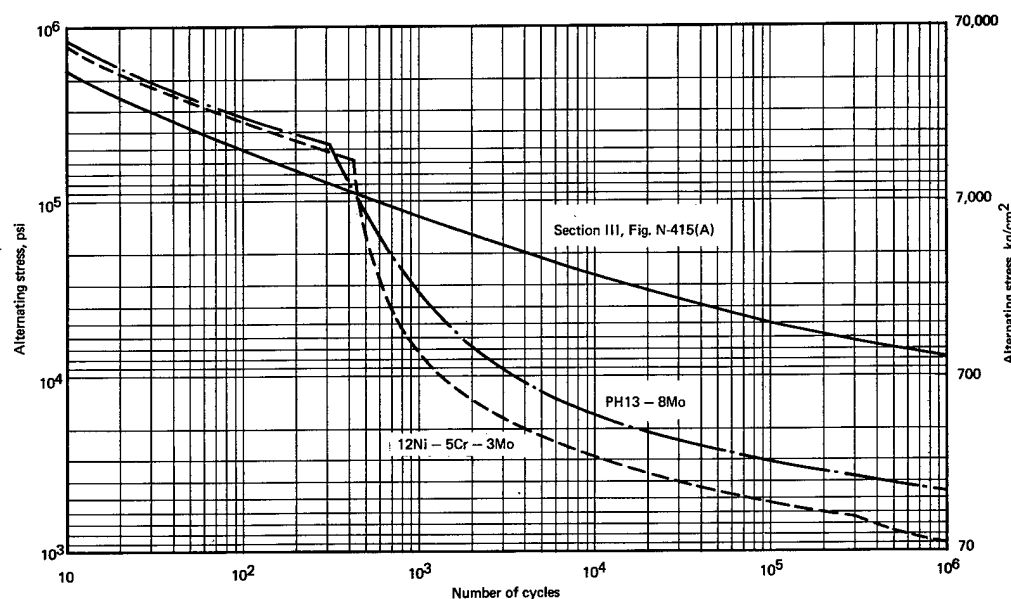


Fig. 7.16 – Comparison of calculated design fatigue curves for PH13-8Mo and 12Ni-5Cr-3Mo (using the Linear Rule to correct for the maximum effect of mean stress) with design fatigue curve for carbon and alloy steels from Section III of ASME Boiler and Pressure Vessel Code for Nuclear Vessels

Another item which should be considered in evaluating the maximum effect of mean stress correction is the fact that, in general, high yield strength materials tend to exhibit a high degree of cyclic strain softening, a decrease in the stress range with cycles during strain cycling tests. This amounts to a decrease in the effective yield strength with cycles, eventually stabilizing at some asymptotic value after many cycles. This asymptotic value is commonly referred to as the dynamic yield strength. It has been suggested¹⁴ that it may be more realistic to base the mean stress correction on the dynamic yield strength rather than

¹⁴Dr. W. E. Cooper, private communication.

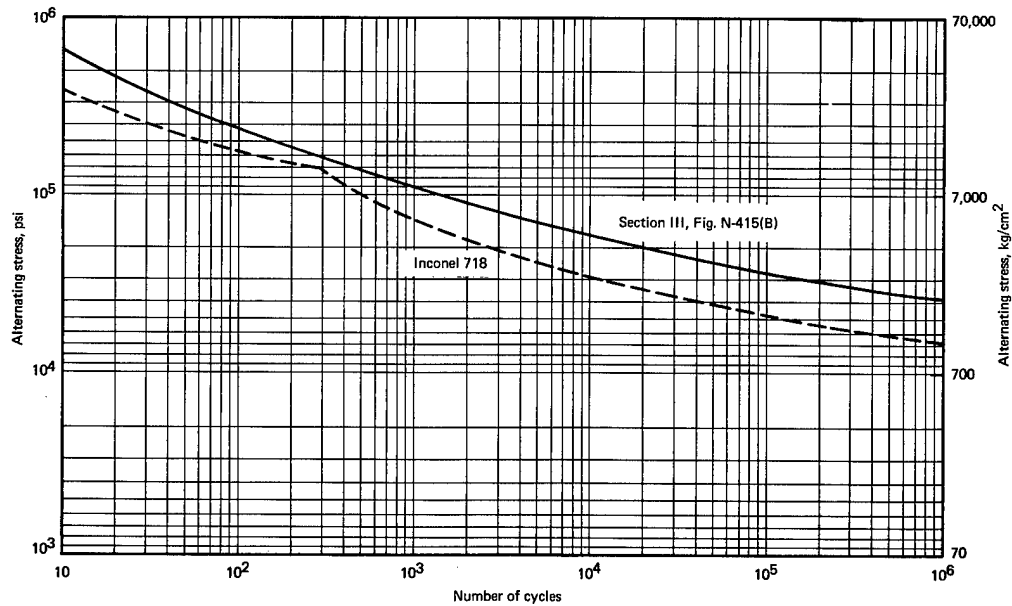


Fig. 7.17 — Comparison of calculated design fatigue curve for Inconel 718 (using the Linear Rule to correct for the maximum effect of mean stress) with design fatigue curve for 18-8 stainless steels and nickel-chrome-iron alloy from Section III of ASME Boiler and Pressure Vessel Code for Nuclear Vessels

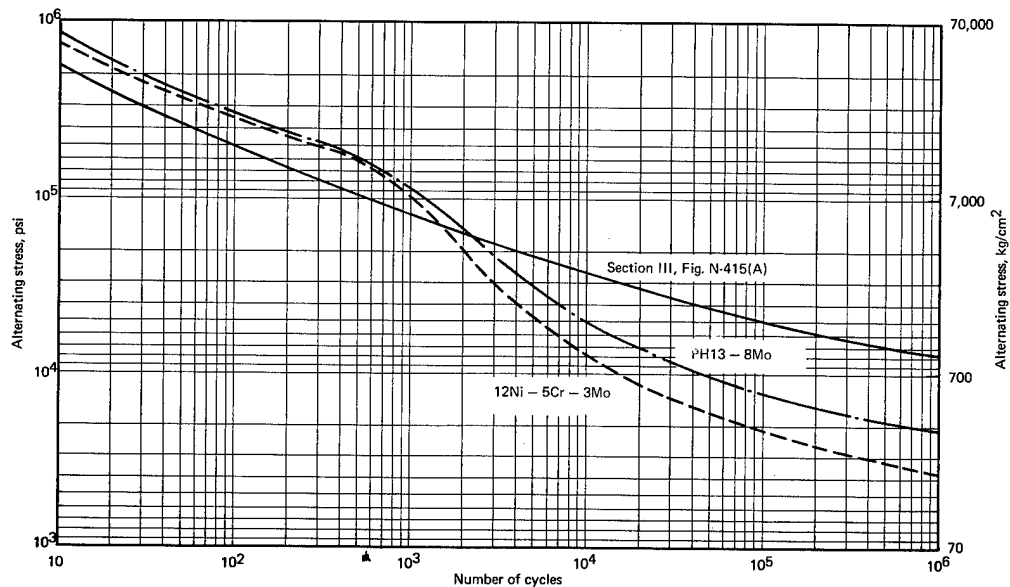


Fig. 7.18 — Comparison of calculated design fatigue curves for PH13-8Mo and 12Ni-5Cr-3Mo (using the Peterson Cubic Rule to correct for the maximum effect of mean stress) with design fatigue curve for carbon and alloy steels from Section III of ASME Boiler and Pressure Vessel Code for Nuclear Vessels

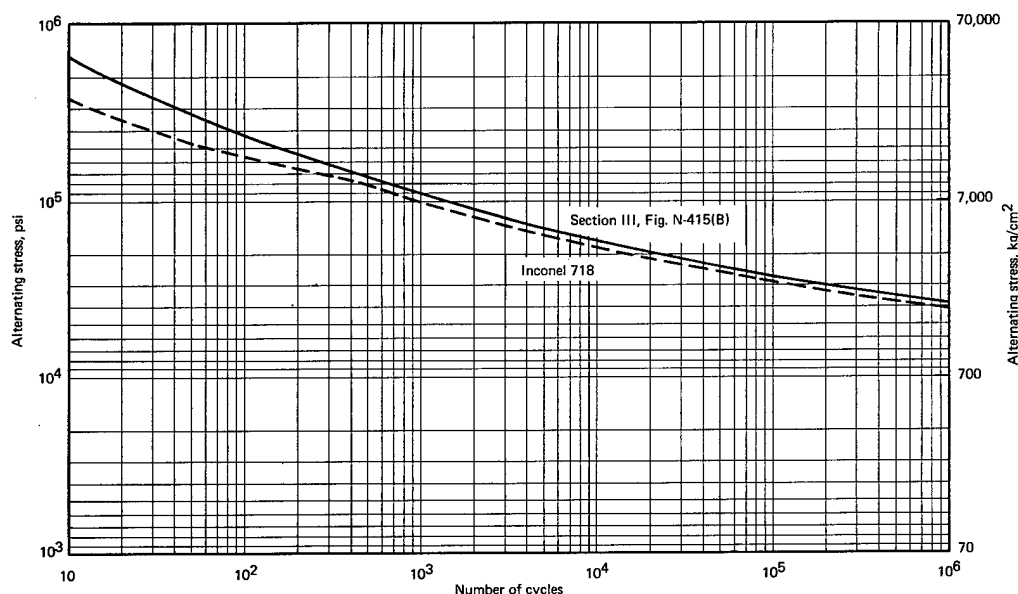


Fig. 7.19 — Comparison of calculated design fatigue curve for Inconel 718 (using the Peterson Cubic Rule to correct for the maximum effect of mean stress) with design fatigue curve for 18-8 stainless steels and nickel-chrome-iron alloy from Section III of ASME Boiler and Pressure Vessel Code for Nuclear Vessels

the static yield strength for these high yield strength materials. Manson¹⁵ shows data for a 4340 steel in which the asymptotic value of the stress range is only about two-thirds its initial value. To examine the potential significance of this factor, assumed values of dynamic yield strength, σ_{dy} , of 8790 and 10,540 kg/cm² were used to obtain calculated design fatigue strength curves for the 12Ni – 5Cr – 3Mo material, and these are compared with the calculated curve based on the static yield strength, σ_{sy} , and with the corresponding Section III design fatigue strength curve in Figure 7.20 using the linear rule and in Figure 7.21 using the Peterson Cubic Rule. These figures demonstrate that the use of dynamic yield strength and the Peterson Cubic Rule can greatly influence assessment of the fatigue behavior of these high-strength materials.

The preceding discussion of fatigue properties is only an indicator, at best, of the potential fatigue properties of the candidate pressure vessel materials, but it does serve to identify significant facets of the fatigue aspects which will be considered in evaluating the candidate materials.

In summary, the foregoing analysis indicates:

1. Up to about 400 cycles, the 12Ni – 5Cr – 3Mo and PH13-8Mo materials appear to be potentially somewhat better than the conventional materials regardless of the type of mean stress correction used, but this remains to be demonstrated through actual fatigue test data. (Many reactor pressure vessels are currently designed on the basis of fewer than 500 specified operating cycles.)
2. The Inconel alloy 718 appears to have a somewhat reduced fatigue strength over the full cyclic range compared to the Section III curve for the 18-8 stainless steels and Ni-Cr-Fe alloy. This remains to be demonstrated through actual fatigue tests.

¹⁵Manson, op. cit.

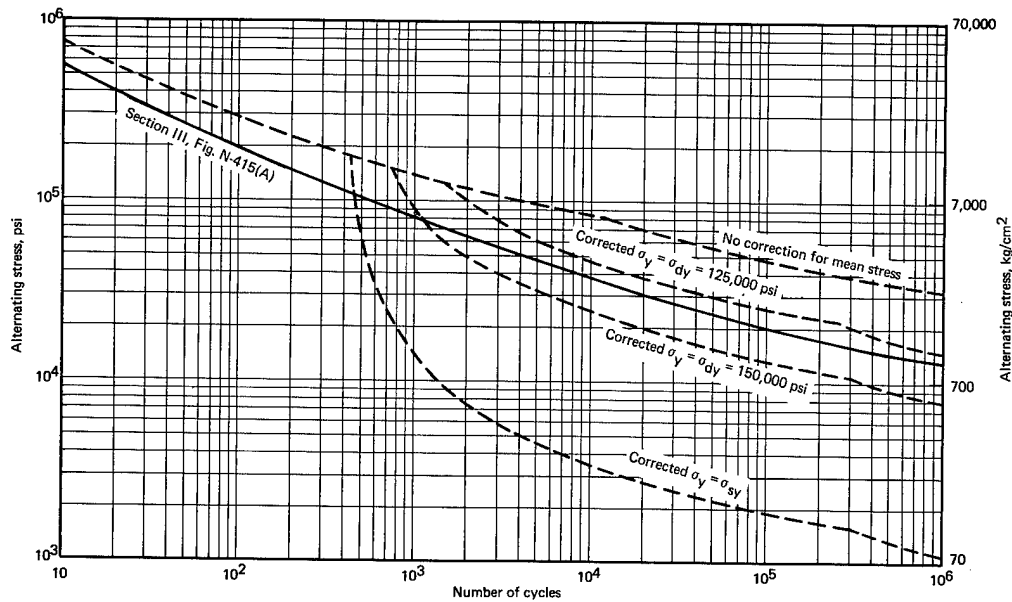


Fig. 7.20 — Comparison of calculated design fatigue curves for 12Ni — 5Cr — 3Mo corrected (Linear Rule) for mean stress using assumed values for the dynamic yield strength, σ_{dy} , with the uncorrected curve and with the curve corrected using the static yield strength, σ_{sy}

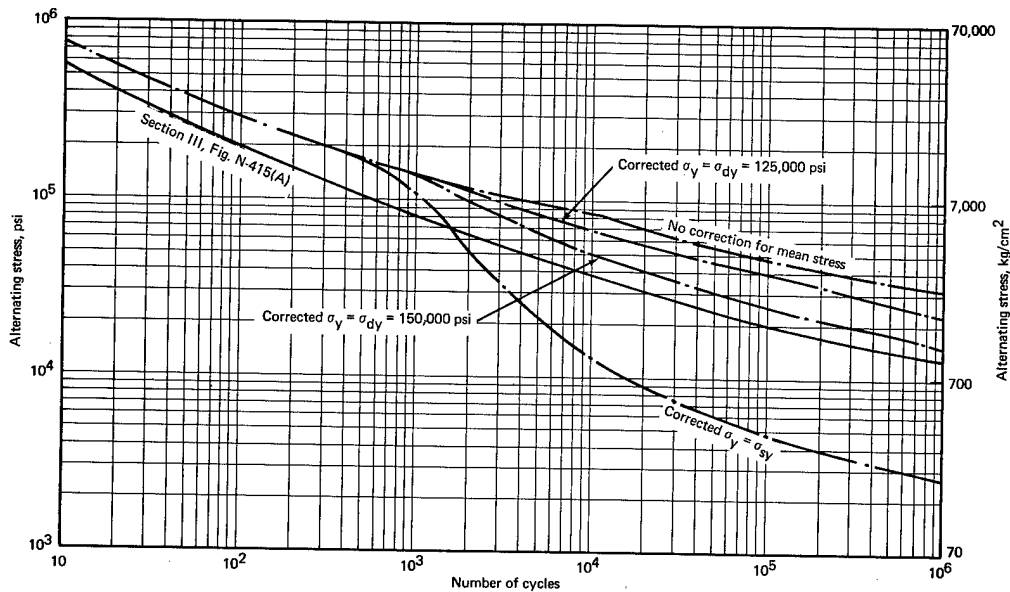


Fig. 7.21 — Comparison of calculated design fatigue curves for 12Ni — 5Cr — 3Mo corrected (Peterson Cubic Rule) for mean stress using assumed values for the dynamic yield strength, σ_{dy} , with the uncorrected curve and with the curve corrected using the static yield strength, σ_{sy}

3. The use of the Peterson Cubic Rule indicates significant potential gains in design fatigue life. The validity of the cubic rule should be investigated experimentally if such gains need to be exploited.
4. Potentially even more significant than the use of the cubic rule are the gains indicated through the use of the dynamic yield strength in lieu of the static yield strength in making mean stress corrections. These results identify the need for experimental investigations exploring use of the dynamic yield strength in lieu of the static yield strength in making the mean stress corrections. They demonstrate specifically the need to establish the actual dynamic yield strength of these materials in the presently planned fatigue tests to determine whether it would be advantageous to use dynamic data in making the mean stress correction.

FAST FRACTURE BY EITHER BRITTLE FRACTURE OR LOW-ENERGY TEARING

As used herein the term fast fracture refers to either brittle fracture or low-energy tearing. These types of failure are characterized by high-velocity crack propagation with little prior plastic deformation. These types of failure have been studied extensively in recent years, but no single approach has achieved wide acceptance for the full spectrum of significant strength levels. The two approaches most widely accepted are the NRL Fracture Analysis Diagram Procedure¹⁶ and the fracture mechanics approach which is the outgrowth of Griffith's failure theory for brittle materials and its subsequent modifications for metallic materials by Orowan¹⁷ and Irwin.¹⁸

Brittle Fracture

NRL Fractural Analysis Diagram Procedures – These procedures are generally accepted as providing a usable procedure for the lower-strength steels with yield strengths below about 3500 kg/cm². Pellini and Puzak have used the fracture analysis diagram procedures to correlate numerous service failures,¹⁶ including some examples for higher-strength materials. This procedure applies only to materials having a "well defined transition temperature," according to Pellini and Puzak; which is apparently not true of Inconel 718 material.¹⁹ Since this procedure has not been specifically validated for materials of the strength levels involved in this program, considerable experimental data will be needed if this approach is to be employed in fracture-safe evaluation of these advanced pressure vessel materials. To establish a fracture analysis diagram for these materials one needs (1) crack initiation data to define the crack initiation curves, (2) crack arrest data to define the crack arrest (CAT) curve, (3) Charpy V-notch or drop-weight test data to define the nil-ductility transition temperature (NDT), (4) explosion tear test¹⁶ data to define the fracture transition plastic (FTP) point, and (5) correlation with service failures of model pressure vessels to establish validity of the procedure in this strength range.

Fracture Mechanics Approach – This approach is currently limited to the linear fracture mechanics range in which stress levels are in the elastic range everywhere except very locally at the crack tip. This limits current usefulness to very high strength materials (yield strengths 14,000 kg/cm²) and to materials operating below their nil-ductility transition temperature (NDT). Since the materials of interest in this program approach the 14,000 kg/cm² yield strength level, it appears appropriate to consider determination of

¹⁶W. S. Pellini and P. P. Puzak, "Fracture Analysis Diagram Procedures for the Fracture-Safe Engineering of Steel Structures," NRL Report 5920, March 1963.

¹⁷E. Orowan, "Fundamentals of Brittle Behavior in Metals," *Fatigue and Fracture of Metals*, J. Wiley and Sons, New York, N.Y., 1952.

¹⁸G. R. Irwin, "Fracture Mechanics in Structural Mechanics," *Proceedings of the First Symposium on Naval Structural Mechanics*, Pergamon Press, New York, N.Y., 1960.

¹⁹GEMP-1002, p. 115.

plane-strain fracture toughness (K_{IC}) values for these materials. Of the many different test specimens currently in use for the determination of K_{IC} values, it has been suggested²⁰ that the wedge-opening loading (WOL) specimen developed by Westinghouse is most applicable for use with the heavy sections appropriate for pressure vessels.

Low-Energy Tearing – The term low-energy tearing has been used by Pellini and Puzak to describe "fracture propagation not involving a cleavage mode but resulting from a very low energy absorption in tearing." Neither the fracture mechanics approach nor the NRL fracture analysis diagram procedures have been proved applicable for analysis of the low-energy tearing problem. Pellini and Puzak²¹ indicate modifications to the fracture analysis diagram which they apparently feel would make the same type of procedure applicable to the low-energy tear case. This remains to be demonstrated and much more work is required before this procedure or the specific tests required to define the procedure can be explicitly identified. Pellini and Puzak point out that the higher-strength materials may be particularly susceptible to low-energy tearing of the welds or the heat-affected zone; they recommend using their explosion bulge test of welded sections to obtain at least a relative picture of the weld and heat-affected zone low-energy tearing problem.

7.3 GENERAL DISCUSSION

All alloys for which data have been obtained have relatively high yield-to-tensile strength ratios which would cause their Design Stress Intensity Values (S_m) to be based on the one-third tensile strength criterion of the Code. Table 7.21 is a compilation of tentative values for three alloys studied in this program, based upon the tests made to date. Modified heat

TABLE 7.21
ESTIMATED DESIGN STRESS INTENSITY VALUES, S_m ,
FOR ADVANCED PRESSURE VESSEL MATERIALS

Grade	Maximum Allowable Stress, ^a for Maximum Metal Temperature, psi				
	38°C	315°C	371°C	427°C	538°C
12Ni – 5Cr – 3Mo	59,000	47,800	—	41,000	—
PH13 – 8Mo	65,000	54,000	—	48,000	—
Inconel alloy 718	63,300	—	—	59,000	56,600
SA212B ^b	23,300	18,700	18,300	—	—
SA302B ^b	26,700	26,700	26,700	—	—
SA533B, ^b Class I	26,700	26,700	26,700	—	—

^aThe maximum allowable stress values for the materials based on the lowest of the following:

1/3 of the specified minimum tensile strength at room temperature.

1/3 of the tensile strength at temperature.

2/3 of the specified minimum yield strength at room temperature.

^bActual values listed in Section III of ASME Boiler and Pressure Vessel Code.

treatments and multiheat data would alter these values somewhat. Included in the table are corresponding Code-approved values for three materials of current use in pressure vessels. Of significance is the potential strength margin possessed by the advanced materials, although this is only one of many aspects which must be considered before any materials can be proved suitable for advanced pressure vessels. In the following paragraphs, an attempt has been made to assess the relative potential of these alloys, based on results to date.

²⁰Dr. W. E. Cooper, private communication.

²¹W. S. Pellini and P. P. Puzak, "Practical Considerations in Applying Laboratory Fracture Test Criteria to the Fracture-Safe Design of Pressure Vessels," NRL Report 6030, November 1963.

12Ni - 5Cr - 3Mo

Properties determined thus far for base metal and welded joints have involved one plate composition (heat No. 01378) and one filler metal composition, 12Ni - 3Cr - 3Mo (heat No. 01434). Both base metal and weldments, when given the recommended aging treatment of 480°C for 3 hours, showed room-temperature properties which were lower than expected. Re-aging of the base metal and weldments for longer times, however, resulted in improved hardness and strength. A major advantage of the alloy is its favorable aging characteristics (slow rise to peak hardness) in the temperature range which produces a favorable balance in strength and toughness.

Weld efficiencies have exceeded 90 percent and the possibility exists that improvements can be made with modified aging procedures. The 12Ni - 3Cr - 3Mo filler metal on hand is apparently not optimum from a weld efficiency standpoint, however, and current efforts center on a matching 12Ni - 5Cr - 3Mo filler metal. The new 2.54-cm plate (heat No. 1PO193) and weld filler wire (heat No. V91230) are expected to develop higher properties under the same heat treatments with better joint efficiencies. Welding characteristics of heavier sections remain to be determined.

It was expected from the outset that this alloy could achieve satisfactory weld properties by aging only after welding. The attractiveness of 12Ni - 5Cr - 3Mo, as well as the other two age-hardening alloys, PH13-8Mo and Inconel alloy 718, would be much reduced if a complete heat-treating cycle after welding is required. It appears that a suitable aging treatment can be devised which will make it unnecessary to solution-treat prior to aging after welding the 12Ni - 5Cr - 3Mo alloy, although this is not clearly established.

Table 7.22 and Figure 7.22 compare some properties of this alloy with those of PH13-8Mo and Inconel alloy 718. The 12-5-3 (heat 01378) shows the lowest tensile strength, is intermediate in yield strength, shows little or no orientation effects in tensile tests but some in impact tests, and has the best overall Charpy V-notch energy absorption values.

If the alloy responds favorably relative to the foregoing considerations, achieves the low cycle fatigue life estimated for it, and continues to show the radiation resistance found in early tests at NRL,²² it must be considered a primary candidate for advanced pressure vessels.

In any case, continued consideration of this alloy is planned with emphasis on determining DWTT, low-cycle fatigue behavior, radiation effects, weldability, and weld properties in heavy sections.

PH13-8Mo

Studies of PH13-8Mo have involved one heat (heat No. VC5281) of 1.27-cm-thick plate and one heat of wire filler metal (heat No. 5178). The alloy showed the highest room-temperature tensile and yield strengths, but also the highest degree of anisotropy. Its Charpy V-notch impact energy absorption level fell somewhat more rapidly with temperature than the 12-5-3 alloy.

PH13-8Mo developed the highest weld strength and had the best joint efficiency (98%), based on an average plate strength of the two orientations tested. It is not yet clear, however, whether the alloy will develop satisfactory properties after welding by aging alone. Weldments planned for the 2.54-cm-thick plate will be used to further evaluate this question. Aging studies on parent metal indicate that for aging temperatures which produce adequate toughness (e.g., 565°C), the alloy ages quite rapidly to a very high level and then

²²L. E. Steele, J. R. Hawthorne, R. A. Gray, "Neutron Irradiation Embrittlement of Several Higher Strength Steels," NRL-6419, September 7, 1966.

TABLE 7.22
COMPARISON OF ROOM-TEMPERATURE PROPERTIES OF THREE ALLOYS IN PLATE AND WELD JOINT^a

Heat Treatment ^b	Orientation		Variation in		Plates		Welded Joint		Joint		
	to Rolling Direction ^c	Tensile Strength, %	Strength, kg/cm ²		Elongation in 4D, %	CVN Energy, m-kg	Strength, kg/cm ²		Elongation in 4D, %	CVN Energy, m-kg	Efficiency, %
			Tensile	Yield			Tensile	Yield			
12Ni - 5Cr - 3Mo (2.54 cm)											
A	T	5	11,900	11,400	22	14.7	11,000	10,400	14	8.5 - 11.0	92
	P		12,550	12,250	22	9.7	11,000	10,400	14	8.5 - 11.0	92
B	T	0	12,600	12,200	19	12.7	-	-	-	-	-
	P		12,600	12,200	19	10.0	-	-	-	-	-
C	-	-	-	-	-	-	11,840	11,250	14	-	93 ^e
PH13 - 8Mo (1.27 cm)											
D	T	12	15,500	14,400	18	10.7	14,200	12,250	11	6.1	98
	P		13,700	13,200	20	9.7	14,200	12,250	11	6.1	98
Inconel 718 (2.54 cm)											
E	T	0	13,300	9,900	13	1.6	10,600	9,500	12	1.7 est.	80
	P		13,500	9,650	15	2.8	10,600	9,500	12	1.7 est.	80
F	T	2	14,350	12,970	18	1.3	12,600	10,550	7	2.8	87 ^f
	P		14,700	11,900	21	2.7	12,600	10,550	7	2.8	87 ^f
G	T	2	13,900	11,300	19	-	-	-	-	-	-
	P		13,590	10,000	24	-	-	-	-	-	-

^a Average properties.

^b Heat treatment A - Age at 480°C - 3 hr - air cool, weld direct aged.

B - A + 480°C - 3 hr - air cool.

C - A + 450°C - 24 hr - air cool.

D - Age at 565°C - 4 hr - air cool.

E - Heat Treatment I, see Table 7.14 for details.

F - Heat Treatment II, see Table 7.15 for details.

G - Heat Treatment III, see Table 7.16 for details.

^c T = Transverse, P = Parallel.

^d Joint efficiency = tensile strength of joint/tensile strength of base metal x 100.

^e Treatments differ, but other studies showed hardness to be about the same. Value is included as example of what can be expected.

^f Weld double-aged directly after welding per heat treatment II.

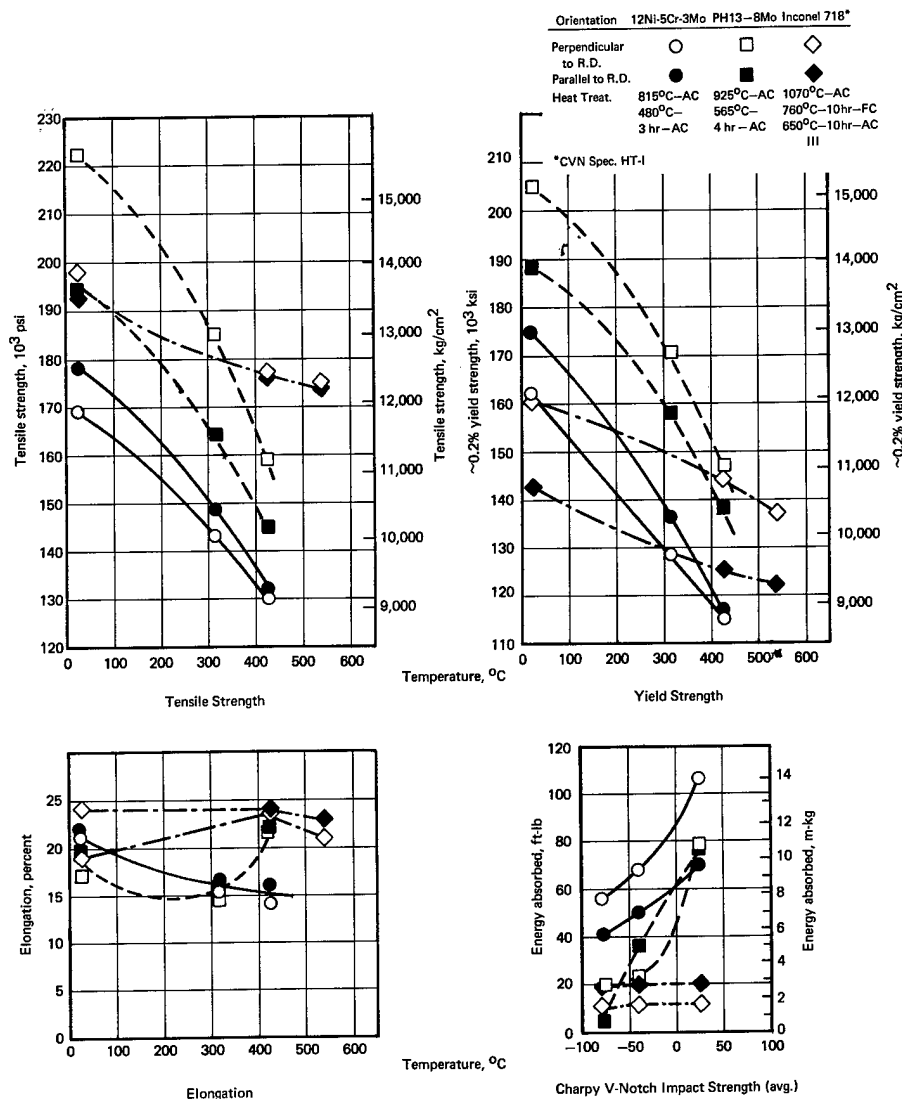


Fig. 7.22 — Comparison of tensile and impact properties of 12Ni — 5Cr — 3Mo, PH13 — 8Mo, and Inconel 718 alloys at various temperatures

overages to a significant degree within about a 20-hour period. This type of aging behavior is not favorable for heavy, complex shapes.

The estimated low-cycle fatigue behavior and indicated radiation resistance of PH13-8Mo²³ appear to favor its consideration as an advanced pressure vessel material.

Continued evaluation of this alloy is planned for the immediate future, with emphasis on further delineating aging behavior, weldability, weld properties, DWTT, preliminary low-cycle fatigue characteristics, and completing radiation effects studies currently in process.

INCONEL ALLOY 718

Investigation of Inconel alloy 718 has involved one composition of plate and one lot of filler metal. Figure 7.22 and Table 7.22 show a comparison of certain properties of Inconel alloy 718 with the PH13-8Mo and 12Ni — 5Cr — 3Mo alloys. Tensile properties of this alloy

²³Unpublished data, NRL.

are only slightly lower than those of PH13-8Mo at room temperature but, as expected, they eventually exceed that alloy as test temperature increases. The low toughness values for both parent metal and welds place the potential of this alloy in some question, however. An alternate heat treatment (III) expected to improve toughness is being investigated. Toughness values do not change significantly with temperature nor are they apparently worsened by radiation to approximately 10^{19} n/cm² ($E_n \geq 1$ Mev). Drop-weight tear tests will be conducted at NRL for additional information on the toughness of this fcc alloy.

Weld joint properties of Inconel alloy 718 show welding efficiencies of 80 percent with heat treatment I and 87 percent with heat treatment II. No testing has been done on weldments given heat treatment III. Compared to the parent metal, weld joint properties of Inconel alloy 718 show lower tensile ductility and reduced toughness.

No new work is contemplated on this alloy in the immediate future, although efforts will be made to complete studies already initiated.

7.4 SUMMARY AND CONCLUSIONS

The following data have been obtained on approximately 2.54-cm-thick ^{Al1 heat A} plate of 12Ni - 5Cr - 3Mo, PH13-8Mo, and Inconel alloy 718, relative to the potential of these candidate high-strength materials for advanced pressure vessels.

12Ni - 5Cr - 3Mo

The 12Ni - 5Cr - 3Mo alloy possesses ^{FCC} aging characteristics which appear to be suited to the uniform aging of heavy sections. Its tensile properties and toughness are most promising. ^{FCC} Low-cycle fatigue data and effects of irradiation on toughness remain to be determined. The alloy gives ^{FCC} evidence of adequate structural stability at temperatures up to at least 315°C. The weldability of the 12-5-3 composition with 12-3-3 filler metal is good but the resulting weld efficiency should be even better if a filler metal composition (12-5-3) matching the base metal is employed. Further data are necessary to indicate whether post-weld aging alone will produce adequate properties.

The 12-5-3 alloy continues to be regarded as a promising candidate for advanced pressure vessels, and will be evaluated in thicknesses ≥ 10 cm.

PH13-8Mo

The ^{SS} aging characteristics of PH13-8Mo, at least for aging temperatures which produce high toughness levels, may not be suited to the uniform aging of heavy sections. Excellent tensile properties and good toughness can be developed in the alloy. Low-cycle fatigue data and effects of irradiation on toughness remain to be determined. PH13-8Mo appears acceptably stable structurally upon longtime heating at temperatures to 425°C. The alloy has good weldability and weld strength with filler metal of matching composition; weld ductility and toughness are only fair. It is not yet clear whether aging alone will be an acceptable post-weld heat treatment.

Further qualification of this alloy will be made on a 2.54-cm-thick plate, before heavy section studies are considered.

INCONEL ALLOY 718

Excellent strength properties characterize Inconel alloy 718, particularly at higher temperatures. It is much superior to the 12-5-3 alloy or PH13-8Mo in this respect. Its toughness is quite low, based on Charpy V-notch tests, under two conditions of heat treatment; a third ^{N.B.} heat treatment is being evaluated for toughness. Initial radiation effects indicate no reduction in toughness levels. ^{N.B.} Low-cycle fatigue data remain to be determined. The alloy apparently possesses good structural stability at temperatures to at least 540°C. In-

Inconel alloy 718 developed sound welds with filler metal of matching composition, although weld strength and toughness were significantly lower than those of the parent metal.

No new work will be initiated on this alloy; studies presently underway will be completed.

A heat-treatable steel, ^{F1C} HP 9Ni - 4Co - 0.20C, has been added to the program.

Consideration has been given to the types of failure which need to be prevented in pressure vessel applications, and special material properties which are related, e.g., strain-hardening coefficient, dynamic yield strength, and plane strain fracture toughness. It is estimated that the 12-5-3 and PH13-8Mo alloys, at least, possess satisfactory low-cycle fatigue behavior, particularly if dynamic yield strength and the Peterson Cubic relationship can be employed in applying mean stress corrections.) *end*

7.5 PLANS AND RECOMMENDATIONS

Prepare additional weldments of 2.54-cm-thick plate of the 12-5-3 alloy using filler metal of matching composition.

Initiate preparation for welding of 10-cm-thick plate of 12-5-3 alloy.

Complete initial property determinations on the 10-cm-thick plate of 12-5-3 alloy.

Continue heat-treating studies on 12-5-3 and PH13-8Mo alloys.

Prepare weldments of 2.54-cm-thick plate of PH13-8Mo.

Continue study of heat treatment influence on toughness of Inconel alloy 718.

Complete initial determination of irradiation effects on toughness of 12-5-3 and PH13-8Mo.

Complete preparation of low-cycle fatigue specimens of 12-5-3, PH13-8Mo, and Inconel alloy 718.

Complete preparation of DWTT specimens of 12-5-3, PH13-8Mo, and Inconel alloy 718.

8. PHYSICO-CHEMICAL STUDIES OF CLAD UO_2 IN POTENTIAL MELTDOWN ENVIRONMENTS

(1175)

J. F. White*

The objective of this program is to study the behavior of zirconium-alloy-clad UO_2 fuel elements in steam and steam plus air from 1000°C to the melting point of UO_2 . This includes measurement, when necessary, of physical and mechanical properties of the cladding, the oxidized cladding, and UO_2 to their respective melting points.

During the period covered by this report, CY-67, the properties of stainless steel cladding material were also investigated. Since recent reactor designs have employed Zircaloy-4 exclusively for all claddings, spacers, and coolant channels, the effort on stainless steel property measurements is being phased out of the program.

The behavior of zirconium-alloy-clad and stainless-steel-clad UO_2 fuel elements during temperature excursions to the melted condition in the presence of steam or steam plus air has not been studied sufficiently to permit suitable hazard analyses when loss of coolant occurs. This program is being conducted to investigate the reactions that occur during meltdown in these atmospheres at heating rates which approximate those likely to be encountered in nuclear afterheat temperature excursions when the coolant has been lost. These investigations include the following studies:

1. Dynamic testing to determine the behavior of clad UO_2 when oxidized by steam, reactions between the various reactor core components, internal pressure effects, hydrogen release by the metal – steam reactions, and flow aspects of the molten constituents.
2. Measurements of the rates of metal – steam reactions, oxidation of UO_2 by steam, and reactions between core constituents.
3. Property measurements, including thermal properties of UO_2 , Zircaloy-4, and Type 304 stainless steel, and the mechanical properties of Zircaloy-4 and Type 304 stainless steel.

8.1 DYNAMIC TESTING OF ZIRCONIUM-BASE ALLOYS (K. M. Emmerich and E. F. Juenke)

INTERNAL PRESSURE EFFECTS

The effects of internal gas pressure and temperature on the deformation behavior of Zircaloy-4 cladding material during a thermal surge were investigated using the pressure test facility shown schematically in Figure 8.1. Figure 8.2c shows a typical tube sample prepared for testing. The composition and characterization of the Zircaloy-4 material used in these experiments meet LOFT specifications reported previously.¹ Details of the experimental procedure have been reported.²

*Project leader and principal investigator.

¹"Fifth Annual Report – High-Temperature Materials Program, Part A," GE-NMPO, GEMP-400A, February 28, 1966, p. 205.

²"AEC Fuels and Materials Development Program Progress Report No. 71," GE-NMPO, GEMP-1002, December 29, 1967, p. 123.

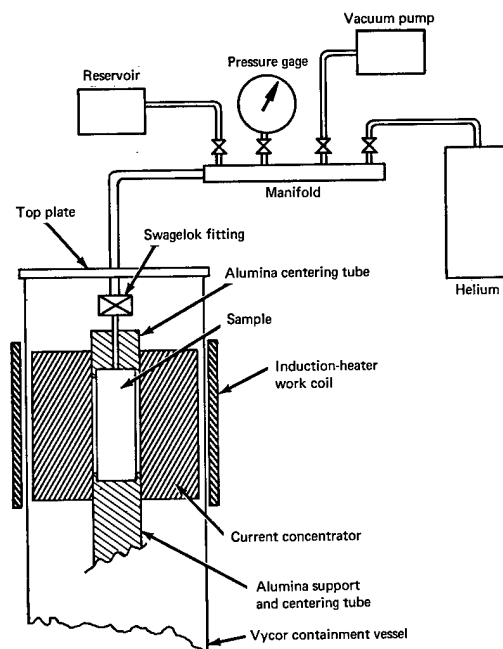


Fig. 8.1 — Schematic diagram of pressure test circuit

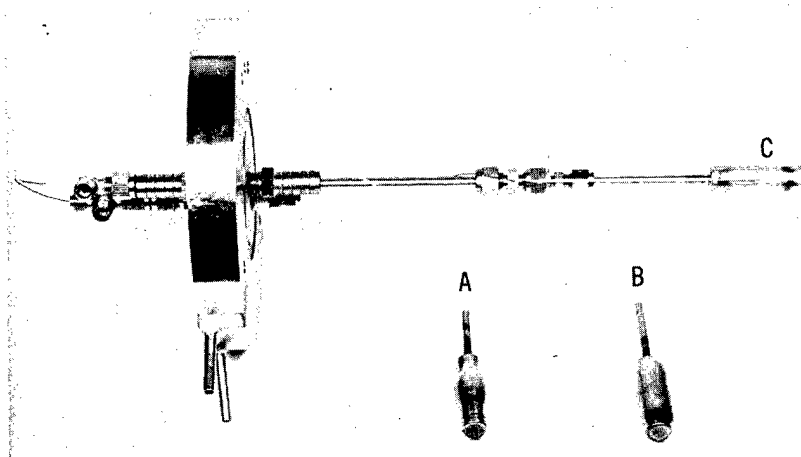


Fig. 8.2 — Typical pressure-test samples of Zircaloy-4 before and after testing at 1.11 kg/mm^2 . Sample length is 5.7 cm. (Neg. P67-11-1)

- a. Heated at 0.3°C per second to 668°C .
- b. Heated at 20°C per second to 753°C .
- c. Unheated.

In this series of tests, heating rates of 20°C and 0.3°C per second and internal helium pressures from 0.024 to 1.21 kg/mm^2 were used. The tubes were heated at a constant rate under fixed pressure in an argon atmosphere until 34 percent diametral expansion occurred, approximately the expansion which would result in major blockage of coolant channels in a typical reactor. Results for this series of tests are given in Table 8.1 which lists final internal pressure, surface (maximum) temperature when the sample had expanded 34 percent diametrically, tensile strength of the material at the maximum temperature, and calculated effective stress. Two typical samples tested at the same internal pressure ($\sim 1.11 \text{ kg/mm}^2$) are compared with an untested sample in Figure 8.2. The 34 percent diametral expansion was

reached at 668°C for sample A, heated at 0.3°C per second; and at 753°C for sample B, heated at 20°C per second.

Tensile tests at various constant-load levels were conducted on Zircaloy-4 for comparison with the internal pressure tests. In these experiments, sheet specimens cut parallel to the rolling direction were heated from room temperature to rupture temperature at rates of approximately 0.3°, 3°, and 20°C per second. Data are presented in Table 8.2.

In both the pressurized-tube tests and the constant-load tensile tests, the temperature attained at failure (34 % expansion in the case of the pressurized tubes or rupture of the tensile specimens) showed heating rate dependence. At fixed pressures or load levels, higher maximum temperatures were obtained for the higher heating rates in all instances.

TABLE 8.1
EFFECTS OF INTERNAL PRESSURE ON ZIRCALOY-4 TUBING HEATED IN ARGON

Heating Rate, °C/sec	Internal Pressure (Gage), ^a kg/mm ²	Maximum Temperature, °C	Calculated Effective Stress, ^a kg/mm ²	Tensile Strength, at Maximum Temperature, kg/mm ²
0.3	1.125	666	8.114	6.9
0.3	1.118	668	8.065	6.9
0.3	0.721	723	5.205	4.6
0.3	0.541	758	3.901	3.7
0.3	0.214	860	1.550	1.8
0.3	0.144	915	1.040	1.4
0.3	0.065	924	0.469	1.2
0.3	0.065	933	0.469	1.15
0.3	0.074	953	0.534	1.0
0.3	0.037	1020	0.267	0.68
0.3	0.036	1027	0.260	0.68
0.3	0.025	1187	0.181	0.38
23.1	1.209	737	8.727	4.0
22.8	1.055	753	7.615	3.8
20.9	0.703	820	5.074	2.5
22.0	0.352	881	2.541	1.6
21.9	0.352	886	2.541	1.6
20.4	0.141	955	1.031	0.99
21.5	0.141	1003	1.013	0.74
22.3	0.141	1024	1.013	0.68
22.6	0.037	1165	0.263	0.39
20.1	0.037	1282	0.266	0.29

^aBased on pre-test tube dimensions.

TABLE 8.2
CONSTANT LOAD CONTROLLED HEATING-RATE TEST
RESULTS FOR ZIRCALOY-4^a IN ARGON

Sample No.	Heating Rate, °C/sec	Initial Stress, kg/mm ²	Rupture Temperature, °C	Elongation, %	DPH Hardness (2-1/2 kg)	
					Before Test	After Test
22	0.3	1.195	945	68	209	245
18	3.0	6.327	765	48	220	215
19	3.0	12.654	665	28	225	206
17	3.0	3.164	900	54	224	218
15	3.0	1.195	1020	81	198	223.5
16	3.0	0.504	1120	102	221	206
21	20.0	1.195	1120	69	227	218
23	20.0	0.504	1235	102	215	200

^aSpecimens were 0.076 cm thick, 0.63 cm wide, with a gage length of 2.54 cm.

Data obtained in the two series of tests were analyzed to determine the inter-relationship of applied stress, rate of uniform heating, total strain, and maximum temperature. This was accomplished by examining the theoretical solutions for a uniaxial test under constant load and a linearly increasing temperature, and a test of a thin-walled tube with constant internal pressure and linearly increasing temperature under the following assumptions:

1. Deformations are primarily those due to second-stage creep.
2. Second-stage creep behavior can be represented by an equation of the form

$$\frac{d\epsilon}{dt} = A e^{-Q/RT} \sigma^n \quad (8.1)$$

where

ϵ = strain
 t = time
 T = absolute temperature
 R = gas constant
 Q = activation energy for creep
 σ = effective stress *
 A and n = material parameters.

3. Deformations are small.

4. For the case of the tube, the radial stress is negligible, i. e., $\sigma_r \approx 0$.

Under these assumptions, and letting $T = \beta t$, the governing equations are: for the uniaxial case,

$$d\epsilon_x = A e^{-Q/R\beta t} \sigma^n dt \quad (8.2)$$

and for the tube case,

$$d\epsilon_\theta = \frac{\sqrt{3}}{2} A e^{-Q/R\beta t} \sigma_e^n dt \quad (8.3)$$

where

$\sigma_e = \sqrt{3} \frac{p\rho}{h}$
 p = pressure
 ρ = inside radius
 h = wall thickness
 ϵ_θ = hoop (tangential) strain
 ϵ_x = axial strain

Letting $Q/RT = z$ and integrating these equations [(8.2) and (8.3)], gives the general result

$$\epsilon = \frac{a S^n Q}{\beta R} \left[-\frac{e^{-z}}{z} - \{-Ei(-z)\} \right]_{z=z_1}^{z=\infty} \quad (8.4)$$

where, for the uniaxial case and the tube case, $a = A$ and $\sqrt{3}/2 A$, $S = \sigma$ and σ_e , and $\epsilon = \epsilon_x$ and ϵ_θ , respectively.

*Based on the von Mises flow criterion, the effective stress for the multi-axial (tube) case is

$$\sigma_e = \frac{1}{\sqrt{2}} [(\sigma_1 - \sigma_2)^2 + (\sigma_2 - \sigma_3)^2 + (\sigma_3 - \sigma_1)^2]^{0.5},$$

where $\sigma_1, \sigma_2, \sigma_3$ are the principal stresses which, for the case of the tubes, are the radial (σ_r), hoop (σ_θ), and axial (σ_x) stresses.

The exponential integral function may be approximated for $z_1 > 10$ by

$$-Ei(-z) = e^{-z_1} \left\{ \frac{1}{z_1} - \frac{1}{z_1^2} + \frac{2!}{z_1^3} - \frac{3!}{z_1^4} + \dots \right\} \quad (8.5)$$

Since Q is the order of $40 T_m$ cal/mole, z_1 will always be much greater than 10. Therefore, neglecting all but the first two terms of the expansion, equation (8.4) becomes:

$$\epsilon \cong \frac{a S^n RT^2}{\beta Q} e^{-Q/RT} \quad (8.6)$$

Taking the logarithms of both sides and rearranging terms gives:

$$\ln S = \frac{1}{n} \left[\ln \epsilon - \log \frac{aR}{Q} + \ln \beta - 2 \ln T + \frac{Q}{RT} \right] \quad (8.7)$$

The exponent n for stress dependence and the activation energy Q are essentially constant for temperatures above about one half the absolute melting point (788°C for Zircaloy-4).

Logarithmic (true) strain, $\ln(1 + \epsilon)$, is more valid in this case than engineering strain because the expansion cannot be considered small. Accordingly, the combined data in Tables 8.1 and 8.2 for temperatures above 788°C were fitted to an equation of the form of (8.6), giving the final equation with a standard deviation of ± 40 percent:

$$S = 0.0113 k \exp \left(\frac{78,470 \pm 8900}{3.96 RT} \right) \left(\frac{r \epsilon_\ell}{T^2} \right)^{1/3.96} \quad (8.8)$$

where $k = 1$ for tensile tests and $(\sqrt{3}/2)^{1/3.96}$ for pressurized tube tests, and

$$\begin{aligned} S &= \text{stress, kg/mm}^2 \\ R &= \text{gas constant, } 1.987 \text{ cal/mole-}^\circ\text{K} \\ T &= \text{temperature, } ^\circ\text{K} \\ r &= \text{heating rate, } ^\circ\text{K/sec} \\ \epsilon_\ell &= \text{logarithmic strain} = \ln(1 + \epsilon). \end{aligned}$$

The logarithm of stress versus $1/T$ for this equation is shown in Figures 8.3 and 8.4 for the several heating rates used in the tests described above. Experimental data for all temperatures are also plotted on these figures. A stress dependence (exponent n) of 3.96 and an activation energy (Q) of 78.5 kcal/mole for creep in Zircaloy-4 are indicated by this analysis. The value of n agrees well with the expected value of 4.0,³ and the value of the activation energy agrees with the estimated value of 81 kcal/mole for zirconium self-diffusion, using the approximation $Q = 38T_m$, where T_m is the melting point in $^\circ\text{K}$.⁴

This analysis does not consider the effect of the α - β zirconium phase transformation which may occur in the temperature range of 900° to 1000°C in Zircaloy-4. Tensile data appear to show a difference in behavior above and below this range, but separate analyses of the two temperature regions are of dubious validity, due to the limited number of data points. The pressurized tube experiments showed no difference in behavior in the two temperature regions.

EFFECT OF OXIDATION ON TUBE DEFORMATION

The effects of oxidation on the deformation behavior of Zircaloy-4 tubing were studied under dynamic heating conditions. Initial tests were made with 0.3°C/sec heating rates and at various internal pressures of 0.040 to 0.141 kg/mm^2 to study the effect of steam

³J. M. Dorn, editor, The Mechanical Behavior of Materials at Elevated Temperatures, McGraw-Hill, 1961, p. 95.

⁴Ibid., p. 88.

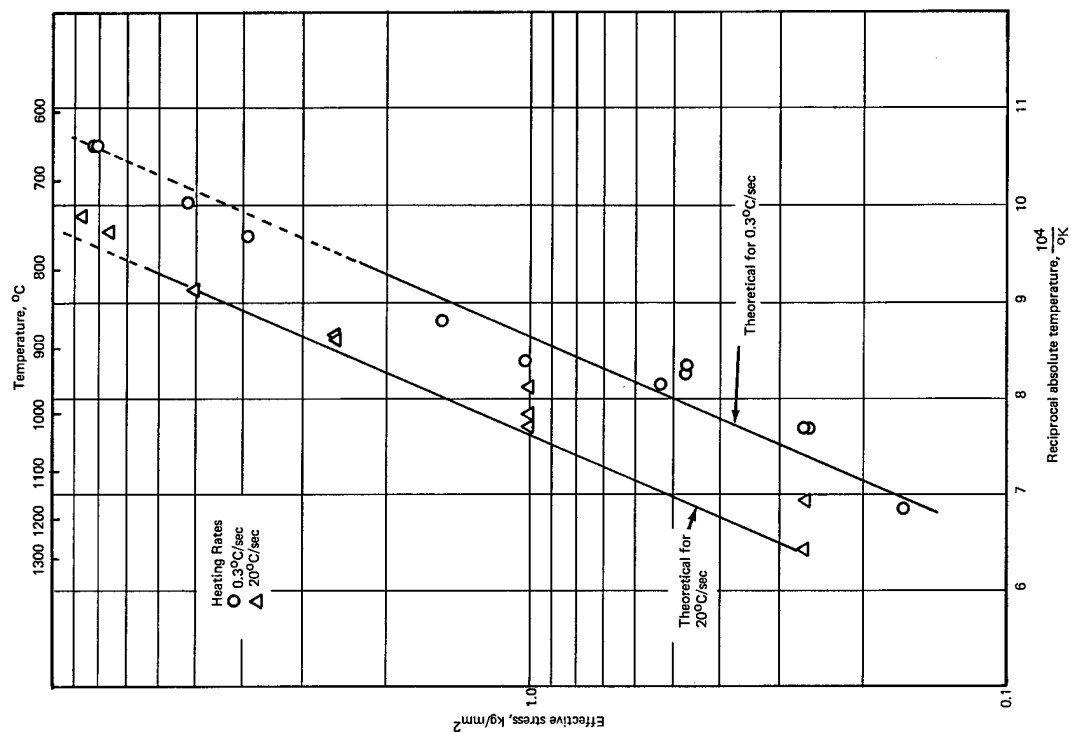


Fig. 8.4 — Effective stress versus temperature for constant pressure tube tests in argon + 3 vol % H₂

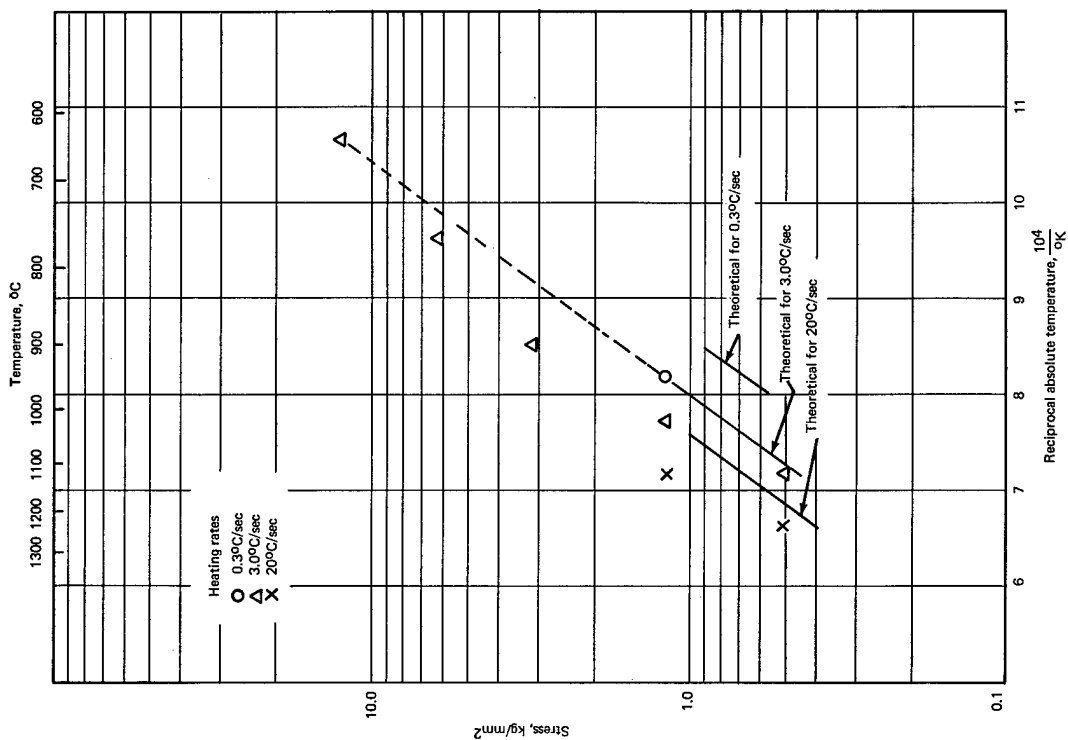


Fig. 8.3 — Stress versus temperature for constant load tensile tests in argon

atmosphere. Results of these measurements are shown in Table 8.3 with the results of comparison tests in argon. These data show that in a steam atmosphere failure of partially oxidized Zircaloy-4 tubes due to internal pressure will occur at temperatures higher than predicted from the base metal strength data. Typical fracture failure for a tube heated in steam is compared in Figure 8.5 to a sample heated in argon.

TABLE 8.3
EFFECTS OF INTERNAL PRESSURE ON ZIRCALOY-4
TUBING HEATED AT 0.3°C PER SECOND

Atmosphere	Internal Gage Pressure, kg/mm ²	Maximum Temperature, °C	Diametral Expansion, %
Argon	0.040	1180	33
Steam	0.040	1475	12.5 ^a
Argon	0.057	1055	34
Steam	0.058	1460	11.4 ^a
Argon	0.078	970	34
Steam	0.077	1035	18.6 ^a
Argon	0.141	905	34
Steam	0.141	905	33

^aFailed by fracture.

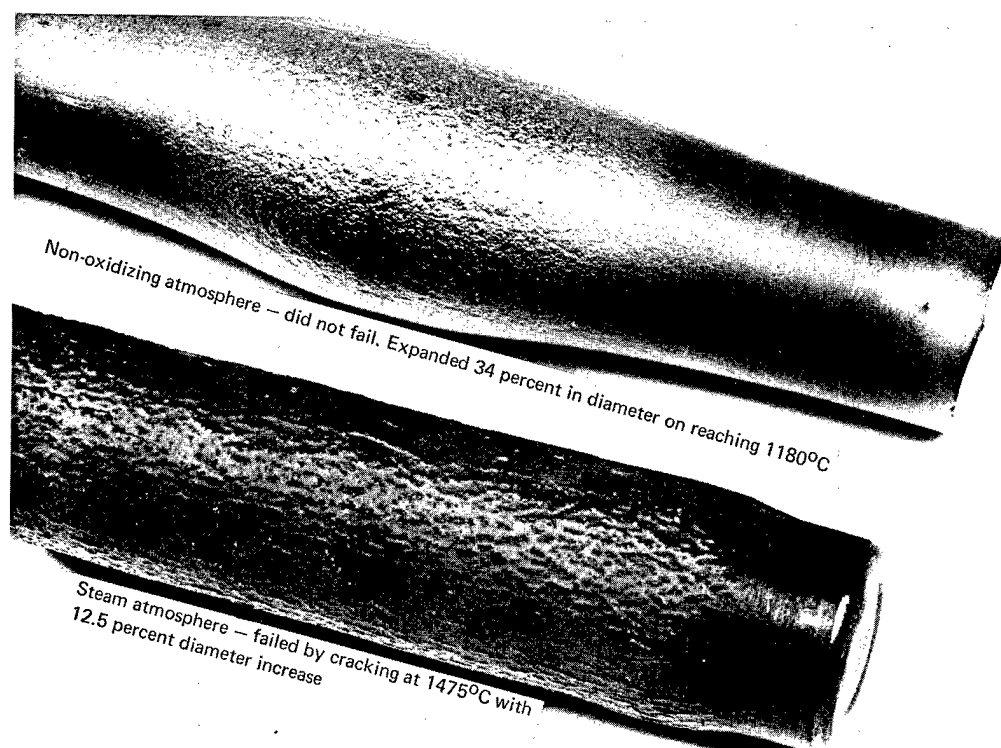
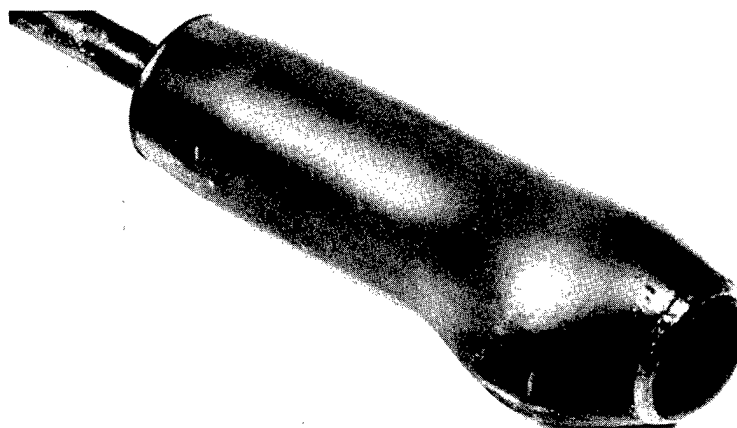


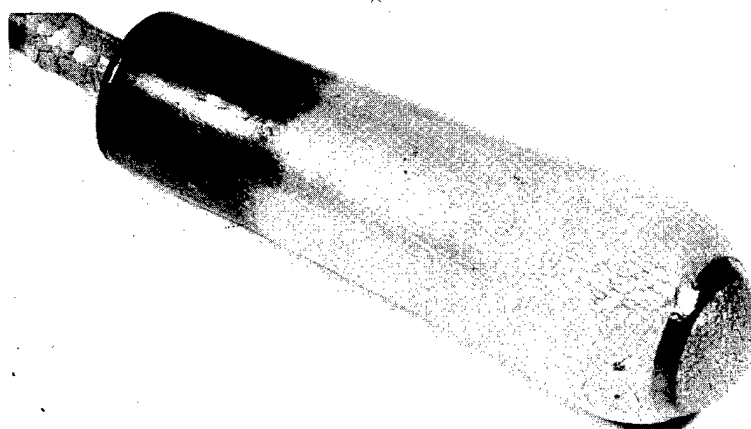
Fig. 8.5 — Effect of atmosphere on the failure of Zircaloy-4 tubes heated at 0.3°C/sec with 0.040 kg/mm² internal pressure (Neg. 68-1-42)

The effects of atmosphere on the expansion rate of Zircaloy-4 tubes at constant temperature and constant internal pressure were studied in argon and in steam by measuring the rate of diametral expansion with a cathetometer. Test temperatures selected for a given pressure were about 50°C below the maximum temperature achieved in the argon atmosphere dynamic heating tests at 0.3°C per second. Two comparisons have been made between the behavior of Zircaloy-4 in argon and in steam. At 0.131 kg/mm^2 (195 psig), a Zircaloy-4 tube heated at 860°C required 260 minutes for 34 percent expansion in steam, but only 74 minutes in argon. At 995°C and 0.051 kg/mm^2 (72 psig), 34 percent expansion required 106 minutes in steam, compared to 20 minutes in argon. Figure 8.6 shows the post-test appearance of these latter two samples.

These tests show that (1) under the dynamic conditions of a thermal surge, oxidation permits the Zircaloy cladding to achieve higher temperatures before failure, and (2) at constant temperature and pressure, the rate of expansion is retarded by oxygen absorption in the Zircaloy. Figure 8.6 shows that the presence of steam results in a more uniform expansion of the tube. Steam oxidation, like strain hardening, results in more uniform expansion.



a. Heated in argon required 20 minutes for 34% expansion (Neg. P68-1-34A)



b. Heated in steam required 106 minutes for 34% expansion (Neg. P68-1-34B)

Fig. 8.6 — Zircaloy-4 tubes heated at 995°C with an internal pressure of 0.051 kg/mm^2

TESTING OF 50-cm-LONG ZIRCALOY-4-CLAD UO_2 FUEL ELEMENTS

A furnace capable of heating a 50-cm-long Zircaloy-4-clad UO_2 sample in steam was constructed for simulating the axial thermal gradient imposed upon a fuel element in a reactor loss-of-coolant accident. This equipment is being used to determine whether there are corrosion rate effects in Zircaloy-4 cladding due to a hydrogen boundary layer buildup, and to establish effects of internal pressure, conditions under which cladding rupture occurs with loss of internal pressure, and behavior under meltdown. Figure 8.7 is a schematic drawing of the furnace; construction and operation details were reported previously.⁵ Figure 8.8 shows a typical 50-cm-long Zircaloy-4-clad UO_2 sample assembled for test.

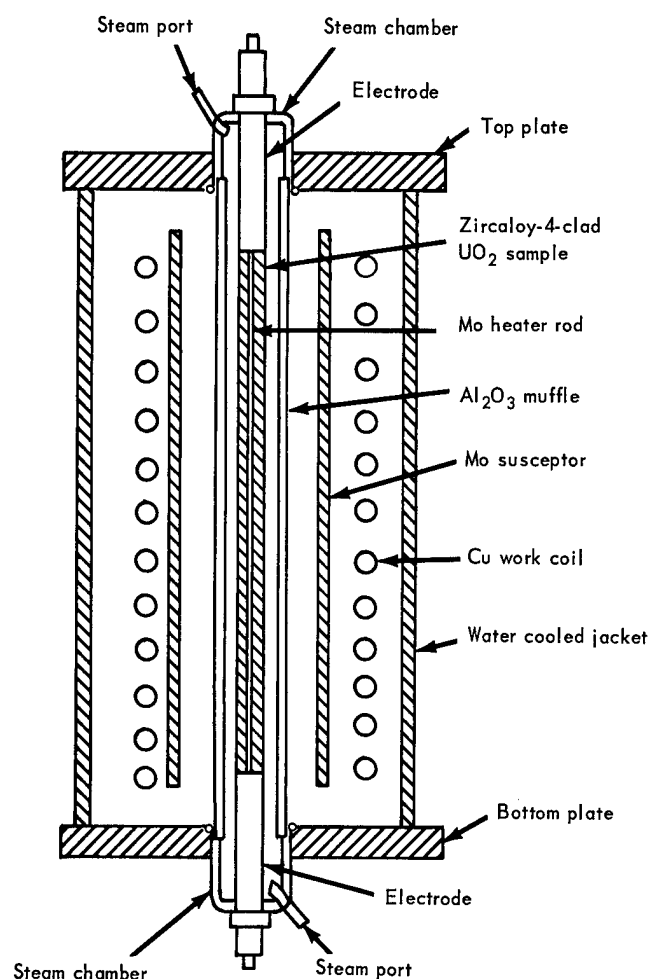


Fig. 8.7 — Schematic diagram of furnace for simulating reactor thermal and atmospheric environment during a loss-of-coolant accident

⁵"AEC Fuels and Materials Development Program Progress Report No. 69," GE-NMPO, GEMP-69, September 30, 1967, p. 139.

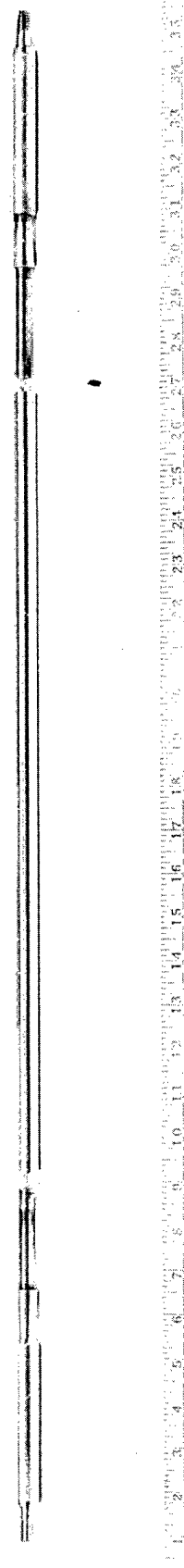


Fig. 8.8 — Typical 50-cm-long Zircaloy-4-clad UO_2 sample assembled for test (Neg. P67-7-24B)

Oxidation tests were run to study thickness of the oxide layers formed on 50-cm-long Zircaloy-4-clad UO_2 samples heated at rates of 0.3°C and 1.0°C per second in steam flowing at the rate of 3.4 standard liters (6×10^{-3} lb) per minute. The oxide thickness at the midpoint of the sample and at 7.6 cm from each end were determined metallographically and are summarized in Table 8.4. Circumferentially the thickness varied less than 50 percent. Longitudinally the oxide thickness at the midpoint, the hottest portion of the specimen, was from 1.5 to 2.5 times the thickness at the ends of the tube. For these tests, no difference was observed between the oxide thicknesses at the two ends. Consequently, assuming laminar flow under the test conditions, there was no evidence of a hydrogen-rich boundary layer at the metal - gas interface.

TABLE 8.4
VARIATION OF OXIDE THICKNESS ON 50-cm-LONG
ZIRCALOY-4-CLAD UO_2 ELEMENTS HEATED IN STEAM

Heating Rate, $^\circ\text{C}/\text{sec}$	Maximum Temperature, $^\circ\text{C}$			Oxide Thickness, microns ^a		
	Top	Middle	Bottom	Top ^b	Middle	Bottom
0.3	786	900	776	<13	13	<13
0.3	934	1098	922	19	32	16
0.3	c	1313	1222	25	86	60
0.3	c	1500	1430	117	200	102
1.0	c	1100	923	13	19	13
1.0	c	1300	1170	32	70	28
1.0	c	1510	1475	66	140	91
1.0	c	1510	1300	73	133	60

^aAverage of four circumferential measurements.

^bSteam entered furnace from the top.

^cTop thermocouple failed before maximum temperature was attained.

DYNAMIC TESTING OF IRRADIATED ZIRCALOY-2 AT CONSTANT INTERNAL PRESSURE

A test fixture for pressure testing irradiated Zircaloy-2 tubing at various heating rates is being constructed. Test pieces will be Zircaloy-2 and fuel rod cladding tubes from the spent fuel of an industrial reactor from which UO_2 has been removed. Tubes will be cleaned and cut to 8-inch lengths. The material is highly radioactive and must be handled remotely; equipment is being designed with the simplified assembly and disassembly features shown in Figure 8.9. The Zircaloy tube will be pressurized with helium from a line attached to the bottom of the fixture. The top and bottom of the tube will be made pressure tight with O-ring seals. The thermocouple will be attached in the form of a loop which is drawn against the sample by a constant weight. This permits about 1 cm of the thermocouple wire from the bead to contact the tubing, thus minimizing errors in temperature measurement arising from thermal losses due to heat transmission along the wires.

8.2 REACTION MECHANISMS AND KINETICS (J. T. Bittel and L. H. Sjødahl)

OXIDATION OF ZIRCONIUM ALLOYS BY STEAM OR AIR

Effects of the variation of steam flow rate and oxygen partial pressure on the oxidation kinetics of zirconium alloys were determined to 1585°C . Studies of Zircaloy-4 in steam were also extended to 1835°C .

Steam Oxidation

A thermogravimetric technique⁶ was used to determine the oxidation kinetics of Zircaloy-4 in steam at various flow rates. Parabolic rate constants determined from these tests are

⁶R. E. Latta, J. T. Bittel, and G. B. Hadesty, "Continuous Recording Strain Gauge Thermobalance," Rev. of Sci. Instr., Vol. 38, No. 11, November 1967, p. 1667.

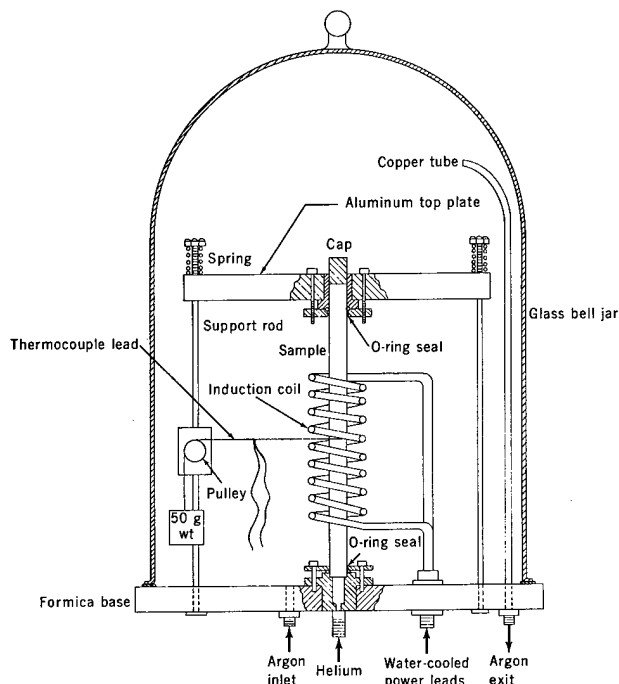


Fig. 8.9 — Furnace assembly for internal pressure tests on irradiated Zircaloy-2 tubing

shown in Table 8.5 and plotted as log rate versus reciprocal temperature in Figure 8.10, along with the curve determined previously for steam oxidation of zirconium alloys.⁷ Results of the steam tests at various flow rates agree with previously reported corrosion data using lower flow rates; this indicates that the steam oxidation rate of Zircaloy-4 is independent of the steam flow rate in the range examined.

Although zirconium would not be expected to hydride appreciably at the temperatures of the steam corrosion tests, Lemmon⁸ reported that part of the hydrogen which formed as a result of the $\text{Zr-H}_2\text{O}$ reaction was found in tested Zircaloy-2 samples; 12.5 percent of the hydrogen formed in a 1600°C test and 6.8 percent in a 1000°C test. Hence hydrogen content of Zircaloy-4 samples tested in steam at 1200°C and at 1600°C was determined by hot extraction analysis. Two samples tested at 1200°C showed 40 and 332 ppm; the 1600°C test sample showed 98 ppm. The highest concentration of hydrogen found, 332 ppm or 1.3 percent of the hydrogen produced, is equivalent to less than 0.5-mg weight gain in this sample. This would have an insignificant effect (0.16%) on the total weight gain. The greater amounts of hydrogen reported by Lemmon may result from his testing in steam at a total pressure of 50 psi (0.035 kg/mm²) or from the fact that Zircaloy-2 absorbs hydrogen more readily than Zircaloy-4.

Tests on the steam oxidation of Zircaloy-4 were extended to 1835°C using solid cylindrical samples in an inductively heated furnace. Experimental details have been reported previously.⁹ A spectrographic analysis of the Zircaloy used in the present tests is given in Table 8.6.

⁷"Sixth Annual Report — High-Temperature Materials Program, Part A," GE-NMPO, GEMP-475A, March 31, 1967, pp. 240–245.

⁸A. W. Lemmon, "Studies Relating to the Reaction Between Zirconium and Water at High Temperatures," BMI-1154, 1957.

⁹GEMP-1002, p. 134.

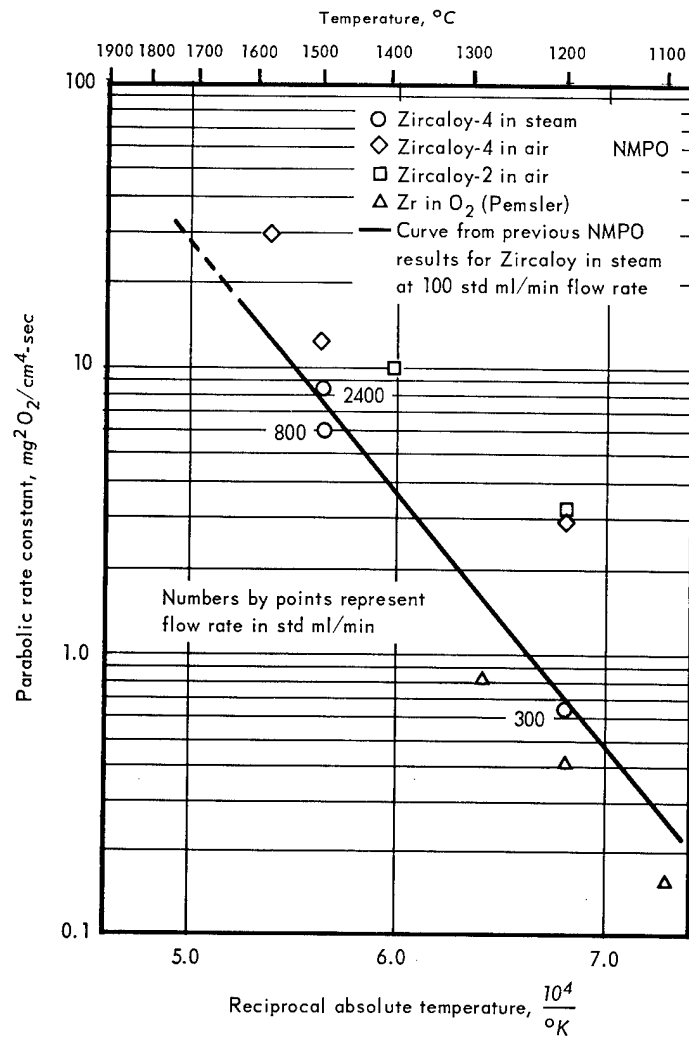


Fig. 8.10 — Oxidation of zirconium alloys by steam and air

TABLE 8.5
RESULTS OF STEAM AND AIR CORROSION
OF ZIRCONIUM ALLOYS

Sample Material	Gas Composition	Gas Flow Rate, std. ml/min.	Temperature, °C	Parabolic Rate Constant, (mg O ₂) ² /cm ⁴ ·sec
Zr-4	Steam	300	1200	0.63
Zr-4	Steam	800	1500	5.96
Zr-4	Steam	2400	1500	8.3
Zr-4	Air ^a	300	1200	2.99
Zr-2	Air ^a	300	1200	3.17
Zr-2	Air ^a	300	1400	9.87
Zr-4	Air ^a	300	1500	12.2
Zr-4	Air ^a	300	1585	29.5
Zr ^b	O ₂	—	1100	0.158
Zr ^b	O ₂	—	1200	0.415
Zr ^b	O ₂	—	1290	0.800

^aDewpoint — 66°C.^bPemsler, gas flow rate unknown.

Test results from the steam oxidation of Zircaloy-4 in this high-temperature range are shown in Table 8.7 and Figure 8.11. Although these results fall nearly within the 95 percent confidence limits calculated from the lower-temperature data,¹⁰ they are about 36 to 70 percent higher than the extrapolated low-temperature Arrhenius curve. This indicates a possible change in controlling mechanism to one with higher activation energy for these higher temperatures. Fitting the $\ln W^2/t$ for the four data points above 1600°C, the previously measured data at 1600°C and 1615°C,¹⁰ and the datum point of Baker¹¹ for 1852°C to a linear equation by least squares, yields:

$$W^2/t = 1.5 \times 10^8 \exp \left(\frac{-60,600 \pm 5,400}{RT} \right) \quad (8.9)$$

where

W = weight gain per unit area, mg/cm²

t = time, sec

R = gas constant, cal/mole-°K

T = temperature, °K

This can be compared to the expression derived for the least-squares fit to the data for temperatures between 1000° and 1600°C¹⁰:

$$W^2/t = 5.56 \times 10^5 \exp \left(\frac{-39,700 \pm 2300}{RT} \right) \quad (8.10)$$

TABLE 8.6

COMPOSITION OF ZIRCALOY-4^a
USED IN OXIDATION STUDIES

Element	Analysis	
	percent	ppm
Sn	1.45	-
Fe	0.186	-
Cr	0.108	-
Fe+Cr+Ni	0.294	-
Al	-	67.0
B	-	0.3
C	-	186.0
Cd	-	< 0.25
Co	-	< 5.0
Cu	-	< 20.0
Hf	-	60.0
Mg	-	< 10.0
Mn	-	< 20.0
Mo	-	< 20.0
Na	-	< 10.0
Ni	-	< 20.0
Pb	-	< 20.0
Si	-	31.0
Ti	-	20.0
V	-	< 20.0
W	-	< 20.0
U	-	< 0.2
Zr	-	Bal

^aIngot analysis provided by vendor.

TABLE 8.7

RESULTS OF STEAM CORROSION OF ZIRCALOY-4
BETWEEN 1500° and 1800°C

Temperature, °C	Time, min	Weight Gain, g	Area, cm ²	Parabolic Rate Constant
				(Kp), (mg O) ² /cm ⁴ -sec
1540	12	0.9827	11.09	10.9
1700	10	1.3687	10.83	26.6
1733	10	1.8820	11.19	47.2
1742	10	1.9041	10.92	50.0
1800	10	1.9437	10.77	54.3

¹⁰GEMP-475A, pp. 240-242.

¹¹L. Baker and L. C. Just, "Studies of Metal-Water Reactions at High Temperatures, III. Experimental and Theoretical Studies of the Zirconium-Water Reaction," ANL-6548, p. 1962.

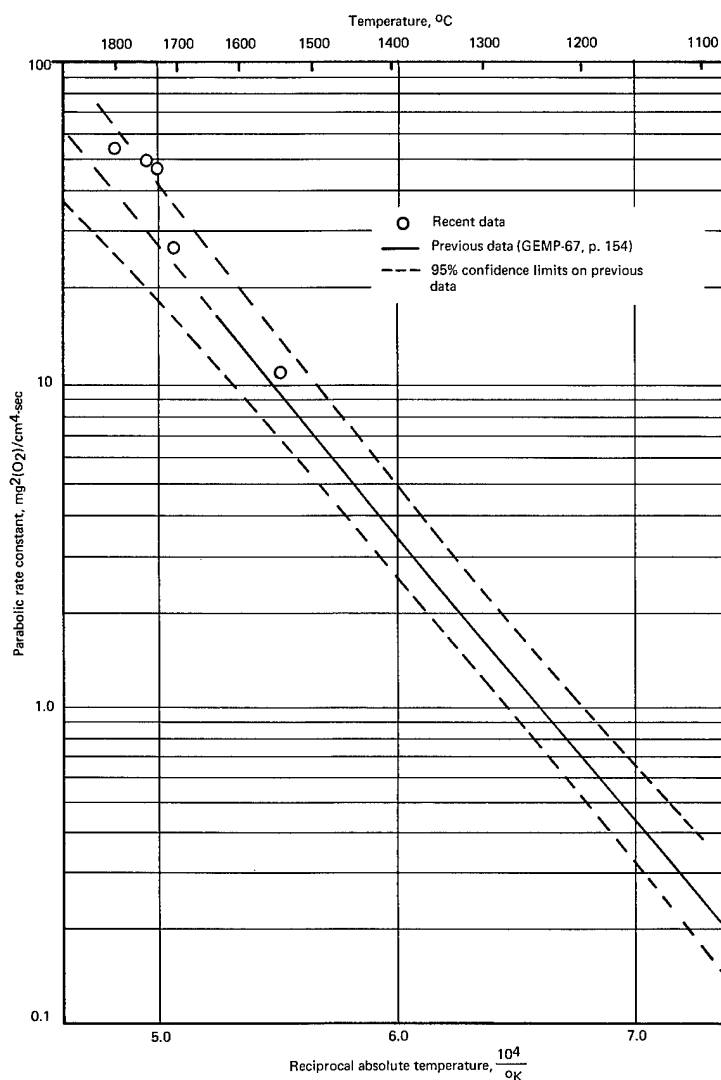


Fig. 8.11 — Parabolic rate constant versus reciprocal temperature for oxidation of Zircaloy-4 by steam.

The oxidation of zirconium and Zircaloy proceeds by a combination of oxygen solution in the metal and growth of an oxide coating. Debuigne, et al.,¹² from investigation of zirconium in oxygen, concluded that diffusion of oxygen in the alpha metal was the rate-controlling step in the temperature range from 668° to 1200°C and that the process is parabolic but has exponents slightly greater than 2. Oxidation rates calculated from his data using an exponent of 2 agree with those of Pemsler¹³ for zirconium heated in oxygen. Although the crystal structure of the oxide films on zirconium are monoclinic at room temperature, the work of Ruh and Garrett on the system Zr-O^{14} predicts that the crystal

¹²J. Debuigne, J. P. Guerlet, and P. Lehr, "Aspects Fundementaux des Phenomenes D'oxydation du Zirconium sous Oxygene Pur," Etude Sur La Corrosion et la Protection Du Zirconium et de Ses Alliages, Presses Universitaires de France, Paris, 1966.

¹³J. P. Pemsler, "Studies on the Oxygen Gradients in Oxidizing Metals, V. The Oxidation of Oxygen Saturated Zirconium," J. Electrochem. Soc., 1966, pp. 1241-1244.

¹⁴R. Ruh and H. J. Garrett, "Nonstoichiometry of ZrO_2 and Its Relation to Tetragonal-Cubic Inversion in ZrO_2 ," J. Am. Ceram. Soc., Vol. 50, No. 5, May 1967, p. 257.

structure is tetragonal above about 1100°C and that it is cubic at temperatures as low as about 1500°C. Klepfer¹⁵ has suggested that since oxygen may diffuse at different rates through the different oxide crystallographic forms, the activation energies for the oxidation process may be different also. If so, the higher rates measured in this present work may be related to the change in crystallographic structures of the oxide film.

Air Oxidation

Corrosion tests in dry (-66°C dewpoint) air flowing at 300 std ml/min were conducted with Zircaloy-4 at 1200°, 1500°, and 1585°C and, for comparison, with Zircaloy-2 at 1200°C and 1400°C. Results of these tests are given in Tables 8.5 and 8.10. Also given, for comparison, are data on steam corrosion at 1200°C and 1500°C, and Pemsler's data on oxygen oxidation of unalloyed zirconium at 1100°, 1200°, and 1290°C. These data show that Zircaloy corrosion in air is more erratic and two to five times as rapid as in steam.

Figure 8.12 shows the microstructure of Zircaloy-4 corroded in air at 1200°C. A sample corroded in steam at the same temperature is shown in Figure 8.13. The coating on the air-tested sample varied greatly in thickness and density around the periphery of a cross section. Figure 8.12a and b show, respectively, the relatively thin, dense reacted layer and the thicker, more porous reacted layer which contains up to 10 percent crescent-shaped separations or large voids. Below the dense areas of coating on the air-tested samples is an oxygen-rich alpha zirconium zone similar to that seen in steam corrosion. Below the more porous oxide is a porous yellow phase identified by X-ray diffraction as zirconium nitride. The oxygen-stabilized alpha-phase metal layer beneath the yellow phase is very thin compared to that observed in the microstructure of steam-oxidized metal. Table 8.8 records measurements of the total sample diameter and of thicknesses of the coating and of the oxygen-stabilized, alpha-phase metal formed at 1200°C in both atmospheres.

TABLE 8.8
ZIRCALOY-4 OXIDIZED FOR 1 HOUR AT 1200°C
IN AIR AND IN STEAM

Atmosphere	Coating Thickness, microns	Alpha-Phase Metal Thickness, microns	Original Diameter, mm	Post-Test Diameter, mm
Air	356 to 1016	0 to 200	12.6	13.0
Steam	200	180	12.6	12.8

The higher rates for air corrosion relative to steam oxidation apparently result from the formation of zirconium nitride and its effect on the coating structure. Nelson¹⁶ reports that zirconium reacts more rapidly with air than with oxygen, producing a mixture of the nitride, oxide, and oxynitride of zirconium. Since Pemsler's results¹⁷ for zirconium in oxygen show even lower rates than those reported here for steam, the higher corrosion rates in air do not result from higher oxygen partial pressure in air, but rather from the presence of nitrogen.

¹⁵H. H. Klepfer, private communication.

¹⁶L. S. Nelson, "Combustion of Zirconium Droplets Ignited by Flash Heating," Western States Section, Combustion Institute, Paper WSS/CI 64-23, 1964.

¹⁷Pemsler, loc. cit.

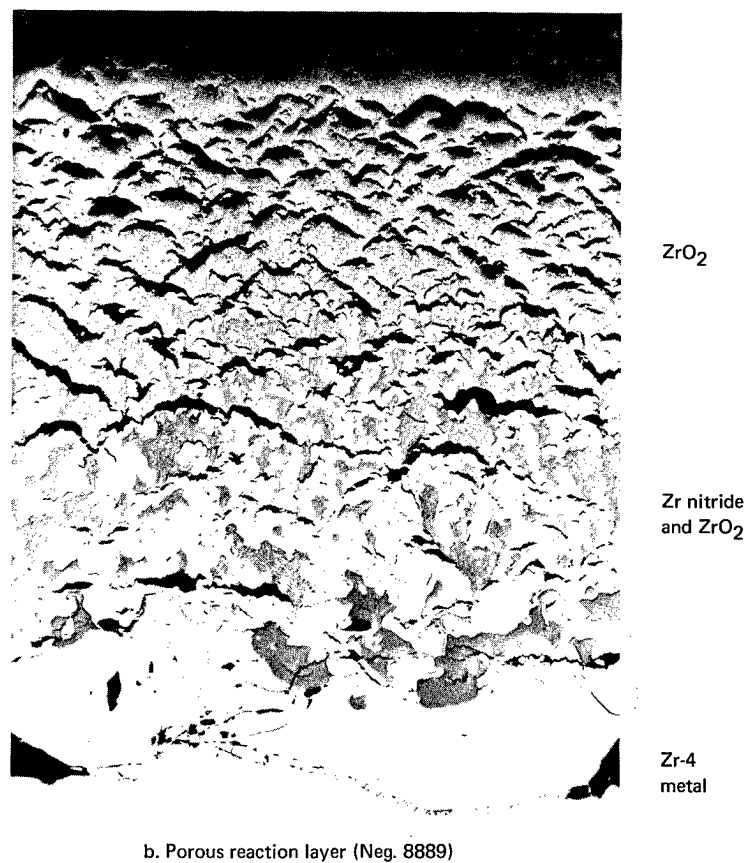
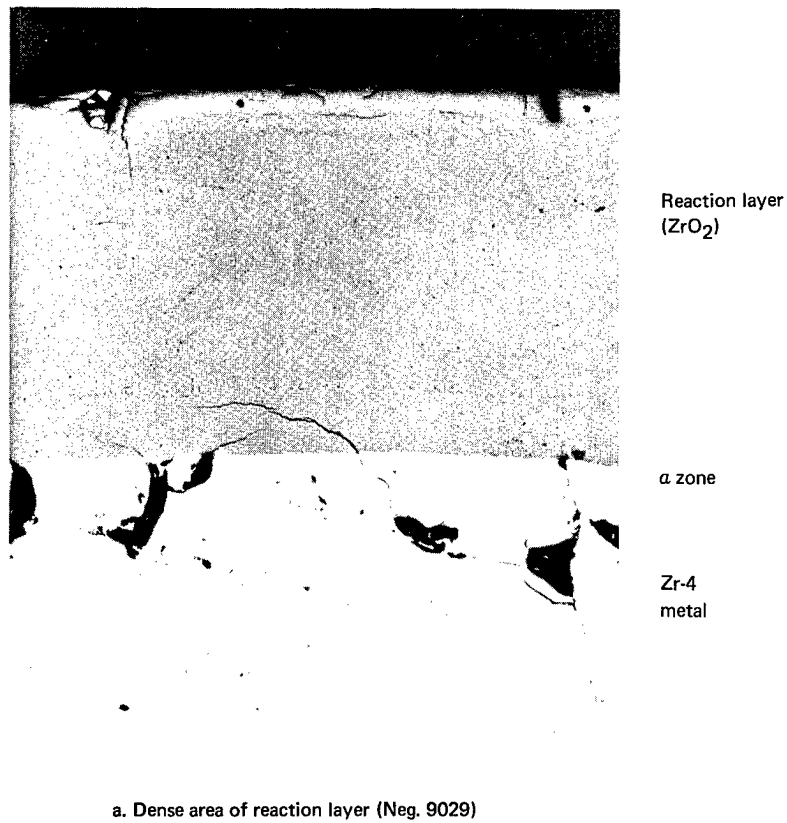


Fig. 8.12 — Photomicrographs of Zircaloy-4 tested at 1200°C for 1 hour in air (As-polished, 100X)

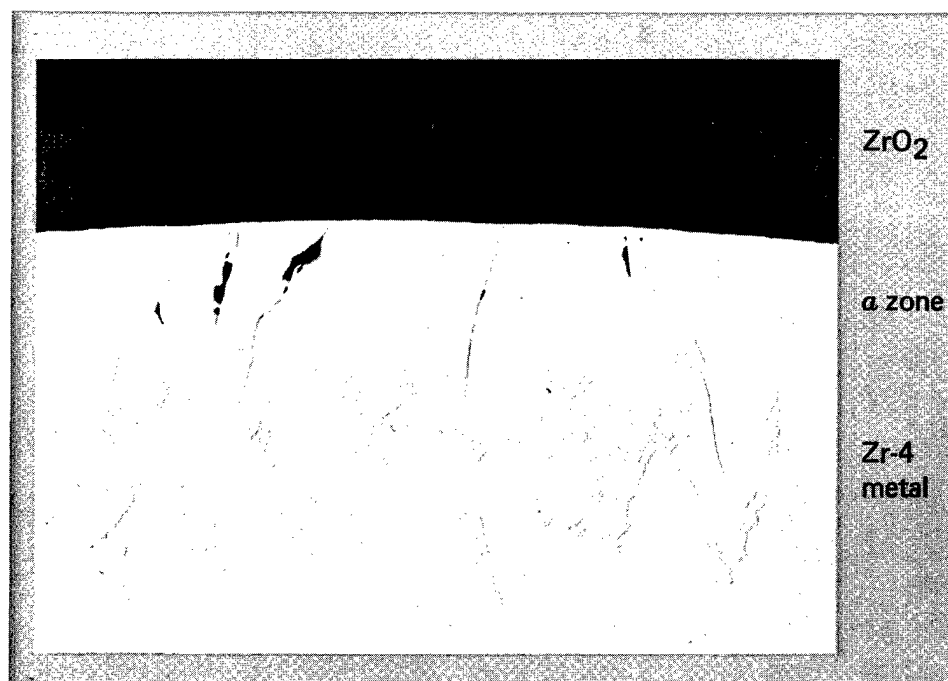


Fig. 8.13 — Photomicrograph of Zircaloy-4 tested at 1200°C for 1 hour in steam (Neg. 8890, as-polished, 100X)

OXIDATION OF TYPE 304 STAINLESS STEEL IN STEAM OR AIR

Steam Oxidation

In the previous annual report,¹⁸ results of studies of the oxidation kinetics of Type 304 stainless steel in steam at temperatures between 1000° and 1350°C were presented. Scales which formed at 1200°C and above remained in place upon cooling although they cracked; those formed at lower temperatures tended to spall when cooled. The microstructure of the oxidized surface formed at the higher temperatures showed a multi-layer coating. The scales, formed on the surface of 304L stainless steel samples oxidized in steam at 1200°C and 1300°C, have been studied by microprobe analysis.

These microprobe analyses previously discussed¹⁹ in detail are summarized in Table 8.9. Both samples contain high-chromium oxide inner layers of a spinel structure, as revealed by X-ray diffraction analysis. Similar high concentrations of chromium as Fe-Cr spinel in the inner oxide layer have been observed by Fujii and Meussner²⁰ in studies of the oxidation of Fe-Cr alloys in argon plus steam at temperatures between 700° and 1100°C.

Previous studies of steam corrosion kinetics of 304 stainless steel at temperatures between 1000° and 1375°C showed that an initial linear oxidation rate (for 6 to 28 minutes) preceded the parabolic behavior.²¹ The parabolic rate was represented by the equation

$$W^2/t = 2.4 \times 10^{12} \exp \left(\frac{-84,300 \pm 2400}{RT} \right) \quad (8.11)$$

¹⁸GEMP-475A, pp. 246–251.

¹⁹GEMP-69, pp. 144–147.

²⁰C. T. Fujii and R. A. Meussner, "High Temperature Oxidation of Iron-Chromium Binary Alloys in Water Vapor, Part 1," U.S. Naval Research Laboratory, NRL Report 5506, September 21, 1960.

²¹GEMP-475A, p. 246.

TABLE 8.9
DESCRIPTION OF OXIDE LAYERS FORMED ON STAINLESS STEEL
DURING OXIDATION IN STEAM AT 1200°C AND 1300°C

Temperature, °C	Oxide Layer	Electron Probe Analyses, ^a wt %			Metallography of Oxide
		Fe	Cr	Ni	
1200	Outer Oxide	75	—	2	Two phases with large grains and large voids.
	Inner: Oxide	45	27	4	Small grains and voids plus metal.
	Metal	47	10	43	
1300	Outer: Oxide	77	—	— ^b	Two phases, large oxide grains, large voids, metallic inclusions.
	Metal	30	—	77 ^c	
	Inner: Oxide	47	22	7	Two phases, small grains and voids, metallic particle.
	Metal	40	5	60 ^c	

^aAverage values for weight percent metal at center of oxide layers.

^bApproximately 2% Mn concentrated near surface of oxide layer.

^cAlthough corrected for absorption and fluorescence, the calculated compositions totaled more than 100% in the metal phase. This does not affect the conclusions drawn in the text.

Recent analysis of the linear portion of the data yields a least-squares fit given by the equation

$$W/t = 1.1 \times 10^5 \exp \left(\frac{-44,350 \pm 2300}{RT} \right). \quad (8.12)$$

The linear rates for steam oxidation are plotted in Figure 8.14. The results of Higgins²² for steam oxidation of Type 321 stainless steel at 1260°C are included for comparison.

Air Oxidation

To compare the behavior of 304L stainless steel in air with its oxidation in steam, tests were run in flowing dry air (-66°C dewpoint) between 1100° and 1375°C using the thermogravimetric technique. Although weight gains in air at 1360°C and below were too small to accurately determine rate behavior, parabolic behavior is assumed because the low rates imply protective film formation. Parabolic rate constants, calculated for comparison with the parabolic and linear portions of the steam oxidation of 304L stainless steel, are included in Table 8.10.

The logarithms of parabolic rate constants in air are plotted in Figure 8.15 together with those for steam oxidation. The rate in air is less than that in steam by a factor of about 10³. Oxidation behavior of 304 stainless steel in air including the point at 1100°C may be represented by Hagel's²³ curve for chromium oxidation in air, which is included in Figure 8.15. Data of Caplan and Cohen²⁴ for 302 stainless steel in dry air, which show good agreement with the data of Hagel²³ for chromium, are also included in Figure 8.15. Oxidation rates determined by Hagel²³ and by Gulbransen²⁵ for chromium in oxygen are shown in this figure; they differ only slightly from the rates in air.

Tests of 304L stainless steel at 1375°C in air show oxidation rates comparable to those for steam at this temperature, much higher than the rates in air between 1100° and 1360°C.

²²H. M. Higgins, "A Study of the Reaction of Metals and Water," AECD-3664, April 15, 1955.

²³W. G. Hagel, "Factors Controlling the High Temperature Oxidation of Chromium," ASTM Trans., Vol. 56, 1960, p. 583.

²⁴D. Caplan and M. Cohen, "High Temperature Oxidation of Chromium-Nickel Steels," Corrosion, Vol. 15, 1959, p. 141t.

²⁵E. A. Gulbransen and K. F. Andrew, "Kinetics of the Oxidation of Chromium," J. Electrochem. Soc., Vol. 104, 1957, p. 334.

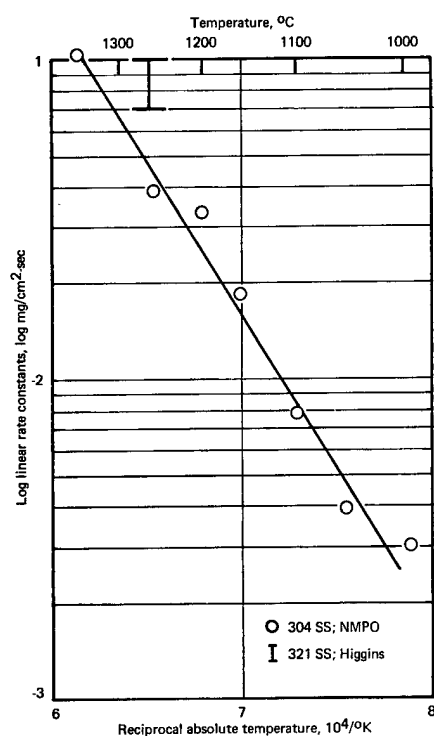


Fig. 8.14 — Linear rate constant versus temperature for steam oxidation of Type 304 stainless steel

TABLE 8.10 RESULTS OF OXIDATION OF 304L SS FROM 1000° TO 1375°C IN STEAM AND IN AIR ^a			
Atmosphere	Temperature, °C	Rate Constants ^b	
		Linear, mg/cm ² -sec	Parabolic, mg ² /cm ⁴ -sec
Steam	1000	0.0030	0.0095
	1050	0.0039	0.030
	1100	0.0087	0.095
	1150	0.016	0.18
	1150	0.017	—
	1200	0.033	0.75
	1200	0.034	0.80
	1250	0.038	2.1
	1300	—	4.4
	1350	0.11	13
	1375	Not observed	17
Air	1100	—	0.00025
	1200	—	0.00005
	1225	—	0.00012
	1350	—	0.0074
	1360	—	0.0079
	1375	—	21
	1375	—	25

^aDry air (−66°C dewpoint).

^bFor tests in steam, there was a change from linear to parabolic behavior after times ranging from 6 to 28 minutes.

The increased rate reflects the presence of a liquid phase, consistent with a temperature above the Fe-FeO solidus.²⁶ A sample after testing at this temperature is shown in Figure 8.16, where it is compared with an unoxidized sample and a sample oxidized at 1360°C in air. The scale formed at 1360°C is thin and uniform compared to that at 1375°C which is much thicker, very irregular, and shows evidence of melting. X-ray diffraction revealed the composition of the scale surface formed in air at 1360°C and below to be principally Fe₃O₄, with a minor amount of Fe₂O₃. The surface of the scale formed at 1375°C was Fe₃O₄. When the poorly adherent outer layer was removed from a sample tested at 1332°C,* however, a green oxide layer was exposed which was identified by X-ray diffraction as rhombohedral Cr₂O₃ with less than 20 percent Fe₂O₃.

Electron microprobe analysis of the sample oxidized in air at 1375°C showed a distribution of the iron, nickel, and chromium in both oxide and metallic phases which was very similar to that observed in the sample oxidized in steam at 1300°C. A sample oxidized at 1310°C in air, however, showed a very high chromium concentration (48%) and only 8 percent iron in the oxide layer attached to the metal substrate. This is consistent with the presence of a protective layer of Cr₂O₃ and agrees with the data of Yearian.²⁷

Scales formed in air at 1360°C and below generally spalled when the samples were cooled and removed from the furnace; this effect was not so noticeable on samples run in steam above 1200°C.

*These samples were not used in weight gain analysis because much of the oxide layer was lost by spallation.

²⁶L. S. Darkin and R. W. Gurry, "The System Iron — Oxygen, II: Equilibrium and Thermodynamics of Liquid Oxide and Other Phases," J. Am. Chem. Soc., Vol. 68, 1946, pp. 799–816.

²⁷H. J. Yearian, H. E. Boren, Jr., and R. E. Warr, "Structure of Oxide Scales on Nickel-Chromium Steels," Corrosion, Vol. 12, 1956, p. 561t.

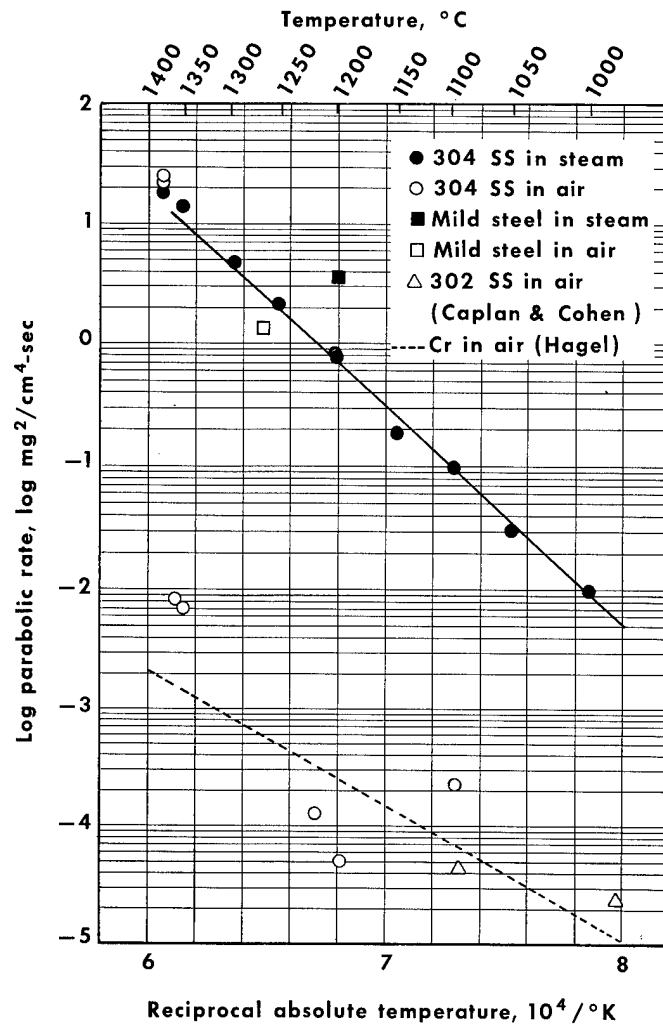


Fig. 8.15 — Parabolic rate constant versus temperature for steam and air oxidation of Type 304L stainless steel

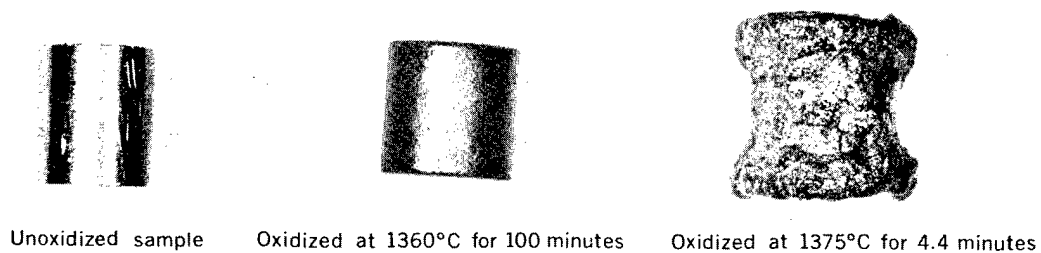


Fig. 8.16 — 304L stainless steel samples oxidized in air

A sample of mild steel was heated in air for 1 hour at 1280°C for comparison with the 304L stainless steel behavior. The parabolic rate constant was 1.26 mg²/cm⁴-sec compared to about 0.001 mg²/cm⁴-sec for 304L stainless steel under the same conditions.

The unusually low oxidation rate of stainless steel in air compared to that in steam at 1360°C and below is due to formation of a protective Cr₂O₃ layer which forms in air but not in steam. Seybolt²⁸ has shown that at 1300°C the oxide of an 0.8Fe - 0.2Cr alloy is rhombohedral (Cr, Fe)₂O₃ only at oxygen partial pressures above 0.05 atmosphere, whereas spinel forms below 0.01 atmosphere. Since oxygen pressures in steam vary from about 2 x 10⁻⁴ to 8.8 x 10⁻⁶ atmospheres in the temperature range employed, the Fe-Cr spinel layer observed in the steam oxidation of 304L stainless steel is consistent with the results of Seybolt.²⁸ An increase of chromium in the oxide of alloys which have up to 0.85Cr, 0.15Fe, approximately the composition observed in the oxide formed on 304L stainless steel by air below 1360°C, stabilizes the rhombohedral phase down to 10⁻⁴ atmospheres oxygen, accounting for the Cr₂O₃ layer in the air-oxidized samples. Possibly because of reactions of Cr₂O₃ with liquid Fe-FeO, no Cr₂O₃ was observed at 1375°C in air, and protection was no greater than that in steam.

OXIDATION OF UO₂ BY STEAM

Oxidation Kinetics

The steam oxidation of UO₂ was investigated in the temperature range from 885° to 1835°C. Data for the range from 1100° to 1500°C were presented previously.²⁹ Recent oxidation studies at 885°C and 1000°C were conducted using the thermobalance apparatus described earlier.³⁰ Investigations from 1600° to 1835°C were carried out in an induction-heated furnace with a dense Al₂O₃ muffle to prevent oxidation of the molybdenum susceptor. Test specimens of UO_{2.002} or UO_{2.004} were right circular cylinders sintered to about 95 percent of theoretical density at 1700°C. The spectrographic analysis of a typical sample is given in Table 8.11. Sample dimensions were varied with oxidation temperature to compensate for the variation in oxidation rates. Details of the experimental procedures were given in earlier reports.^{31,32}

Exact dimensions of each sample, experimental data, calculated rate constants, and calculated oxygen diffusion coefficients for all UO₂ steam oxidation tests are listed in Table 8.12. The parabolic rate constants are plotted in Figure 8.17. The least-squares equation for these rates is:

$$W^2/t = 8.4 \times 10^4 \exp\left(\frac{-48,000 \pm 1900}{RT}\right) \quad (8.13)$$

Experiments using UO₂ of 98 percent theoretical density were run at 1390°C and 1520°C for comparison with the results of the tests using 95-percent-dense material. Data and results of these tests are included in Table 8.12 and Figure 8.17. The good agreement between these data and the data from 95-percent-dense samples is predictable using the data of Belle,³³ which show no open porosity in UO₂ for densities greater than 91 percent.

²⁸A. U. Seybolt, "Observations on the Fe-Cr-O System," J. Electrochem. Soc., Vol. 107, 1960, p. 147.

²⁹GEMP-475A, pp. 251-256.

³⁰Latta, Bittel, and Hadesty, loc. cit.

³¹"High-Temperature Materials Program Progress Report No. 63," GE-NMPO, GEMP-63, December 30, 1966, p. 120.

³²GEMP-1002, pp. 130-131.

³³J. Belle, "Uranium Dioxide: Properties and Nuclear Applications," Naval Reactors, Div. of Reactor Development, USAEC, 1961, p. 333.

TABLE 8.11
CHEMICAL ANALYSIS^a OF UO₂ USED
IN STEAM OXIDATION STUDIES

Element	ppm
C	68.5
N	65
S	40
F	1.5
P	6
Ag	<5
Al	<20
B	<0.2
Cd	<0.2
Co	<9
Cr	<10
Cu	<10
Fe	27
Mg	<10
Mn	<10
Mo	<10
Ni	17.5
Pb	<10
Si	11
Sn	<10
Ti	<10
Ca	<10
W	<10
O/U	2.002 ± 0.003

^aAverage of duplicate analyses

TABLE 8.12
RESULTS OF UO₂ OXIDATION BY STEAM

Temperature, °C	Test Time, sec	Sample Diameter, cm	Sample Height, cm	Original Weight, g	Weight Gain, g	Final Average O/U Ratio	Theoretical Equilibrium O/U Ratio	Parabolic Rate, mg ² /cm ⁴ -sec	Oxygen Diffusion Coefficient, cm ² /sec
1835	600	3.091	1.905	148.5231	0.6141	2.090 ^a	2.158	0.892 ^a	1.16 × 10 ^{-4a}
1795	600	3.089	1.911	148.9234	0.6828	2.074	2.162	0.691	8.10 × 10 ⁻⁵
1720	600	3.096	0.949	74.3928	0.4079	2.095	2.165	0.470	5.30 × 10 ⁻⁵
1715	600	3.086	1.921	148.9461	0.4703	2.055	2.166	0.327	3.20 × 10 ⁻⁵
1625	1200	3.109	0.948	74.3039	0.4001	2.093	2.170	0.223	2.37 × 10 ⁻⁵
1610	1200	3.086	1.908	148.6701	0.6365	2.074	2.171	0.302	3.00 × 10 ⁻⁵
1600	1800	3.084	1.903	148.5232	0.8587	2.100	2.171	0.368	4.21 × 10 ⁻⁵
1520 ^b	1200	2.731	0.8585	53.9598	0.2127	2.071	2.176	0.104	8.68 × 10 ⁻⁶
1500	1140	1.250	1.283	16.4467	0.0876	2.094	2.177	0.12	1.28 × 10 ⁻⁵
1500	2400	1.255	1.267	16.2287	0.1009	2.109	2.177	0.076	8.86 × 10 ⁻⁶
1500	4560	1.255	1.273	16.1417	0.1226	2.132	2.177	0.059	8.33 × 10 ⁻⁶
1410	3600	3.096	1.904	148.9666	0.6357	2.074	2.183	0.100	8.48 × 10 ⁻⁶
1400	5700	1.254	1.256	16.0962	0.1206	2.131	2.183	0.046	5.71 × 10 ⁻⁶
1400	6900	1.254	1.275	16.3291	0.1029	2.110	2.183	0.027	2.91 × 10 ⁻⁶
1390 ^b	2400	2.695	1.084	67.9490	0.2064	2.053	2.184	0.042	2.81 × 10 ⁻⁶
1200	7020	1.396	1.310	20.6454	0.0649	2.057	2.198	0.0077	5.23 × 10 ⁻⁷
1200	10800	1.403	1.272	20.5758	0.0735	2.064	2.198	0.0066	4.48 × 10 ⁻⁷
1100	10500	1.288	1.265	16.9978	0.0331	2.037	2.207	0.00175	1.02 × 10 ⁻⁷
1100	10860	1.263	1.275	16.5417	0.0187	2.023	2.207	0.00056	3.10 × 10 ⁻⁸
1000	24480	1.256	0.2525	15.0666 ^c	0.410	2.050	2.243 ^d	0.00023	1.04 × 10 ⁻⁸
885	17400	1.400	0.1259	9.8528 ^c	0.0210	2.039	2.262 ^d	0.00012	2.58 × 10 ⁻⁹

^aSome loss of UO₂ occurred in this test; consequently, the parabolic rate and oxygen diffusion are based on post-test chemical analysis. All others are based on weight gain.

^bHigh-density sample, 98% theoretical density. All other samples approximately 95% theoretical density.

^cThese two samples consisted of five pieces each.

^dCalculated by equation of Aronson and Belle; others by equation of Anthony et al.

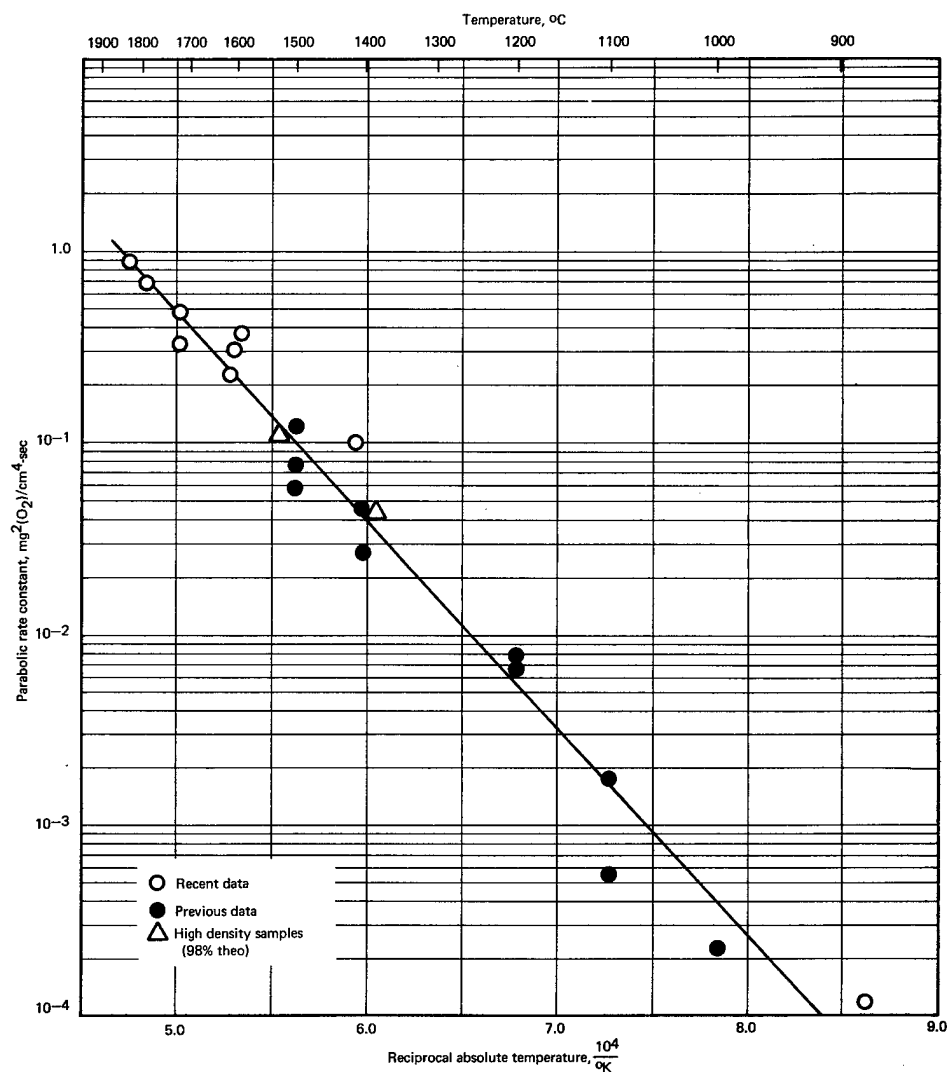


Fig. 8.17 — Parabolic rate constant versus reciprocal temperature for oxidation of UO_2 by steam

Oxygen Diffusion in UO_2

Experimental — The controlling mechanism of steam oxidation of UO_2 is believed to be primarily interstitial bulk diffusion of oxygen. If oxidation of UO_2 is controlled by diffusion of oxygen through the crystal lattice, it follows that a composition gradient should exist in tested samples whose average composition is below that at equilibrium with the steam atmosphere. To test this hypothesis the outer surface, a layer approximately 80 microns below the surface, and the center of a UO_2 sample oxidized in steam for 1 hour at $1400^{\circ}C$ were studied by X-ray diffraction. Lattice parameters of the major phase (UO_{2+x}) from the center outward were 5.4705, 5.4695, and 5.4689, corresponding to O/U ratios of 2.003, 2.023, and 2.030. There was evidence in all areas of a second phase. Both the amount of the second phase and its oxygen content (estimated from lattice parameter measurements) increased from the center to the surface. In the vicinity of the surface the second phase, with a composition of approximately U_4O_9 , represented 30 percent of the material. From these data the overall surface region O/U ratio was estimated to be $2.03 \times 0.7 + 2.25 \times 0.3 = 2.10$. An O/U ratio of 2.180 is calculated to be the O/U ratio

in equilibrium with steam at 1400°C. The entire sample of this test had a final average O/U ratio of 2.074 calculated from the weight gain.

Portions of this sample taken from the center and from the surface regions were analyzed chemically and O/U ratios of 2.072 in the interior and 2.084 toward the exterior were obtained, consistent with X-ray and weight gain analyses.

The O/U ratio for various portions of a sample heated 10 minutes at 1715°C showed 2.007 in the interior and 2.075 on the surface by X-ray analyses, and an overall average of 2.055 from the weight gain data; the O/U at equilibrium for this temperature is 2.166. Some redistribution of oxygen in the surface layer of the test sample occurs during the cooling cycle, but the discrepancy between the surface O/U and the equilibrium O/U value appears somewhat larger than can be explained on this basis.

Overall results indicate that the oxidation is primarily controlled by diffusion of oxygen, but the difference between the equilibrium O/U ratios and that measured for the exterior indicates that the surface reaction rate may be low enough to affect the results. If so, the true diffusion coefficients may be slightly higher than the values reported below.

Oxygen diffusion coefficients were calculated from the weight gain of the UO_2 tested in steam assuming a bulk diffusion mechanism and using the following equation derived by Jain³⁴ for right circular cylinders:

$$\bar{v} = 1 - \left[1 - 4 \left(\frac{\tau_H}{\pi} \right)^{1/2} \right] \left[1 - 4 \left(\frac{\tau_\rho}{\pi} \right)^{1/2} + \tau_\rho \right] \quad (8.14)$$

where

\bar{v} = fractional completion of the oxidation

$\tau_x = Dt/x^2$

D = diffusion coefficient, cm/sec²

x = radius (ρ) or height (H), cm

t = time, seconds

Values of τ were obtained using \bar{v} calculated from the weight gain and the UO_{2+x} composition in equilibrium with steam at test temperature. The latter was calculated from basic thermodynamic data and appropriate relationships between UO_{2+x} composition and equilibrium oxygen partial pressure. Data of Anthony, et al.,³⁵ were used for temperatures of 1100°C and above, and those of Aronson and Belle³⁶ were used for the lower temperatures.

Figure 8.18 shows the results of these calculations plotted as $\log D$ versus $10^4/T$. The least-squares equation for the curve fitted to those data and previously reported data³⁷ for the temperature range 1100° to 1600°C yields the following for the diffusion coefficient in cm²/sec.

$$D_{\text{chem}} = 151 \exp \left(\frac{-58,000 \pm 2000}{RT} \right) \quad (8.15)$$

³⁴S. C. Jain, "Simple Solutions of the Partial Differential Equation for Diffusion," Proc. Roy. Soc., A243, 1957, pp. 359–374.

³⁵A. M. Anthony, R. Kiyoura, and T. Sata, "Les Equilibres des Composes Oxygenes de l'Uranium entre 1500 et 2000°K," J. Nuc. Mat., Vol. 10, 1963, pp. 8–14.

³⁶S. Aronson and J. Belle, "Nonstoichiometry in Uranium Dioxide," J. Chem. Phys., Vol. 29, 1958, pp. 151–158.

³⁷"AEC Fuels and Materials Development Program Progress Report No. 67," GE-NMPO, GEMP-67, June 30, 1967, p. 160.

Theoretical – Thorn and Winslow³⁸ have derived the following theoretical relationship between oxygen self-diffusion coefficients in UO_{2+x} and the composition of UO_{2+x} :

$$D = \frac{Z}{4} \langle \ell^2 \rangle \nu \left\{ x + \left[x^2 + \frac{8q_i}{q_v} \exp \left(\frac{-(E_v - E_i)}{RT} \right) \right] \right\}^{1/2} \exp \left(\frac{-U_\ell}{RT} \right) \quad (8.16)$$

where

- D = self-diffusion coefficient for oxygen in UO_{2+x}
- Z = number of nearest neighbors
- $\langle \ell^2 \rangle$ = mean square of diffusional jump
- ν = mean vibrational frequency of lattice
- U_ℓ = energy composed of energies associated with correlation of the diffusing species vibrating out of phase with its shell of neighbors
- E_v = energy required to produce vacancies
- E_i = energy required to remove atoms from interstitial sites
- q_i = vibrational partition functions associated with interstitial sites
- q_v = vibrational partition functions associated with vacancy sites
- x = fractional deviation from stoichiometric (x in UO_{2+x})

They selected the following values for the parameters of the above equation:

$$\frac{Z}{2} \langle \ell^2 \rangle = 22.4 \times 10^{-6} \text{ cm}^2$$

$$\nu = 18 \times 10^{12} \text{ sec}^{-1}$$

$$E_v = 131.1 \text{ kcal/mole}$$

$$E_i = 93.8 \text{ kcal/mole}$$

$$U_\ell = 35.1 \text{ kcal/mole}$$

$$8q_i/q_v \cong 500$$

All the above values were derived from basic information except for the shell energy value which was derived from the experimental diffusion data of Auskern and Belle³⁹ for $\text{UO}_{2.002}$. In a later publication Thorn and Winslow⁴⁰ introduce new values for E_v and U_ℓ whereby the quantity $(E_v - E_i)$ becomes 40.9 kcal/mole and U_ℓ is 29.7 kcal/mole (the activation energy of Auskern and Belle for oxygen diffusion in UO_{2+x} having an O/U of 2.004 and 2.067 in the temperature range 300° to 600°C). Using either set of values for $(E_v - E_i)$ and U_ℓ in equation (8.16) gives correlation with the results of Auskern and Belle; the later set of values better explains their results for nearly stoichiometric material ($\text{UO}_{2.002}$).

Chemical diffusion coefficients for oxygen in UO_{2+x} (diffusion resulting from a chemical potential gradient) can be related to the coefficients for oxygen self diffusion (determined by tracer experiments) by the following equation:

$$D_{\text{chem}} = D_{\text{self}} \left(\frac{2+x}{2x} \right) \left(\frac{d \ln P_{\text{O}_2}}{d \ln x} \right) \quad (8.17)$$

where: P_{O_2} = oxygen partial pressure

Using Thorn and Winslow's equation (8.16) to calculate D_{self} values for $\text{UO}_{2.05}$ and converting these to D_{chem} by equation (8.17) gives good correlation between theory and

³⁸R. J. Thorn and G. H. Winslow, "Correlation of Thermodynamic Properties and Atomic Transport in the Uranium Dioxide Phase," Thermodynamics: Proceedings of the Symposium on Thermodynamics, Vol. 2, IAEA, 1966, p. 234.

³⁹A. B. Auskern and J. Belle, "Oxygen Ion Self Diffusion in Uranium Dioxide," J. Nucl. Mat., No. 3, 1961, pp. 267-276.

⁴⁰R. J. Thorn and G. H. Winslow, "Oxygen Self-Diffusion in Uranium Dioxide," J. Chem. Phys., Vol. 44, April 1966, p. 2822.

the experimental results of the present study, as shown in Figure 8.18. The dashed line is the theoretical curve and the solid line is the least-squares fit to the experimental data. The theoretical line in Figure 8.18 represents the composition $\text{UO}_{2.05}$, for which there is general agreement in the literature concerning the value of the thermodynamic function $\left(\frac{d \ln P_{\text{O}_2}}{d \ln x}\right)$. Furthermore, the composition $\text{UO}_{2.05}$ selected here is a reasonable first approximation to the composition of the test samples since the average O/U values changed from 2.003 to between 2.023 and 2.132 during the present experiments.

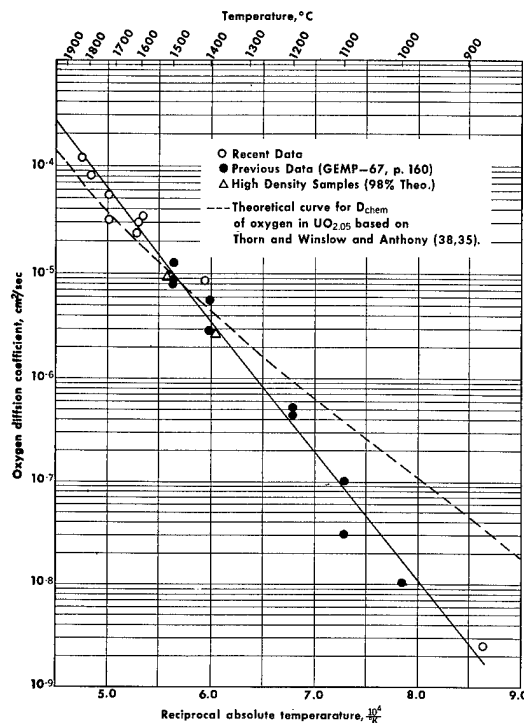


Fig. 8.18 — Oxygen diffusion coefficient versus reciprocal temperature for oxidation of UO_2 by steam compared to theoretical curve for oxygen diffusion coefficient in $\text{UO}_{2.05}$

Although good correlation is established between theoretical and experimental values, effort is continuing to determine the best theoretical values with which to compare experimental results. This includes selection of the best set of constants for the Thorn and Winslow equation (8.16) and of the most valid equation for determining the thermodynamic function to be used in the conversion from self- to chemical-diffusion coefficients in equation (8.17). It also remains to be determined which O/U value best represents experimental data obtained under oxidizing conditions in which the average O/U is constantly changing with time.

8.3 PHYSICAL AND MECHANICAL PROPERTIES (A. D. Feith, E. F. Juenke, and W. L. McCullough)

TENSILE STRENGTH OF TYPE 304 L STAINLESS STEEL

The tensile strength of annealed 304 L stainless steel sheet was measured from room temperature to 1375°C . The test specimens were fabricated from 0.076-cm-thick sheet and had a 2.54-cm gage length in the major rolling direction of the sheet. Table 8.13 shows the chemical analysis for this material.

TABLE 8.13
CHEMICAL ANALYSIS OF TYPE 304L
STAINLESS STEEL TENSILE SPECIMENS

Element	Percent
C	0.024
Co	0.05
Cr	18.00
Cu	0.28
Mn	1.69
Mo	0.16
Ni	10.95
P	0.024
Si	0.70
S	0.011

Measurements from room temperature to 800°C were performed in air, utilizing an extensometer to determine the 0.2-percent yield point and to control the strain rate at 0.005 cm per minute. The measurements from 800° to 1375°C were performed in argon at a crosshead speed of 0.15 cm per minute without using an extensometer. In all cases, the measurements were performed 0.6 hour after start of heat-up to temperature, allowing 0.3 hour to reach test temperature and 0.3 hour at temperature to attain constant temperature throughout the specimen. Ductility was measured as elongation at rupture, and the hardness (DPH) of each tested specimen was measured after test.

Strength, ductility, and hardness results are given in Table 8.14. The tensile strength data versus temperature are plotted in Figure 8.19. Strength data for 800°C measured in argon are somewhat higher than in air, possibly because of the effect of oxidation or because of a higher strain rate. Ductility and hardness data are plotted in Figure 8.20.

THERMAL CONDUCTIVITY OF 304 L STAINLESS STEEL

The thermal conductivity of Type 304 L stainless steel was measured in the 520° to 1340°C temperature range by the radial heat flow method described previously.^{41,42} Single Pt / Pt - 10Rh thermocouples were used to measure the temperatures at two radial locations of the test specimen over the entire temperature range studied. Although the thermal gradient was small (3° to 8°C), it was determined to a reasonable degree of precision (approximately ± 5%) by dividing the difference between the thermocouple outputs at the two radial locations by the sensitivity of the couple at the mean temperature value. This technique is widely employed when measuring small gradients, rather than using differential thermocouples.

The specimen was fabricated from a commercial grade 304L stainless steel of the composition listed in Table 8.15. Shown also in this table are the compositions of other 300 series stainless steels whose conductivities are compared with that of the tested material in Figure 8.21.

The thermal conductivity of this material increased with temperature; this appears to be typical of the stainless steels. The results of this study have been fit to the following linear equation with a standard deviation of 1.770×10^{-2} watt/cm-°C:

$$k = 8.924 \times 10^{-2} + 1.970 \times 10^{-4} T \quad (8.18)$$

⁴¹A. D. Feith, "A Radial Heat Flow Apparatus for High Temperature Thermal Conductivity Measurements," GE-NMPO, GEMP-296, August 1963.

⁴²A. D. Feith, "Measurements of the Thermal Conductivity and Electrical Resistivity of Molybdenum," GE-NMPO, GE-TM 65-10-1, October 1965.

TABLE 8.14
TENSILE TEST RESULTS FOR TYPE 304 STAINLESS STEEL SHEET

Specimen No. ^a	Atmosphere	Temperature, °C	0.2% Yield Strength, kg/mm ²	Tensile Strength, kg/mm ²	Elongation at rupture (in 2.54-cm gage length), percent	Hardness, DPH ^b
1	Air	25	27.3	65.4 ^c	65	174
10		25	28.5	66.5	64	174
2		200	22.4	46.4	36	203
11		200	22.9	47.2	38	227
3		400	20.0	44.9	32	266
12		400	20.3	44.8	31	254
4		600	16.1	33.2	23 ^d	218
13		600	15.9	33.9	34	218
5		800	8.1	10.4	44 ^e	173
14		800	8.0	10.0	46	164
6	Ar	800	—	13.0 ^f	53	164
15		800	—	13.0	52	170
7		1000	—	4.9	51	143
16		1000	—	5.0	44	145
8		1200	—	1.9	65	157
17		1200	—	2.1	53	127
9		1300	—	1.4	46	105
18		1300	—	1.3	48	110
19		1350	—	0.91	41	104
20		1375	—	0.86	43	107

^a0.076-cm-thick by 2.54-cm gage length, annealed condition.

^bAfter test; kg load.

^cStrain rate in air, 0.005/min.

^dFracture at extensometer knife edge.

^eFracture outside gage length.

^fLoading rate in argon, 0.15 cm/min. (cross-head speed).

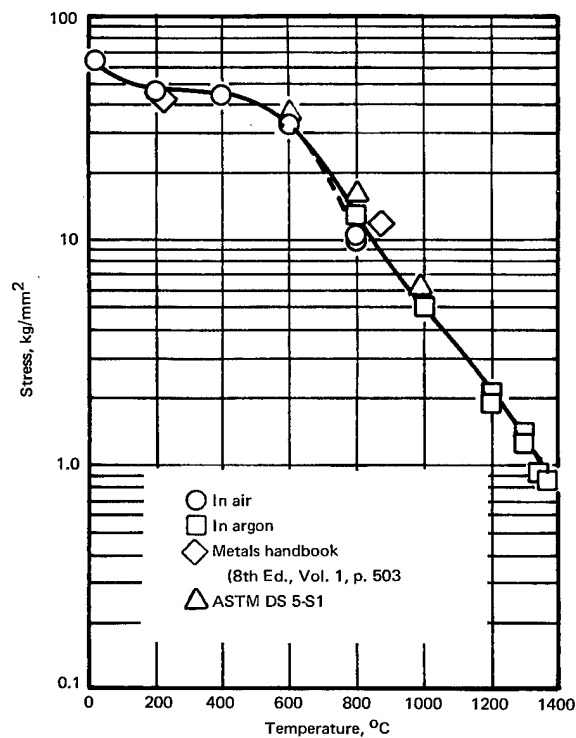


Fig. 8.19 — Ultimate tensile strength of Type 304 stainless steel sheet

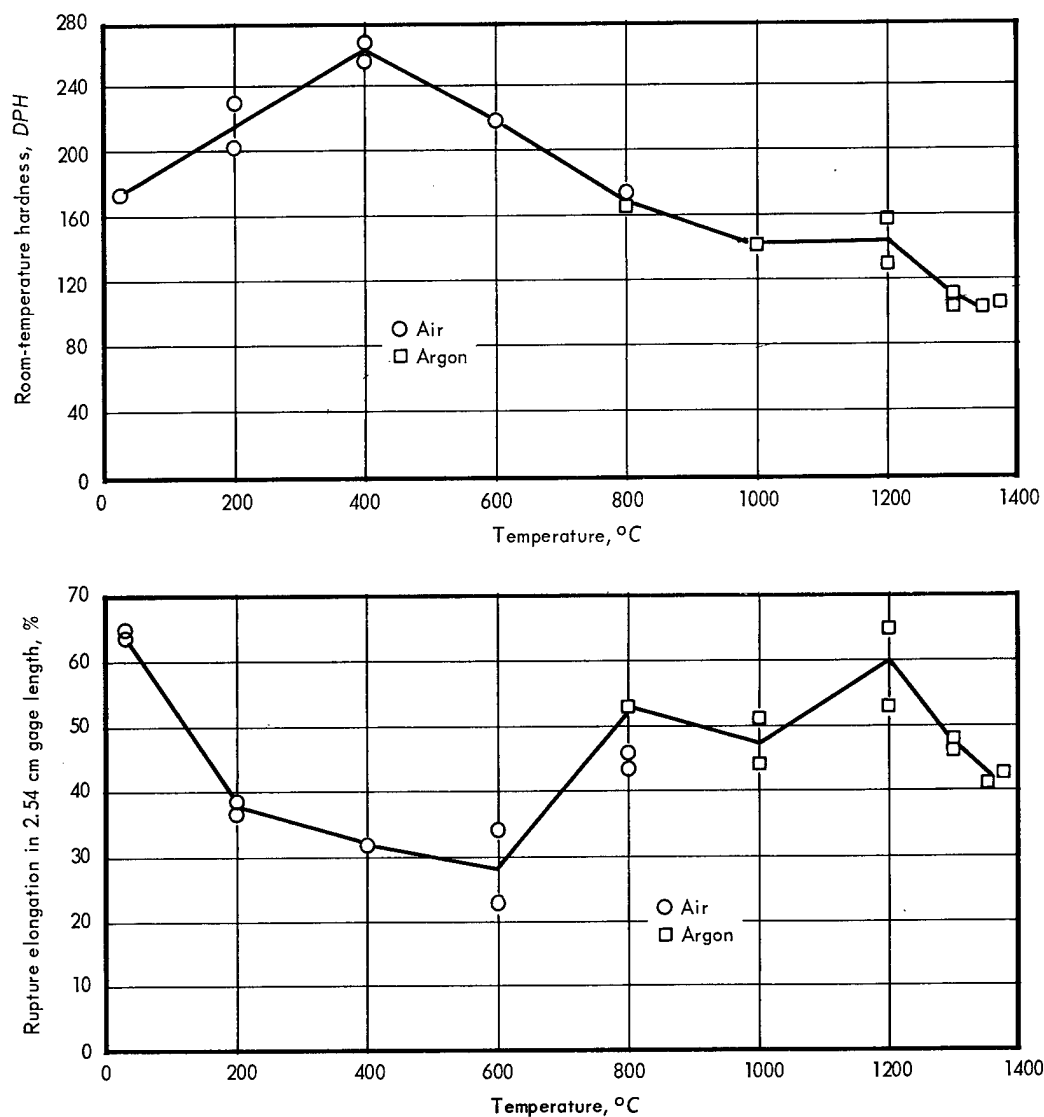


Fig. 8.20 — Ductility and hardness versus temperature as a result of tensile testing Type 304 stainless steel sheet

where

k = thermal conductivity, watt/cm-°C

T = temperature, °C

Values below 700°C are somewhat lower than other reported values, although the high-temperature data appear to agree well with values recommended by the TPRC data book.⁴³ The recommended values for Type 304 stainless steel were extrapolated above 900°K (627°C) and apparently maintain a uniform displacement above the values for Type 347 stainless steel. Values for Type 347 stainless steel above 1500°K (1227°C) were also extrapolated.

Thermal diffusivity data for this same 304L stainless steel have been obtained in the 300° to 1100°C temperature range and are reported under Task 1503. Enthalpy measurements are being made over the same temperature range and electrical resistivity measurements are planned. When these studies are complete, an adequate correlation

⁴³Thermal Physical Properties Research Center Data Book, Table 1089R, Vol. 1, June 1966.

TABLE 8.15
COMPOSITION OF STAINLESS STEELS USED IN
VARIOUS THERMAL CONDUCTIVITY TESTS

Element	This Study Type 304L	TPRC ^a Type 304	TPRC ^a Type 347	Silverman ^b Type 302	Lucks ^c Type 301 ^d	Powell ^e Type 18/8
C	0.024	0.053	0.06	0.116	0.15	0.08
Cu			0.09			
Mn	1.131	0.67	1.64		2.0	1.23
Si	0.70		0.58	0.13	1.0 Max.	0.62
P	0.014	0.025	0.013	0.021		
S	0.12		0.017	0.013		
Cr	18.37	18.51	17.65	18.4	16-18	18.68
Ni	9.89	9.09	10.94	9.6	6-8	8.85
Mo	0.09		0.02			
Nb						0.99
Ti						0.14

^aThermal Physical Properties Research Center Data Book, Vol. 1, June 1966, Table 1089R.

^bL. Silverman, "Thermal Conductivity Data Presented for Several Metals and Alloys Up to 900°C," J. Metals, Vol. 5 (1953) pp. 631-2.

^cC. F. Lucks and H. W. Deem, "Thermal Properties of Thirteen Metals," ASTM Special Tech. Pub. No. 227, 1958.

^dAnalysis not reported — values presented are typical for this material based on stainless steel catalogs.

^eR. W. Powell and R. P. Tye, "New Measurements on Thermal Conductivity Reference Materials," Proceedings of the Sixth Conference on Thermal Conductivity, Dayton, Ohio, 1966.

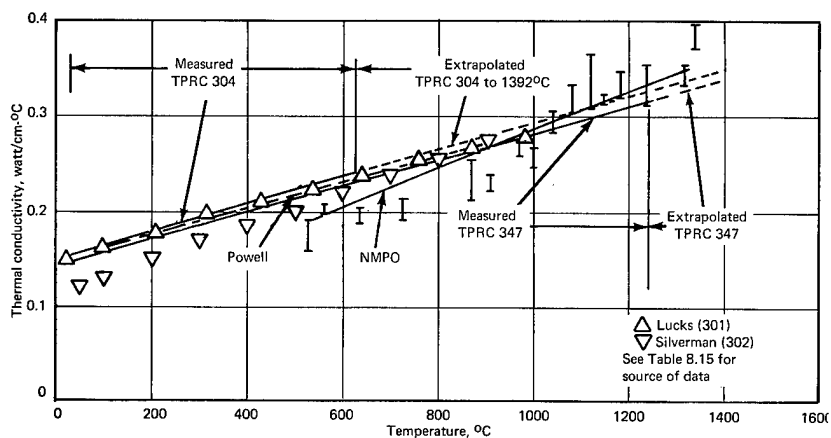


Fig. 8.21 — Thermal conductivity as a function of temperature for stainless steels

between the thermal conductivity and thermal diffusivity of this material can be made. This correlation will be used to ascertain the correct positioning of the low-temperature portion of the curve representing conductivity data presented above.

SPECTRAL AND TOTAL EMITTANCE MEASUREMENTS OF OXIDIZED ZIRCALLOY-4

Spectral and total hemispherical emittance measurements were carried out on both unoxidized and oxygen-saturated Zircaloy-4. The hole-in-tube method of measurement used in these studies is similar to that employed by Lemmon⁴⁴ for similar measurements on zirconium alloys and by Jain and Krishnan⁴⁵ in their studies on graphite. Figure 8.22

⁴⁴A. W. Lemmon, op. cit., p. A-1.

⁴⁵S. C. Jain and K. S. Krishnan, "The Distribution of Temperature Along a Thin Rod Electrically Heated in Vacuo. III: Experimental," Proc. Roy. Soc., Series A, Vol. 225, September 1954, p. 7.

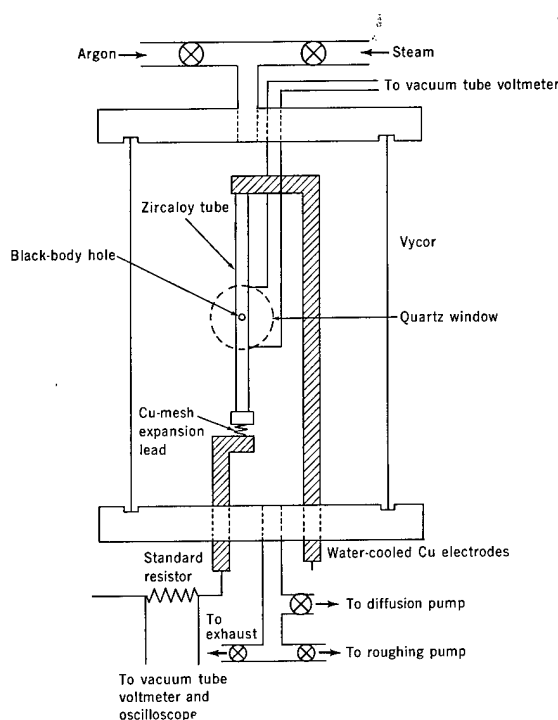


Fig. 8.22 — Schematic diagram of furnace used for emittance measurements

is a schematic diagram of the sample and important features of the apparatus. The sample was a tube of Zircaloy-4 about 15.2 cm long and 0.71 cm in diameter with a wall thickness of 0.038 cm. A hole, 0.079 cm in diameter, was drilled through one wall of the tube near the center. Two 0.025-cm-diameter tungsten wire voltage probes were spot-welded to the tube approximately 1.27 cm above and below the hole. Electrical power was supplied to the sample through water-cooled copper electrodes. The sample was surrounded by a Vycor chamber; the system was capable of operating with atmospheres of argon, steam, or vacuum. The black-body temperature and the surface temperature adjacent to the hole were measured optically through a quartz window. A vacuum tube voltmeter was used to determine both the voltage between the voltage probes and the sample current, calculated from the voltage drop across a calibrated standard resistance in series with the sample. An oscilloscope across the standard shunt was used to ensure a pure sinusoidal wave form for the sample current.

The tube used in these experiments was long enough that the temperature at the middle of the tube in the region of the black-body hole was sensibly constant over a considerable length of the tube, approximately 5 cm. Under these conditions, the loss of heat from the region of the temperature measurement was due almost entirely to radiation from its surface, and little loss resulted from either thermal conduction toward the ends of the tube or from radiative transfer in the tube cavity.

The spectral emittance was determined using the relationship:

$$\ln E_2 = \frac{-C_2}{2} \frac{(T - S)}{TS} \quad (8.19)$$

where

E_{λ} = spectral emittance
 λ = observed wavelength
 C_2 = radiation constant, = 1.438 cm/°K
 S = surface temperature, °K
 T = black-body temperature, °K

The wavelength observed in these measurements was 0.65 microns.

Total hemispherical emittance was determined using the following equation:

$$E_T = \frac{IV}{2\pi r \ell \sigma T^4} \quad (8.20)$$

where

E_T = total hemispherical emittance
 I = sample current, amperes
 V = potential drop across measured section, volts
 r = radius of sample, cm
 ℓ = length of measured section, cm
 σ = Boltzman's constant = 5.673×10^{-12} watt/cm²-°K⁴
 T = black-body temperature, °K

Preliminary tests were run to compare spectral and total emittance values between 900° and 1300°C for unoxidized Zircaloy-4, oxygen-saturated Zircaloy-4, and Zircaloy-4 oxidized sufficiently to have a substantial ZrO₂ coating on the surface. The Zircaloy-4 tubes used in the experiments meet LOFT specifications and ASTM specifications B-353-645 Grade RA-2, and have a surface finish of 63 RMS or better inside and out. Table 8.16 gives the vendor's ingot analysis.

The measurements for unoxidized Zircaloy-4 were conducted on two samples heated in a vacuum (<10⁻³ Torr). On initial heat-up of these samples the spectral emittance was in the range of 0.6 to 0.7 up to a temperature between 1100° and 1200°C, at which point it dropped to about 0.4. It is assumed that a change in surface condition, possibly oxidation or evaporation, accounts for this change in emittance behavior. The high emittance values are believed to result from oxidation of the metal by residual oxygen in the furnace during the initial heat-up. At high temperatures the oxygen dissolves rapidly in the metal and the emittance approaches that of the unoxidized metal. These initial experiments show that spectral emittance, E_{λ} , varies between 0.56 at 885°C and 0.43 at 1550°C. The value for 1100° to 1500°C is relatively constant, between 0.40 and 0.45. The total emittance, E_T , for the same temperature range lies between 0.20 and 0.28. These values are in fair agreement with the values obtained by Lemmon⁴⁴ for unoxidized Zircaloy-2 and Zircaloy-B in the same temperature ranges; E_{λ} = 0.43 to 0.44 and E_T = 0.22 to 0.26.

Application of an oxide layer by steam oxidation appreciably increased the spectral and total emittance. Several samples were oxidized for 30 minutes at temperatures between 950° and 1050°C. In each case both the spectral and total emittance increased to between 0.80 and 0.90 and remained thus through several thermal cycles. When steam oxidation was carried out for shorter periods of time, 5 to 10 minutes, the emittance reached high values as above. As heating continued, however, the oxygen of the scale dissolved in the metal and both spectral and total emittance values dropped, approaching the original values for the unoxidized metal.

These observations prove that in order to measure the effect of oxide layer thickness on the emittance of Zircaloy-4, it is necessary to saturate the metal with oxygen before

applying the oxide layers. Table 8.17 gives the calculated conditions for saturation of Zircaloy-4 tubes of the dimensions used in these experiments by steam oxidation at various temperatures. The time required to deposit enough oxygen to saturate the metal and the time required to homogenize the sample by diffusing oxygen into the metal have been calculated using equation (8.10):

$$W^2/t = 5.56 \times 10^5 \exp \left(\frac{-39,700 \pm 2300}{RT} \right)$$

developed in the reaction rate study described above and Lemmon's⁴⁴ equation for oxygen diffusion in alpha-zirconium, respectively. After saturation, oxide layers will be formed by additional oxidation in steam. Emittance values will then be determined and the oxide layer thickness will be measured metallographically.

8.4 SUMMARY AND CONCLUSIONS

Dynamic heating tests of Zircaloy-4 tubes with an internal pressure show that steam oxidation of the metal will result in lower deformation rates, less deformation, and higher failure temperatures. A model has been developed for expressing the tube failure by deformation when oxidation is negligible, as a function of tensile strength and rate of heating.

TABLE 8.16

CHEMICAL ANALYSIS OF ZIRCALOY-4
TUBING USED IN EMITTANCE MEASUREMENTS^a

Element	Ingot Analysis, wt %	
	Top	Bottom
Cr	0.09	0.09
Fe	0.19	0.20
Sn	1.45	1.40
Ni	<0.004	<0.004
Zr	Bal	Bal

Impurities	Ingot Impurities, ppm	
	Top	Bottom
C	<80	100
H	11	6
N	25	35
O	1400	1000
Al	<20	<20
B	<0.2	<0.2
Cd	<0.2	<0.2
Cl	<10	<10
Co	<10	<10
Cu	<20	40
Hf	<100	<100
Mg	<10	<10
Mn	<20	<20
Mo	<20	<20
Pb	<20	<20
Si	<30	30
Ti	<20	<20
V	<20	<20
W	<50	<50

^aAnalysis by vendor.

TABLE 8.17

CALCULATED TIMES FOR SATURATION
OF ZIRCALOY-4 TUBES^a BY STEAM OXIDATION

Temperature, °C	Oxidation	
	Time, ^b min	Solution Time, ^c min
1000	17	337
1050	10	183
1100	5	103
1150	3	61
1200	2	37
1250	1	23
1300	0.8	15
1350	0.6	10
1400	0.4	7
1450	0.3	5
1500	0.2	3

^aCalculations based on a sample dimension of 15.2-cm length, 0.71-cm diameter, 0.038-cm wall thickness.

^bCalculated from equation (8.10):

$$W^2/t = 5.56 \times 10^5 \exp \left(\frac{-39,700 \pm 2300}{RT} \right)$$

^cCalculated from $D_a = 0.196 \exp \left(\frac{-41,000 \pm 1500}{RT} \right)$

The oxidation of Zircaloy-4 and zirconium by steam shows a higher rate above about 1600°C which can be expressed as

$$W^2/\text{sec} = 1.5 \times 10^8 \exp \left(\frac{-60,600 \pm 5400}{RT} \right).$$

Oxidation of Zircaloy-4 in air is somewhat erratic and occurs at a greater rate than in steam; the difference is attributed to the reaction with nitrogen in the air.

The rate-controlling mechanism for oxidation of UO_2 by steam is considered to be diffusion of oxygen through the UO_{2+x} lattice. This proposed mechanism was verified by measuring an oxygen gradient in samples which had not reached equilibrium conditions.

The oxidation rate of 304 L stainless steel in air is about 10^3 times less than in steam up to 1370°C. This behavior is believed to be due to the presence of Cr_2O_3 as a protective film. During steam oxidation, however, formation of a film having the spinel structure provides less resistance to oxidation. The air oxidation rate becomes equal to or greater than that for steam at 1370°C and above, since molten Fe-FeO destroys the protective Cr_2O_3 film.

The tensile strength of annealed 304L stainless steel decreased from about 66 kg/mm² at room temperature to 0.86 kg/mm² at 1375°C.

The thermal conductivity of Type 304L stainless steel increased with temperature between 520° and 1340°C. The variation of thermal conductivity with temperature for this temperature range may be expressed as follows:

$$k = 8.924 \times 10^{-2} + 1.970 \times 10^{-4}T.$$

The spectral emittance of unoxidized Zircaloy-4, at a wave length of 0.65 microns, varied between 0.56 at 885°C and 0.43 at 1550°C. Total hemispherical emittance varied between 0.20 and 0.28 over the same range. The presence of an oxide layer increased the values for both spectral and total emittance to between 0.8 and 0.9. For thin oxide films, however, solution of the oxygen in the metal during prolonged heating caused both spectral and total emittance to approach original values for the unoxidized metal.

8.5 PLANS AND RECOMMENDATIONS

Spectral and total hemispherical emittance measurements will be continued on unoxidized, oxygen-saturated, and oxidized Zircaloy-4 to determine the effect of oxide layer thickness on the emittance of oxidized Zircaloy-4.

A thermal-arrest technique will be employed to study the solidus temperatures for the system Zr- UO_2 from the zirconium-rich end to compositions in the range likely to be encountered in a loss-of-coolant meltdown accident. Phases present in quenched samples will be examined to augment the lower-temperature, pseudo-binary information presently available.

Measurement of the effect of internal pressure on Zircaloy-4 tubing will continue with emphasis on the effect of oxide film thickness on the deformation and failure characteristics of this material.

Irradiated Zircaloy-2 from the spent fuel discharge of a power-producing reactor will be studied to determine the effect of radiation damage on the behavior of pressurized tubes under dynamic heating conditions.

9. FAST BREEDER REACTOR THERMOCOUPLE DEVELOPMENT

(1414)

E. S. Funston,* W. C. Kuhlman†

The objective of this program is to identify and establish the properties of reliable high-temperature thermocouple, electrical, and electronic materials to provide instrumentation and electrical components for use in fast breeder reactors.

9.1 W VERSUS W - 25Re THERMOCOUPLE CHARACTERISTICS AT HIGH TEMPERATURE

Determining the centerline fuel temperature of LMFBR fuel elements requires temperature measurements to approximately 2500°C. Thermocouple systems used to measure this temperature must be constructed of materials that are metallurgically and chemically compatible with each other and with the anticipated environment. Although these materials may be compatible, the electrical properties (resistivity and thermoelectric power) of the sheath, insulators, and environmental gas may still influence the thermoelectric signal, making validity of indicated temperatures uncertain. Loss of effective electrical insulating properties of ceramic oxides when used in conjunction with a high resistance of thermoelements has been observed at high temperatures by several investigators,^{1,2} and this effect was measured as a function of temperature.

Investigations during the past year have been primarily concerned with the many factors influencing the thermoelectric output generated in a thermocouple system. The various parameters that have received attention are: effects of gaseous environments, size of thermocouple wires, electrical insulation, and sheathing materials. By varying materials combinations and gaseous environments, and measuring the thermoelectric output as a function of temperature against calibrated standards, abnormal thermoelectric responses could be easily detected. Thermocouples using wire of 0.125-mm and 0.25-mm diameter were made and tested to determine whether optimization of wire diameters would be necessary. Electrical insulating characteristics of thorium and hafnia were compared at temperatures ranging from 1600° to 2600°C. Research on different sheathing materials has been limited to the Mo - 50Re alloy tubing and pure molybdenum tubing. The effects of high-temperature gaseous environments on the thermoelectric response from W versus W - 25Re[‡] thermocouples were determined in hydrogen and helium. An in-pile nuclear irradiation program was performed to determine the reactor stability of W versus W-25Re thermocouple systems. Data were obtained showing thermoelectric deviations as a function of temperature and neutron dosage. Each parameter investigated and significant results and conclusions of the individual experiments are discussed and illustrated.

*Project leader.

†Principal investigator.

‡ All compositions are in weight percent unless otherwise noted.

¹ E. A. Brown, B. G. Goodier, J. E. Perry, Jr., R. L. Petty, W. R. Prince, and C. R. Tallman, "Thermocouple Development for Project Rover," High Temperature Thermometry Seminar, Washington, D.C., February 24-26, 1965, WASH-1067.

² G. F. Popper and T. Z. Zeren, "Refractory Oxide Insulated Thermocouple Analysis and Design," High Temperature Thermometry Seminar, Washington, D.C., February 24-26, 1965,

ELECTRICAL INSULATION EVALUATION

Comparative tests were made at temperatures ranging from 1600° to 2600°C to determine the electrical insulating properties of the hafnia and thoria insulators. The construction of each thermocouple used was essentially identical for these experiments, except for insulating materials and the web thickness between the two thermocouple holes separating the thermocouple legs. The web thickness of the HfO_2 insulator measured 0.3 mm; the ThO_2 insulator had a web thickness of 0.75 mm. No sheathing was used, and tests were performed in an electrical heat-resistant furnace (Figure 9.1). Both helium and hydrogen atmospheres were used as test environments. The differences in thermocouple response during the experimental testing for electrical insulating characteristics are shown in Figure 9.2. The thermoelectric signals measured are shown by two curves which reveal that the thermocouple insulated with HfO_2 had the strongest thermoelectric response, even though the web thickness separating the W and W - 25Re thermoelements was less than one-half the thickness of the ThO_2 insulator.

EFFECT OF GASEOUS ENVIRONMENT

The next series of tests were primarily to establish effects on the thermoelectric response from thermocouples insulated with HfO_2 and ThO_2 when used in hydrogen or helium environments. The thermocouples were made of 0.25-mm stranded W and W - 25Re alloy wire. The stranded wires were separated with HfO_2 and ThO_2 electrical insulators. The

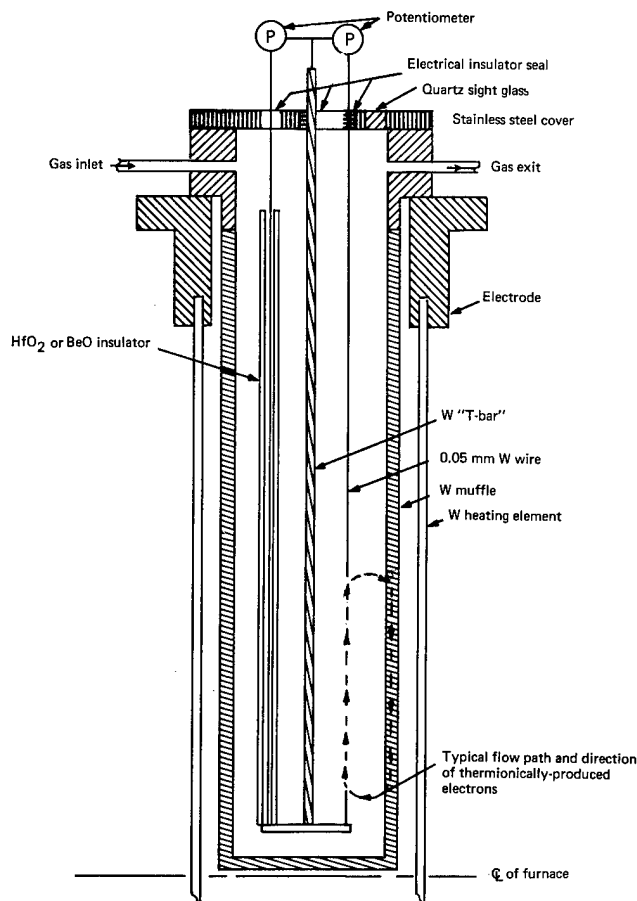


Fig. 9.1 — Test equipment to measure thermoelectric and thermionic anomalies in thermocouple wires

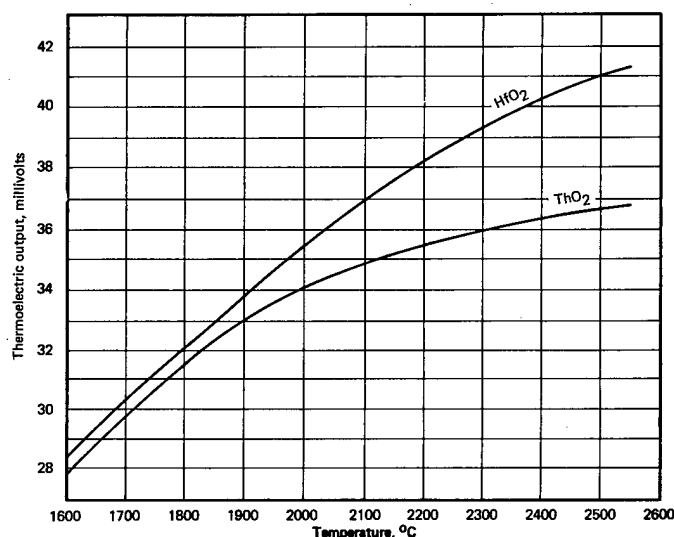


Fig. 9.2 — Comparative curves showing measured thermoelectric signals as a function of temperature in helium atmosphere from W versus W — 25Re thermocouples insulated with thoria and hafnia

HfO₂ insulator measured 2.1-mm OD with two 0.6-mm holes. The ThO₂ insulator measured 3-mm OD with two 0.3-mm diameter holes. The thermoelectric output as a function of temperature was determined using a direct-current electrical heat-resistant furnace (Figure 9.1). Initially the thermoelectric response of HfO₂-insulated thermoelements was measured in a hydrogen environment. After data had been compiled, the system was purged with helium and electrical measurements were taken in helium. The experiments were repeated using thermocouples insulated with thoria. The changes measured are graphically illustrated in Figure 9.3. The two sets of curves show that the response was lowered considerably for the ThO₂-insulated thermocouple in hydrogen. The helium atmosphere shifted the thermoelectric output downward, but its overall effect was far less than hydrogen on the thoria insulator. The data show that hafnia as an electrical insulator is much less affected by hydrogen or helium atmosphere. All measurements in this series of tests were referenced against black-body measurements using an optical pyrometer calibrated against a NBS calibrated instrument.

SHEATHING STUDIES

Concurrent with the tests on thermocouple evaluation, test thermocouples were sheathed in molybdenum and Mo — 50Re alloy seamless tubing. Measuring the voltage output as a function of temperature for thermoelements insulated with HfO₂ or ThO₂ in either hydrogen or helium gas showed only relatively small changes from calibrated values. The direction of the small shift in voltage output was similar to those previously determined for unsheathed thermocouples.

EFFECT OF UNMATCHED THERMOCOUPLE WIRE DIAMETERS

To determine the effect of unmatched wire sizes in the construction of a thermocouple probe, a series of tests was initiated studying the effects of unmatched pairs on the emf signal. Wire sizes chosen were 0.25-mm- and 0.125-mm-diameter W and W — 25Re. Unmatched systems were made using 0.25-mm W versus 0.125-mm W — 25Re wire; the matched thermocouples had only 0.25-mm-diameter wire. The wires comprising the two thermoelements of the couple were separated physically by HfO₂ ceramic insulation. The thermoelements and electric ceramic insulator were sheathed in Mo — 50Re and unalloyed molybdenum tubing.

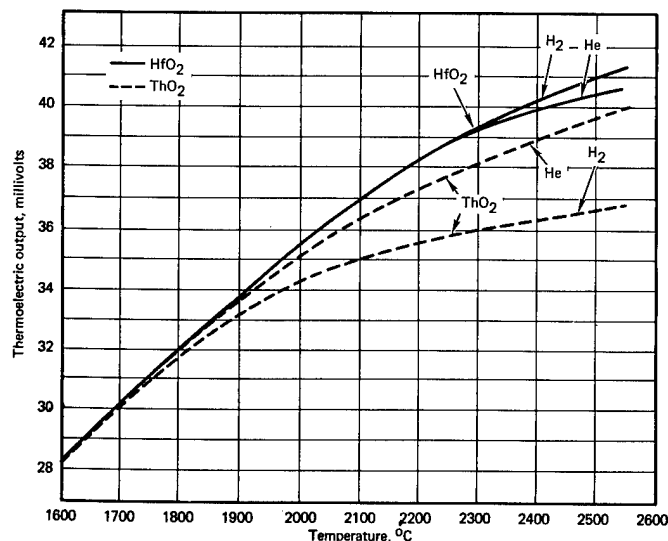


Fig. 9.3 — Comparative curves showing measured thermoelectric signals as a function of temperature in hydrogen and helium from W versus W — 25Re thermocouples insulated with thoria and hafnia

The insulation and sheathing materials were selected for their maximum reliability in high-temperature thermocouple measurements, as shown by previous studies. The major variable in the thermocouple probe was in wire diameters. Testing was again performed in a direct-current electrical heat-resistant furnace (Figure 9.1). The thermoelectric signals were measured against a standard calibration for the W versus W — 25Re wire. Temperatures were verified against optical pyrometer temperature readings on a black-body hole. The family of four curves shown in Figure 9.4 represent the deviations found, and appear to be well within the sensitivity of measuring techniques. The curves overlap each other up to 2200°C. In the higher temperature ranges the spread is insignificant.

These tests strongly indicate that thermoelement wire sizes do not need to be matched in thermocouple systems.

9.2 ELECTRICAL INSULATION FOR HIGH-TEMPERATURE THERMOCOUPLES

A vital part of the thermocouple system is the electrical insulator. Measuring temperatures up to 1700°C is usually fairly easy, because there is a wide choice of materials. Alumina is generally preferred for its economy, excellent electrical insulator properties, and fabricability in all sizes.

For temperature measurements above 1700°C the choice of materials narrows. In an attempt to expand present choices and discover better insulator materials, work was undertaken on compound oxide systems. Previous research studies^{3,4} showed that the CaZrO_3 system had a potential for high-temperature insulation. Although its melting point was not high enough (~2375°C), similar compounds such as SrHfO_3 , SrZrO_3 , and CaHfO_3 have higher melting points: 2680°, 2550°, and 2500°C, respectively. These materials have been considered possible insulators of thermocouples for center-core fuel element temperature measurements above 2500°C. Initial studies were made below

³"AEC Fuels and Materials Development Program Progress Report No. 69," GE-NMPO, GEMP-69, September 29, 1967, pp. 67-69.

⁴"Sixth Annual Report — High-Temperature Materials Program, Part A," GE-NMPO, GEMP-475A, March 31, 1967, pp. 270-271.

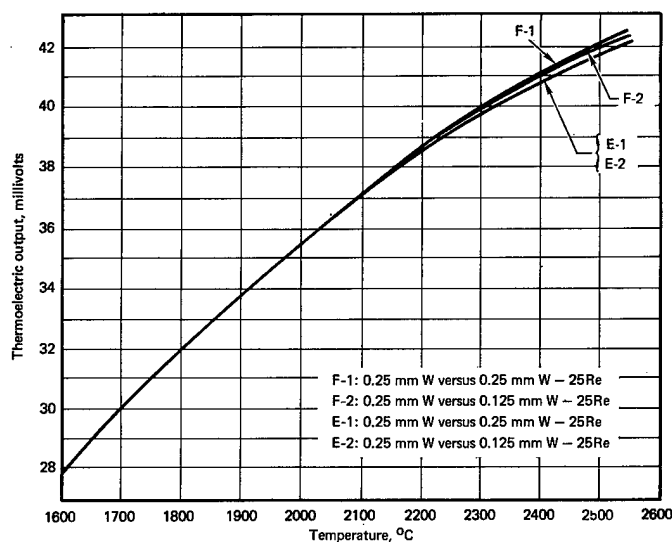


Fig. 9.4 — Comparative curves showing measured thermoelectric signals generated between matched and unmatched wire sizes as a function of temperature

this temperature so that the insulators could be compared with BeO (MP-2450°C), the highest resistivity insulator currently available as a thermocouple insulator.

In three separate tests, each of the above insulators was evaluated by comparing the thermoelectric output of W versus W - 25Re thermocouples insulated with BeO and one of the above three materials. The thermocouples to be compared were placed in Mo - 30Re sheaths which were closed only at the hot end. The sheathed thermocouples were placed together in an apparatus similar to that shown in Figure 9.1. Temperatures measured were referenced against black-body hole temperatures determined by a NBS calibrated optical pyrometer. The calibrations of the three different BeO-insulated thermocouples in all three tests were identical within ± 0.5 percent of the same temperature for the same millivoltage output. The thermoelectric outputs of the SrZrO_3 -, SrHfO_3 -, and CaHfO_3 -insulated thermocouples were within ± 0.5 percent of the BeO-insulated thermocouples up to 2000°C. Above this temperature, deviations occurred which are shown in Figure 9.5. The curve for SrHfO_3 shows the least deviation from the BeO-insulated thermocouple of the three materials and is therefore a potential high-temperature thermocouple insulator.

INTRINSIC VARIABLES AFFECTING THERMOCOUPLE VOLTAGE

During the course of thermocouple testing, several synergistic effects were noted which resulted in abnormalities of the thermocouple signal, especially above 2000°C. In laboratory tests exploring these effects, experiments were performed on a non-insulated loop of W wire and on a HfO_2 -insulated loop of W wire inserted into a high-temperature furnace; the thermoelectric output between the two ends of the W wires was measured. Appreciable electric outputs were obtained in both cases, although theoretically no output should be obtained.

In the test furnace (Figure 9.1) an electrically insulated W T-bar made of 3-mm-diameter material was suspended inside a W muffle. Two 0.05-mm-diameter W wires, one with and one without an electrical insulator, were connected to the W T-bar as shown. This assembly was suspended in a resistively heated W tube furnace. Thermoelectric potential measurements were made between the W T-bar and both the bare and insulated 0.05-mm-dia-

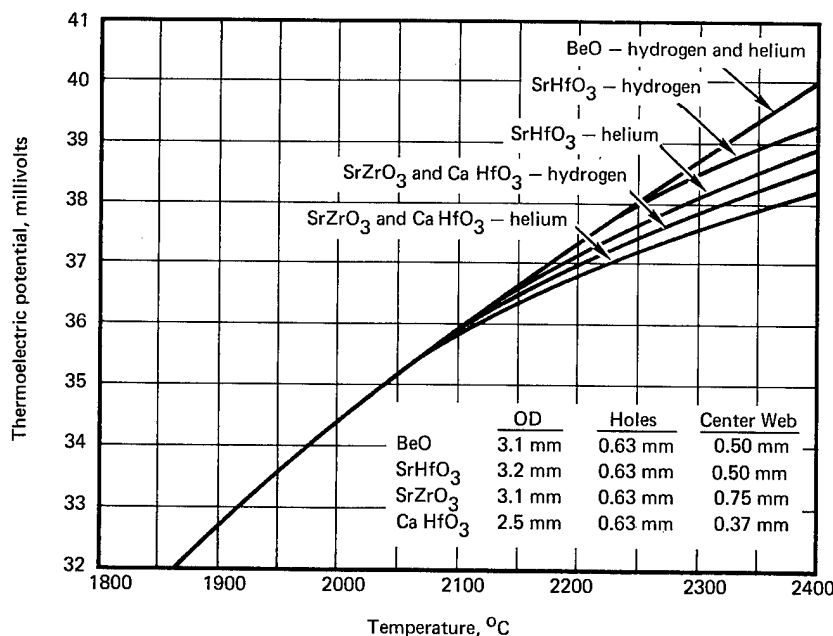


Fig. 9.5 — Thermoelectric output of W-versus W — 25Re-stranded wire (ten 0.075-cm thick wires) thermocouples using BeO, SrZrO₃, SrHfO₃, and CaHfO₃ for electrical insulation in hydrogen or helium

ter wires as a function of temperature. Temperatures were measured using an optical pyrometer by focusing on the bottom surface of the W muffle. The relatively large-diameter (3 mm) W T-bar was used to provide a thermoelectrically stable reference material which could then be used to measure thermoelectric anomalies in the small-diameter W wires by forming an electric circuit with the 0.05-mm-diameter wires. A thermoelectric study was made on bare 0.05-mm wires and on 0.05-mm wires surrounded by BeO or HfO₂. Small-diameter (0.05 mm) wires were used because it was believed they would give an exaggerated effect to any causes of abnormalities.

The curves shown in Figures 9.6 through 9.8 are plots of measured voltage changes as a function of temperature between the W T-bar and either the 0.05-mm-diameter W wire or the BeO-insulated 0.05-mm-diameter W wire in hydrogen, helium, or argon. Each test was run with a new piece of 0.05-mm-diameter W wire. In these three curves, the thermoelectric output developed between the reference W T-bar and the BeO-insulated 0.05-mm-diameter W wire was more consistent than between the W T-bar and the bare 0.05-mm-diameter W wire, as the environmental gas was changed from hydrogen to helium to argon. The reference W T-bar versus 0.05-mm W bare wire output in hydrogen increased rapidly to approximately 0.6 millivolts and then remained fairly steady to 2000°C. In argon the output increased to approximately 1800°C, then began to decrease. In helium, the output increased rapidly to approximately 1.7 millivolts at approximately 1872°C, three times the values in hydrogen or argon.

This wide variation in thermoelectric signals generated between the tungsten T-bar versus bare tungsten wire in the three gases, compared to the relatively stable signals found in the insulated wire in the same gases, suggests that insulation prevents pickup of extraneous electrical signals within the muffle.

The electrical measurements made in the specialized setup (Figure 9.1) indicate that the calibration of bare wire thermocouples must be done with care since there are a number of possible sources leading to errors in calibration measurements:

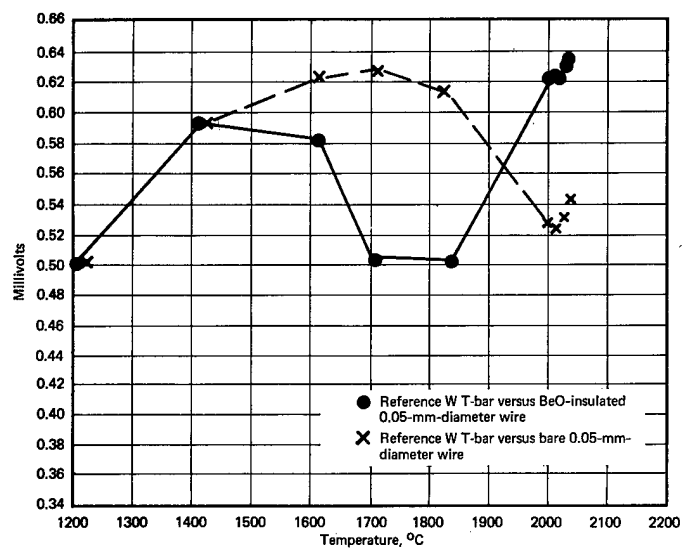


Fig. 9.6 — Measured thermoelectric voltage in a hydrogen atmosphere test apparatus (Figure 9.1) designed to detect causes of anomalies noted during thermocouple calibration experiments

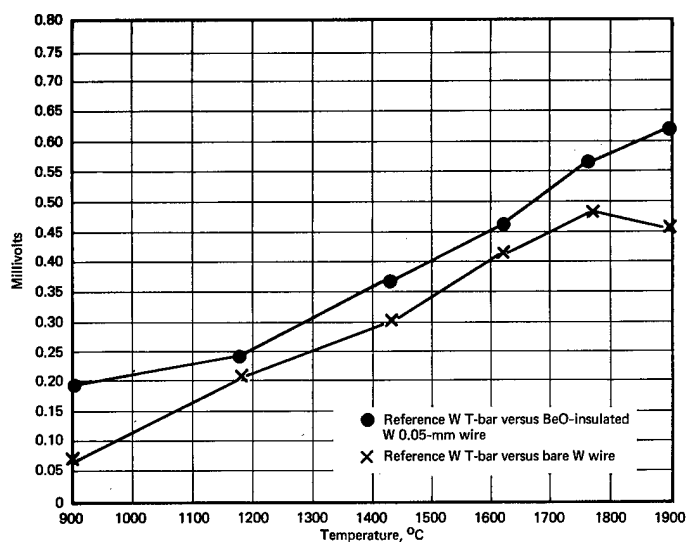


Fig. 9.7 — Measured thermoelectric voltage in an argon atmosphere test apparatus (Figure 9.1) designed to detect causes of anomalies noted during thermocouple calibration experiments

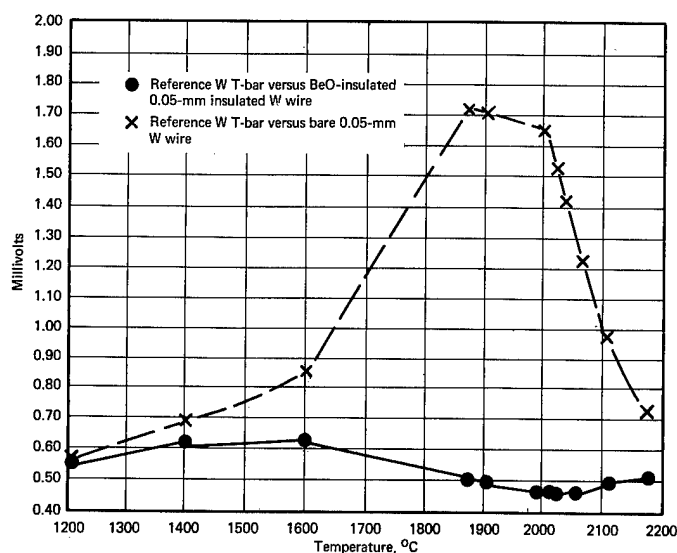


Fig. 9.8 — Measured thermoelectric voltage in a helium atmosphere test apparatus (Figure 9.1) designed to detect causes of anomalies noted during thermocouple calibration experiments

1. Electrical leakage through the insulation.
2. Electrical leakage through ionized gases.
3. Induced emf if container is charged.
4. Thermionics.
5. Thermoelectric effect between "insulator" and thermocouple wire.

9.3 THERMOELECTRIC CHANGES IN W - 25Re DUE TO TRANSMUTATION

The thermoelectric changes of an alloy representing the composition of W - 25Re after 1 year in 10^{14} neutron/cm²-sec thermal flux was previously evaluated and described in detail.⁵ Theoretical calculations on transmuted effects indicate that the W - 25Re alloy composition will change to W - 21.5Re - 5.4 Os (at. %) after 1 year. An alloy rod of this composition was fabricated for thermoelectric tests after heat treating at 2770°C for 3 hours; it was a single-phase alloy. When this rod was placed in a calibrating furnace which imposed a temperature gradient from room temperature to 2300°C along its length, two other phases precipitated in the rod between 2000° to 2300°C causing inhomogeneities along the rod length. This temperature-induced inhomogeneity caused differences (as much as 0.9 mv) in the emf-versus-temperature relationship, depending upon whether calibration was made while increasing or decreasing the temperature. The combination of neutron-induced thermoelectric changes (transmutation) and temperature-induced thermoelectric changes (phase precipitation) would make questionable the use of W-25Re as a thermoelement for temperature measurements when 1-year exposure in a 10^{14} neutron/cm³-sec thermal flux is required.

REACTOR STABILITY OF W VERSUS W - 25Re THERMOCOUPLE

A second reactor test of W versus W - 25Re thermocouples was performed under conditions very similar to one previously reported.⁶ This test was designed to measure the neutron-induced thermoelectric changes in the W and W - 25Re thermoelements and to

⁵GEMP-69, pp. 67-69.

⁶GEMP-475A, pp. 268-270.

minimize the uncertainty previously experienced⁷ in interpreting data relating to the W - 25Re leg. The test had considerable difficulty with W wires breaking; the small amount of W data obtained were inconclusive. Figures 9.9 and 9.10 show the results of thermoelectric deviations of W and W - 25Re as a function of temperature and time in the ORR with a flux of 1.2×10^{14} neutron/cm²-sec thermal and 2.1×10^{13} neutron/cm² sec fast ($E_n \geq 1$ Mev). Data of Figure 9.9 indicate that the W thermoelement at low temperature (600°C) becomes more thermoelectrically positive with dosage, and at approximately 1400°C changes very little with dosage. At approximately 1800°C no data were obtained, but the shape of the curve indicates that W becomes more thermoelectrically negative in this region. The W data appear to confirm previous findings⁶ although at 600°C the latest test shows a greater positive increase in thermoelectric potential. The data of Figure 9.10 for W - 25Re indicate that the shapes of the curves are very similar to those obtained for W; this differs from conclusions of the first test⁷ whose data were difficult to interpret. The similarity of the W and W - 25Re curves indicates that changes in the W thermoelement are compensated by changes in the W - 25Re thermoelement. There is a degree of difference between the W and the W - 25Re thermoelectric changes which results in a small net increase in thermoelectric output of a W versus W - 25Re thermocouple. For the time period represented by the two curves, the maximum increase in indicated temperature would be approximately 5°C.

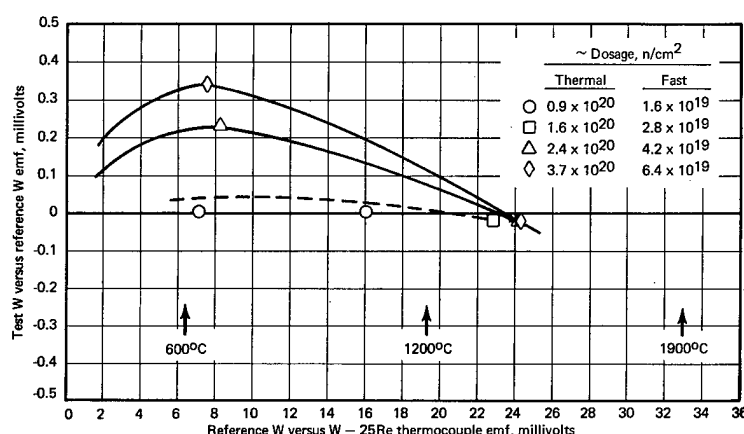


Fig. 9.9 — Relative stability of W thermoelements as a function of temperature and time in a 1.2×10^{14} n/cm²-sec thermal flux

REACTOR TESTING OF THERMOCOUPLE MATERIALS

Test capsules containing 0.25-mm-diameter wires of W, W - 25Re, W - 3Re, Mo, Fe, Chromel, Alumel, Constantan, BeO, and Al₂O₃ were shipped to the EBR-II. They were originally scheduled for insertion in December 1967, but have been delayed until March 1968. These capsules contain 15-cm lengths of the above thermocouple materials. After exposure to approximately 10^{22} to 10^{23} neutron/cm² fast neutrons, all materials will be removed from the reactor and each will be compared thermoelectrically in the laboratory with unirradiated specimens of the identical materials.

9.4 SUMMARY AND CONCLUSIONS

Studies of very high-temperature thermocouple characteristics revealed that the thermoelectric emf produced along BeO, HfO₂, or ThO₂ insulators can affect the output of the

⁷"High-Temperature Materials Program Progress Report No. 63," GE-NMPO, GEMP-63, December 30, 1966, pp. 129-133.

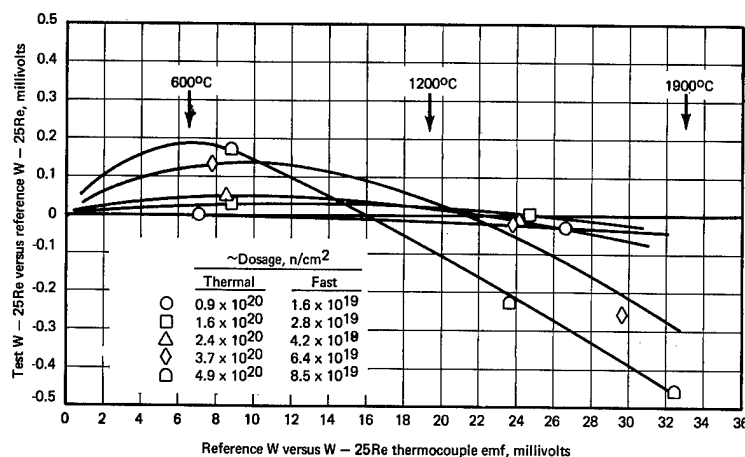


Fig. 9.10 — Relative stability of W — 25Re thermoelements as a function of temperature and time in a 1.2×10^{14} n/cm²-sec thermal flux

thermoelements. Bare-wire thermocouples were found to be influenced by the environment.

The nuclear radiation effect on W versus W — 25Re thermocouples in the ORR after approximately 2 months in a 1.2×10^{14} neutron/cm²-sec thermal and 2.1×10^{13} neutron/cm²-sec fast flux was studied. Results indicate that the W and the W — 25Re thermoelements shift similarly in thermal emf, resulting in a small (5°C) positive error.

SrHfO₃, SrZrO₃, and CaHfO₃ were found to be inferior to BeO and HfO₂ as thermocouple insulator materials.

9.5 PLANS AND RECOMMENDATIONS

Evaluations will continue of neutron-flux-induced thermoelectric changes with emphasis on the effects of fast neutron dosage.

Methods will be investigated to improve thermocouple performance at very high temperatures by improving techniques and optimizing material selection. This effort is aimed at improving reliability and accuracy of center-core temperature measurement of LMFBR fuel pins.

Studies will be made to improve the reliability of thermocouples for measuring the liquid metal coolant temperature of fast breeder reactors.

10. PHYSICO-CHEMICAL STUDIES OF Fe-Cr-Al-CLAD FUEL SYSTEMS

(7076)

H. S. Edwards,* K. M. Bohlander†

The objective of this program, which was terminated at the end of FY-66, was to define and to understand the reactions which can occur between oxidation-resistant Fe-Cr-Al-base alloys and UO_2 in the temperature region from 500° to 1200°C.

Early attempts to use Fe-Cr-Al-base alloys as cladding for UO_2 or metal- UO_2 fuels resulted in the appearance of uranium as surface contamination on specimens tested in air at elevated temperatures for extended periods of time. The tentative explanation of this result was that UO_2 was reduced by aluminum in the cladding, thus producing uranium which diffused to the surface. Final work on this program during CY-67 included diffusion studies and fueled capsule tests. A summary of the conclusions derived from the overall work program is presented.

10.1 DIFFUSION STUDIES

Fe, Cr, AND Al DIFFUSION

Diffusion couples of Fe-Cr-Al versus Fe and Fe-Cr-Al versus Cr were studied to determine the rate of influx of cladding alloy constituents, such as Al, into the core area, which normally contains a cermet fuel of Fe- UO_2 or Cr- UO_2 . The couples were fabricated from 2.54-cm-long by 1.27-cm-diameter rods of the Fe-Cr-Al alloys listed in Table 10.1. A 0.32-cm-diameter axial hole was drilled into the rods and the core portion of the diffusion couple (usually Fe or Cr) press-fitted into the opening in the cladding. The diffusion capsules were completed by fitting a closure rod of the same alloy as the cladding into the top of the capsule and sealing by electron-beam welding in vacuum. After checking for leaks, the capsules were autoclaved for 2 hours at 1000°C and 700 kg/cm² gas pressure to insure core-cladding contact. Sufficient couples were placed on test at 1000°C that a complete set could be removed for destructive analysis after 100, 300, and 1000 hours.

The initial results of transverse electron microprobe analyses presented previously¹ were not quantitatively accurate; trends in the data, however, indicated that cladding materials containing greater quantities of Al will increase the distance Al diffuses into Fe cores, and that Cr most effectively curtails the diffusion of cladding constituents. The diffusion couples were re-examined using the electron microprobe in the step-scan scanning mode with fixed-time counting. Corrections were applied to the data and plots made of the normalized concentrations as a function of radial distance.² A solution of the diffusion equation, appropriate for the geometry of the test specimens, was determined and

*Project leader.

†Principal investigator.

¹"Sixth Annual Report - High-Temperature Materials Program, Part A," GE-NMPO, GEMP-475A, March 31, 1967, pp. 178-179.

²"AEC Fuels and Materials Development Program Progress Report No. 67," GE-NMPO, GEMP-67, June 30, 1967, pp. 79-86.

numerical values for diffusion coefficients of Fe, Cr, and Al in Fe-base alloys were calculated (Table 10.2). No diffusion coefficients were calculated for samples with Cr cores. The markedly lower diffusion rates in Cr were apparent from a qualitative examination of the plots.

URANIUM DIFFUSION

The objective of the uranium diffusion studies was to determine the manner in which the U-bearing reaction products formed in the core were transported through the cladding to the surface. An attempt was made to determine the diffusion coefficient of U in Fe-Cr-Al alloys and to differentiate between volume diffusion and grain boundary diffusion of U in these alloys.

Determination of the diffusion coefficients of U in Fe-Cr-Al alloys was hampered by the lack of an accurate method for measuring very small concentrations of U in these alloys. Initially, the electron microprobe and spark-source mass spectrograph were used in attempts to measure U concentration gradients and solubilities. The extremely low U solu-

TABLE 10.1

COMPOSITIONS^a OF ALLOYS FABRICATED FOR PROGRAM USE

Fe - 5Cr - 4Al	Fe - 5Cr - 7Al	Fe - 5Cr - 10Al	Fe - 4Al
Fe - 15Cr - 4Al	Fe - 15Cr - 7Al	Fe - 15Cr - 10Al	Fe - 10Al
Fe - 25Cr - 4Al	Fe - 25Cr - 7Al	Fe - 25Cr - 10Al	Fe - 5Cr
			Fe - 25Cr

^aNominal compositions are in weight percent.

TABLE 10.2

DIFFUSION COEFFICIENTS AT 1000°C

Nominal Composition, wt % Core	Cladding	Time, hr	Diffusion Coefficient, cm ² /sec		
			D _{Fe}	D _{Cr}	D _{Al}
Fe	Fe - 4Al	100	— ^a	—	6.5 x 10 ⁻¹⁰
Fe	Fe - 4Al	300	—	—	5.0 x 10 ⁻¹⁰
Fe	Fe - 10Al	100	7.8 x 10 ⁻¹⁰	—	6.7 x 10 ⁻¹⁰
Fe	Fe - 10Al	300	—	—	8.0 x 10 ⁻¹⁰
Fe	Fe - 25Cr	100	2.9 x 10 ⁻¹⁰	3.1 x 10 ⁻¹⁰	—
Fe	Fe - 25Cr	300	—	9.0 x 10 ⁻¹⁰	—
Fe	Fe - 5Cr - 4Al	100	—	2.9 x 10 ⁻¹⁰	5.8 x 10 ⁻¹⁰
Fe	Fe - 5Cr - 10Al	100	6.3 x 10 ⁻¹⁰	2.8 x 10 ⁻¹⁰	5.3 x 10 ⁻¹⁰ to 21.0 x 10 ⁻¹⁰
Fe	Fe - 25Cr - 4Al	100	2.9 x 10 ⁻¹⁰	2.4 x 10 ⁻¹⁰	9.5 x 10 ⁻¹⁰
Fe	Fe - 25Cr - 10Al	300	8.1 x 10 ⁻¹¹	3.5 x 10 ⁻¹⁰	1.3 x 10 ⁻⁹
Fe - 10Al	Fe - 5Cr - 10Al	1000	—	5.5 x 10 ⁻¹⁰	—
Fe - 10Al	Fe - 25Cr - 10Al	100	4.7 x 10 ⁻¹⁰	3.4 x 10 ⁻¹⁰	—
Fe - 25Cr	Fe - 25Cr - 4Al	100	—	—	3.5 x 10 ⁻¹⁰
Fe - 25Cr	Fe - 25Cr - 4Al	300	—	—	4.0 x 10 ⁻¹⁰
Fe - 25Cr	Fe - 25Cr - 10Al	100	—	—	6.8 x 10 ⁻¹⁰

^aNot measured.

bilities in Fe-Cr-Al alloys (~ 0.1 wt %) were at or below the detection limit of the electron microprobe, and the relatively low spatial resolution of the spark-source mass spectrograph rendered it unsuitable for accurate analysis of a solid diffusion couple.

The high sensitivity and accuracy of the X-ray fluorescence spectrograph in determining microgram quantities of U on the surface of Fe-Cr-Al-clad fueled specimens (discussed later), prompted an investigation of this instrument as a potential tool in determining U diffusion coefficients. As originally fabricated, the diffusion couple to be analyzed consisted of two solid right cylinders of Fe-5Cr-4Al-1U and Fe-5Cr-4Al (both wt %) butted together and sealed in Fe-Cr-Al tubing. The couple was autoclaved at 1000°C to insure contact and then heat treated for 3450 hours at 1000°C . Parallel sections were removed by machining and analyses were made perpendicular to the specimen length with the periphery masked to eliminate surface effects. A graph of the U concentration as a function of distance (shown in Figure 10.1) agreed with pertinent chemical analyses, microprobe, and metallographic data; however, part of the experimental data in the region of the interface appeared suspect and would need to be verified. Also, the

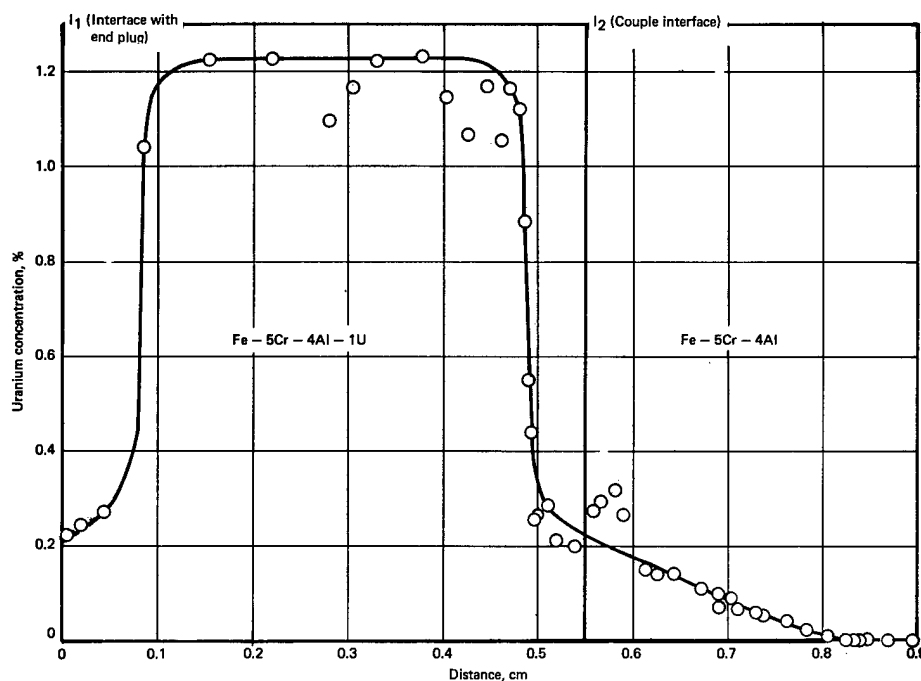


Fig. 10.1 — Uranium concentration profile in Fe-5Cr-4Al-1U versus Fe-5Cr-4Al (wt %) diffusion couple after 3450 hours at 1000°C

unsymmetrical shape of the data points in the vicinity of the interface does not fit available solutions of the diffusion equation. However, the extended length of diffusion time and the length of the diffusion zone may partly compensate for experimental errors. The maximum diffusion distance measured by this technique correlates well with data obtained from the fission track etching method (discussed later). This correlation adds credence to the present data and prompted calculating an approximate value of the diffusion coefficient for U in the Fe-5Cr-4Al alloy. Using a semi-infinite diffusion model with an extended source, the diffusion coefficient was determined to be in the range 10^{-9} to 10^{-10} cm^2/sec , or approximately the same as the coefficients determined for Fe, Cr, and Al. Although supporting data are necessary before this coefficient can be considered accurate, the results

do show the potentialities of the X-ray fluorescence spectrograph to perform difficult and sensitive analyses. It is believed that improved sectioning and standardizing techniques could significantly increase the accuracy of this technique for future diffusion studies of this type.

An attempt was made to differentiate between volume and grain boundary diffusion of U in Fe-Cr-Al alloys using the fission track etching technique.³ Diffusion couples of the type Fe-Cr-Al-U versus Fe-Cr-Al were heat treated for 500 and 1000 hours at 1000°C and 100 hours at 1050°C. These specimens were longitudinally sectioned, metallographically polished, and shipped to a reactor site where they were coated with plastic and irradiated. After irradiation, the location of U in the Fe-Cr-Al side of the couple was determined in relation to existing grain boundaries. This method showed that U diffusion through Fe-Cr-Al alloys at 1000° to 1050°C is by volume diffusion, unaffected by grain boundaries. This method also confirmed the existence of U in the U-depleted zone of the original Fe-Cr-Al-U portion and an abrupt decrease of U at the depleted zone - Fe-Cr-Al-U boundary. Because of the relatively small number of diffusion couples irradiated and the failure of several to develop reliable fission track patterns, no diffusion constant was obtained; however, maximum U diffusion distances were measured and are shown in Figure 10.2 together with the maximum distance of U penetration as measured by X-ray fluorescence on Fe-5Cr-4Al-1U versus Fe-5Cr-4Al after 3450 hours at 1000°C. These data verify that the diffusion of U is unaffected at 1000°C by grain boundaries and is independent of Fe-Cr-Al composition (within the limits studied).

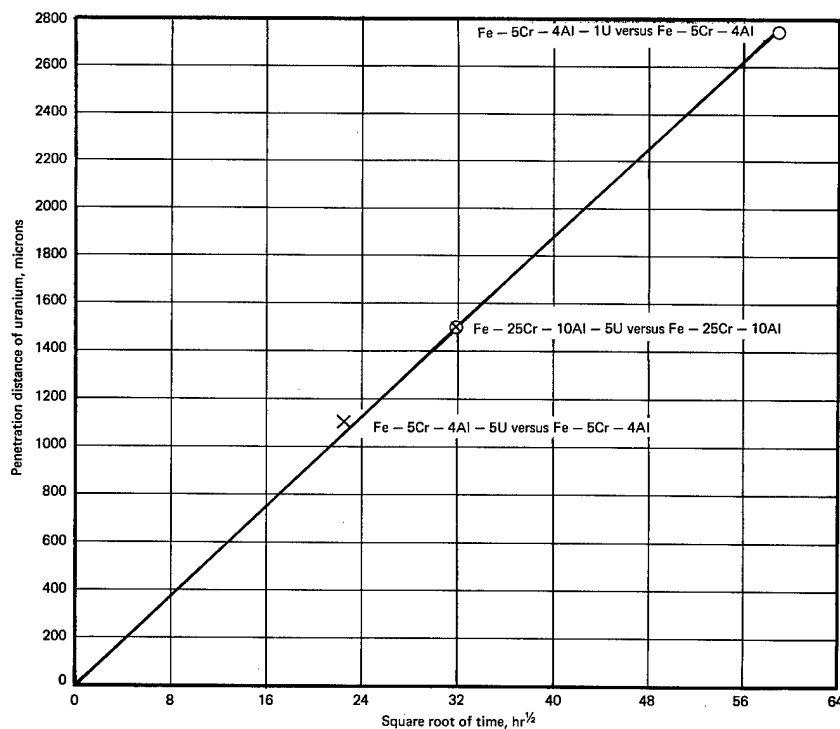


Fig. 10.2 — Maximum penetration of uranium in Fe-Cr-Al-base alloys at 1000°C as measured from the interface by fission track etching or sectioning methods

³H. S. Rosenbaum and J. S. Armijo, "Fission Track Etching as a Metallographic Tool," Journal of Nuclear Materials, Vol. 22, April 1967, pp. 115-116.

10.2 FUELED CAPSULE TESTS

Capsule tests were performed to quantitatively determine the rate of U accumulation on the surface of Fe-Cr-Al-clad UO_2 -containing cermet fuel specimens as a function of the cladding and core composition. The specimens in these tests were 2.5-cm-diameter discs approximately 0.25 cm thick, with 0.038-cm-thick cladding on one flat side and 0.076-cm-thick cladding on the other. The cladding compositions were those listed in Table 10.1 and the fueled cores were predominantly $\text{UO}_{2.00}$, $\text{UO}_{1.989}$, and Fe-40 $\text{UO}_{2.00}$ (vol %) sintered to densities exceeding 95 percent of theoretical. A few Cr-40 $\text{UO}_{2.00}$ (vol %) cores clad with 0.051-cm-thick Fe-25Cr-4Al (wt %) were fabricated. The capsules were evacuated, sealed by electron-beam welding, and autoclaved at 600°C and 140 kg/cm² gas pressure to achieve uniform core-cladding contact during testing. Testing was done under 2 atmospheres of argon gas containing 3 volume percent oxygen to maintain core-cladding contact, oxidize any U diffusing to the cladding surface, and prevent catastrophic oxidation of the low-alloy claddings.

Partial results from testing capsules at 1200°C and 800°C were reported previously,⁴ together with information for a series of capsules containing Fe-40 $\text{UO}_{2.00}$ cores and $\text{UO}_{1.989}$ cores which completed 1000 hours at 600°C. Analysis for surface U was by X-ray fluorescence spectrograph with a 7 to 9 microgram U/cm² lower limit of detection.

Two series of clad specimens completed 1000 hours at 1200°C; one series contained $\text{UO}_{2.00}$ cores and the other $\text{UO}_{1.989}$ cores. Figure 10.3, which shows the quantity of U on the surface of specimens containing $\text{UO}_{1.989}$ cores, demonstrates that free U (present in the core) diffuses completely through the cladding within 6 hours at 1200°C. The quantity of Al present in the Fe-Cr-Al cladding appeared to have little, if any, influence on the rate of accumulation of surface U; however, complete absence of Al from the cladding (Fe-5Cr and Fe-25Cr) decreased the U diffusion rate. The presence of U in the claddings had a detrimental effect on the cladding or cladding-core interface and resulted in many cladding failures due to radial cracking.

Results for representative capsules containing $\text{UO}_{2.00}$ cores during 1000 hours at 1200°C are shown in Figure 10.4. Only minor differences arising from different cladding thickness are indicated, the first detection of surface U on the 0.76-mm-thick cladding occurred 20 to 40 hours after the first indication on the 0.38-mm-thick side (13 hours). No definite relationship was established between the quantity of Al in the Fe-Cr-Al cladding and the amount of surface U contamination. The data show that binary Fe-Al claddings will produce greater amounts of U on the surface than Fe-Cr-Al alloy claddings and claddings containing no Al will produce no detectable U during 1000 hours testing at 1200°C. Thus, it appears that Al in the cladding does produce subsequent U contamination on the surface, probably due to reducing UO_2 to U. The comparatively high U concentration on the capsules without Cr in the cladding may indicate that Cr has an inhibiting effect on the diffusion of Al. A slight but similar trend was noted among the Fe-Cr-Al-clad capsules; those with 25 percent Cr had smaller surface concentrations than those with 5 percent Cr, even though the Al concentrations of the claddings were the same. In this group of specimens, there was no evidence of oxidation or cracking in any of the claddings as in the group of substoichiometric specimens.

The preceding observations were in agreement with the diffusion results on Cr and Al and suggested that the diffusion of Al into the core (containing $\text{UO}_{2.00}$) could be curtailed or eliminated with a Cr barrier layer; thus, no U would be produced to diffuse to the surface of the cladding. Accordingly, several capsules were fabricated from 0.51-mm-thick Fe-25Cr-4Al (wt %) cladding and Cr-40 $\text{UO}_{2.00}$ (vol %) fuel was fabricated as the usual

⁴GEMP-475A, pp. 181-182.

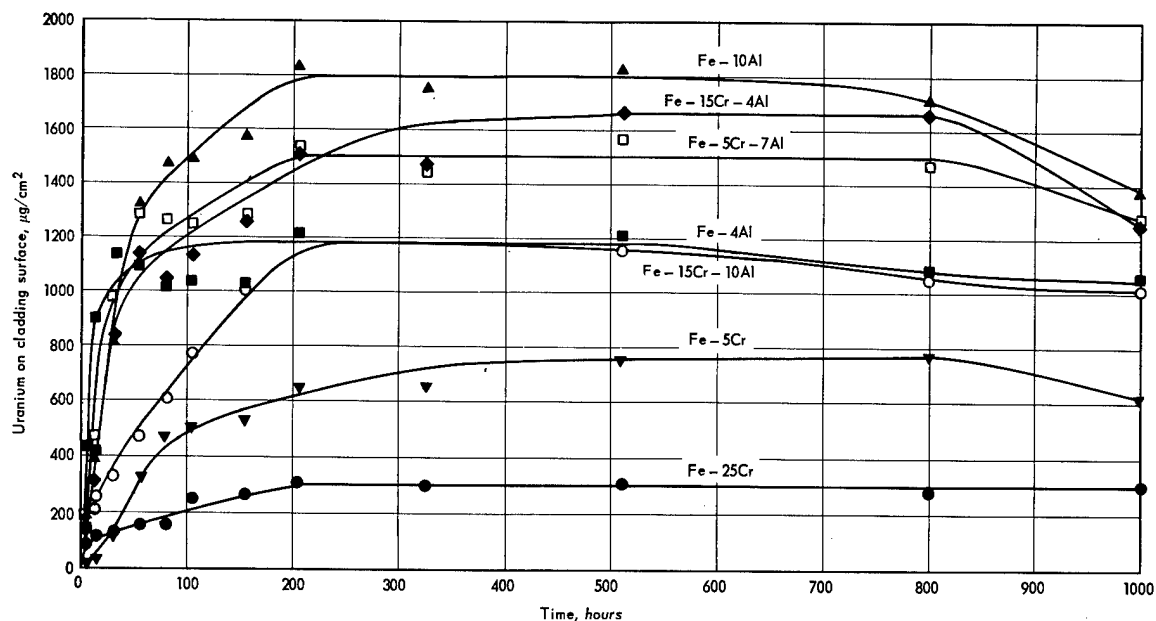


Fig. 10.3 — Concentration of U on surface of various claddings after 1000 hours at 1200°C (clad specimens contained $\text{UO}_{1.989}$)

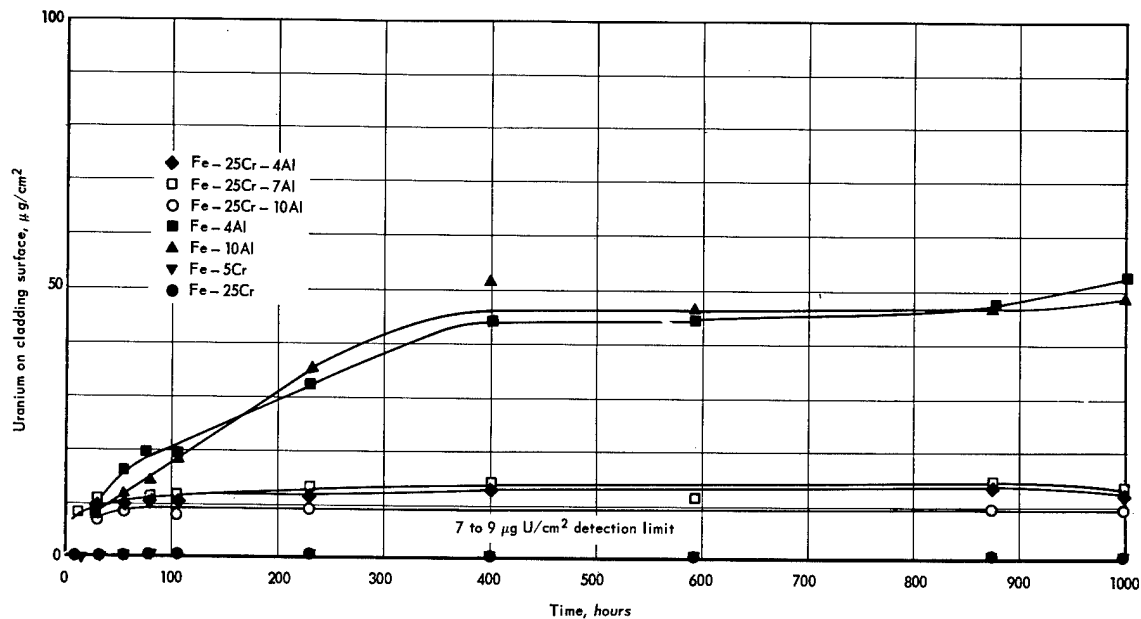


Fig. 10.4 — Concentration of U on surface of various claddings after 1000 hours at 1200°C (clad specimens contained $\text{UO}_{2.00}$)

disc-shaped core. A 0.08-mm-thick layer of Cr separated the core and cladding. Capsules were tested in the usual manner at 1200°C with control capsules and a capsule containing a substoichiometric $\text{UO}_{1.989}$ core separated from the Fe - 25Cr - 4 Al cladding by a Cr barrier. Results from the control capsules duplicated previous results (Figures 10.3 and 10.4). The capsule containing the $\text{UO}_{1.989}$ core showed no improvement over previously tested capsules with no Cr layer; hence, a Cr barrier does not impede the diffusion rate of U through the cladding after U is formed. Results from capsules containing Cr- $\text{UO}_{2.00}$ fuel and Cr barriers showed no surface U in 900 hours at 1200°C plus 125 hours at 1300°C. This appears to be a significant improvement over non-Cr-barrier capsules, but the extent was difficult to assess because of the lower limit of detection of 7 to 9 micrograms U/cm^2 and the usual range of U concentration formed on Fe-Cr-Al-clad capsules (10 to 20 micrograms U/cm^2) after 1000 hours at 1200°C.

When examined, a metallurgical bond between the Cr and the core and cladding made the exact interface difficult to determine. There were a few small voids and oxide particles in the interface area, fewer than in capsules containing Fe- $\text{UO}_{2.00}$ or Cr- $\text{UO}_{2.00}$ with no Cr barrier. From this limited amount of testing, it appears that a Cr barrier impedes the inward diffusion of Al to the UO_2 core and thus prevents the formation of U; it does not, however, prevent the outward diffusion of U if it is already present in the fuel.

Two series of capsules containing Fe - 40 $\text{UO}_{2.00}$ (vol %) cores and $\text{UO}_{1.989}$ cores were initially tested at 600°C for 1000 hours in argon containing 3 percent oxygen. Intermediate analyses by X-ray fluorescence during and after the test showed no surface U contamination on any of the capsules. The temperature was increased to 800°C and the same specimens were tested an additional 1000 hours. Intermediate and final analyses indicated again that no surface U was on the claddings (within the 7 to 9 micrograms U/cm^2 detection limit of the instrument).

The capsules were returned to test at 1000°C. After 100 hours, analyses showed U on all Fe-Cr-Al- and Fe-Al-clad $\text{UO}_{1.989}$ core capsules. The amount varied from 10 to 60 micrograms U/cm^2 and increased regularly with time until after 1000 hours it ranged from 30 to 380 micrograms U/cm^2 . The results were similar to the previous test at 1200°C in that no definite relationship was established between Cr or Al content of the cladding and the amount of U measured. No U was detected on the cladding alloys which did not contain Al; thus corroborating 1200°C test data showing enhanced U diffusion rates through cladding alloys containing Al. There were no cladding failures due to cracks during this 1000°C test as there were at 1200°C; however, metallographic examination disclosed that U diffusing through the claddings had a detrimental effect. Most of the claddings bore evidence of intergranular oxidation; oxide penetration up to 0.35 mm was found in some specimens.

Analyses of the series of clad capsules containing Fe - 40 $\text{UO}_{2.00}$, both during and after the 1000-hour test at 1000°C, detected no U on the surface of any capsule. Post-test metallographic examination showed no deterioration of the cladding (as occurred with substoichiometric fuels) and good core-to-cladding contact with a thin discontinuous film, approximately 3 microns thick, of Al_2O_3 at the interface.

10.3 CONCLUSIONS

Aluminum in Fe-Cr-Al-base cladding alloys reduces UO_2 in cermet fuels, beginning in the temperature range between 1000° and 1200°C. Free U formed in this reaction dissolves in and diffuses rapidly through the cladding to the surface where it is converted to an oxide. At 1000°C and below, no reaction of Al with UO_2 takes place within the lower limits of detection of the surface analytical method used (7 to 9 micrograms U/cm^2). Oxygen liberated during the reduction of UO_2 combined with Al from the cladding to form Al_2O_3 at the clad-

ding - core interface. This stable compound inhibits subsequent diffusion of Al into the UO_2 -containing fuel and consequently limits the quantity of U formed. This process of Al_2O_3 barrier formation indicates that increasing the Al content of the cladding above 4 weight percent, to increase oxidation resistance, would not significantly influence the amount of surface U contamination.

The diffusion coefficient of Al in Cr was found to be significantly lower than other elements in the Fe-Cr-Al-U system and led to the development of a Cr barrier between the fuel and cladding to reduce Al- UO_2 interaction and potentially eliminate surface U contamination.

If free U is initially present in the fuel, for example, as substoichiometric UO_{2-x} , or if free U is formed in the fuel during operation, then the U would diffuse through 0.38-mm-thick cladding within 100 hours at 1000°C or within 6 hours at 1200°C . Uranium diffusion through binary Fe-Cr alloys is curtailed in comparison with ternary Fe-Cr-Al alloys, in which the diffusion rate is virtually unaffected by the composition of the cladding (within the composition limits of this study 5 to 25% Cr and 4 to 10% Al). No U was detected on the surface of any specimen after 1000 hours at 600°C or after the test temperature was increased to 800°C for an additional 1000 hours. At 1000°C , U solubility in Fe-Cr-Al alloys is 0.1 to 0.2 percent, and its diffusion coefficient is in the range 10^{-9} to 10^{-10} cm^2/sec .

11. HIGH-TEMPERATURE RESEARCH ON CARBIDES FOR FUEL AND STRUCTURAL APPLICATIONS

(7073)

J. F. White,* E. F. Juenke†

The objective of this program was to determine the high-temperature physico-chemical properties of refractory carbides for fuel and structural applications.

This program terminated at the end of Fiscal Year 1967; significant results are presented below.

11.1 PREPARATION AND FABRICATION OF REFRACTORY CARBIDES

The results of reaction studies for the preparation of well-characterized carbides of Ta, Zr, and Hf from their respective oxides are shown in Table 11.1. Spectrographic-grade graphite – oxide reactions require higher temperatures, in the range of 2200° to 2300°C, to form well-crystallized single-phase material. While zirconium oxide reacts with C to form ZrC in about 1 to 2 hours at temperatures between 1850° and 2000°C, com-

TABLE 11.1
X-RAY DIFFRACTION AND CHEMICAL ANALYSES OF CARBIDES PRODUCED FROM THE METAL OXIDES IN VACUUM

Material	Reaction Temperature, °C	Time at Temperature, hr	Lattice Parameter, Å	Combined Carbon, wt % (± 0.05) ^a	Uncombined Carbon, wt %	Oxygen, ppm	Nitrogen, ppm	Combined Carbon-to-Metal Ratio
TaC ^c	1800	1	Two phases TaC + Ta ₂ C	4.91	1.48 \pm 0.05	700 \pm 100	23 \pm 20	0.79 \pm 0.01
TaC ^c	1800	5	TaC + Ta ₂ C	—	—	—	—	—
TaC ^c	2000	1	4.455	5.74	0.37 \pm 0.05	700 \pm 100	< 5 \pm 5	0.93 \pm 0.01
TaC ^c	2000	5	4.456	5.86	0.28 \pm 0.02	600 \pm 100	< 5 \pm 5	0.94 \pm 0.01
TaC ^c	2200	1	4.455	6.07	0.12 \pm 0.02	350 \pm 30	< 5 \pm 5	0.98 \pm 0.01
TaC ^c	2200	5	4.456	6.23	0.10 \pm 0.02	1640 \pm 100	< 5 \pm 5	1.00 \pm 0.01
ZrC ^b	1850	2	4.698	11.47	0.529 \pm 0.05	—	330 \pm 30	0.99 \pm 0.01
ZrC ^b	2000	1½	4.649	12.39	0.18 \pm 0.02	450 \pm 30	77 \pm 30	1.08 \pm 0.01
ZrC ^b	2150	¾	4.699	11.74	0.18 \pm 0.02	1140 \pm 100	398 \pm 30	1.01 \pm 0.01
ZrC ^c	2000	5	4.698	10.07	1.31 \pm 0.05	430 \pm 30	580 \pm 100	0.86 \pm 0.01
ZrC ^c	2200	1	4.699	11.31	0.62 \pm 0.05	1340 \pm 100	252 \pm 30	0.97 \pm 0.01
ZrC ^c	2200	5	4.698	11.59	0.56 \pm 0.05	1300 \pm 100	5 \pm 5	1.00 \pm 0.01
HfC ^c	2200	2	4.638	5.84	0.36 \pm 0.05	920 \pm 100	350 \pm 30	0.92 \pm 0.02
HfC ^c	2300	2	4.638	6.35	0.36 \pm 0.05	720 \pm 100	280 \pm 30	1.01 \pm 0.01
HfC ^c	2300	5	4.638	5.94	0.62 \pm 0.05	470 \pm 30	350 \pm 30	0.95 \pm 0.01

^aPercent carbon for stoichiometric carbides (1:1 C/M) are as follows:

TaC 6.22

ZrC 11.63

HfC 6.30

^bPrepared from oxide and carbon.

^cPrepared from oxide and spectrographic graphite.

*Project leader.

†Principal investigator.

plete reaction between this oxide and spectrographic-grade graphite requires 5 hours at 2200°C to produce single-phase ZrC. Hafnium oxide – graphite reactions to form HfC require temperatures of at least 2300°C to obtain a well-crystallized, homogeneous, single-phase product.

Typical analyses of scaled-up lots (2 kg) of TaC, ZrC, and HfC (preparation based on the conditions determined in the above experiments) are shown in Table 11.2.

Analyses of Ta and Zr carbides prepared from the hydrides appear in Table 11.3. These data indicate that a 2200°C treatment was required to form single-phase TaC, whereas single-phase ZrC was formed at 1800°C. Reacting the Zr hydride with C at 2000°C and above, however, produced a higher carbon-to-metal ratio. In general, the oxygen content of the product is lower than in the graphite – oxide reactions; the nitrogen content is about the same.

Vacuum hot pressing was used to form dense cylindrical specimens of various carbides. Table 11.4 summarizes the results. TiC and ZrC were fabricated at nearly theoretical density by hot pressing in graphite dies at 2125°C for 5 to 30 minutes. TaC and HfC required temperatures of 2200° to 2300°C for 15 to 30 minutes to achieve densities from 94 to 97 percent of theoretical.

TABLE 11.2
CHEMICAL AND X-RAY ANALYSES OF TYPICAL BATCHES OF TaC, ZrC,
AND HfC PREPARED BY OXIDE-GRAPHITE REACTION IN VACUUM

Material	Reaction Conditions	Free Carbon, %	Oxygen, ppm	Nitrogen, ppm	X-Ray Analysis
TaC	5 hr at 2200°C	0.16	950	8	Single-phase fcc
ZrC	5 hr at 2200°C	0.56	1300	<5	Single-phase fcc
HfC	2 hr at 2400°C	0.28	91	52	Single-phase fcc

TABLE 11.3
X-RAY DIFFRACTION AND CHEMICAL ANALYSES OF ZrC AND TaC PRODUCED FROM
METAL HYDRIDE – GRAPHITE REACTIONS IN VACUUM

Material	Reaction Temperature, °C	Phases	Combined Carbon, wt % (± 0.05)	Uncombined Carbon, wt %	Oxygen, ppm	Nitrogen, ppm	Combined Carbon-to-Metal Ratio (± 0.01)
TaC ^a	1800	Inhomogeneous TaC plus graphite	5.67	0.39 \pm 0.05	320 \pm 30	13 \pm 5	—
TaC ^b	1800	Inhomogeneous TaC plus graphite	5.50	0.56 \pm 0.05	280 \pm 30	34 \pm 10	—
TaC ^a	2000	Inhomogeneous TaC	5.73	0.29 \pm 0.05	330 \pm 30	<5 \pm 5	—
TaC ^b	2000	Inhomogeneous TaC	5.89	0.27 \pm 0.05	2.90 \pm 30	18 \pm 5	—
TaC ^a	2200	TaC, $a_o = 4.453_7$	6.07	0.050 \pm 0.007	260 \pm 30	29 \pm 10	0.97
TaC ^b	2200	TaC, $a_o = 4.454_1$	6.07	0.032 \pm 0.005	180 \pm 30	<5 \pm 5	0.97
ZrC ^a	1800	ZrC, $a_o = 4.698_5$	10.83	0.40 \pm 0.05	650 \pm 50	345 \pm 30	0.93
ZrC ^b	1800	ZrC, $a_o = 4.698_1$	10.94	0.38 \pm 0.05	590 \pm 50	369 \pm 30	0.94
ZrC ^a	2000	—	11.55	0.18 \pm 0.02	310 \pm 30	299 \pm 30	0.99
ZrC ^b	2000	—	11.16	0.33 \pm 0.05	350 \pm 30	351 \pm 30	0.96
ZrC ^a	2200	ZrC, $a_o = 4.697_9$	11.33	0.075 \pm 0.005	1570 \pm 100	96 \pm 20	0.97
ZrC ^b	2200	ZrC, $a_o = 4.697_7$	11.36	0.19 \pm 0.02	2910 \pm 100	133 \pm 20	0.98

^aMaterial prepared by reaction of stoichiometric 1:1 graphite-to-metal ratio.

^bMaterial prepared with 0.5 percent excess graphite.

TABLE 11.4
DENSITY OF VARIOUS CARBIDE COMPACTS PREPARED
BY VACUUM HOT-PRESSING

Material ^a	Vacuum Hot-Pressing Conditions				Density, percent of theoretical
	Temperature, °C	Time, min	Pressure, kg/cm ²	Vacuum, 10 ⁻² Torr	
TiC	1750	5	105.4	5.0	97.4
TiC	2030	5	105.4	2.0	100.0
TiC	2135	15	140.6	1.5	100.0
ZrC	2000	45	126.5	2.5	99.9
ZrC	2125	30	140.6	1.5	99.76
ZrC	2125	30	140.6	1.5	99.2
HfC	2175	30	105.4	3.5	90.1
HfC	2225	30	140.6	2.5	94.5
TaC ^b	2150	30	105.4	8.0	89.6
TaC ^c	2225	30	140.6	2.5	~85
TaC ^d	2250	20	140.6	0.8	95.3
TaC ^d	2235	15	140.6	2.5	96.8

^aCylindrical samples about 2.54 cm diameter x 3.18 cm high.

^bPressed from commercial powder.

^cPressed from powder prepared by vacuum reaction of Ta and carbon.

^dPressed from powder prepared by vacuum reaction of Ta₂O₅ and carbon.

This work was discussed in detail in a previous report.¹

11.2 Ta CARBIDE

THERMAL STABILITY

The kinetics of the evaporation of TaC were studied in Ar + 3H₂ (vol %) and in hydrogen atmospheres, at temperatures between 2000° and 3000°C. Weight loss from TaC in its homogeneity range followed a parabolic rate law indicating a diffusion-controlled mechanism. Rates of C loss at the surface, determined by following surface compositional changes by X-ray analysis, were atmosphere dependent. In each atmosphere the surface lattice parameter (and, therefore, the composition) decreased more rapidly at higher temperatures.

Color changes were observed on the surface of the sample during vaporization tests. Surface depletion of C results in a change from the characteristic golden color of TaC to a silver-gray color. The interior of the samples, however, retained the golden color, as, for example, did samples heated for 100 hours in hydrogen at 2000°C and 55 hours at 2930°C in Ar + 3H₂. X-ray analysis showed that the center was nearly stoichiometric TaC in both cases. These observations indicate a severe compositional gradient near the surface of the test samples and are consistent with a diffusion-controlled mechanism for loss of C from TaC in this temperature range.

Diffusion coefficients were calculated from the weight changes for the loss of C from TaC through a C deficient (TaC_{1-x}) layer. The results are shown in Table 11.5.

The loss of carbon from TaC is a reversible process. Carbon evaporates preferentially from TaC in an atmosphere of C activity lower than that of the solid throughout its homogeneity range. Substoichiometric TaC will absorb C from atmospheres of higher C activities. Thus, by controlling the C activity of the atmosphere, preferential evaporation of

¹"Fourth Annual Report — High-Temperature Materials and Reactor Component Development Programs, Volume II — Materials," GE-NMPO, GEMP-334B, February 26, 1965, pp. 107–112.

TABLE 11.5

DIFFUSION COEFFICIENTS FOR CARBON IN TaC _{1-x}			
Specimen	Atmosphere	Temperature, °C	Diffusion Constant, cm ² /sec
22A	Ar + 3H ₂	2000	1.45 × 10 ⁻¹⁰
22B	Ar + 3H ₂	2300	{ 3.22 × 10 ⁻¹⁰ 9.42 × 10 ⁻¹⁰
16	Ar + 3H ₂	2930	1.37 × 10 ⁻⁸
18B	H ₂	2300	{ 9.32 × 10 ⁻¹⁰ 1.99 × 10 ⁻⁹
20	H ₂	2650	2.74 × 10 ⁻⁹

C from a TaC_{1-x} sample of any composition in the single-phase region can be suppressed. When this is accomplished, the C activity of the solid in equilibrium with an atmosphere of known activity is also known.

The stability studies have been reported in detail previously.^{2, 3}

EFFECT OF STRAIN ON LATTICE PARAMETERS

As noted above, severe compositional gradients occur due to preferential C evaporation from heat-treated TaC. X-ray lattice parameter measurements indicate that carbide surfaces are often strained due to this C depletion. These strains, in turn, cause the calculated lattice parameters to be biased, and significant errors are introduced into compositions estimated from lattice parameter. X-ray data from the present studies on TaC, as well as from similar data on NbC reported in the literature,⁴ were analyzed to develop a means for determining when strain exists and to develop an analytical technique for taking strain into account when estimating composition from lattice parameter measurements.

The relative magnitude and direction of the strain may be calculated from lattice parameters measurements on carbides with the cubic NaCl structure. The parameters of TaC_{1-x} in this study were calculated from both the Cu K α_1 and Cu K α_2 peaks of the (331), (420), (422), and (333) (511) planes. These parameters were analyzed statistically by multiple regression against the variables $\cos\theta \cot\theta$ for the instrumental error, and a strain parameter Γ^* for the error due to strain.

These studies have shown that strain effects are present in lattice parameter measurements whenever Ta or Nb carbides are heated under non-equilibrium conditions. The degree and sense of the strain is dependent upon the thermal history of the specimen.

On the basis of these analyses, an analytic expression was derived which permits determination of the lattice parameter (a_0) from the measured parameter (a) corrected for instrumental error ($\cos\theta \cot\theta$ term) and the strain parameter (Γ term) by the following equation:

$$a = a_0 + b \cos\theta \cot\theta + c (\Gamma - \Gamma_0).$$

A positive strain coefficient (c) indicates that the strain is due to C depletion from the surface, whereas a negative coefficient indicates a higher C concentration at the surface.

* Γ is a parameter which varies roughly in proportion to Poisson's ratio, and which for planes in cubic lattices equals $(h^2k^2 + k^2l^2 + l^2h^2)/(h^2 + k^2 + l^2)^2$.

²GEMP-334B, pp. 114-120.

³"Fifth Annual Report - High-Temperature Materials Program, Part B," GE-NMPO, GEMP-400B, February 28, 1966, pp. 140-143.

⁴E. K. Storms, N. H. Kirkorian, and C. D. Kempter, "Crystallographic Data: Niobium Carbide," Analytical Chemistry, Vol. 32, No. 12, 1960, p. 1722.

The coefficient is zero for a constant composition within the layer penetrated by the X-ray beam, as, for example, when the carbide has been equilibrated with an atmosphere of fixed C activity.

The analysis of compositional gradients in carbides and strain analyses based on these measurements were discussed more fully in a previous report.⁵

11.3 NON-STOICHIOMETRY IN Ta AND U MONOCARBIDES

Refractory carbides, such as TaC_x and UC_x , are of interest for high-temperature applications principally because of their high melting points. These materials, however, characteristically undergo compositional variations and deviations from stoichiometry at high temperatures; hence, the reactivity of C must be examined from the standpoint of C activity as a function of composition. The object of this work was, therefore, to establish the C activity of Ta and U monocarbides as a function of composition and temperature. Related thermodynamic properties were deduced from an analysis of the data making use of the model proposed by Hoch⁶ for nonsubstitutional solid solutions.

EXPERIMENTAL PROCEDURE

The experimental procedure consisted of equilibrating the monocarbide powder with an atmosphere of controlled C activity. The desired C activities were obtained by introducing hydrogen-methane gas mixtures at a pressure of 1.2 atmosphere into a Re muffle, as shown in Figure 11.1. The exterior portions of the furnace were maintained in hydrogen at 1.1 atmosphere. Carbon content of the controlled atmosphere was checked by chemical analysis of the exit gas, and oxygen content, as water, by a Beckman Electrolytic Hygrometer. Unit C activity was achieved in some runs by heating the powders in hydrogen in a closed graphite crucible in the presence of graphite powder. The principal gas species in the atmosphere in each run were determined by use of the thermodynamic functions of McBride, et al.⁷ The measured amount of CH_4 at room temperature was taken to be the total C in all species at the temperature of the experiment, except where unit C activity was assumed to calculate the concentration of the gaseous species in hydrogen in equilibrium with graphite. The methane content of the gas was varied between 1 and 100 ppm, and the oxygen content was found to vary between 1 and 15 ppm.

Tantalum monocarbide samples consisted of powder of average particle size < 44 microns whose X-ray and chemical analyses are given in Table 11.6. These powders, in Re crucibles, were equilibrated with the gas mixtures at temperatures between 1800° and 2350°C. X-ray diffraction analysis of equilibrated powders showed no evidence of strain due to compositional gradients.

Samples were heated in increments of 1 to 12 hours depending upon temperature. After each interval, the samples were weighed and lattice parameters were measured to establish when equilibrium was being approached; i. e., powders were heated until the strain effect due to compositional gradients was insignificant and lattice parameters varied by less than 0.0010 Å between successive readings. Compositions were calculated from the lattice parameter a_0 , corrected for strain effects and instrumental error, using the equation determined by Bowman⁸ for the variation of lattice parameter with C-to-Ta ratio.

⁵GEMP-400B, pp. 143-146.

⁶M. Hoch, "Statistical Model for Nonsubstitutional Solutions," Trans. Met. Soc. of AIME, Volume 230, 1964, p. 138.

⁷B. J. McBride, S. Heibel, J. C. Ehler, and S. Gordon, "Thermodynamic Properties to 6000°K for 210 Substances Involving the First 18 Elements," NASA SP-3001, 1963.

⁸A. L. Bowman, "The Variation of Lattice Parameter with Carbon Content of Tantalum Carbide," J. Phys. Chem., Vol. 65, 1961, p. 1596.

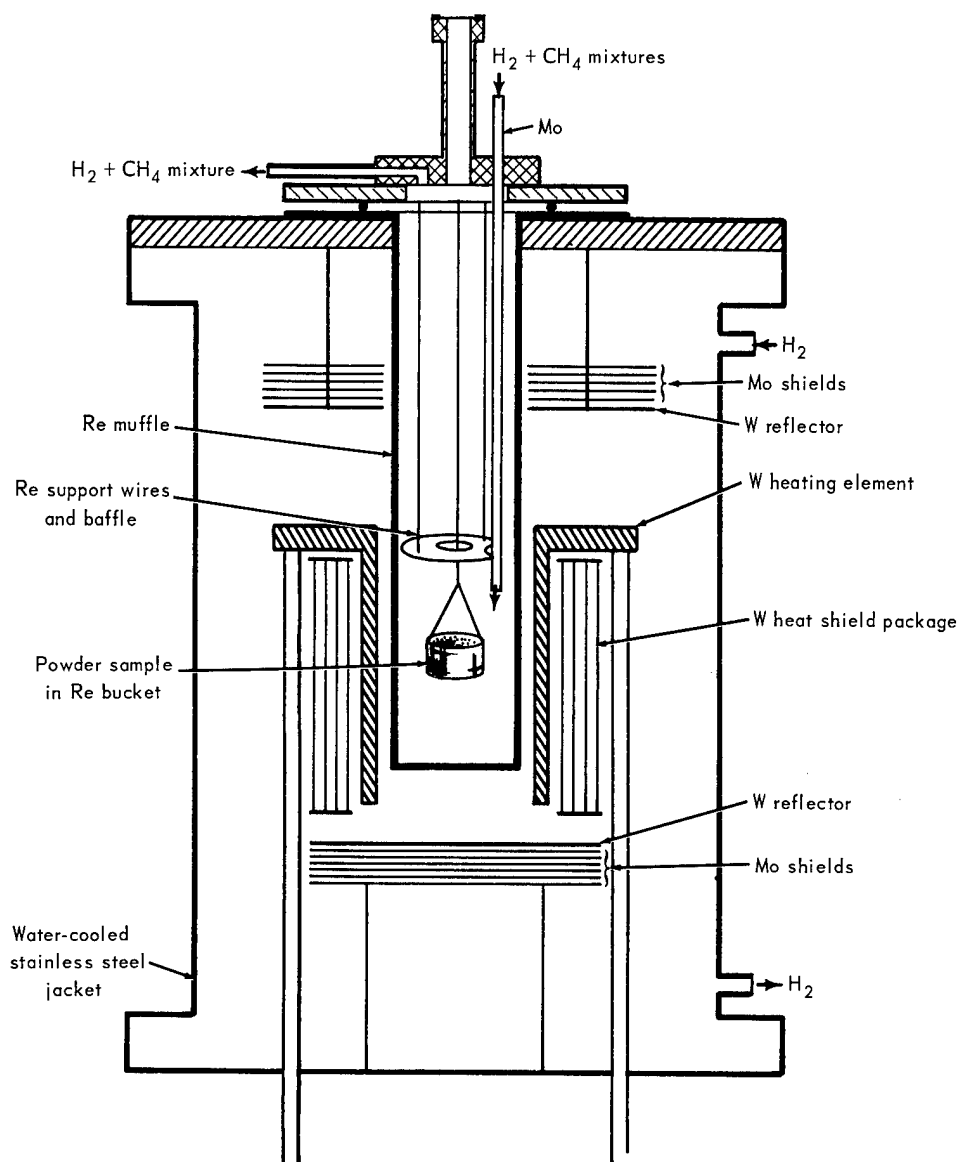


Fig. 11.1 – Schematic diagram of experimental set-up for equilibrium studies

TABLE 11.6

CHEMICAL AND X-RAY ANALYSES OF TANTALUM CARBIDE
COMPOSITIONS USED IN EQUILIBRATION EXPERIMENTS

Nominal Composition	TaC _{0.8}	TaC _{0.90}	TaC _{0.99}
Carbon, %	4.94	5.76	6.32
Uncombined carbon, ppm	134	<100	2700
Oxygen, ppm	167	177	163
Nitrogen, ppm	105	40	21
X-ray lattice parameter (a_0), Å	4.42577	4.44303	4.45585
C/Ta (chemical analysis)	0.784	0.921	0.973
C/Ta (X-ray analysis) ^a	0.800	0.910	0.992

^aBased on: A. L. Bowman, "The Variation of Lattice Parameter with Carbon Content of Tantalum Carbide," Journal of Physical Chemistry, Vol. 65, 1961, pp. 1596–1598.

To ensure equilibrium, $\text{TaC}_{0.80}$ and $\text{TaC}_{0.99}$ powders were heated side-by-side in a divided crucible in some tests. The change in composition of each powder was determined periodically by lattice parameter measurements. An exponential curve of the form $A = A_{\infty} + Be^{-Ct}$ fitted to the data yielded the asymptotic lattice parameter from which equilibrium compositions were calculated by Bowman's⁸ equation. Results of a typical run are shown in Figure 11.2. The calculated compositions for samples approaching equilibrium from both sides in this manner agree to within 1.0 percent.

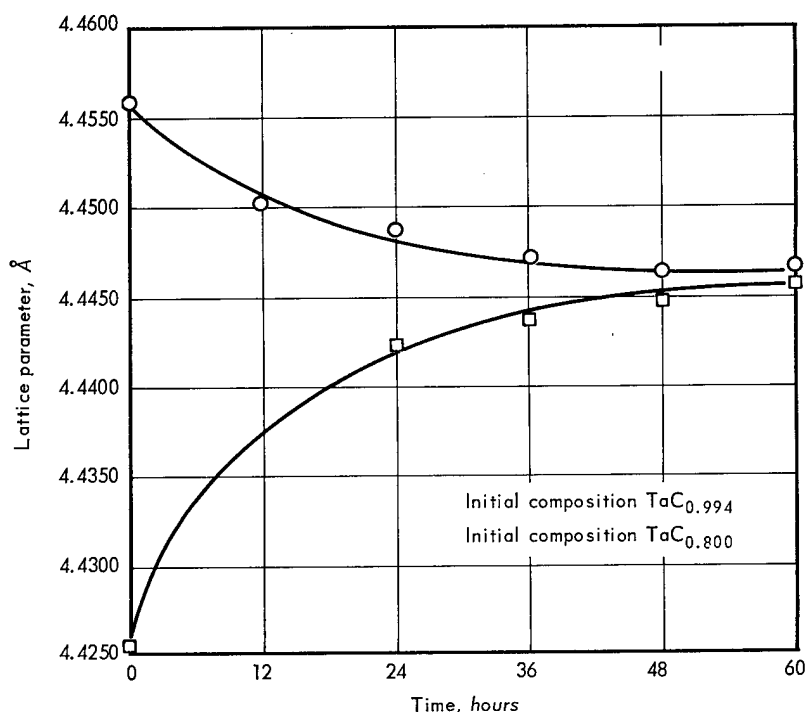


Fig. 11.2 — Extrapolated lattice parameter versus time at 1800°C for $\text{TaC}_{0.800}$ and $\text{TaC}_{0.994}$ in $\text{H}_2 + 14 \text{ ppm CH}_4$

Uranium monocarbide samples consisted of powders (< 44 microns particle size) encapsulated in 0.05-cm-thick Re capsules formed from Re sheet and sealed in vacuum by electron-beam welding. Since Re does not form a stable carbide but dissolves up to 11.7 atomic percent C,⁹ it serves as a membrane permeable to C through which the carbide may be equilibrated with the C activity of the outside gas atmosphere. In this way, evaporation of U is suppressed.

The composition of the commercially processed starting material is given in Table 11.7.

The samples were heated at 1500°C and 1700°C in the hydrogen – methane mixtures. They were weighed at regular intervals and assumed to have achieved equilibrium when a weight change less than 0.01 percent of the sample weight was observed in a 6-hour period. The total weight loss in a 2.5-g sample was about 0.030 g. Samples for X-ray diffraction analysis of the starting powder and of equilibrated powders after each series of runs were sealed in glass capillary sample holders under argon to avoid exposure of the sample to air.

⁹J. E. Hughes, "A Survey of the Rhenium-Carbon System," J. Less Common Metals, Vol. 1, 1959, p. 377.

Results

The C activity versus composition data measured for TaC_x and UC_x at various temperatures are summarized in Tables 11.8 and 11.9, respectively, along with a calculated activity coefficient for each data point, using a method described below.

In the TaC studies, chemical analyses showed the oxygen content to be less than 600 ppm in all the samples analyzed. This concentration is low enough to be ignored in subsequent discussions. In the case of UC_x , however, the oxygen content is high enough that the system under study must be considered as a portion of the U-C-O ternary system, as discussed below.

DISCUSSION

The variation of the C activity with composition and temperature was analyzed in terms of the statistical model of Hoch⁶ to (1) study the implications of deviations from stoichiometry in TaC and UC, (2) establish the defect interaction energies, and (3) to determine the Frenkel

TABLE 11.7

CHEMICAL AND X-RAY ANALYSES OF URANIUM CARBIDE USED IN EQUILIBRIUM EXPERIMENTS

Carbon, %	4.77
Uncombined carbon, ppm	2300
Oxygen, ppm	6300
Nitrogen, ppm	140
X-ray lattice parameter (a_0), Å	4.960 ^a
C/U (chemical analysis)	0.951

^aVery diffuse lines.

TABLE 11.8

CARBON ACTIVITY AS A FUNCTION OF TEMPERATURE AND COMPOSITION IN TaC_x

Temperature, °C	x in TaC_x		Oxygen, ppm	Carbon Activity (a_c)	$A = RT \ln \left(a_c \frac{1-x}{x} \right)$
	X-Ray Analysis	Chemistry			
1800	0.805			0.0014	-32.8
1800	0.926			0.0247	-25.7
1800	0.931			0.0283	-25.4
1800	0.925			0.0147	-25.6
1800	0.936			0.0283	-25.7
1830	0.927	0.864	390	0.0418	-23.9
2035	0.928	0.959	561	0.0287	-28.0
2035	0.933	0.955	369	0.0450	-26.3
2150	0.845			0.0085	-31.0
2150	0.823			0.0073	-31.0
2220	0.914	0.869	547	0.0342	-28.4
2220	0.924			0.0449	-27.5
2250	0.995			1.0000	-26.5
2260	0.897			0.0401	-27.1
2300	0.872			0.0185	-30.2
2300	0.875			0.0225	-29.3
2300	0.869			0.0225	-29.1
2300	0.866			0.0185	-30.0
2300	0.994			1.0000	-26.3
2345	0.900			0.0292	-29.8
2345	0.994			1.0000	-26.6
avg.					-27.9 ± 1.9

TABLE 11.9
CARBON ACTIVITY AS A FUNCTION OF TEMPERATURE
AND COMPOSITION IN $UC_xO_{0.099}$

Temperature, °C	Composition, x + y	Carbon Activity a_c	$RT \ln \left(a_c \frac{1-x-y}{x} \right)$ kcal/mole
1500	0.992	0.010	-32.8
1500	0.994	0.044	-29.4
1500	0.991	0.039	-28.4
1700	0.990	0.061	-29.5
1700	0.971	0.010	-32.5
1700	0.993	0.033	-32.4
1700	0.952	0.012	-29.9
			avg. -30.7 ± 1.6

energy associated with a transfer of a C atom from a singly occupied site to a site already occupied by another C atom in the U monocarbide phase region.

Activity coefficients for TaC derived in this analysis are included in Table 11.8. The activity coefficient, to a first approximation, is independent of composition for $0.805 < x < 0.995$ and may be only slightly dependent on temperature for $1800^\circ < T < 2350^\circ\text{C}$. The average value for the activity coefficient, $RT \ln \left(a_c \frac{1-x}{x} \right)$, is -27.9 ± 1.9 kcal/mole. This agrees with the value of approximately -27 kcal/mole obtained by Hoch¹⁰ in an analysis of the evaporation rate data of Fries¹¹ for NbC, and of Coffman, et al.,¹² for TaC.

The experimental results for U carbide ($UC_xO_{0.099}$) are given in Table 11.9. The data show that the activity coefficient is fairly constant as a function of temperature and composition, with an average value of -30.7 ± 1.6 kcal/mole. If the carbon-oxygen interaction energy is assumed to be equal to the value deduced by Hoch⁶ for the carbon-oxygen interaction in the iron-carbon-oxygen system (-26.4 kcal/mole), the activity coefficient for C in UC_x ($x < 1$) to a first approximation is

$$RT \ln \left(a_c \frac{1-x}{x} \right) = -28.1 \pm 1.6 \text{ kcal/mole.}$$

This value was deduced from data on compositions close to stoichiometry (average $x = 0.983$), ignoring double occupancy of some C lattice sites. When double occupancy is taken into account, the activity coefficient becomes:

$$RT \ln \left(a_c \frac{1-x}{x} \right) = -26.9 \pm 1.6 \text{ kcal/mole.}$$

Calculations of the C activity coefficient using the data of Storms¹³ for $UC_{0.995}$ gives

$$\begin{aligned} RT \ln \left(a_c \frac{1-x}{x} \right) &= -25.9 \text{ kcal/mole (} T = 2100^\circ\text{K)} \\ &= -25.3 \text{ kcal/mole (} T = 2300^\circ\text{K)} \end{aligned}$$

This agrees with the above value.

¹⁰M. Hoch, private communication.

¹¹R. J. Fries, "Vaporization Behavior of Niobium Carbide," Journal of Chemical Physics, Vol. 37, No. 2, July 1962, pp. 320-327.

¹²J. A. Coffman, G. M. Kibler, T. R. Riethoff, and A. A. Watts, "Carbonization of Plastics and Refractory Materials Research, Part I," WADD-TR-60-646, Part I, February 1961.

¹³E. K. Storms, "A Mass Spectrographic Study of the Vapor Pressure of U(g) and UC_2 (g) Over Various Compositions in the Uranium-Carbon System," Thermodynamics, Vol. 1, IAEA, Vienna, 1966.

The activity coefficient for the second C atom on a C site in U monocarbide is 6.8 ± 0.5 kcal/mole. Therefore, the Frenkel energy for UC_x , i. e., the energy required to move a C atom from a C site to a second site already occupied by a C atom, is 33.7 ± 1.7 kcal/mole.

Based on this analysis, the disorder in stoichiometric uranium carbide ($UC_{1.0}$) was estimated. The results indicated that at 2000°K the fraction of available C sites occupied is 0.986; at 2500°K, it is 0.967. In other words, in $UC_{1.0}$ at 2000°K, 1.4 percent of the C sites are doubly occupied; at 2500°K, 3.3 percent are doubly occupied.

The experimental procedure and results for the equilibration studies have been discussed extensively in previous reports.^{14, 15} A detailed discussion of the data analysis in terms of the statistical model has been published.¹⁶

11.4 PLANS AND RECOMMENDATIONS

This task terminated June 30, 1967. A topical report will be issued covering the work accomplished in this program.

¹⁴GEMP-400B, p. 146-155.

¹⁵"Sixth Annual Report - High-Temperature Materials Program, Part A," GE-NMPO, GEMP-475A, March 31, 1967.

¹⁶M. Hoch, E. F. Juenke, and L. H. Sjodahl, "Non-Stoichiometry of Tantalum Carbide and Uranium Monocarbide," GE-NMPO, GEMP-540, prepared for presentation at IAEA Symposium on Thermodynamics of Nuclear Materials, Vienna, Austria, September 4-8, 1967.